DEBRIS HAZARD ASSESSMENT IN EXTREME FLOODING EVENTS

Dissertation

(Cumulative Work)

approved by the

Faculty of Architecture, Civil Engineering and Environmental Sciences

Technische Universität Braunschweig

in Cotutelle with the

Ottawa-Carleton Institute for Civil Engineering

University of Ottawa

in candidacy for the degree of a

Doktor-Ingenieur (Dr.-Ing.) /

Doctorate in Philosophy Civil Engineering*)

by

Jacob Stolle
born 06 September 1991
from Ottawa (Canada)

Submitted on	20 May 2019
Oral examination on	23 August 2019
Professorial advisors	Prof. Dr.-Ing. Nils Goseberg
	Prof. Dr.-Ing. Ioan Nistor
	Prof. Dr.-Ing. Emil Petriu

2019

***) Only one of both titles may be used.**

Abstract

Coastal areas are often important to economic, social, and environmental processes throughout the world. With changing climate and growing populations in these areas, coastal communities have become increasingly vulnerable to extreme flooding events, such as tsunami, storm surges, and flash floods. Within this new paradigm, there has been an effort to improve upon current methods of hazard assessment, particularly for tsunami. Recently, the American Society of Civil Engineers (ASCE) released the ASCE 7 Chapter 6 which was the world's first standard, written in mandatory language, that addressed tsunami resilient design in a probabilistic manner for several of its prescriptions. While often the focus tends to be on mapping the hazards related to hydraulic loading conditions, post-tsunami field surveys from disaster-stricken coastal communities have also shown the importance of also considering the loads exerted by solid objects entrained within the inundating flows, commonly referred to as debris loading. Limited research has addressed debris hazard assessment in a comprehensive manner.

Debris loading can be generally divided into two categories: impact and damming. Debris impact loads are caused by the rapid strike of solid objects against a structure. Debris damming loads are the result of the accumulation of debris at the face of or around a structure, causing thus an obstruction to the flow. The primary difference between these loads is the time period over which they act. The rapid loading due to debris impacts requires structural properties be considered in assessing the associated loads whereas debris damming loads are generally considered in a quasi-static manner. In assessing the hazard associated with both impact and damming loading conditions, methodologies must be developed to consider the likelihood of the load occurring and the magnitude of that load.

The primary objective of this thesis was to develop a probabilistic framework for assessing debris hazards in extreme coastal flooding events. To achieve this objective, the components of the framework were split into three general categories: debris transport, debris damming, and debris impact. Several physical experimental studies were performed to address each of these components, representing the most comprehensive assessment of debris hazards in extreme flooding events to date.

Debris transport was addressed to estimate the likelihood of debris loading occurring on a structure. The studies presented herein examine the different parameters that must be considered in assessing the motion of debris with the flow. The studies showed that the initial configuration of the debris and hydrodynamic conditions were critical in determining the motion of the debris. The stochastic properties of the debris motion were also assessed. It was shown that the lateral displacement of the debris could be approximated by a Gaussian distribution and the debris velocity by a Kumaraswamy (1980) distribution. The study of debris impact was further used to develop the current models used in estimating the impact force. The rigid body impact model was compared to models where the structural response was considered. The analysis showed that the effective stiffness model proposed by Haehnel and Daly (2004) was best suited to provide a conservative estimation of the impact force. Additionally, the impact geometry was taken into consideration examining the influence of various parameters on the impact force. Furthermore, debris damming was examined for the first time in transient loading conditions. This particular study examined the influence of the transient wave condition on the debris dam formation as well as the influence of different debris geometries. The influence of the debris dam geometry was correlated to increases in loading and overtopping conditions at structures. The assessment of debris hazards is critical in the development of accurate design conditions. The probabilistic framework presented within this thesis is expected to provide a basis for estimating debris hazards and inform future studies in the development of hazard assessment models.

Acknowledgements

I would first and foremost like to thank my advisers, Professor Ioan Nistor, Professor Nils Goseberg, and Professor Emil Petriu for the opportunities that they provided me throughout my graduate studies, despite my humble beginnings as an Environmental Engineer. Without their tireless work, expertise and guidance, I highly doubt I would have been able to have such an excellent experience as a graduate student. They gave me endless opportunities to explore the academic world by attending conferences, publishing papers and working in scientific laboratories in different countries. These experiences helped me grow as a researcher and develop my own project ideas by interacting with researchers globally.

I would also like to thank the large group of people that, in one way or another, supported my PhD thesis. Professor Shibayama for his support in helping develop my research program in Japan as well as giving me the invaluable opportunity to visit the site of the 2018 Indonesian Tsunami and develop a deeper understanding of why this research is important. Professor Torsten Schlurmann who gave me the opportunity to experience a wide-range of coastal engineering topics and develop an appreciation for inter-disciplinary work. Dr. Tomoyuki Takabatake who was invaluable in the development of my research projects in Japan and helped me develop a deeper appreciation for Japanese engineering. Furthermore, I would like to thank all of the graduate students that helped with this project from around the world: Caren Derschum, Hajo von Häfen, Gabriella Mauti, Go Hamano, Hidenori Ishii, Kotaro Iimura, and Shinsaku Nishizaki.

Finally, I would like to thank my family (Mother, Father, Anna, and Ben) and girlfriend (Alicia) for supporting me throughout my PhD. They continuously helped out me, showed up to research talks when I was close by, and helped me stay sane during the more challenging parts. I love them all the more for it.

I would also liked to acknowledge the NSERC Canadian Graduate Scholarship (Doctorate), the Mitacs-Japanese Society for the Promotion of Science Fellowship, and the DAAD Short-term Fellowship for their financial support throughout my PhD in various capacities as well as the support provided by my supervisors through their research funds, particularly the NSERC Discovery grants of Profs. Nistor and Petriu and the Marie Curie Fellowship grant of Prof. Goseberg.

Table of Contents

List of Figures

List of Tables

List of Acronyms

2DOF	Two Degree-of-Freedom
ACC	Accelerometer
ADV	Acoustic Doppler Velocimeter
ANCOVA	Analysis of Covariance
ANOVA	Analysis of Variance
ASCE	American Society of Civil Engineers
B	Board
CAM	High-definition Camera
DAQ	Data Acquisition System
ECM	Electro-current Meter
EEMD	Ensemble Empirical Mode Decomposition
FT	Force Torque Transducer
HP	Hydro Pole
HS	High-speed Camera
IMF	Intrinsic Mode Function
K1980	Kumaraswamy (1980)
LC	Load Cell
LVDT	Linear Variable Differential Transform
NBCC	National Building Code of Canada
NRSME	Normalized Root Mean Squared Error
RMSE	Root Mean Squared Error
SC	Shipping Container
SDOF	Single Degree-of-Freedom
USDS	Ultrasonic Distance Sensor
VC	Video Camera
VIF	Variable Inflation Factor
WG	Wave Gauge

List of Symbols

Δx	Lateral displacement of debris (m)
Δy	Distance from the debris source (m)
A	Cross-sectional area (m^2)
a	Shape parameter for Kumaraswamy (1980) distribution (-)
A_d	Cross-sectional area of dam (m^2)
b	Shape parameter for Kumaraswamy (1980) distribution (-)
B_d	Breadth of dam (m)
b_s	Dimensionless factor relating stiffness (-)
c	Wave celerity (m/s)
c, ξ	Damping coefficient (kg/s)
C_{area}	Agglomeration coefficient (-)
C_d , C_D	Drag coefficient (-)
C_M	Added mass (-)
C_R	Resistance Coefficient (-)
$_d$	Debris
d_{lon}	Displacement in the longitudinal direction (m)
e	Impact eccentricity (m)
E	Young's Modulus (Pa)
f	Darcy-Weisbach coefficient
F_{dm}	Damming force
F_i	Impact force (N)
Fr	Froude number (-)
g	Gravitational constant (m/s^2)
h, d	Water depth (m)
h_0	Initial impoundment depth (m)
k	Contact stiffness (Nm)
L_z	Cantilever arm (m)
L_c , l	Characteristic Length (m)
L_T	Straight line distance between center of gravity and impact point (m)
M	Moments (Nm)
m_d	Mass of the debris (kg)
n	Number of debris per column (-)
N_S	Dimensionless factor relating scale (-)
p	impact load applied over time (N)
R	Wave run-up (m)
r	Number of columns of debris (-)
R^2	Coefficient of determination
Re	Reynolds number (-)
R_i	Radius of gyration (m)
$_s$	Structure
S	Spacing between outer edge of debris (m)

t	Time (s)
t_i	Impact duration (s)
t_{open}	Gate opening time (s)
u	Flow velocity (m/s)
U, u_b	Bore front velocity (m/s)
$\overline{u}$	Mean debris velocity (m/s)
$\overline{U}$	Normalized debris velocity (-)
V_d	Volume of debris (m^3)
W	Width of dam (m)
We	Weber number (-)
X	Displacement in x-direction (m)
$\dot{x}$	Velocity (m/s)
$\ddot{x}$	Acceleration (m/s^2)
Y	Displacement in y-direction (m)
Z	Displacement in z-direction (m)
α,β	Impact orientation (^{o})
γ	Fitted parameter for velocity distribution (-)
ε_0	Lateral distance between center of gravity and impact point (m)
η	Water surface elevation (m)
η_u	Dispersion parameter for Kumaraswamy (1980) distribution (-)
θ	Angle between the debris velocity vector and the normal force (^{o})
Θ	Orientation of long axis of debris (^{o})
λ	Ratio of oblique and maximum impact forces (-)
μ	Dynamic viscosity (Ns/m^2)
μ_0	Coefficient of friction (-)
ν	Kinematic viscosity (m^2/s)
ρ_d	Density of Debris (kg/m^3)
ρ_s	Density of fluid and sediment (kg/m^3)
ρ_w	Density of water (kg/m^3)
σ	Standard deviation (-)
τ	Time elapsed since impact (s)
ω	Natural modes of frequency (^{o}/s)
ω_d	Damped modes of frequency (^{o}/s)

Chapter 1. Introduction

1.1 Background

Recent major coastal flooding events, such as the 2017 Hurricane Harvey and the 2018 Indonesian Tsunami, indicate the need for improved hazard assessment methods. With the changing climate and rising sea levels, coastal communities are increasingly vulnerable to extreme flooding events (IPCC 2014). As these events can have severe economic, environmental, and social impacts on coastal communities, accurate estimation of flooding hazards is critical in resilient, sustainable design.

Within the Canadian context, the coastal environment is a significant part of the Canadian landscape as the country is not only bordered by the world's three main oceans (Atlantic, Arctic, and Pacific) but also encompasses several important internal marine waters, such as the Gulf of St. Lawrence and the Hudson Bay, as well as the shores of the world's largest fresh water lakes. The economic and recreational value of these environments is compounded by the fact that 25 percent of the Canadian population lives in these coastal areas (DFO 2002). As a result of urban development, expansion, and intensification, this percentage will likely rise as global trends indicate population density in coastal areas will continue to increase (Manson 2005). However, these areas pose inherent hazards due to the proximity to large marine water bodies. These hazards can manifest in the form of extreme flooding events caused by storm surges, hurricanes, and tsunami, leaving millions of Canadians vulnerable to such disasters.

The vulnerability of Canadian coastal communities is further accentuated by the ongoing and future climatic changes (Manson 2005). Already, as a result of flooding, there has been a significant rise (160%) in the average cost of water damage claims over the period of 2000 – 2011 (Friedland et al. 2014). Sea-level rise and coastal erosion will only escalate the susceptibility of coastal areas to extreme flooding events by reducing their natural protection and extending flood plains (Chouinard et al. 2008, Boon 2012). Increased intensity, duration, and frequency of storm events will likely exceed the present design conditions and lead to the futility of many current engineered protection measures (IPCC 2014). The National Research Council of Canada (NRC) has recently expressed a desire to include the effects of climate change in upcoming versions of the National Building Code of Canada (NBCC). However, these changes have not yet been implemented (Barrett and Hannoush 2016).

Tsunami, while occurring less often than storm surge and hurricane events, can be significantly more devastating as observed during the 2004 Indian Ocean and the 2011 Tohoku Japan tsunami. This is of particular concern for the West Coast of Canada, where the nearby Cascadia Subduction Zone (CSZ), that has historically triggered major tsunami events (Priest et al. 2010), could potentially rupture (7-12% certainty) in the next 50 years (Goldfinger et al. 2012). Additionally, tsunami from far-field sources, such as the case of the 1964 Alaska Earthquake were shown to potentially induce significant damage to Canadian West Coast communities. Canada's East Coast is not immune to tsunami hazard as it has been hit by the two most damaging tsunami in Canadian history: the one generated by the 1917 Halifax Port Explosion and the 1929 Grand Banks Earthquake and subsequent (localized) tsunami (Clague et al. 2003).

In the National Building Code of Canada (NBCC), limited prescriptions exist for the design of structures in extreme flooding events (Palermo et al. 2009). As previously mentioned, the standard does not currently address the issue of climate change (Barrett and Hannoush 2016). In tsunami engineering, a recent paradigm shift due to the devastation of the 2011 Tohoku Tsunami has revised the practice of

addressing tsunami design. The system has moved from a historical to a system utilizing a probabilistic approach (Chock 2015). This shift has led to the development of the world's first design standard (ASCE 7 Chapter 6), written in mandatory language, specifically for the design of tsunami-resilient infrastructure (ASCE 2016a). The standard relies on a variety of tsunami sources and magnitudes to develop a stochastic catalogue of tsunami scenarios, which are then used to assess probabilistically quantifiable hazards. Similar changes may be necessary in the assessment of other coastal flooding mechanisms as the local historical record likely will no longer reflect future design conditions.

Historically, the estimation of flooding hazards has focused on the hydraulic conditions (i.e. floodplain mapping, hydraulic loading), field investigations of flood-stricken communities have indicated the necessity for considering secondary effects, such as erosion and debris (Ghobarah et al. 2006, Robertson et al. 2007, Palermo et al. 2013). The focus of this thesis will address debris hazards, where debris are defined as any solid object entrained within the flow. Fig. 1-1 shows examples of the effects of debris loading on structures in the aftermath of the 2018 Indonesian Tsunami. Fig. 1-1(a) shows debris loading on structures where a naval ship was washed onshore impacting the structure causing damage to the outer facade. Fig. 1-1(b) shows fuel tanks which had been picked up within the flow and impacted the structures around a gas station. Fuel tanks have become of particular concern due to the potential environmental concerns associated with chemical spills (Bernier et al. 2018).

Fig. 1-1. Examples of erosion and debris loading from the 2018 Indonesian Tsunami at (a) Watusampu Naval Base and (b) Gas Station near the Palu City Shopping Mall.

Debris loading can be broadly defined in two categories: impact and damming. Debris impact is a rapid impulse force applied to a structure caused by the debris striking the structure. Debris damming occurs due to the accumulation of debris at the face of or around structures. The accumulation results in an increase in the drag forces exerted on the structure and is generally treated as a static load. While both of these loading conditions involve solid objects entrained within the flow, the different time scales on which they act requires different considerations (i.e. structural response in the case of debris impact) from a design perspective. With the objective of developing methodology for addressing debris hazards in extreme flooding events, this thesis outlines the results of several studies examining the various concerns influencing this complex topic.

1.2 Objectives

The intent of this thesis is to validate and improve upon the current design standards proposed in the ASCE 7 Chapter 6 for the assessment of debris hazards in extreme flooding events. Due to the relatively

large scope of the research conducted, the thesis was separated into three distinct programs, each with their own objectives: (1) debris transport, (2) debris impact, and (3) debris damming. Hence, the overall objectives of the thesis consist of:

1) Establishing a framework for evaluating the vulnerability of coastal communities to debris loading conditions.
2) Identify key characteristics of debris loading that can improve upon the current standards and aid practicing engineers in assessing debris loading potential.
3) Provide comprehensive, high-quality data to be further used in the calibration and validation of numerical models.

Based on these overall objectives, the objectives of each program include:

1) Debris Transport
    a. Examining and quantifying the stochastic distributions of debris spreading and debris velocity.
    b. Examining the influence of the initial spatial distribution of the debris on debris spreading and velocity characteristics.
    c. Developing a framework for determining the likelihood of debris loading conditions occurring during a major flooding event.
    d. Providing concise data and empirical models regarding the trajectory, orientation, and velocity of debris when transported in high-energy flows.
2) Debris Impact
    a. Examining and quantifying the impact characteristics of the debris.
    b. Evaluating the influence of multi-debris impacts on the maximum loading conditions.
    c. Assessing and identifying challenges associated with the current conservative impact models used in the design standards.
3) Debris Damming
    a. Examining key characteristics influencing the capture and formation of a debris dam.
    b. Evaluating the secondary effects associated with a debris dam (flow accelerations, backwater rise, etc.).
    c. Determining a methodology for assessing the maximum loads associated with the formation of a debris dam.

1.3 Scope

The primary objective of this thesis is to provide comprehensive, high-quality data for the assessment of the current ASCE 7 Chapter 6 design guidelines. The study focuses on providing this information through physical modelling experiments. Due to time constraints and physical constraints of the laboratory environment, the study has some inherent limitations in the evaluation of debris transport and loading:

- The focus is on the impact of large debris acting in a Lagrangian manner. Smaller debris are generally assumed to be ubiquitous and therefore are addressed as a debris flow by changing the density of the inundation flood. Generally, all structures are designed for smaller debris impacts due to relatively small loads and, therefore, there is less need for hazard assessment measures.
- The experiments were performed at a relatively small-scale (1:40 or smaller). Due to limitation of the available laboratory facilities, the issues of scale was assessed through physical modelling. The

geometric scale was chosen to be as large as possible while maintaining reasonable prototype scale flow conditions. A discussion of these implications are presented in Chapter 6.

- Due to the lack of field investigation data regarding debris, the physical modelling experiments could not be directly validated using field data. However, the candidate did validate the prescriptions of ASCE7 Chapter 6, *which are derived from limited field data*. Further investigations will be needed to address scale effects before any conclusions should be confidently applied.
- The number of debris investigated in the experiments were limited by both the available equipment as well as the analysis techniques. Additionally, a large number of debris would interact with the flume walls, therefore, biasing the results.
- The physical modelling experiments employed an idealized topography. The influence of complex topographies was not investigated within this thesis. A secondary objective of the thesis was to provide benchmarking data for numerical models. As such, complicated, site-specific topography was not used to simplify any calibration efforts.

There are a wide range of factor that will influence debris motion and impact loading, many of which are site specific (Parola 2000). Therefore, the factors that were chosen to be investigated were generalized to be applicable in a wide range of situations. As a secondary objective of the thesis is to provide benchmark data for numerical modelling, it was decided to maintain an idealized setting. Additionally, this will allow for future experiments at larger scales to address scale issues in a simple setting.

1.4 Contributions and Novelty of the Study

The novelty of the present study lies in the comprehensive approach to the evaluation of debris hazard assessment within extreme flooding events. Previous studies have been limited in scope, failing to address the stochastic nature of the debris hazard. The study presented herein is the first study to examine the probabilistic properties of debris transport in extreme flooding events, aiding in the development of a framework for estimating debris hazard. The study also examines the evolution of the debris motion allowing for the development of analytical models addressing the important transport characteristics, such as debris velocity and orientation, which dictate the forces exerted on structures.

The comprehensive approach further enables an in-depth examination of the impact forces exerted on structures in extreme flooding events. Previous studies into debris impact examined carefully controlled impact conditions which limit the interactions of the debris within the surrounding fluid. This can have implications due to the added mass and damping effects. In this study, the influence of the surrounding hydrodynamics was captured under *transient* hydrodynamic conditions. Most critically, as the debris motion was not constrained, multiple debris impacts could be investigated, examining these consequences on design equations.

This study, also for the first time, investigates debris damming under *transient* loading conditions. While debris damming has been identified in several field investigations as a potential loading condition, limited studies exist examining the phenomenon in transient loading conditions. Previous studies have predominantly focused on the likelihood of debris damming occurring in riverine environments. An examination of formation mechanisms and resistance coefficients under transient loading may better represent debris damming during the initial phases of a flood event.

1.5 Publications

Journal Articles

1) **Stolle, J.**, Goseberg, N., Nistor, I., and Petriu, E. (2019). Physical Modelling of Flood-Driven Debris Hazard. *Journal of Waterway, Port, Coastal, and Ocean Engineering*. ASCE. Under Review.

    - The author (Jacob Stolle) was responsible for the development of the statistical model and analysis used in the manuscript as well as was part of the planning of the experimental program used in the validation of the model. The manuscript can be found in Chapter 3.

2) Mauti, G., **Stolle, J.**, Takabatake, T., Nistor, I., Goseberg, N., and Mohammadian, M. (2019). Experimental Investigation of Idealized Debris Dams in Steady-Flow Conditions. *Journal of Hydraulic Engineering*. ASCE. Under Review.
    - The author helped in the development of the experimental program and initial development of the analysis tools. The author also provided scientific editing on the final manuscript. The manuscript was not included within this thesis.
3) Mikami, T., Shibayama, T., Esteban, M., Nakamura, R., Nishida, Y., Achiari, H., Rusli, A., Marzuki, G., Marzuki, M., **Stolle, J.**, Krautwald, C., Robertson, I., Aránguiz, R., and Ohira, K. (2019). Tsunami Heights and Damage Caused by the 2018 Sulawesi Earthquake. Pure and Applied Geophysics. Springer. 176(8), pp. 3291-3304.
    - The author was part of the international reconnaissance team that travelled to Palu, Indonesia in the aftermath of the disaster. The author provided support and scientific editing in the development of the manuscript. The manuscript was not included within this thesis.
4) Aránguiz, R., Esteban, M., Takagi, H., Mikami, T., Takabatake, T., Gomez, M., González, J., Shibayama, T., Okuwaki, R., Yagi, Y., Shimizu, K., Achiari, H., **Stolle, J.**, Robertson, I., Ohira, K., Namakura, R., Nishida, Y., Krautwald, C., Goseberg, N., and Nistor, I. (2019) The 2018 Palu Tsunami as a combination of several landslides and co-seismic tsunami effects. Nature Scientific Reports. Springer. Under Review.
    - The author was part of the international reconnaissance team that travelled to Palu, Indonesia in the aftermath of the disaster. The author provided support and scientific editing in the development of the manuscript. The manuscript was not included within this thesis.

5) Takabatake, T., St-Germain, P., Nistor, I., **Stolle, J.**, and Shibayama, T. (2018). Numerical Modelling of Coastal Inundation from Cascadia Subduction Zone Tsunami and Implications for Coastal Communities on Western Vancouver Island, Canada. *Natural Hazards*, Springer. 0, pp. 1-25.

    - The author aided in the development in the manuscript by providing scientific and editing help to the author during the development and review of the manuscript. The manuscript was not included within this thesis.

6) **Stolle, J.**, Krautwald, C., Robertson, I., Achiari, H., Mikami, T., Nakamura, R., Takabatake, T., Nishida, Y., Shibayama, T., Esteban, M., Nistor, I., and Goseberg, N. (2019). Engineering Lessons from the 28 September 2018 Indonesian Tsunami: Debris Loading. *Canadian Journal of Civil Engineering*. Canadian Science Publishing. In-Press.

- The author was part of the international reconnaissance team that travelled to Palu, Indonesia to examine the aftermath of the 2018 disaster. The author was responsible for the synthesis of the results and the drafting of the original manuscript. The manuscript can be found in Appendix B.

7) **Stolle, J.**, Nistor, I., Goseberg, N., and Petriu, E. (2019). Multiple Debris Impact Loads in Extreme Hydrodynamic Conditions. *Journal of Waterway, Port, Coastal and Ocean Engineering*. ASCE. In-Press.

    - The author was responsible for the development of the analytical model used in this manuscript as well as a part of the development of the experimental plan on which the validation was based. The manuscript can be found in Chapter 5.

8) **Stolle, J.**, Takabatake, T., Hamano, G., Ishii, H., Iimura, K., Shibayama, T., Nistor, I., Goseberg, N., and Petriu, E. (2019). Debris Transport over a Sloped Surface in Tsunami-like Flow Conditions. *Coastal Engineering Journal*. Taylor and Francis. 61(2), pp. 241-255.
    - The author was responsible for the development of the experimental program and analysis that contributed to the bulk of the manuscript. The manuscript can be found in Chapter 3.

9) Von Häfen, H., Goseberg, N., **Stolle, J.**, and Nistor, I. (2019). Gate-Opening Criteria for Generating Dam-break Waves using Smoothed Particle Hydrodynamics. *Journal of Hydraulic Engineering*. ASCE. 145(3), 04019002.

    - The author acted as the secondary supervisor for the primary author (H. Van Häfen). Additionally, the author performed the experiments necessary for the calibration of the numerical model and aided in the initial development as well as editing of the manuscript. The manuscript was not included within this thesis.

10) **Stolle, J.**, Goseberg, N., Nistor, I., and Petriu, E. (2018). Debris Impact Forces on Flexible Structures in Extreme Hydrodynamic Conditions. *Journal of Fluids and Structures*. Elsevier. 84, pp. 391 – 407.

    - The author was responsible for the development of the analytical model used in this manuscript as well as a part of the development of the experimental plan on which the validation was based. The manuscript can be found in Chapter 5.

11) **Stolle, J.**, Derschum, C., Goseberg, N., Nistor, I., and Petriu, E. (2018). Debris Impact under Extreme Hydrodynamic Conditions Part 2: Impact Force Responses for Non-Rigid Debris Collisions. *Coastal Engineering.* Elsevier. 141, pp. 107 – 118.

    - The author was responsible for the initial development of the manuscript. Additionally, the author performed the experiments used in the analysis as well as aided in the development of the experimental protocol. The manuscript can be found in Chapter 5.

12) Derschum, C., Nistor, I., **Stolle, J.**, and Goseberg, N. (2018). Debris Impact under Extreme Hydrodynamic Conditions Part 1: Hydrodynamics, Wave-Structure Interactions and Impact Geometry. *Coastal Engineering.* Elsevier. 141, pp. 24 – 35.

    - The author was responsible for the final analysis and development of the manuscript. Additionally, the author performed the experiments used in the analysis as well as

aided in the development of the experimental protocol. The manuscript can be found in Chapter 5.

13) **Stolle, J.**, Takabatake, T., Nistor, I., Mikami, T., Nishizaki, S., Hamano, G., Ishii, H., Shibayama, T., Goseberg, N., and Petriu, E. (2018). Experimental Investigation of Debris Damming Loads under Transient Supercritical Flow Conditions. *Coastal Engineering*. Elsevier. 139, pp. 16 – 31.

    - The author was responsible for the development of the experimental plan as well as the execution of the experiments. The author was also responsible for the development of analysis techniques and writing of the manuscript. The manuscript can be found in Chapter 4.

14) **Stolle, J.**, Ghodoosipour, B., Derschum, C., Nistor, I., Petriu, E., and Goseberg, N. (2018). Swing Gate Generated Dam-break Waves. *Journal of Hydraulic Research, IAHR*, Taylor & Francis. DOI: 10.1080/00221686.2018.1489901

    - The author was responsible for the development of the experimental plan as well as the execution of the experiments. The author was also responsible for the development of analysis techniques and writing of the manuscript. The manuscript can be found in Appendix A.

15) Esteban, M., Glasbergen, T., Takabatake, T., Hofland, B., Nishizaki, S., Nishida, Y., **Stolle, J.**, Nistor, I., Bricker, J., Takagi, H., and Shibayama, T. (2017). Overtopping of Coastal Structures by Tsunami Waves. *Geosciences*. MDPI. 7, 121.

    - The author aided in the development of the experimental facilities used in the experimental program. In addition, the author provided scientific and editing aid in the development of the manuscript. The manuscript was not included within this thesis.

16) **Stolle, J.**, Takabatake, T., Mikami, T., Shibayama, T., Goseberg, N., Nistor, I., and Petriu, E. (2017). Laboratory Study of Debris Damming Loads and Effects in Flood Events. *Geosciences.* MDPI. 7, 74.

    - The author was responsible for the development of the experimental plan as well as the execution of the experiments. The author was also responsible for the development of analysis techniques and writing of the manuscript. The manuscript can be found in Chapter 4.

17) **Stolle, J.**, Goseberg, N., Nistor, I., and Petriu, E. (2018). Probabilistic Investigation and Risk Assessment of Debris Transport in Extreme Hydrodynamic Conditions. *Journal of Waterways, Port, Ocean, and Coastal Engineering*. ASCE. 144(1), 04017039.

    - The author was responsible for the initial development of the manuscript. Additionally, the author performed the experiments used in the analysis as well as aided in the development of the experimental protocol. The manuscript can be found in Chapter 3.

18) **Stolle, J.**, Nistor, I., Goseberg, N., Mikami, T. and Shibayama, T. (2017). Entrainment and Transport Dynamics of Shipping Containers in Extreme Hydrodynamic Conditions. *Coastal Engineering Journal*, JSCE, 1750011.

- The author was responsible for the initial development of the manuscript and final analysis. The author was not present for the experimental program. The manuscript was not included in this thesis.

Other Refereed Contributions

19) **Stolle, J.**, Nistor, I., Takabatake, T., Goseberg, N., Petriu, E., and Shibayama, T. (2018). Debris Damming Loads and Effects in Tsunami-Like Events. *Canadian Society of Civil Engineering General Conference 2018, Fredericton, Canada.*

20) **Stolle, J.**, Takabatake, T., Hamano, G., Ishii, H., Iimura, K., Shibayama, T., Nistor, I., Goseberg, N., and Petriu, E. (2018). Debris Transport over a Sloped Surface in Tsunami-Like Flow Conditions. *Coastlab 2018, Santander, Spain.*

21) Derschum, C., **Stolle, J.**, Nistor, I., and Goseberg, N. (2017). Influence of Wave-Structure Interaction on Tsunami-driven Debris Impact. *International Short Course and Conference on Applied Coastal Research 2017, Santander, Spain.*

22) Goseberg, N., Heunecke, M., **Stolle, J.**, and Nistor, I. (2017). Numerical Modelling of Shipping Container Transport over a Horizontal Bottom. *International Short Course and Conference on Applied Coastal Research 2017, Santander, Spain.*

23) Nistor, I., Goseberg, N., and **Stolle, J.** (2017). Flood-Induced Debris Motion in a Built-in Environment. *IAHR World Congress 2017, Kuala Lumpur, Malaysia.*

24) Goseberg, N., **Stolle, J.**, and Nistor, I. (2017). Swing Gate Generated Dam Break Waves. *IAHR World Congress 2017, Kuala Lumpur, Malaysia.*

25) **Stolle, J.**, Goseberg, N., Derschum, C., and Nistor, I. (2017). Debris Dynamics and Associated Loads in Extreme Hydrodynamic Conditions. *IAHR World Congress 2017, Kuala Lumpur, Malaysia.*

26) **Stolle, J.**, Goseberg, N., Nistor, I., and Petriu, E. (2017). Debris Entrainment Dynamics During Extreme Flooding Events. *Canadian Society of Civil Engineering 23rd Canadian Hydrotechnical Conference, Vancouver, Canada.*

1.6 Outline of the Thesis

To address the objectives stated in Section 1.2, the thesis details a set of studies examining debris hazard assessment within the context of the three stated areas: debris transport, debris impact, and debris damming. To address these issues, the thesis was divided into the following chapters:

- Chapter 2.0 outlines the current state-of-the-art in regards to debris hazard assessment. A detailed literature review was performed in each of the three areas. A section also addresses the numerical modelling of solid bodies to develop an understanding of necessary validation parameters for numerical model. In addition, a section was added addressing the current methodology for debris hazard assessment in the major tsunami design guidelines.
- In Chapter 3.0, a series of studies were performed examining the properties of debris transport. The objective of the section was, along with Section 2.0, to identify variables important in estimating the displacement of debris along with developing an understanding of the probabilistic properties of debris transport. The section cumulates with a proposal for a basic probabilistic framework estimating debris hazard.

- Chapter 4.0 outlines studies examining debris damming in tsunami-like flow conditions. Based on the river studies outlined in Section 2.0, the studies aim to provide a basic understanding of debris damming behaviour in transient, energetic flow conditions while also providing a preliminary estimation of loading and potential overtopping conditions.
- Chapter 5.0 examines a series of studies aimed at developing a more in-depth understanding of debris impact loading. The studies examine the influence of the hydrodynamic conditions on the debris impact geometry and force distribution. An analytical model is presented to examine cases where debris impact flexible structures. Additionally, a study examines the consequence of assessing only a single debris impact compared to an agglomeration of multiple debris.
- In Chapter 6.0, the potential limitations of the previous sections are discussed, particularly related to how the results can be applied at prototype scale. The application of the probabilistic model is also outlined with an example.
- Chapter 7.0 summarizes the thesis by outlining the general conclusions drawn from the studies in each area. Future work is also proposed to address some of the issues outlined in Section 6.0.
- The Appendices include a series of studies that were also part of the development of thesis, but which did not directly contribute to the objectives outlined in Section 1.2.

Chapter 2. Literature Review

2.1 Debris Transport

Debris transport in extreme hydrodynamic events has been extremely difficult to assess in the field. Debris, defined as any solid object entrained within the flow, can vary from anything from construction materials to vehicles to shipping vessels and often have multiple sources (Naito et al. 2014). This makes associating debris in the aftermath of an event with a specific source challenging. Naito et al. (2012) examined the performance of fuel storage tanks in the aftermath of the 2011 Tohoku Tsunami outlining the vulnerability of these system to damage from hydrodynamic loading, and therefore, the likelihood to become debris.

Naito et al. (2014) examined the position of displaced shipping vessels after the 2011 Tohoku tsunami as they had a very clear source (the port) and substantial documentation of their exact position before the tsunami occurred. From the forensic engineering survey, Naito et al. (2014) was able to develop a conservative estimation of the maximum spreading angle of the shipping vessels in relation to their source. Based on the analysis of the relatively limited data set, Naito et al. (2014) developed a method of assessing the maximum area vulnerable to debris loading from a specific source (Fig. 2-1). The maximum displacement of the debris was calculated based on the debris concentration, which was defined as the plan area of the debris divided by the spreading area of the debris. Again a conservative estimate was made to establish a debris concentration of 2% would contain the majority of the debris. Therefore, the debris limits are defined by the ±22.5° cone containing an area 50 times the plan area of the debris.

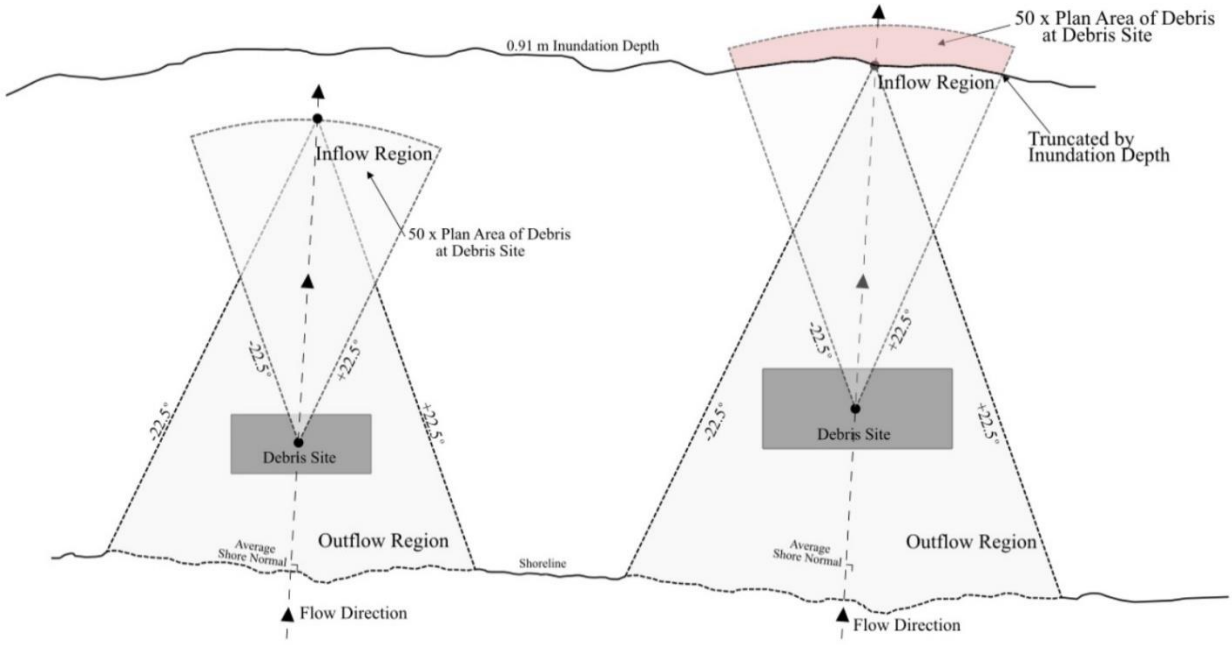

Fig. 2-1. Method of assessing maximum debris transport area from Naito et al. (2014).

However, if the spreading area encroached on an area where the inundation depth is less than 0.91 m, this area is not considered as it was expected the debris would ground and no longer propagate forward, as a

result this would be the maximum inundation limit of the debris (red area). Additionally, from the center of the inundation limit, a spreading area can be again determined using the ±22.5° cone from the inundation limit to the shoreline. The second area represents the potential spreading as a result of the outflow. Therefore, any critical buildings within the two spreading areas (shaded area in Fig. 2-1) should be designed for a potential debris impact.

Matsutomi (2008) examined the transport of driftwood in steady-state flow conditions. The study showed that given an appropriate acceleration distance (estimated as 20 times the length of the driftwood), the debris would reach the local flow velocity. Additionally, the lateral displacement of the debris could be approximately modelled as a Gaussian distribution. Yao et al. (2014) examined the mass transport of boxes over a sloped surface in a broken solitary wave. The study showed that the inertia of the boxes caused the maximum displacement to be less than the maximum inundation of the wave. The reduced displacement resulted in several boxes being washed offshore due to the retreating wave. Rueben et al. (2014) also examined the transport of boxes in a broken solitary wave, however, using a optical tracking algorithm, allowed for the trajectory of the boxes to be tracked. The study found that the on-shore motion of the debris was relatively repeatable, contrasting the off-shore motion which appeared to be random. Additionally, Rueben et al. (2014) found that the offshore velocity was 20 – 40% of the onshore velocity.

Nistor et al. (2016) investigated the transport of shipping containers over an idealized, flat harbour setting to validate the field results from Naito et al. (2014). The study found that the ±22.5° cone was a very conservative estimation of the spreading area. The authors noted that the debris transport was dependent on the number of debris present at the source, due to debris-debris and debris-fluid interactions. Goseberg et al. (2016b) extended the study to investigate the influence of obstacles on debris transport. The study found that obstacles placed within the flow resulted in a decrease in the longitudinal displacement, however, no difference was noted in the lateral spreading. A force balance based on the entrained debris resulted in the equation (Shafiei et al. 2016b):

$$m_d \ddot{x}_d = \frac{1}{2} C_d \rho_w A_d (u_b - \dot{x}_d)^2 \tag{2-1}$$

$$\dot{x}_d = u_b - \left(\frac{C_d \rho_w A_d}{2 m_d} t + \frac{1}{u_b} \right)^{-1} \tag{2-2}$$

$$x_d = u_b t - \frac{2 m_d}{C_d \rho_w A_d} \ln \left(\frac{C_d \rho_w A_d u_b}{2 m_d} t + 1 \right) \tag{2-3}$$

where m_d is the mass of the debris, $\ddot{x}_d$ is the acceleration of the debris, C_d is the drag coefficient, ρ_w is the density of water, A_d is the cross-sectional area exposed to the flow, u_b is the wave front velocity, $\dot{x}_d$ is the velocity of the debris and x_d is the displacement of the debris. Stolle et al. (2017a) used the same experimental setup to investigate the influence of multiple debris on the entrainment process. The study found that the increased number of debris resulted in a slower acceleration, however, similar peak velocities were observed. Stolle et al. (2017a) proposed an extension of Eq. (2-2) to include the number of debris present within the agglomeration (n):

$$\dot{x}_d = u_b - \left(\frac{C_d \rho_w A_d}{2 n m_d} t + \frac{1}{u_b} \right)^{-1} \tag{2-4}$$

While the primary method of evaluating debris transport in extreme hydrodynamic events has been physical modelling, there are still multiple challenges that must be overcome to properly model debris motion in an experimental setting. The motion of debris is a highly random process (Bocchiola et al. 2006, Matsutomi 2009), therefore, extensive data is needed to establish meaningful results. Additionally, further research is needed investigating scale effects related to the laboratory experiments.

2.2 Debris Loading

2.2.1 Debris Impact

The focus of debris impact modelling in hydraulic engineering has emphasized single debris impact. The majority of studies to date have been in steady-state flow conditions. In deriving an analytical approach of estimating the maximum impact loading, the most common methodology uses a Single Degree-Of-Freedom (SDOF) model (Haehnel and Daly 2002). The model is based on the assumption that the structure will be rigid and the impact duration short, reducing the SDOF model (Fig. 2-2) to the following differential equation:

$$m_d\ddot{x} + kx = 0 \tag{2-5}$$

where m_d is the mass of the debris, x is the displacement of the structure and debris, k is the contact stiffness (generally taken as the stiffness of the debris).

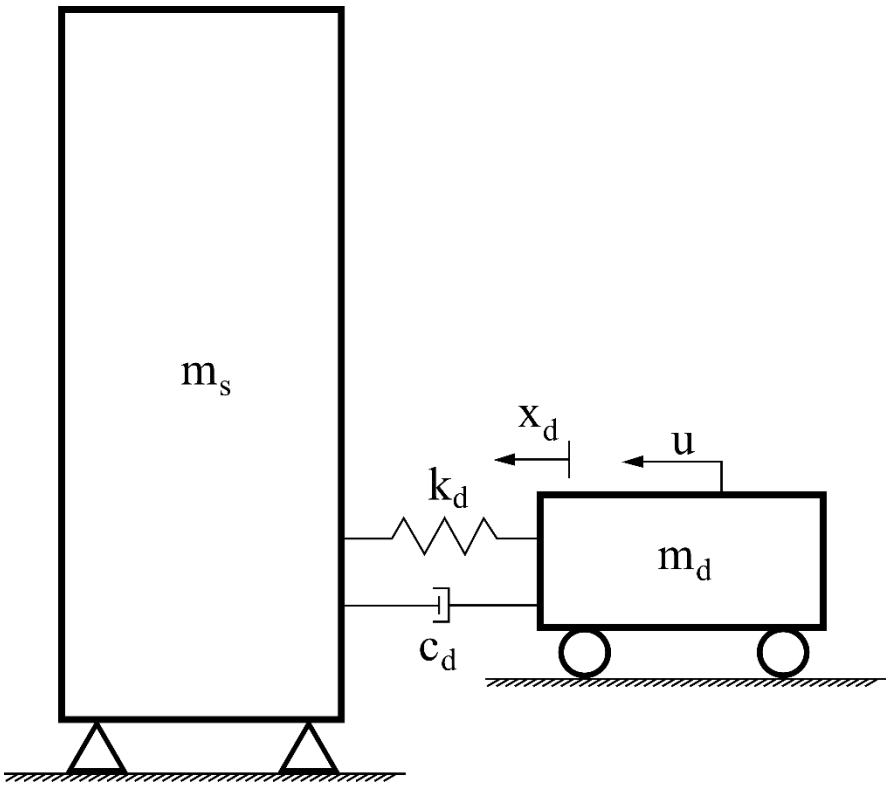

Fig. 2-2. Single Degree-of-Freedom (SDOF) model for debris impacts.

The solution of the SDOF model requires an assumption of one parameter either: the contact stiffness, impact duration, or impact displacement. When the contact stiffness is assumed the solution of Eq. (2-5), for the maximum impact force (F_i) can be calculated as:

$$F_i = u_i\sqrt{m_d k} \tag{2-6}$$

$$\frac{1}{k} = \frac{1}{k_s} + \frac{1}{k_d} \tag{2-7}$$

where u_i is the impact velocity, k_s is the stiffness of the structure, and k_d is the stiffness of the debris. This method is referred to as the contact-stiffness approach and is most commonly used in design guidelines (see Section 2.4). When the impact duration (t_i) is estimated, the impulse-momentum approach

is used. This assumes that the momentum of the debris goes to zero and the debris exerts an impulse on the structure. Using this approach, the following equation can be derived:

$$F_i = \frac{\pi}{2}\frac{u_i m_d}{t_i} \tag{2-8}$$

This assumes the impulse is shaped as a sinusoid. When the impact displacement (x_s) is assumed, the work-energy approach can be used. This assumes that the kinetic energy of the debris goes to zero when impacting the structure, resulting in the equation:

$$F_i = \frac{m u_i^2}{x_s} \tag{2-9}$$

Theoretically, these estimations of the maximum impact forces are equivalent, however, due to the difficulty in properly estimating the parameters, they have resulted in large variations in their accuracy in an experimental setting.

Another common approach to debris impacts is the use of the Hertzian contact model (Hertz 1882), where the deformation is assumed to occur at the face of the structure (as opposed to be distributed throughout the structure). Matsutomi (2008) proposed the following equation to estimate the impact force of a single tsunami-driven debris:

$$\frac{F_i}{\gamma_w D^2 L} = 1.6 C_M \left(\frac{u}{\sqrt{gD}}\right)^{1.2} \left(\frac{\sigma}{\gamma_w L}\right)^{0.4} \tag{2-10}$$

where γ_w is the specific weight of the debris, D is the diameter of the debris, L is the length of the debris, C_M is the inertia coefficient with $C_M = 1+C_0$, C_0 is the added mass coefficient, u is the debris impact velocity and σ_f is the yield stress of the debris.

Arikawa et al. (2007) performed 1:5 scale experiments of shipping containers impacting structures under tsunami-like surge fronts. Based on Hertzian contact mechanics, the following empirical equation was developed:

$$F_i = 0.25\left(\frac{4\sqrt{a}}{3\pi}\frac{1}{K_s + K_d}\right)^{\frac{2}{5}} \left(\frac{5}{4}\frac{m_s m_d}{m_s + m_d}\right)^{\frac{3}{5}} u^{\frac{6}{5}} \tag{2-11}$$

$$K = \frac{1-\upsilon^2}{\pi E} \tag{2-12}$$

where a is half of the radius of the contact face, υ is Poisson's ratio, and E is the modulus of elasticity. Ikeno et al. (2013) further tuned the empirical equation (Eq. (2-11)) to include a wider range of debris types:

$$F_i = 0.243(C_M m_d)^{\frac{3}{5}} u^{\frac{6}{5}} D^{\frac{1}{5}} \left(\frac{1}{\pi(K_s + K_d)}\right)^{\frac{2}{5}} \tag{2-13}$$

where D is the width of the side of the debris impacting the structure.

The variations in experimental data from the analytical equations listed above tend to be a result of the difficulty in addressing the other influences on the impact. Haehnel and Daly (2004) identified that the mass of the debris does not uniformly act around the impact point, resulting in the rotation or redirection of the debris. This is commonly referred to as obliqueness (β), where the debris velocity vector is at an angle from the impact vector, and eccentricity (e), where the impact occurs out of line with the center-of-gravity (CG), which were addressed as added parameters to Eq. (2-6):

$$\beta = \cos\theta \tag{2-14}$$

$$e = \frac{1}{\sqrt{1 + \frac{\varepsilon_0}{r_i}}} \tag{2-15}$$

where θ is the angle between the debris velocity vector and the normal force (Fig. 2-3), ε_0 is the distance between the CG and the impact point, and r_i is the radius of gyration. Additionally, due to the rapid deceleration of the debris upon impact, the water behind the debris needs to be similarly decelerated. However, the extent of this influence is difficult to address as it depends on the debris geometry, degree of submergence, orientation upon impact, and natural frequency. Generally, the issue is addressed as an added mass (C_M) added to the mass of the debris. Riggs et al. (2014) in a physical modelling experiment comparing in-air and in-water impacts of shipping containers found an insignificant influence of the added mass coefficient. Shafiei et al. (2016b), in a similar study, found that the impact force increased 1.5 times in the in-air experiments. The authors noted that the submergence ratio was significantly greater than Riggs et al. (2014), which was likely why the difference was so pronounced. Further research is needed in addressing an appropriate value for the added mass due to the highly specific nature of the parameter.

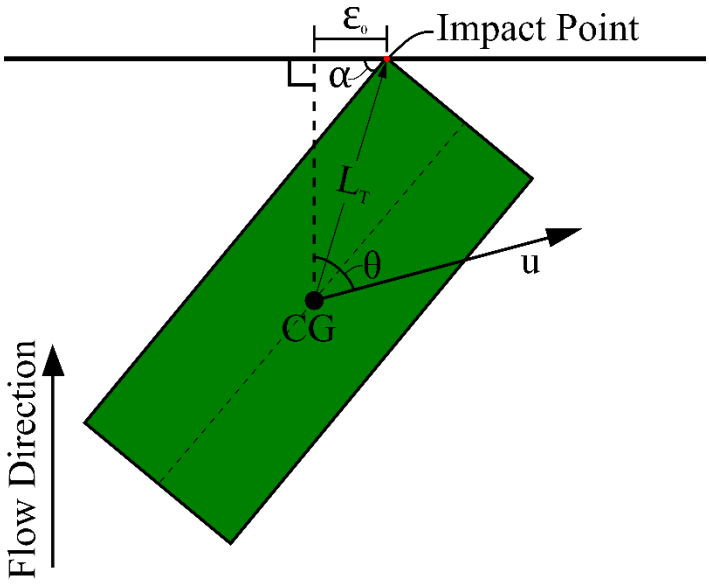

Fig. 2-3. Conceptual plan view drawing of the debris impacting a structure.

Blok et al. (1983) used the SDOF model to estimate a ship's impact onto a structure. However, in their study, the stiffness of the structure was used as opposed to the stiffness of the impacting object. They furthered the spring-mass system to examine eccentric impacts that result due to yaw (around the z-axis) rotations. The resulting coefficient could be multiplied by Eq. (2-6) to reduce the magnitude of the impact force:

$$\nu = \sqrt{\frac{L_T^2}{r_i^2 + L_T^2}} \tag{2-16}$$

where L_T is the shortest straight line distance between the CG and the impact point. Ikeno et al. (2016) noted that the equations from Haehnel and Daly (2004) tend to overestimate oblique impact forces. Ikeno et al. (2016) determined that a portion of the kinetic energy of the debris is transformed into rotational

energy, with the remainder transferred into the structure. Based on the conservation of energy, Ikeno et al. (2016) developed the dimensionless parameter, λ, as a ratio of the oblique and maximum impact forces:

$$\lambda(\theta) = \sqrt{\frac{1 + \left(\frac{L_T}{r_i}\right)^2 \sin^2\theta}{1 + \left(\frac{L_T}{r_i}\right)^2}} \tag{2-17}$$

where L_T is the length between the CG and the impact point. Based on a comparison with physical experiments, Eq. (2-17) tended to over predict the experimental impact force.

Khowitar et al. (2014) examined the longitudinal impact by a pole on a column governed by Timoshenko (1914) beam theory (Fig. 2-4). The impacting pole is governed by the one-dimensional wave equation (Paczkowski et al. 2012). The impact is considered to be sufficiently short that the deformation of the beam is dominated by shear. The shear force in the column is given as:

$$F = 2\kappa G A \gamma \tag{2-18}$$

where κ is the shear coefficient, G is the shear modulus, A is the cross-sectional area of the column, and γ is the positive direction shear ($\gamma = \partial^2 \overline{w}/\partial \bar{x}_1^2$). The corresponding force in the pole is:

$$F = E_p A_p \varepsilon_p \tag{2-19}$$

Where E_p is the elastic modulus of the pole, A_p is the cross-sectional area of the pole, and ε_p is the strain in the pole. The force in the spring is equal to the difference in the deformation ($F = k(\Delta_2 - \Delta_1)$).

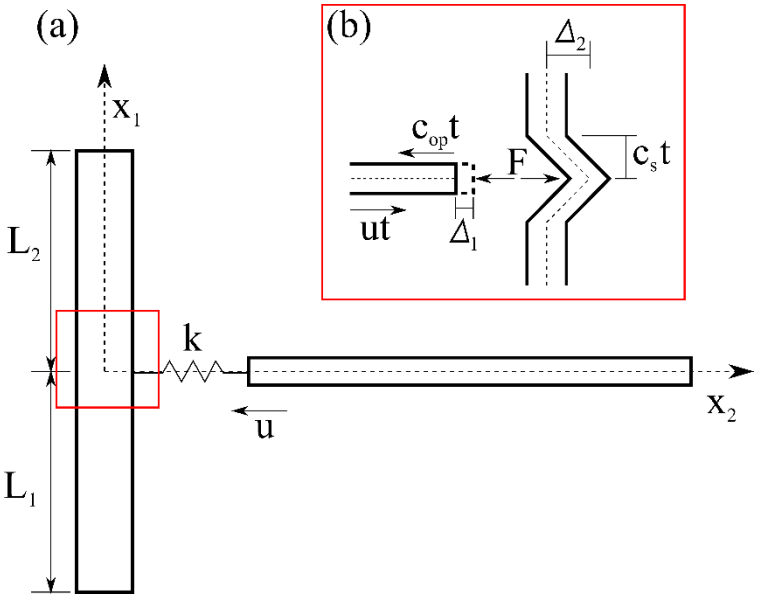

Fig. 2-4. (a) Longitudinal impact by a pole with a beam (adapted from Khowitar et al. (2014)). (b) Impact zone after impact.

Solving for the equilibrium condition of Fig. 2-4(b) and assuming a rigid column will result in Eq. (2-6). However, if the column has an associated stiffness, re-arranging the equation results in the terms:

$$\alpha_1 = 1 + \alpha_m \mu \frac{\sqrt{\tau}}{2} \tag{2-20}$$

$$\alpha_2 = 1 + \frac{2}{\alpha_m \mu \sqrt{\tau}} \tag{2-21}$$

where α_m is the ratio of mass per length of the pole and column, μ is the non-dimensional specific stiffness of the pole and τ is the non-dimensional specific stiffness of the column. Khowitar et al. (2014) showed that as α_1 approaches 1, the impact force is dictated by the axial response of the pole. Alternatively, if α_2 approaches 1, the force is dominated by the shear response of the column.

The current body of research has emphasized single debris impacts and constrained flow conditions. Due to the random nature of debris transport, further investigation is needed for more realistic scenarios where there are multiple, free-floating debris. Additionally, the current models do not capture the response of the structure to rapid impulse loading and should be extended and validated for structures that are not rigid.

2.2.2 Debris Damming

Debris damming is often considered as a debris static load: they form as debris agglomerate onto the face of a structure resulting in increased loading due to a larger exposed area to the incoming flow. Fig. 2-5 shows examples of debris damming from recent tsunami events. In Fig. 2-5(a), large agglomerations of debris come in contact with structures causing large debris dams. Fig. 2-5(b) shows two shipping vessels which constricted the flow between the houses causing rapid backwater rise. Field interviews (see Appendix B) with residents indicated that large accumulation of debris during in Wani Harbour (Central Sulawesi, Indonesia) resulted in the constriction of flow to an extent that it limited the inundation of the tsunami.

Fig. 2-5. Field evidence of debris damming loads in (a) the 2011 Tohoku Tsunami (YouTube, 2011) and (b) the 2018 Palu Indonesian Tsunami.

Debris impact and debris damming have been examined within the context of steady and unsteady-state flow conditions. Debris damming loads (F_{dm}) are often considered as an adjustment to the drag force equation associated with hydrodynamic forces, tending to act as a static load (Yeh et al. 2014):

$$F_{dm} = \frac{1}{2} \rho_w C_D B_d h u^2 \tag{2-22}$$

where ρ_w is the density of the fluid, C_D is the drag coefficient (commonly taken as that used for a rectangular pier = 2.0), B_d is the cross-stream width of the debris dam, h is the water depth, and u is the flow velocity.

Debris damming has not been extensively examined for cases of coastal flooding where non-stationary hydraulic conditions may uniquely govern the process of dam formation and build-up. Significant research has been conducted by hydraulic researchers investigating the formation of debris dams at bridge piers in steady-state conditions. Parola (2000) prepared a report on the design of highway bridge piers resistant to debris damming loads. His study found that the drag coefficient was dependent on the blockage ratio (the fraction of the total unobstructed cross-section blocked by the debris dam) and on the Froude (Fr) number.

While the debris dam influences the loads exerted on a structure, the formation of the dam also can have secondary effects that must be considered in the design process. The constriction of the flow path results in backwater rise, potentially overtopping flood protection structures adjacent to those at the location of interest (Schmocker and Hager 2011). Debris dam-induced flow constrictions also causes flow accelerations underneath and downstream of the dam (Pagliara and Carnacina 2013), which can results in significant scouring (Melville and Dongol 1992).

Fenton (2003) used the conservation of momentum equations to calculate the increase of backwater levels due to the presence of obstacle in an open channel. The solution used a linear approximation of the momentum equation, making the proposed equation only applicable over a small reduction in momentum flux:

$$\Delta\eta = \frac{u^2}{2g}\frac{C_d}{\beta Fr^2 - 1}\frac{a}{A} \tag{2-23}$$

where u is the velocity of the fluid at the obstacle, A is the cross-sectional area of the channel, β is the Boussinesq coefficient and a is the cross-section area of the obstacle transverse to the flow direction.

Schmocker and Hager (2013) examined the formation of debris dams at a debris rack. The study examined the influence of opening size, debris density and debris volume. Schmocker and Hager (2013) qualitatively showed the temporal evolution of the debris dam formation stayed relatively similar regardless of experimental conditions. The study also found the dam formation and backwater rise to be dependent on the Froude number as the dam tended to compact horizontally and be forced further into the cross-section of the flow at higher Froude numbers:

$$\frac{h}{V_D^{\frac{1}{3}}} = 0.3Fr^{0.3} \tag{2-24}$$

where h is the backwater rise and V_D is the volume of debris. Pagliara and Carnacina (2010) examined the influence of debris dam roughness and porosity on scour profiles. Both the roughness and the porosity of dam had significant influence on the scour depth and final bed profile. Stancanelli et al. (2015), in a study of stony debris flows at channel confluences, determined that a decreased dam porosity resulted in an increase in backwater rise.

The study of debris damming in tsunami-like flood events has not often been addressed. Pasha and Tanaka (2014) examined the capture of debris at inland forests under steady-state flow conditions with a Froude number of 0.7. The study examined several different debris geometries and found that the capture mechanism varied based on the contact area with obstacles. Cylindrical debris, with the smaller contact area, tended to oscillate at the front of the structure forming less stable dams. Similar to Bocchiola et al. (2008), the capture efficiency was determined to decrease with increasing flow velocity and increase with debris length. Limited studies have addressed debris damming in transient loading conditions, considering the prevalence in field observations, further research is needed into this phenomenon.

2.3 Numerical Modelling

The modelling of floating solid objects has been one of the challenges that has traversed the fields of hydraulic, environmental, and mechanical engineering. Various attempts have been made using a host of computational fluid dynamics (CFD) models solving the Navier-Stokes equations. The models have utilized both Eulerian (looking at a single location and observing the fluid properties through that location) and Lagrangian (following individual fluid packets) approaches. Within these two approaches, two discretization techniques are common: Volume-of-Fluid (VOF) and Smoothed Particle Hydrodynamics (SPH) methods. The VOF method extends the typical Finite Volume Method (FVM) Eulerian fixed mesh discretization to allow for free-surface tracking by storing information regarding the extent to which a cell contains a fluid (1 – being fully submerged, 0 – being empty) (Hirt and Nichols 1981). SPH discretizes the domain into a set of particles for which the Navier-Stokes equations are numerically solved for each particle using a differentiation of interpolation formulae (Monaghan 1992). The following section will provide a comprehensive examination of the available literature for the modelling of floating solid objects, particularly focused on the attempts on two-way coupling the solid-fluid interaction.

2.3.1 Eulerian

The initial phases of floating solid body transport were focused primarily on completely immersed bodies. Peskin (1977) examined the flow pattern of blood in the heart which solved the Navier-Stokes equation using a Laplacian solver, where the heart contractions were modelled using a spring system. Glowinski et al. (1997) extended this work using a technique called fictitious domain where the entire domain was considered to be an incompressible fluid but the markers within the solid body had a fixed distribution. These techniques required the motion of the body to be known before hand and could not represent the physical phenomenon actually occurring within the immersed flow. Moreover, all these techniques were extremely computationally expensive. The introduction of the VOF method allowed for the free-surface boundaries to be clearly defined within the cells, and more realistic boundary treatments to be examined.

The primary challenge of using the fixed cell Eulerian approaches, like VOF, is discretizing the solid boundaries within the individual cells. Xing et al. (2001) applied the VOF technique with a moving grid strategy, which adapts the grid to fit the surfaces of the body. The technique was compared to the free-floating motion of a solid body under wave motion, however, significant deviations were observed from experimental results. Swidan et al. (2013) used a dynamic unstructured grid (Hadzic 2006) to model water impact loads on wedge shaped hulls.

Other techniques involve using a fixed Cartesian grid system that considers the solid objects to be an additional phase. Fekken (2004) assigned uniformly distributed markers to the solid in the initial discretization of the domain. The number of markers within each cell was then used to determine the amount of the solid within a cell. The markers acted as a "sub-grid" that cuts the control volumes of the fixed fluid grid. The method was limited as the rotation of an object resulted in spaces occurring between the sub-grids resulting in small losses (~0.01%) in the conservation of mass equations.

Kleefsman et al. (2005) utilized the VOF method to investigate the application to green-water wave impacts on marine infrastructure. The model was tested by examining the impingement of falling wedges, cones, and cylinders into an initially stationary, free surface. Visual observations comparing the model to experimental results showed reasonable accuracy. However, a noticeable spike was noted when comparing the pressure information. The spike resulted from cells initially empty being seeded with a

small amount of water causing the VOF method to rapidly fill in the cell with water. In the following time steps, the subsequent unstable flow velocity caused spurious spikes in the pressure.

Wu et al. (2014) developed a Partial-Cell Treatment (PCT) to incorporate the VOF method into solving the solid-fluid interface. The technique was incorporated into a Large Eddy Simulation (LES) model using the VOF method to track the free-surface. The PCT treatment calculates an effective mesh cell size by reducing the size of the cell based on the presence of the object within the cell. This treatment preserves mass and continuity features of the flow around the solid by imposing a porous effect on all fluxing quantities. The motion of the fluid was then determined by the Discrete Element Method (DEM) which sums all of the forces acting on an element (cell) and solving the Euler equations for the rotation and translation of the solids. The treatment was tested against floating and sinking block cases with good agreement between the measured and modelled trajectories.

2.3.2 Lagrangian

The research around the application of SPH modelling of floating solid objects has primarily focused on the implementation of the boundary conditions to accurately reproduce the solid body motion. The most commonly used boundary conditions in SPH are: repulsive, ghost particles, and dynamic (Gomez-Gesteira et al. 2012). The repulsive boundary conditions exert a force normal to the wall, where the magnitude of the force is a function of the distance between the particle and the wall (Monaghan 1994). Ghost particles are a set of particle placed outside the domain with the physical quantities necessary to enforce the necessary boundary conditions (Fourtakas et al. 2015). The dynamic boundary conditions are the most commonly used of these conditions where the boundary particles are enforced to satisfy the same equations as the fluid particles, however, instead of moving, the density of the boundary particles fluctuate exerting a pressure on the surrounding fluid particles (Crespo et al. 2007).

Rogers et al. (2009) implemented the repulsive boundary conditions under the conclusion that the repulsive boundary most accurately represents the physical phenomenon. The object was considered to be a rigid body and the forces on each boundary particle were summed from all the surrounding fluid particles. The frictional force was a function of the normal force. The forces on each boundary particle were then summed to determine the force on the solid body. The translation and rotation of the solid body was determined using the equation of rigid body dynamics. The model was compared to experimental data examining the motion of a caisson breakwater under wave loading. Qualitatively, the motion of the caisson breakwater was well represented, however, the measured forces showed large fluctuations due to gaps in the fluid continuum formed as violent flow forcing anisotropic particle distributions. This has been reasonably handled in future version of the code (Lind et al. 2012) using particle shifting schemes, however, further investigation is needed to address free surface instabilities.

Another method of calculating the motion of solid objects is to initially treat the solid as a deformable fluid. The motion is calculated based on the conservation of momentum between the fluid and solid particles. An additional treatment is performed to correct the relative locations of the particles within the solid object to a fixed distance. Shao and Gotoh (2004) utilized this technique within an SPH-LES coupled model to analyze the motion of a floating curtain wall. The technique performed reasonably well compared to the experimental results but tended to have some inconsistencies near sharp corners. This method tends to be less straightforward compared to the Newton's law of motion but less prone to the effects of spurious pressure fluctuations (Ren et al. 2015).

Hashemi et al. (2012) compared the use of dynamic boundary particles to the ghost particle technique while also introducing a particle shifting and time stepping scheme to reduce the pressure fluctuations common to the SPH models. The model was validated against a falling cylinder through a water column

case study. The model showed significantly improved motion of the cylinder as well as consistent pressure surfaces around the cylinder. However, the authors noted that at high particle accelerations near the solid boundaries, the particle spacing needed to be considerably reduced to get consistent results. Omidvar et al. (2013) extended this work to include a variable mass technique which allowed for progressively finer resolution near areas of interest which reduced the computational cost of the dynamic boundary procedure in high acceleration flows.

One of the other causes of the pressure fluctuations in the SPH formulation is a result of the solid-fluid and solid-solid boundary. Canelas et al. (2015) introduced a δ-SPH term into the continuity equation to control the density fluctuations caused by the dynamic boundary and to handle the interfacial interaction. The δ-SPH term is a diffusive term which contributes to the density field and smooths out the high-frequency oscillations. The result of this smoothing at the interface between two materials allows for a more uniform ordering of the particles and reduces the chances of particle "locking" resulting in spurious increases in pressure. This model was compared to previous versions of SPH where the boundary layer around a falling cylinder was considerably more continuous than the previous models

One of the advantages of the SPH method is the relatively simple coupling with commonly used Lagrangian solid solvers, like DEM. Canelas et al. (2013) coupled a non-linear Hertzian contact mechanics DEM to calculate the normal and tangential components of the force. The friction at the solid face is modelled as a spring-dashpot system using Coulomb's Law. The model was compared to experimental results qualitatively examining the collapse of a stack of cubes in a dam-break flow. The authors noted that the increased computational load resulted in a reduced resolution which influenced the propagation of the wave. This resolution also affected the scales at which momentum transfer occurred between the cubes and the fluid which resulted in differences between the experimental and numerical results.

Canelas et al. (2016) extended the SPH-DEM coupling to the updated Distributed Contact DEM (DC-DEM) model to improve the models application to complex geometries. The contact mechanics is calculated similarly to the DEM model from Canelas et al. (2013). However, instead of a direct calculation of the forces between solids, the particles are constrained together by a spring-dashpot system where the deformation of the system is dependent on the overlap of the two particles in contact. This approach allows for a generalization of the geometry and information is not needed regarding the normal and tangential directions of the interacting topologies.

2.3.3 Lagrangian-Eulerian

An additional option exists regarding the modelling of floating solid objects that addresses the shortcomings of the Eulerian and Lagrangian models by combining the approaches in the Arbitrary Lagrangian-Eulerian (ALE) method. The method relies on the development of a kinematical description of the deforming continuum to allow for better descriptions of distortions than the Lagrangian models and more detail than the Eulerian models (Donea et al. 1982). In the ALE description, the nodes may move with the material as in the Lagrangian model or be held fixed as in the Eulerian model. Alternatively, the nodes could also be moved in an arbitrary manner to give continuous re-meshing capabilities. The primary drawback of this method is the extreme computational costs related to the calculation as studies carrying out this method tend to be performed on supercomputers. Kan et al. (1998) applied a coupled Eulerian-Lagrangian technique for modelling the motion of leukocytes within the bloodstream which allowed the model to handle higher Reynolds numbers, extending the work of Glowinski et al. (1997) to a fully Eulerian-Lagrangian technique.

Yang et al. (2017) used an Immersed Boundary Method (IBM) to investigate the entrance of a falling wedge into a still basin. The IBM introduces a forcing term (usually in the form of a spring stiffness) to the momentum equation to represent the influence of the solid boundary on the fluid (Yang and Stern 2015). The force on the structure is calculated through a surface integration of the pressures acting on the immersed boundary. The method was relatively successful at predicting the dropping velocity and pressures acting on the falling wedge. Additionally, the air entrapment was well represented which has been shown to be an important consideration in the water entry problem.

An additional Eulerian-Lagrangian coupling uses the Eulerian fixed window technique to calculate the fluid flow features and the solid phase is treated as a discrete phase where the pressures are integrated onto each individual particle (Lagrangian). Iqbal and Rauh (2016) examined the settling velocity of particles for application in process engineering. The model coupled a DEM solver for the Lagrangian solid particle and utilized the Eulerian PISO solver in the OpenFOAM package for the fluid components. A semi-analytical term was added to the momentum equation to include the momentum exchange between the Lagrangian and Eulerian phases. The inclusion of the momentum exchange allowed for the viscous (drag) forces to be considered. However, the authors noted that the correct selection of the momentum transfer model is necessary as in some settling velocity cases the model used in this study did not compare well to experimental results.

One of the challenges in ALE is of addressing the discrepancy in scales between the phenomenon influencing the object motion (generally influenced by the bulk flow characteristics) and the finer scales of the fluid (needed to resolve flow features such as eddies). Pozzetti and Peters (2018) examined the coupling of OpenFOAM and a DEM model over multiple scales. The application was applied to large particles where bulk flow dominates the motion of the particle. Again, the model considered the particles as a Lagrangian object and the fluid as a fixed mesh. A dual-mesh system was used where the coarse mesh maps the Lagrangian properties of the particles to Eulerian and fluid-particle interactions are solved. The fine mesh solves the Navier-Stokes equations to identify smaller scale turbulent properties. This splitting of the responsibilities reduces the calculation burden on the fine mesh allowing for improved computational efficiency. The results of this model compared well to experimental results and the conservation of energy was significantly improved over the single scale models.

2.4 Design Specifications

2.4.1 Design of Structures for Vertical Evacuation from Tsunami (FEMA P646)

The guidelines set by FEMA P646 (2012) use the contact-stiffness method of determining the impact force caused by debris in the inundating tsunami flow. The guidelines use the following equation to estimate the impact force:

$$F_i = C_m u_{max} \sqrt{km} \tag{2-25}$$

where C_m is the added mass coefficient (recommended to be 2.0), u_{max} is the maximum flow velocity, k is the effective stiffness of the debris and m is the mass of the debris. The impact force should be considered locally on a single member of the structure at the elevation of the water surface. The type of debris should be determined based on the location of the vertical evacuation structure and potential debris in the surrounding area. The use of the maximum flow velocity should also take into consideration the inundation depth as smaller debris with little to no draft will travel at a higher velocity than larger debris requiring larger depths to float. The maximum flow velocity should be determined using a numerical

simulation, unless unavailable, in which case the flow velocity of a wooden log on a uniformly sloping beach can be determined using the following equation:

$$u_{max} = \sqrt{2gR(1 - \frac{z}{R})} \tag{2-26}$$

where R is the design runup height and z is the ground elevation at the structure. The FEMA P646 also addresses debris damming loads by modifying the equation for the drag force caused by the inundating flow, the following equation is derived:

$$F_{dm} = \frac{1}{2}\rho_s C_d B_d (hu)_{max}{}^2 \tag{2-27}$$

where C_d is the drag coefficient, B_d is the breadth of the debris dam, $(hu)_{max}$ is the maximum product of the water depth and flow velocity. The force should be assumed to act uniformly over the extent of the debris dam and at the submerged height of the structural components.

2.4.2 Coastal Construction Manual (FEMA P-55)

The Coastal Construction Manual is primarily concerned with flooding and debris impact loads associated with the flooding. Determining whether or not the impact will occur is less of a concern as long as reasonable allowance is made for the debris impact. The following equation is recommended for determining debris impact force:

$$F_i = m_d g V C_D C_B C_{Str} \tag{2-28}$$

where W is the weight of the object, V is the velocity of water, C_D is the depth coefficient, C_B is the blockage coefficient and C_{Str} is the building structure coefficient. The method is largely an empirical approach relying upon engineering best practices to determine the coefficients.

2.4.3 Tsunami Loads and Effects (ASCE 7 Chapter 6)

The ASCE 7 applies debris impact loads to buildings where the minimum inundation depth exceeds 0.91 m and the forces will be applied to the perimeter gravity-load carrying structural components perpendicular to the inflow and outflow directions specified elsewhere in the code. The loads will be applied to points critical for flexure and shear within the inundation depths. All buildings will be designed for impact by floating wooden poles, logs, vehicles, tumbling boulders and concrete debris; and building in proximity to a port or shipping yard the potential for strikes from shipping containers, ships and barges will be determined.

The design impact force of wood logs and poles is determined using the following equation:

$$F_l = I_{tsu} C_0 u_{max} \sqrt{k m_d} \tag{2-29}$$

where I_{tsu} is an importance factor specified by the type of building, C_0 is the orientation coefficient (0.65 for logs and poles), u_{max} is the maximum flow velocity at depth sufficient to float debris, k is the effective stiffness of the debris and m_d is the mass of the debris. The impulse duration for elastic impact will be:

$$t_d = 2m_d \frac{u_{max}}{\sqrt{k m_d}} \tag{2-30}$$

The ASCE 7 Chapter 6 was the first standard to provide a method of assessing if extreme debris impacts were of concern. The method was adapted from Naito et al. (2014), a full description can be found in Section 2.1. The ASCE 7 does not explicitly address debris damming, however, the influence of debris accumulation is mentioned within hydrodynamic loads. A common practice in mitigating hydrodynamic loading is breakaway walls, which reduce the drag loads by reducing the cross-sectional area of the

structure. The ASCE 7 sets a lower limit to the reduction in cross-sectional area as a result of debris accumulating and filling the sections where the walls break away.

Debris damming is addressed through calculating the overall drag forces as:

$$F_d = \frac{1}{2}\rho_s I_{tsu} C_d C_{cx} B(hu^2) \tag{2-31}$$

where C_D is the drag coefficient (dependent on the width to inundation depth ratio), ρ_s is the density of the fluid (considering density changes due to entrained sediment and small debris), I_{tsu} is the importance factor dependent on the type of building, h is the water depth, and U is the flow velocity. C_{cx} is the closure coefficient, calculated as:

$$C_{cx} = \frac{\sum(A_{col} + A_{wall}) + 1.5A_{beam}}{Bh_{sx}} \tag{2-32}$$

where A_{col} and A_{wall} are the projected area of column and wall elements, A_{beam} is the combined projected area of the slab and beam exposed to the flow, B is the width of the building, and h_{sx} is the average story height. Debris damming is incorporated into this equation by restricting the minimum closure coefficient (ratio of area enclosed to the total project vertical plane area) to 0.70 (Carden et al. 2015).

2.5 Research Needs

Field surveys of recent major flooding events have shown the necessity for considering debris loading in the design of critical infrastructure (Yeh et al. 2014, Nistor and Palermo 2015). However, there has been limited work in addressing the potential hazard in a comprehensive manner. Based on the literature review conducted above, the follow points are important in the development of a hazard assessment framework:

- Current methods of assessing debris dynamics are limited due to the lack of data regarding debris transport in major flooding events (Naito et al. 2014). Current estimations rely on the final resting positions of debris transported within the event and do not capture the intermediate processes, such as acceleration and velocity, that may influence the magnitude of loading events.
- The probabilistic properties of debris transport have not been adequately addressed. A comprehensive study is needed to address the complex interaction between variables that dictate the trajectory of debris in extreme flooding events.
- The single degree-of-freedom model has limitations due to the assumption of a rigid body impact. This limits the potential influence of the structural response and inertia of the structure on the impact force. Extending the model would allow it to be more flexible in handling “extraordinary” debris impacts where the inertia of the debris would be similar to that of the structure.
- Limited studies have addressed the impact geometry and, in particular, the appropriate geometric coefficients for design standards. The current standards provide an engineering estimation for the coefficients, however, limited information exists regarding mean values or the distribution of these values.
- Video evidence from the 2011 Tohoku Tsunami (Fig. 2-5(a)) showed large agglomerations of debris impacting structures. Current studies have focused on the impact of a single object

impacting the structure. Extending these models to include multiple debris impacts could improve estimations of impact conditions within major flooding events.

- Studies into debris damming have primarily focused on steady-state flow conditions. Studies into transient flow have shown the formation of complex hydraulic conditions around obstacles (St-Germain et al. 2013), which may influence the formation of a debris dam.
- Debris damming studies have tended to focus primarily on the likelihood of debris dam formation. Combining these studies to examine the drag forces and backwater rise would develop a comprehensive picture of debris damming from a design perspective.
- Several numerical modelling techniques have been developed for addressing solid body transport. However, limited data sets exist for the validation of these models. Comprehensive data sets addressing the different processes involved in debris transport are necessary for the further development of these numerical models.

Based on this literature review, there is clear need for developing a deeper understanding of debris hazard in extreme flooding events. Leveraging the results from the studies outlined above, the following program aims to develop probabilistic methodology for assessing debris loading in major flooding events. A framework will be developed that considers the different variables that have been shown to influence debris transport. Additionally, the study will aim to address the shortcomings of debris loading assessment by extending the current models to apply to a wider range of scenarios, particularly related to multiple debris impacts and “extraordinary” debris impacts.

Chapter 3. Debris Transport

3.1 Debris Transport over a Sloped Surface in Tsunami-Like Flow Conditions

Preprint of an article printed in the Coastal Engineering Journal © 2019 Taylor & Francis.
https://www.tandfonline.com/doi/abs/10.1080/21664250.2019.1586288

3.1.1 Objectives

Currently, the research has predominantly focused on developing empirical relationships between the number of debris and their spreading characteristics due to a multitude of variables that influence debris transport. To further describe the physical phenomena of debris transport, the study presented in this section aims to investigate, for the first time, the influence of the bed topography and friction on debris entrainment and transport. The study of friction was motivated by the work of Imamura et al. (2008) where the friction contributed to the type of motion (sliding, saltation, entrainment) of boulders in tsunami-like flow conditions. The objectives of this study are to extend this work to address positively-buoyant objects:

- Investigate the influence of bed friction on the lateral spreading and longitudinal displacement of the debris.
- Determine the influence of the bed friction on the maximum velocity of the debris.
- Examine the relationship between the longitudinal and lateral displacement of the debris

3.1.2 Experimental Setup

Facilities

The experiments were performed in the Tsunami Wave Basin (TWB) (4.0 m x 9.0 m) at Waseda University (Tokyo, Japan), shown in Fig. 3-1. The TWB consists of a vertical reservoir attached to a shallow basin. Two bed topographies simulating a nearshore coastal zone were used for these experiments: a 1:10 slope and a horizontal section. The chosen slope represents some of the commonly shoreline characteristics such as those typically found in Japan or Chile. The limit of 1:10 slope and flat section was located 4.20 m from the vertical reservoir outlet and continued for a distance of 4.00 m. The flat bed had a constant elevation of 0.20 m above the flume bottom. The flat bed was made of stainless steel and, for the experiments involving increased surface roughness, the slope was covered entirely with a 0.0035 m thick carpet, made of 100% polypropylene with a density of 180 kg/m^3. For all experiments, the bed was impermeable. The still-water depth in the basin was kept constant at 0.15 m for each experiment. The initial water head in the reservoir was 0.90 m before each experiment. The reservoir was filled and accurately maintained using a vacuum pump. To initiate the wave generation, the air valves located at the top of the reservoir were opened at 50% of their cross-sectional area to allow the release of the water column. An elongated solitary (Goseberg et al. 2013) was formed by the release of the water column - a full description of the hydrodynamic conditions is presented in the Results section.

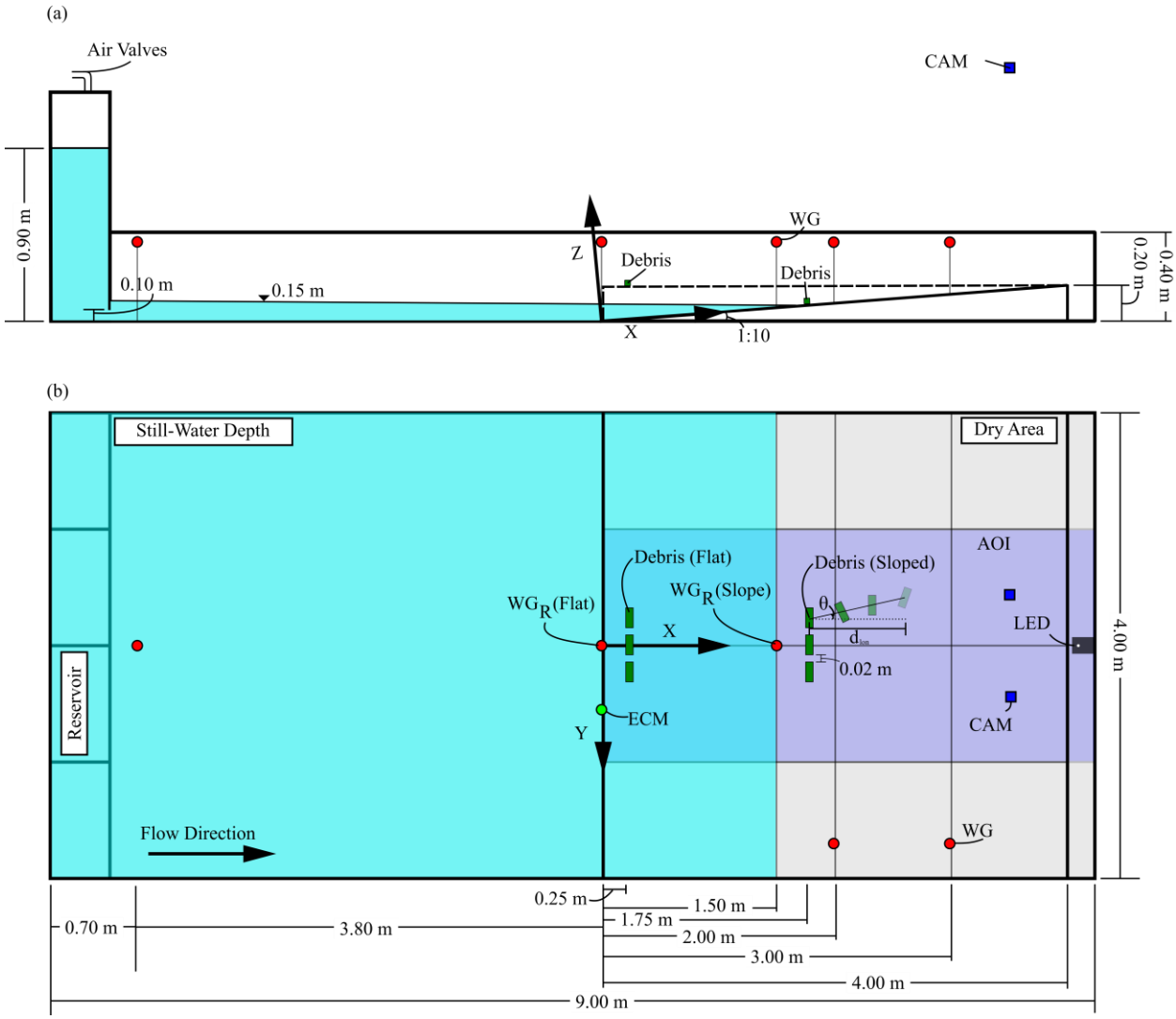

Fig. 3-1. Waseda Tsunami Wave Basin: (a) side view and (b) plan view. The wave gauges are shown as red circles, and the video cameras are shown as blue squares. The model debris are displayed as green rectangles. The slope section is shown as a solid line, the flat section as a dashed line.

The origin of the coordinate system (0,0) was placed at where the slope or horizontal section began, along the longitudinal axis of the basin. The positive *x*-direction was in the onshore direction of the flow along the bed surface, the positive *y*-direction was in the span-wise direction, and the positive *z*-direction was upwards. The centroids of the debris were placed at x = 1.78 m (on the slope) and x = 0.28 m (on the flat section), both at 0.28 m from the water line. The debris were placed with the long axis perpendicular to the flow direction. In cases with more than one debris, the initial inter-debris spacing was 0.02 m.

For the remainder of this paper, time (t) = 0.00 s refers to the instant when the water depth at the reference wave gauge (WG_R) exceeded 0.002 m. Wave gauge WG_R was kept at the same position (0.28 m upstream of the debris site) for all of the experiments. The remaining three wave gauges (WG, accuracy: 0.15%) (Table 3-1) were rotated among the 4 positions shown in Fig. 3-1 (red circles), ensuring that a minimum 10 experiments were measured at each position.

The video cameras (CAM, 1920 px × 1080 px, Table 3-1) were fixed over the dry section to track the motion of the debris. The area of interest (AOI) is shown as the blue shaded area in Fig. 3-1. The CAM were synchronized with the hydrodynamic data using an LED light. The LED was controlled by the data acquisition system (DAQ). Before the experiments began, the LED was switched on; once the water column was released, the LED was instantaneously switched off. The CAM monitored the intensity of the pixels associated with the LED light in each image; once the LED was switched off, the CAM began to track the debris in post-processing. The 5 V voltage signal controlling the LED was recorded with the DAQ; when the voltage dropped below 2.5 V the light was set to be off. The estimated synchronization error was +/- 0.017 s.

Table 3-1. Instrumentation.

Instrument	Manufacturer	Sampling Rate
Wave Gauge (WG)	KENEK Co. Ltd.	50 Hz
Video Camera (CAM)	Sony Co.	60 Hz
Data Acquisition System (DAQ)	KENEK Co. Ltd.	

Debris Models

The debris were modelled as 1:50 geometrically-scaled 6.1 m long prototype shipping containers (model dimensions: 0.12 m x 0.045 m x 0.045 m). The mean mass of the debris was 0.111 kg (+/- 0.003 kg) with a draft of approximately 0.021 m. Using Froude similitude, the mass of the model debris at prototype scale (13,875 kg) approximately represents an average, fully-loaded shipping container (14,400 kg). The model debris were built of solid pine wood (with a specific gravity, SG = 0.45) and the wood was homogeneous. To adjust the friction between the bed and the debris, sandpaper was fixed to the face of the debris (Fig. 3-2). Each model debris was painted with a water resistant paint to limit the intrusion of the water and differentiate the color from the bed as well as between individual debris. The debris were painted either blue, green, or red; however, the color did not correspond with the material on the debris surface.

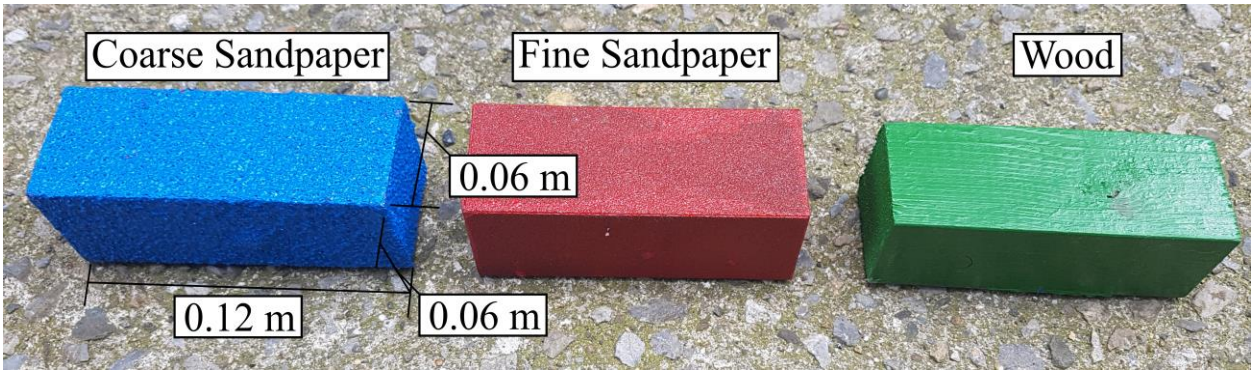

Fig. 3-2. Model debris - 1:50 shipping containers (model dimensions 0.12 m x 0.045 m x 0.045 m).

The coefficient of static friction for each debris-bed pairing was estimated through dry tests. The debris was placed on the bed and the bed slope was gradually increased until it started to move. The coefficient of static friction was determined based on a force balance of the debris. The mean coefficients of static friction are shown in Table 3-2. The dry test was repeated five times for each setting and the mean error in the estimation of the coefficient was determined to be +/- 20%.

Table 3-2. Coefficient of static friction between debris-bed pairs.

Coefficient of Static Friction (μ)	Stainless Steel (S) [Min. Max.]	Carpet (C) [Min. Max.]
Wood (W)	0.41 [0.35 0.50]	0.50 [0.41 0.56]
Fine Sandpaper (FS)	0.45 [0.37 0.53]	0.75 [0.65 0.91]
Coarse Sandpaper (CS)	0.59 [0.49 0.66]	0.85 [0.60 0.95]

The debris were tracked using a camera-based object tracking algorithm (Stolle et al. 2016, 2017a). Previous validations of the algorithm have shown that the approximate error of the tracking was +/- 0.01 – 0.03 m. The algorithm geo-rectified each image using six control points placed on the dry area of the slope. The individual debris are identified in each image based on the color of the debris by a thresholding technique. The original validation of the algorithm noted that the error tended to increase with increasing number of debris. This was a result of the algorithm incorrectly passing unique identifiers between different individual debris. By expanding the number of colors used to identify the debris from one to three, this issue was averted for up to 10 debris used within these experiments. A full description of the algorithm can be found in Stolle et al. (2016). The debris were tracked as long as they were in the dry area of the basin. If the debris overtopped the dry area and fell into the stilling basin or were washed offshore, the tracking was truncated.

Experimental Protocol

Table 3-3 outlines the experimental variables used in these experiments. Each variation of the variables was used for 3 repetitions which resulted in a total of 36 experimental categories and 108 experimental trials. For each trial, the same initial wave condition was used. Sandpaper was added to the outer faces of the debris to change the friction between the debris and the bed. The debris were placed at x = 0.28 m from the edge of the water (Fig. 3-1), with the first debris placed with the centroid onto the center basin. The flow resistance was adjusted by including an artificial carpet on the bed of the slope while the friction between the debris and the bed was adjusted by adding sandpaper to all faces of the individual debris.

Table 3-3. Experimental Variables (abbreviations used to label experimental runs throughout this work).

Bed Slope	Surface Roughness	Debris Material	Number of Debris
1:10 (S)	Stainless Steel (SS)	Wood (W)	1
Flat (F)	Carpet (C)	Fine Sandpaper (FS)	3
		Coarse Sandpaper (CS)	5

For the single debris case, the centroid of the debris was placed at y = 0.00 m. For the subsequent additions of debris, a single row of debris was maintained with a 0.02 m spacing between their outer faces (Fig. 3-3). In the following section, the debris trajectories are compared between the tests with different debris positions (displayed a integers in Fig. 3-3). The position refers to the debris that had the same initial centroid y-position.

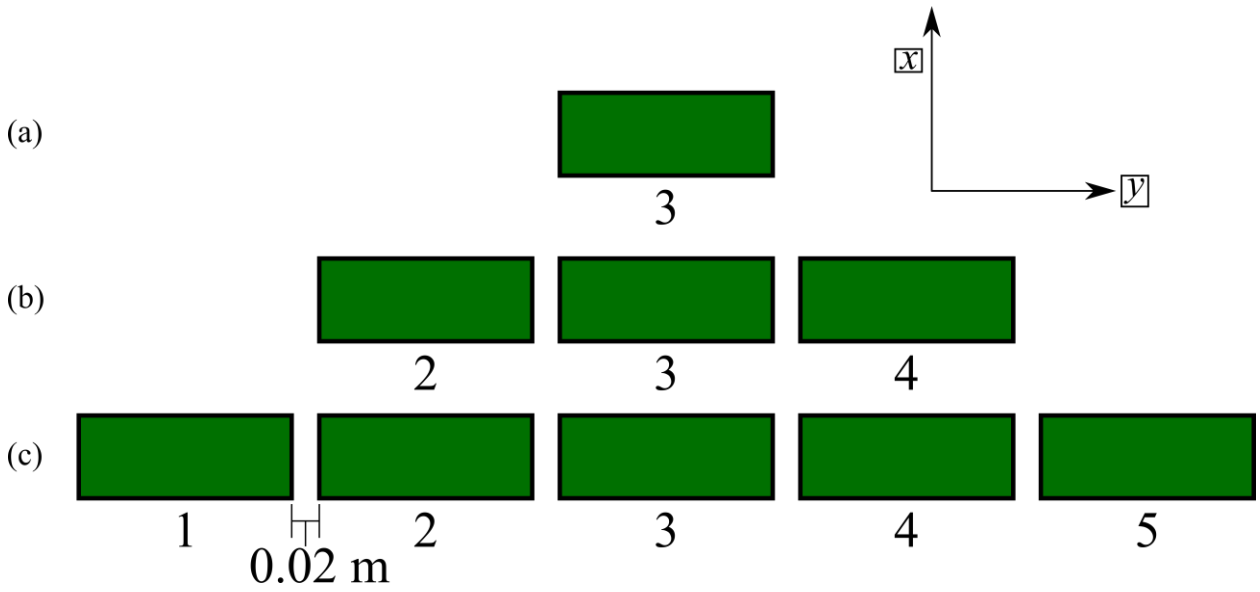

Fig. 3-3. Debris configuration for (a) 1, (b) 3, and (c) 5 debris. Debris positions indicated as numbers throughout the remainder of the study.

3.1.3 Results

Hydrodynamics

The hydrodynamic forcing condition was developed by releasing a 0.90 m column of water from the vertical tank (Fig. 3-1). The release of the water column generated an elongated solitary wave (Nistor et al. 2016) profile that propagated over the still-water section. The bed topography was initiated at a distance of 4.00 m from the outlet of the vertical tank. For the case of the 1:10 slope, the wave begun to shoal at x = 0.00 m, eventually breaking over the slope off-shore. For the flat-bed, the incoming wave was reflected by the sharp vertical discontinuity, which simulated a harbor-like environment. The reflection caused a strong amplification of the wave front and breaking over the edge of the vertical quay. In both cases, the wave traveled onshore as a turbulent, surge. Fig. 3-4 shows the mean water surface elevation (η) over time (t) for each of the bed topographies. Time instant 0.00 s represents the arrival of the wave tip (when η exceeded 0.002 m) at a distance of - 0.25 m from the debris site (at WG_R). The wave shows a pronounced steep front, common to a broken solitary wave (Hafsteinsson et al. 2017), followed by an elongated tail which increases the duration of the flow. A second peak can be observed at approximately 0.50 s behind the wave front. A numerical study of the basin (Douglas 2016) showed that the reduced head, as a result of the vacating chamber, caused the water entering the still-water section to cease building the initial wave, forming a secondary smaller wave behind the initial wave form.

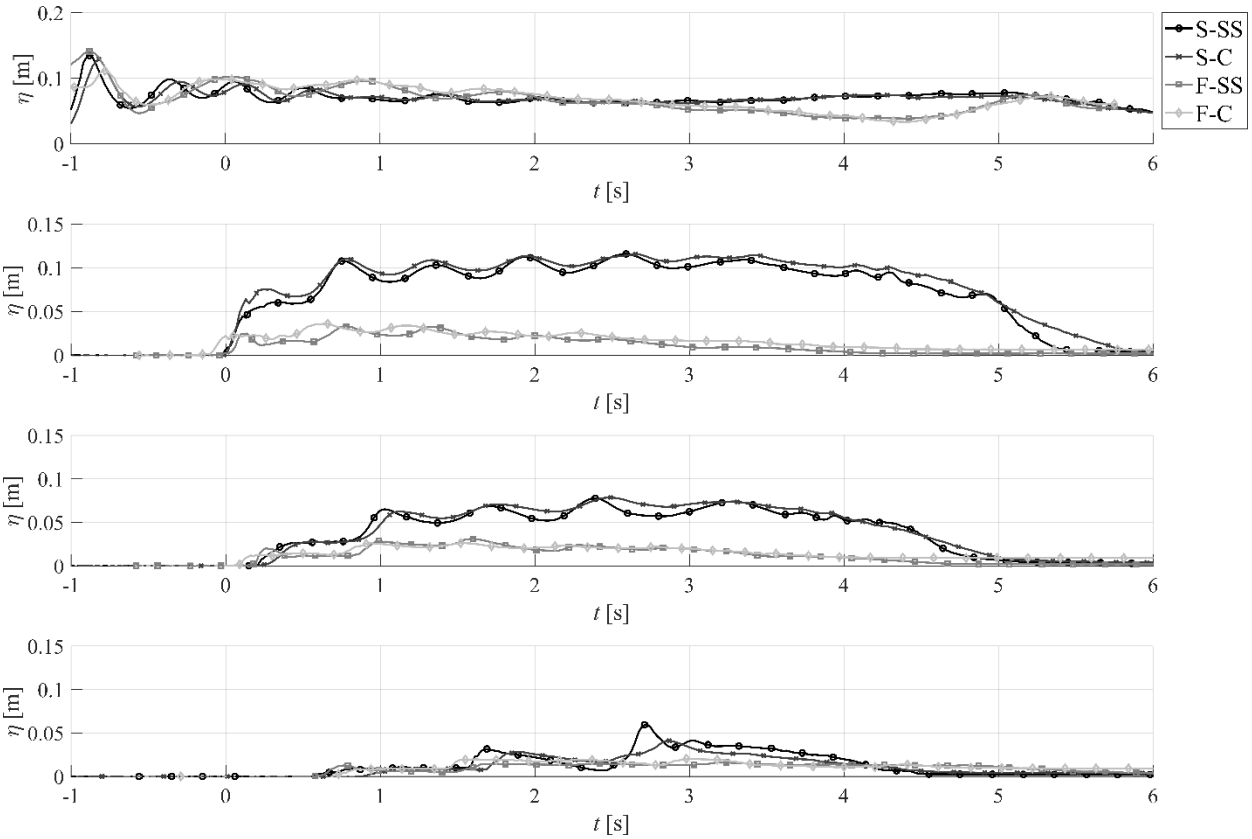

Fig. 3-4. Time-histories of the mean water surface elevations (η) at x = -0.05 m and distances of (b) -0.25 m, (c) 0.5 m, and (d) 1.25 m from the debris site.

Table 3-4 outlines the hydrodynamics conditions associated observed at the debris site (Fig. 3-4b). The wave front velocity was calculated using the difference in the arrival times between the WG upstream of the debris site and the WG 1.25 m downstream of the debris site. The maximum wave height was the maximum wave height at 0.25 m upstream of the debris site and the standard deviation was the one between the individual experiments. Overall, the wave showed strong repeatability with limited deviation between the wave profiles. For all cases, the wave tip traversed the length of the dry area, overtopping into the end of the stilling basin.

Table 3-4. Hydrodynamic conditions at debris site.

Bed Topography	Wave Front Velocity [m/s]	Maximum Wave Height [m]	Standard Deviation [m]	Weber Number [-]	Reynolds Number [-]
S-SS	2.027	0.115	0.003	6537	6.35×10^5
S-C	1.515	0.116	0.005	3647	1.75×10^5
F-SS	2.419	0.033	0.002	2655	7.98×10^4
F-C	1.724	0.036	0.004	1472	6.21×10^4

Studies into the physical properties of solitary waves have shown that the duration of the wave does not adequately capture the duration of a tsunami-like event (Madsen et al. 2008). Within these experiments, the flow durations were approximately 5 s, corresponding to 35.5 s at prototype scale, which is an order of magnitude smaller than a typical tsunami event (Kamphuis 2010). The issue of flow duration is common in tsunami engineering studies due to the large wavelengths associated with tsunami flow conditions and technical limitations of most experimental facilities. Some facilities have been shown to

accurately reproduce tsunami wave runup (Rossetto et al. 2011, Goseberg 2013a, Schimmels et al. 2016); however, these experiments require a large facility and using small scales, leading to potential scale effects. Solitary waves have previously been used to investigate wave loading and debris motion (Yao et al., 2014). The authors of the present study acknowledge that the current wave conditions allow for only the analysis of the incipient motion of debris and cannot capture all phenomena associated with a tsunami flood event.

The measured hydrodynamic conditions compare well to field and numerical modelling of the 1993 Hokkaido-Nansei-Oki Tsunami (water depths of 5 – 15 m, flow velocities of 3 – 15 m/s). As the experiments were scaled considering Froude similitude (Fr - ratio of gravitational to inertial forces), Bricker et al. (2015) noted the importance of properly considering the surface tension and viscous forces when addressing tsunami modelling by showing how flow resistance can be significantly influenced when improperly scaled. As shown in Table 3-4, within these experiments, the Weber number (We) (ratio of surface tension to inertial forces) exceeded the critical value of 120 determined by Peakall and Warburton (1996). Furthermore, the Reynolds number (Re) (ratio of viscous and inertial forces) was in the fully turbulent regime (Te Chow 1959). However, the Reynolds number did not achieve the 1.00×10^6 typically associated with a tsunami, therefore, the boundary layer within the flow may not be properly represented (Bricker et al. 2015).

Debris Transport

This section focuses on the maximum spreading area of the debris in onshore direction. The maximum displacement of the debris in the flow direction will be referred to as the longitudinal displacement while the maximum displacement of the debris in the cross-flow direction will be herein referred to as the lateral displacement. The lateral displacement is normalized by the longitudinal displacement to obtain the spreading angle.

Debris Spreading

Fig. 3-5 shows the spreading angle for all the cases organized by the debris position (as indicated in Fig. 3-3). The debris position is defined by the initial centroid *y*-position of the debris. The lateral spreading is defined by the spreading angle (θ), given as:

$$\tan\theta = \frac{y_f - y_i}{x_f - x_i} \tag{3-1}$$

where y_f is the position in the *y*-direction at the maximum *x*-position, y_i is the initial *y*-position of the debris, x_f is the maximum *x*-position, and x_i is the initial *x*-position of the debris. The spreading angle was only considered for the onshore motion and, therefore, one value would be associated with each debris for each trial. The spreading angle at the maximum displacement was selected to maintain a consistent definition with previous literature (Goseberg et al. 2016b, Nistor et al. 2016).

An ANOVA test was performed with the null hypothesis that the mean spreading angles for each debris position were the same. The test showed that the mean spreading angles for each debris position were significantly different (*p*-value << 0.005, *F*-statistic = 64.1, degrees-of-freedom (dF) = 320).

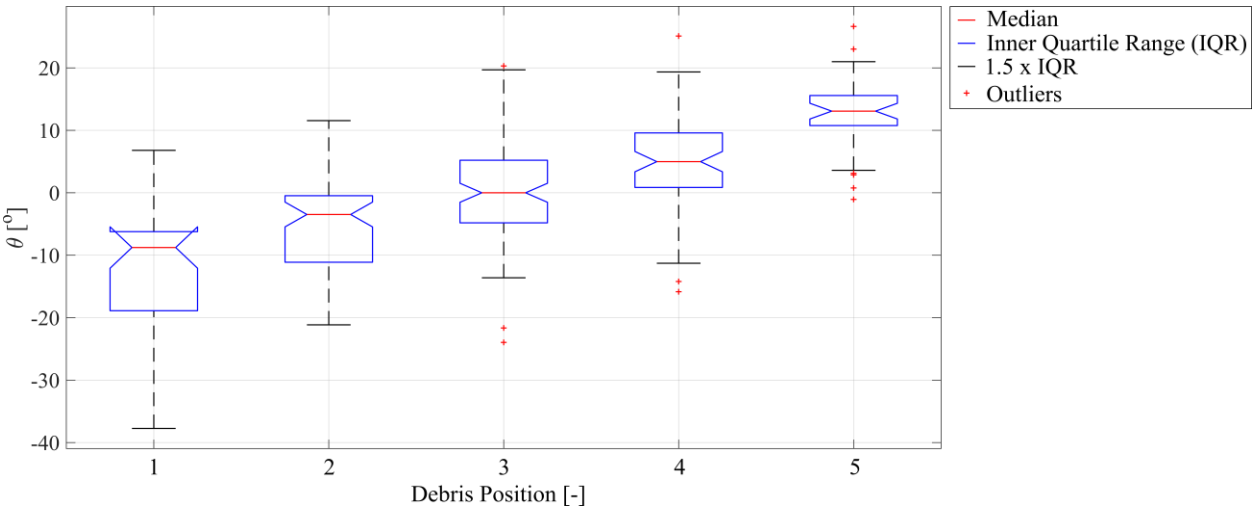

Fig. 3-5. Debris spreading angle (θ) for all tests as a function of the initial debris position (as shown in Fig. 3-3). The mean spreading angle for each position is shown as a red line, the blue lines indicated the second and third quartile, the dashed lines show the first and fourth quartile, the outliers are shown as red crosses.

Fig. 3-5 shows that the debris tended to be driven away from the geometric center of their source. The debris in the center of the configuration (y = 0.00 m) had a spreading angle close to 0. Therefore, the debris moved in essentially a straight line, as it had been observed in previous experiments (Stolle et al. 2018c). As the debris position moved further from the center position in the longshore direction, the mean spreading angle increased. The difference in spreading may be a result of a non-symmetric pressure distributions caused by the obstruction of flow and gaps between debris (Tutar and Oguz 2002, Alam et al. 2011) resulting in unequal forces acting across the debris face. Considering the debris configuration as a porous solid object, the stagnation point would occur at y = 0.00 m, resulting in a symmetrical force acting on the central debris, with increasingly asymmetrical forces on the debris further from the center. However, further investigation is needed to address these forces as high resolution water depth and velocity data are needed to examine this pattern of debris spreading. Additional considerations are also needed to investigate the influence of turbulent eddies (Rueben et al. 2014) and gap size (Alam et al. 2011).

As was shown through the ANOVA test performed above, the spreading angle was dependent on the initial position of the debris. Therefore, to address the influence of friction on debris spreading, the debris positions must be **considered individually**. Fig. 3-6 shows the spreading angle for the sloped (a – e) and horizontal (f – j) bed topographies by debris position. The mean spreading angle is shown as a solid line and the raw data points as markers. The standard deviation and 95% CI are shown as patches. A two-sample *t*-test was performed between the stainless steel and carpeted cases with the null hypothesis that the spreading angles were the same. The t-test showed no significant difference between the spreading angles for 27 of the 30 sets. The sets, in this case, refer to the paired slope and carpeted measurements for each debris position. It is unclear why significant differences were observed for the 3 cases (S-W, F-W, and F-FS); further experiments may be necessary to better capture the mean distributions.

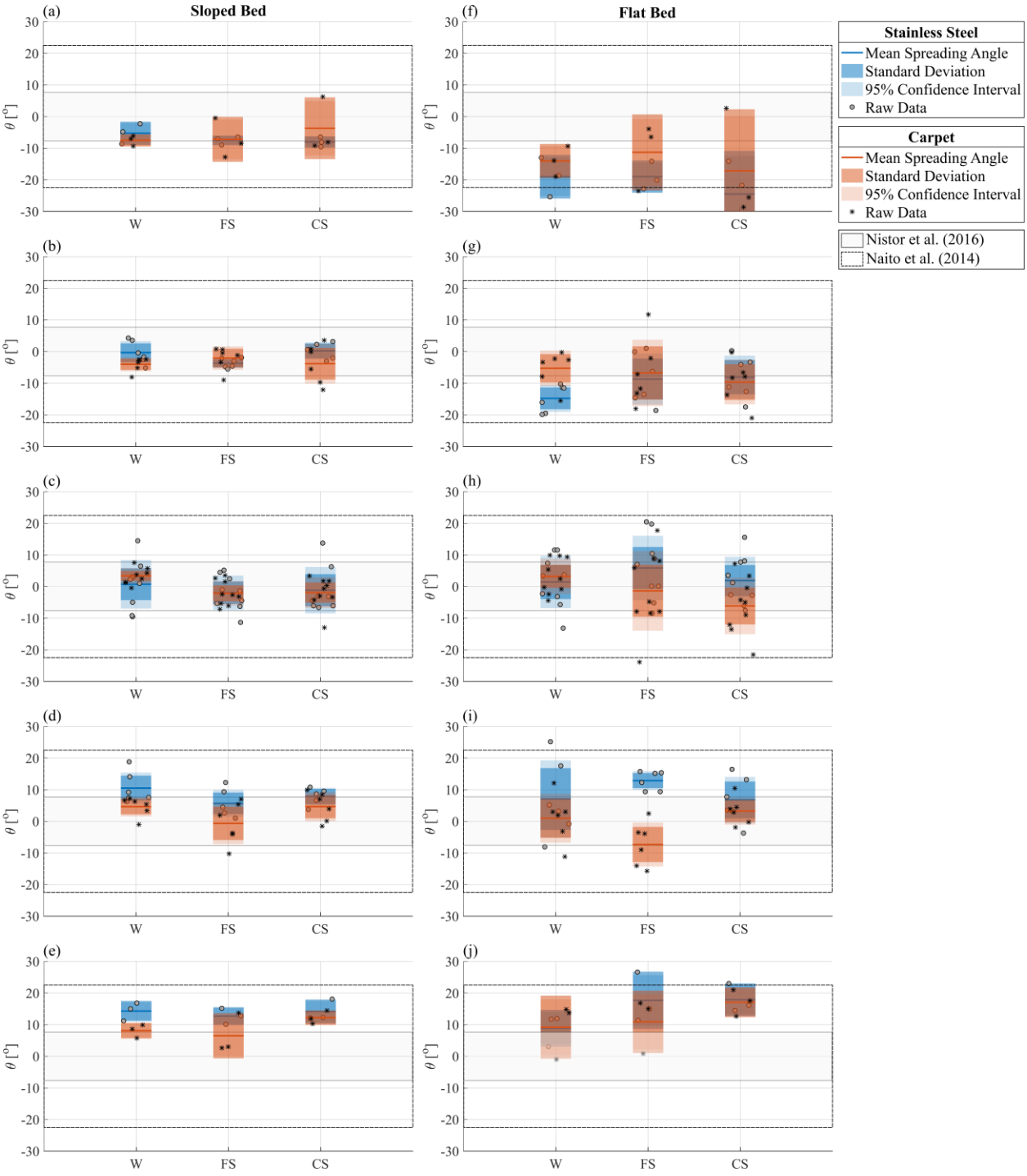

Fig. 3-6. Spreading angle (θ) as a function of the debris surface friction for stainless steel (blue) and carpeted case (orange). The sloped bed is shown in the left hand column (a-e) sorted by the *y* debris position: (a) -0.28 m, (b) -0.14 m, (c) 0 m, (d) 0.14 m, and (e) 0.28 m. The horizontal bed is similarly organized in the right hand column. The maximum spreading angle estimated by Eq. (1) is shown as a grey box and the +/- 22.5° spreading angle predicted from Naito et al. (2014) as a dashed box in each figure.

An ANOVA test was used to examine the influence of the debris surface friction on the spreading angle. Similar to the influence of the bed friction, no significant difference between the mean spreading angle

for 18 of the 20 sets were observed. The sets in this case refer to the paired means based on the debris friction for each debris position and bed friction. Therefore, friction appears to have no significant influence on the debris spreading. The debris spreading angle seems to be primarily dependent on the initial configuration of the debris. This phenomena had not previously been examined in the study by Nistor et al. (2016) and, as can be seen by the comparison with Eq. (1) which shows that, for the outer debris, the spreading angle is underestimated. Nistor et al. (2016) used fewer numbers of debris to the lateral (only three) which may have contributed to the reduced spreading angle. Comparing to field estimation of spreading (Naito et al. 2014), for the outermost debris, the spreading angle could potentially be under predicted. Naito et al. (2014) used field data where confounding influences, such a channelization and direction of flow as a result of irregular terrain, cannot be accurately estimated. Furthermore, as this study examines the incipient motion of the debris, the spreading behaviour of the debris in the latter stages of the flow may vary.

However, it should be noted that the debris trajectory was measured under idealized settings, with a flat propagation surface. Bocchiola et al. (2008), in a study of large woody debris transport in rivers, noted that the trajectory of debris over bars present in the river was dependent on the contact of the debris with the bar, as it dictated the rotation of the debris. A larger coefficient of friction would require a greater force to dislodge from the bar and potentially influence the rotation of the debris. Further investigation is needed to address the influence of obstacles present in the moving path of debris.

As the friction had no influence on the spreading angle, the mean trajectory of the debris for all the cases can be averaged over the longitudinal displacement. Fig. 3-7(a) shows the mean trajectory (solid line) and the 95% confidence interval (CI) (dashed line). Comparing the trajectories of the sloped and flat bed shows a relatively similar evolution of the lateral spreading. In the initial stages of the propagation, where the peak acceleration occurs, limited spreading can be observed. However, as the debris continue to propagate, the deviation from the mean trajectory increases. Additionally, an increase in the mean spreading angle can be observed for the debris located at the outer edges of the configuration as the mean trajectory deviates from the straight line path observed for the central debris.

To address the stochastic nature of debris transport, empirically derived statistical models have been used to estimate the debris trajectory. Stolle et al. (2018c) used a 1-D Gaussian model to examine the lateral spreading of a single shipping container using the development of the variance over distance to analyse the normal probability density function of the lateral deviation. However, this model is limited in addressing the stochastic nature of the transport of debris in the flow direction. Lin and Vanmarcke (2010), in a study of wind-driven debris, used a 2-D Gaussian model which could adequately capture the variation in the wind direction. A 2-D distribution requires an understanding of the covariance between the two variables, in this case, the *x*- and *y*-positions. Fig. 3-7(b) shows the development of the Pearson correlation coefficient (Fisher 1925), which is the normalized value of the covariance:

$$\rho(t) = \frac{\sum_{i=1}^{n}(x_i - \bar{x})(|y_i| - \bar{y})}{\sqrt{\sum_{i=1}^{n}(x_i - \bar{x})^2}\sqrt{\sum_{i=1}^{n}(|y_i| - \bar{y})^2}} \tag{3-2}$$

where $\bar{x}$ is the mean *x*-position at an instance in time, and $\bar{y}$ is the mean *y*-position. The lateral displacement was taken as the absolute value to address only the magnitude of the displacement. To adhere to the assumptions of the correlation coefficient, the latter was calculated at each time step to ensure independent samples. A ρ-value equal to 1 represents a perfect positive correlation between the variables while -1 denotes a perfect negative correlation. As it can be observed in Fig. 3-7(b), for both bed slopes, the correlation coefficient in the latter stages of the flow approached zero. This indicates that the

x- and *y*-positions are statistically independent, quantitatively confirming this assumption made in the wind-driven debris model by Lin and Vanmarcke (2010).

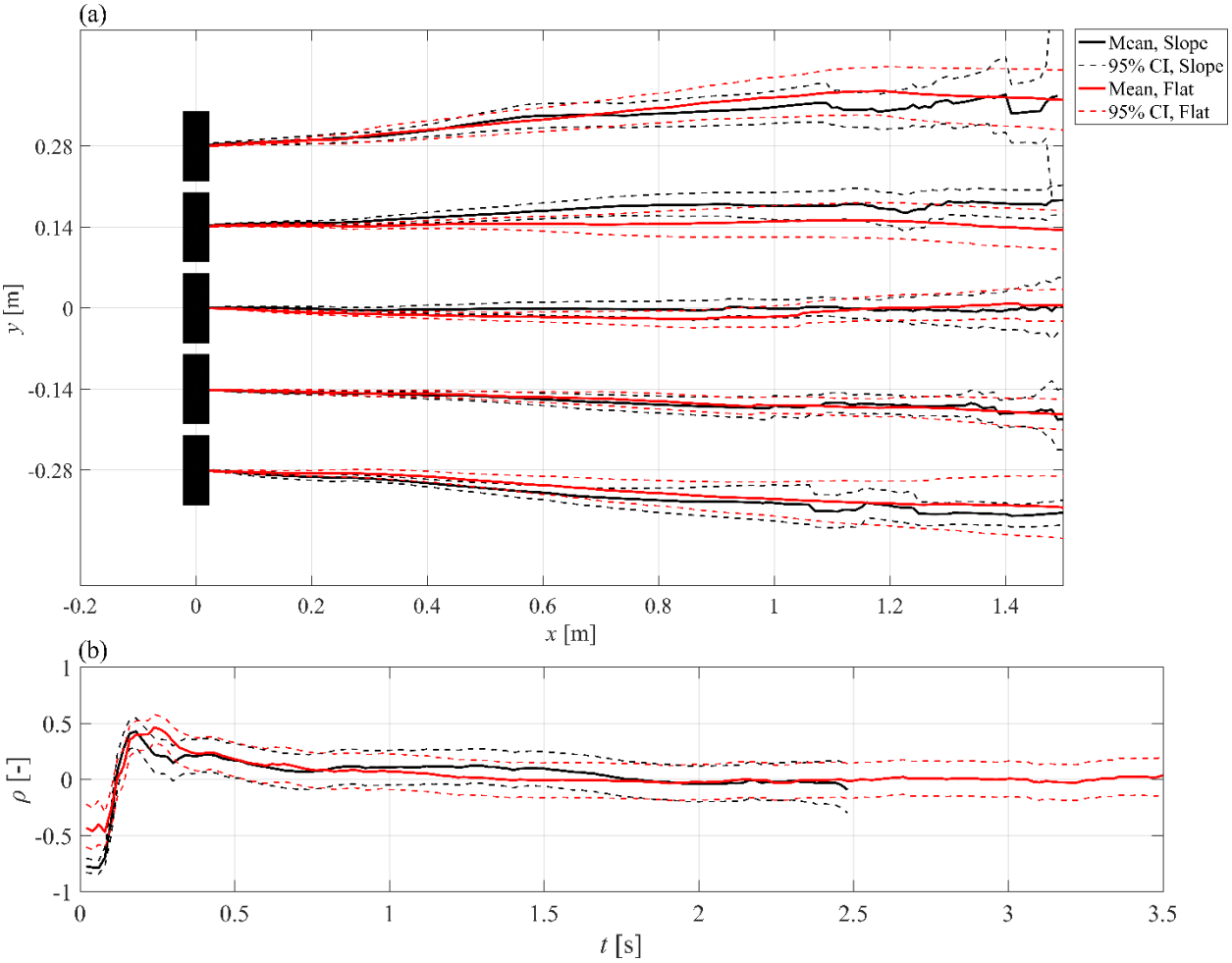

Fig. 3-7. (a) Debris trajectory as a function of the distance from the debris origin for sloped (black) and horizontal (red) beds. (b) Pearson correlation coefficient (ρ) as a function of time (t).

Longitudinal Displacement

Fig. 3-8 shows a comparison of the longitudinal displacement (displacement in the *x*-direction) for each of the debris positions for all cases. The longitudinal displacement is defined as the maximum displacement of the debris in the *x*-direction. An ANOVA test between the groups showed that there was no significant difference ($p = 0.78$, F-statistic = 0.44, $dF = 320$) in the longitudinal displacement of the debris. Therefore, unlike the spreading angle, all debris positions will be considered simultaneously in the analysis presented in Fig. 3-9.

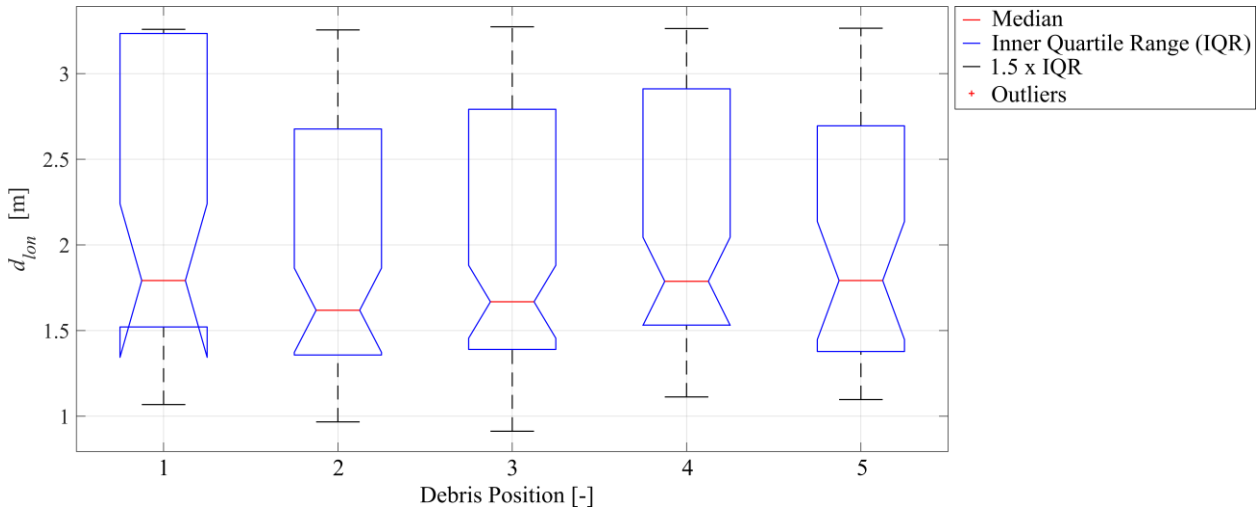

Fig. 3-8. Longitudinal debris displacement (d_{lon}) for all cases as a function of the debris position.

Fig. 3-9 shows the longitudinal displacement for each of the experimental cases, as outlined in Table 3-3. The mean values are shown as a solid line and the raw data as markers. The longitudinal displacements are compared to Nistor et al. (2016). An examination of the influence of the coefficient of friction shows that it did influence the longitudinal displacement. The greater the coefficient of friction, the smaller the longitudinal displacement. This was likely due to the friction being most critical during the initial entrainment of the debris and whenever grounding occurred. The greater coefficient of friction would require a larger initial force to overcome the friction force, as well as substantial losses in moment as the container was dragged along the bed. It was also observed that, for the cases with the coarse sandpaper and the carpet; the debris was initially entrained in a rolling/saltation type motion as opposed to sliding. The additional rotational component of the motion would result in less energy applied to the longitudinal displacement (Imamura et al. 2008). The roughness of the debris surface, as well as induced turbulence within the flow, could also have influenced the drag forces, specifically the drag coefficient (Sumer and Fredsøe 2006) acting on the debris. However, this effect would likely be negligible in comparison to the frictional losses.

The influence of friction was more pronounced for the flat bed slope (Fig. 3-9b). Due to the shallower water depths in the initial stages of the flow, the debris tended to be dragged across the bed surface as opposed to being completely entrained (afloat), as was observed for the sloped bed case (Fig. 3-9(a)). The constant interaction between the bed surface and the debris would result in substantial kinematic friction losses in summation. Unlike the sloped bed, the debris on the flat bed cases with low coefficients of friction tended to overtop at the end of the slope, resulting in a truncated maximum value. Thus, the influence of friction was likely more substantial than indicated within this study, as the values were normalized by this truncated value.

Goseberg et al. (2016b) and Nistor et al. (2016), in a study using similar hydrodynamic conditions, found that the number of debris present at the debris source influenced the maximum longitudinal displacement. However, in this study, there was no significant correlation between the number of debris and the longitudinal displacement. This was likely due to the initial configuration of the debris, as this study only used a single row of debris, whereas Nistor et al. (2016) employed multiple rows parallel to the apron edge. The multiple rows of debris resulted in collisions between the debris which resulted in additional energy loss. Additionally, as was noted in Stolle et al. (2017a), the entrainment of multiple rows of debris caused the formation of agglomerations of debris which acted as a single object with a reduced cross-

sectional area transverse to the flow direction and greater mass, thus, reducing the acceleration, and therefore the displacement, of the debris (Eq. (2-2)). Based on the results of this study, the number of rows of debris, as opposed to number of debris, is likely the primary driver of the longitudinal displacement. However, further investigation into the influence of the gap between debris in the initial configuration may be necessary (Alam et al. 2011).

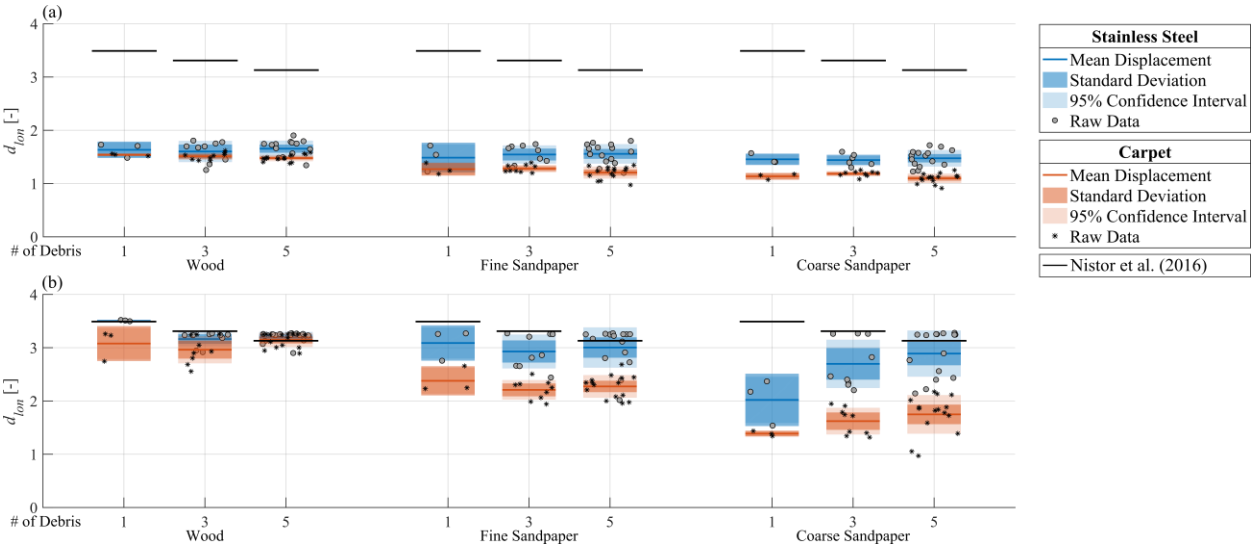

Fig. 3-9. Longitudinal displacement for the (a) sloped and (b) flat bed cases. The stainless steel bed surface is shown in blue and the carpeted surface is shown in orange. The black lines show a comparison of longitudinal displacement to the empirical solution presented in Nistor et al. (2016).

Comparing the present results to Nistor et al. (2016), the equation reasonably estimated the longitudinal displacement for the case most resembling the experiments with the flat bed and similar coefficients of friction in the case of wood (0.30 in Nistor et al. (2016)). As expected with increasing friction, there was an increase in discrepancy between the empirical and experimental results. For the case of the sloped bed, the empirical equation significantly over predicts the longitudinal displacement. This is likely a result of the kinetic energy of the wave now also contributing to the change in gravitational potential energy of the debris, in addition to the kinetic energy, causing a reduction in the longitudinal displacement.

Therefore, the debris/bed friction as well as the slope must be considered when estimating the longitudinal displacement of debris. Imamura et al. (2008), in a study of boulder transport, suggested a time-varying friction factor. Weiss and Diplas (2015) used an impulse-based approach to estimate the entrainment of boulders. However, neither of these procedures considers the grounding process of positively-buoyant debris. Therefore, further analytical development is needed to adequately address frictional influences on longitudinal displacement.

Debris Velocity

Fig. 3-10 shows the debris velocity (in the flow direction) for all cases normalized by the mean wave front velocity, as displayed in Table 3-4, for both the sloped (a) and flat (b) beds. The debris velocity showed a distinct profile, regardless of bed topography and debris-bed friction. This was expected, as the wave profile was not changed throughout the experiment. The initial wave front entrained the debris

causing an acceleration to 80 – 90% of the bore front velocity. Due to the relatively short duration of the flow, the debris may have not reached the maximum surrounding flow velocity.

For the incipient motion of the debris, the evolution of the debris velocity was reasonably well represented by Eq. (2-2), except for a time delay related to the initial entrainment of the debris. The cases with the larger coefficient of friction have a slightly increased time delay due to the larger momentum required to overcome static friction. However, due to the short duration of the wave used in this study, as the local flow velocity decreased as the wave reached its maximum inundation extent, Eq. (2-2) did not capture the deceleration due to the assumed constant wave front velocity.

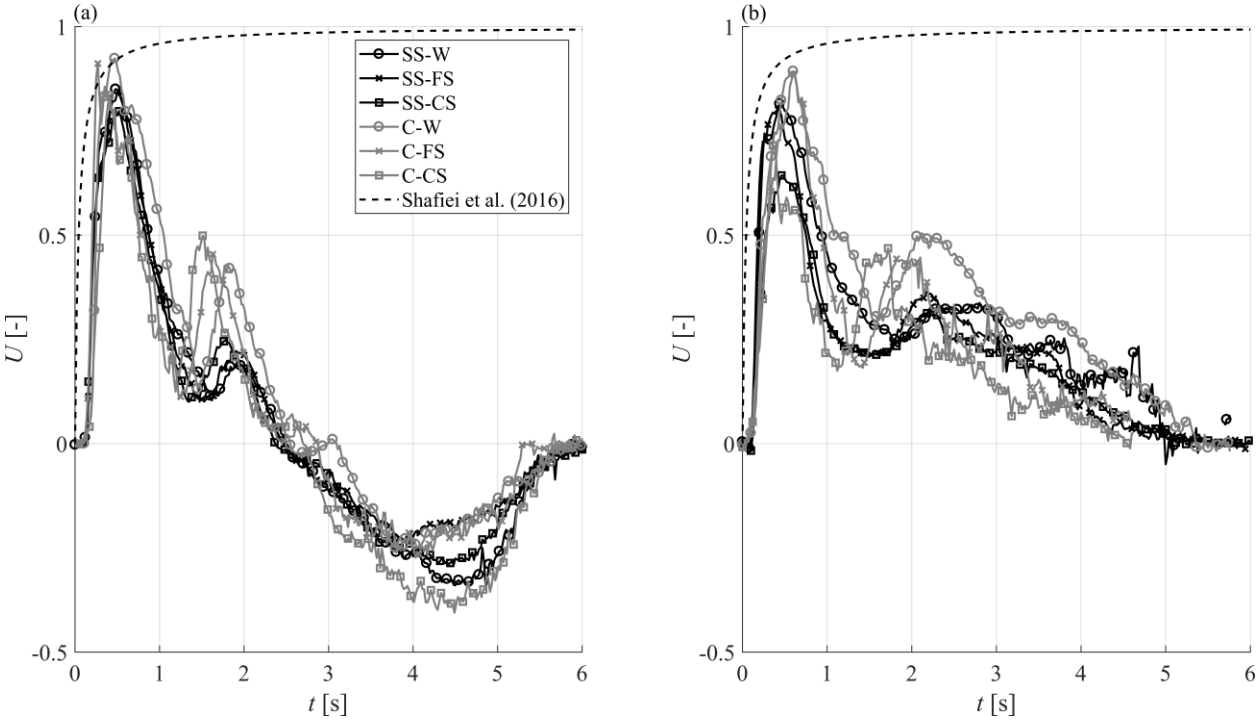

Fig. 3-10. Debris velocity (U) normalized by the mean wave front velocity at the debris site for (a) sloped bed and (b) flat bed. The dashed line shows the theoretical evolution of the debris velocity from Eq. (2-2).

The debris rapidly decelerated due to the reduced flow velocity and shallower flow conditions causing grounding of the debris. The influence of the friction can be readily observed within this stage of the flow as the debris with the greater coefficients of friction tended to have a sharper reduction in velocity. The later results in a reduced longitudinal displacement of the debris in the first stages of the flow. However, due to the closer proximity to the shoreline, the increased water depth and flow velocity as a result of the secondary wave results in the debris with the greater friction having a larger and earlier secondary velocity peak. For the flat bed case (Fig. 3-10b), the debris continued propagating until the flow depth was insufficient and permanent grounding occurred.

For the sloped bed case, due to the drawdown of the wave, the debris were then washed in the offshore direction, resulting in the negative velocities observed in Fig. 3-10a. Similar to the secondary wave, the debris with the greater coefficient of friction experienced greater flow depths and velocities due to their proximity to the shoreline resulting in increased offshore velocity. Rueben et al. (2014), in a study of the motion of generic boxes in a broken bore, found that the onshore velocities were approximately 4 to 6 times greater than the offshore velocities. In this study, the ratio of onshore to offshore velocities was 2.5

to 4. The discrepancy between this study and that of Rueben et al. (2014) is likely due to the gentler composite slope (1:30 to flat bed) used by the later which resulted in reduced off-shore flow velocities.

3.1.4 Discussion

This study examined the transport of debris in a tsunami-like wave, however, as was noted in the Hydrodynamics section, the wave profile used within this study has a flow duration an order of magnitude lower than that of an actual tsunami event (Madsen et al. 2008). As the influence of the friction within this study primarily occurred during the initial entrainment (and re-entrainment) of the debris, the longer duration of the flow may result in a less significant influence of friction on the maximum spreading area of the debris. Therefore, the conclusions of this study should only be used in addressing the incipient motion of the debris. Weiss and Diplas (2015) noted, in a parametric study of boulder transport in tsunami and storm waves, that the duration of the flow above the critical entrainment force (impulse) dictated if a boulder would be mobilized. While in this study the debris were mobilized in all cases, the duration of flow in smaller wave conditions may become a crucial parameter. To the authors' knowledge, no study has examined entrainment criteria considering the impulse approach for positively and neutrally buoyant objects such that further research is needed to address this issue.

While this study does not address the development of an analytical equation assessing debris transport, the conclusions drawn from this study are critical in its future development. There are essentially four phases of transport, for positively buoyant debris, that need to be addressed: initiation of motion, entrainment, fully entrained, and grounding. The initiation of motion requires several considerations related to the type of motion. A force and moment balance on the object would need to be simultaneously assessed to determine whether the object would initially slide, saltate, or roll. Therefore, as was shown in this study, the friction between the debris and the bed will be of critical importance. The entrainment of the debris would be dependent on the buoyancy of the debris: the more buoyant the object, the more easily it would be entrained. Within the fully entrained phase, for positively buoyant debris, Eq. (2-2) has been shown in several studies to approximate the displacement of debris (Shafiei et al. 2016b, Stolle et al. 2017a). For the grounding phase, essentially the same parameters as the entrainment and initiation of motion would be relevant, resulting in the deceleration of the debris motion as it once again comes in contact with the bed. The critical challenge within all these phases is coupling the force balance with a hydrodynamics solution capable of capturing the varying local flow velocity and water depth which, as shown, is also influenced by the flow resistance. Furthermore, this study also showed that the slope of the bed also plays a decisive role in determining the displacement of the debris.

While this study focused on the onshore conditions for debris transport, Fig. 3-10 showed that offshore debris velocity can reach up to 40% of the onshore velocity. Additionally, due to overtopping of the wave into the still basin and the relatively short duration of the flow, the offshore velocity could exceed the measured values within this study. Limited studies have addressed the offshore motion of debris due to the wave drawdown and limited guidelines exist within the current standards and guidelines. Further research is needed to address this important aspect of the debris as this study has shown that the velocities can reach magnitudes large enough to cause structural damage if not properly addressed.

This study is limited to addressing the motion of a single type of debris in an idealized setting. Matsutomi (2009) noted in a study of driftwood motion that the shape of the object played a significant role in the acceleration and orientation of the debris within the flow. The orientation can alternatively have an effect on the acceleration as it has an influence on the added hydrodynamic mass. Moreover, while previous studies have shown that the debris velocity does not exceed that of the wave front (Rueben et al. 2014, Yao et al. 2014, Stolle et al. 2017a), these studies have also been performed under idealized topographical

(flat) conditions. The presence of bed features and obstacles may cause flow accelerations that have a significant influence on the maximum debris velocity.

3.1.5 Conclusions

The study outlined herein examines the influence of friction on the entrainment and transport of 1:50 geometrically-scaled shipping containers over a sloped and flat surface in tsunami-like flow conditions. For the first time in a study pertaining to debris motion, the friction was varied through the bed friction as well as the skin friction at the surface of the model shipping containers and by using multiple initial debris configurations were used to analyze the influence of their number. Based on the results of this study, the following conclusions can be made:

- The obvious assumption that the initial position of the individual debris had an influence on the spreading angle could be confirmed. Asymmetric water depths and turbulent eddies formed by the obstruction of the debris were the likely cause of the difference in lateral displacement.
- The variation of skin and bed friction was observed to have no significant influence on the spreading angle of the debris.
- The friction had a however a significant influence on the longitudinal displacement (in the flow direction) of the debris. Due to the reduced flow velocities caused by the bed friction and due to greater forces required to initially entrain (and re-entrain) the debris, longitudinal displacement was reduced.
- The number of debris did not have a significant influence on the longitudinal displacement of the debris. As the debris were placed in a single row in this study, limited inter-debris interactions occurred, which previously had been shown to reduce longitudinal displacement (Nistor et al. 2016).
- The debris velocity reached between 80-90% of the wave front velocity. The offshore velocities were consistently 2.5 – 4 times less than the onshore velocities.

This study provides an exploratory examination on the influence of friction on debris entrainment and transport. Due to the relatively short duration of the wave used within this study, the conclusions reached should only be applied to the incipient motion of the debris. The study also only examined a single hydrodynamic boundary condition, field surveys of disaster-stricken communities showed that several wave types can occur in the event of a tsunami, dependent on the local topography (Takahashi et al. 2011). Due to challenges related to the measurement of flow conditions around the debris, the use of these results to calibrate a numerical model may be necessary to fully evaluate the phenomenon around debris motion.

3.1.6 Link to Section 3.2

The study presented here examined the variables that influence debris transport of a flat surface. The results of this study were used to provide a basic understanding of debris dynamics to be extended into a probabilistic model in the following sections.

3.2 Probabilistic Investigation and Risk Assessment of Debris Transport in Extreme Hydrodynamic Conditions

Preprint of an article printed in Journal of Waterways, Ports, Ocean, and Coastal Engineers © 2018 American Society of Civil Engineers. https://ascelibrary.org/doi/abs/10.1061/(ASCE)WW.1943-5460.0000428

3.2.1 Objectives

While the previous literature has focused on the physical phenomena related to debris transport in extreme hydrodynamic conditions, each discussed the stochastic nature of the debris transport. While the randomness of debris motion was acknowledged by most authors as a crucial aspect, little work has been accomplished to probabilistically investigate how debris tend to spread out from their initial location. Reasons as to why this goal has been difficult to investigate are twofold: first, in-situ studies only allow to analyse debris distribution from a singular event, and, secondly, many past experimental programs lacked sufficient repetitions which would have provided the required data to assess data from a probabilistic perspective. Hence, this study investigates for the first time debris spreading using a probabilistic approach which involved a sufficiently large number of test repetitions while providing a framework to probabilistically describe debris' spreading. With the long-term objective of assessing the risk related to extreme debris loading, the specific objectives of this study are:

- Evaluate the influence of the hydrodynamic forcing factor, namely a dam-break wave generated by the sudden release of water impounded in the reservoir section with various initial depths, on wave velocity profile and the debris spreading.
- Study the influence of multiple debris configuration at initial origin on debris spreading and their velocity time-history.
- Investigate the probabilistic properties of debris transport and spreading and propose a framework to guide future studies in this regard.

3.2.2 Experimental Setup

Experimental Facilities

The experimental work presented in this paper was performed in the Hydraulic Laboratory of the University of Ottawa (Ottawa, Canada) in the High-Discharge Flume (Fig. 3-11) as part of a joint research collaboration program between University of Ottawa, Canada, and Universität Hannover, Germany. The experimental flume was modified to simulate a harbour area with a flat horizontal topography.

The flume was 30 m long, 1.5 m wide, and 0.80 m deep. The impoundment reservoir which was used to generate the dam-break wave was 21.55 m long with the full 0.80 m depth. The flume was fitted with a swing gate placed on top of a 0.20 m high horizontal false floor, which was installed in the flume to avoid damaging the protective membrane of the flume. The false floor was 8.45 m long (see Fig. 3-11). The false floor was painted with a mixture of paint and sand particle (mean grain size (d_{50}) = 0.001 m). A steady-state test was performed to determine the Darcy-Weisbach friction coefficient which was determined to be 0.014 for the entire length of the false floor. The swing gate was fitted with a counter-weight (12.5 kg) which helped increase the opening velocity of the gate. The rapid gate opening was critical in ensuring the generation of a well-defined dam-break wave (Lauber and Hager 1998).

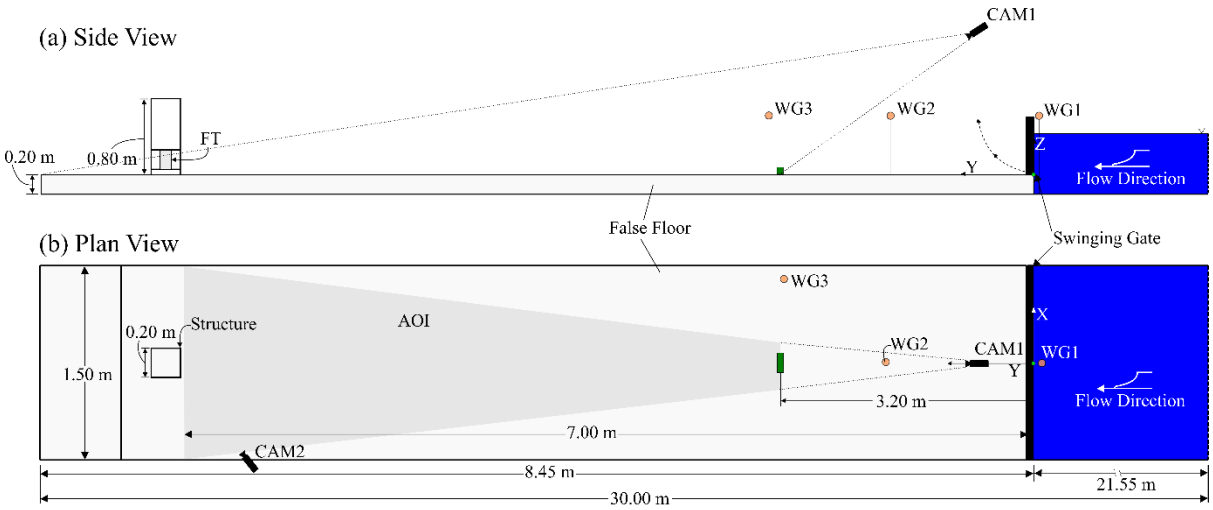

Fig. 3-11. University of Ottawa dam-break flume showing the position of the structure, the swing gate, the impoundment reservoir, the false floor and instrumentation used as well as its location.

The origin of the right-handed reference system was placed center-flume on the upstream edge of the swing-gate. The positive *x*-direction was to the right when facing the upstream direction, positive *y*-direction was in the flow direction, while positive z-direction pointed upwards.

A free-standing structure was placed at a distance of 7.03 m downstream of the swing gate and was used in a series of experiments examining debris impact loads. As the dam-break flow conditions were initially supercritical ($Fr > 1$) and the debris propagated within the bore front, additionally, the analysis in the following section truncated the presented results to a point 0.5 m from the front of the structure. Therefore, the presence of the structure did not influence the results presented in the following sections.

Debris Model

The 1:40 scale of the experiment was set using the Froude similitude. The individual debris was modelled as a fully-loaded 6.1 m long x 2.4 m wide x 2.4 m high shipping container, 14 400 kg at prototype scale (Knorr and Kutzner 2008). The debris model had dimensions of 0.06 m x 0.06 m x 0.15 m, with a mass of 0.226 kg, and was hollow, with a wall thickness of 0.005 m. The debris were made from high-molecular weight polyethylene (PE-UHMW) with a material specific gravity (SG) = 0.93. The design and weighting of the model debris, as a result of the presence of instrumentation within the debris, resulted in a draft of 0.025 m in still water. For each experimental test, the debris was placed at a distance of 3.20 m from the gate. Before the beginning of each test, the debris was dried and the excess water was removed from the flume bed. Debris were smothered with petroleum jelly to reduce water infiltration inside the debris models.

The debris was designed to have a solid green color to ensure significant contrast between the debris and the flume bed. Using the camera-based object tracking algorithm, developed by Stolle et al. (2016), the debris were tracked throughout the area of interest (AOI) shown in Fig. 3-11. The object tracking algorithm was tested in similar experiments as presented in Stolle et al. (2016) with in a position determination error of 0.01 m – 0.03 m.

The theoretical coefficient of static friction between the debris model and the false floor surface was approximately 0.4 (Malhotra and Subramanian 1994). The suggested coefficient of static friction used in the design of shipping containers (for transportation guidelines) is 0.3 (GDV 2003). The initiation of

motion of the debris resulted in the immediate floating of the debris, resulting in little influence of the dynamic friction on the motion of the debris.

Instrumentation

The location of the instruments utilized in these experiments is shown in Fig. 3-11; instrumentation was used to collect in parallel data on the hydrodynamic forcing factor and the resulting debris motion. The data provides the basis for the probabilistic analysis in this study. The raw data was collected using two data acquisition (DAQ) systems (HBM MX840B and HBM MX1601B), synchronized using a FireWire (IEEE 1394) connection. The water surface elevations were measured using capacitance-type wave gauges (WG) with a sampling rate of 1200 Hz. Each of the WG were calibrated before installation with a calibration coefficient greater than 0.99. WG1 was placed within the reservoir, immediately upstream of the swing gate (y = -0.01 m) to act as a reference point for its opening. The incipient drop in the water level recorded by WG2 was taken as time origin, t = 0.000 s. WG2 and WG3 were placed 2.00 m and 3.20 m, respectively, downstream from the gate to measure the time-history of the water surface elevation of the propagating bore, a result of the almost instantaneous opening of the gate impounding the water volume.

A HD camera (CAM1) was placed to analyze the motion of the debris as the debris propagated through the AOI. CAM1 was externally triggered with a 25 Hz trigger signal output from a third DAQ system (National Instruments USB-6009). WG6 was additionally used to evaluate the synchronization between the DAQ systems and camera system. Six reference points were placed within the AOI to geo-reference each image within the flume coordinate system.

Experimental Protocol

The experimental protocol was separated into four categories, as shown in Table 3-5. The experimental work focused partly on the influence of the hydrodynamic forcing factor, the dam-break wave generated by the 0.20 m or 0.40 m impoundment water depth behind the gate in the reservoir section of the flume (h_0). The initial configuration of the debris was of interest and the guiding question was: how will debris placed with the long axis perpendicular to the flow direction (0^o) or with the long axis of the debris parallel to the flow direction (90^o) influence how debris would eventually spread? Each experimental test was repeated at least fourteen (14) times.

Table 3-5. Experimental Protocol

Experimental Test	Impoundment Depth [m]	Initial Debris Orientation [^{o}]	Experimental ID [#]	Number of Repetitions [#]
E01	0.40	0	254-263, 274-283	20
E02	0.20	0	219-222, 294-303	14
E03	0.40	90	101-110, 264-273, 284-293	30
E04	0.20	90	111-120, 223-226	14

3.2.3 **Results**

Hydrodynamics

The hydrodynamic forcing factor used in this experiment was a dam-break wave. In recent years, the generation of dam-break waves has been one of the methods used to physically model the inland inundation due to a broken tsunami wave (Imamura et al. 2008, Al-Faesly et al. 2012, Shafiei et al. 2016b). Chanson (2006) demonstrated, using data from the 2004 Indian Ocean Tsunami, that of the

characteristics of an instantaneous dam-break were similar to those of an inundating bore propagating over a coastal plain. Additionally, the dam-break wave has a longer flow duration than solitary waves, especially when a sufficient impounding reservoir length is provided. The unrealistic wave period of solitary waves traditionally used to model tsunami waves was one of the primary drawbacks to other tsunami physical modelling techniques (Madsen et al. 2008).

Fig. 3-12 shows the measured time-history of the water surface elevations recorded by the three WG, whose location is shown in Fig. 3-11. The mean water depths obtained over the test repetitions are displayed as solid lines with the 95% confidence interval indicating the accuracy of the water surface measurements. For both the 0.20 m impoundment depth and the 0.40 m impoundment depth, the results showed good repeatability of the water surface elevations and the arrival times of the bore front at each wave gage. The time-averaged standard deviation in water surface elevation was 0.0078 m and 0.0019 m for the 0.40 m and 0.20 m impoundment depths, respectively.

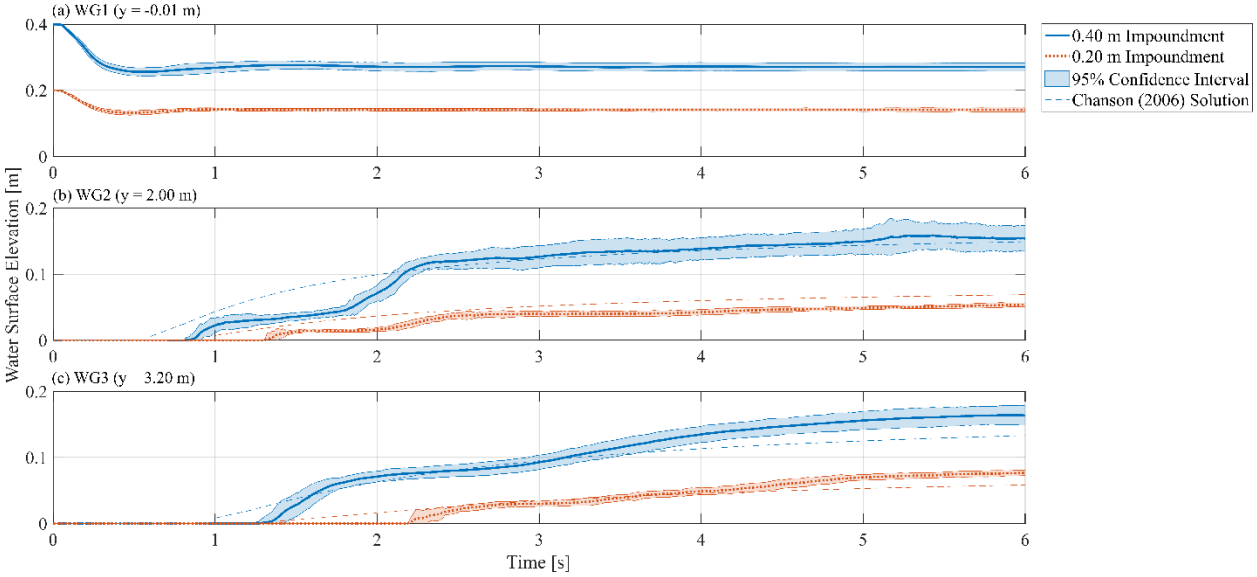

Fig. 3-12. Averaged time-history of the water surface elevation profiles for 0.20 m and 0.40 m impoundment depths for: (a) WG1 (y =-0.01 m); (b) WG2 (y = 2.00 m); and (c) WG3 (y = 2.40 m).

The results of the inundating bore were compared to the analytical solution of a dam-break wave proposed by Chanson (2006). The Chanson (2006) solution builds upon the Ritter (1892) solution for a dam-break wave propagating over a frictionless surface in a semi-infinite reservoir, by including the frictional effects in the rounded tip of the bore front. Using the arrival of the bore front at WG5 and WG6, the average bore front velocity at the debris site was 2.46 m/s and 1.35 m/s for the 0.40 m and 0.20 m impoundment depths, respectively. Using the Chanson solution, the velocity of the bore front at the initial location of the debris site was estimated to be 2.65 m/s and 1.68 m/s, which slightly over predicted the velocity.

As can be observed in Fig. 3-12, the bore front arrived later than predicted by the analytical solution and, additionally, the bore was not as steep as predicted by the same solution. The time-averaged difference of the bore front arrival between the experimental results and the analytical solution was 0.0132 s and 0.0157 s for the bores generated by the 0.40 m and 0.20 m impoundment depths, respectively. The discrepancy between the bore front and the analytical solution was likely a result of the design of the swing gate. To ensure proper gate sealing, two metal columns protruded 0.06 m into the cross-section of

the flume were set on the later sides of the gate frame. The protrusion resulted in the formation of cross-waves as a result of the flow acceleration into the shielded areas behind the columns. The influence of the cross-wave can be observed by the rapid increase in water surface elevation around ~1 s after the bore arrival, similar effects were observed as a result of cross-wave in Khankandi et al. (2012). As debris propagated within the initial phase of the bore, the influence of the cross-waves was negligible.

Debris Transport

As discussed in the introduction, in assessing the vulnerability to debris impact and subsequent potential structural failure, two aspects to consider are the debris spreading angle (the lateral displacement of the debris), which would determine the likelihood of debris impact; and debris velocity in the onshore (positive y) direction, which would influence the maximum impact force. The following section will examine the stochastic properties of the debris trajectory, defined as the propagation path of the debris geometric centroid, solely as a result of the inundating wave. Using the camera-based object tracking algorithm discussed in "Debris Model", the debris were tracked as they propagated through the AOI. Due to the flat, horizontal bed as well as to relative size of the flume, the debris spreading as a result of drawdown was not considered. The subsequent section addresses the debris velocity profile.

Fig. 3-13 outlines a typical debris transport mechanism of the debris in the E01 and E03 cases. The difference between the debris transport trajectories can be observed as E03 resulted in a larger deviation in the lateral direction due to the rotation of the debris. Previous studies using the same type of debris showed that the equilibrium orientation of the debris was with the long axis perpendicular to the flow direction (Stolle et al. 2015, 2017a). In the case of the debris initially placed with the long axis perpendicular to the flow direction (Fig. 3-13a), little to no rotation of the debris occurred which resulted in a relatively uniform force acting on the cross-section of the debris facing the incoming flow. However, in the case of the long axis of the debris placed parallel to the flow direction (Fig. 3-13b), the debris was rotated towards the equilibrium orientation, resulting in an uneven distribution of forces onto the cross-section of the debris, forcing thus the debris to deviate from the central axis of the flume.

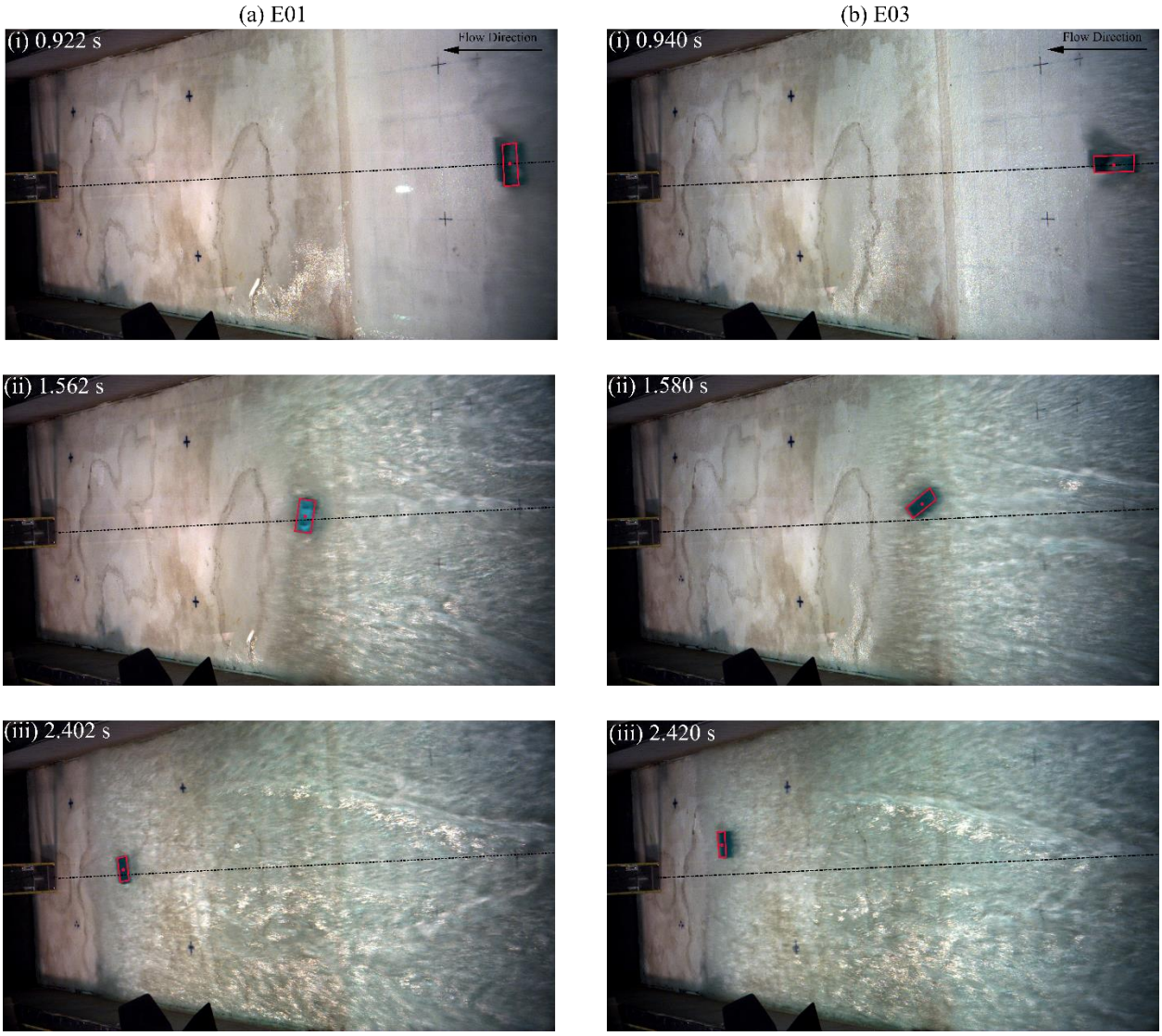

Fig. 3-13. Comparative images depicting the debris transport through the AOI for E01 and E03. The box outlines the top-most face of the debris tracked by the object-tracking algorithm. The internal point represents the centroid of the debris which was used to estimate the displacement of the debris. The black dashed line represents the central axis of the flume.

Debris Spreading

Fig. 3-14 details the debris trajectories for each of the categories listed in Table 3-5. Each test shows the mean trajectory, as a solid line, and the 95% confidence interval, as a shaded patch. Within each figure, the trajectory is compared to the spreading angles proposed by Naito et al. (2014) (dotted line) and Nistor et al. (2016) (dashed line). Table 3-6 displays the statistical parameters related to debris transport. A Bartlett test (Snedecor and Cochran 1989) was performed over the entire length of the AOI, with a null hypothesis that all the categories come from population with the same variance. The Bartlett test was performed to determine if any significant deviations occurred along the AOI. These deviations would potentially influence the distance-averaged values or be the result of a significant topographical or hydraulic feature. The *p*-value was above 0.05 throughout the AOI and, therefore, spreading distance and standard deviation displayed in Table 3-6 were averaged across the trajectory of the debris. The mean

trajectory was shown to compare to the commonly used assumption that the debris trajectory can be approximately estimated as a straight line. The mean and maximum standard deviation are displayed to show the variation of the debris trajectory.

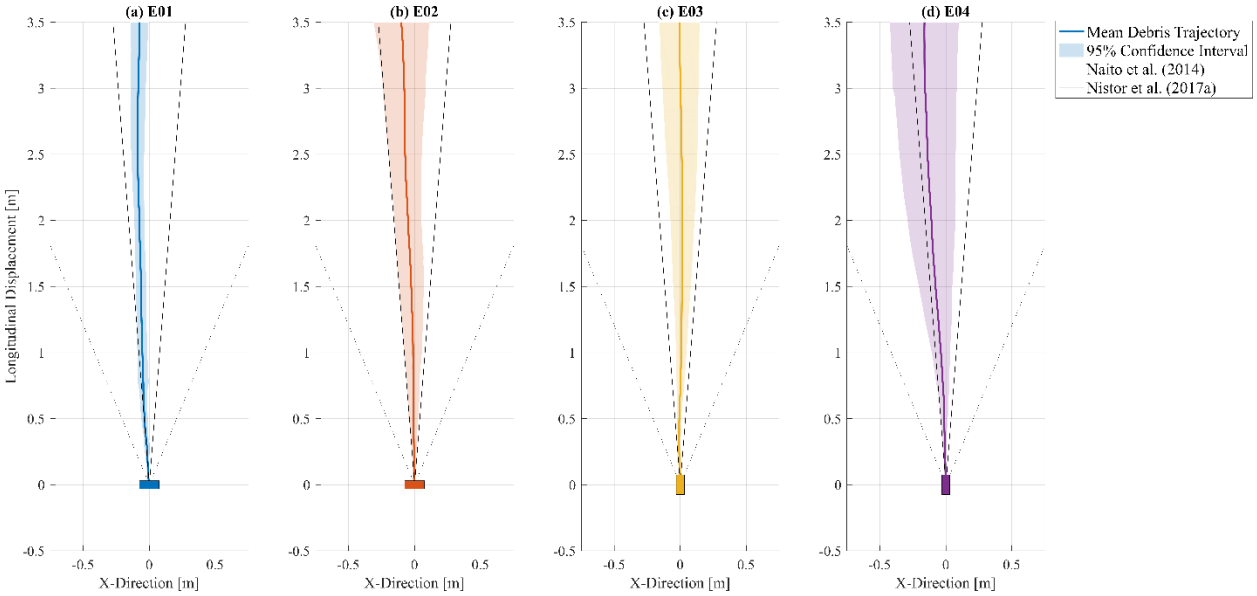

Fig. 3-14. Debris mean trajectory for each of the experiments tests: (a) E01, (b) E02, (c) E03, and (d) E04. The trajectories are enclosed by the 95% confidence interval (shaded region). The predicted spreading angles from Naito et al. (2014) (dotted line) and Nistor et al. (2016) (dashed line) are displayed in black.

Predominantly, the debris was enclosed within the proposed spreading areas. However, in the case of E04, the debris propagated outside of the exposed spreading area proposed by Nistor et al. (2016). In both methods of estimating the propagation paths, the proposed spreading area assumed that the mean trajectory would be a straight line. As can be observed in Table 3-6, the mean trajectory was not a straight line, resulting in the overlap of the debris spreading area with the predicted spreading area. As can be observed in both Fig. 3-14 and Table 3-6, within each category, there was a slight bias to in the negative x-direction. Previous studies have indicated a straight trajectory has generally been observed in steady-state conditions (Bocchiola et al. 2006, Matsutomi 2009). As the bias was in the same direction between the categories, the deviation of the trajectory could be a result of non-uniformity of the friction or topography across the flume bed. The formation of the cross-wave as a result of the constriction at the gate formed a distinctly 3-D wave profile, which could cause lateral debris deviation due to the water surface slope. However, cross-waves did not form until after the initial wave front had passed the debris site, as can be observed by the stepped wave profile in Fig. 3-12b at around 2.0 s. Therefore, the cross-waves were unlikely to have had a significant influence on the consistent deviation. The deviation trend in the negative direction in each case suggests that these inconsistencies were common across experiments. Therefore, any additional deviations related to the manual opening of the gate did not represent a major source of inaccuracies.

Table 3-6. Distance-average statistics related to the debris trajectory for the four experimental categories.

	Trajectory Statistics			Trajectory Distribution	
Experimental Category	Mean Spreading Distance [m]	Mean Standard Deviation [m]	Maximum Standard Deviation [m]	Two-sided *t*-test *p*-value ($\alpha = 0.05$)	Shapiro-Wilk test *p*-value ($\alpha = 0.05$)
E01	-0.075	0.025	0.036	1.17×10^{-9}	0.379
E02	-0.056	0.064	0.108	0.042	0.539
E03	0.009	0.053	0.079	0.337	0.336
E04	-0.118	0.096	0.134	8.50×10^{-4}	0.683

In the cases with smaller impoundment depths, the debris had a wider variance around the mean, associated with the standard deviation of the trajectory (Fig. 3-14b and d); reasons for this behavior lie in the physics of the entrainment and advection processes by which the debris are transported. As a result of the smaller water depths, the debris come in contact with the flume bed more often and over longer durations as the water depth to draft ratio is smaller than for the waves generated by larger impoundment depth. This contact of the debris resulted in them pivoting around their contact point as frictional forces would initiate torque around the debris' center of mass. This would additionally change the exposed surface area facing the forcing flow which in turn causes the debris to deviate from their previous trajectory vector, therefore resulting in a wider spreading area. At each instant of grounding, deviation could potentially lead the debris closer to or further away from to the ideal straight propagation path, with increased grounding eventually resulting in larger deviations overall. The pivoting of debris hence influenced the maximum spreading area of the debris. The equilibrium orientation of the debris was with the long axis of the debris perpendicular to the flow direction, which counters previous results in steady-state conditions experimental work (Bocchiola et al. 2008). Matsutomi (2009) suggested that the slenderness ratio (length divided by width of debris) influenced the propagation characteristics of the debris, though this study does not examine multiple slenderness ratios to evaluate that aspect of the propagation. As a result, the debris initially parallel to flow (E03 and E04) would pivot to propagate perpendicular to the flow. As described by Fig. 3-13, the rotation of the debris towards the equilibrium propagation orientation resulted in asymmetric forces acting around the debris centroid causing the debris to pivot about the central vertical axis. The resulting pivoting caused an increase in the spreading area as well as its variance associated with each experimental category.

While debris propagation has been examined in a variety of experimental settings (Imamura et al. 2008, Matsutomi et al. 2008, Matsutomi 2009, Naito et al. 2014, Rueben et al. 2014, Goseberg et al. 2016b, Nistor et al. 2016), one of the primary comments in most of the analysis conducted in these previous studies was related to the probabilistic nature of debris motion, yet this was never explicitly demonstrated. One of the most commonly used statistical distributions, and one of the key assumption in many statistical tests (Rachev 1991), is the Gaussian distribution. As discussed earlier, there was a bias related to the flume bed, therefore the normalcy of the data was tested around the mean trajectory. As the real mean and variance was unknown, the Shapiro-Wilk test (Shapiro and Wilk 1965), in which the null hypothesis states that the distribution of the data is normal, was selected. A reliability level (α) of 5% was selected to be consistent with previous debris propagation studies. The resulting distance-averaged *p*-values are shown in Table 2. In each case, the *p*-value exceeded 0.05 suggesting that the debris trajectory was

normally distributed around the mean trajectory and thus, the previously assumed normalcy of the processes involved could be, for the first time, used with confidence.

As stated in the introduction, in previous studies analyzing debris trajectory, debris tended to propagate in a straight line. A two-sided *t*-test (Table 3-6), with a null hypothesis that the spreading distance comes from a normally distributed function with a mean of 0 m, indicated that E02 and E03 were not significantly different than the expected 0 m (corresponding to a straight line). While E01 and E04 showed a significant difference (p-value << 0.05), the trend of the mean trajectory in the negative x-direction suggests that the difference was likely the result of the experimental facilities and was not influenced by the inherent statistical nature of the process. While the lateral displacement was statistically different than 0, the standard deviation and mean lateral displacement were less than the length of the debris. From a practical engineering perspective, the difference would not be significant and the assumption of a straight trajectory would still hold.

A quantified analysis of each experimental category was performed to evaluate the difference between each experimental category. For this comparison, a two-sample *t*-test was performed between each experimental category (Rachev 1991), in which the null hypothesis states that the two categories come from distributions with equal means and variances. As shown in Table 3-7, the categories were not significantly different. E03 appears to be the only category that was significantly different, with each comparison consistently resulting in the lowest p-values. As the difference between category means was not significant, the negative deviation of the debris was common between experimental categories and therefore a result of a factor common between experimental categories, in this case most likely the bed surface.

A second evaluation was performed to analyze the difference in the standard deviations between the experimental categories. A two-sample *F*-test (Box 1953) was performed, with a null hypothesis that the two categories come from normal distributions with the same variance.

Table 3-7. Comparison p-values between trajectory profiles of the experimental categories.

	Two-sample *t*-test ($\alpha = 0.05$)				Two-sample *F*-test ($\alpha = 0.05$)			
Experimental Category	E01	E02	E03	E04	E01	E02	E03	E04
E01	--	0.293	4.76×10^{-5}	0.185	--	0.002	0.065	5.17×10^{-4}
E02	0.293	--	0.004	0.065	0.002	--	0.342	0.220
E03	4.76×10^{-5}	0.004	--	3.30×10^{-6}	0.065	0.342	--	0.006
E04	0.182	0.065	3.30×10^{-6}	--	5.17×10^{-4}	0.220	0.006	--

As shown in Table 3-7, significant differences were observed between the experimental categories, particularly in the case of E01, where relatively small standard deviations were observed. A comparison between the p-values of the impoundment depth influenced more significantly the variance than the initial orientation of the debris, with the standard deviation increasing with lower impoundment depths. Additionally, a difference can be observed in both Table 3-7 and Fig. 3-14 between the standard deviations of the cases with the same impoundment depth and different orientations. As described above, the rotation of the debris towards the equilibrium orientation resulted in asymmetric forces acting on the debris causing increased lateral spreading.

Debris Velocity

The second issue related to the debris impact forces was the need to assess the impact velocity of the debris. Based on Eq. (2-2), the debris velocity is limited by the bore velocity (u_b), which was defined in Shafiei et al. (2016b) as the flow velocity directly behind the bore front, assumed to be constant.

Fig. 3-15 shows the mean on-shore (y-direction) velocity profiles, as a solid line, along with the 95% confidence interval (the faded area) for each experimental category, for two different initial debris orientations: 0 and 90 degrees. The velocity was normalized by the wave celerity ($\sqrt{gh_0}$). As can be observed in Fig. 3-15, there is initially a high standard deviation, particularly for E01 corresponding to an impoundment depth of 0.4 m, which was related to the overtopping of the debris during the initial entrainment phase which resulted in the temporary occlusion of the debris from the camera. The mean acceleration distance, defined as the distance travelled by the debris to reach maximum propagation velocity, is shown as a dashed line and is compared to the acceleration distance for steady-state velocity which was proposed by Matsutomi (2009).

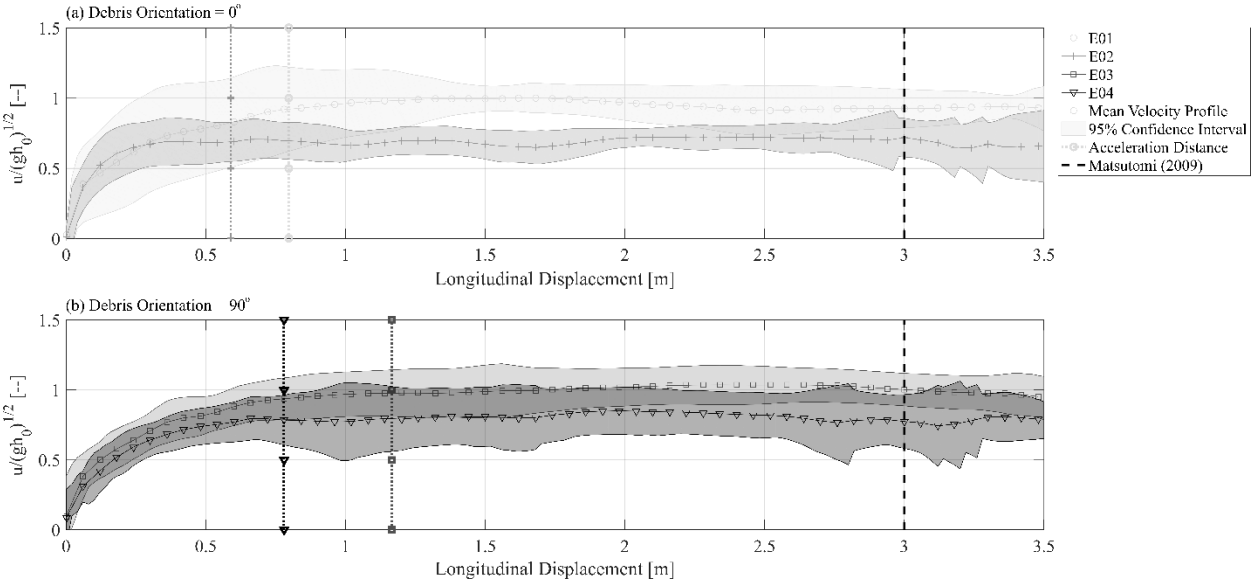

Fig. 3-15. Debris mean trajectory for each of the experiments tests: (a) E01, (b) E02, (c) E03, and (d) E04. The trajectories are enclosed by the 95% confidence interval (shaded region). The predicted spreading angles from Naito et al. (2014) (dotted line) and Nistor et al. (2016) (dashed line) are displayed in black.

Fig. 3-15 shows that the debris reached a quasi-equilibrium propagation velocity within the AOI after approximately 0.75 m from their initial location. Comparing the maximum velocities of each category, as expected, those with the larger impoundment depths consistently had a higher normalized propagation velocity. However, for all cases, the maximum velocity approximately approached unity. The discrepancy between the normalized velocities for the smaller impoundment depth may be a result of viscous scale effects. Lauber and Hager (1998) indicated that dam-breaks with an impoundment of less than 0.25 m showed viscous effects in the bore profile and, as discussed in "Hydrodynamics", the bore profile for the 0.20 m impoundment depth had a larger difference comparing to the analytical profile proposed by Chanson (2006).

The acceleration distances for all experimental categories were significantly smaller than the 20 times the length of the debris proposed by Matsutomi (2009). The deviation in the acceleration distances are likely due to the differences in both the hydrodynamic forcing factor and the differences in the type of debris.

The dam-break wave eventually reached a quasi-steady state flow velocity equal to $\sqrt{gh_0}$, however, the theoretical, initial bore front velocity is approximately $2\sqrt{gh_0}$, and tends towards the quasi-steady state velocity over the AOI (Chanson 2006). The flow velocity, initially higher due to the unsteady flow conditions, increased the acceleration of the debris, and therefore reduced the acceleration distance compared to the steady-state flow case. Comparing the results as a function of the initial orientation of the debris, the debris initially perpendicular to the flow direction (0^o) reached maximum velocity before the debris placed parallel to the flow direction (90^o). Considering Eq. (2-2), as all other variables are constant, the larger area of the debris projected to the flow resulted in increased acceleration. Shafiei et al. (2016b) additionally noted that the density of the debris influenced the contribution of the added mass of water in the case of debris impacts. Similarly, the differing densities between the type of debris used in this study and Matsutomi (2009) may influence the added mass of water acting on the debris throughout the acceleration process.

For a quantified analysis of the debris velocity, the mean normalized equilibrium velocity is shown in Table 3-8. The mean normalized velocity was considered to be the mean velocity from the distance taken for the debris to reach maximum velocity to the end of the AOI. The normalized velocity was tested using a two-sided *t*-test, where the null hypothesis was that the mean velocity was equal to the wave celerity. As it can be observed in Table 4, the mean equilibrium velocity was generally significantly different than the wave celerity. As discussed earlier, this was potentially a result of viscous scaling effects. Additionally, the friction associated with the flume bed was not considered within the wave celerity. In the case of the larger impoundment depths, the debris moved closer with the wave front. According to the analytical solution for a dam-break flow (Chanson 2006), the bore front velocity decays from $2\sqrt{gh_0}$ to the $\sqrt{gh_0}$ as the bore propagated, resulting in the increased velocities observed in Fig. 3-15. Therefore, given a sufficient propagation distance, the debris' velocity would likely reduce to $\sqrt{gh_0}$.

Table 3-8. Test statistics for the equilibrium velocity for each experimental category.

Experimental Category	Normalized Equilibrium Velocity ($\frac{\bar{u}}{\sqrt{gh_0}}$)	Standard Deviation [--]	Two-sided *t*-test ($\frac{\bar{u}}{\sqrt{gh_0}}$ = 1, α = 0.05)
E01	1.040	0.078	0.28
E02	0.754	0.067	8.47×10^{-6}
E03	1.095	0.080	0.001
E04	0.879	0.111	0.004

Probabilistic Approach for Debris Transport

In a similar problem in structural engineering, the Eurocode 1 – Action on Structures (EU 2006) addresses accidental impacts on structures, where the motion of an impacting object has a typical trajectory (e.g. car travelling along a road, a ship passing underneath a bridge) characterized by a normal distribution to determine the probability of accidental impact. As determined in "Debris Spreading", the spreading of the debris around the mean trajectory was normally distributed. As a result, in assessing the likelihood of debris impact, a normal probability density function (*P*) related to the position of the centroid of the debris could be utilized and can be expressed mathematically as follows:

$$P(x) = \frac{1}{\sqrt{2\pi}\sigma} e^{-\frac{(x-\mu)^2}{2\sigma^2}} \tag{3-3}$$

where x is the lateral spreading, σ is the standard deviation, and μ is the mean trajectory. As discussed in "Debris Spreading", in the cases presented in this study, the mean trajectory was significantly different than 0 m. However, as previously discussed, while the result was statistically significant, the magnitude

of the deviation was less than the length of the debris, making thus the difference not significant from a practical engineering perspective. Combined with previous studies conducted in steady-state flow conditions which indicated that the mean trajectory of the debris was approximately 0 m (Bocchiola et al. 2008, Matsutomi 2009), the assumption of a straight trajectory is likely valid. However, the influence of an irregular bed surface profile has not been examined in detail and may influence the validity of this assumption. In those cases, the difference in the trajectory was likely biased by inconsistencies in the experimental setup. Assuming that the mean trajectory would be at 0 m, the only variable should be the standard deviation. Within the context of the spreading distribution, the standard deviation (σ) is related to the spreading angle (θ) as proposed by Naito et al. (2014) and Nistor et al. (2016). Eq. (3-4) shows the relationship between the number of debris and the spreading angle, where the hydrodynamic forcing factor was not considered. Nistor et al. (2016) determined that an increased number of debris in an experimental trial resulted in an increase in the spreading angle due to inter-debris collisions. Additionally, Rueben et al. (2014) postulated that the presence of other debris within the vicinity of the debris of interest resulted in turbulent eddies which further influence the debris spreading. However, the influence of the turbulent eddies has not been confirmed within an experimental setting. Comparing to the current study, Nistor et al. (2016) used a different forcing factor in the form of a broken elongated solitary wave. However, Baldock et al. (2012) showed that a broken solitary wave propagating over a horizontal plane acts similar to a dam-break wave. Therefore, isolating the initial wave height of the solitary wave, 0.075 m from Stolle et al. (2017a), the following equation can be used to estimate the standard deviation:

$$\sigma = \frac{1}{h_0}\tan\theta\, d_{lon} = \frac{1}{h_0}\tan(0.277 + 0.06N)\, d_{lon} \tag{3-4}$$

where h_0 is the impoundment depth, N is the number of debris within the experiment and d_{lon} is the longitudinal displacement. Fig. 3-16 shows the change in the standard deviation across the 3.5 m AOI compared to the standard deviation predicted by Eq. (3-4). Eq. (3-4) (black lines) slightly underestimates the slope of the line of best fit by 16.5% and 14.5% for 0.20 m and 0.40 m impoundment depths, respectively. The discrepancy may be a result of the coefficients related to the influence of the number of debris, an aspect which was beyond the scope of this study. Moreover, the initial orientation of the debris was shown to have a significant influence on the standard deviation of the lateral spreading. As it can be observed in Fig. 3-16, the orientation influenced the debris lateral displacement between the cases with similar impoundment depths. However, as the influence of this parameter is affected by the equilibrium orientation of the specific debris type, which is dependent on the physical debris properties, such as slenderness ratio (Matsutomi 2009), the influence of the orientation was not considered in the present work. The moment of inertia (I) also has a significant influence on the angular acceleration around the debris centroid (Ikeno et al. 2016). Considering that only a single debris type was used in this study, further research on multi-debris motion is needed to fully investigate the influence of the initial orientation on Eq. (3-4).

Given the need of practitioners and planning engineers in the field of tsunami mitigation and engineering to estimate the lateral spreading for an analysis of site-specific vulnerability, the predictive Eq. (3-4) is hence an improvement, allowing to estimate the standard deviation from a mean trajectory based on a number of debris and their distance away from the initial location. While the limits to use this proposed equation lie within the bounds of the current study (number of debris, N < 18), future research will allow for a more sophisticated insight as the number of experimental datasets will hopefully increase.

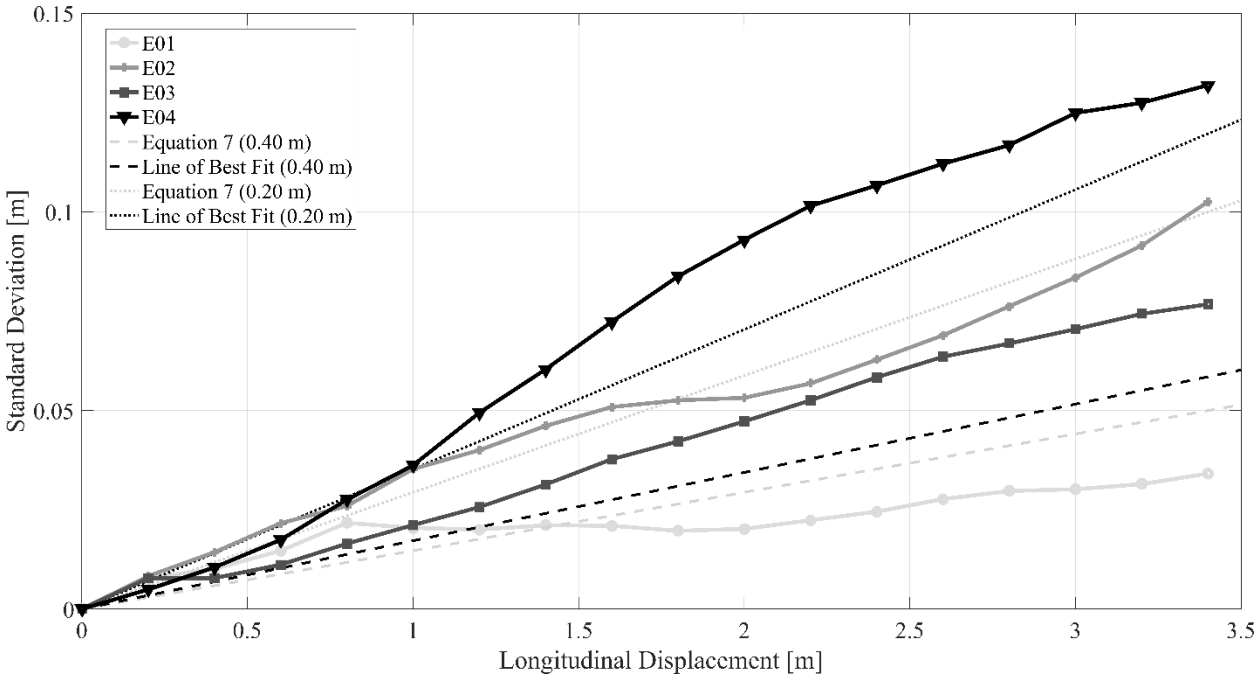

Fig. 3-16. Standard deviation as the debris propagated through the AOI compared to the predicted standard deviation from Eq. (3-4).

With an understanding of the change in the standard deviation as a function of longitudinal displacement, Eq. (3-4) can be applied together with Eq. (3-3) to develop a probability density function along the propagation path of the debris. Fig. 3-17 shows the probability distributions for the 0.20 m and 0.40 m impoundment depths, enclosed within the bounds proposed by Naito et al. (2014). Developing similar probability distributions from known debris sources, such as shipping yards in coastal communities, will allow local authorities to assess vulnerability of critical infrastructure to extreme debris impacts.

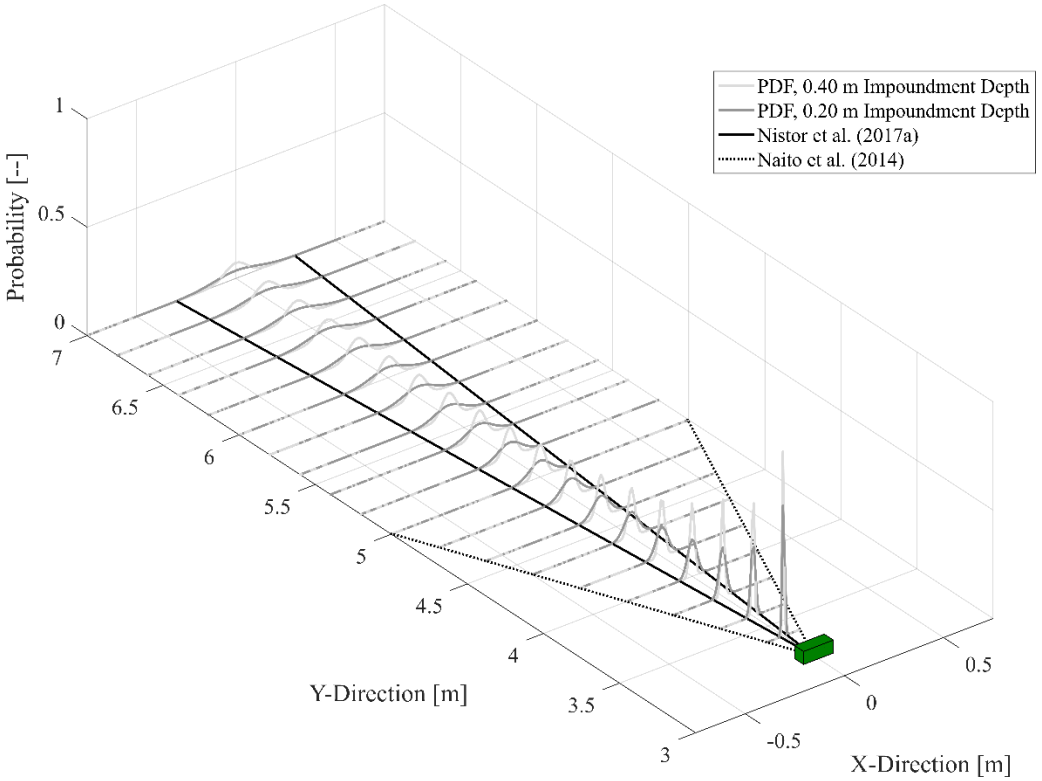

Fig. 3-17. Probability density function for the two different hydrodynamic forcing factors: bores generated by the 0.20 m and 0.40 m impoundment depths. The debris spreading bounds are displayed as a black line: Nistor et al. (2016) – solid and Naito et al. (2014) – dotted.

3.2.4 Discussion

Scale Effects

Investigating the debris transport processes requires the use of hydraulic scale models. Laboratory investigations are inherently based on the assumption of similarity of Froude numbers: the use of model scaled-down flow velocities based on maintaining the ratio of inertial to gravitational forces. This particular choice of scaling violates other scaling laws by introducing scale effects; these are discussed herein. The application of the dam-break wave in these experiments has a two-fold justification. Firstly, dam-break waves have commonly been used in tsunami engineering, particularly in studies related to hydrodynamic loads on near-shore structures (Palermo et al. 2009, Al-Faesly et al. 2012, St-Germain et al. 2013, Shafiei et al. 2016b). Chanson (2006) demonstrated the similarity between a broken tsunami wave propagating over dry land and the analytical solution for dam-break waves. The longer period associated with the dam-break wave is also more representative of that of a tsunami wave compared to previous methods of physically reproducing a tsunami wave (Madsen et al. 2008). Secondly, the dam-break wave has been comprehensively evaluated both in physical models (Lauber and Hager 1998, Khankandi et al. 2012) and theoretical studies (Ritter 1892, Chanson 2006). The application of analytical solutions allows for an easy comparison to experimental results and the prevalence of dam-break laboratory facilities allows for similar studies to reproduce and improve on the presented results.

This study examined the probabilistic nature of debris motion propelled by a dam-break wave. However, the relatively small-scale of the experiments resulted in potential scale effects that need to be addressed. The smaller impoundment depth (0.20 m) was smaller than the threshold impoundment depth from the comprehensive experiments performed by Lauber and Hager (1998) for viscous effects to influence the

dam-break bore propagation. However, the experiments performed by Lauber and Hager (1998) were only evaluated for one non-dimensional distance ($Y = \frac{y}{h_0} = 10$) from the gate, thus posing questions as to whether their criteria is comprehensively applicable along the propagation distance. Lauber and Hager (1998) noted that, in the far-field of propagation, the influence of many factors that influenced bore front profiles, such as the gate opening time, diminished and the wave profile approached that of the analytical solution. To additionally assess any influences of the surface tension on the initial entrainment of the debris, the calculated Weber number was in the range of 1924 to 2721, which significantly exceeds accepted critical values of 2.5 to 160 (Peakall and Warburton 1996).

Rueben et al. (2014) postulated that one of the factors influencing debris spreading was the formation of turbulent eddies. As turbulence generally does not scale well with Froude scaling (She and Leveque 1994), to avoid the influence of viscosity on the experimental study, the flow should be within the fully turbulent domain with Reynold's number (Re) > 12 500 (Te Chow 1959). As determining flow velocities for dam-break flow conditions tends to be difficult to assess, a slightly modified Re will be used (Jánosi et al. 2004):

$$Re = \frac{Uh}{\nu} \tag{3-5}$$

where U is the bore front velocity, h is the characteristic wave height behind the wave front, and ν is the kinematic viscosity. Using Eq. (3-5), the Re number at the debris site ranged from 1.50 x 10^5 - 1.67 x 10^5 for the 0.40 m impoundment depth and 4.87 x 10^4 – 5.17 x 10^4 for 0.20 m one. Hence, the Re number was maintained within the fully turbulent zone. However these numbers were significantly lower than ones that have been observed in the field: 10^6 (Bricker et al. 2015). Therefore, the turbulent boundary layer typically present in coastal flooding events was not reproduced in these experiments. Though, as the debris in these experiments tends to float in the upper portion of the flow, the boundary layer is unlikely to have had a significant influence on debris propagation.

The flume bed significantly influenced bore characteristics and debris propagation. As the experiments were run successively, water was removed from the flume bed; however a thin layer of water remained on the flume bed, which slowed down the bore propagation (St-Germain et al. 2013). Additionally, in undistorted models, the influence of bottom friction tends to be disproportionately greater at model scale for both the debris-bed and fluid-bed interactions (Hughes 1993). At the same time, prototype frictional elements on the ground of coastal areas such as medium-size vegetation, fences and other roughness elements do have an effect on the propagation of the tsunami inundation over dry terrain. Reproducing scaled-down roughness elements is difficult and researchers often resort to using a rather uniformly distributed equivalent friction instead. The difficulties in assessing these scale effects at the small-scale presented suggest that further research is needed to quantify these effects for use at prototype scale.

The flat, horizontal bed slope was chosen to represent an idealized coastal setting, where no gravitational acceleration affected the debris' motion as a result of the bed slope. Theoretical research into the influence of bed slope on dam-break wave propagation had shown that the wave front velocity would be reduced (Chanson 2005), and therefore, based on Eq. 3, the maximum debris velocity would be reduced. To the authors' knowledge, no research has examined the influence of bed slope on the lateral motion of debris. This represents a gap in the understanding of debris transport which requires further investigation.

Vulnerability Assessment of Debris Loads

As discussed in the Introduction section, assessing the vulnerability of coastal areas to debris impact has been difficult due to problems related to identifying debris sources and impact sites in the aftermath of a

tsunami event (Charvet et al. 2014). Building design guidelines and standards considered all areas are at-risk of debris impact (FEMA 2012, ASCE 2016a), whereas the consideration of debris loads in fragility curves analysis has been mostly ignored. Lin and Vanmarcke (2010) proposed a stochastic vulnerability model for wind-borne debris during extreme events. The basis of their model considered the distribution of debris entrainment, debris velocity, and debris trajectory. Within the vulnerability model, the debris trajectory model was modelled, similarly to this study, using a Gaussian distribution. The debris velocity was modelled using a Beta distribution, which is a continuous probability distribution to represent random qualities on the interval of [0,1] (Gupta and Nadarajah 2004), in this case as a ratio of the maximum debris velocity. The development of the Beta distribution of debris velocity within a tsunami-like flow was however outside the scope of this study.

Currently, debris entrainment parameters have yet to be fully developed with regards to unsteady flow conditions. However, basic force balance of a floating object can provide a starting point in determining the hydraulic condition needed to entrain debris (Nistor et al. 2017). However, Braudrick and Grant (2000) noted that, in steady-state conditions, logs were entrained slightly before the force balance suggest, stating also that future research was needed. Applying a similar vulnerability model as Lin and Vanmarcke (2010) to debris loads in extreme flooding events would be possible with further development of stochastic debris parameters, particularly with respect to debris impact conditions.

The application of a stochastic approach to debris motion could also help improve the analysis of the fragility curve for tsunami-prone coastal communities. Charvet et al. (2015) applied a binary method of assessing if a debris impact occurred. Using a probabilistic analysis of debris motion can improve the accuracy when assessing potential damage from debris impact by providing a better understanding of potential debris impacts. Hatzikyriakou and Lin (2017) modelled the 2012 Hurricane Sandy to examine both the positive and negative influences of seaward buildings on building survival rates by shielding and debris generation. The inclusion of surrounding buildings into fragility assessment improved the performance of fragility curves in their case study. Goseberg et al. (2016b) showed that the debris trajectory was not influenced by the presence of obstacles, the focus of the study was on the absolute magnitude of the spreading angle. The presence of major topographical features, as well as the presence of other debris, may influence the assumption of a normal distribution. Hence, further research is needed to evaluate this aspect. However, significant work is still needed to apply such methods particularly to extreme debris loads from large-scale debris, such as vehicles and shipping containers.

3.2.5 Conclusions

This study analyzes the motion of debris in extreme hydrodynamic conditions, focusing on a dam-break wave as forcing factor for debris motion. The debris were modelled as a scaled-down shipping containers and were tracked using a camera-based object tracking algorithm developed by Stolle et al. (2016). Four experimental categories were examined for two hydrodynamic forcing conditions and two initial debris configurations. The analysis investigated the probabilistic nature of debris motion, concluding that:

- The hydrodynamic forcing condition had a significant influence on the debris (lateral) spreading. In the case of the dam-break waves generated with a larger impoundment depth, less lateral spreading occurred.
- The initial placement configuration of the debris did have a significant impact on the standard deviation of the lateral spreading. Additionally, the initial placement configuration had a significant impact on the debris acceleration distance to reach equilibrium propagation velocity.
- The debris spreading was normally distributed around the mean debris trajectory.

- The standard deviation of the debris distribution increased with longitudinal displacement of the debris.
- The equilibrium propagation velocity of the debris can be modelled as approximately the dam-break wave celerity ($\sqrt{gh_0}$).

The application of the probabilistic nature of debris motion could significantly improve the accuracy of fragility curve analysis by better predicting both the probability of a potential impact and its maximum impact force. While significant research is still needed to address issues related to the scaling of debris motion in laboratory conditions, a basic understanding of debris spreading distribution could improve the already well-developed fragility curves and eventually be included in comprehensive vulnerability models.

3.2.6 Link to Section 3.3

The investigation of the motion of a single debris piece was used to provide preliminary insight into debris motion to be extended into more complex conditions. The following section examines the motion of multiple debris building upon the basic characteristics outlined in this study, using this development to outline a preliminary framework for assessing debris hazard from a probabilistic perspective.

3.3 Physical Modelling of Flood-Driven Debris

3.3.1 Objectives

The following study intends to build upon the framework outlined in Lin and Vanmarcke (2010) and applying this framework to "extraordinary" debris impacts in flood-like events using results obtained from physical modelling. Debris hazard assessment has important applications in the design of flood-resistant structures (Chock 2016) and fragility analysis (Charvet et al. 2015) while also potentially informing recovery of valuable objects efforts in the aftermath of flooding events. With the overall aim of developing a stochastic framework for estimating debris hazard, the specific objectives of this study are:

- Based on previous literature, develop an understanding of the parameters governing debris transport.
- Establish a methodology, based on physical processes, for estimating the displacement of the debris both in the flow direction and laterally.
- Develop a method for estimating the design loading conditions through the physical behaviour of debris motion.

This study will focus on applying the framework in tsunami-like flow conditions, in this case, a dam-break wave. The physical model was designed as an idealized, flat topography to limit the influence of aspects, such as bed slope and obstacles within the flow. In order to test and build the framework, the study will address one type of positively buoyant debris, scaled-down shipping containers, scaled considering Froude similitude.

3.3.2 Methodology

Experimental Facilities

The physical modelling was performed at the University of Ottawa dam-break flume (Ottawa, Canada) (Fig. 3-18). The facility is 30 m long, 1.5 m wide, and 0.8 m deep, with a false floor 8.45 m long, 0.20 m high placed at one end of the flume. The remainder of the flume was used as a reservoir to impound a volume of water, which was released by a swinging gate (Häfen et al. 2018, Stolle et al. 2018b). The coordinate system of the facility is defined from the upstream side of the gate on the bed of the false floor. The positive *x*-axis is in the direction of the flow, the positive *y*-axis is flume right, and the positive *z*-axis in the upwards direction.

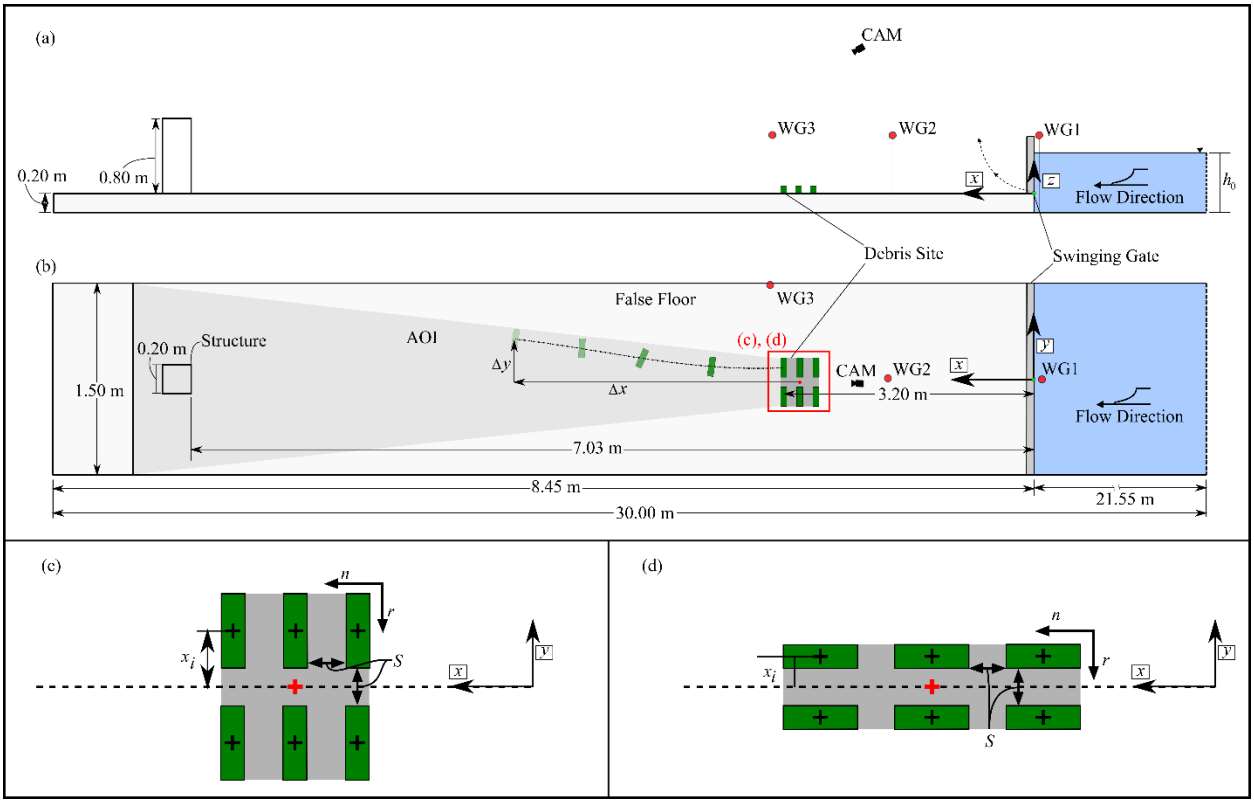

Fig. 3-18. University of Ottawa dam-break flume (30 m × 1.5 m × 0.8 m) side view (a) and top view (b). The red circles indicate the position of the wave gauges and the green box indicates the position of the debris. The red cross represents the geometric center of the debris site. The parameters for the debris configuration are shown in (c) for orientation (Θ) = 0° and (d) 90°.

The debris used in this experiment were 1:40 geometrically scaled shipping containers (0.15 m × 0.06 m × 0.06 m); made of high molecular weigh polyethylene (PE-HMW). The shipping containers were scaled as the mean weight of fully-loaded shipping container (Knorr and Kutzner 2008), considering Froude similitude (m_d = 0.236 +/- 0.005 kg). The resulting density (ρ_d) and draft of the containers was approximately 416 kg/m^3 and 0.025 m, respectively. The debris were placed with the centroids of the furthest downstream debris at x = 3.20 m. The number and configuration of the debris were varied throughout the experiment to examine the influence of the initial entrainment of the debris on debris transport. Before each experiment, the debris were sealed and covered in petroleum to prevent water intrusion.

The experiments were performed within the context of a larger experimental protocol examining debris impact forces on a structure (Derschum et al. 2018, Stolle et al. 2018a, 2018c, 2019a). The structure (0.20 m × 0.20 m × 0.80 m) was placed at a distance of 7.03 m from the gate. To eliminate potential interference from the structure, as well as from the reflected wave, the motion of the debris was tracked only to a distance of 6.50 m from the gate, resulting in a maximum longitudinal displacement (Δx) of 3.30 m. The debris continued to be displaced by the flow until captured in a net covering the bottom drain of the flume.

The bed of the false floor was covered with 1 mm-sieved sand and painted to have a fixed bed surface. Stolle et al. (2018b), in a hydrodynamic analysis of the flume, determined that the approximate Darcy-Weisbach friction factor was 0.0293 by fitting the instantaneous wave profile of various impoundment

depths to the Chanson (2006) solution for a dam-break wave. The coefficient of static friction (μ_0) between the debris model and the false floor was approximately 0.40 (Stolle et al. 2018c), which slightly exceeds the suggested coefficient (0.30) used in the design of shipping container transportation methods (GDV 2003).

Instrumentation

Three wave gauges (WG, RBR WG-50, capacitance-type, accuracy = +/- 0.1%, 0.50 m measurement range, 1200 Hz) were placed in the flume (Fig. 3-18). Wave gauge (WG1) was placed in the reservoir (at x = -0.10 m) to determine the opening of the gate. When the water surface in the reservoir dropped 2% of the initial impoundment depth (h_0), the gate was considered to be completely open indicating the start of each individual experiment (reference time, t = 0.00 s). Wave gauges WG2 and WG3 were placed on the false floor, z = 0.005 m above the bed at distances of x = 2.00 m and 3.20 m, to measure the propagation of the wave downstream. Before the WG were placed in the flume, they were calibrated ensuring an R^2 value of 0.99.

The debris were tracked through the area-of-interest (AOI) using a high-definition camera (CAM, Basler pi1900-32gc). The CAM was externally triggered using a 25-Hz output signal from a data acquisition system (DAQ, National Instruments USB-6009). The signal was simultaneously sampled by a second DAQ system (HBM MX1601B), also sampling the WGs, to synchronize the images with the hydrodynamic data. The estimated synchronization error was approximately +/- 0.04 s.

Debris Tracking

The position of the debris were tracked using a camera-based tracking algorithm (Stolle et al. (2016), however, it was adapted to and modified for the purpose of this study. As noted in Stolle et al. (2016), the algorithm has difficulties tracking more than six debris of the same colour throughout image sequences. This is due to the algorithm passing the identifiers of the individuals between debris. As a result, the algorithm cannot reliably distinguish the trajectory of a single debris across the AOI. As outlined in Stolle et al. (2016), the algorithm was separated into two distinct features: object detection and object tracking. The object tracking feature was mainly responsible for maintaining the unique identifier. As in this study up to 12 debris were used, the object tracking feature was eliminated to avoid challenges related to the passing of identifiers. The object detection algorithm was then used to identify the position of the centroid of the individual debris within each frame. The accuracy of the method without the object tracking algorithm was compared to manual selection of the individual debris within the image in three experimental trials resulting in an approximate error of +/- 0.045 m.

The challenge with removing the object tracking feature is the motion of the individual debris cannot be assessed. To address this issue in terms of the lateral displacement of the debris, the displacement discussed in the following section (Δy) refers to the lateral displacement of each debris' centroid (in each frame) from the geometric center of the initial configuration of the debris (at rest). The geometric center is determined based on the position of the centroid of each debris (black crosses in Fig. 3-19). The geometric center was determined by conceptualizing a rectangle that would capture the position of all the debris centroids in each image (green rectangle in Fig. 3-19) and taking the mean of the outmost coordinates (red cross). Within this study, the initial geometric center was always positioned at y = 0.00 m. For the debris velocity, as the displacement of an individual debris could not be tracked, the velocity of the group of debris was assumed to be relatively constant. Therefore, the velocity of the group was calculated by the trajectory of the geometric center of the debris within each frame (Fig. 3-19).

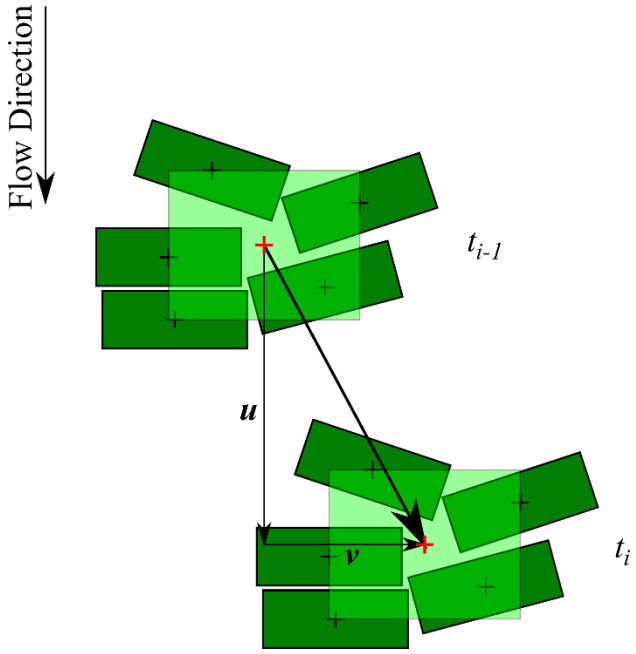

Fig. 3-19. Measurement of debris position and velocity using the object detection algorithm. The green box represents a single debris, the black crosses are centroids of individual debris, and the red crosses are the centroid of the debris group. The faded green box represents the conceptualized rectangle used in the determination of the centroid of the group.

Experimental Protocol

With the main objective of developing a probabilistic framework regarding the debris dynamics based on physical processes, dimensional analysis (Hughes 1993) was performed based on force balances (outlined in the following section). To address the relevant parameters found through the dimensional analysis, several hydrodynamic forcing conditions and debris configurations were experimentally tested and used for the analysis (Table 3-9). The hydrodynamic forcing conditions was varied by changing the water depth impounded in the reservoir (h_0). The debris configuration was adjusted by changing the number of columns of debris (r), the number of debris within each column (n), the spacing between the edges of the debris (held constant in the *x*- and *y*-directions) (S), and the orientation of the long axis of the debris (Θ). An Θ -value of 0° refers to the long axis of the debris perpendicular to the flow direction. Ten repetitions were performed per experimental category for a total of 170 experimental trials.

Before each experimental trial, excess water from the previous trial was removed from the bed of the flume. The debris were placed in the flume using set guides indicated on the bottom of the flume. The reservoir was filled to the set impoundment depth, wave absorbers were placed within the cross-section of the reservoir to aid in the attenuation of wave caused by the filling process. The impounded volume of water was released by operating the opening mechanism of the swing gate (Stolle et al. 2018b), entraining the debris and propagated the debris downstream. After each experiment, the debris were opened to remove any intrusion of water and were resealed with petroleum jelly.

Table 3-9. Experimental Protocol. The experimental categories are named to represent the initial conditions. C – impoundment depth (h_0), N – number of debris, R – number of columns of debris (r), S – debris spacing (S), O – debris orientation (Θ).

Experimental Category	Impoundment Depth (h_0) [m]	Number of Columns (r)	Number of Debris per Column (n)	Debris Spacing (S) [m]	Debris Orientation (Θ) [°]
C20N1 R1S1O1	0.20	1	1	0	0
C40N1 R1S1O1	0.40	1	1	0	0
C40N1 R1S1O2	0.40	1	1	0	90
C20N3 R1S1O1	0.20	1	3	0.03	0
C40N3 R1S1O1	0.40	1	3	0.03	0
C20N6 R1S1O1	0.20	1	6	0.03	0
C20N6 R2S1O1	0.20	2	3	0.03	0
C40N1 R1S1O1	0.40	1	6	0.03	0
C40N1 R2S1O1	0.40	2	3	0.03	0
C50N6 R2S1O1	0.50	2	3	0.03	0
C20N12 R2S1O1	0.20	2	6	0.03	0
C20N12 R2S1O2	0.20	2	6	0.03	90
C40N12 R2S2O1	0.40	2	6	0.015	0
C40N12 R2S1O1	0.40	2	6	0.03	0
C40N12 R2S3O1	0.40	2	6	0.06	0
C40N12 R2S1O2	0.40	2	6	0.03	90
C50N12 R2S1O1	0.50	2	6	0.03	0

3.3.3 Results

Dimensional Analysis

To determine the relevant parametersfor flood-driven debris hazard, dimensional analysis (Hughes 1993) was performed assuming the propagation of debris over a flat, horizontal bed with no flow obstructions. The dependent parameter was the lateral displacement of the debris (Δy).

The most relevant parameters to consider are the type of fluid defined by the density (ρ_w) and viscosity (μ). Generally, for extreme flood events, this corresponds to water; however, the ASCE 7 Chapter 6 allows adjustments to the fluid density based on the salinity and presence of small debris and sediment in the water. Next, the type of debris that was studied, is important. As the debris is assumed to be fully entrained, it can be defined by its geometry, i.e. characteristic length (l), and density (ρ_d). How the debris reacts to the hydrodynamic forcing condition is dependent on the surrounding environment (Rueben et al. 2014, Nistor et al. 2016, Stolle et al. 2017a). As the assumption is the debris is entrained within unobstructed flow, the surrounding environment can be defined by the number of other debris present (n), the number of rows of debris (r), the spacing between the debris (S) and the friction between the debris and the bed (μ_0). Finally, the debris are driven by the surrounding hydrodynamics, defined by the flow depth (d) and velocity (c). Using the Buckingham Π-theorem, the resulting non-dimensional pi-groups were identified as:

$$\frac{\Delta y}{d} = f\left(\Theta, n, r, \frac{\Delta x}{d}, \frac{S}{d}, \frac{l}{d}, \frac{\rho_d}{\rho_w}, Re, Fr, \mu_0\right) \tag{3-6}$$

where Re is the Reynolds number ($Re = \mu cd/\rho_w$) and Fr is the Froude number ($Fr = c/\sqrt{gd}$). Within this study, the material of the debris and the bed surface were kept constant, therefore, the Π-group μ_0 was not examined. Additionally, the material and geometry of the debris was not changed, therefore, the Π-group ρ_d/ρ_w was also not considered. Therefore, the Π-groups being investigated were:

$$\frac{\Delta y}{d} = f\left(\Theta, n, r, \frac{\Delta x}{d}, \frac{S}{d}, \frac{l}{d}, Re, Fr\right) \tag{3-7}$$

The dimensional analysis was used to inform the development of the experimental protocol (Table 3-9). The following sections further examine the factors influencing the trajectory of debris using statistical methods with the objective of developing a model of estimating the lateral displacement of debris under transient flow conditions.

Hydrodynamics

The hydrodynamic forcing condition was a dam-break wave, generated by releasing a volume of water from behind a manually opened swinging gate. Fig. 3-20(a) – (c) shows the water surface elevations at *x* = - 0.10 m, 2.00 m, and 3.20 m for each impounded water depth (h_0 = 0.20 m, 0.40 m, and 0.50 m). For a full hydrodynamic analysis of the University of Ottawa dam-break flume, see Stolle et al. (2018b). The wave profiles were repeatable between experimental trials with a standard deviation in wave arrival time of 0.053 s and a standard deviation of the water surface of 0.008 m at the debris site (*x* = 3.20 m).

Due to challenges in measuring the flow velocity around the debris, the wave front velocity (c) was used as a proxy for the local flow velocity. The wave front velocity was calculated by the difference in the wave arrival time between WG2 and WG3. Fig. 3-20(d) plots the measured wave front velocity against the impoundment depth. The wave front velocity is a function of the impoundment depth, flow resistance, and distance from the gate (Chanson 2006). Therefore, the velocity represents the mean velocity from *x* = 2.00 m and 3.20 m, and due to flow resistance, the wave front velocity will decrease due to flow resistance across the AOI. Eq. (3-8) is commonly used to describe the mean wave front velocity (Wüthrich et al. 2018)

$$c = \alpha\sqrt{gh_0} \tag{3-8}$$

where α is a fitted coefficient. Literature values for the α-value can range from 0.66 (Matsutomi and Okamoto 2010) to 2.00 (Ritter 1892). Fig. 3-20(d) shows the fitted Eq. (3-8), along with the 95% Confidence Interval (CI), for the mean wave velocity at the debris site resulting in α = 1.29. Stolle et al. (2018b) performed a similar analysis for the length of the propagation section resulting in a fitted α-value of 1.09. Due to the relatively high flow resistance (*f* = 0.0293), the wave front velocity (and therefore α) decays rapidly across the AOI.

As the wave front velocity decays as it propagates downstream (Chanson 2006), the maximum drag forces acting on the debris occurred at the debris site. Therefore, for the remaining analysis, the wave front velocity will be used as the proxy for the local flow velocity. Due to the rapid nature of the debris entrainment and similar challenges measuring the local water depth, the maximum water depth (D) at the debris site attained during single experimental runs was used for the following analysis. Table 3-10 outlines the mean ($\bar{c}$ and $\bar{D}$) and standard deviation (σ) for the wave front velocity and maximum water depth at the debris site for each impoundment depth. The data confirms the general trend of higher front velocities as well as increasing maximum water depth at the debris site with increasing impoundment

depth. Low levels of standard deviation indicate the high degree of repeatability throughout the experimental campaign.

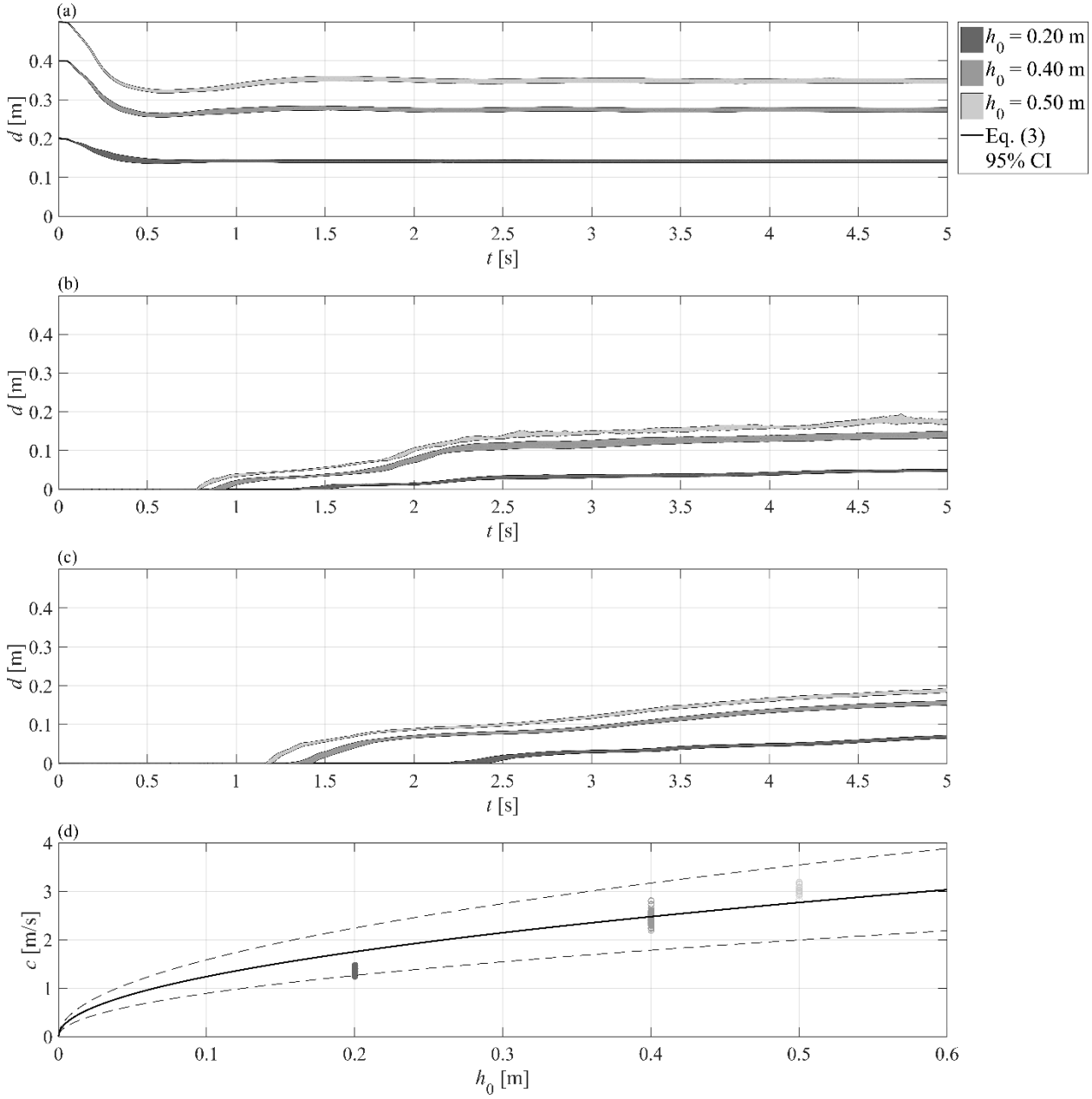

Fig. 3-20. Time history of mean surface water elevation of the dam-break waves. The mean water surface elevations are given for each impoundment at (a) WG1 (x = -0.10 m), (b) WG2 (x = 2.00 m), and (c) WG3 (x = 3.20 m). The wave front velocity (c) between WG2 and WG3 for each trial are shown in (d). The wave front velocity was fit to Eq. (3-8) (solid line), the 95% confidence interval of the fit is shown as the dashed line.

Table 3-10. Wave hydrodynamics at the debris site (x = 3.20 m).

h_0 [m]	Wave Front Velocity (c)		Maximum Water Depth (D)	
	$\bar{c}$ [m/s]	σ_c [m/s]	$\bar{D}$ [m]	σ_D [m]
0.20	1.364	0.057	0.093	0.006
0.40	2.466	0.112	0.173	0.012
0.50	3.030	0.111	0.209	0.005

From a design perspective, information about the hydrodynamics driving the debris entrainment and consecutive downstream propagation is very important for the derivation of a probabilistic debris impact assessment. In the following, the path of the debris –its trajectory- will be discussed and evaluated for the given hydrodynamic conditions in the experiments.

Debris Trajectory

Assessing the likelihood of "extraordinary" debris impact has predominantly been performed in a binary manner (impact or no impact) due to challenges in identifying what parameter influence the trajectory of the debris. This section addresses the lateral (cross-flow) displacement ($Y = \Delta y/D$) of the debris, the following section will address the displacement in the flow direction through assessing the debris velocity. The parameters addressed in this study were based on analysis of previous literature and the dimensional analysis performed in the previous section. The displacement was taken as the displacement from the geometric center of the initial configuration of debris.

In the framework develop by Lin and Vanmarcke (2010), the distribution of the debris trajectory was assumed to be a normal distribution with a mean of 0 (i.e. the debris propagates in a straight line). Stolle et al. (2018c) validated this assumption for a single shipping container in a similar experimental setup. Table 3-11 shows the mean ($\bar{Y}$) and standard deviation (σ_Y) of the lateral displacement across the AOI for each experimental category. A one-sample t-test (Anderson et al. 1958) was performed with the null hypothesis that the mean of the lateral displacement was equal to zero; the statistical test outcome is presented in Table 3-11. The data predominantly confirms that the assumption of a mean of zero ($p >$ 0.05) proves to be correct except in the two cases with a single debris and an impoundment depth of 0.40 m. In addition, Stolle et al. (2018c) investigated similar test series and determined that the deviation from the mean was sufficiently small (less than the width of the shipping container). The remaining discrepancy was likely due to small inconsistencies in the bed topography.

The second assumption made in Lin and Vanmarcke (2010) was the lateral displacement of the debris was normally distributed. To test this assumption, a Shapiro-Wilk (1965) test was performed with the null hypothesis that the lateral displacement was normally distributed around the mean. For the cases with a single column of debris the lateral displacement is normally distributed about the mean throughout the trajectory (Fig. 3-21(a)), however, for the cases with two columns, this was not observed ($p < 0.05$) (Fig. 3-21(c)). Fig. 3-21 shows the trajectory of debris for two experimental category (C40N6 R1S1O1 and C40N12 R2S1O1). Due to the configuration of the debris, the lateral displacement has a distinct bimodal distribution (Fig. 3-21(d)). As the debris continues to propagate from the debris site, the bimodality of the displacement decreased.

Table 3-11. Statistical properties of debris trajectories for each experimental category. The mean and standard deviation of lateral displacement are determined from the normalized lateral displacement ($Y = \Delta y/D$).

Statistical Test	One sample t-test			Shapiro-Wilk	Goodness-of-Fit
Experimental Category	$\bar{Y}$ [-]	σ_Y [-]	p-value [-]	p-value [-]	NRMSE [-]
C20N1 R1S1O1	-0.14	0.53	0.40	0.26	0.629
C40N1 R1S1O1	-0.19	0.13	0.01	0.24	-3.060
C40N1 R1S1O2	0.21	0.21	0.02	0.16	-0.077
C20N3 R1S1O1	0.22	1.06	0.12	0.16	0.341
C40N3 R1S1O1	0.06	0.35	0.20	0.12	0.528
C20N6 R1S1O1	-0.37	1.76	0.20	0.14	0.637
C20N6 R2S1O1	0.33	3.15	0.33	0.11	0.621
C40N6 R1S1O1	-0.06	0.60	0.33	0.13	-0.500
C40N6 R2S1O1	-0.03	1.18	0.60	0.15	0.768
C50N6 R2S1O1	-0.11	0.88	0.16	0.14	-2.138
C20N12 R2S1O1	0.37	3.41	0.19	0.13	0.314
C20N12 R2S1O2	0.13	4.61	0.57	0.13	0.315
C40N12 R2S2O1	0.12	1.40	0.38	0.10	0.721
C40N12 R2S1O1	0.01	1.44	0.63	0.10	0.788
C40N12 R2S3O1	-0.11	1.36	0.32	0.11	0.386
C40N12 R2S1O2	0.20	1.41	0.36	0.10	0.337
C50N12 R2S1O1	0.11	0.99	0.27	0.13	0.824

To address this issue, the Shapiro-Wilk (1965) test was performed over the final X = 5 (faded red box in Fig. 3-21) to reduce the influence of the initial configuration on the distribution. As can be seen from Table 3-11, in the latter stages of the propagation, all experimental categories displayed normally distributed lateral displacement about the mean (p > 0.05).

Based on the assumption of a normal distribution with a mean of zero, the probability density function (P) can be expressed as:

$$P(X) = \frac{1}{\sqrt{2\pi\sigma_Y^2}} e^{-\frac{Y^2}{2\sigma_Y^2}} \tag{3-9}$$

Therefore, the only free parameter is the standard deviation. While the Shapiro-Wilk (1965) test showed that the initial configuration did not influence the distribution of the debris in the latter stages of the flow, it did influence the standard deviation. To address the various parameters outlined in the dimensional analysis, multiple linear regression was performed to examine the influence of the outlined parameters on the standard deviation. The standard deviation was determined as a function of the displacement (X) from the debris source for each experimental category.

The variance inflation factor (VIF) (Kenney 1962a) was calculated between each of the parameters outlined in the dimensional analysis to test for multicollinearity between the parameters. Multicollinearity can result in large fluctuations in estimated coefficients from the regression. Generally, VIF values greater than 10 indicate collinearity between variables (Farrar and Glauber 1967). In this case, Fr and Re showed high collinearity (VIF > 10). The Fr and Re are not necessarily collineated for all hydrodynamic forcing conditions; however, in this specific case, due to the physics of a tsunami-like, Re tends to increase with Fr. Additionally, as the model was scaled considering Froude similitude, the Reynolds number would not

represent ranges that are typical of tsunami. Therefore, the Reynolds number was not considered in the regression analysis. The ratio l/D and parameter Θ also displayed high VIF values, as the parameter Θ was related to the orientation of the long axis. The parameter Θ was hence removed from the analysis as it does not represent a physical characteristic in the force balance and the length of exposed area to the flow has application in a wide range of geometries. As the remaining factors are a function of the initial configuration, the parameters are assumed to influence the change in standard deviation over distance from the site, resulting in the equation:

$$\sigma_Y = \left|\left(\lambda_1 Fr + \lambda_2 \frac{l}{D} + \lambda_3 \frac{S}{D} + \lambda_4 n + \lambda_5 r\right) X + X_i\right| \tag{3-10}$$

where λ_j are the regression coefficients (with j the numbers of coefficients) and X_i is the position of the outermost columns of debris in the initial configuration (Fig. 3-18).

The multiple linear regression showed that the linearized model could explain 62% of the margin of variance ($R^2 = 0.617$) and was statistically significant ($p << 0.05$). A Kolmogrov-Smirnov test (Smirnov 1948) was performed with the null hypothesis that the residual were normally distributed, ensuring the validation of the assumption of normally distributed residuals ($p = 0.10$). Each of the coefficients were considered to show a statistically significant trend, except in the case of spacing. This is potentially due to the limited number of cases that examined the influence of spacing as well as a high potential for a non-linearity that cannot be captured by the regression model. Rueben et al. (2014) noted, in a study of debris dynamics over a slope surface, that the debris appeared to have an "area of influence" related to its obstruction of the flow. Similar to a fixed obstacle, debris influence the surrounding flow, as they tend to propagate slower than the surrounding fluid, therefore, it is likely the area of influence is a function of the inertia of the debris, hydrodynamics, and spacing. Further investigation is necessary to address the importance of spacing within this context.

The calculated regression coefficients (

Table 3-12) are subject to potential scale effects and are influence by the parameters not include within the regression, such as friction and buoyancy. However, the standardized coefficient, where the regression was performed with each parameter standardized (i.e. mean of 0 and standard deviation of 1), show the relative influence of each parameter on the lateral displacement.

Based on the standardized coefficients (

Table 3-12), the hydrodynamic conditions, exposed length of the debris, and number of columns have the most substantial influence on the lateral displacement. This is consistent with previous literature, Stolle et al. (2018c) indicated for a single debris, the greater water depths and velocities resulted in smaller lateral displacement due to less interaction with bed surface. Braudrick and Grant (2001) determined that the debris tended towards a equilibrium orientation, in the case of shipping containers with the long axis perpendicular to the flow, during the rotation process this causes an increase in the lateral displacement. Stolle et al. (2019b) showed that the debris tended to diffuse away from the initial configuration as a function of the number of columns present. Nistor et al. (2016) showed that the increase in the number of debris resulted in an increase in the lateral displacement.

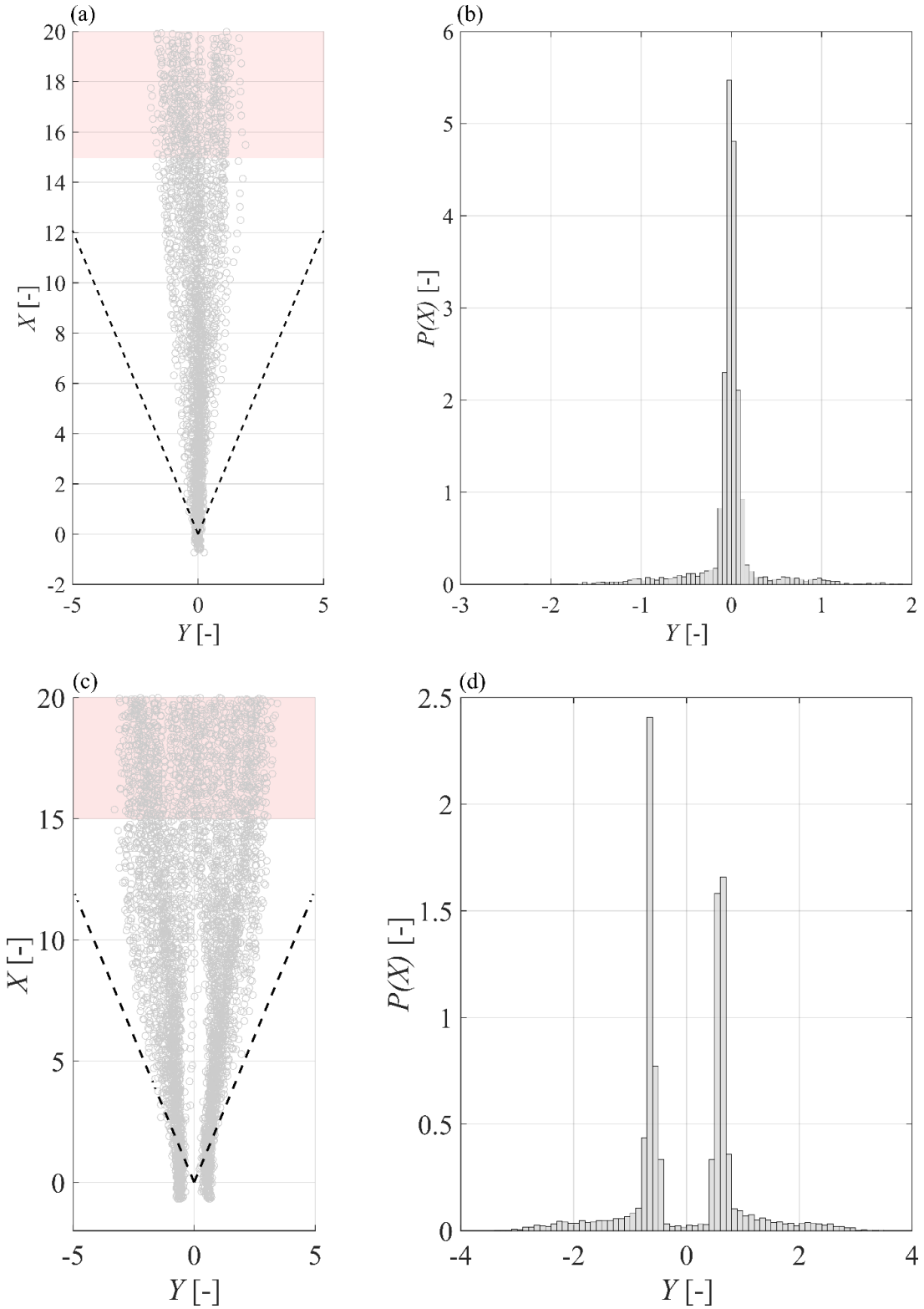

Fig. 3-21. Debris transport for experimental category C40N6 R1S1O1 and C40N12 R2S1O1. (a, c) The position of each debris throughout the AOI compared to the +/- 22.5º spreading angle suggested in Naito et al. (2014). The faded red box shows where the Shapiro-Wilk (1965) test was performed. (b, d) Probability density of the lateral displacement.

Table 3-12. Multiple linear regression of the standard deviation of the debris displacement (Y).

	Multiple Linear Regression			
Parameter	Regression Coefficients (λ_j)	Standardized Coefficients (β)	p-value	VIF
Froude Number (Fr)	-0.390	-0.865	$p << 0.05$	2.337
Length (l/D)	-0.208	-0.591	$p << 0.05$	1.792
Spacing (S/D)	0.020	0.039	0.218	2.200
Number of Debris per column (n)	0.008	0.238	$p << 0.05$	1.260
Number of columns (r)	0.051	0.409	$p << 0.05$	1.273

The fit of Eq. (3-10) to each experimental category was estimated using the normalized root mean squared error (NRMSE):

$$NRMSE = 1 - \frac{\sum_{j=1}^{m}\left(\sigma_Y(X_j) - \widehat{\sigma_Y}(X_j)\right)}{\sum_{j=1}^{m}\left(\sigma_Y(X_j) - \overline{\sigma_Y}\right)} \tag{3-11}$$

where σ_Y is the standard deviation from the experimental data, $\widehat{\sigma_Y}$ is the standard deviation estimated from Eq. (3-10), $\overline{\sigma_Y}$ is the mean standard deviation, and m is the number of data points. The NRMSE can range from 1 (perfect fit) to -∞ (bad fit). The NRMSE for each experimental category is shown in Table 3-11. Fig. 3-22 shows a comparison of the fit for three identical debris configurations with different hydrodynamic forcing conditions with NRMSE equal to 0.621 (a), 0.768 (b), and -2.138 (c), respectively. Eq. (3-10) had difficulty modelling small changes in standard deviation over AOI (i.e. Fig. 3-22(c)), though overall modelled each experimental category well.

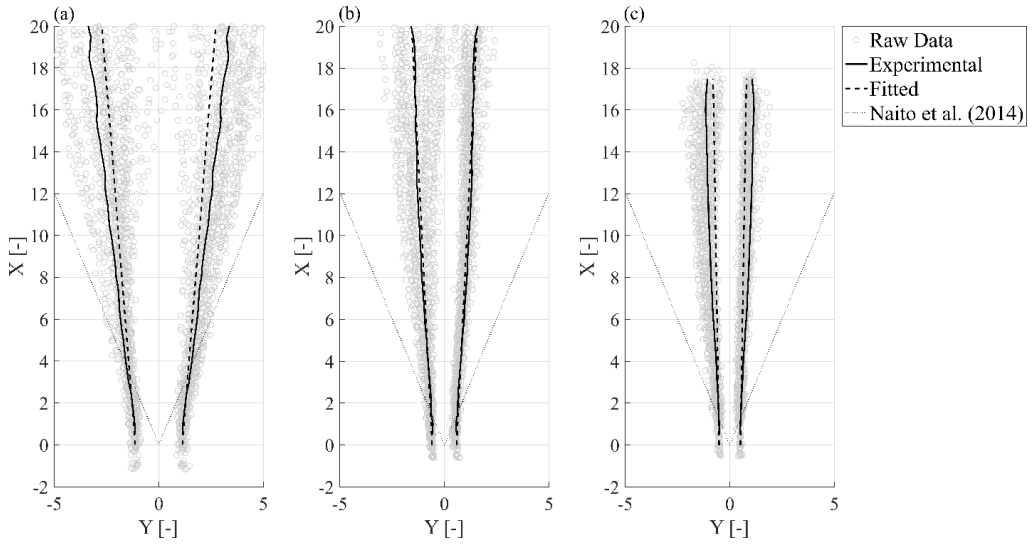

Fig. 3-22. Comparison of the fitted standard deviation (dashed line), standard deviation from the experimental data (solid line), and the raw experimental data (circular markers) for experimental categories with 6 debris, 2 columns, 0.03 m spacing, and 0° orientation: (a) C20N6 R2S1O1; (b) C40N6 R2S1O1; and (c) C50N6 R2S1O1.

Debris Velocity

The debris velocity is a critical intermediate component of debris hazard assessment as it dictates the magnitude of the impact force exerted on the structure (Eq. (2-6), Nistor et al. (2017)). Stolle et al. (2017a) examined the transport of multiple shipping containers in similar configurations as this study. Based on a force balance of fully entrained debris, the following equation was determined to describe the debris velocity profile:

$$u = c - \left(\frac{C_d \rho_w A_d}{2nm_d} t + \frac{1}{c}\right)^{-1} \tag{3-12}$$

where C_d is the drag coefficient of the debris and A_d is the cross-sectional area of the debris exposed to the flow. Eq. (3-12) does not consider the entrainment of the debris, which requires further development due to the different potential modes of transport (i.e. sliding, rotation). Furthermore, as the local flow velocity around the debris is a difficult parameter to estimated, the wave front velocity is used as a proxy for the flow velocity. Eq. (3-12) represents a conservative estimation of the debris velocity over a flat horizontal surface as the wave front velocity will represent the maximum flow velocity.

Fig. 3-23 shows the mean group velocity of the debris for each of the experimental categories as a function of time, separated by the initial impoundment depth. Eq. (3-12), based on the number of debris present within each column, is shown as a dotted line. As can be seen from Eq. (3-12), the debris velocity approaches the wave front velocity asymptotically. Comparing the debris velocity profile to the mean wave front velocity at the site (Eq. (3-8), α = 1.29), the debris group velocity does not exceed the wave front velocity, as expected. As the wave front velocity decays over the AOI, the debris does not reach the wave front velocity at the debris site and instead approaches the mean wave front velocity over the AOI (α = 1.09), as determined from Stolle et al. (2018b).

The rapid acceleration of the debris in the initial phases of entrainment are not captured by Eq. (3-12). As described in Stolle et al. (2015), at smaller impoundment depths, the initial wave impact does not initiate the motion of the debris. As a result, a wake forms downstream from the debris, causing a large hydraulic gradient between the upstream and downstream faces of the debris. Once the horizontal force induced by the hydraulic gradient overcomes the static friction force, the debris rapidly accelerates, in some cases, briefly exceeding the wave front velocity. However, as the debris settles within the wave front, the debris velocity reduces to below the wave front velocity. In the case of h_0 = 0.50 m, the momentum of the wave immediately overcomes the coefficient of static friction, resulting in no rapid spike in the acceleration of the debris.

While Eq. (3-12) does not capture the entrainment phase of debris transport, the equation does represent a conservative estimation (with n = 1) of the evolution of the mean velocity profile over time. To capture the probabilistic nature of debris transport, Lin and Vanmarcke (2010) suggested the application of a bounded distribution to capture the evolution of debris velocity between rest and the maximum flow velocity. Lin and Vanmarcke (2010) used a Beta distribution (McDonald 2009), however, the challenge with the Beta distribution is the distribution requires a specialized Beta function to ensure the total probability remains constant.

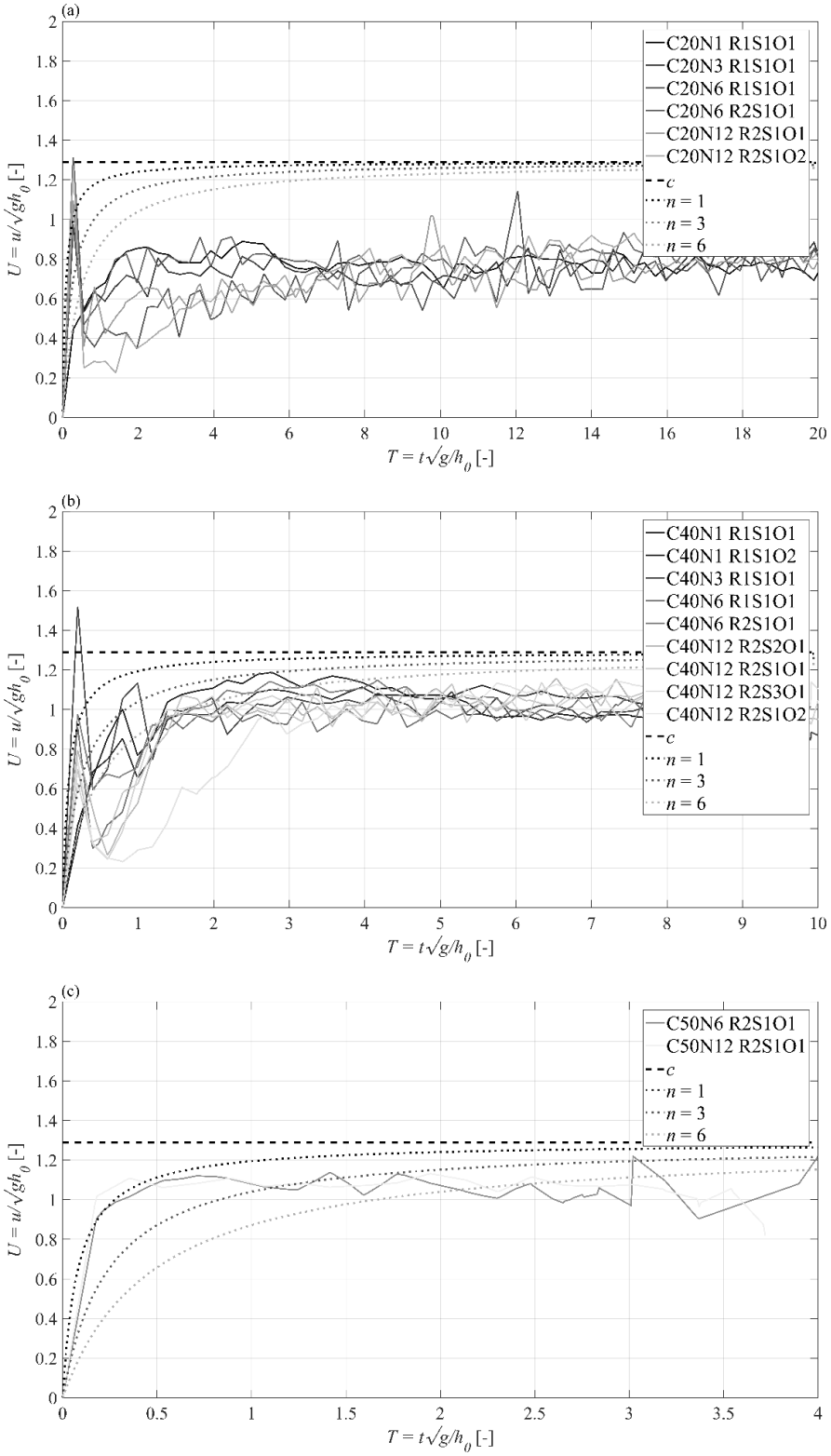

Fig. 3-23. Mean debris velocity profiles (solid lines) for each experimental category for (a) h_0 = 0.20 m, (b) h_0 = 0.40 m, and (b) h_0 = 0.50 m. The dotted line shows the estimated velocity profile from Eq. (3-12). The thick dashed line details the mean wave front velocity based on Eq. (3-8).

The Kumaraswamy (1980) (K1980) two-parameter (a and b) bounded distribution, developed for hydrology application (Jones 2009), is within the same family as the Beta distribution. The K1980 distribution represents a similarly shaped distribution with the distinct advantage of having a closed form for both the probability ($f(x;a,b)$) and cumulative distribution ($F(x;a,b)$) functions:

$$f(U;a,b) = abU^{a-1}(1-U^a)^{b-1} \tag{3-13}$$

$$F(x;a,b) = 1-(1-U^a)^b \tag{3-14}$$

Similar to the Beta distribution, the K1980 distribution is determined by its mean ($\overline{U}$) and dispersion (η_U), expressed in the shape terms as:

$$a = \overline{U}\eta_u \tag{3-15}$$

$$b = (1-\overline{U})\eta_u \tag{3-16}$$

Using Eq. (3-12), the normalized debris velocity can be determined as:

$$\overline{U} = \frac{u}{c} = 1-\left(\frac{C_d\rho_w A_d}{2nm_d}ct+1\right)^{-1} \tag{3-17}$$

The K1980 distribution can take on different shapes depending on a and b, however, for the purpose of debris transport, the distribution should be unimodal (Lin and Vanmarcke 2010). Therefore, the values of a and b, must be greater than one (Jones 2009). Based on Eq. (3-15) and (3-16), the dispersion must then be defined as:

$$\eta_u = \max\left(\frac{1}{\overline{U}}, \frac{1}{1-\overline{U}}\right)+\gamma \tag{3-18}$$

where γ is a positive fitted parameter based on the type of debris. Using the experimental data, the parameter γ was iteratively fit to the data set (γ = 2.32) by comparing the mean squared errors between the experimental and theoretical probability density functions (PDF). The applicability of the K1980 distribution was then evaluated using the Kolmogorov-Smirnov test, which compares the experimental cumulative distribution function (CDF) to the theoretical one (Smirnov 1948), with the null hypothesis that the experimental data follows the K1980 distribution at each time step.

For each experimental category, the null hypothesis was not rejected with a mean *p*-value of 0.30 (+/- 0.09). Therefore, the K1980 distribution can be assumed to reasonably capture the experimental dataset. Fig. 3-24 shows a comparison of the experimental data set ((a) and (c)) to the proposed K1980 distribution ((b) and (d)) for two experimental categories (C40N1 R1S1O1 and C40N12 R2S1O1, respectively) at three arbitrarily selected time steps. As the time passes, the mean velocity of the debris increased towards the wave front velocity in both experimental cases. However, the influence of the added inertia in the case with 12 debris (Fig. 3-24(c)) can be observed by the reduced velocity in the later time steps compared to the single debris case.

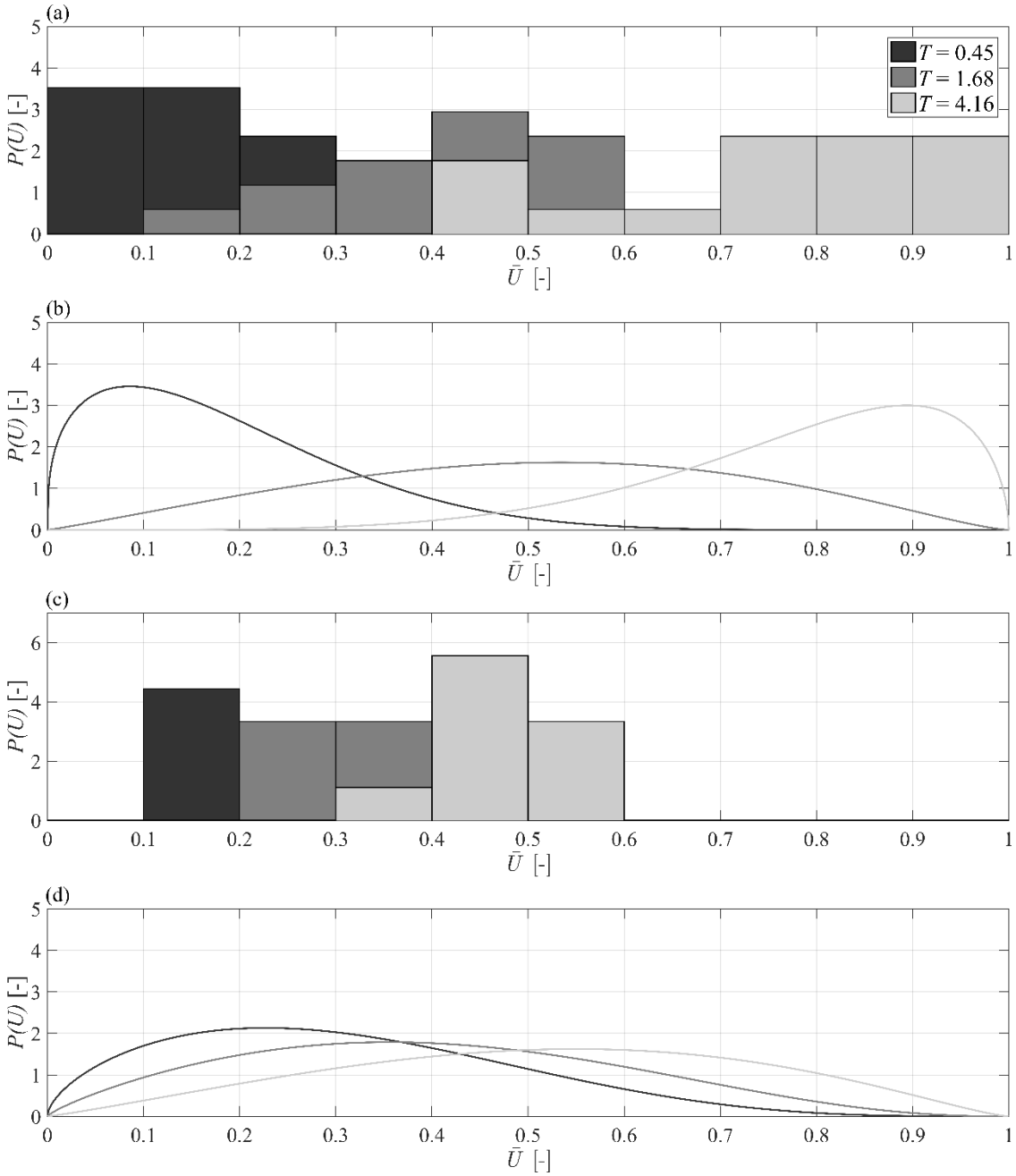

Fig. 3-24. Comparison of the probability density function ($P(U)$) for the experimental data set (a, c) to the theoretical Kumaraswamy (1980) distribution (b, d) for three time steps for C40N1 R1S1O1 and C40N12 R2S1O1, respectively.

3.3.4 Discussion

The experimental setup was intended to represent an idealized case of a tsunami propagating over coastal plain (Chanson 2006). To ensure the experiment could adequately address the probabilistic nature of debris transport, the scope was limited to represent this specific scenario. As such, the hydrodynamic boundary condition only examined the initial inundation of a tsunami wave and did not consider the results of drawdown or subsequent wave entrainment. The number of debris was limited to a maximum of 12 as further additions resulted in significant model effects due to interactions with the walls of the flume.

The inter-debris friction, debris-bed friction, and the buoyancy of the debris were not investigated. As these factors have been shown to have an influence on debris transport, further research is necessary to address these issues.

Bricker et al. (2015), in a study examining Manning's roughness coefficients used in tsunami modelling, indicated the critical importance in adequately addressing viscous and surface tension effects. Within this experiment, the Reynold's number ranged from 1.59×10^4 to 6.85×10^5 which place the flow within the turbulent flow regime (Te Chow 1959). However, as the Reynolds number at prototype scale are often in excess of 1.00×10^6, the experiments presented here do not capture the turbulent boundary layer that is potentially present (Sumer and Fredsøe 2006), influencing the drag acting on the debris. The Weber number ($We = \rho U^2 D/\sigma$), the ratio of surface tension and gravitational forces, ranged from 152.4 to 671.2 exceeding the critical Weber number of 120 prescribed by Peakall and Warburton (1996). However, concerns potentially exist between the debris where adhesion may occur.

For the lateral displacement of the debris, it would be expected that the general importance and influence of the parameters discussed in the dimensional analysis would remain similar at prototype scale. However, the magnitude of regression coefficients (λ_j) could potentially vary significantly. To date, no study has investigated debris motion at sufficiently large scales to address scale effects while this work depicts the first approach towards describing the debris transport process probabilistically where extreme flow conditions are concerned. In particular, parameters, such as turbulence (She and Leveque 1994) and drag (Granville 1976), which scale considering Reynolds similitude are not properly scaled. Additionally, this study did not address parameters that would have a significant influence on debris transport, in particular, buoyancy and friction. As shown in the dimensional analysis, the Eq. (3-10) could not describe 38% of the variance from the mean, leaving potential to build upon the current data set to address these issues.

The evolution of the debris velocity should theoretically be more robust to scale effects as the underlying Eq. (3-12) is based on a closed solution of the forces acting on the debris. However, the equation was based on fully entrained debris, and therefore, does not consider the influence of debris entrainment or other forms of motion, such as sliding or saltation. Though, as these phases of motion would result in loss of energy and, therefore, reduced acceleration, Eq. (3-12) represents a conservative estimation of the potential debris velocity at a given time.

The experimental study presented here examined the transport of "extraordinary" debris in a dam-break wave over a flat, horizontal surface. Therefore, limitation need to be addressed in the application of the model in a built environment. Aspects, such as flow channelling or typical surface roughness of debris, are not captured with the current model. Investigation is necessary to address debris transport through flow obstructions (Goseberg et al. 2016b), likely influencing the underlying assumption that the mean displacement of the debris is equal to zero. Flow accelerations and impact with other structures within these constricted environments may influence the evolution of the debris velocity. Furthermore, the model examines "extraordinary" debris impact where the debris has a distinct source and is immediately entrained within the flow. Other probabilistic models have also included terms that consider debris generation (i.e. from the destruction of houses), the generation of individual debris objects is then modelled as a Poisson distribution (Lin and Vanmarcke 2010, Hatzikyriakou and Lin 2017). However, as the accurate modelling of collapsing structures under hydraulic loading has yet to be addressed, this aspect was not included within this study (Heller 2011).

3.3.5 Conclusions

The experiments presented here were used in the development of a probabilistic framework for addressing debris hazard in extreme flooding events. Using the measured trajectory of debris within energetic flow events and dimensional analysis, empirical formulas were developed capturing the physical motion in a probabilistic framework. Based on the results of these experiments the following conclusions can be derived:

- The mean trajectory of debris over a horizontal surface, with no flow obstruction, can be estimated with no lateral displacement. The distribution of lateral displacement around the mean can be assumed to be Gaussian.
- The hydrodynamic conditions, geometry of the debris, as well as the initial configuration of the debris are important factors in estimating the distribution of debris around the mean.
- A force balance of completely entrained debris can be used to conservatively estimate the evolution of debris velocity as a function of time.
- The distribution of debris velocity as a function of time can be estimated using a two-parameter bounded distribution, the Kumaraswamy (1980) distribution.

The proposed model was developed analyzing the general trends regarding debris motion, in particular, the lateral motion. However, potential scale effects need to be addressed before the application of such a model. With the challenges in assessing debris trajectory in the aftermath of events through field studies, future investigations into debris hazard assessment will be needed at sufficiently large scale to limit scale effects related to the Reynolds number, in particular, turbulence and drag. The results discussed here should aid in the development of such experimental series as it helps inform general parameters that are critical in the assessment of debris displacement.

Chapter 4. Debris Damming

4.1 Experimental Investigation of Debris-Induced Loading in Tsunami-Like Flood Events

4.1.1 Objectives

The objective of hydraulic research into debris damming has primarily focused on the effects associated with the formation of the debris dam. This study will examine the variables related to design considerations of coastal structures subject to extreme inflows: horizontal in-stream loads, associated drag coefficients and backwater rise. With the eventual intention to provide design consideration related to the design of coastal structures for debris damming loads in coastal flooding events, the objectives of this study are:

- Examine the influence of the supplied debris volume on the debris dam formation.
- Determine the influence of debris mixtures, based on the quantity and type of debris supplied, on debris dam formation.
- Evaluate the horizontal in-stream loads caused by the formation of a debris dam at the face of the structure.
- Examine the influence of debris dam properties such as non-structural void fraction and size on loads and backwater rise.

4.1.2 Experimental Setup

Experimental Facilities

Complex fluid-structure interaction between debris and a fixed obstacle governs the process of dam formation. Hence, experimental work is currently most promising to explore this problem at hand. As such, the experiments were performed at the High-Discharge Flume at Waseda University, Tokyo, Japan. The flume was 14.0 m long, 0.40 m wide and 0.80 m high (Fig. 4-1) and is currently used for modelling 2D fluid problems. The experimental setup was placed on top of a 0.20 m false floor. The debris was released into steady-state flow conditions using a trapdoor placed on top of the flume (0.50 m from the water surface). The trapdoor opening was chosen to allow for all the debris to be released simultaneously for each experimental trial and improve repeatability. The debris were arranged on the trapdoor in the same manner for each experimental trial. The trapdoor was released and dropped into the steady-state flow. As each debris type was positively buoyant, the debris only briefly penetrated the water surface before surfacing and propagating in the flow direction. The origin of the experimental setup was considered to be on top of the false floor at the center point of the trapdoor, using a right-handed coordinate system with the flow direction as the positive x-direction with the positive y-direction flume left. The distance between the trapdoor and the obstacle was chosen based on Matsutomi (2009) where the distance for the debris to reach steady-state flow velocity was 20 times the debris length, therefore giving the debris sufficient distance to reach steady velocity.

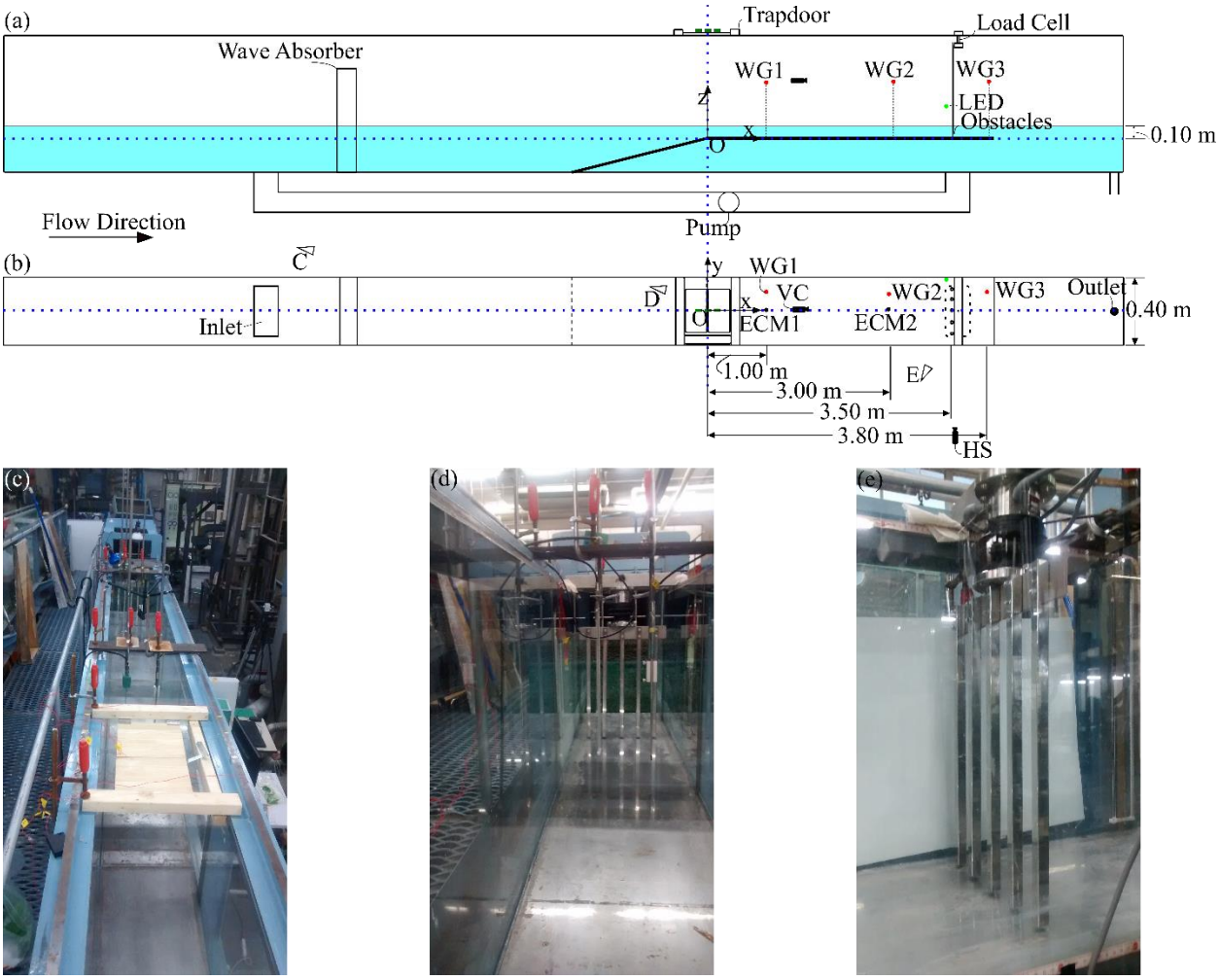

Fig. 4-1. High-discharge flume at Waseda University. (a) side view of the flume; (b) top view along with the view of the three subsequent images (c-e). The WG are shown as red circles, the ECM are shown as black dots. The coordinate system is indicated as a blue dotted line in (a) and (b).

The obstacles to be impacted by the debris were modelled as a set of columns using a 1:50 length scale (Fig. 4-2). The obstacles were modelled after structural columns in a building where breakaway walls had previously been destroyed by the inundating flow. The columns were 0.016 m wide with an opening width (W) of 0.06 m between each of the obstacles. The gap between the obstacles and the flume wall were 0.04 m on both sides and the obstacles were 0.40 m high. The width of the columns was chosen based on prescriptions from the National Building Code of Canada (2005) corresponding to a general office building based on selected column spacing. The obstacles were placed 0.005 m above the bed surface to prevent them from touching the bed surface and thus influencing the force measurements from the load cell.

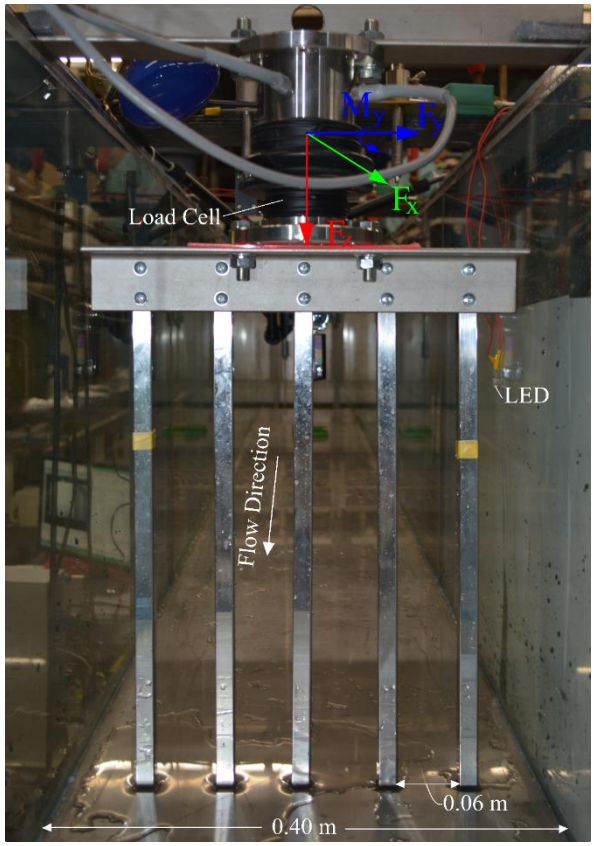

Fig. 4-2. Downstream view of the obstacle setup.

Instrumentation

The instrumentation setup is outlined in Fig. 4-1 and Table 4-1. The wave gauges (WG) were placed 0.10 m from the flume wall and the electro-current meters (ECM) were placed 0.20 m from the flume wall (center flume), 0.06 m from the bed. The WG and ECM were removed from the flume during the experiments containing debris to prevent damage due to accidental debris impact. The load cell was connected to the top of the obstacle setup, as shown in Fig. 4-2. The load cell had a maximum rating force of 500 N, which exceeded any forces measured in these experiments. The load cell was calibrated by placing known weights along its three axis of coordinates. The load cell had a coefficient of calibration exceeding 0.99 for F_x, F_y and M_y. The load cell was firmly connected to the top of the flume to ensure a rigid reference point. The sampling rate of all instruments was 100 Hz. The data from the load cell was filtered using an Empirical Mode Decomposition (EMD) filter (Huang et al. 1998) to remove signal noise as well as the impulses caused by the debris impacting the structure. All the data from the hydraulic measurement equipment was collected into a single Data Acquisition (DAQ) system to assure synchronicity between the instruments.

Table 4-1. Instrumentation used in experimental setup.

Instrumentation	Model	Instruments
Wave Gauge (WG)	KENEK CH-601	WG1, WG2, WG3
Electro-current Meter (ECM)	KENEK MT2-200	ECM1, ECM2
Video Camera (VC)	JVC Everio GZ-HM440	
High-Speed Camera (HS)	KATO KOKEN k4	
Load Cell	SSK LB120-50	
Data Acquisition System (DAQ)	KENEK ADS2016	

Two cameras were setup to measure the formation of the debris dam. The video camera was placed upstream of the obstacles, facing the front face. The video camera (VC) recorded in an Advanced Video Coding High Definition (AVCHD) codec standard at 30 Hz. Before each experimental run, the video camera was manually triggered. The second camera was a high-speed camera (HS), commonly used in particle image velocimetry (PIV). The HS camera recorded each experiment using an Audio Video Interleaved (AVI) format at 100 Hz. The HS camera was manually triggered during the experiments.

As both camera systems were independent, a synchronization system was designed to minimize time discrepancies between the cameras and the DAQ recorded data (Fig. 4-3). The trapdoor used to release the debris was connected to a simple circuit that, when broken, would turn off an LED light placed within the view of the video camera. Within each experimental video, the frame in which the LED light turned off would be considered as time zero. The voltage of the simple circuit was also input into the DAQ to indicate the time when the trapdoor was opened. The HS camera had a limited sampling window, therefore an output signal (5 V) was manually triggered by an operator as the debris approached the obstacles. The output signal triggered the HS camera to begin capturing images and the DAQ recorded the output signal to relate the trigger signal to time zero.

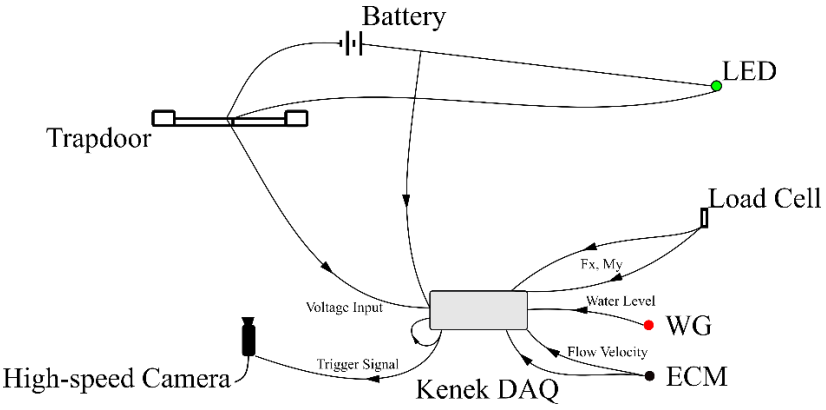

Fig. 4-3. Data Acquisition (DAQ) system setup for the experimental setup.

Model Debris

The debris were selected to model debris commonly found in coastal communities (Chock 2016). The experiments were scaled using a 1:50 length scale and were scaled geometrically using Froude similitude. Previous research on debris damming pertaining to debris mixtures is generally scarce with few exceptions, such as Schmocker and Hager (2013), this work predominantly investigates mixtures of debris, as this is the most likely scenario for debris transported in an extreme flow condition in a coastal setting. Hence, three different types of debris were selected (Fig. 4-4): shipping containers (SC), hydro poles (HP), and boards (B).

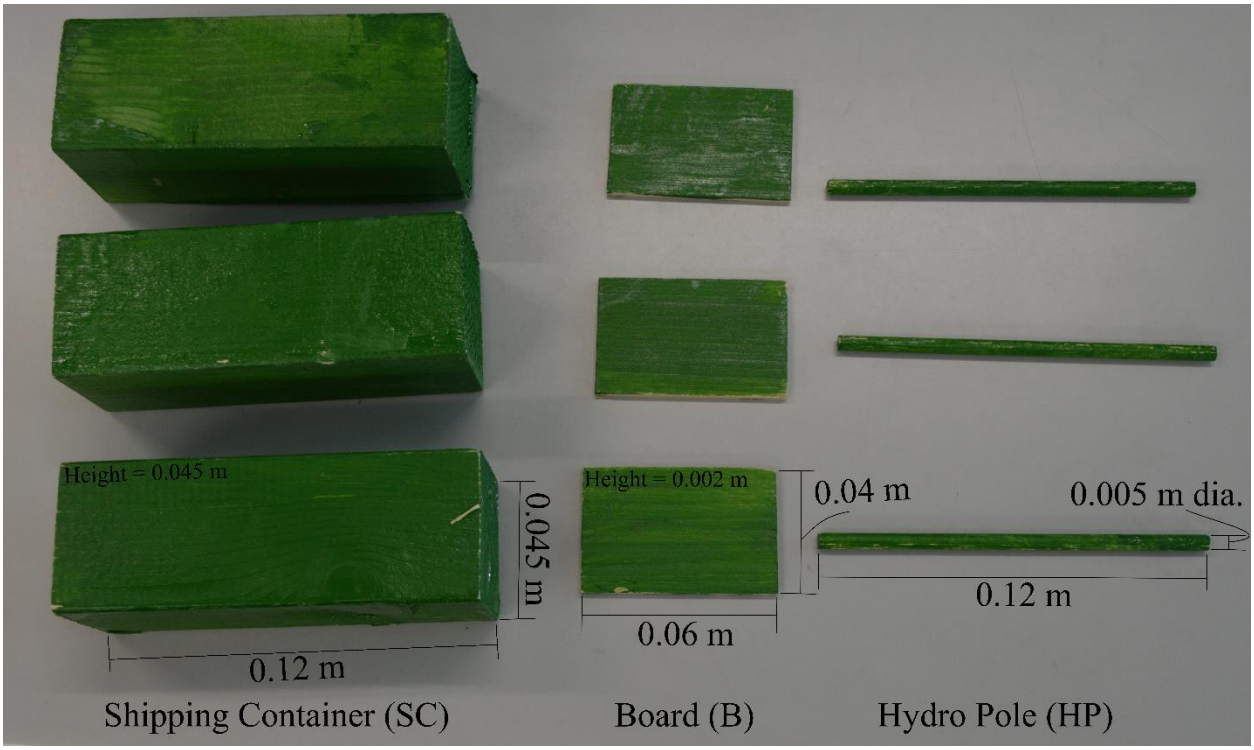

Fig. 4-4. Type of debris:(a) Shipping Container (SC); (b) Board (B); and (c) Hydro Pole (HP).

The debris were modelled after standard debris used in current building guidelines (Chock 2016). The properties of each debris type are outlined in Table 2 and their geometry and aspect is shown in Figure 4. The shipping containers were modelled as standard 6.00 m long shipping containers (Knorr and Kutzner 2008). The hydro poles were modelled as standard 6.00 m (0.25 m dia.) long hydro poles (Aghl et al. 2014). The boards were selected to model sheets of dry wall and plywood observed in images of debris damming that occurred in field studies (Nistor and Palermo 2015). The dry wall and plywood were generally of arbitrary shape as they were severely damaged when entrained within the flow; however, to maintain repeatability between cases, a single type of board (0.06 m x 0.04 m x 0.002 m) was selected.

The characteristic length is a variable often used to describe the physical properties of an object, however the definition varies widely depending on the application. As the focus of this study is on the formation of a debris dam, the primary factor influencing the dam formation is whether the debris contacts the obstacle or not. Visual observations of the debris propagation towards the obstacles showed that the orientation of the debris relative to the flow direction was a probabilistic process. Therefore, it was assumed that each dimension of the debris had equal chance of contacting the obstacles. Therefore, an average of the physical dimensions of the debris (length, width, and height) was used as the characteristic length. The characteristic length of the debris mixture was taken as the averaged characteristic length, weighed by the volume of debris present within each configuration. The dimensionless length (L) was the characteristic length of the debris divided by the opening width (W) of the obstacles.

$$L_c = \frac{V_{SC}L_{SC} + V_{HP}L_{HP} + V_B L_B}{V_{SC} + V_{HP} + V_B} \tag{4-1}$$

where V is the volume of the debris and L is the length of the debris.

Table 4-2. Debris Properties

	Dimensions					Dimensionless Variables
Type of Debris	Length [m]	Width [m]	Height [m]	Characteristic Length [m]	Surface Area-to-Volume Ratio [m^{-1}]	Length [--]
Shipping Container (SC)	0.12	0.045	0.045	0.070	105.56	1.17
Hydro Pole (HP)	0.12	0.005	0.005	0.043	816.67	0.72
Board (B)	0.06	0.04	0.002	0.034	1083.33	0.57

The debris was scaled using the 1:50 length scale for the dimensions and mass of the objects. However, due to the heterogeneous nature of prototype shipping containers and size-strength ratio of the boards and hydro poles, material properties (stiffness, yield strength, etc.) of the debris and the obstacles were not properly scaled (Bazant 2005). Additionally, as shown in images from the 2005 Hurricane Katrina (Robertson et al. 2007), significant damage affected the debris which could potentially influence the observed stability of the debris dam as well as the roughness of the dam within this study.

Experimental Protocol

This study aims to assess the influence of the debris concentration and flow velocity on dam formation and loads. The experiment employed three different flow velocities (0.3, 0.45, and 0.60 m/s), in combination with a large variety of debris configurations (Table 4-3). Within each experimental category, three repetitions were performed except in the case with the clear water conditions (Category 1, 11, and 21), for a total of 93 individual experiments. Three repetitions were chosen to examine the repeatability of each test case. Experiments were run for 60 s to allow for the dam to reach an equilibrium condition.

The experimental protocol was designed to fit within the framework of the risk associated with debris impact used in the ASCE 7 Tsunami Loads and Effects (Chock 2016, Nistor et al. 2017). The framework assesses the risk associated with debris impact as a function of the plan area of the debris. By extension, the occurrence of debris impact would also carry an associated risk of debris damming. As such, six cases were performed with similar plan area of the debris with different mixtures of the three debris types. Two cases were then performed with multiples of the plan area to evaluate the influence of the plan area. For the flow velocity of 0.45 m/s, three other experimental sets (31, 32, and 33) were performed to investigate the influence of the debris shape on the repeatability and loads associated with the dam formation by performing test with similar volumes.

Table 4-3. Experimental Protocol

Category	**Experimental Condition**	**Water Depth (h) [m]**	**Flow Velocity (v) [m/s]**	$Fr = v/\sqrt{gh}$ **[--]**	**Debris Cases [SC,HP,B]**
1	A	0.10	0.60	0.60	0,0,0
2					9,0,0
3					0,81,0
4					0,0,20

5					3,27,7
6					7,9,2
7					1,63,2
8					1,9,16
9					6,54,14
10					9,81,20
11	B	0.10	0.30	0.30	0,0,0
12					9,0,0
13					0,81,0
14					0,0,20
15					3,27,7
16					7,9,2
17					1,63,2
18					1,9,16
19					6,54,14
20					9,81,20
21	C	0.10	0.45	0.45	0,0,0
22					9,0,0
23					0,81,0
24					0,0,20
25					3,27,7
26					7,9,2
27					1,63,2
28					1,9,16
29					6,54,14
30					9,81,20
31					1,0,0
32					0,103,0
33					0,0,52

Debris Dam Measurement

The debris dam formation was monitored using the two-cameras setup shown in Fig. 4-1. Due to difficulties with occlusion of sections of the dam from the side, as well as due to the 3D nature of the dam, the latter was conservatively defined as a uniform box related to its maximum width, depth, and length. The HS camera was used to monitor the depth (d) and length (l) of the dam (Fig. 4-5b). To be consistent, the depth and length were selected based on the debris closest to the camera. The depth was considered for the free-surface water elevation at the structure to be consistent with the definition used for cross-sectional area of the debris dam in Equation 3. The video camera was used to monitor the width of the dam (Fig. 4-5c). The width (w) was defined as the width of the debris dam at the face of the obstacles.

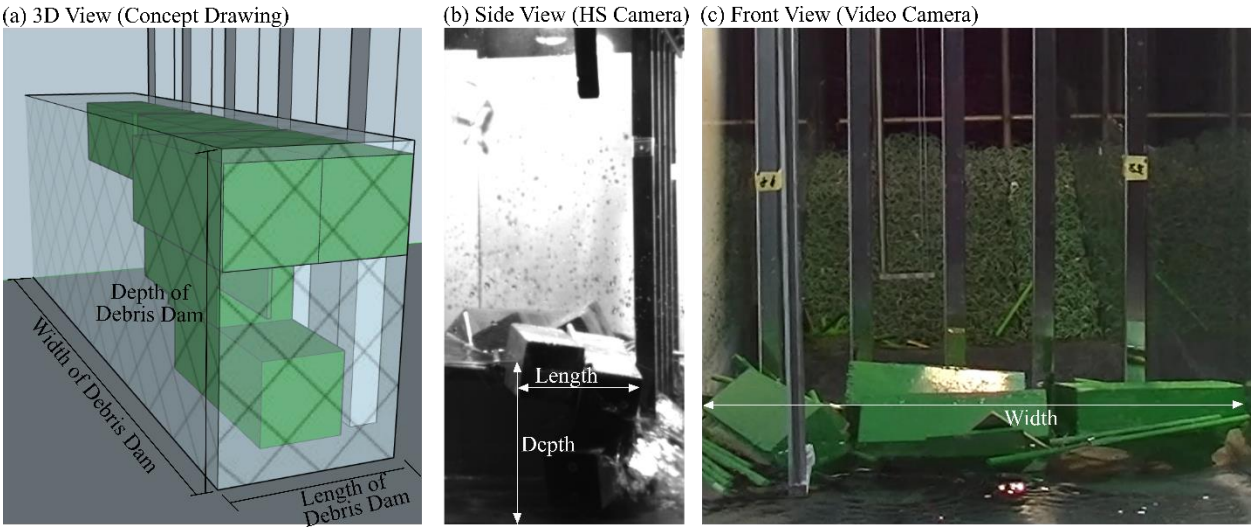

Fig. 4-5. Measurement of debris dam dimensions using a two-camera system. (a) conceptual drawing of the dam dimensions; (b) image from the HS Camera; and (c) image from the video camera.

The dimensions of the dam were manually selected for each image within the experiment. Repetitions of four experimental trials found the standard deviation of the equilibrium dam length to be 0.01 m. Determining the correct debris dam shape could not be captured by the two camera system and there was not a system in place to capture such 3D images in a hydraulic environment due to potential for damage from the free-floating solid objects.

Statistical Analysis

Throughout the following section, statistical analysis is used to quantitatively determine the significance of the results. The following two tests, in particular, are used extensively and are explained within the context of this study. Through this section, the results of the statistical test are reported as the test statistic and p-value.

Welch's T-Test

The paired t-test was used to examine the difference between the mean values between the different flow conditions. The basis of the Welch's t-test is to examine the change of a dependent variable between two related, independent groups with unequal variances (McDonald 2009). The null hypothesis of the test states that the difference between each paired measurement is zero. For this study, the paired measurements are the mean value of the three repetitions for the various debris configurations.

Analysis of Covariance (ANCOVA)

The analysis of covariance is typically used to compare two or more regression lines to determine if the trends are significantly different (McDonald 2009). The test is used to examine the change in a dependent variable between groups while controlling for the change in the variable as a function of a second measurement variable. The null hypothesis of the test states that both the slope and the y-intercept of the regression lines are statistically the same. For this study, the regression lines between the flow conditions were compared to determine if the flow conditions had a significant influence on the described results.

4.1.3 Results

Experimental Hydrodynamics

Steady-state flow conditions were selected for the investigation of debris damming loads and effects due to the relatively long duration needed for the formation of an equilibrium debris dam condition (Schmocker and Hager 2013). Transient flow conditions often found during rapid coastal inundation events occurring as a result of storm surges or tsunami will be addressed in a separate study. Three flow velocities (0.30 m/s, 0.45 m/s, and 0.60 m/s) were selected for the experiments with a constant water depth. The time-history of the water depths, flow velocities and associated horizontal in-stream forces can be observed in Fig. 4-6 for the clear-water conditions (no debris). As observed in Fig. 4-6a-b, the flow was steady throughout this experimental run. The standard deviation from the mean, averaged across categories, was 2.91×10^{-4} m and 0.005 m/s for water heights (WG1) and flow velocity (ECM1), respectively.

The horizontal force measured in the flow direction (in-stream) for each clear water condition is shown in Fig. 4-6c. The force measurement had a standard deviation of 0.203 N across the three categories. The rigid point in which the load cell was connected to the flume wall, which was also connected to the pump. As a result, slight vibrations were noted; however, the resulting noise was negligible. For each category, the mean drag coefficient per unit width was calculated for the entire obstacle as 0.60 ± 0.057 [95% Confidence Interval (CI)].

While it is widely established that coastal flooding events are characterized by transient flow conditions, there are significant difficulties in physically modelling the long duration flow events, particularly in the case of tsunami (Madsen et al. 2008). As a preliminary investigation of debris damming, the transient nature of coastal flooding was not considered herein. However, comparing to tsunami, the time scale of the local flow conditions, in field studies of tsunami-stricken areas, (~ 7 min at prototype scale) is significantly shorter than the tsunami wave period (> 10 min) (Mitobe et al. 2016). The flow velocities at prototype scale (2 – 7 m/s) in these tests compared well to the velocities observed in the 2004 Indian Ocean Tsunami (2 – 5 m/s) (Fritz et al. 2006).

The drag coefficient varies with the Reynolds number in incompressible flow (Hughes 1993). As the experiments were scaled using Froude similitude, scale issues potentially exist. Bricker et al. (2015) outlined the necessity for properly scaling the Reynolds and Weber numbers to correctly address issues related to turbulence and surface tension. The experiment presented herein had Reynolds numbers in the range of $3 – 6 \times 10^5$, representing the fully turbulent flow condition needed to avoid significant scale effects. Additionally, the Weber number ranged from 123.6 – 494.5 which exceeds the critical values of 120 presented by Peakall and Warburton (1996).

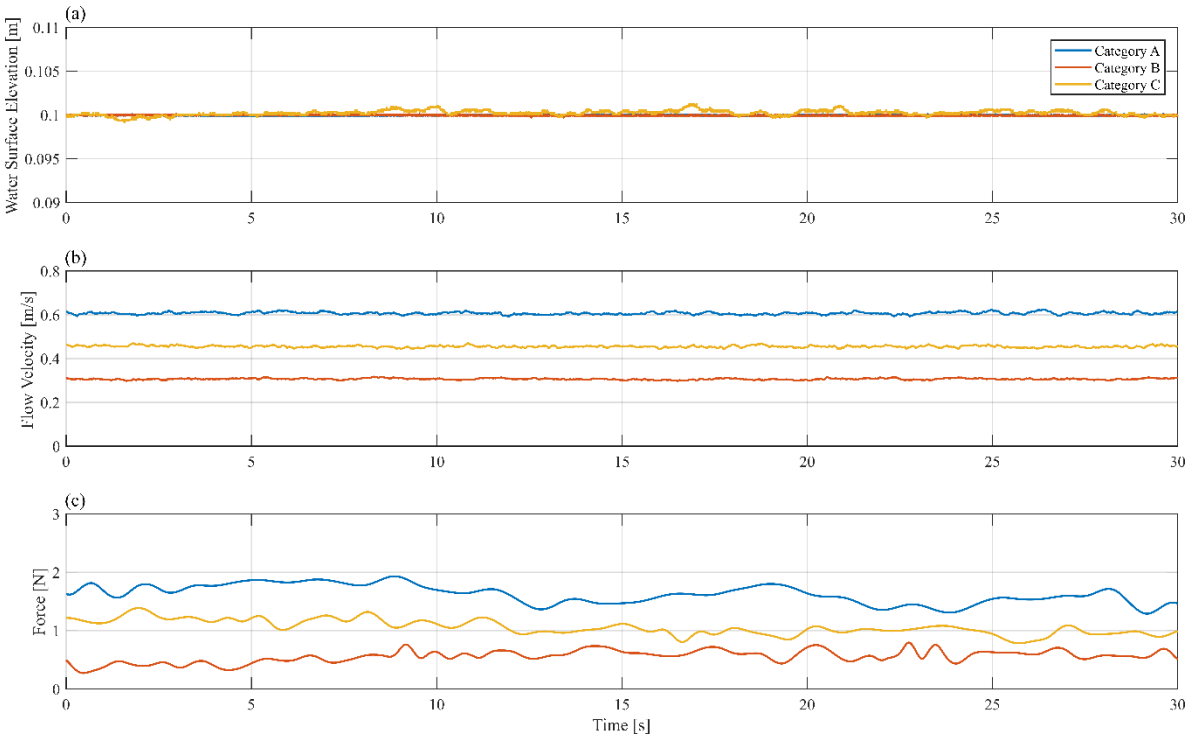

Fig. 4-6. Hydrodynamic conditions in clear-water conditions for the three experimental categories listed in Table 3. (a) WG1 (x = 1.00 m); (b) ECM1 (x = 1.00 m); and (c) FT (x = 3.50 m).

Debris Geometry

To examine the influence of the debris geometry, three experimental categories were conducted with the same volume of debris (categories 31, 32, and 33). While each case resulted in an increase in the forces acting on the obstacles, there was noticeable deviation in the magnitude and repeatability of the equilibrium force condition. Fig. 4-7 shows the difference in force-time histories for each of the same volume cases and compares with the base case where not debris was added into the water.

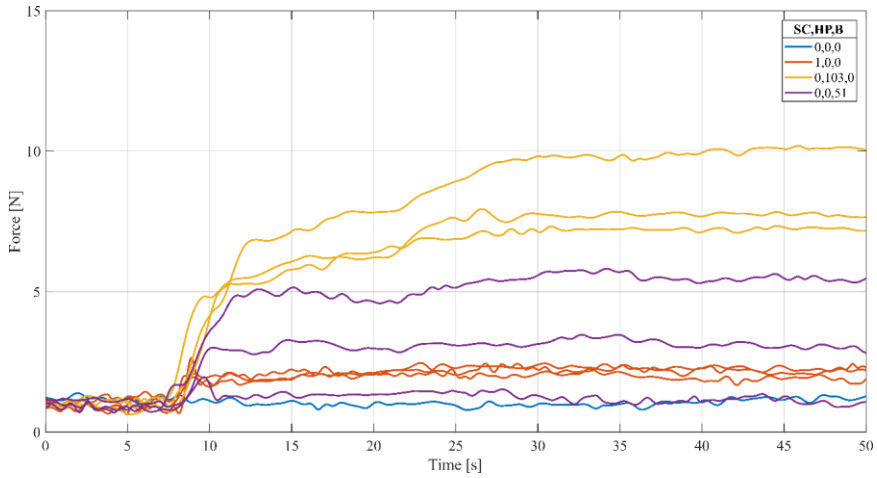

Fig. 4-7. Force-time history of same volume cases and comparison with the base case without debris. The debris category is displayed in colors. The number of each type of debris are displayed within the legend (SC, HP, B).

The differences in the debris geometry resulted in varying dam formation characteristics. The cases with a single shipping container consistently formed a dam with similar characteristics and loads, whereas the characteristics of the hydro pole and boards varied between trials. Bocchiola et al. (2008) discussed the importance of the *"key" log* in the formation of a debris dam. The "key" log refers to the first object to get caught on the obstacle and initiates the formation of the dam.

The formation of the *"key" log* influenced the deviations observed in the force-time histories. The case with the single shipping container consistently resulted in the dam forming as the length of the shipping container exceeded the width between the obstacles. Similarly, the hydro pole length exceeded the distance between the obstacles; however, the smaller characteristic length (a function of the dimensions of the debris) resulted in larger deviation between trials. The boards' length was equal to the distance between the obstacles, resulting in the board being unable to bridge between two obstacles and an inconsistent formation of the dam.

A comparison of the capture efficiency (the number of debris capture divided by the total number of debris) for each debris type for all the experiments (regardless of debris mixture) shows the influence of the physical properties of the debris (Fig. 4-8). The probability in this case was the count of the number of experiments divided by the number of experiments that contained the debris type. The mean capture rate (average percentage of each type of debris captured in the experiment) and standard deviation (SD) are shown on each histogram. Due to the larger size of the shipping container, the debris was consistently captured with a significantly greater capture rate and less deviation. Whereas, the smaller characteristic length of the hydro poles and boards resulted in smaller capture rates with greater deviation between experiments.

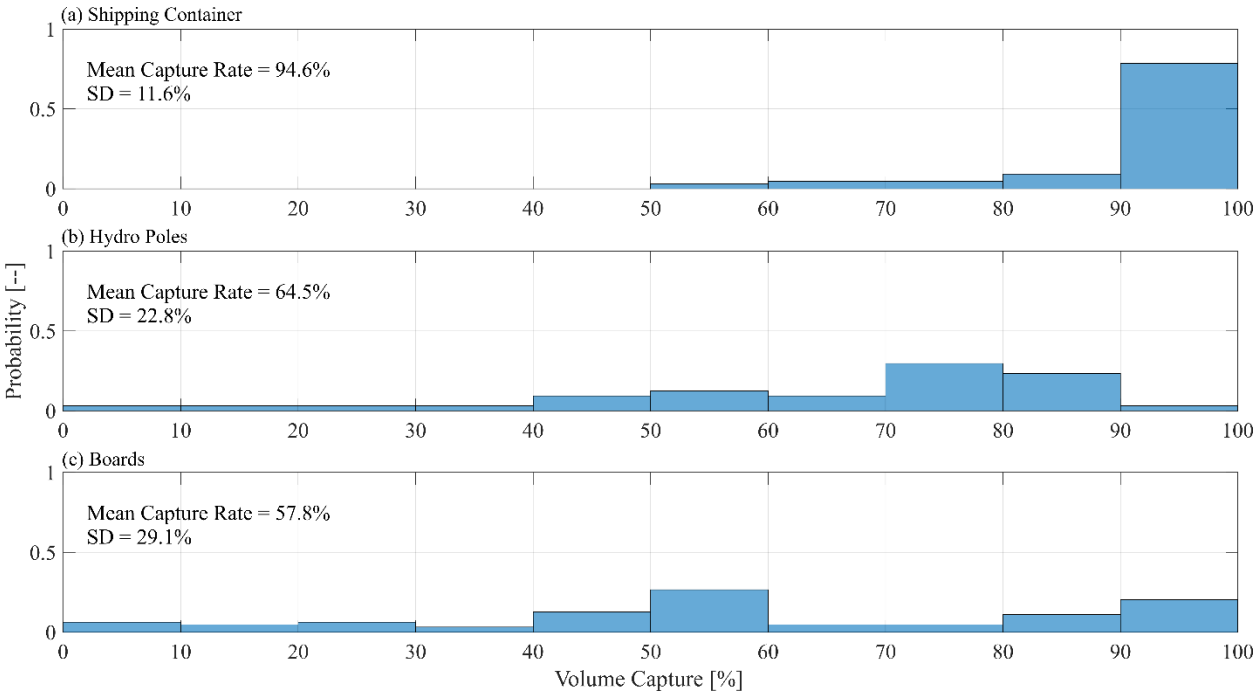

Fig. 4-8. Capture efficiency of the debris types for all experiments. (a) Shipping Containers (SC); (b) Hydro Poles (HP); and (c) Boards (B).

The difference in the magnitude of the load as a result of the debris dam formation was a function of the blockage ratio (B) caused by the debris dam (the area of the dam transverse (a) to the flow direction

divided by the total available cross-section of the flow (*A*)). While each case depicted in Fig. 4-7 had the same volume, the hydro poles and boards had an increased available surface area due to their increased surface area-to-volume ratio. Therefore, for a given volume of debris and flow condition, the characteristic length of the debris influenced the consistency of the formation of the dam and the surface area-to-volume ratio influenced the magnitude of the debris damming load.

Debris Dam Properties

The formation of a debris dam has been well-established by Bocchiola et al. (2008) and Schmocker and Hager (2013). The initial formation of the dam begins once the *"key" log* has become blocked at the obstacle face (Fig. 4-9a). The initial formation results in the streamlines forcing the incoming debris to begin to span the width of the flume (y-direction) (Fig. 4-9b) (Schmocker and Hager 2013). As the debris continue to accumulate on the face of the obstacle (increasing the width of the dam), the power of the flow causes the dam to compact at the obstacle face, forcing the debris at the face towards the flume bottom (increasing the depth of the dam) (Fig. 4-9c). Throughout this process, the dam continually increases the blockage of the flow, causing a rise in water level (backwater rise) and a reduction in the flow velocity. Once the flow velocity has been sufficiently reduced, a debris carpet begins to form upstream of the dam (increasing the length of the dam) (Fig. 4-9d).

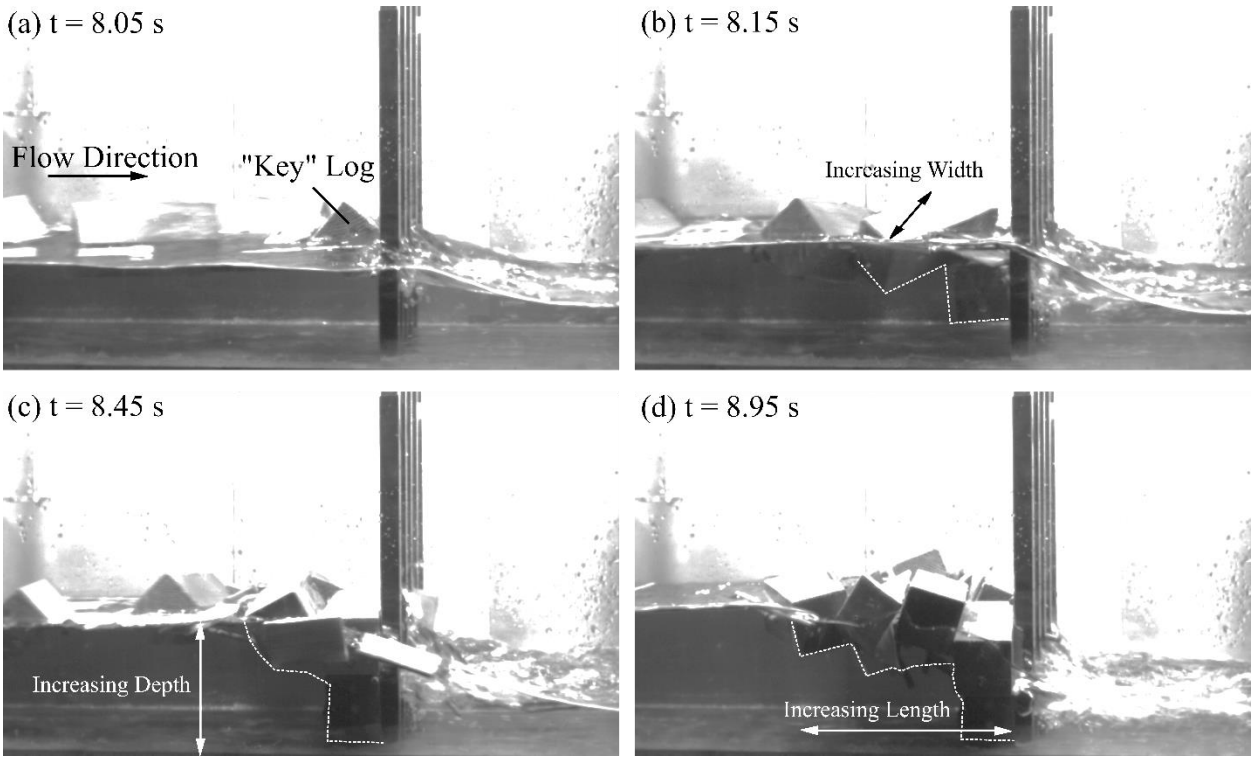

Fig. 4-9. Qualitative examination of debris dam formation. (a) Capture of the "key" log; (b) Increasing width of the dam; (c) Increasing depth of the dam; and (d) Increasing length of the dam. White dashed line shows the outline of the dam under the water surface.

Pfister et al. (2013) showed that the capture efficiency was dependent on the diameter (D) of the debris, in this case large woody debris, for a piano key weir. Their study showed that the capture efficiency of the large woody debris was high when the diameter was greater than 1.

$$\frac{V_c}{V} = 1.5\left(\frac{D}{W}\right) - 0.5 \quad (4\text{-}2)$$

Fig. 4-8 shows the individual debris capture efficiency for each experiment. Fig. 4-10 shows the capture efficiency of each experiment based on the volume-averaged dimensionless length. As can be observed, the capture efficiency approximately linearly increased as the characteristic length increased ($R^2 = 0.512$):

$$\frac{V_c}{V} = 0.818\frac{L_c}{W} \quad (4\text{-}3)$$

where V_c is the captured volume of debris at the obstacle face and V is the total volume of debris. An ANCOVA comparison of the trends for the different flow conditions showed no significant difference between the capture efficiency regression lines ($F(2,81) = 0.45$, $p = 0.641$). Previous studies indicated with increased Froude number, the stability of dam decreased (Bocchiola et al. 2008), however this was not observed in this study, potentially due to the relatively small range of Froude numbers examined.

Eq. (4-3) represents a deterministic evaluation of the volume capture as a function of the dimensionless characteristic length. However, as discussed earlier, debris transport is a stochastic process. The propagation orientation of the debris, which influenced weather the debris would contact the obstacle or not, is a probabilistic process influenced by a variety of factor, such as the flow conditions and surrounding topography (2008). As a result, significant scatter can be observed around the regression line. In this study, the characteristic length was calculated assuming that each side had an equal opportunity of forming the "key" log. Previous studies of debris transport have discussed the prevalence of a mean orientation (Stolle et al. 2017a) around which the likely debris orientations within the flow would be distributed. Detailed stochastic analysis of solid object orientation within the flow is needed to get a more accurate estimation of the characteristic length, something which is outside the scope of this study.

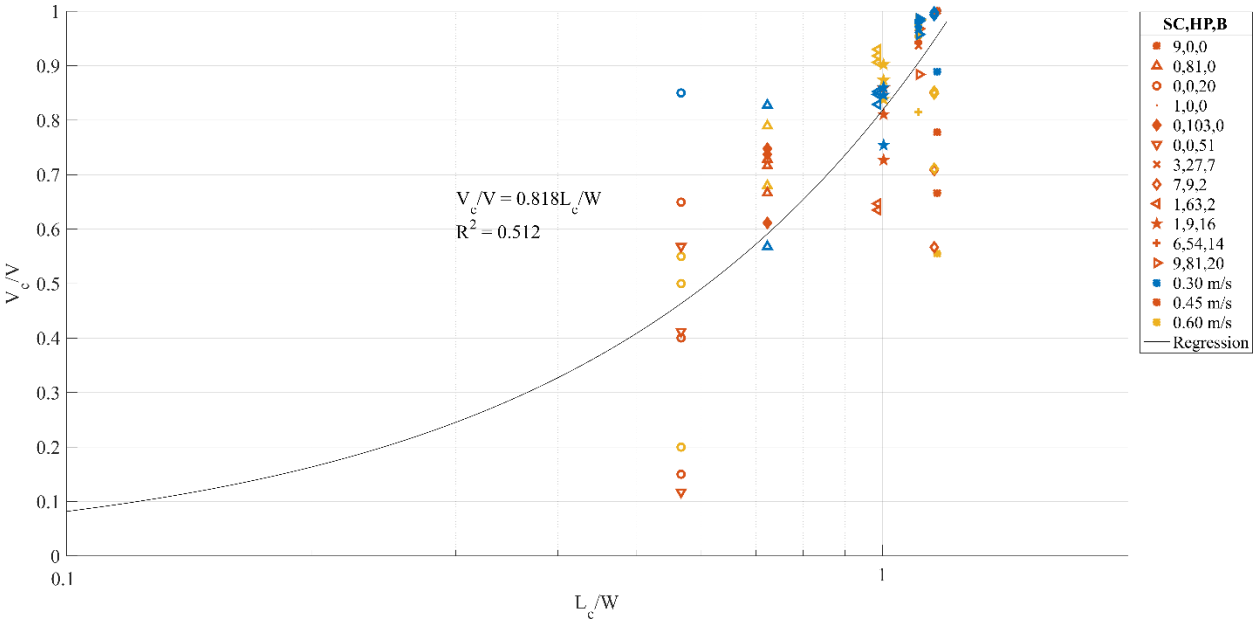

Fig. 4-10. Capture efficiency as a function of the characteristic length of the debris source. The debris configuration indicated by the marker type, flow condition indicated by the color.

Fig. 4-11 shows the formation properties of the dam, namely its width, length, and depth as a function of the debris volume. As expected, all properties of the dam increased with an increase in the debris supply. In this study, the width of the dam was limited by the flume width (0.40 m). Similarly, the depth of the

debris dam was limited by the flume bottom; however, this limitation was offset by the increasing flow depth as a result of flow blockage. This resulted in dam depths potentially greater than the initial flow depth. The debris length was influenced by the flow velocity as sufficiently high flow velocities would cause the dam to compact at the obstacle face as opposed to forming the debris carpet.

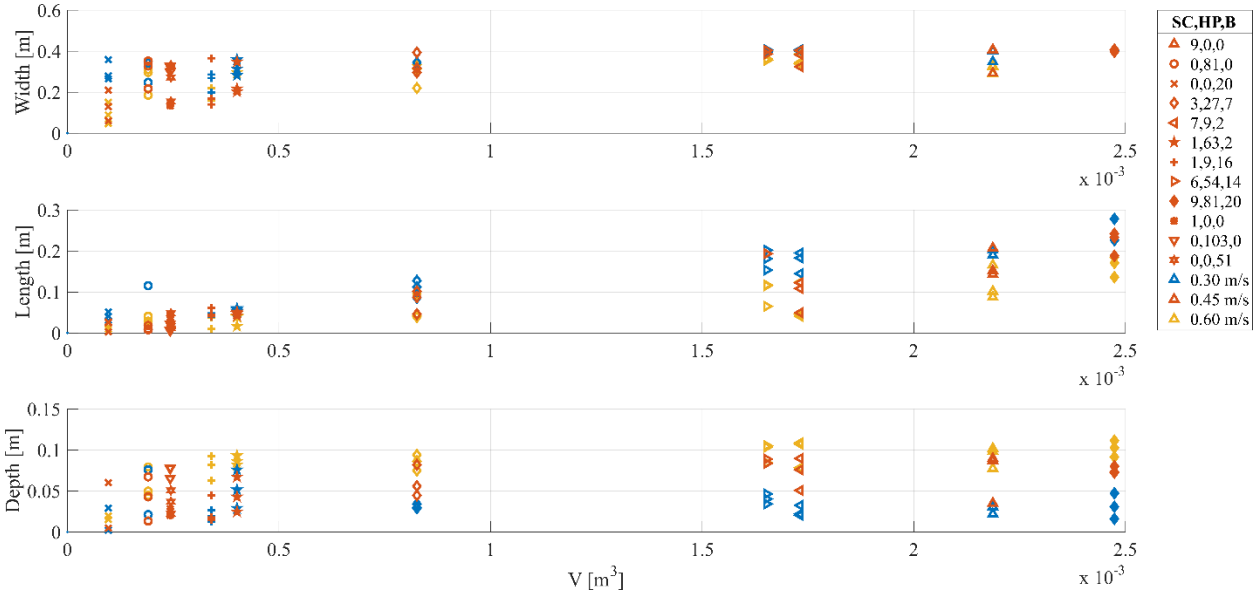

Fig. 4-11. Debris dam properties (a) Width (y-direction), (b) Length (x-direction), and (c) Depth (z-direction) as a function of the debris volume. The debris configuration is indicated with differing symbols; the flow velocity is also displayed.

A comparison of the dam formation with the differing flow velocities further confirms the dam formation process outlined by Schmocker and Hager (2013). In the cases with the larger flow velocity, compaction of the dam at the face of the structure occurred, forcing the debris towards the bed. As shown in Fig. 4-11c, the cases with the larger flow velocities consistently had larger depths. Additionally, the cases with lower flow velocities resulted in the dam lengthening as the debris carpet formed, and, alternatively, shallower dams. The width of the debris dam appeared to be primarily driven by the amount of debris supplied to the obstacle.

Additional considerations are needed when addressing the formation of the dam in coastal settings. Pasha and Tanaka [40], in their study of debris damming in coastal forests during a tsunami event, found that debris with a larger surface contacting the structure were more stable and less likely to be forced towards the bed. In Fig. 4-11, cases with larger volumes of the hydro poles (circle and star markers) tended to form deeper dams as a result of less contact area with the obstacle. Whereas, the boards and shipping containers tended to contact the obstacles and become immediately stable forming shallower dams.

Considering Eq. (2-22), an important aspect of the debris dam governing the debris loads is the transverse cross-sectional area of the dam. In the case of this study, the transverse cross-sectional area was designated by the width and depth. As the flow velocity influenced the formation of the dam, Fig. 4-12 shows the cross-sectional area (a), normalized by the available cross-sectional area (A), herein referred to as the blockage ratio (B), as a function of the Froude number.

$$B = \frac{a}{A} \tag{4-4}$$

As the width of the debris dam was primarily determined based on the volume of debris supplied to the site, increasing the Froude number resulted in deeper dams. Fig. 4-12 shows an increase in the mean blockage ratio as a function of the Froude number. A paired t-test was performed between the three flow velocities and found significantly greater blockage ratio as the Froude number increased. Between Froude numbers of 0.3 and 0.45, the blockage ratio was significantly greater ($t(8) = -2.805$, $p = 0.023$) and similarly for Froude number 0.45 and 0.6 ($t(8) = -3.278$, $p = 0.0112$).

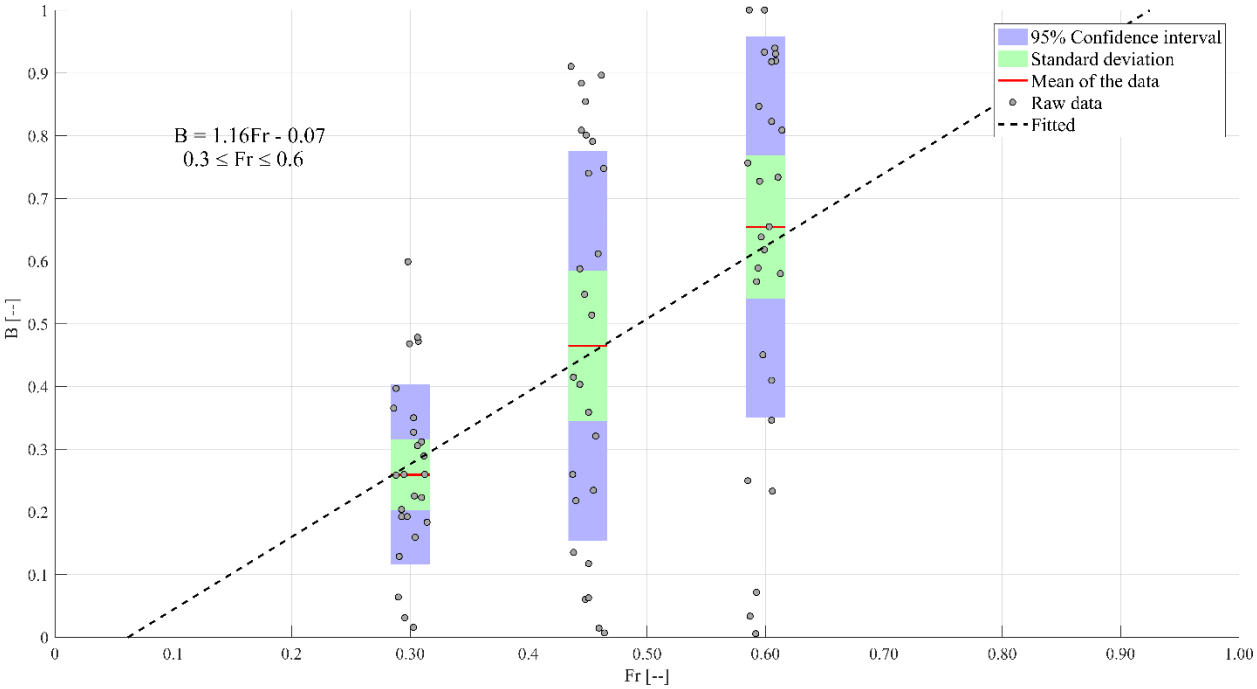

Fig. 4-12. Blockage ratio of the dam as a function of the Froude number. All equilibrium blockage ratios are displayed as grey dots; the mean blockage ratio is displayed as a solid line.

As shown in Fig. 4-12, there was significant deviation in the cross-section of the dam. Considering the random nature associated with debris motion (Matsutomi 2009, Rueben et al. 2014), the formation of the "key" log varied between experimental cases which influenced when the dam began to form and the amount of debris trapped within it. The increased Froude number additionally resulted in increased stability of the initial "key" log, which aided in the formation of the dam. While the porosity of the dam could not be established in this study, the increase compaction of the dam caused by the increased flow power would decrease the porosity of the dam. However, further research is needed to evaluate the extent of this influence.

While general observations can be made regarding the dam formation, the relatively small width of the flume resulted in a limit to the dam formation influencing the effectiveness in developing comprehensive methods of estimating dam size from debris volume and flow conditions. Additionally, due to difficulties in directly assessing the cross-sectional area, the selection method was conservative as it did not consider the porosity of the dam.

Backwater Rise

The application of the energy equations across an obstruction in a channel in subcritical flow conditions shows that a corresponding increase in the channel constriction results in a rise of the water surface upstream of the obstruction (El-Alfy 2009). In the context of this study, backwater rise ($\Delta\eta$) is defined as:

$$\frac{\Delta\eta}{\eta_0} = \frac{\eta - \eta_t}{\eta_0} \tag{4-5}$$

where η_0 is the initial water level without the obstacles (for all cases 0.10 m), η is the water level upstream of the dam, η_t is the water level without the dam (as a result of the obstruction of the obstacles).

Using the momentum equations, Fenton (2003) showed that backwater rises as a function of the Froude number. Fig. 4-13 displays the backwater rise, normalized by the initial water depth, as a function of the Froude number. The backwater rise showed a significant increase as the Froude number increased as expected due to the increase in the blockage ratio. Between a Froude number of 0.3 and 0.45, the backwater rise increased ($t(8) = -5.433$, $p < 0.001$) as well as between 0.45 and 0.6 ($t(8) = -6.764$, $p < 0.001$).

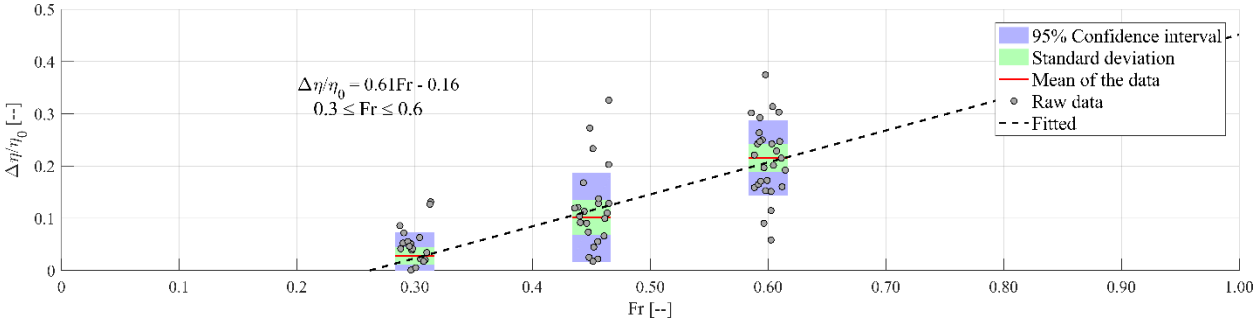

Fig. 4-13. Backwater rise as a function of the Froude number. For each hydrodynamic boundary condition, all equilibrium backwater rise is displayed as a grey dot; the mean of hydrodynamic boundary condition is displayed as a solid line.

Fig. 4-14 shows a comparison of the backwater rise in the experiments to the analytical solution from Fenton (2003). A constant drag coefficient was used, estimated in the following section for the cases where blockage ratios (B) exceed 0.46 (C_D = 1.417). The analytical solution well represents the trend of the backwater rise, however tends to overestimate the magnitude. Fenton (2003) noted that the linear explicit approximation of the momentum across the obstruction used in Eq. (2-23) would only be valid over a small obstruction of the channel, as large obstructions were generally observed this potentially resulted in the discrepancy. Additionally, Schmocker and Hager (2013) noted that the Froude number and available volume of debris influenced the backwater rise by influencing the compaction of the dam. This is particularly significant as the blockage of the dam was conservatively estimated. Additionally, porosity and irregular shapes were not considered in the calculation of the cross-sectional area of the dam.

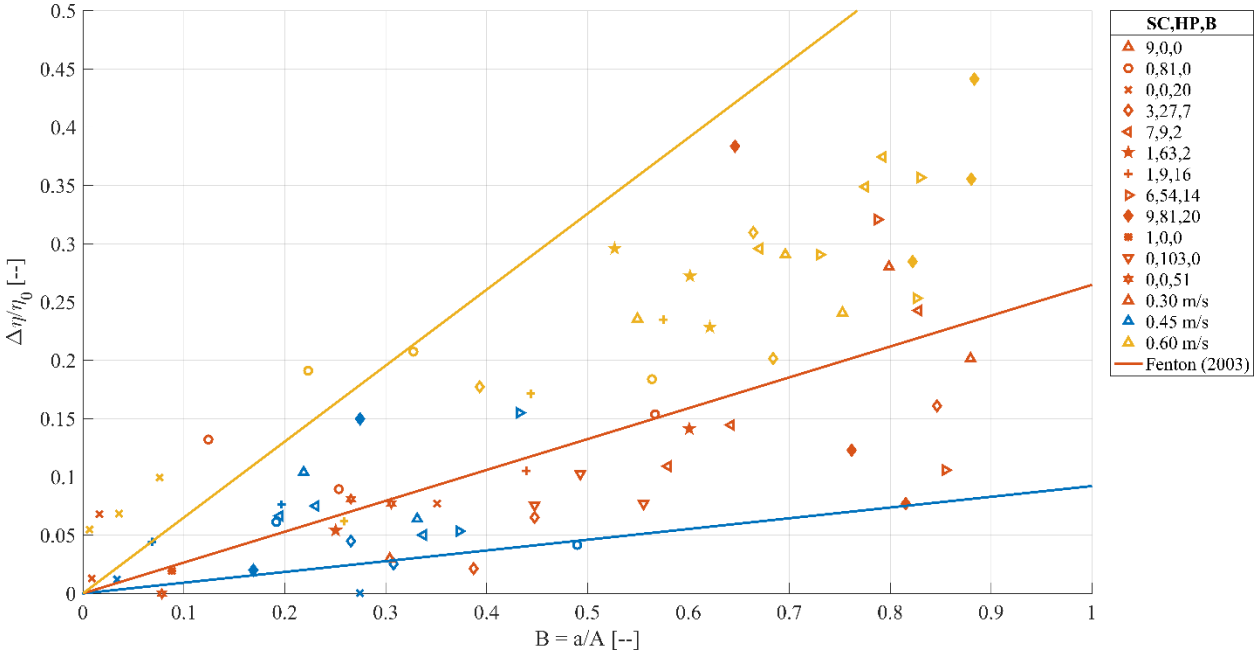

Fig. 4-14. Backwater rise as a function of the blockage ratio. The backwater rise is compared to the analytical solution from Fenton (2003). The different debris configurations are displayed by differing symbols, the hydrodynamic conditions are displayed by color.

Drag Forces

Debris damming has often been discussed within the context of increase drag forces acting on the obstacles. As can be observed from Eq. (2-22), the drag force is a function of the exposed cross-section area and the drag coefficient. A comparison of all the experiments showed than an increase in the Froude number resulted in a corresponding increase in the blockage ratio (Fig. 4-12). Fig. 4-15 shows a similar comparison between the equilibrium force, normalized by the equilibrium force with no debris present, and the Froude number. The increase in force did not follow the expected trend related to the increase in the blockage ratio.

The discrepancy between the blockage ratio and force trends is likely a results of the backwater rise associated with the restriction of the channel caused by the dam. As discussed in the previous section, the backwater rise is a function of the Froude number. Following the continuity equations, as the water surface increased upstream of the dam, flow velocity decreased. Considering Equation 1, the drag force is influence by water depth by $O(h)$, whereas the force is influenced by water velocity by $O(u^2)$. The decrease in flow velocity overcomes the increase cross-sectional area of the dam, resulting in the decrease in average force seen between 0.45 and 0.60. Between each case, no significant difference was observed. Significant deviation in equilibrium force values can be observed in all cases; however, this was most prominently observed for Fr = 0.6. Analyzing the results in Fig. 4-12, the larger variation in the blockage ratio associated with the higher Froude number results in an associated increase in the deviation in measured forces.

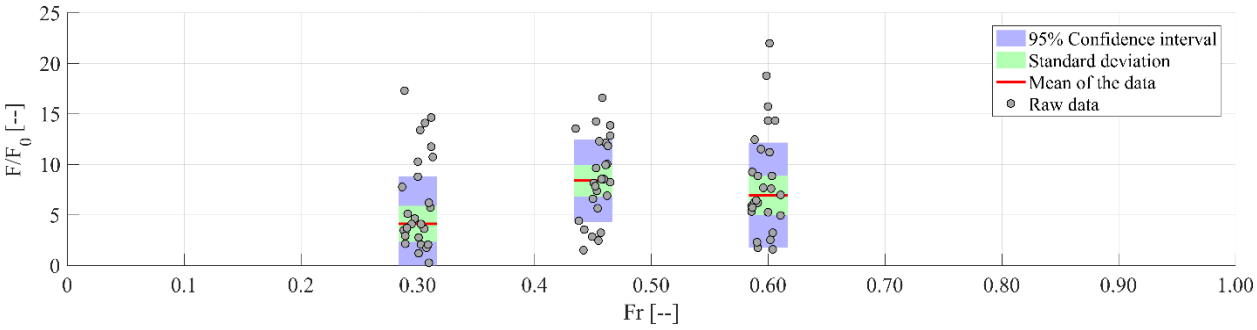

Fig. 4-15. Load on the obstacles as a function of the Froude number. All equilibrium forces are displayed as the grey dots; the mean of the data is displayed by the solid red line.

Fig. 4-16 shows the increase in force as a function of the blockage ratio. Using Eq. (2-22), the dashed line in Fig. 4-16 represents the increase in force as a result of the change in cross-section, exclusively. As can be observed, the force in all cases exceeds the force predicted by the change in blockage ratio, therefore the FEMA [19] guidelines, as the drag coefficient is considered to be constant, would underestimate of debris damming force. Particularly since the porosity of the dam could not be evaluated, therefore the blockage ratio would tend to be overpredicted. However, the FEMA guidelines use a conservative estimation drag coefficient (C_D = 2.0), which was significantly greater than the drag coefficient used in this study (C_D = 0.6).

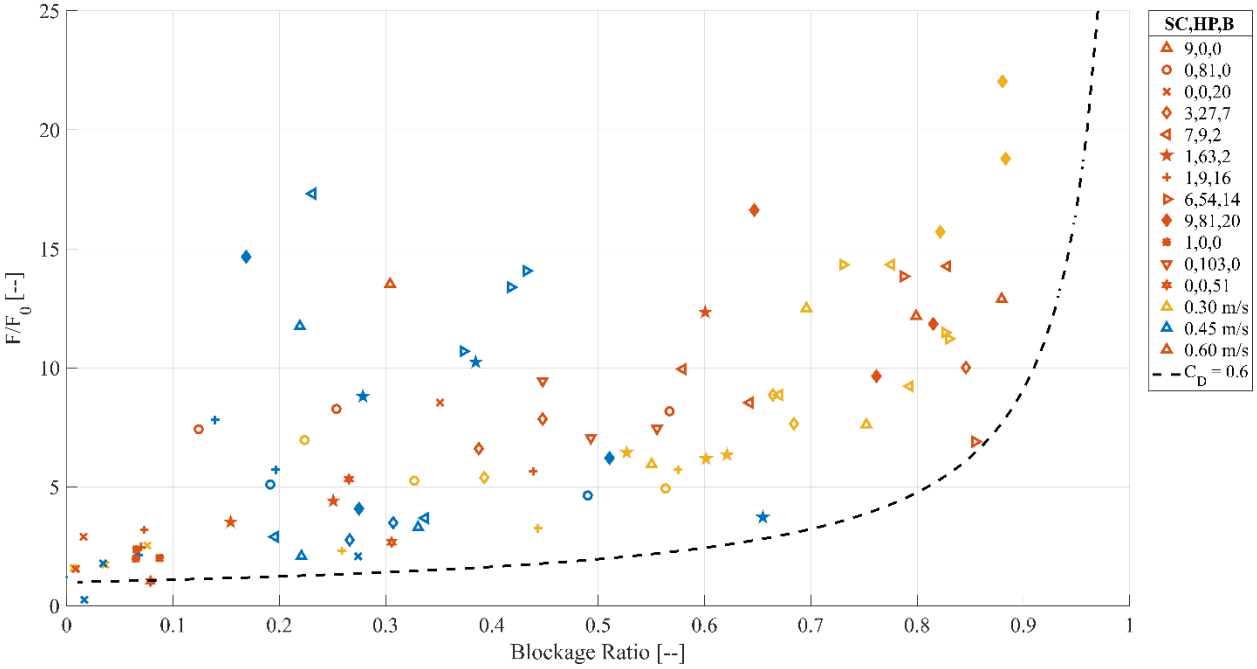

Fig. 4-16. Equilibrium force, normalized by equilibrium force before debris dam forms, as a function of blockage ratio. The debris configuration is denoted by the marker type; the color represents the hydrodynamic boundary condition. The dashed line represents the theoretical increase in force if only the change in blockage ratio is considered.

As discussed earlier, the formation of the blockage at the obstacles resulted in both an increase in upstream water surface and a decrease in the upstream flow velocity. Functional relationships of drag and flow conditions has shown that viscosity (and therefore the Reynold's number) is an important

consideration in assessing the drag coefficient. Therefore, with the change in flow conditions, the forces acting on the obstacles cannot be properly addressed exclusively examining the change in cross-sectional area.

Fig. 4-17 displays the drag coefficients per unit width as calculated from Eq. (2-22). Parola (2000), in a similar study of debris damming in steady-state conditions, determined drag coefficients using a contracted flow velocity, which is the flow velocity within the obstacle. In this study, due to difficulties in determining the contracted flow velocity without damaging instrumentation, the initial free-stream flow velocity before the dam forms was used in the calculation of the drag coefficient.

Due to the difference in the definition of flow velocity, a direct comparison to the Parola (2000) framework was not possible. However, examining the trends observed in the Parola (2000), for blockage ratios less than 0.36 showed significant deviation between experiments, resulting in the author taking a constant drag coefficient. For blockage ratios between 0.36 and 0.77, a distinctly negative trend could be observed, following by a levelling of the trend for blockage ratios between 0.77 to 1.

Fig. 4-17 shows qualitatively displays similar trends, for blockage ratios from 0 to 0.2, there was large deviations in the drag coefficient from 2.5 to 10. From 0.2 to 0.46, a distinctive negative trend can be observed, followed by a levelling off of the slope for blockage ratios exceeds 0.46. The 0.46 cut off value was chosen based on visual observation of the data set.

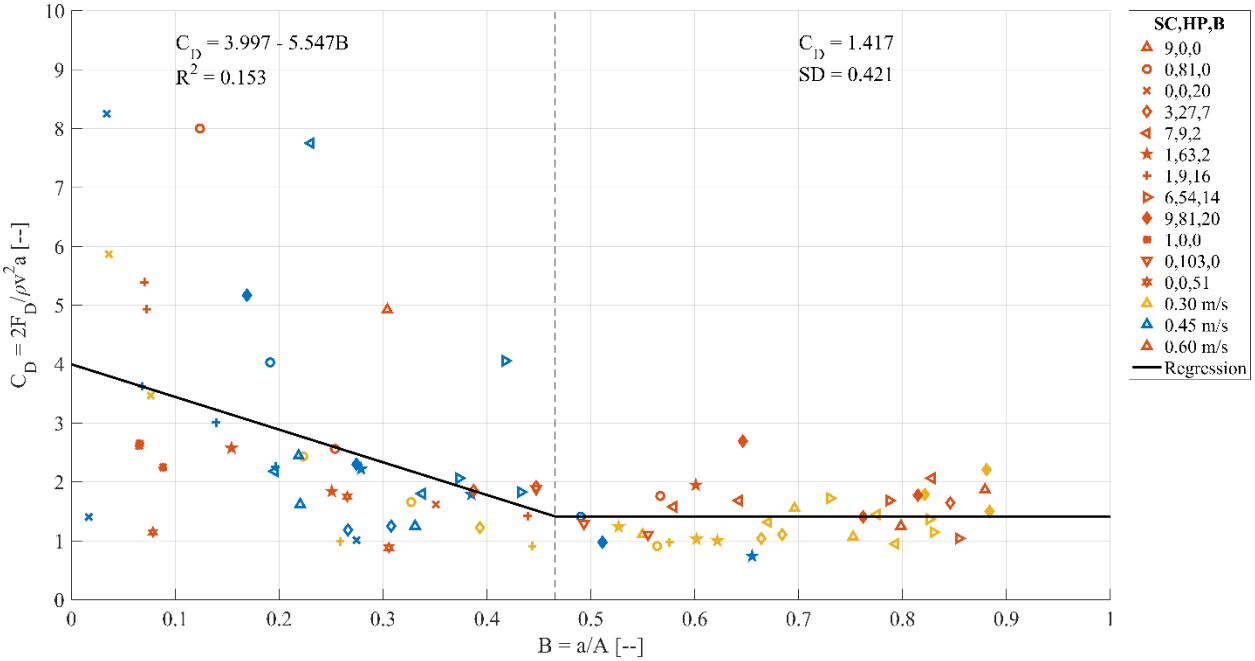

Fig. 4-17. Drag coefficient as a function of blockage ratio. The debris configuration is shown by marker type; the hydrodynamic boundary condition by color.

Quantitatively, the regression line displayed in Fig. 4-17 does not represent well the experimental data (R^2 = 0.153), suggesting that the mean of the data ($C_{D,mean}$ = 2.138, 95% CI [1.798, 2.477]) is a better representation of the drag coefficient. In the case of the smaller blockage ratios, the mean was difficult to assess due to large variations in the C_D values. The smaller blockage ratios were a result of fewer debris being captured, with less compaction occurring. As the estimation of the drag coefficient was dependent on the exposed frontal cross-sectional area of the dam, less compaction would result in increased porosity

of the dam and, therefore, the cross-sectional area would be less accurate than the highly compacted cases.

However, from an engineering standpoint, the smaller blockage ratios represent smaller force values due to the small cross-sectional area and consequently the smaller drag forces. In the case where the blockage ration exceeded 0.46, the data was well-represented by the mean (C_D = 1.417, 95% CI [1.277, 1.577]). The mean drag coefficient was similar to those recommended by the Canadian Standards Association (CSA) (2006) and the American Association of State Highway and Transportation Officials (AASHTO) (2012) for the design of bridge piers under debris damming loads (C_D = 1.40).

4.1.4 Discussion

The experimental setup used in this study was modelled as a generalized obstacle to examine the formation of debris dams during flooding events. The debris and obstacles were generally scaled using a 1:50 length scale employing Froude similitude. However, limitations exist in regards to the properties of the debris. Robertson et al. (2007) examined the aftermath of the 2006 Hurricane Katrina and noted significant inelastic deformation of the debris and the structures on which the debris dam formed. Additionally, as the debris forms the debris dam, there is potential for the debris to break apart due to the increase in drag forces (Schmocker and Hager 2013). The deformation and damage to the rigid debris was not investigated in this study and likely would influence the formation and stability of the dam. Pasha and Tanaka [28] noted the frictional forces between the debris and obstacles influenced the dam formation. The model debris was relatively smooth in comparison to prototype models therefore the influence of friction in the dam formation and stability would not be adequately captured by the model (Pasha and Tanaka 2016).

The focus of this study addressed the debris loads related to the drag forces caused by the formation of a debris dam. However, debris also exert loads on structures as a result of an impact. Due to rapid nature of the impact loading, the sampling rate of the load cell (100 Hz) in these experiments was insufficient to capture the impulses caused by the debris impacting the obstacle. To isolate the maximum loads caused by the formation of the dam, the impact loads were filtered out of the force signal using an Empirical Mode Decomposition EMD filter (Huang et al. 1998). While both loads are an important consideration in the design for extreme loading, generally, debris impact and damming loads are addressed separately due to the different nature of their load characteristics (Nistor et al. 2017). The debris impact is a dynamic force: as a result, several structural properties, such as natural frequency, must be taken into account into their design. Whereas, debris damming loads are commonly addressed as a static load as a function of the flow conditions and dam size (Eq. (2-22)). As such, debris design loading must be dealt with through different methods in the structural design.

The drag coefficient on the debris dam is a complex concept due to the dependency of the drag coefficient on the Reynold's number as well as dam properties, such as physical dimensions and porosity. As the experiments were scaled in the Froude domain, the Reynold's number must be carefully considered (Bricker et al. 2015). All the experiments were performed with a Reynold's number between 3.0 – 6.0 x 10^4, well within the fully-turbulent zone. Boundary layer experiments for both flat plates and spheres have shown similar characteristics regarding the drag coefficient (Yunus and Cimbala 2006). For fully developed turbulent flow, the drag coefficient can be considered to be independent of the Reynold's number until the point where the boundary layer transitions from laminar to turbulent, however this zone is well outside the range of these experiments (~2.0×10^5).

Due to the 2D nature of the flume, the formation of the dam resulted in a significant difference in hydrodynamic condition due to an increase in water depth, and a corresponding decrease in flow velocity.

Additionally, the large blockage ratios in the flume do not allow for adequate formation of the wake resulting in overestimations of the drag coefficient (Anthoine et al. 2009) for a given Reynold's number. In future studies, the investigation of the drag forces should be addressed within a 3D flume with adequate blockage ratios to limit wall effects.

Additional considerations are needed bearing in mind that the debris dam itself is a 3D process. The drag coefficient in this study (and commonly used in design guidelines) considers the 2D drag coefficient where the area was considered as the area of the dam exposed in the flow direction. Therefore, the drag coefficient neglects the effects of the skin friction acting on the surface of the debris parallel to the flow direction (Granville 1976). The calculation of the drag coefficient is dependent on the chosen reference area, in cases where the object is submerged within the fluid, such as an aircraft, the drag coefficient is often calculated using the surface area or the squared cubed root of the volume (Stevens et al. 2015). However, the squared cubed root of the dam would not adequately express the surface area due to the porous nature of the dam and the surface area could not be determined within the context of this study. Considering the need to maintain consistency within hydraulic engineering, the 2D drag coefficient was calculated using the area of the dam transverse the flow direction.

For the potential future application of these results in the design of coastal structures, careful consideration is needed for the granular material present within coastal flooding events (Robertson et al. 2007, Yeh et al. 2013). Stancanelli (2015), in the study of stony debris in river channels, showed that the grading of the debris can have significant influence on the dam properties and associated effects. Granular material has the potential to block the pores associated with the larger debris dam formation, influencing the porosity and size of the dam. As the results presented herein focus on clear water cases, further investigation into debris grading will be needed to properly address this issue.

4.1.5 Conclusions

This paper examines the formation of debris dams at a generic column obstacle under steady-state flow conditions. The study examined the influence of the debris hydrodynamics and their mixtures on the dam formation, as well as the associated backwater rise and loading on the structure.

Based on the presented results, the following conclusions can be drawn:

- The capture efficiency of the debris was dependent on the physical dimensions (length, width, and height) of the debris relative to the opening width of the obstacle. The larger characteristic length of the debris, the more readily the debris were captured at the obstacle.
- An increase in the supplied volume of debris to the obstacle resulted in an increase in the length, width, and depth of the debris dam.
- Flow velocity had a significant influence on the blockage of the channel. The increased velocity resulted in the debris being pushed towards the bed resulting in an increased depth of the dam. Decreased velocity resulted in the formation of a debris carpet at the free-surface in front of the obstacle.
- Hydrodynamic conditions (initial flow depth and velocity) had a significant influence on the backwater levels. An increase in the Froude number resulted in a larger blockage ratio and a more pronounced backwater rise.
- Hydrodynamic conditions did not have a significant influence on the drag forces acting on the obstacle. The increase in the water depth due to the backwater rise and decrease in flow velocity resulted in no significant increase. However, the restriction of the flow around the obstacle as a result of the two-dimensional (2-D) characteristics of the flow contributed to this results and should therefore be addressed in a 3-D setting.

This study is a preliminary investigation into the mechanics of debris dam formation in flooding events. Post-tsunami field surveys of affected communities demonstrated that debris damming is a major concern in coastal flooding events. As the debris dam can influence key design criteria, such as overtopping height, flow velocities, and scour depths, careful consideration is needed in the design of infrastructure prone to such hazard. Assessing the dam formation potential and its dimensions is needed to in determine design loads for tsunami resistant infrastructure. As in this experimental program the hydrodynamic forcing condition was steady-state, these results can also be applied across the wider discipline of hydraulic engineering, particularly related to design of infrastructure in debris-laden creeks and rivers.

4.1.6 Link to Section 4.2

The study investigated debris damming characteristics in steady-state flow conditions, which is a relatively well-established topic in hydraulic engineering. However, as the type of debris considered in tsunami engineering often deviates significantly from hydraulic engineering (who mainly focuses on large woody debris), this study acts as a bridge between coastal and hydraulic engineering. Using the lesson derived from this study, Section 4.2 will examine the different behaviour of debris damming in transient, high-energy flow conditions.

4.2 Experimental Investigation of Debris Damming Loads under Transient Supercritical Flow Conditions

Preprint of an article printed in Coastal Engineering© 2017 Elsevier.
https://www.sciencedirect.com/science/article/pii/S0378383918300504

4.2.1 Objectives

A thorough review of debris damming literature leads to the conclusion that the examination of debris damming has been predominantly performed in steady-state subcritical flow conditions. However, many flooding events, particularly tsunami and flash-floods, have transient flow properties (Saatcioglu et al. 2005, Ghobarah et al. 2006, Ioualalen et al. 2007) and can enter into trans-critical/supercritical ($Fr > 1$) flow regimes (Titov and Synolakis 1997, Fritz et al. 2006, Matsutomi and Okamoto 2010). Previous research into the hydraulic loads and flow-structure interaction associated with unsteady tsunami-like waves has shown distinctive wave profiles of transient nature that significantly differ from steady-state conditions (Arnason et al. 2009, St-Germain et al. 2013, Goseberg and Schlurmann 2014). Previous studies into debris loading in transient flow conditions have focused on loading related to debris impact (Ikeno et al. 2016, Shafiei et al. 2016b). Therefore, this study examines the formation and loading conditions associated with a debris dam in unsteady supercritical flow conditions with the objectives of:

- Studying the formation of debris dams in unsteady flow conditions and contrasting that to the formation mechanisms described by Schmocker and Hager (2013).
- Examining the influence of debris shape on the formation and stability of the debris dam.
- Determining the runup of the supercritical flow on the obstacle as a result of the debris dam formation.
- Evaluating the loading conditions on the obstacle as a result of the debris dam formation.

This study was coupled with a steady-state examination of debris damming in subcritical flow conditions in the same facility to allow for a direct comparison to steady-state conditions.

4.2.2 Experimental Setup

Experimental Facilities

The experiments were performed in the High-Discharge Flume at Waseda University, Tokyo (Japan). The flume shown in Fig. 4-18 was 14.0 m long × 0.40 m wide × 0.80 m high and is typically used in the physical modelling of 2D hydraulic problems. The flume was separated into two sections: the reservoir (light blue) and the propagation section. The floor of both sections was stainless steel. The propagation section consisted of a 2.0 m long 1:10 slope followed by a 4.0 m flat section. The 1:10 slope was used to provide adequate storage from the high-discharge flow to avoid any backwater effects caused by the flow exceeding the outlet capacity. Rapid opening of the lift gate resulted in a dam-break wave which propagated along the flume axis as a hydraulic bore (Chanson 2006). The debris used in this study were scaled-down versions of common coastal debris: shipping containers (SC), hydro poles (HP), and damaged drywall panels (referred to herein as boards) (B). The debris were placed 1.0 m from the edge of the slope downstream to allow for adequate time for the bore to develop once they had passed the sloped section as well as sufficient time to reach maximum velocities before impacting the obstacles. The time for the entrained debris to reach maximum velocity was determined based on the equation (Shafiei et al. 2016b, Stolle et al. 2017a):

$$u(t) = u_b - \left(\frac{C_d \rho_w A_d}{2m_d} t + \frac{1}{u_b}\right)^{-1} \tag{4-6}$$

where u_b is the bore front velocity, C_d is the debris drag coefficient, ρ_w is the density of water, A_d is the area of the debris transverse to the flow direction, m_d is the mass of the debris, and t is the time since the bore front reached the debris. To ensure all debris reached maximum velocity, the shipping container (specifications in the following section) was used to determine the required acceleration distance to reach approximately 99% of the bore front velocity.

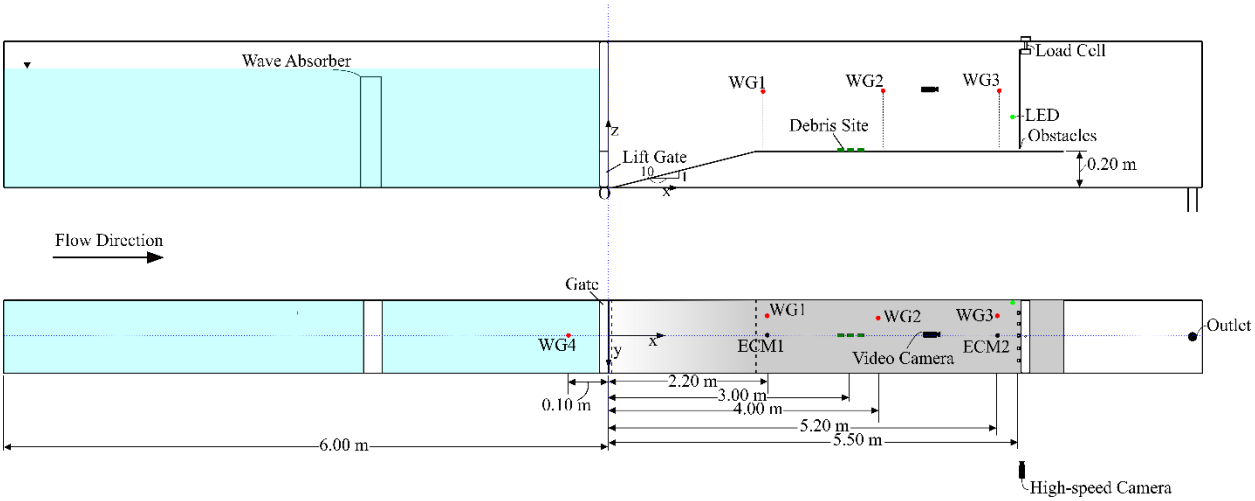

Fig. 4-18. High-Discharge Flume at Waseda University, Tokyo. Red dots indicate the position of a wave gauge (WG); black dots represent a position of the electromagnetic current meter (ECM).

The obstacles to be impacted by the debris were modelled as a set of columns using a 1:50 length scale and placed 5.50 m downstream from the gate (Fig. 4-19). The obstacles were modelled as structural columns in a building where breakaway walls had previously been destroyed by the inundating flow. The width of the columns was chosen based on the general office prescriptions from the National Building Code of Canada (2005). The columns were 0.014 m wide with an opening width (W) of 0.06 m between each of the obstacles. The gap between the obstacles and the flume wall were 0.04 m on both sides. The obstacles were 0.40 m high. The obstacles were placed 0.005 m above the bed surface to prevent them from touching the bed surface and thus biasing the force measurements from the load cell.

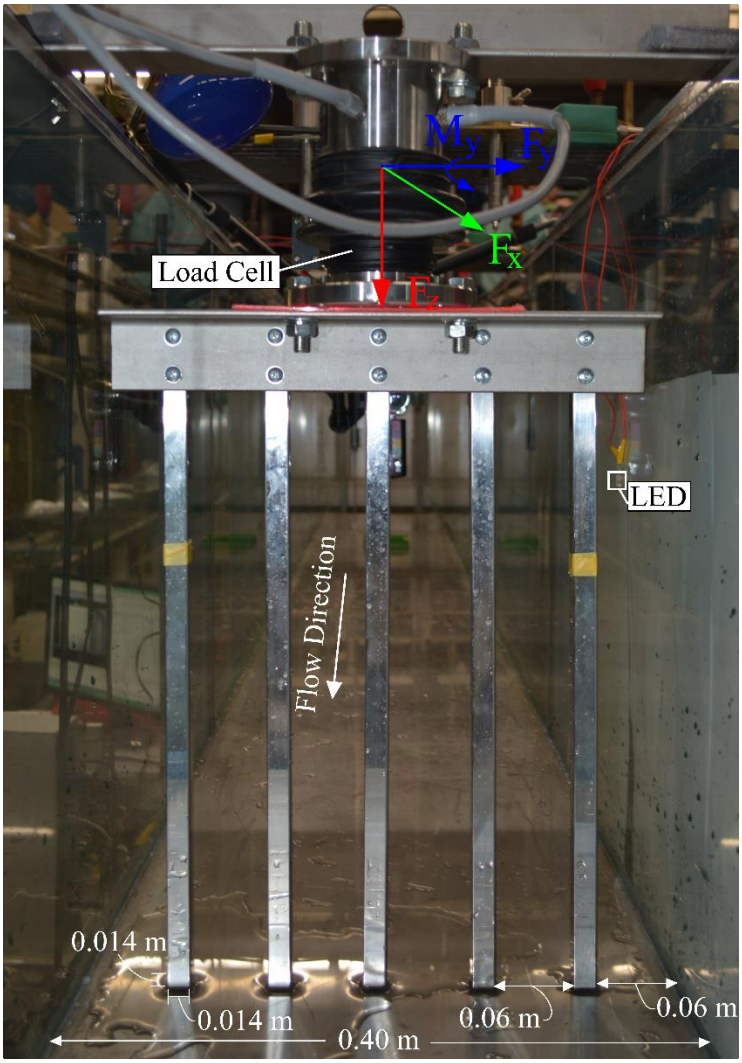

Fig. 4-19. Obstacle configuration - view pointing in the upstream direction. F_x is positive in the direction of the flow (towards the view point), F_y is positive towards the left of the flume with respect to the direction of the flow and F_z is positive in downwards direction.

Lift Gate

In tsunami studies, one of the primary concerns regarding the reproduction of a tsunami-like wave in a laboratory setting is the duration of the flow conditions (Goseberg 2013b, Goseberg and Schlurmann 2014). Additionally, the study of debris damming required sufficient flow duration for the debris dam to form and stabilize (Schmocker and Hager 2013). Chanson (2006) showed that a dam-break wave well represented the propagation of a tsunami wave over a coastal plain. However, due to the physical limitation of the described flume length, an ideal dam-break with full opening wave would not have adequately sustained the flow. Therefore, a partial gate opening was selected to control the release of the water from the reservoir and elongate the flow duration.

The lift gate was designed to obstruct the entire cross-section of the flume (0.40 m x 0.80 m) (Fig. 4-20). In this work, an opening at the bottom of the gate (0.40 m x 0.10 m) was set to be opened by lifting the gate vertically. This process was initiated and controlled with a mass-and-pulley system; once the mass was released, the gate opened rapidly. The selected mass was 10 kg, resulting in an approximate opening

time of 0.1 s. The mass was placed on a roller system to prevent any swaying of the mass and ensuring a repeatable release of the gate. The hydrodynamics and repeatability of the wave generated by the partial opening of the gate are further discussed in the "Results" section.

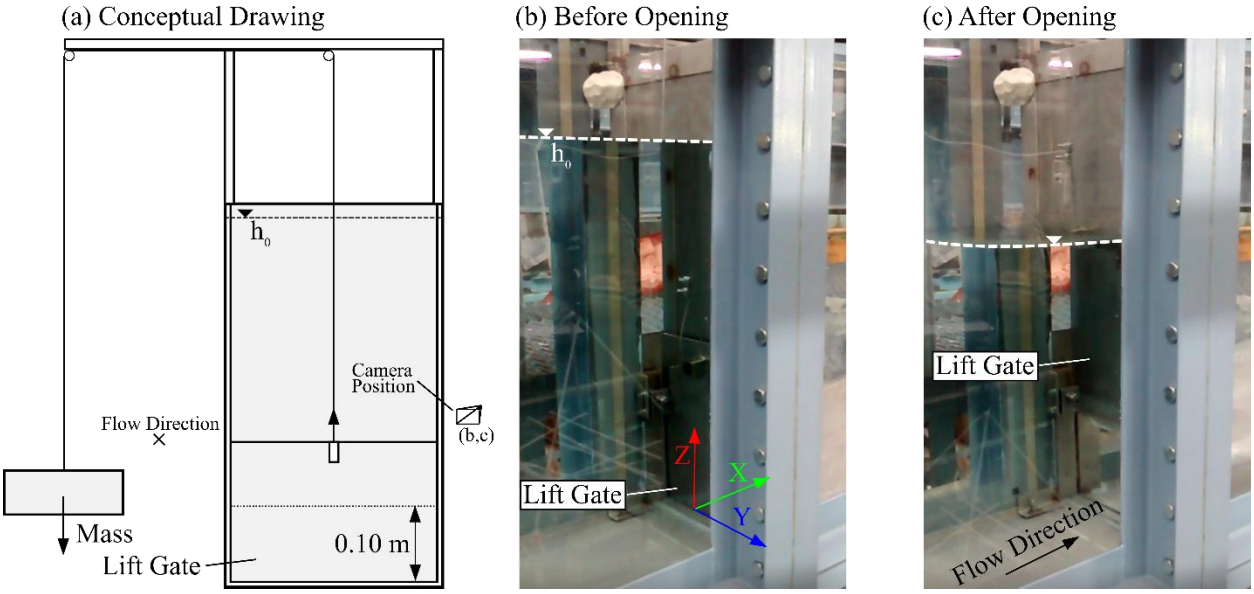

Fig. 4-20. Partial gate opening. (a) Conceptual drawing of the gate, (b) gate before the opening, and (c) gate after opening. Camera angle for (b-c) shown in (a).

Instrumentation

The instrumentation setup can be observed in Fig. 4-18. Table 4-4 details the specifications of the various instrumentation. For the no obstacle (no debris and no obstacles) and clear water cases (no debris), wave gauges (WG, KENEK CH-601, 100 Hz) were placed at distances of -0.10 m, 2.20 m, 4.00 m, and 5.50 m from the gate. The electro-current meters (ECM, KENEK MT2-200, 100 Hz) were placed at a distance of 2.20 m and 5.50 m, measuring flow velocities in the X- and Y-direction. A WG placed in the reservoir section was used to determine the opening time of the gate. Time = 0 s herein will refer to the time when the water level began to drop at the WG in the reservoir (WG4). For the cases where debris were present, the WG and ECM were removed from the sections downstream of the debris site to avoid accidental damage.

Table 4-4. Instrumentation Specifications.

Instrumentation	Model	Instruments	Sampling Rate
Wave Gauge (WG)	KENEK CH-601	WG1, WG2, WG3	100 Hz
Electro-current Meter (ECM)	KENEK MT2-200	ECM1, ECM2	100 Hz
Video Camera (VC)	JVC Everio GZ-HM440		60 FPS
High-Speed Camera (HS)	KATO KOKEN k4		100 FPS
Load Cell	SSK LB120-50		100 Hz

The load cell was a 6 degrees-of-freedom system that allowed for the monitoring of F_x, F_y, F_z, M_x, M_y, and M_z. However, due to channel limitation of the DAQ (KENEK ADS2016), only F_x, F_y and M_y were recorded. As the flow was primarily one-dimensional, the focus of this study will be on the forces in the *x*-direction. The load cell was mounted to the upper edge of the flume walls and secured tightly with clamps to ensure a rigid point for the force measurements. The load cell (SSK LB120-50, with a sampling

rate of 100 Hz) was bolted to both the beam spanning the flume width and the obstacles (Fig. 4-19). The sampling rate of the load cell (100 Hz) was limited by the Data Acquisition System (DAQ). Due to the low sampling rate, the peaks of the debris impact force could not be captured, however, as the focus of this study is addressing the drag load, the sampling rate should not influence the results presented below. The data from the load cell was filtered using an Empirical Mode Decomposition (EMD) filter (Huang et al. 1998) to remove signal noise as well as the impulses caused by the debris impacting the structure.

The video camera (VC, JVC Everio GZ-HM440, 60 fps) was synchronized with the DAQ system using a LED placed within the field-of-view (FOV) of the VC. Upon the opening of the gate, the LED was manually switched on. The voltage signal from the LED was monitored using the DAQ, allowing for the step voltage signal to be recorded and associated with the gate opening time. In post-processing, the LED was monitored using a color thresholding technique (Stolle et al. 2016). Once the LED turned on within the video, the time in the video could be associated with the voltage signal captured by the DAQ. The synchronization error between the VC and DAQ was estimated to be ±0.015 s. The high-speed camera (HS, KATO KOKEN k4, 100 fps) was manually triggered using the DAQ system. Upon the opening of the gate, a signal was initiated and simultaneously recorded by the DAQ, sending a step signal to the high-speed camera, initiating the recording of the HS.

Debris Properties

The experiments were performed considering Froude similitude (1:50 geometric length scale). Three different types of debris were selected based on the debris indicated in the ASCE 7 Chapter 6 (Chock 2016) and the FEMA P646 (FEMA 2012) (Fig. 4-21). All the debris were built from pine wood (specific gravity (SG) = 0.47), and were therefore positively buoyant. The shipping container (SC) was modelled as a standard ISO 6.1 m shipping container (0.12 m × 0.045 m × 0.045 m) (Goseberg et al. 2016b, Stolle et al. 2016, Nistor et al. 2016). The hydro poles (HP) were modelled as standard 6.1 m hydro poles (0.12 m × 0.005 m diameter). The board (B) was designed considering an arbitrary shape of a piece of drywall washed away from another structure (0.06 m × 0.04 m × 0.002 m). Each debris was weighed for an average weight of 0.111 kg (prototype scale = 13 875 kg), 0.002 kg (250 kg), and 0.004 kg (500 kg) for the SC, B, and HP, respectively. The standard deviation of the weight between debris was 0.001 kg. The mass of a shipping container can range from 2,300 kg (empty) to 30,480 kg (fully loaded) (Aghl et al. 2015), with an average mass of 14,400 kg (Knorr and Kutzner 2008). The mass of a hydro pole can range depending on the material, FEMA (2012) recommended using a mass of 450 kg for debris impact analysis.

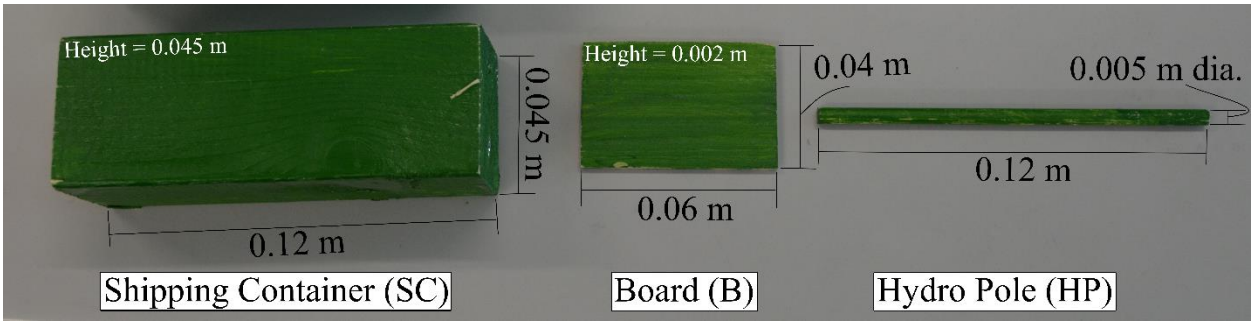

Fig. 4-21. Type of debris modelling in tsunami-like conditions: Shipping containers (SC), board (B), and Hydro poles (HP).

The characteristic length (L_c) of debris is commonly used to describe the potential of forming a debris dam, the definition of which can vary depending on the application. In debris damming studies, the

primary factor influencing the dam formation is whether the debris contacts the obstacle (Bocchiola et al. 2006, Pfister et al. 2013). In studies conducted in river engineering applications, the characteristic length was often taken as the maximum geometric dimension of the debris. However, this does not necessarily capture that fact that the debris may pass by the obstacles with a different geometric dimension. Visual observations of the debris propagation towards the obstacles showed that the orientation of the debris relative to the flow direction in these violent flow conditions was a random process. This was similarly observed in studies of debris transport under other types of violent flow conditions (dam-breaks and broken waves) (Stolle et al. 2017a, 2018c). Therefore, it was assumed that each dimension of the debris had equal chance of contacting the obstacles. An average of the physical dimensions of the debris (length, width, and height) was used as the characteristic length. The characteristic length of each was then 0.07 m, 0.043 m, and 0.034 m for SC, HP, and B, respectively.

Experimental Protocol

The experiments can be separated into three categories: same volume cases (SV), same plan area cases (PA), and the debris mixture cases (DM). An additional set of tests were performed to examine the repeatability of the hydrodynamics with (clear water) and without (no obstacles) the structure. The same volume cases (equally combined volume of all debris in a test) were performed to examine the influence of the individual debris properties on the capture efficiency and associated loads. The plan area experiments refer to the plan area of the debris when observing the debris from a top view. For each category, the experiments were performed with three different impoundment water depths: 0.40 m, 0.50 m, and 0.60 m. Each experiment was performed with 3 repetitions for a total of 125 experimental trials. Table 4-5 shows the various experimental setting used within this study; the debris mixtures are designated based on the number of individual debris within each experiment.

Table 4-5. Experimental Protocol.

Impoundment Water Depth [m]	Debris Mixture [SC, HP, B]	Experimental Category
0.4	0,0,0	
0.5	9,0,0	PA
0.6	0,81,0	PA
	0,0,20	PA
	3,27,7	PA/DM
	7,9,2	PA/DM
	1,63,2	PA/DM
	1,9,16	PA/DM
	6,54,14	DM
	9,81,20	DM
	1,0,0	SV
	0,103,0	SV
	0,0,51	SV

For each experiment, before the debris was placed at the debris site (Fig. 4-18), excess water was removed from the flume floor. A thin film of water was present on the bed of the flume for all of the experimental trials as all water could be removed. The debris were randomly mixed and then placed in the center of the flume in the same manner for each of the experimental trials to ensure repeatability. Water was added to the reservoir side of the flume to the designed impoundment depth. After the reservoir was filled, adequate time (~3 min) was allowed for the water surface in the reservoir to settle. The mass of the

opening mechanism was then released to initiate the lift gate motion, followed by the voltage signals manually triggering the LED and HS.

Debris Dam Measurement

The debris dam formation was monitored using the two-cameras setup shown in Fig. 4-18. Due to challenging occlusion of sections of the debris dam as observed from the side, as well as due to the 3D nature of the dam, it was conservatively defined as a uniform box related to its maximum width, height, and length (Fig. 4-22a). In the definition of drag force, the area used in its calculation (Eq. (2-22)) is the projected area of the obstruction exposed to the flow (Elger and Roberson 2016): in this case, these were the depth and width of the debris dam. The HS camera was used to monitor the depth (d) and length (l) of the debris dam (Fig. 4-22b), as the sections of the dam could be occluded by debris closer to the camera. To be consistent, the depth and length were selected based on the debris closest to the camera. The depth was considered for the free-surface water elevation at the structure to be consistent with the definition used for cross-sectional area of the debris dam. The VC was used to monitor the width of the dam (Fig. 4-22c). The width (*w*) was defined as the maximum width of the dam at the face of the obstacles.

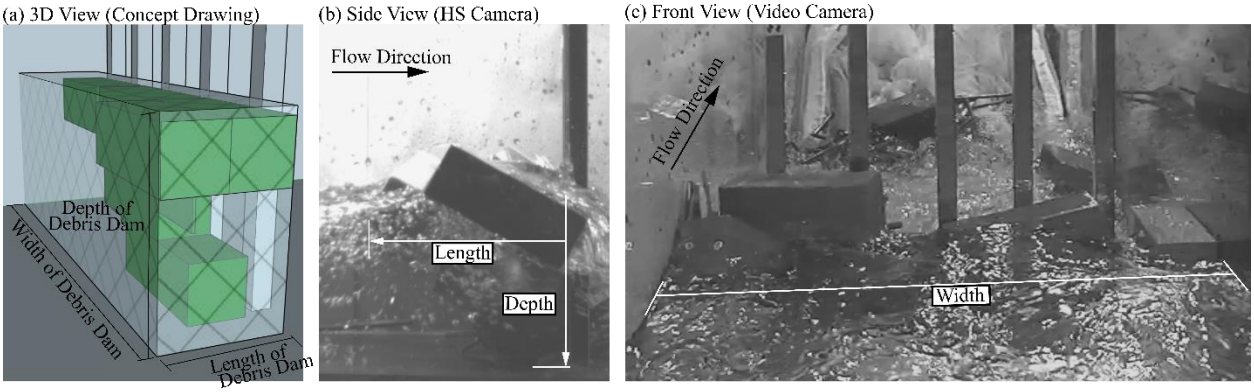

Fig. 4-22. Measurements of the debris dam properties. (a) conceptual image; (b) view from the HS; (c) view from the VC.

The dimensions of the debris dam were manually selected for each image within the experiment. The images were first rectified using four control points placed on the plane of interest (the face of the obstacles for VC and the glass wall of the flume for HS). The outermost edges of the debris dam were selected to determine the dimensions of the dam. An accuracy of ±10 pixels for the photos was estimated due to occlusions from the water surface. Based on the pixel-to-real world transformation the estimated real-world error was in the range of 0.025 – 0.035 m. Determining the correct absolute debris dam shape could not be captured by the two camera system and no such system in place to capture such 3D images in a hydraulic environment due to the potential for damage from free-floating solid objects. As similar concerns were noted for the WG, the maximum runup onto the obstacles was also measured using the same technique.

Due to the transient nature of the debris dam formation and the air entrainment in the initial process of its formation, its dimensions could not be accurately assessed until after the surface roller had propagated upstream. Therefore, to maintain consistency between experiments, the debris dam properties were measured at the time of maximum force in the clear-water conditions (outlined in following section), as this occurred when the dam properties could be accurately assessed.

4.2.3 Results

Hydrodynamic Conditions

The wave profile produced by the partial opening gate can be observed in Fig. 4-23. Chanson (Chanson 2006) showed using video images from the 2004 Indian Ocean Tsunami that a dam-break wave can approximately represent an inundating tsunami wave propagating over a coastal plain. WG4 (Fig. 4-23a) was the WG placed within the reservoir and was used to estimate the opening of the gate. A comparison of the wave profiles at the three downstream WG (WG1, WG2, and WG3) showed good repeatability between the three repetitions for both the profile (standard deviation (SD) = 0.015 m) and the wave arrival time (SD = 0.028 s). Slight deviations in the water surface elevation in the wave tip were noted due to oscillations, particularly closer to the gate. These oscillations are commonly observed in many other dam-break studies due to the turbulence within the wave tip (Nouri et al. 2010). An outline of the maximum water depths and wave front velocities is shown in Table 4-6.

Table 4-6. Flow conditions for each impoundment depth.

Impoundment Depth [m]	Mean Maximum Water Depth [m]	Maximum Water Depth Standard Deviation (SD) [m]	Mean Wave Front Velocity [m/s]	Wave Front Velocity Standard Deviation (SD) [m/s]
0.40	0.065	0.012	2.22	0.033
0.50	0.102	0.014	2.88	0.016
0.60	0.133	0.017	3.43	0.083

A comparison of the wave profiles in Fig. 4-23 to the Ritter (Ritter 1892) solution for a dam-break wave with a semi-infinite reservoir showed a reasonable correlation for the initial phases of the experimental wave used in these tests. However, the influence of the limited volume reservoir can be observed as the wave height begins to drop below the analytical solution in its latter stages. Additionally, the wave tip exhibited a steeper front, which was likely due to the flow resistance caused by the bed as friction is not considered in the Ritter solution.

At prototype scale, the maximum water depth corresponds to a range of 3.5 – 6.65 m and wave front velocities of 15.69 – 24.25 m/s. The conditions compared well to field estimations and numerical modelling of the 1993 Hokkaido-Nansei-Oki Tsunami (water depths of 2 – 10 m, flow velocities of 10 – 19 m/s) (Titov and Synolakis 1997) and the 2011 Tohoku Tsunami observations in a built environment (water depths of 5 – 15 m, flow velocities 3 – 15 m/s) (Yeh et al. 2013). The flow duration (~ 6 s model scale, corresponding to 42 s at prototype scale) was an order of magnitude less than typically observed for a tsunami wave (Madsen et al. 2008). However, the flow was sufficient to allow for the debris dam to form and peak loads were observed well before the water depths began to decrease. Therefore, these flow conditions were deemed to be sufficient as a preliminary examination of debris damming in transient flow conditions.

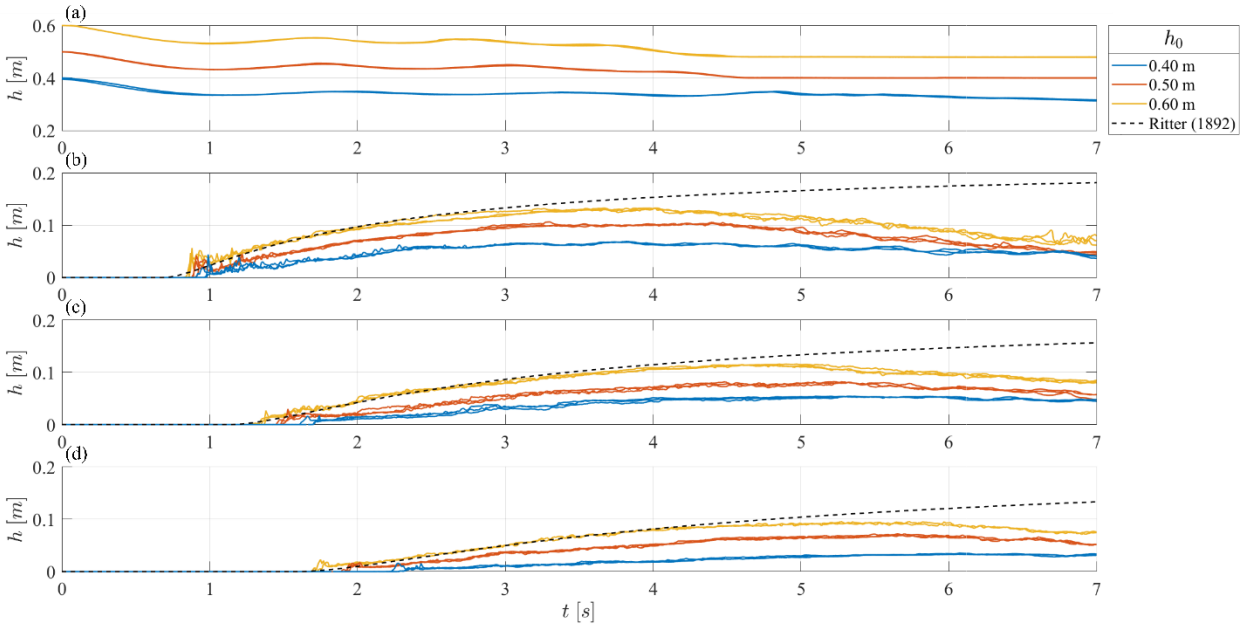

Fig. 4-23. Time-history of the water surface elevation profiles for the case with the obstruction in place (Figure 1). (a) WG4; (b) WG1; (c) WG2; and (d) WG3. The black dashed line shows the Ritter (Ritter 1892) solution for a dam-break wave in a semi-infinite frictionless flume.

Fig. 4-24 shows the clear-water (no debris) conditions at the obstacle. Fig. 4-24a-b show the water depth and the flow velocity at the obstacle site, unbiased by the presence of any obstacle. The time-history of the wave front velocities at the obstacle site are also plotted as open circles in Fig. 4-24b. Flow velocities were measured (solid line) using ECM2; however, due to air entrainment and cavitation occurring in the initial wave front, data could not be accurately captured for the first ~2 s of the wave front. To get a rough estimation of the flow velocities not captured by the instruments, the fluid dynamics in the reservoir were modelled in a simplified manner, as a reservoir releasing water through a pipe. The estimated velocity of the fluid released from the reservoir would therefore be approximately linear ($v = \sqrt{2gh}$). Ritter's (1892) solution for a dam-break wave over a frictionless surface showed that the flow velocity at a fixed point would decrease linearly from the wave front velocity. However, bed friction (Lauber and Hager 1998) and the sloping bed (Chanson 2006) cause significant non-linearity in the velocity profile. Additionally, the formation of the negative wave in the reservoir resulted in a non-linear variation (+/- 4.5%) of the water depth in the reservoir (h) compared to the water depth estimated by the idealized reservoir case. Despite the inherent issues with the linear assumption, to estimate the momentum flux, flow velocities were assumed to decrease linearly from the wave front velocity to the measured flow velocities (dotted line).

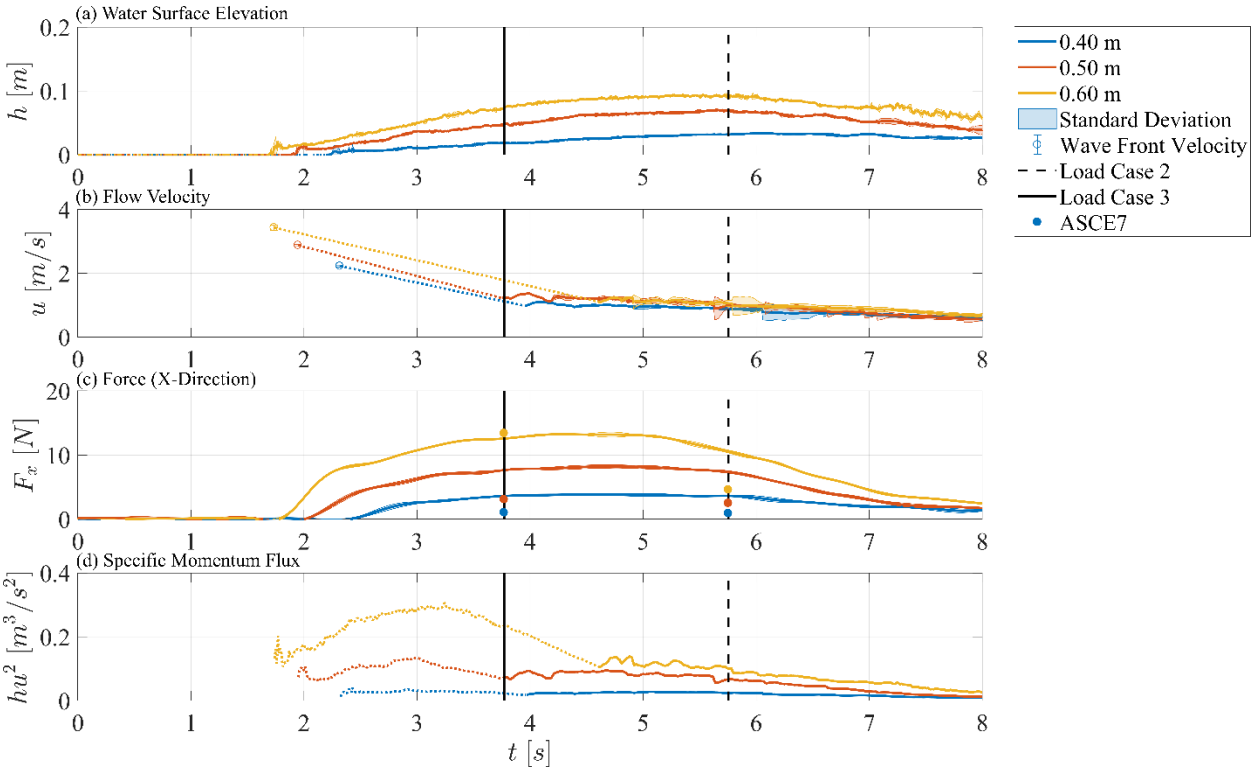

Fig. 4-24. Hydrodynamic conditions at the site of the obstacle (no debris case). The water surface elevation and flow velocity taken without the structure in place. The dotted line represents the estimated flow velocities. The black lines represent the load cases outline by the ASCE 7 Chapter 6 (Chock, 2016). The filled circular markers represent the calculated drag forces from the ASCE 7 Chapter 6.

The clear-water force profile in the flow direction (Fig. 4-24c) was measured with the obstacles in place. The clear-water cases demonstrated the repeatability of the gate opening as the force (in the flow-wise direction) showed minimal variation (standard deviation/maximum force = 0.0254) between similar experiments. Comparable variations were noted for F_y, with a mean maximum value of 0.52 N, indicating that the forces in the *y*-direction could be considered negligible and that the flow was essentially one-dimensional. As flow conditions (water depth and flow velocity) at the point of maximum force were known at the time of maximum force, and the air bubbles had sufficiently cleared to observe the debris dam, comparisons between the clear-water cases and the debris cases will be performed at the time of maximum force. An overview of the hydrodynamic conditions at the time of maximum force are displayed in Table 4-7. The Froude number from field investigations of tsunami events have ranged from 0.6 – 1.4 (Fritz et al. 2006, 2012, Matsutomi and Okamoto 2010). Bricker et al. (2015), in an examination of Manning's *n* values used in tsunami modelling, emphasized the necessity of properly scaling experiments, particularly related to the Reynolds (Re) and Weber (We) numbers. The Re and We number were calculated at the point where the ECM first recorded consistent velocity values. Te Chow (1959) noted that flow conditions should be fully turbulent ($Re > 1.25 \times 10^4$) and Peakall and Warburton (1996) indicated that We > 120 - both of these conditions are achieved in these experiments.

Table 4-7. Hydrodynamic conditions at the time of maximum force for each impoundment depth.

Impoundment Depth [m]	Force [N]	Time [s]	Water Depth [m]	Flow Velocity [m/s]	Froude number ($Fr = u/\sqrt{gh}$) [--]	Reynolds number ($Re = uh/\nu$) [--]	Weber number ($We = \rho u^2 h/\sigma$) [--]
0.40	3.86	4.29	0.03	0.99	1.99	2.51×10^4	345
0.50	8.22	4.56	0.06	1.11	1.41	6.63×10^4	913
0.60	13.23	4.72	0.09	1.21	1.29	1.08×10^5	1 493

As discussed in the Introduction section, the ASCE 7 Chapter 6 considers three load cases for the design of structures (Chock 2016). The first case considers the influence of the buoyant forces acting on the structure, which was not measured in this experiments. The second case (black dashed line) occurs when the maximum water depth occurs and the third case at two-thirds the flow depth (black solid line). Both cases occurred at similar times for each impoundment depth, therefore, the mean time was displayed in Fig. 4-24. The flow conditions in these experiments varied slightly from the flow conditions assumed in the design of the load cases and, as such, the maximum velocity was assumed to occur near the two-thirds water depth case (Chock 2016). For bores, as the ones used in these experiments, the maximum flow velocity occurred at the wave tip. However, in the clear-water case, the peak force occurred close to the point of maximum water depth (Load Case 2). The calculated drag forces for the two load cases are shown as filled circular markers. Based on the ASCE 7 Chapter 6 guideline, the drag coefficient was selected to be C_D = 1.25, where the C_D value is dependent on the width to depth ratio. The drag force was under predicted by Eq. (2-22), potentially due to the influence of the constrained channel (Qi et al. 2014) and the estimation of the flow velocity.

As can be observed from Eq. (2-22), debris damming is dependent on the specific moment flux (momentum flux per unit mass per unit width (hu^2)). Examining the momentum flux of the bore (Fig. 4-24d), the maximum debris damming load would be expected to occur close to Load Case 3. However, due to the assumption of a linear reduction in the flow velocity, further research is needed to confirm this result.

Debris Damming

The formation of a debris dam in steady-state subcritical flow conditions has been well-established by Schmocker and Hager (2013). According to these authors, the debris initially passed through the obstacles until the first debris was caught in the obstacle, commonly referred to as the "key log." Once the "key log" had formed, the debris were pushed by the streamlines surrounding the "key log" to fill the width of the obstacle. As the width was filled, the debris would begin to compact those at the front of the structure, forcing them towards the bed and obstructing thus the channel cross-section. As a result, the water depth upstream of the dam began to rise and the flow velocity decreased. Once the flow velocity had decreased, compaction no longer occurred and a debris carpet on the water surface began forming upstream of the obstacle. The extent of each of these steps could be dependent on the flume dimensions and initial flow conditions. However, the companion study to the work performed here (Stolle et al. 2017b) with the same debris under steady-state flown conditions displayed a similar behavior.

Fig. 4-25 shows the formation of the debris dam in unsteady supercritical flow conditions. Due to the supercritical flow conditions and the high flow velocity, unlike the steady-state case, stream lines did not fully form (Soares-Frazão and Zech 2007) and debris were not pushed to obstruct the full width of the obstacle. The violent flows caused the rapid compaction of the dam resulting in the constriction of the

cross-section. As the constriction formed, the water would runup the structure and form a surface roller directly upstream of the structure (Fig. 4-25b), similar to the surface piercing columns in dam-break flows (St-Germain et al. 2013). Due to the supercritical flow conditions, the rise in water surface level did not propagate upstream as was observed in the steady-state case. Instead, the surface roller expanded in cross-stream direction until it reached the walls of the flume; at that point, the surface roller propagated upstream. St-Germain et al. (2013) also noted that this was the point of maximum runup. Similarly, the maximum force and runup corresponded with the instant just before the surface roller began to propagate back upstream (Fig. 4-25e). The vortices formed by the surface roller destabilised the dam formation causing parts of the it to break apart and be washed downstream, past the obstacles (Fig. 4-25c). As the surface roller propagated upstream, the reduction of flow velocity and return of predominantly unidirectional flow resulted in the dam stabilizing (Fig. 4-25d). It should be noted that the obstacles spanned the width of the flume which caused the surface roller to rapidly form. Given a wider area, the reduction in flow velocity would likely have occurred over a longer period, influencing the occurrence of the maximum runup, as well as the propagation of the surface roller upstream.

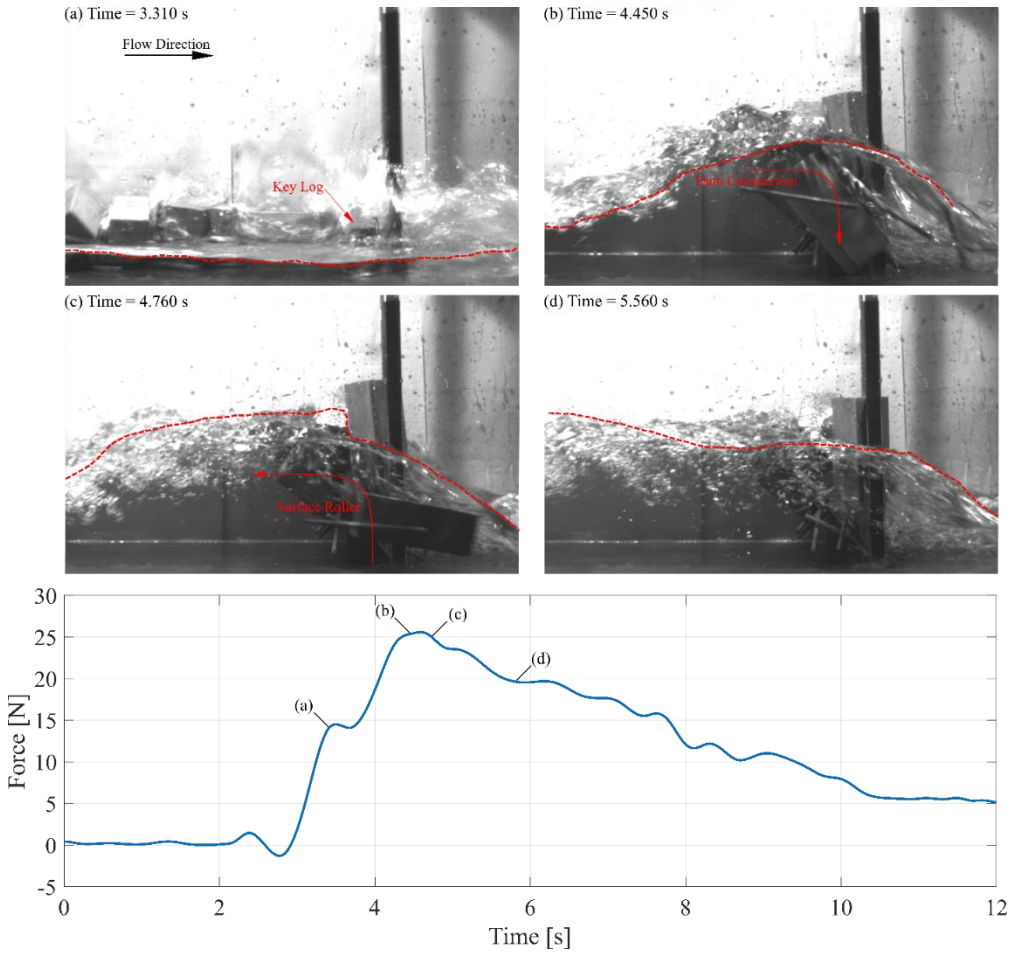

Fig. 4-25. Debris dam formation for the case with 9 SC, 81 HP, 20 B and 0.40 m impoundment depth. Panels (a)-(d) show still images from the HS at various key point. The red dashed line is marking the water surface elevation. Panel (e) shows the force-time history for the experiment, the times corresponding to the above images are indicated within the figure.

Debris Capture

Throughout the experiments, three different types of debris were used in various quantities. As a general comparison of the capture efficiency for the different debris types, the volume percentage of the debris captured (volume of debris captured/initial volume of debris) within each experimental trial are displayed in Fig. 4-26(a-c). Pfister et al. (2013) showed in a study on debris capture at a piano key weir that the length of the debris influenced the capture of the debris at the obstacle. With the same cases in steady-state (SS) conditions, the debris was also found to be captured at an increased rate with greater characteristic length (Stolle et al. 2017b). However, in the experiments presented here, the HP had a capture efficiency less than that of the B and SC debris. Pasha and Tanaka (2016) observed a similar result in the study of forest trapping efficiency of logs in tsunami-like conditions. They compared circular and square cross-sectional logs and determined the circular cross-section of the log had a smaller contact area with the obstacle. As a result, the circular logs tended to oscillate along the front face of the obstacle. A similar phenomenon was observed in this study, with the movement of the HP resulting in the dam being less stable than the case of the SC and B, often resulting in it being washed away entirely during the initial stages of the dam formation in the cases with only HP (Fig. 4-26d).

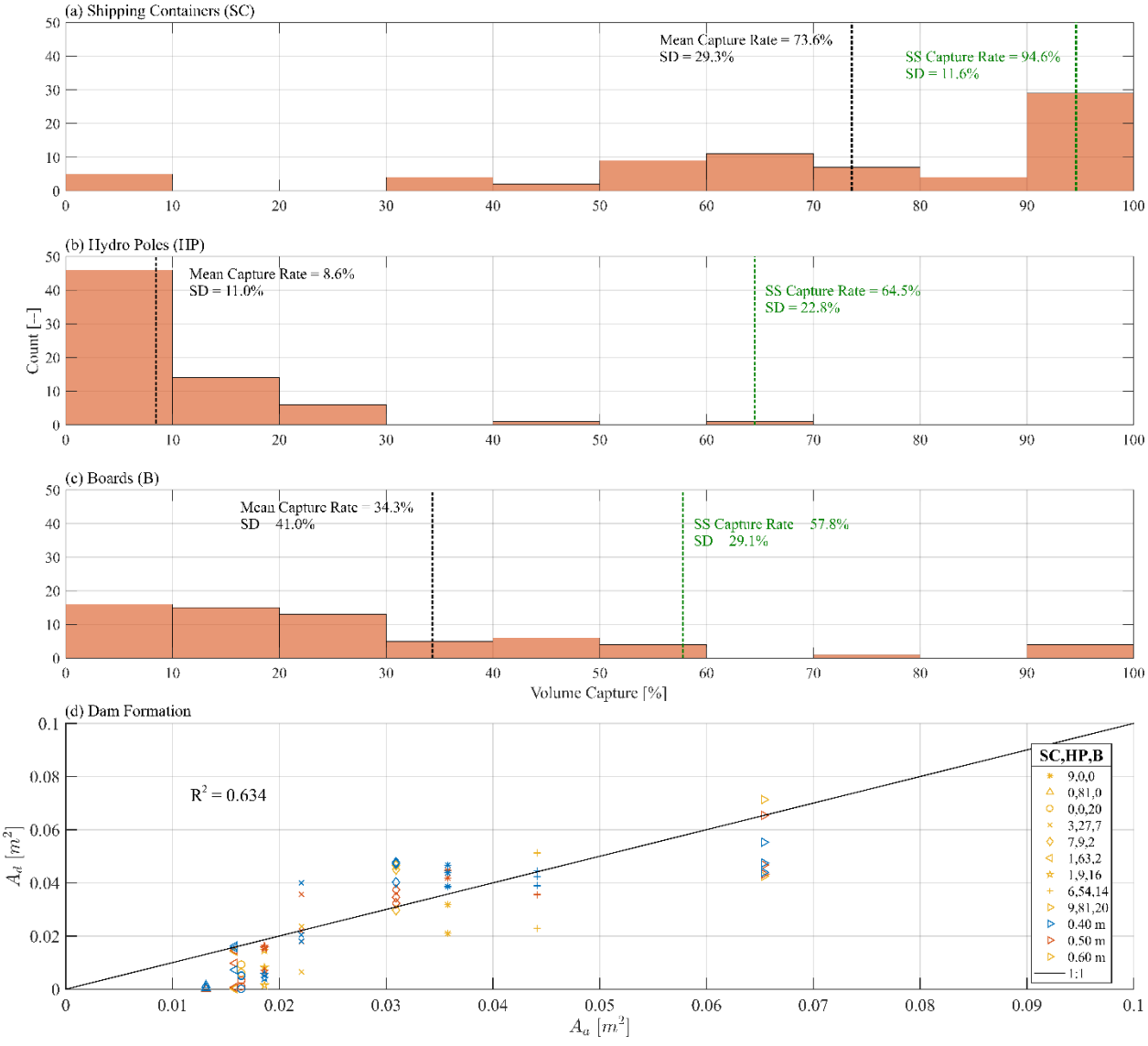

Fig. 4-26. Debris capture efficiency for (a) SC, (b) HP, and (c) B for all experimental trials, compared to the steady-state (SS) experiments presented in Stolle et al. (2017). Panel (d) comparison of the available debris to the debris dam cross-section. The type of experiment is indicated by marker type; the hydrodynamic forcing condition is indicated by color.

In comparing the two flow conditions, the capture rate was consistently less for the unsteady cases (Fig. 4-26). Bocchiola et al. (2008), while examining the debris capture efficiency in rivers, found that the Froude number influenced the rate of debris capture. Higher Froude numbers resulted in a lower capture efficiency due to the increased turbulence around obstacles. The highly unstable flow conditions resulted in more lateral motion of the debris causing them to be dislodged from the structure and be washed away. Additionally, in the case of the unsteady flow conditions, the formation of the surface roller at the front of the structure resulted in the break-up of the debris dam, resulting in some of the debris being washed away from it. Stolle et al. (2017b) noted that the variation in the dam formation was dependent on the characteristic length of the debris. In these experiments, the HP had the lowest variability, however this was due to the low capture efficiency of the debris. Comparing to the SC (L_c = 0.07 m) and B (L_c = 0.034 m) cases, the larger debris (SC) had less variability in the capture efficiency compared to the smaller ones. Considering the HP experiments, the contact area of the debris appears to have a significant role in the capture efficiency of the debris. Due to the relatively small number of debris geometries observed in these experiments, further investigation is needed to accurately assess the influence of the contact surface area.

Fig. 4-26d compares the available area of the debris (A_a), defined as the plan area of the debris multiplied by the mean capture rate of each debris type, to the area of the debris dam transverse to the flow direction. The experimental results show good comparison to the best fit line. Significant deviations can be observed in the cases with a large number of HP due to the instability of the dams with the HP. The debris dams formed in the high *Fr* number cases presented here tended to form in a single layer, resulting in the close correlation between the number/volume of available debris and area of the dam. Previous studies into debris damming in lower velocity flows showed that the dam often had multiple layers and that a debris carpet formed at the water surface (Braudrick and Grant 2001, Bocchiola et al. 2006, Schmocker and Hager 2013). These features of the debris dam would result in the available debris over predicting the area of the dam. As a conservative estimation, determining the mean capture rates of common coastal debris may aid in the design of appropriate debris dam sizes.

Runup on the surface of obstacles

One of the concerns related to debris damming is the overtopping of structures due to the formation of flow obstruction and associated rise in water level (Waldner et al. 2007). Fig. 4-27 shows the maximum runup (R) normalized by the width of the debris dam (w) as a function of the debris dam Froude number ($Fr_d = u/\sqrt{gw}$) at the time of maximum runup for the clear-water case. The width of the dam was selected as the normalization of the parameter to fit within the framework of other drag force estimation studies (Qi et al. 2014, Foster et al. 2017). As the time of maximum runup occurred before the ECM could accurately measure the velocity, the linear interpolation shown in Fig. 4-24 was used to estimate the flow velocity. The dashed line represents the implication of Bernoulli's equation (Equation (4-7)), indicating that the maximum runup at the upstream face of the structure would occur at the stagnation point (Chaplin and Teigen 2003). The runup was defined from the water surface elevation in the clear water case to the runup height at the time of maximum runup - therefore the potential energy could be neglected. As shown in Fig. 4-27, the relationship between the runup and Froude number closely matched the quadratic relationship estimated by Bernoulli (1738).

$$\frac{R}{w} = \frac{Fr^2}{2} \tag{4-7}$$

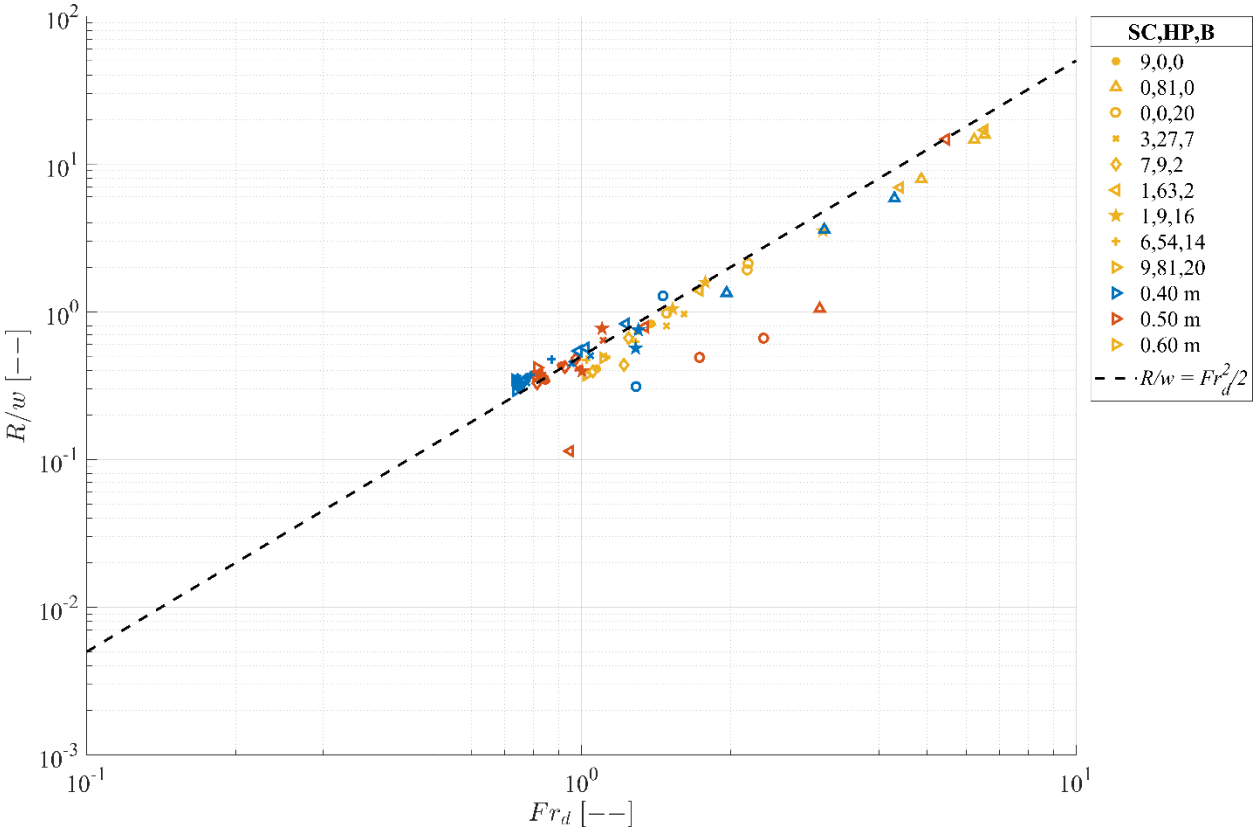

Fig. 4-27. Surface runup at the upstream face of the obstacles. The debris mixture is indicated by the marker type, the initial impoundment depth by the color.

Hay (1947), in the study of runup on semi-submerged cylinders, noted that the runup was approximately linearly related to the Froude number at low values of Re/Fr, but the relationship progressed towards quadratic with an increase in *Re/Fr*, though the relationship tended to breakdown when Fr > 8. The *Re/Fr* values used in the experiments presented here ($Re/Fr > 2.0 \times 10^5$) exceeded those in the Hay (1947) experiments ($535 < Re/Fr < 9.83 \times 10^4$), therefore the relationship would be expected to approximately be quadratic (black dashed line).

The deviations observed in Fig. 4-27 can be attributed to two aspects. As previously discussed, flow velocity was estimated using a linear relationship between the wave front velocity and the one measured by the ECM. As the bed friction and changes in bed elevation, were not considered in this assumption, the flow velocity can only be considered as a rough estimation. The application of the width of the dam as the characteristic length in the Bernoulli equation assumed that the width of the dam was solid. Due to the arrangement of the debris dam, the dam has a porosity associated with the formation characteristics. It value would have varied between the various debris dams, attributing to the discrepancy from the quadratic relationship. The outliers observed in Fig. 4-27 were predominantly the result of the occasional unusual capture of the boards. Due to the shape of the boards, they were occasionally captured with the long axis pointed outward from the dam, resulting in a large increase in the width of the dam, with little increase in the blockage. Additionally, it should be noted that the obstacles spanned the width of the

flume. In the case of a wider flume, the passing of flow around the obstacle may result in less of the velocity head being transferred to the wave runup height.

Debris Dam Loading

Fig. 4-28 shows the filtered force-time histories of the SV cases (solid lines), which were performed to examine the influence of the different type of debris. Impact forces were filtered from the total force signal as they were outside of the scope of this study. Additionally, due to the rapid nature of the impact, the sampling rate used by the FT was insufficient to fully capture the maximum impact load (Aghl et al. 2014). The mean time of occurrence of the maximum force is indicated with the dashed line of the color corresponding to the water depth in each figure. The clear-water case (no debris) can be observed in Fig. 4-28a, followed by the SC case (Fig. 4-28b), HP case (Fig. 4-28c), and B case (Fig. 4-28d). The maximum forces for each category of debris and impoundment depth are displayed in Fig. 4-28e. Comparing the categories, case B showed the largest maximum forces. Stolle et al. (2017b) determined that, for cases with the same volume, the debris with the higher surface area-to-volume ratio (as in the B case) resulted in larger loading. A possible reason for this is that these debris could form larger dam cross-section. A similar trend was observed in the present work: however, due to the low capture rate of the HP, the larger loads could not be observed for the HP cases. Except for the case with 0.40 m impoundment depth, the reduced energy of the flow resulted in a more stable dam formation, while for the larger impoundment depths, the dams in the HP cases were rapidly washed away.

Contrasting the time of the occurrence of the maximum force with the clear water cases, the cases with debris resulted in a maximum force occurring earlier in the force-time history. The shift in the maximum force condition could influence the determination of the critical design condition during the design process. The earlier occurrence of the maximum force can be attributed to several aspects of the flow conditions: Firstly, comparing the influence of the flow velocity ($O(u^2)$) and water depth ($O(h)$), the higher velocity in the initial part of the wave had a greater influence on the drag forces acting on the debris dam. Therefore, as discussed earlier, when comparing to the ASCE 7 Chapter 6 load prescriptions, Load Case 3 represents the largest risk related to debris damming due to the higher flow velocities. The second aspect is related to the breakup of the dam caused by the propagation of the surface roller upstream. Comparing the occurrence of this phenomena to the occurrence of the maximum force in the case of using clear water, the upstream propagation of the surface roller occurred at an earlier instant. The propagation of the surface roller caused the dam to break up and some of the debris were washed downstream. Therefore, when the flow conditions that resulted in the maximum force in the clear water case reached the obstacle, a smaller dam and, therefore, a smaller force was recorded.

The influence of the surface roller can be further observed for Fig. 4-28e. The more energetic flows due to the higher impoundment depths caused less debris to be captured, the dam to be less stable and break up earlier. As a result, comparing the normalized maximum forces, the higher impoundment depths resulted in smaller increases in the peak force. However, these experiments were performed with all the debris generated at a single source point. In cases where debris would be constantly supplied upstream of an obstacle, the dam would likely continue to grow after the surface roller had propagated upstream. Additionally, due to the relatively short duration of the flow, the dam may have not reached an equilibrium state. Further investigation into the debris dam formation is needed for a variety of debris supply conditions to develop a more comprehensive understanding of debris damming in tsunami-like conditions.

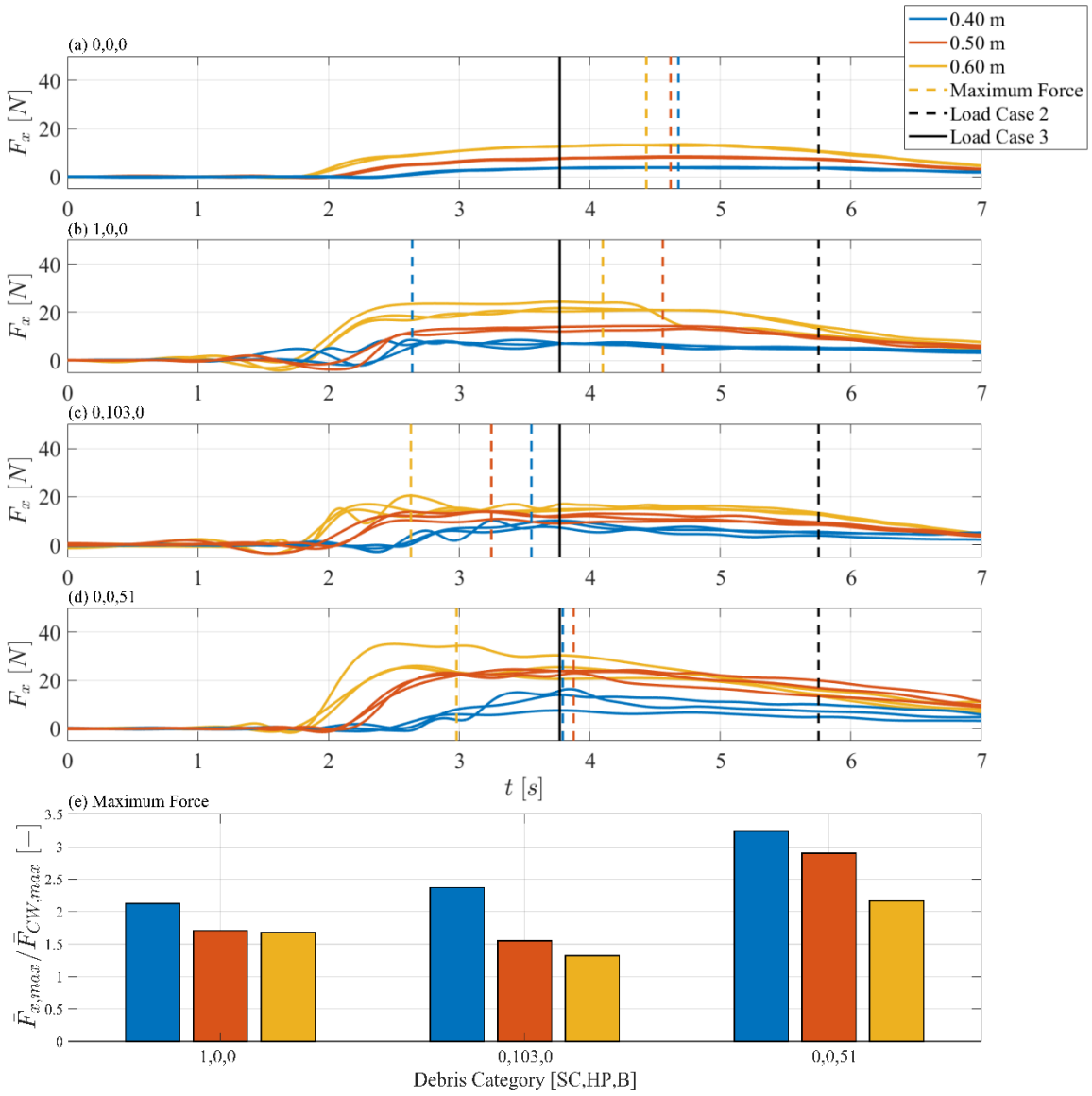

Fig. 4-28. Force-time history from the SC experimental categories. The initial impoundment depth is indicated by the color, the mean time of maximum loading indicated by the dashed line. (a) Clear-water case; (b) 1 SC, 0 HP, 0 B; (c) 0 SC, 103 HP, 0 B; (d) 0 SC, 0 HP, 51 B. The mean maximum force normalized by the clear water maximum force in each category is shown in (e).

In Eq. (2-22), the drag coefficient (C_D) was used to calculate the drag force acting on a structure. However, the classical definition of the drag coefficient refers to the case when the obstacle is fully submerged in the flow (Qi et al. 2014). In the experiments presented here, due to the unsteady, energetic nature of the flow, a wake formed behind the structure resulting in an unbalanced hydrostatic force acting on the structure (Fig. 4-25). As such, the drag coefficient cannot be determined within this study. Arnason et al. (2009), in a study of bore impingement on a vertical column, instead used a similar resistance coefficient (C_{R0}) which acts as a time history due to the fluctuation in the hydrostatic component.

$$C_{R0} = \frac{2F_x}{\rho h b u^2} \tag{4-8}$$

Additionally, the flume used in this experiments was meant for 2D experiments; however, the formation of the streamlines around the dam blockage displayed a distinctly three-dimensional (3D) nature. C_D is generally defined over an infinite cross-section, as such the volume of fluid can be injected over the infinite cross-section (Anthoine et al. 2009). However, in the confined conditions of this 2D flume, the fluid was forced through a smaller cross-section, resulting thus in increased flow accelerations around the blockage. As such, in these constricted flow conditions, C_D would be overestimated. To correct for the blockage, Qi et al. (2014) to be the average of the upstream and downstream flow velocities. A similar adjustment (Árnason 2005) was applied to calculate the resistance coefficient in unbounded flow (C_R):

$$C_{R0} = C_R \left(1 + \frac{C_R b}{w}\right)^2 \tag{4-9}$$

where w is the width of the channel. Fig. 4-29 shows the C_R as a function of the product of the Froude and Reynolds (Re_d) number. C_R was taken as mean resistance coefficient in the first 5 seconds after the wave arrival to avoid any influence from the reservoir. The characteristic length used in the calculation of the Fr_d and Re_d was the dam width at the time of occurrence of the maximum force. Due to the unsteady conditions and formation of the surface roller, a reference unperturbed upstream state could not be achieved. Therefore, the velocity and water depth used in the calculation of C_R was taken from the clear-water condition (Bremm et al. 2015) at the same instant. The focus of this study addressed the forces in supercritical flow conditions: it is therefore unclear if the same trend could be extended to subcritical flow conditions, rendering thus necessary future research on transient subcritical conditions.

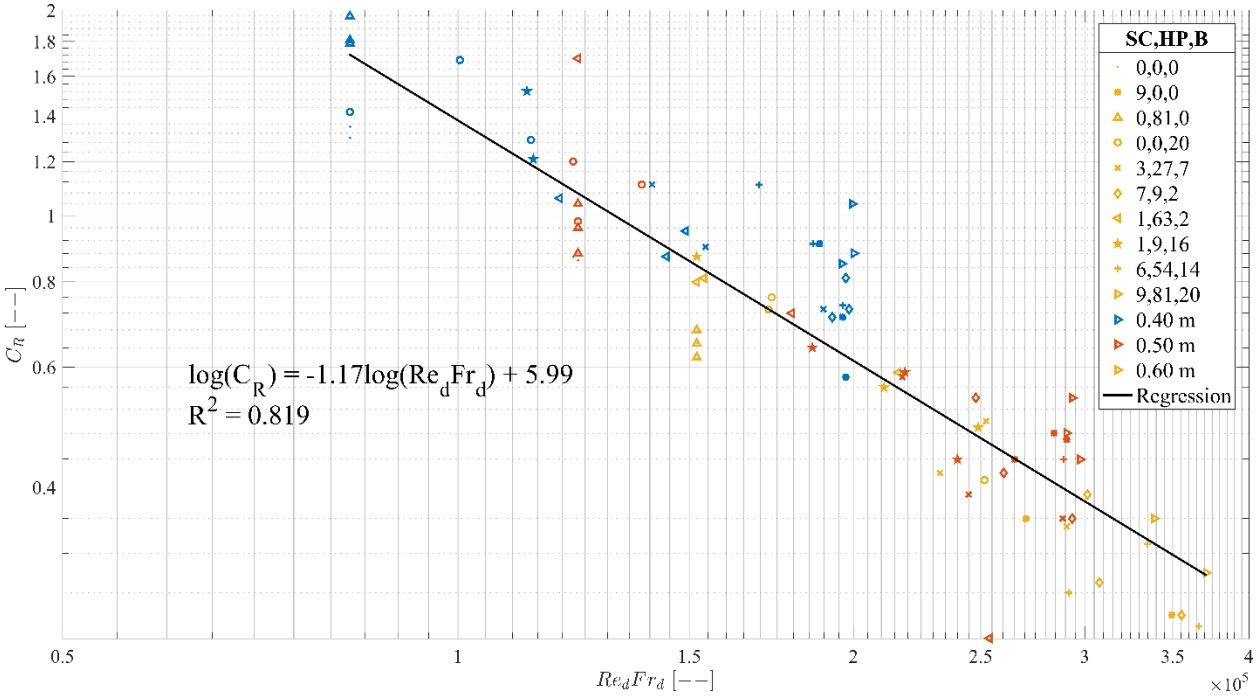

Fig. 4-29. Resistance coefficient, C_R as a function of the product of the Reynolds and Froude number. The different debris mixtures are indicated by the marker type and the initial impoundment depth by the marker color. The log-log regression line is displayed as a solid black line.

Generally, it has been well-established that the drag coefficient and Re are correlated (Yalin and Kamphuis, 1971). However, as the resistance coefficient (unlike the drag coefficient) includes forces

related to two physical phenomena (viscous and gravitation), spurious correlation could potentially exist. To analyze potential spurious correlation between C_R, Fr_d and Re_d (Kenney, 1982), the correlation was checked independently for u, w, Re_d, and Fr_d with F_x. Table 4-8 shows the results of the Pearson correlation analysis showing that a significant correlation existed between each of the variables. Therefore, it is concluded that minimal spurious correlation exists.

Table 4-8. Correlation between hydrodynamic variables and resistance force.

Variables	u		w		Re_d		Fr_d		F_x		C_R	
	R^2	p	R^2	p	R^2	p	R^2	p	R^2	p	R^2	p
u	-	-	0.026	0.140	0.942	<<0.05	0.819	<<0.05	0.432	<<0.05	0.574	<<0.05
w	0.026	0.140	-	-	0.002	0.666	0.187	<<0.05	0.244	<<0.05	0.108	<<0.05
Re_d	0.942	<<0.05	0.002	0.666	-	-	0.699	<<0.05	0.599	<<0.05	0.699	<<0.05
Fr_d	0.819	<<0.05	0.187	<<0.05	0.699	<<0.05	-	-	0.200	<<0.05	0.379	<<0.05
F_x	0.432	<<0.05	0.244	<<0.05	0.599	<<0.05	0.200	<<0.05	-	-	0.434	<<0.05
C_R	0.574	<<0.05	0.108	<<0.05	0.699	<<0.05	0.378	<<0.05	0.434	<<0.05	-	-

The discrepancy between the data and the regression line was potentially the result of the characteristic length used in the calculation of the dimensionless numbers. Due to significant aeration of the flow obstructing the side view of the dam, a single value was used to represent the width of the dam at an equilibrium position. However, throughout the formation of the dam, the width varied as the dam was highly unstable due to the energetic flow conditions. Additionally, due to the porous nature of the dam, the width of the dam may overestimate the actual blockage ratio. Chaplin and Teigen (2003) also noted that the calculation of C_R could be highly unstable around $Fr = 1$ due to rapid variations in the water depth. The variation could also be a function of the random nature the turbulence and debris motion (She and Leveque 1994, Matsutomi 2009).

4.2.4 Discussion

The study presented herein examined, for the first time, the formation of debris dams and the associated effects in transient, supercritical flow conditions. The physical model was scaled using 1:50 length scale (Froude similitude). Further consideration is needed to address the relatively short duration of the flow in this study compared to a real tsunami inundation. Longer duration flow may have an influence on the occurrence of the maximum load as increased dam compaction (Schmocker and Hager 2013) as well as potential for additional accumulating debris and debris sources to reach the site may reduce the porosity and increase or decrease the stability of the dam.

Further limitations exist in relation to the debris properties. The debris were scaled on the basis of the dimensions and mass, however physical properties, such as stiffness and yield strength, were not considered in the scaling process. As a result, the debris in the study maintained structural integrity, whereas, in images of field surveys of various flooding events, significant damage to the debris was observed (Robertson et al. 2007, Esteban et al. 2015). The deformation of the debris would inevitably influence the stability of the debris dam formation. Pasha and Tanaka (2016) noted in their study of debris dam formation that friction between the obstacle and debris was important in determining dam stability. The frictional aspects of the debris and obstacle were not considered in the scaling and therefore this aspect would not be captured within these experiments. Pagliara and Carnacina (Pagliara and Carnacina 2013) additionally noted that roughness elements related to the debris shape also had a significant influence on the dam formation while also influencing the flow field around the dam. Previous studies of debris damming have also indicated that the debris mixture (different sizes, buoyancies, and materials) can influence the formation of the dam. While different debris mixtures were examined in this study, further investigation with a wider variety of mixtures is needed to evaluate their influence on the debris

dam formation. Furthermore, positively buoyant debris were analyzed within this study. However, forensic field surveys have also indicated that negatively and neutrally buoyant debris, such as boulders and vehicles can be entrained within the flow (Yeh et al. 2013). Schmocker and Hager (2013) determined that the buoyancy of the debris influenced the formation of the debris dam as the negatively buoyant debris would initially block a larger portion of the flow cross-section. Further research is needed to address variations of debris buoyancy and the potential scale effects related to the scaling of the physical properties of the debris.

The focus of this study addressed the debris loads associated with the debris dam. However, as noted in various field surveys (Ghobarah et al. 2006, Takahashi et al. 2010, 2011), debris impact forces can cause significant damage to structures. Debris impact loads are dynamic loads that exhibit a significantly different structural response than debris damming and therefore were not considered within this study. An Empirical Mode Decomposition (EMD) filter was used to isolate the influence of the debris damming from the impact forces (Huang et al. 1998).

The drag coefficient could not be directly measured in these experiments due to the unbalanced hydrostatic pressure acting on the obstacle. As a result, the resistance coefficient was used as a surrogate representing the force from both the form drag and the hydrostatic pressure. Arnason et al. (2009) noted in a study of bore impingement on a column that the resistance coefficient was a function of the Froude number and blockage ratio. In this study, the Froude number and blockage ratio were both estimated using the width of the dam. However, the dam was not a solid object and therefore had an associated porosity that was not captured within the current measurements. The debris dam porosity would result in a smaller cross-sectional area exposed to the flow than used in the calculation and could also potentially influence the formation of the boundary layer by affecting the separation point (Sumer and Fredsøe 2006). Additionally, the dam was assumed to be a uniform box due to challenges associated with assessing its 3D geometry. The assumption of a uniform box was selected as, in the definition of the drag force (Eq. (2-22)), its area is the projected area exposed to the flow. The box would therefore represent a conservative estimation of the projected debris dam area exposed to the flow, potentially resulting in a smaller resistance coefficient. Further investigation is needed to address the influence of the debris dam porosity on the resistance coefficient.

Additional consideration likely needs to address the potential influences of the side wall: the force was corrected to be considered in unbounded flow based on (Árnason 2005). However, as the dam formed, debris were occasionally caught against the wall and the dam, resulting in the load being partially transferred to the side walls. This phenomenon may result in a smaller force measured by the FT; further investigation in a wider flume environment is needed to address the extent of this influence.

Due to concerns over damaging instrumentation, instruments were not placed downstream of the debris site. More in-depth measurements around the obstacle could potentially allow for an accurate estimation of the drag and lift coefficients as a result of debris damming, similar to the work done for free-standing structures performed by Foster et al. (2017) and Qi et al. (2014).

4.2.5 Conclusions

The study discussed herein examined the formation and loads associated with debris dams in supercritical, unsteady flow conditions. The study focused on the debris damming in a coastal setting by modelling debris common to a coastal environment and by using a hydrodynamic forcing condition similar to a tsunami wave. The paper investigated the influence of the debris mixtures on the size of the debris dam, the runup at the structure face, and the loads exerted on the structure.

Based on the results, the following conclusions can be drawn:

- The debris dam formation was initiated similarly to the steady-state cases, as described in Schmocker and Hager (2013). However, due to the formation of the surface roller at the structure face, the dam was less stable than the unidirectional cases.
- Due to the more energetic flow and formation of the surface roller, capture efficiency of the debris was significantly less than that observed in the steady-state cases. Also, capture efficiency decreased with flow velocity and length of the debris.
- As a result of the full development of the stagnation pressure at the structure face, the runup at the front face of the structure closely matched the runup estimated by the Bernoulli equation. The runup normalized by the dam width correlated closely with the quadratic of the Froude number.
- The formation of the debris dam resulted in a shift in the time when the maximum force occurred from ASCE Load Case 2, where hydrostatic pressure dominated, towards the ASCE Load Case 3, where high velocity flow was the primary concern.
- The resistance coefficient showed an approximately log-log linear relationship with the product of the Reynolds and Froude number.

Debris damming has been shown to be a major concern in flooding events, and therefore needs to be carefully considered in the design process of infrastructure exposed to such effects. The study presented herein was the first to examine debris damming in unsteady flow conditions. While the focus of this experimental program was modelling tsunami-like flow conditions, the general conclusions of this study can be applied to rapidly occurring flooding events, such as flash floods and flood waves from breaching dams, where supercritical flow are present. Based on climate change studies on precipitation patters, intensity and possibly frequency of transient flows will likely increase; hence, designing for such extreme flows is of major interest for engineers. However, due to concerns of damage to instrumentation in such conditions, research is further needed into the changing hydrodynamic conditions around the debris dam formation.

Chapter 5. Debris Impact Loading

5.1 Debris Impact under Extreme Hydrodynamic Conditions Part 1: Hydrodynamics and Impact Geometry

Preprint of an article printed in Coastal Engineering© 2018 Elsevier.
https://www.sciencedirect.com/science/article/pii/S0378383918300723

5.1.1 Objectives

With the overall objective of examining debris impact loading in transient violent flow conditions, the specific objectives of the presented study are:

- Investigate the relationship between the flow velocity and the impact velocity of a single debris in a dam-break wave representing a tsunami-like flow.
- Determine the influence of flow features around the structure on debris impact velocity and geometry.
- Examine the influence of debris impact geometry and their statistical distributions on maximum impact loading conditions.

5.1.2 Experimental Setup

Dam-Break Flume

The experimental research reported herein was part of a comprehensive series of tests conducted in the dam-break wave flume at the University of Ottawa, Canada. The flume has a total length of 30.00 m, a width of 1.50 m and a height of 0.72 m. It is divided into two sections: an upstream 21.55 m long reservoir and an 8.45 m long test area. The reservoir and the experimental area were separated by a swing gate designed to generate dam-break wave, simulating tsunami-like flow by suddenly releasing the impounded volume of water. The swing gate has a height of 0.62 m and is made of 0.025 m thick steel frame with marine plywood on its surface and is equipped with a steel counterweight to ease the manual opening process.

Fig. 5-1 provides a schematic overview of the flume setup: the location of the structure, debris and instrumentation. The spatial origin was chosen to be in the center of the flume, at the upstream edge of the gate with the axis directions as shown in Fig. 5-1.

The experimental area was fitted with a 0.20 m high false floor on top of the flume floor. The floor in the entire test area was screened with a mixture of white paint and sand (D_{50} = 0.001 m) which resulted in a measured Darcy-Weisbach friction coefficient of 0.014 for steady-state flow conditions.
The instrument specifications are shown in Table 5-1. One capacitance-type wave gauge (WG1) was placed inside the reservoir, approximately 0.10 m upstream of the swing gate to track the falling head of the impounding water. Two other wave gauges were placed on the experimental area, 2.00 m (WG2) and 3.20 m (WG3) downstream of the swing gate to measure the time-history of the water level as the dam-break wave propagated through the flume. The wave gauges were calibrated with R^2 values greater than 0.99. A high-speed (HS) camera was placed above the flume, near the swing gate and aiming towards the structure. This overhead camera was used to track the surface flow of the wave as well as the debris velocity throughout its entire motion. A high-definition (CAM) camera was aimed towards the structure from the left side of the flume (in the flow direction) and was used to record the flow and debris impact

onto the structure. A second CAM was placed looking downstream of the gate to provide a redundant system to track debris motion.

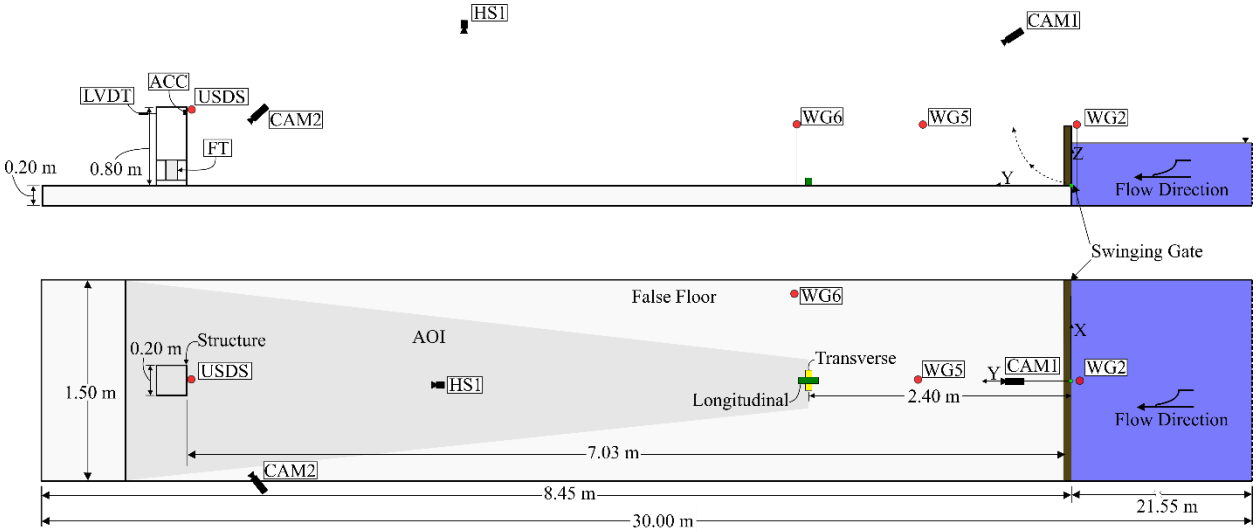

Fig. 5-1. University of Ottawa Dam-break Wave Flume. ACC = accelerometer, USDS = ultrasonic distance sensor, LVDT = linear variable differential transform, CAM = camera, FT = load cell, HS = High Speed Camera, WG = wave gauge.

Table 5-1. Instrumentation used in the wave-flume.

Instrument	Make	Sampling Rate
Wave Gauge (WG)	RBR WG-50 Capacitance (WG1)	1200 Hz
	Akamina AWP-24 (WG2, WG3)	1200 Hz
High-speed Camera (HS)	Flare 2M360-CL	70 Hz
High Definition Camera (CAM)	Basler AG pil900-32gc	25 Hz

Vertical Structure

A hollow, square acrylic structure with side lengths of 0.20 m, a height of 0.80 m, and a 0.00635 m wall thickness was used in the experiments. The acrylic column was attached onto a rigid steel mount which was connected to a load cell further bolted to a steel base plate system (Fig. 5-2). The base plates used for the mount were 0.008 m thick, ensuring a rigid base. The structure was then bolted to the steel mount with two screws on through 0.003 m steel angles. The center of the structure was placed in the centerline of the flume. Its base was located directly on the flume floor and was only connected to the flume with the steel mount in order to allow the structure to move freely upon impact. The vertical gap between the structure and the flume floor was 0.002 m.

The stiffness was calculated using the natural frequency of the structure resulting in a value of k_s = 4.685 $\times$ 10^5 N/m. The mass of the entire structure (acrylic structure, steel mount structure and load cell) was 11.9 kg; the acrylic structure itself had a weight of 6.3 kg. The frequencies of the debris impact measurements were compared with the natural frequencies of the impacted structure and it was concluded that the frequencies did not overlap and thus, the measured forces were not affected by resonance.

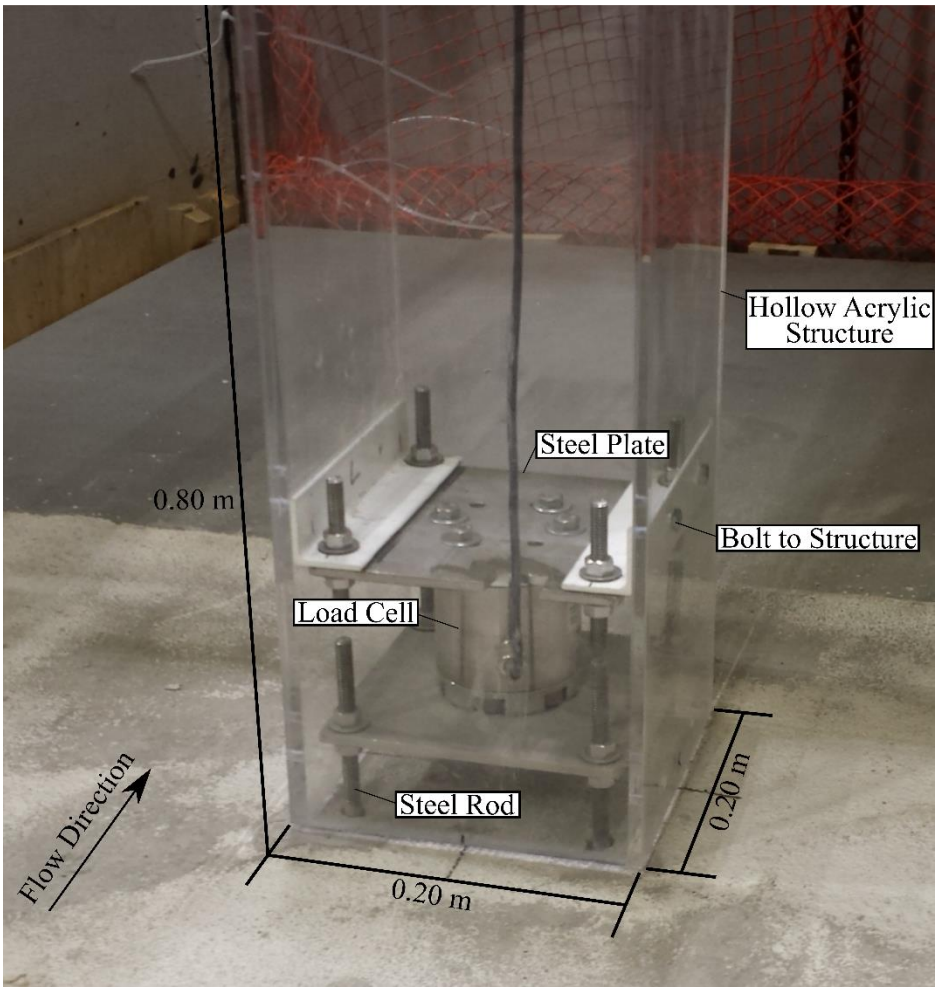

Fig. 5-2. Mounted acrylic structure connected to 6-axis load cell.

A 6-axis load cell with specifications according to Table 5-2 was placed near the base of the structure to simultaneously measure the forces and torques applied around three mutually perpendicular coordinates axes, as shown in Fig. 5-2.

Table 5-2: Instrumentation attached to the impacted structure.

Instrument	Model	Sampling Rate
6-axis Load Cell (LC)	Interface 6A68E	19200 Hz
Accelerometer (ACC)	Kistler 8304A2M2	19200 Hz
Ultrasonic Distance Sensor (USDS)	MassaSonic M-5000/220	1200 Hz
Linear Variable Differential Transform (LVDT)	RDP Electrosense DCV025A	19200 Hz

In addition to the load cell, the structure was equipped with an accelerometer (ACC), an ultrasonic distance sensor (USDS) and a linear variable differential transform (LVDT) connected to the upper end of the structure. The USDS was installed to record the water level right in front of the structure and thus further evaluate the hydrodynamic interaction of the incoming wave with the structure such as the run-up occurring at the initial wave impact. The LVDT measured the motion of the upper end of the structure

upon impact in y-direction (flow direction). To measure the acceleration of the upper end of the structure due to impact, an accelerometer was mounted at the top of the structure. These instruments' specifications are listed in Table 5-2.

Debris Model

Models of 6.1 m (20 ft.) shipping containers with a geometrical length scale of 1:40 were used as debris in this study. Model containers were 0.15 m long and had a square cross section with sides of 0.06 m and regular draft in water was approximately 0.023 m. The model containers were made of buoyant polyethylene (PE-HMW) with a density of 920 kg/m³. Converted at prototype scale, this matches a weight of 14,400 kg, representing a partially-filled shipping container (GDV 2003). At this current stage of research, the structural properties of a prototype shipping container were not modeled.

The stiffness of the debris in the longitudinal direction was measured in a stress-strain test as $k_{d,long}$ = 3 431 N/mm (3 specimen, standard deviation is σ = 523 N/mm). The stiffness in the transverse direction was calculated using the modulus of elasticity (*E*) and the geometrical dimensions of the debris (cross-sectional area (*A*) and its length (*L*)) ($k = EA/L$) (Gere and Timoshenko 1984), resulting in a value of $k_{d,trans}$ = 21 000 N/mm. The proper stiffness value was used, depending on the impact geometry of the debris as shown in the following Table 5-3 (with α and θ as defined in Fig. 2-3). The debris model had a weight of 0.284 kg.

Table 5-3: Stiffness (k_d) and contact stiffness (k) of the debris in dependence of the obliqueness-angle (α) and the impact-angle (θ) of the debris in reference to the structure.

α [°]	θ [°]	k_d [N/mm]	k [N/mm]
< 45	< 45	$k_{d,long}$ = 3 431	876
< 45	≥ 45	$k_{d,trans}$ = 21 000	1115
≥ 45	≥ 45	$k_{d,trans}$ = 21 000	1115
≥ 45	< 45	$k_{d,long}$ = 3 431	876

Experimental Program

The experiments were divided into different test series with at least 10 repetitions each, with the purpose of having a sufficient amount of data to conduct comparative and statistical analyses. With each test series, two different hydrodynamic boundary conditions were examined: (1) by varying the impoundment depth (h_0 = 0.20 m and h_0 = 0.40 m) used to create two dam break waves with different flow depths and associated velocities; and (2) by varying the initial orientation of the debris as they were initially placed either longitudinally (90°) or transversely (0°) to the flow direction before opening the swing gate. Debris could move freely in x-, y- and z-direction. The location of the instrumentation was not changed throughout the test runs. The details of the experimental series are provided in Table 5-4.

Table 5-4: Description of the boundary conditions of the test runs performed in this study.

Experimental Category	Reservoir Water Level (h_0) [m]	Initial Debris Orientation [°]	Repetition
E01	0.4	0	20
E02	0.2	0	10
E03	0.4	90	20

Data Processing

Image Processing

The geometrical impact parameters as well as the impact velocity were derived from the HS camera. The distortion of the camera was corrected and the images were transformed using coordinate transformation by means of measured real-world coordinates of reference points painted on the flume floor and relating them to their counterparts in the image frames (Stolle et al. 2016).

The tracking of the debris motion approaching the impacted structure was achieved by determining the debris location from each image frame. This was performed after the debris entered a target area within a hypothetical circle with a 0.20 m radius around the center of the impacted structure. This radius has been arbitrarily chosen to be the width of the impacted structure (0.20 m) based on a visual examination of the disturbance of the flow in front of the structure. The debris locations were determined by manually selecting from the recorded images the edges of the debris and then by computing the geometrical centroid of the debris with the corner coordinates of the polygon depicting the debris' outline. It should be noted that the centroid coordinates used within this study represent the geometrical centroids and not the center-of-gravity (CG). Because of the symmetrical shape of the debris utilized, the differences were assumed to be negligible. Some image blur originated from the maximum available shutter speed of the camera used and, as such, the debris location (the debris edges in particular) could be attained with an accuracy of +/- 5 pixels. Since the angular field of the camera images is non-orthographic, the ratio of the pixels to real-work coordinates ranged between 286.4 – 290.0 pixels/m in x-direction and 252.2 – 276.7 pixels/m in y-direction. The accuracy of the debris detection thus resulted in 0.0172 – 0.0175 m in x-direction and 0.0181 – 0.0198 m in y-direction.

Extraction of Impact Loads

The load cell measured the response of the structure to the total (hydrodynamic and debris impact) loading. Since the wave impacts the structure in addition to the debris itself, the total measured load does not solely represent the structural response due to the debris. The debris impact is considered a dynamic load while the drag force (hydrodynamic force) exerted to the structure by the flow of water is a quasi-static load. To extract the dynamic forces, the force signal needs to be decomposed into the (quasi) static (hydrodynamic) and the dynamic (impact) load as shown in Fig. 5-3.

To extract only the force due to debris impact, a filtering technique called Ensemble Empirical Mode Decomposition (EEMD) (Huang et al. 1998) was implemented with the specifications as shown in Table 5-5. The EEMD filter decomposes the force signal into intrinsic mode functions (IMF) within the time domain. The IMFs could then be separated into components that contributed to the hydrodynamic, debris impact, and noise signals. The individual IMFs were visually inspected to determine to which category each of them belonged to. Fig. 5-3 shows a comparison of the filtered data signal with the hydrodynamic and impact signals for one experiment. The advantage of the EEMD filter is that it ensures no time shifting in the time domain (Huang et al. 1998). Therefore, there is no concern related to the shifting in the instant when the peak impact force occurred. The comparison of the filter data signal and the impact signal shows a similar standard deviation around the mean (+/- 1.62 N), indicating that the impact signal was reasonably separated from the hydrodynamic load signal.

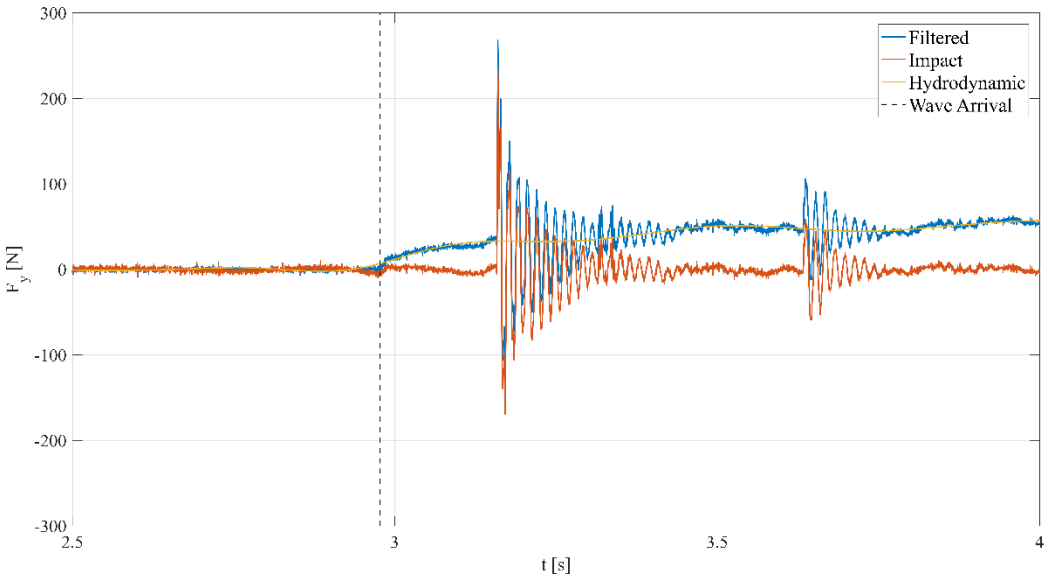

Fig. 5-3. Impact load filtering. The total force measured by the LC compared to the impact and hydrodynamic forces.

Table 5-5: IMF combinations for best matches to raw data for the force and torque signals in x-, y- and z-direction and resulting RMSE.

		F_x	F_y	F_z	M_x	M_y	M_z
EEMD	IMF_{best}	2–12	4–12	2-17	3-10	2–17	2-12
	RMSE [N]	4.11	10.04	12.46	0.44	0.07	1.24

Within this study, the impact force response from the load cells were used without eliminating the reaction of the structure upon impact. Therefore, when discussing the debris impact force within this paper, the measured debris impact force refers to the structural response to the force, not the actual effective force exerted on the structure.

5.1.3 Results

Hydrodynamics

To investigate the flow features around the vertical column, the hydrodynamic properties of the flow employed for this study are outlined as a basis for further analysis. Chanson (Chanson 2006), in a study of tsunami bores from video analysis of the 2004 Indian Ocean Tsunami, determined that a tsunami bore propagating over a coastal plain closely resembled the front of a dam-break wave. The dam-break wave also has a larger period compared to some conventional methods of modelling a tsunami-like wave, such as a solitary wave (Madsen et al. 2008).

Lauber and Hager (Lauber and Hager 1998), in a comprehensive examination of dam-break waves using a vertical lift gate, developed the following criteria for the minimum gate opening time (t_{open}) for dam-break waves:

$$\left(\frac{g}{h_0}\right)^{\frac{1}{2}} t_{open} < \sqrt{2} \tag{5-1}$$

The study by Lauber and Hager (Lauber and Hager 1998) found that when the gate opening time exceeded this criteria, the wave profile would be influenced by the gate. This study found that the gate opening times for h_0 = 0.40 m, the gate opening time adhered to the Lauber-Hager criterion. Due to the reduced hydrostatic pressure acting on the gate for the smaller impoundment depth (h_0 = 0.20 m), the gate opening time was slower than required, likely resulting an influence of the gate opening on the wave profile.

Fig. 5-4 shows a comparison of the experimental data to the analytical dam-break profile (Ritter 1892) for a frictionless dam-break wave with a semi-infinite reservoir. The dam-break waves created within the experiments were similar to the ideal analytical dam-break Ritter solution (1892). However, some discrepancies between the Ritter solution and the hydraulic bore generated within the experiments were observed.

As shown in Fig. 5-4, the drop in the reservoir level observed at WG1 occurred slower than that in the analytical Ritter solution (1892) for both reservoir water levels, particularly for h_0 = 0.20 m. The false floor fitted on top of the flume floor acts as a bottom sill immediately upstream of the gate. This sill changes the flow conditions at the gate and can cause a delay of the water release by restricting the cross-section of the channel. The behavior of the flow around this particular swing gate is further discussed in Goseberg et al. (2017) while the general influence of the shape of the reservoir is discussed in Khankandi et al. (2012). At WG2, the wave front of the experimental bore showed a terraced shape and a steep surge front. This shape likely occured due to the flow resistance imparted by the bed roughness. At WG3, the bore does no longer show a terraced shape though the tip of the bore remained steeper compared to the Ritter solution (1892).

As shown in Fig. 5-4, the wave profile had little variation between the experimental trials. The standard deviation of the water surface elevation was 0.0167 m and σ = 0.0183 m for h_0 = 0.40 m and h_0 = 0.20 m, respectively. Though the gate opening time for the smaller impoundment depth was less than the Lauber-Hager criterion, no significant influence on the repeatability was noted in the wave profile. It also should be noted that the Lauber-Hager criterion was developed for a vertical lift gate and considering the mechanism used in this study (swing gate) a different criterion may be necessary (Goseberg et al. 2017).

Field investigations conducted in the aftermath of major tsunami events revealed flow depth on-land ranging between 0.5 m and 9.0 m in a built environment (Borrero et al. 2006, Fritz et al. 2012). On-land tsunami inundation velocities have also been investigated numerically and experimentally. Borrero et al. (2006) reported flow velocities of up to 2.5 m/s when studying extreme inundation at Banda Aceh (Indonesia) after the 2004 Indian Ocean tsunami. Wave front velocities between 10 - 15 m/s were observed during the Tohoku tsunami in Japan in 2011 (Fritz et al. 2012). The dam-break wave induced bore flow (at prototype scale) of 2.0 to 6.4 m flow depth and associated flow velocities ranging from 5.1 - 9.48 m/s. The flow duration, estimated as the time it takes for the negative wave to propagate the length of the reservoir and reflect back to the structure, was 13.6 s (86 s at prototype scale). The flow duration was an order of magnitude less than a typical tsunami wave (Madsen et al. 2008). The focus of this study is on debris entrained in the initial wave front whose impacts occurred within the initial 5 s of the flow, such that no influence of the further flow duration on this initial impact should be expected. However, as the generation of debris (from destroyed houses to larger objects) can occur throughout the entire duration of a tsunami-induced flood event, further research is needed to investigate debris impacts in the later (quasi-steady) stages of the flow.

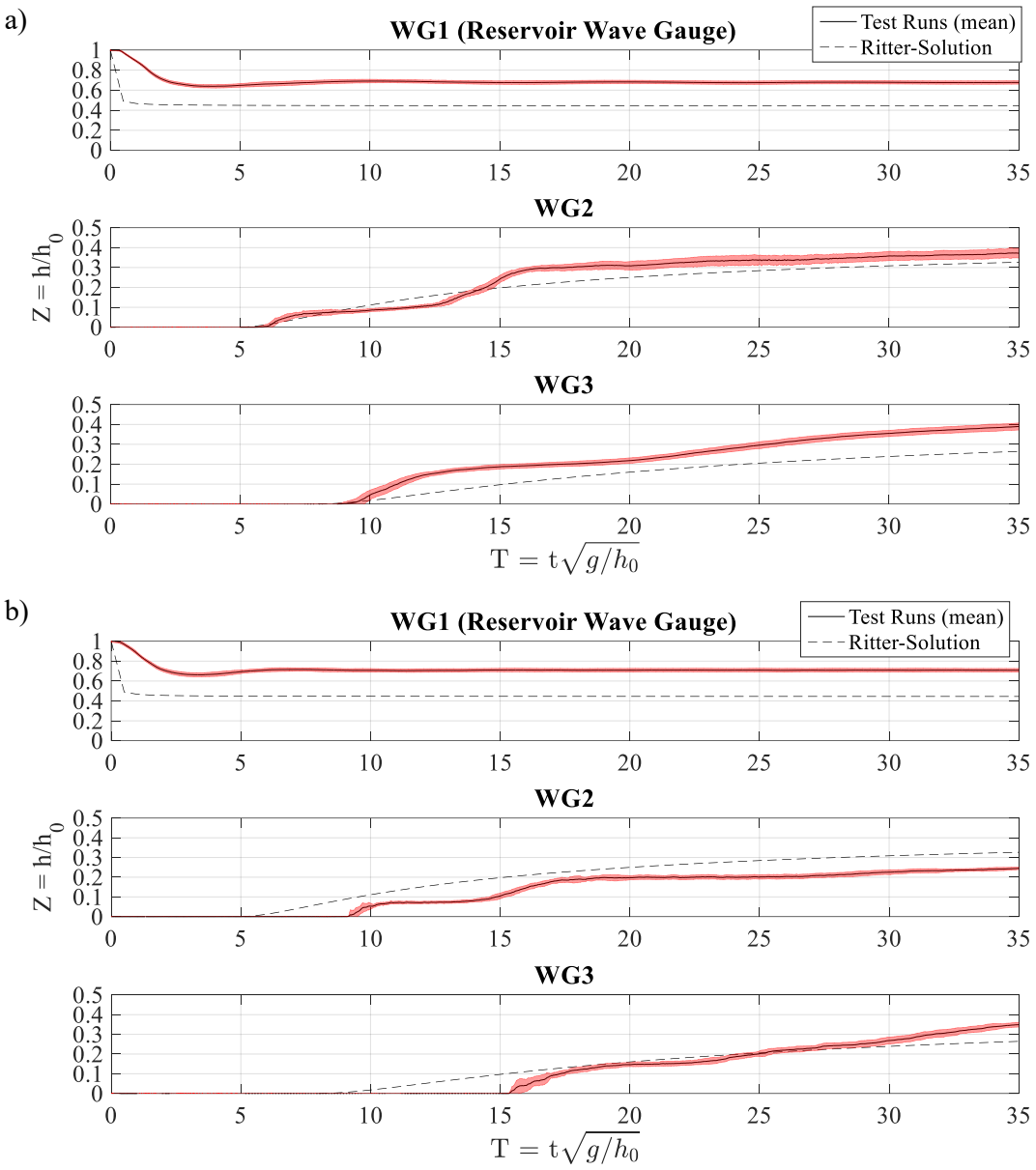

Fig. 5-4. (a) Comparison of the experimental results (solid line) and the analytical Ritter solution (dashed line) for the dimensionless time-history of the water level for an initial reservoir water level of 0.4 m and (b) for 0.2 m for WG1 (y = -0.10 m), WG2 (y = 2.00 m) and WG3 (y = 3.20 m). The red area represents the standard-deviation.

Debris Impact Velocity

FEMA P646 (FEMA 2012) and ASCE 7 (ASCE 2016a) conservatively estimate the impact velocity to be equal to maximum flow velocity at the site. To address this estimation, several factors influencing the debris velocity will be discussed in this section. For this idealized case, with no features inducing flow accelerations, the maximum flow velocity would be assumed to be the flow velocity in the wave tip. The velocity was calculated using the wave tip arrival at each of the wave gauges. The calculated velocity (u_b) represents the mean velocity of the wave tip, however, due to challenges measuring the flow velocity in the wave tip, the wave front velocity was assumed to be approximately equal to the flow velocity

(Chanson 2005). As shown in Table 5-6, the flow velocity was determined to be 2.46 m/s (σ = 0.14 m/s) for h_0 = 0.40 m compared to 1.32 m/s (σ = 0.05 m/s) for the tests with h_0 = 0.20 m.

Table 5-6: Comparison of the flow velocity, impact velocity and delay of the debris in comparison for the reservoir height of h_0 = 0.20 m and h_0 = 0.40 m. μ is the mean value and σ is the standard deviation.

	Bore Front Velocity (u_b)			Debris Velocity (U)			Debris Impact Delay (t_d)		
h_0 [m]	μ [m/s]	σ [m/s]	$u_b/\sqrt{gh_0}$ [-]	μ [m/s]	σ [m/s]	U/u_b [-]	μ [s]	σ [s]	$t_d\sqrt{g/h_0}$ [-]
0.20	1.32	0.05	0.94	0.64	0.25	0.49	0.57	0.02	3.96
0.40	2.46	0.14	1.24	1.57	0.14	0.64	0.18	0.05	0.89

The mean impact velocities (U) of individual debris were 1.57 m/s (σ = 0.14 m/s) for h_0 = 0.40 m and 0.64 m/s (σ = 0.25 m/s) for h_0 = 0.20 m and, thus, were less than the mean flow velocities. The impact velocity was calculated by dividing the distance between the centroid of the debris one frame before impact and the frame at impact by the time between frames. A previous study of this experimental setup (Stolle et al. 2018c) showed that the debris had reached an quasi-equilibrium velocity approaching the bore front velocity.

The impact velocity for each test run was lower than the respective flow velocity for both h_0 = 0.20 m and h_0 = 0.40 m (Fig. 5-5a). Based on the linear regression shown in Fig. 5-5a (solid thin line), the debris impact velocity was approximately 63% of the measure wave front velocity. A portion of the reduced impact velocity is due to the estimation of the wave front velocity; the wave front velocity was determined upstream (y = 3.20 m) of the impact site (y = 7.05 m). Since the bed resistance was present through the propagation section, the wave front velocity will decay over time (Chanson 2006). Therefore, the wave velocity may be slightly overestimated by using the velocity upstream of the impact site. Additionally, the debris was observed to rapidly fall behind the wave front, as there are no features inducing flow accelerations, the wave front velocity would represent the maximum velocity of the flow (Chanson 2005). The flow velocity acting on the debris would be less than the wave front velocity, and therefore, the drag force would be reduced, resulting in reduced debris velocity.

The reduced debris propagation velocity resulted in a delay between the wave and debris impacting the structure (Fig. 5-5b). The difference in the arrival time was calculated by comparing the initiation of the wave force acting on the structure to the first spike in the force related to the debris impact. The mean difference in arrival time was 0.57 s and 0.18 s for 0.20 m and 0.40 m, respectively (Table 5-6). Stolle et al. (2017a), using the same model debris, determined the displacement of debris in bore-like flow conditions could be approximately modelled as Eq. (2-2).

Eq. (2-2) assumes that the wave front velocity and the cross-sectional area exposed to the flow is constant over the area of interest. The thick solid line in Fig. 5-5b shows the estimated difference in arrival time of the wave and the debris based on Eq. (2-2). This equation tends to underestimate the delay in the arrival time. The discrepancy is partially related to the assumption of Eq. (2-2) that the cross-sectional area is a constant along the trajectory. As discussed earlier, the debris propagated in the slower flow behind the wave front, resulting in an overestimation of the drag forces acting on the debris. The cross-sectional area also varied over the area of interest as the debris tended to rotate within the flow. This observation was a result of assuming the maximum cross-sectional as constant; this led to overestimated drag forces acting on the debris.

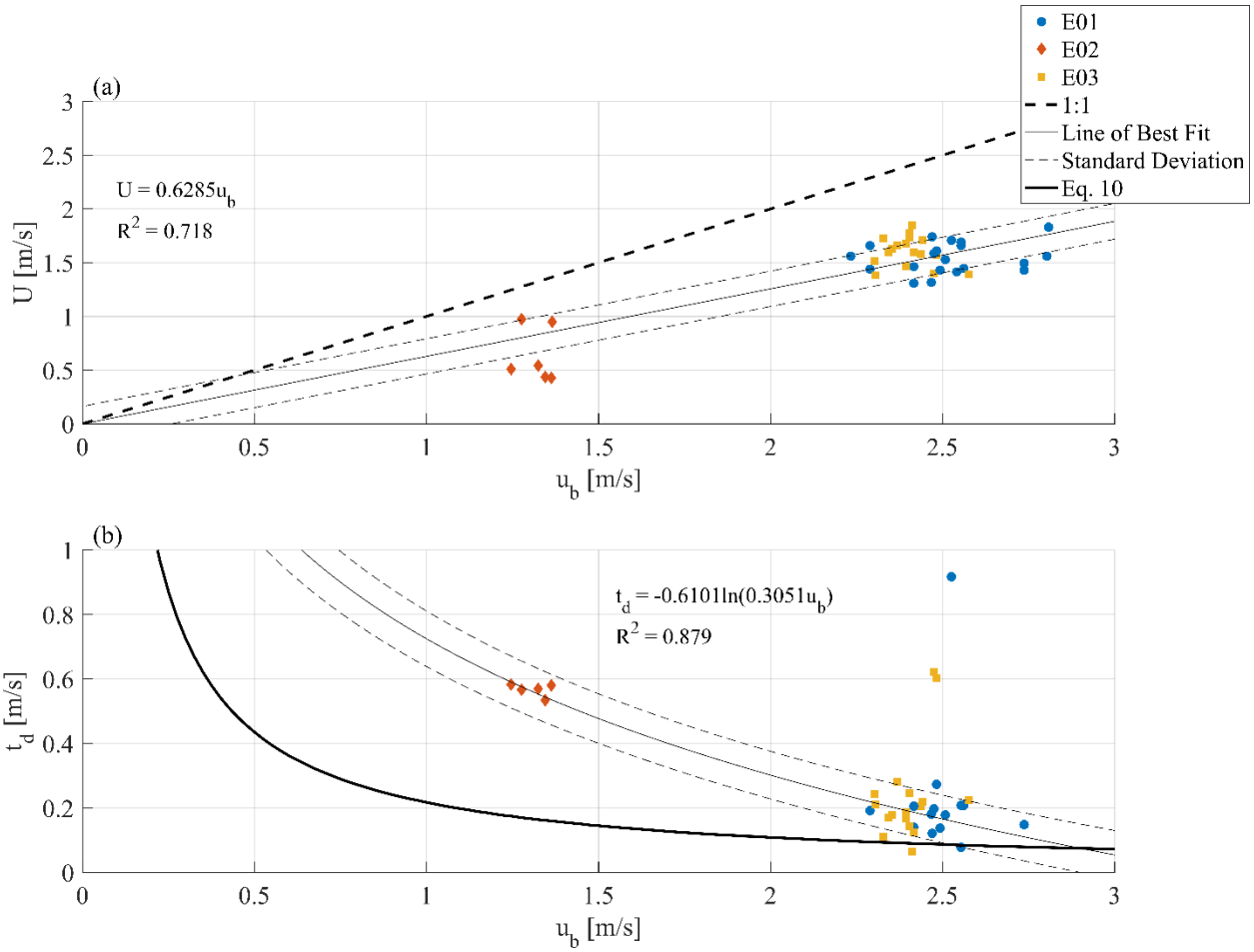

Fig. 5-5. Influence of the wave front velocity on the debris position within the wave. (a) Debris velocity (U) compared to the wave front velocity (u_b); (b) debris impact delay (U) compared to the wave front velocity. The experimental categories are designated by the marker style and color.

Further discrepancies between the bore front velocity and the debris impact velocity, outside of the assumptions of Eq. (2-2), were related to the grounding of the debris. Debris occasionally contacted the bed surface resulting in a rapid reduction in propagation velocity and rotation of the debris. This phenomenon was not captured by Eq. (2-2) as the equation does not consider the local flow depth and could not determine when the grounding would occur. Grounding was the cause of the large deviations shown in Fig. 5-5.

The final aspect not considered with Eq. (2-2) influencing the debris impact velocity would be the formation of the stagnation zone and surface roller at the front face of the structure. The difference between the wave arrival and debris impact would dictate the type of flow features which are occurring around the structure upon impact (St-Germain et al. 2013). A further investigation into the influence of the flow features on the debris impact are discussed in the subsequent sections.

The difference in the debris arrival time and impact velocity to the wave front are dependent on the distance the debris has travelled while entrained within the flow. Since this experimental program solely examined debris entrained at a fixed distance from the structure, the presented relationships vary based on distance; however, Eq. (2-2) would still provide the most rapid arrival time of the debris. Additionally, this study focuses solely on the debris entrained within the leading front of the transient wave and does

not further investigate debris motion due to the quasi-steady component of the tsunami-induced inundation. The authors infer however that Eq. (2-2) likely performs more adequately in the quasi-steady flow due to the assumption of a constant hydrodynamic forcing condition. However, further research is necessary to address this issue in its entirety.

Stagnation Zone

Previous studies investigating dam-break waves impinging upon vertical columns have shown that there are distinctive stages of the flow around the column (Arnason et al. 2009, St-Germain et al. 2013). In the initial stages, the wave front impacts the column and the flow velocity is rapidly reduced, forming a low velocity (stagnation zone) at the base of the structure. The flow around this resulting stagnation zone is redirected around the structure. As the flow continues to build, a surface roller forms at the front of the column, with a horizontal axis perpendicular to the direction of the flow. Due to the restricted width of the flume, the surface roller extends to the side walls of the flume, eventually propagating upstream as the flow transitions from supercritical to subcritical.

Due to the difference in the wave arrival time outlined in the previous section, the flow conditions experienced by the debris upon impact vary based on the arrival time. In the case of h_0 = 0.20 m, the reduced velocities resulted in the stagnations zone being fully realized by the arrival time of the debris. The distinct formation of the flow resulted in a non-linear movement of the debris as it followed the streamlines around the structure. To quantify the non-linear movement, the RMSE in relation to a completely linear approach after entering a hypothetical 0.20 m radius around the structure was used, as shown in Fig. 5-6.

$$RMSE = \sqrt{\sum_{i=1}^{n} \frac{\left(x_i^l - x_i^a\right)^2}{n}} \tag{5-2}$$

where x_i^l is the lateral position of the assumed linear trajectory of the debris, x_i^a is the actual position of the debris, and n is the number of frames captured within the area of interest.

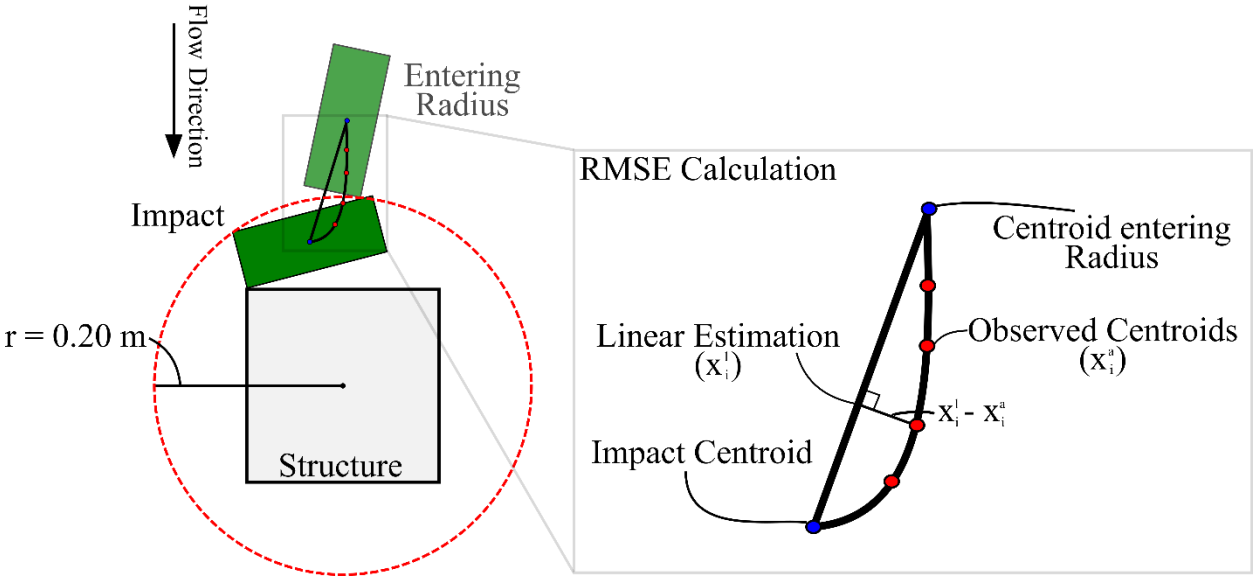

Fig. 5-6. Definition of the RMSE. The comparison of the actual debris centroid positions with an assumed linear approach trajectory.

The RMSE from these experiments had a maximum value of 0.014 m, showing a strong deviation of the observed movement to an idealized linear approach of the debris. For four of the ten test runs with h_0 = 0.20 m, the non-linear movement of the debris resulted in the debris not impacting as the debris followed the streamlines passing around the structure.

Since the stagnation zone had not distinctively formed on arrival of the debris for the larger impoundment depth case (h_0 = 0.40 m), as well as the increased momentum of the incoming debris, the movement of the debris exhibited a significantly straighter trajectory. The RMSE was consistently less than 0.003 m (Fig. 5-7), pointing towards little influence of the stagnation zone on the debris approach geometry. Even for the experiments with a slightly higher RMSE, the curved motion was less visually apparent and higher deviations were related to fluctuations around the theoretical linear approach.

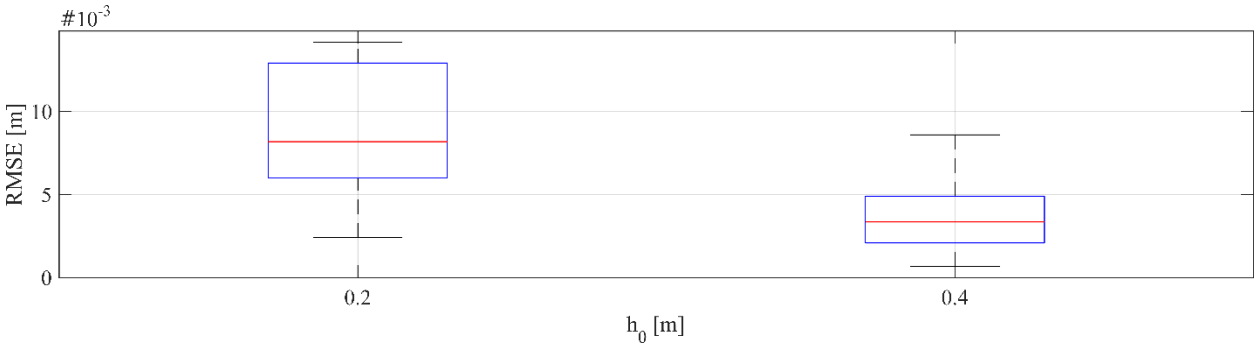

Fig. 5-7. RMSE of the actual debris centroid positions in comparison with a linear approach for different reservoir water levels.

The non-linear movement for the h_0 = 0.20 m tests resulted in gyration of the debris before impact, causing the long axis of the debris to be pushed towards the structure. Ikeno et al. (2016) noted that impacts where the angle between long axis of the debris and the face of the structure were less than 20°, a significant reduction in the impact force was observed due to the transfer of linear kinetic energy to rotational energy around the impact point. Additionally, the presence of the stagnation zone and lateral velocities would reduce the impact forces by reducing the momentum in the direction of the impact.

Surface Roller

A surface roller formed upon the impact of the wave with the structure. For the larger dam-break waves, the surface roller had a larger influence on the debris impact for the cases with h_0 = 0.40 m compared to h_0 = 0.20 m. The movement of the debris tended to follow the formation surface roller. Fig. 5-8 shows a sequence of image frames for the h_0 = 0.40 m case outlining the impact process and the influence of the surface roller.

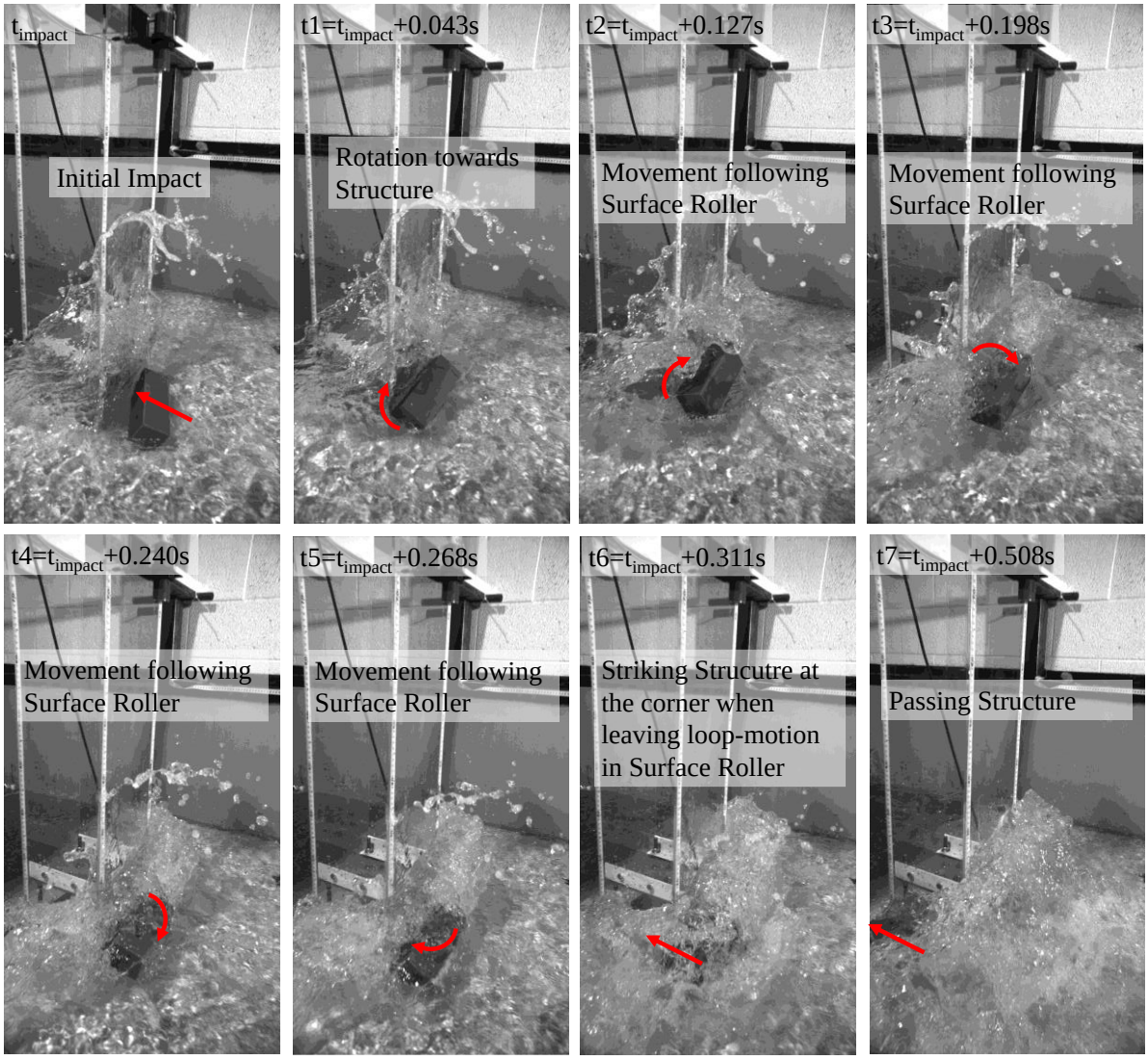

Fig. 5-8. Typical movement of the debris with the surface roller. The arrow represents the direction of the movement and t# indicates the time since impact (t_{impact}).

After the initial impact, the debris followed the movement of the surface roller for the larger impoundment depth. In all cases, the debris rotated around all three axes. The debris was likely to strike the structure again when leaving the surface roller and following the flow around the structure. While being trapped in front of the structure, the debris impacted several times. The first impact tended to exert a greater force on the structure than the secondary impacts, as the majority of the kinetic energy was expended on the first impact, and sufficient acceleration time was not available before the second impact occurred (Fig. 5-9). The multiple impacts could be significant as the structural integrity would potentially decay under multiple impacts as well as the possibility of debris dams forming resulting in further loads (Stolle et al. 2017b).

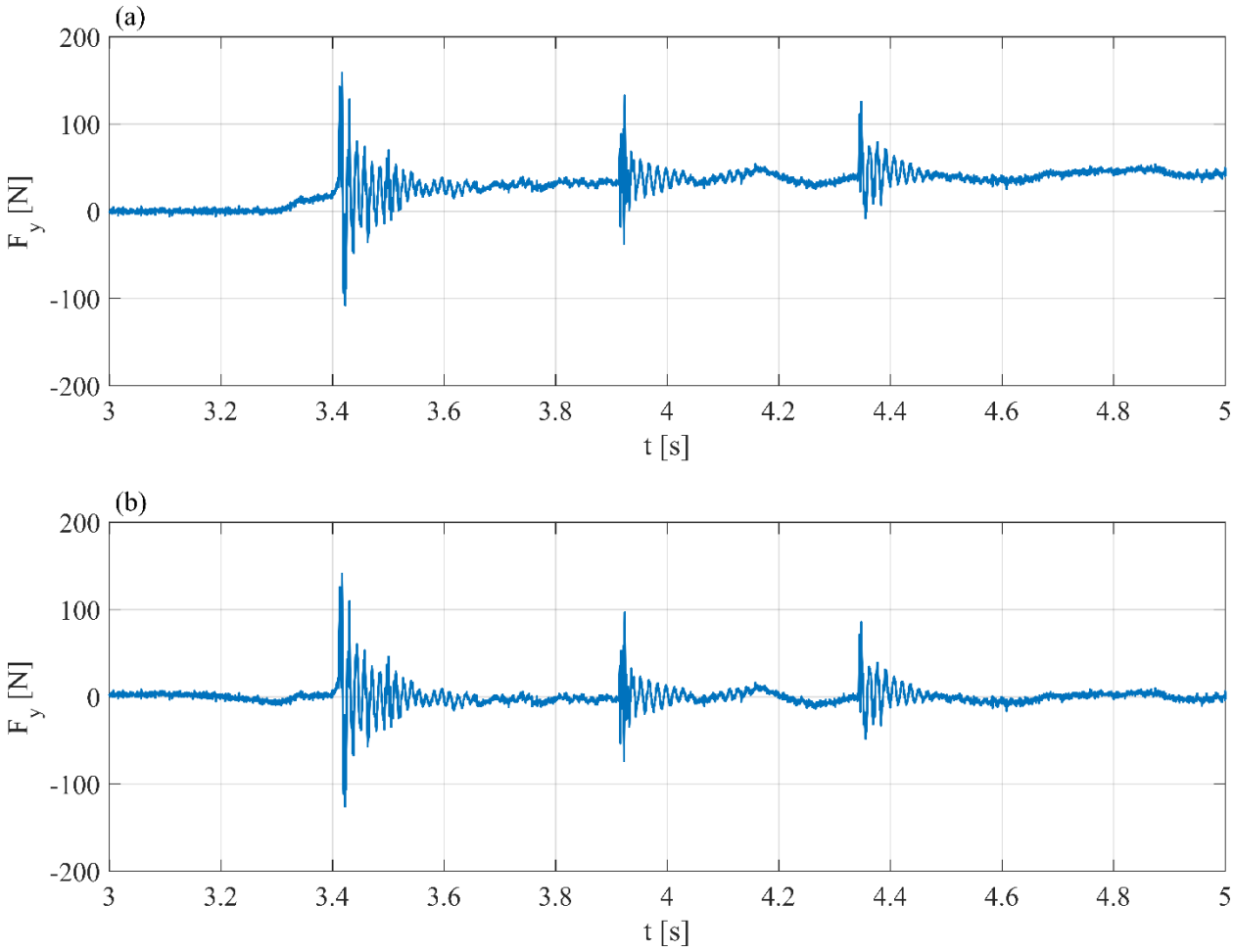

Fig. 5-9. Force-time history in the y-direction. (a) filtered time history using the EMD filter; (b) impact time history with the hydrodynamic load removed.

Debris Impact

During a natural tsunami event, debris transport will occur randomly. This leads to impact events where strikes on obstacles would occur at different angles, orientations, obliqueness and eccentricity. These will hence govern the magnitude of the impact forces, yet there is little information how this occurs. The definitions and terminology pertaining to *debris impact geometry* within hydraulic engineering tend to be fluid. To clarify the designation of each of the terms used in the following section, this section briefly outlines reiterate the definitions outlined in Fig. 2-3.

The impact angle (θ) is the angle between the debris impact velocity vector (U) and the long axis of the debris (DA). The impact obliqueness (β) is the angle between the debris impact velocity and the face of the structure. The impact orientation (α) is the angle between the long axis of the debris and the face of the structure. The impact eccentricity (ε) is the distance (in the lateral x-direction) between the impact point (IP, where the debris first contacts the structure) and the center-of-gravity (CG).

Initial Configuration

The initial orientation (longitudinal or transverse) of the debris prior to entrainment did not have a significant influence on the debris impact on the structure. As can be seen in Fig. 5-10, the maximum

impact force does not show a clear correlation with the initial orientation. A two-sample t-test comparing the h_0 = 0.40 m cases did not show a significant difference in the mean impact forces (p = 0.19, degrees-of-freedom (dF) = 35) comparing the two initial orientations (E01 and E03). The travel distance of the debris before impact (27 x the length of the debris), allowed the debris to rotate within the flow before the initial impact and reach a relatively steady velocity. The initial impoundment depth, h_0, did have a significant influence on the impact force (p << 0.05, dF = 41) as the impact velocity was greater for h_0 = 0.40 m (Eq. (2-6)).

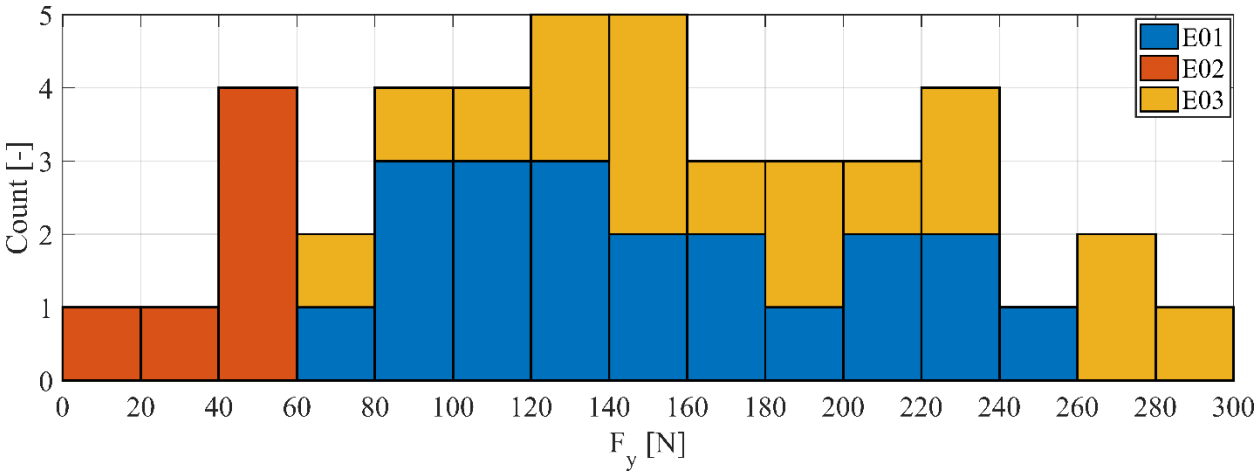

Fig. 5-10. Histogram of maximum impact response for each experimental trial.

Impact Geometry

The following section investigates the influence of the impact geometry parameters on the maximum impact loads as well as the distribution of each parameter. The definitions of each parameter are outlined in Fig. 2-3. The force values presented in this section are normalized by the maximum impact force as determined by the rigid body model (Eq. (2-6)) (Haehnel and Daly 2002):

Fig. 5-11 shows the distribution of impact angles separated by experimental category, which is the angle between the debris impact velocity vector and the long axis of the debris. Examining the line-of-best fit (solid line, R^2 = 0.123) shows an opposite trend, as expected. Haehnel and Daly (2004) determined a similar trend, similar to the one found in this study, noting that the longitudinal impact force only exceeded the transverse impact for a perfect longitudinal hit, where θ = ~0°. As noted by Ikeno et al. (Ikeno et al. 2016), this was likely due to the small value in θ (< 20°) which resulted in a greater amount of kinetic energy being transferred into rotational energy. Due to the free-floating nature of the debris in these experiments, a perfect longitudinal impact did not occur resulting in the observed positive trend with increasing impact angle.

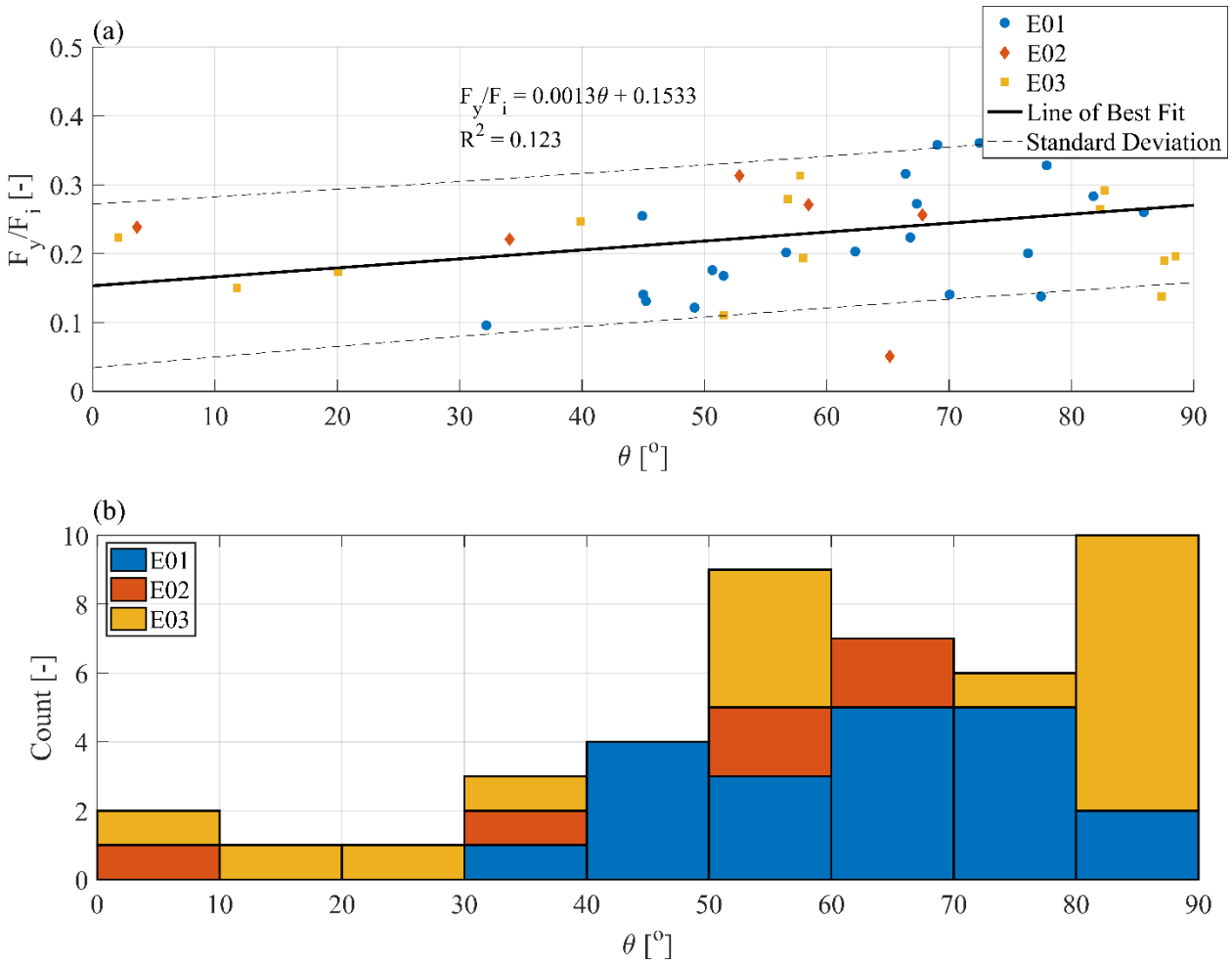

Fig. 5-11. Distribution of Impact Angle (θ). (a) Influence of impact angle on measured force; (b) stacked histogram of impact angle values. The experimental categories are separated by color.

Fig. 5-11b shows the distribution of impact angle for each experimental category. Table 5-7 displays the statistical properties of the impact angle distribution. As can be observed from the mean (μ) impact angle, the debris tended to impact the structure closer to transverse impacts (θ > 45°). A one-way analysis of variance (ANOVA) (McDonald 2009) determined that there was not a significant difference between the means of each of the experimental categories (p = 0.312, dF = 40). Goseberg et al. (2016b), using the same model debris, noted that the debris tended to rotate towards an equilibrium position with the long axis perpendicular to the flow direction. In these experiments, the debris had sufficient distance between entrainment and impact to reach a quasi-equilibrium state resulting in the greater impact angles. The equilibrium position of the floating debris is a function of the inertia of the debris model and may vary depending on the weight distribution. The mass distribution of a prototype shipping container was not considered in the design of the model debris, therefore, the equilibrium condition may vary at prototype scale.

Table 5-7. Statistical properties for the impact geometry parameters: Impact Angle and Impact Obliqueness.

	Impact Angle					Impact Obliqueness				
			Two-sample t-test					Two-sample t-test		
Experimental Category	μ [°]	σ [°]	E01	E02	E03	μ [°]	σ [°]	E01	E02	E03
E01	62.48	14.77	--	0.07	0.97	86.63	2.90	--	5.84×10^{-8}	0.03
E02	46.99	24.40	0.07	--	0.26	41.90	26.64	5.84×10^{-8}	--	3.27×10^{-6}
E03	62.16	28.09	0.97	0.26	--	83.35	5.72	0.03	3.27×10^{-6}	--

Fig. 5-12 shows the distribution of the impact obliqueness, which is the angle between the impact velocity vector and the face of the structure, separated by experimental category. As the angle of attack of the flow, in these experiments, was always perpendicular to the face of the structure, a 90° impact obliqueness would mean the impact velocity vector exclusively had a y-velocity (forward) component. The greater the impact direction angle the greater the energy transferred to the impact, resulting in a large impact force. As can be observed from Fig. 5-12a, the line-of-best-fit (solid line, $R^2 = 0.121$) showed a positive trend, as expected.

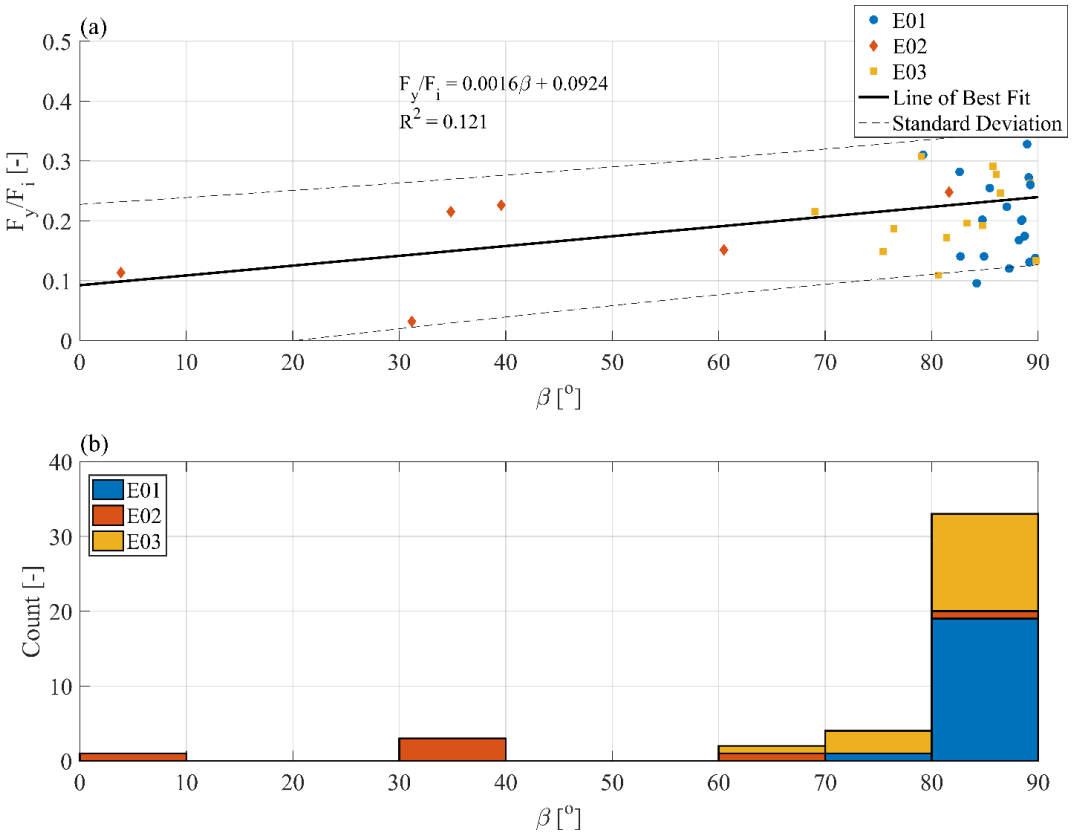

Fig. 5-12. Distribution of Impact Obliqueness (β). (a) Influence of impact obliqueness on measured force; (b) histogram of impact obliqueness values. The experimental categories are separated by color.

Fig. 5-12b shows the distribution of the impact obliqueness angles. A one-way ANOVA determined that there was a significant difference in the mean impact obliqueness between experimental categories ($p << 0.05$). Table 5-7 shows the mean values and standard deviations for each experimental category. A post-hoc two-sample t-test determined that there was a significant difference in means between each experimental category. As discussed earlier, the h_0 = 0.20 m case had larger velocities in the x-direction due to the formation of the streamlines around the structure. The *x*-velocities could induce loading on the structure due to shear loads, however, this type of loading, commonly referred to as glancing impacts, is dependent on the friction between the debris and the structure (Frankel and Weihs 1990), which was not considered within this study. For the h_0 = 0.40 m cases, the debris reached the structure before the streamlines had fully formed, in combination with the greater inertia of the debris, resulted in impact obliqueness close to parallel with the flow direction.

Fig. 5-13a outlines the influence of the impact orientation on the measured impact force. The orientation represents the center-of-mass not acting directly through the impact point resulting in a portion of the kinetic energy being transformed into rotational energy (Ikeno et al. 2016). Occasionally, in cases where the direction of the velocity vector has been challenging to determine, the impact orientation has been used in lieu of the impact angle. Comparing Fig. 5-10a and Fig. 5-13a, a similar trend can be observed as, particularly in the case of h_0 = 0.40 m, the velocity vector was close to perpendicular with the face of the structure. The differences between the impact angle and orientation occurred when significant *x*-velocities resulted in the debris interacting with the streamlines around the structure.

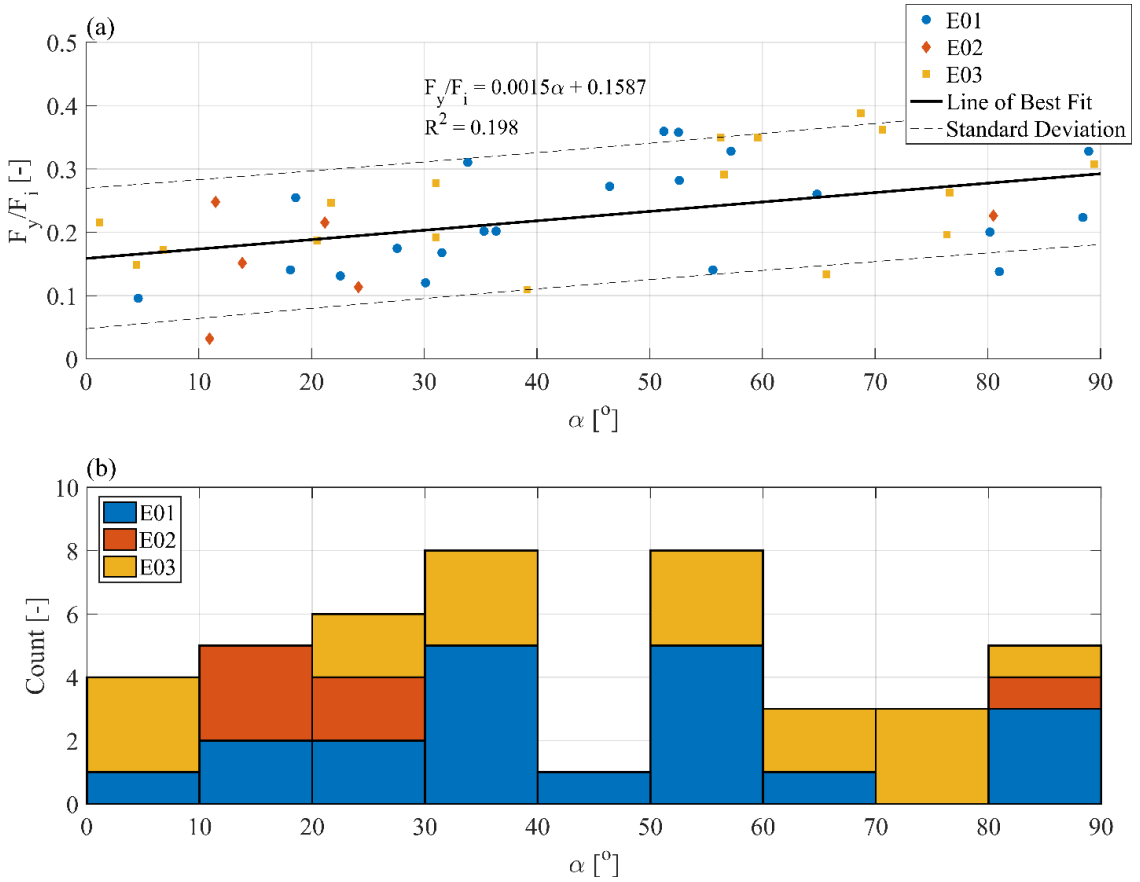

Fig. 5-13. Distribution of Impact Orientation (α). (a) Influence of impact orientation on measured force; (b) histogram of impact orientation values. The experimental categories are separated by color.

Fig. 5-13b details the distribution of the impact orientation for all of the experiments. A one-way ANOVA showed that there was not a significant difference in the mean impact orientation between the experimental categories (p = 0.286, dF = 40). As the debris had sufficient distance to travel from the initial source, the orientation of the debris within the flow seemed to be approximately random. As the orientation does not consider the direction of the velocity vector (as the impact angle does), the equilibrium orientation of the debris is not prevalent within the mean impact orientation angles (Table 5-8).

Table 5-8. Statistical properties for the impact geometry parameters: Impact Orientation and Impact Eccentricity.

	Impact Orientation					Impact Eccentricity				
			Two-sample t-test					Two-sample t-test		
Experimental Category	μ [°]	σ [°]	E01	E02	E03	μ [m]	σ [m]	E01	E02	E03
E01	44.45	22.68	--	0.13	0.89	0.03	0.02	--	0.25	0.46
E02	27.03	26.73	0.13	--	0.17	0.02	0.01	0.25	--	0.70
E03	45.64	28.13	0.89	0.17	--	0.03	0.03	0.46	0.70	--

Fig. 5-14 shows the influence of the impact eccentricity on the measured impact forces. An eccentric impact occurs when the center-of-mass of the debris does not act through the impact axis (Stronge 2004) causing a rotation to occur. The ε-value is the distance (in the x-direction) between the impact axis and the center-of-gravity, representing the rotation arm of the subsequent debris rotation. The greater the length of the impact arm, the greater the rotational energy, and therefore the smaller the impact force. As can be observed in Fig. 5-14, a negative trend can be observed, as expected.

Fig. 5-14b shows the distribution of the measured impact eccentricities. The maximum possible ε-value is half of the length of the long axis (0.075 m). A comparison of the experimental categories, using a one-way ANOVA, showed no significant difference in the mean impact eccentricities (p = 0.553, dF = 40). Similar to the impact orientation, as the cosine of the impact orientation multiplied by the length of the long axis of the debris, the mean impact eccentricities did not have a prevalent mean value, with the observed values spanning the possible range of impact eccentricities.

While the impact geometries displayed trends consistent with the previous literature, the correlations between the parameters were not strong ($R^2 < 0.2$). The primary cause was likely due to the consideration of the impact geometries in a two-dimensional plane. Particularly in the presence of the surface roller, the debris also eccentric and oblique impacts in the *x-z* plane, which was not captured in the impact geometries outlined here. Moreover, the impact geometry and how the debris responds to the hydrodynamic forcing conditions will be dependent on the inertia of the debris. Therefore, the relationships developed in this study would vary depending on the type as well as the mass distribution of the individual debris. Additionally, as will be discussed in Part 2 of this two-parts paper series, the use of the rigid body model to normalize the impact forces may not be adequate to capture the impact conditions due to deflections from the structure.

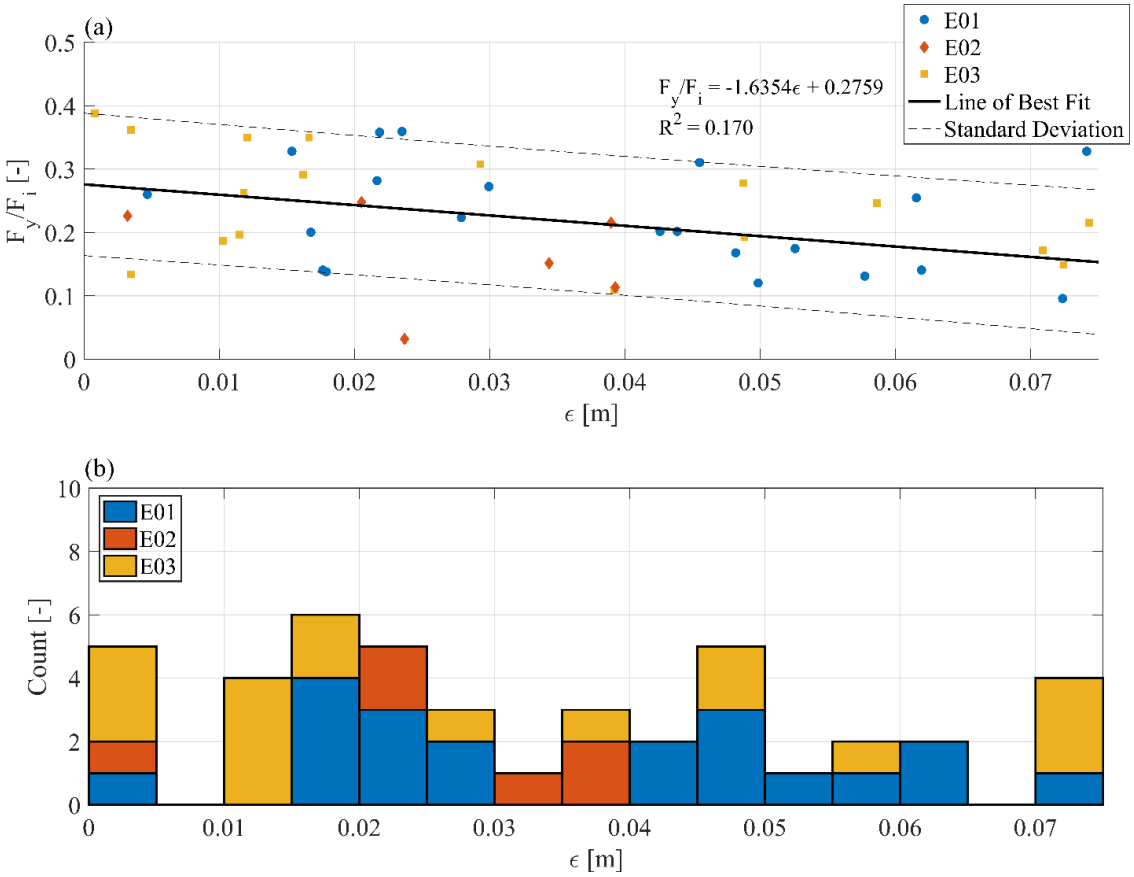

Fig. 5-14. Distribution of Impact Eccentricity (ε). (a) Influence of impact eccentricity on measured force; (b) histogram of impact eccentricity values. The experimental categories are separated by colors.

5.1.4 Conclusions

This study presents the results of physical experiments for debris impact under extreme hydrodynamic conditions; these results presented in the first part of the two-part paper series are pertaining to detailed experimental description, hydrodynamics of the approaching bore interacting with a vertical structure and various parameters to describe the debris impact geometry. A swing gate was used to create the tsunami-like flow conditions (dam-break wave); the debris was depicted as scaled-down (1:40) shipping containers. This study examined the impact of single debris while varying the hydrodynamic boundary conditions and initial orientation of the debris with multiple repetitions of the same test conditions. The aim of this study is to deepen the understanding of how debris entrained in an extreme flow condition would eventually strike a vertical structure. The hydrodynamic and impact forces on the structure were recorded using a six-axis load cell mounted to the bottom of the structure.

Within this paper, the hydrodynamics of the experiments as well as the influences of the flow features around a structure and the impact geometry are evaluated with the following conclusions:

- The debris impact velocity measured within this study showed to be slower than the flow velocity of the bore front. The difference between the velocities was dependent on the initial impoundment depth.
- The formation of the splitting streamlines and stagnation zone in front of the structure resulted in non-linear movement of the debris in close proximity to the structure and reduced impact velocities.

- The formation of a distinct surface roller at the structure upon impact of the bore for greater wave heights influenced debris movement and caused the debris to impact the structures more than once with the additional impact forces less than the initial impact.
- The initial orientation of the debris placement did not have a significant influence on the debris impact conditions as the debris had sufficient time to accelerate and rotate within the flow before impacting the structure.
- The initial impoundment depth had a significant influence on the impact obliqueness as the flow features around the structure resulted in larger velocity components parallel to the face of the structure.

It should be noted that all the results are based on the experimental conditions described in this study and may require further research aimed at variations of hydraulic boundary conditions as well as varying debris such as cars, hydro-poles, dislodged and deteriorated building material. Additionally, due to the experimental nature and stochastic variations in the experimental program results, the described trends have a significant statistical component associated with the linear regressions described that will require future research as well. The focus of this study addressed the leading front of the tsunami wave as images from the 2004 Indian Ocean Tsunami (Fritz et al. 2006) showed debris present throughout the inundation and receding of the wave. Further research is needed to address the subsequent portion of the tsunami-induced inundation to develop a complete picture of the debris impact effects.

5.1.5 Link to Section 5.2

The study presented here examines the interplay between the hydraulic conditions and debris loading on structures. The influence on debris impact geometry on impact forces is well-established within the literature. The study aims to provide qualitative and quantitative reasoning for the variation in impact geometry to establish general trends to aid in the accurate estimation of impact geometry. The study acts as a primer in the explanation of the complex mechanisms involved in estimating impact force response outlined in Section 5.2.

5.2 Debris Impact under Extreme Hydrodynamic Conditions Part 2: Impact Force Responses for Non-Rigid Debris Collisions

Preprint of an article printed in Coastal Engineering© 2018 Elsevier.
https://www.sciencedirect.com/science/article/pii/S0378383918300681

5.2.1 Objectives

This study is part of a two-series paper focusing on a comprehensive experimental program conducted to elucidate debris-structure interaction in a dam-break flume. This part specifically focuses on the impact forces, discussing influencing factors and mechanisms for non-rigid debris impact, an aspect to which little attention was given in the past. With these overall objectives in mind, the following specific problems will be addressed throughout this paper:

- Investigate the relationship between the debris impact forces and associated torques from the perspective of a 6 degree-of-freedom (DOF) impact. Compare the current experimental findings to other research in the literature and discuss discrepancies with regard to structural flexibility non-rigidity on the collision in the present experiments.
- Propose ways to enhance existing the current debris impact force equations to include the flexibility of the impacted structures.

5.2.2 Experimental Setup

Dam Break Flume

The experimental research reported herein was part of a comprehensive program of tests conducted in a dam-break wave flume of the Water Resources Laboratory at the Department of Civil Engineering at the University of Ottawa, Canada. The flume schematically shown in Fig. 5-15 had a total length of 30.00 m (21.55 m reservoir, 8.45 m experimental section), a width of 1.50 m and a maximum depth of 0.72 m.

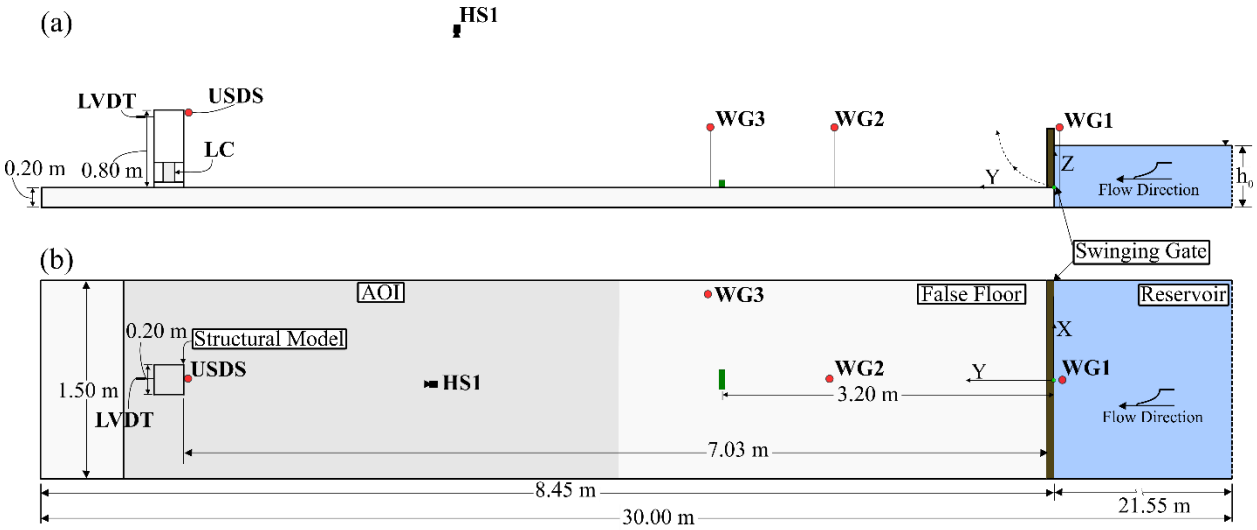

Fig. 5-15. Experimental setup (side view-above and plan view-below). HS = High Speed Camera, LC = Load Cell, USDS = ultrasonic distance sensor, LVDT = linear variable distance transducer, and WG = Wave Gauge.

A right-hand coordinate system was used with its origin at the dam-break gate with the y-axis towards downstream, and the *z*-axis in opposite direction to the gravity vector. A false floor in the form of a poured concrete slab with a glued sand base, was installed 0.25 m above the flume bottom. The floor was screened with 1 mm sand grains and paint resulting in an experimentally-determined steady-state Darcy-Weisbach friction factor (f) of 0.014. The reservoir was used to store a volume of water that was suddenly released by a rapidly-opening swing gate to create a tsunami-like bore. Dam-break generated bores resemble, according to Chanson (2006), tsunami surges or bores propagating over a coastal plain. The swing gate had a height of 0.62 m measured vertically from the false floor and was made of 0.025 m thick steel frame with plywood as surface. The dam-break facility, which is driven by the static hydraulic pressure force and a steel counterweight mounted at the top of a lever, is described in more detail in Goseberg et al. (2017).

Instrumentation

The structural model (0.20 m long, 0.20 m wide, and 0.80 m high), serving as an obstacle to the debris, was modeled as a hollow column placed center-flume at a distance of 7.03 m downstream of the swing gate. The walls of the column were acrylic with a wall thickness of 0.005 m. A small gap (~0.002 m) was left between the bottom of the column and the flume bed to avoid biasing the motion of the structure due to interactions with the bed. The small gap allowed water to enter the inside of the structure, around the load cell. The structural stiffness is an important parameter which was derived by assuming that the structure was a single DOF system. Its natural frequency was determined by employing the natural frequency (ω_s) and the mass of the structure (m_s) and was calculated to be (k_s) of 4.685×10^5 N/m (standard deviation (σ) = 2.09×10^5 N/m).

A stiff steel mount was constructed and embedded into the concrete false floor that served as a base for a 6-DOF load cell (LC). The LC was used to measure the forces and torques in *x*-, *y*- and *z*-direction (specifications shown in Table 5-9). The mount was connected to the structure using four stainless steel bolts at a height of 0.16 m from the false floor. The connection was placed at a height above the floor to limit the distance between the impact site and the connection, reducing the influence of any structural deflection. A linear variable distance transducer (LVDT) was placed behind the structure's top edge (downstream) to measure its displacement.

Models of 6.1 m prototype shipping containers with a 1:40 length scale (based on Froude similitude) were used as debris in this study. The model containers were made of buoyant polyethylene (PE-HMW). The debris were 0.15 m long and had a square cross section with sides of 0.06 cm; the debris' draft was approximately 0.023 m; further specifications of the used container models used for other experimental tests can be found in Nistor et al. (2016), Stolle et al. (2016), and Goseberg et al. (2016b). The scaled container models were tested in an axial stress-strain machine (Instron® Calibration Lab, Norwood, MA, ID4482P3229, range 100 kN) to determine their transversal and longitudinal stiffness which were 21×10^6 N/m and 3.43×10^6 N/m, respectively. The used stiffness was selected depending on the impact geometry of the debris as indicated in the following Table 5-9.

Table 5-9: Stiffness of the debris (k_d) and contact stiffness (k) in dependence of the obliqueness-angle (α) and the impact-angle (θ) of the debris in reference to the structure (CG=center of gravity, IP=impact point, $\vec{u}$=velocity vector of debris).

α [°]	Θ [°]	k_d [N/mm]	k [N/mm]
< 45	< 45	$k_{debris,long}$ = 3 431	876
< 45	≥ 45	$k_{debris,trans}$ = 21 000	1 115
≥ 45	≥ 45	$k_{debris,trans}$ = 21 000	1 115
≥ 45	< 45	$k_{debris,long}$ = 3 431	876

The single debris was manually placed center-flume on the false floor with the centroid 3.20 m upstream of the swing gate (Fig. 5-15) and the accuracy of the placement was estimated to be +/- 0.003 m.

One capacitance-type wave gauge (WG1) was placed inside the reservoir approximately 0.03 m upstream of the swing gate. Two other wave gauges were placed on the experimental section, 2.0 m (WG2) and 3.2 m (WG3) downstream of the swing gate, to measure the time-history of the water level as the dam-break wave propagated through the flume. The wave gauges were calibrated with R^2 values greater than 0.99.

A high-speed camera was aimed towards the structure from the top to document the impact and to analyze the wave-structure interaction: this is explained in more detail in the companion paper. Specifications of the instrumentation are detailed in Table 5-10.

Table 5-10: Instrumentation used in the dam break flume to record hydrodynamic and debris-related parameters.

Instrument	Manufacturer, Model (Symbol)	Sampling Rate
Wave Gauge (WG)	RBR WG-50 Capacitance (WG1)	1 200 Hz
	Akamina AWP-24 (WG2, WG3)	1 200 Hz
High-Speed Camera (HS)	Flare 2M360-CL	70 Hz
6DOF Load Cell (LC)	Interface 6A68E	19 200 Hz
Linear Variable Distance Transducer (LVDT)	RDPE LSC DCV025A	19 200 Hz

Experimental Program

With each test series 1-3, different boundary conditions were employed according to Table 5-11. The varying parameters were the water level in the impounding reservoir (h_0 = 0.20 m and h_0 = 0.40 m), used to create waves with different velocities and water depths and the orientation of debris at its initial position. The debris models were placed either longitudinally or transverse to the direction of flow. The E01 and E02 categories were used to provide an estimation of statistical properties of the debris motion. Using the mean and standard deviation of the lateral deviation of the debris (presented in Stolle et al. (Stolle et al. 2018c)), 10 repetitions were conducted within each test series to ensure a statistical power (Kenney 1962b) greater than 0.80 (probability of correctly rejecting the null hypothesis) when assessing debris motion.

Table 5-11: Description of the boundary conditions of the test runs described within this study.

Experimental Category	Reservoir Water Level (h_0) [m]	Initial Debris Orientation [°]	Repetitions
E01	0.4	0°	20
E02	0.2	90°	20
E03	0.4	0°	10

Data Processing

The impact velocity, as well as the impact geometry, were determined using image processing. The position of the debris was determined manually for every image frame considered. The accuracy with which the debris position was assessed from individual frames was estimated to be +/- 5 pixels resulting in an accuracy of 0.0172 m – 0.0175 m in *x*-direction and 0.0181 m – 0.0198 m in *y*-direction.

The debris impact load was extracted from the total measured load recorded by the 6DOF load cell near the base of the structure with two different filtering techniques. To attain the maximum debris impact force, an Ensemble Empirical Mode Decomposition EEMD-Filter (Huang et al. 1998) was applied with the Intrinsic Mode Functions (IMF), as shown in Table 5-12.

Table 5-12: IMF combinations for best matches to raw data for the force and torque signals in *x*-, *y*- and *z*-direction.

	F_x	F_y	F_z	M_x	M_y	M_z
IMF	2 – 12	4 – 12	2-17	3 - 10	2 – 17	2-12

The 6DOF load cell measured the frequency responses of the structure to the excitation of the system due to the impact (Stronge 2004). The measured force values thus included the oscillation of the structure. Within this study, the impact force responses from the 6DOF load cell were taken without eliminating the effect of the reaction of the structure upon impact. Therefore, when discussing the debris impact force within this paper series, the authors refer to the measured structural response to the debris impact. It is emphasized that the maximum forces discussed in this work do not constitute the adjusted impact forces exerted on the structure as the structure's dynamic response has not been taken into consideration.

5.2.3 **Results**

Forces and Torques

When the wave hits the structure perpendicular to the structure face, as expected, the primary hydrodynamic force occurs in the flow direction (*y*-direction) resulting in a torque in *x*-direction (Fig. 5-16). Because of the orthogonal approach of the wave to the structure, and the uniform separation of the flow, minimal forces occur in the *x*-direction (Fig. 5-16b) which are an expression of the flow's inherent turbulence when surrounding the structure. A buoyant force induced by the submergence of the obstacle was the primary force component in the vertical direction (z-axis). However, due to the hollow construction of the obstacle, thin walls, and intrusion of the water into the center of the structure, negligible buoyant forces were observed.

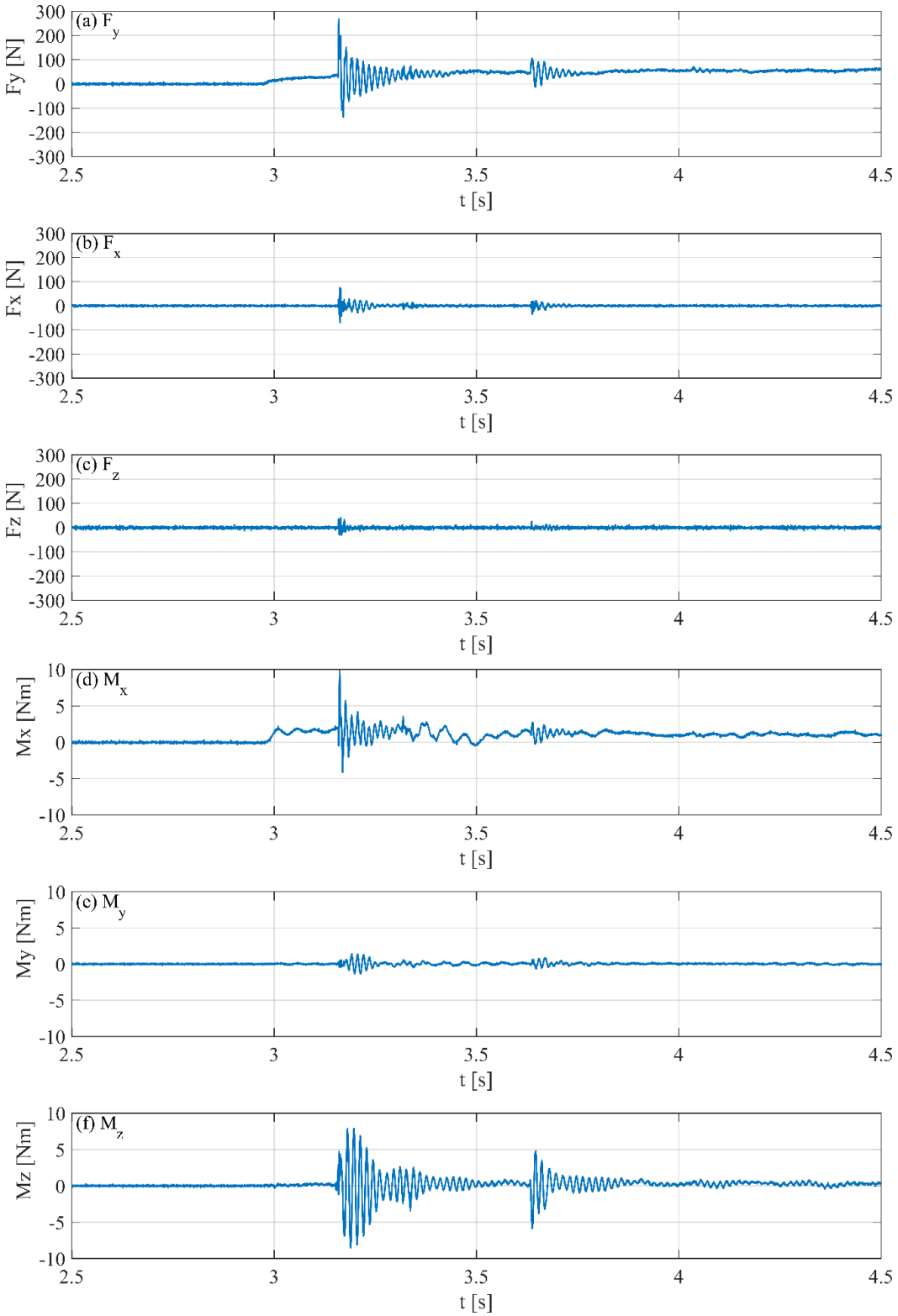

Fig. 5-16. Typical force and moment (torque) time-histories measured from the LC from a single experiment with an impoundment depth h0 = 0.40 m. (a) Fy (N), (b) Fx (N), (c) Fz (N), (d) Mx (Nm), (e) My (Nm), and (f) Mz (Nm).

The shipping container model was transported within the bore, resulting in the maximum impact velocity component in flow direction. For the majority of the tests, the maximum force induced by the debris impact in the flow direction was significantly larger than the forces in the *x*- and *z*-direction, as can be seen in Fig. 5-17. For the range of tests analyzed, a correlation between the lateral and the in-stream maximum forces and torques was observed. This is in agreement with Hertzian contact mechanics (Hertz 1882), as the tangential force is considered to be a direct function of the normal force. The force in the *y*-direction was on average 2.23 and 4.58 times greater than the forces in the *x*- and *z*-directions, respectively.

Shafiei et al. (2016b), in experiments examining circular debris impacting a vertical structure, found that the force in the flow direction exceeded the force in the *z*-direction by 1.67 times. This finding was explained by the authors by a significant frictional force due to an upward angle of the debris. Impact theory on rigid bodies (Thornton and Yin 1991) determined that tangential forces are a result of friction between the colliding objects. In Coulomb's theory of friction (Coulomb 1771), the tangential forces would then be independent of the sliding velocity (*x*- or *z*-directions, in this case) and contact area. Coulomb's law assumes that the normal force is proportional to the contact area between the objects, and due to the rapid nature of the impact, this does not necessarily occur (Hertz 1882). Additionally, significant displacements (of up to 0.004 m) were recorded at the top of the structure; therefore, the impact cannot be considered to be fully rigid. Assuming that Coulomb's law can be applied, this would result in a coefficient of friction (μ) of 0.41 ([0.35 0.46], 95% Confidence Interval). The calculated μ exceeds expected values of ~0.10 for the materials (acrylic, polyethylene) used in the experiments, indicating that Coulomb's law is not capturing the mechanics of the tangential forces.

As shown in Fig. 5-17(b), the torques in the *z*-direction were greater than in the *x*- and *y*-direction. The torque around the *x*-axis was approximately 0.26 times the torque around the *z*-axis. The measured values for the torque around the *y*-axis are approximately 0.10 times the torques around the *z*-axis. As discussed in the first companion paper, the splitting of the flow resulted in the lateral motion and impact of the debris off the center axis the structure's front face. The lateral motion resulted in the debris impacting with a longer moment arm (closer to the edges of the structure) resulting in the moments around the *z*-axis. Similarly, the formation of the surface roller resulted in an increase in the water level in front of the structure (St-Germain et al. 2013). As the debris was positively buoyant, the higher impact location would then result in greater moments around the *x*-axis. Due to symmetry of the flow and limited forces acting in the *x*-component, negligible moments were observed around the *y*-axis.

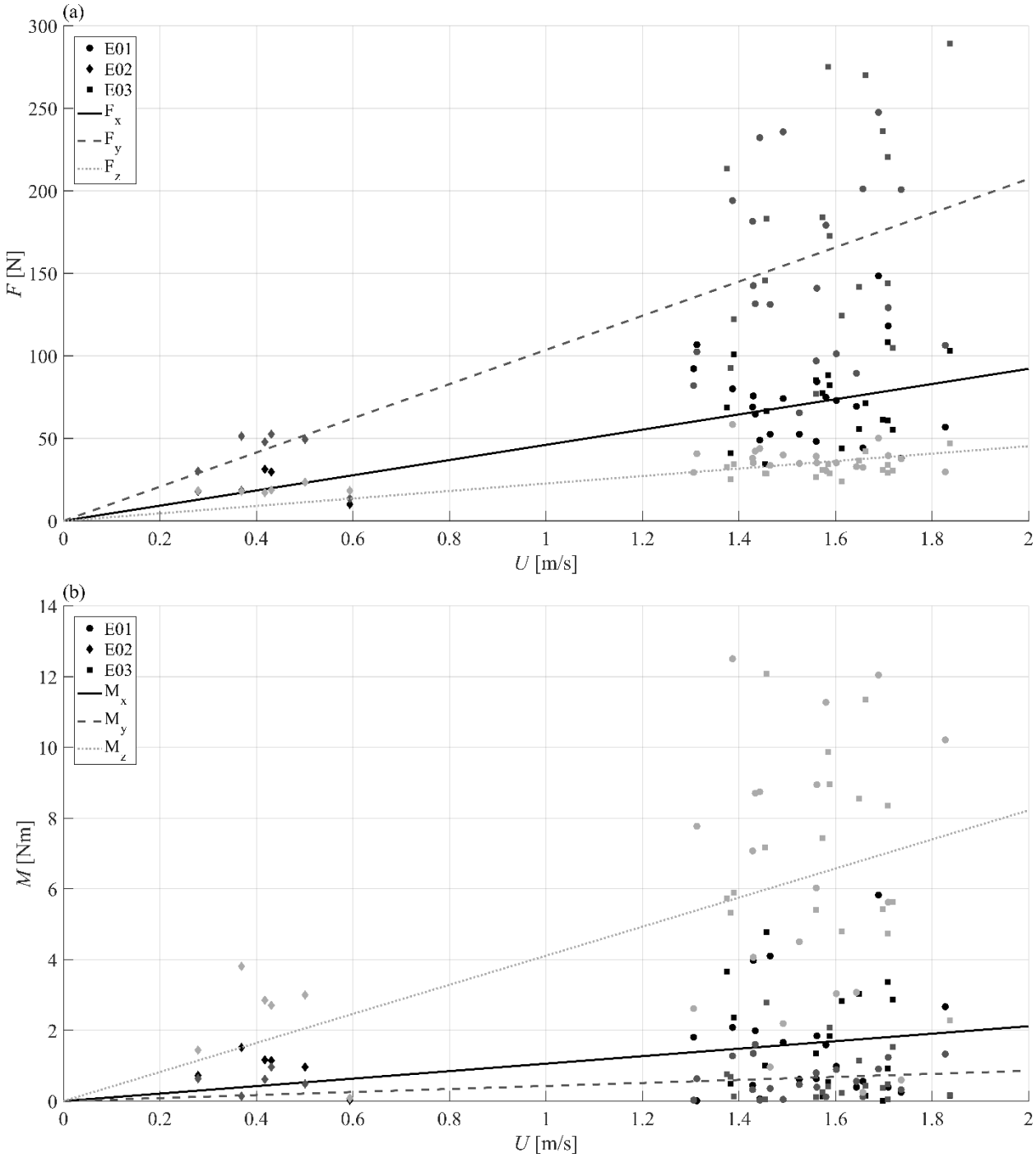

Fig. 5-17. Comparison of the (a) impact force measured with the load cell in the x-, y-, and z-directions and (b) the torques in the x-, y- and z-direction with impact velocity.

Non-Rigid Impacts

The LC was used to measure the impact forces and torques along the three axis of coordinates at the base of the structure. To investigate the elastic response of the structure, an LVDT was attached onto the back face to measure the displacement upon bore and debris impact. Using Hooke's Law ($F_{LVDT} = k_s x_s$) and

assuming linear material behavior for small displacements, the impact force was estimated using the measurements from the LVDT.

Using the two DOF system to represent the complex 3D stiffness and stress-strain evolution of a realistic structure, the displacement at the top of the structure was assumed to be equal to the displacement at the bottom of the structure. Therefore, the LC and LVDT would be measuring the structural response to the same input force. Fig. 5-18 shows the comparison of the measured forces from the LC and LVDT. As the measuring point of the LC was in close proximity to the impact site, the measurement of the LC would be expected to have limited influence from any structural deflection.

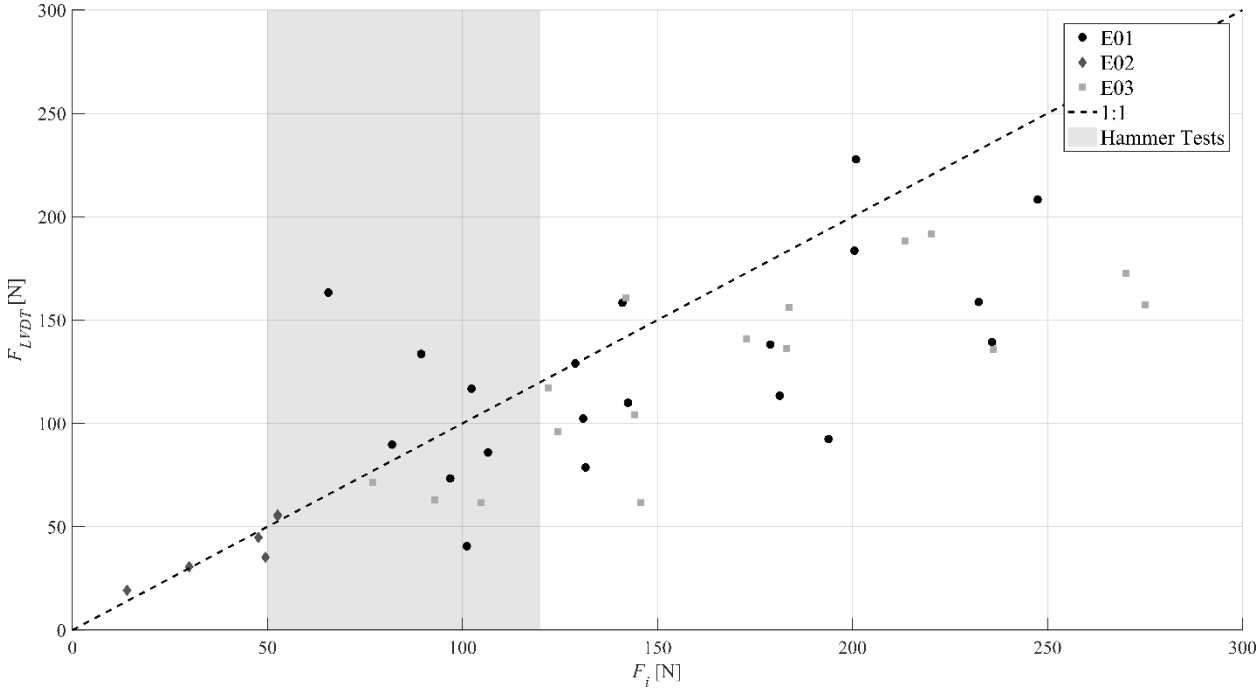

Fig. 5-18. Forces calculated from the displacement data of the LVDT (F_{LVDT}) in relation to the force from the LC (F_i) near the base of the structure. The black dashed line indicates the 1:1 ratio of the measured response from the LC to the LVDT data. The faded rectangle represents the range of force values for which the hammer test was performed.

Unlike previous studies, which assumed the structure to be rigid, a displacement of the structure was actually observed, indicating that a non-rigid impact occurred. Comparing the forces resulting from the F_i and F_{LVDT} measurements showed that the LVDT tended to slightly underestimate the forces measured by the LC. The underestimation may have been due to the structure not only displacing as a result of the impact but also deflecting. Due to the location connection of the structure to the LC above the flume bed (z = 0.16 m), an impact site below z = 0.16 m would cause a deflection in the negative y-direction, reducing thus the measured displacement. This also indicates that the two DOF model may not accurately describe the structural response for slender columns and, as such, more complex models, such as Euler's beam theory, may be necessary (Korobkin 1998).

Further discrepancies may occur due to energy dissipation within the structural connection to the LC (Shafiei et al. 2016b). The greater loads acting on the acrylic structure resulted in increased stress exerted onto the connection between the structure and the load cell. The stress potentially resulted in plastic deformations of the connection and some limited slip between the bolts and the structure.

Another cause of this discrepancy may be due to the assumption in Hooke's Law that stiffness variation with force applied is linear. The stiffness magnitude was estimated from hammer tests over a small range of force values (50 – 120 N, faded area in Fig. 5-18). As shown in Fig. 5-18, within the range used to estimate the stiffness of the structure, the LVDT reasonably estimated the force measured by the load cell. However, with an increasing F_i, the difference between F_i and F_{LVDT} also increased, suggesting that the stiffness (k_s) changed non-linearly with increasing displacement.

Considering the forces measured by the LVDT in the context of the assumption of using a single DOF system, additional discrepancies occur due to the 3D nature of the impact. As was shown in Fig. 5-16, while the hydrodynamic conditions were predominantly in the flow direction, the impact forces resulted in significant magnitudes in both the *x*- and *z*-directions. As the LC was capable of measuring the forces in 3D, the measured forces from the LC are used in the following sections.

Comparison of the experimental results with current force equations

Equations omitting impact geometry

Several equations were proposed by previous researchers to estimate the debris impact force, as outlined in Section 2.2.1. Fig. 5-19 compares the various impact models with the experimental data from this study as a function of the debris impact velocity in the flow direction. The rigid body (Eq. (2-6)) and the Haehnel and Daly (2004) model, using the single DOF system, tend to over-predict the measured impact force. The likely cause of this over-prediction is related to the assumption that structure is rigid. Physically, the motion of the structure absorbs some of the energy from the impacting debris, resulting in a decreased impact force (Haehnel and Daly 2004). While the Haehnel and Daly's (2004) model considers to a certain extent the stiffness of the structure through the use of the effective stiffness, the latter is not capturing the motion of the structure due to the assumption of the single DOF model.

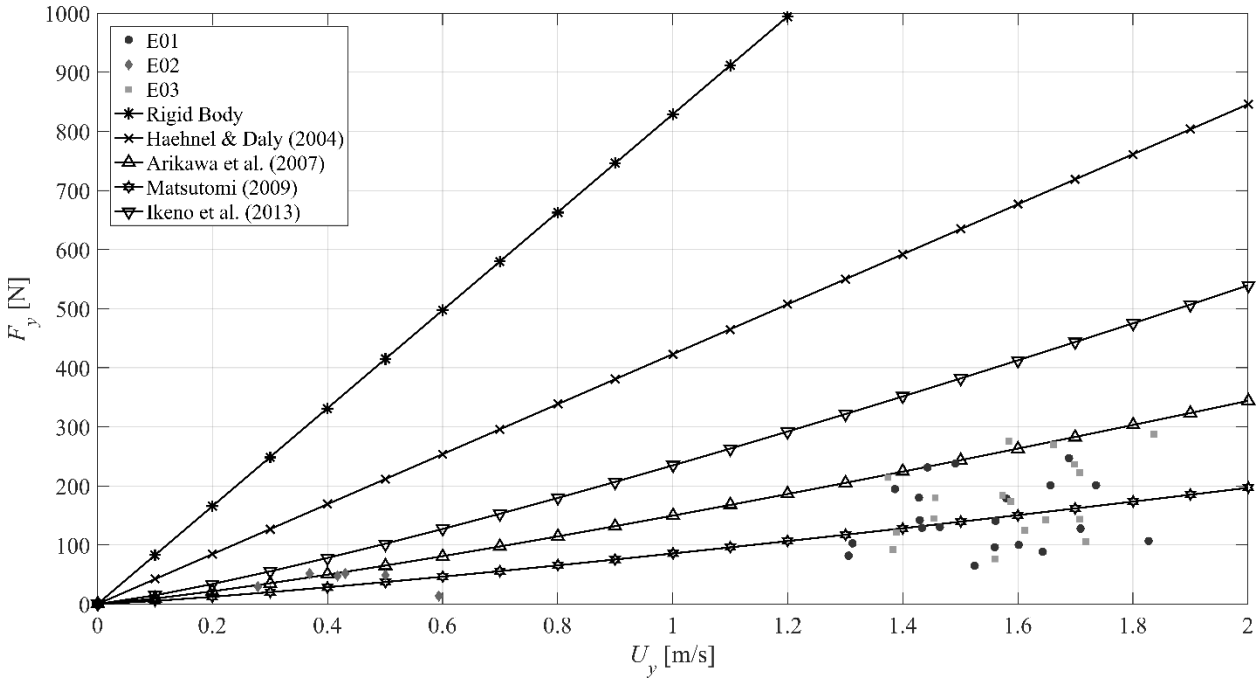

Fig. 5-19. Measured impact force (six-axis LC) and calculated impact force depending on the impact velocity.

The Hertz contact model considers the displacement of the structure through the modulus of elasticity and inertia (mass) of the structure, as in the case of Arikawa et al. (2007). Ikeno et al. (2013), alternatively, did not include the mass of the structure. In the case of the experiments conducted by the authors of the present study, the mass of the structure (30 times greater than the mass of the debris) was not large enough to neglect the influence of inertia. Matsutomi's (2009) equation reasonably accurately estimates the measured impact force, though it underestimated the maximum forces. Matsutomi's (2009) equation was empirically derived using driftwood impact and Riggs et al. (2014) noted that impact behaviour between driftwood and shipping containers can vary. Additionally, Matsutomi's (2009) equation uses the yield stress to model the material behaviour of the shipping container. Yield stress of material cannot necessarily be used to estimate the penetration depth as materials with similar yield stresses could potentially have significantly different modulus of elasticity and, therefore, deformation behaviour.

In the current study, the influence of the added mass was not considered: as such, in all equations where the added mass was considered, the coefficient was set to 1.0. As stated in the FEMA P646 (FEMA 2012), the added mass coefficient is dependent on the debris weight, impact orientation, and impact velocity. Considering the complexity and uncertainties related to the estimation of the added mass coefficient, its value was difficult to assess. Additionally, Riggs et al. (2014), in their study on shipping containers impact, noted no significant influence of the added mass on the maximum force. Shafiei et al. (2016b), in a similar study, did however record a significant difference as a result of the added mass but noted the difference from the findings was related to the density of the debris used in their study. The denser the debris, the more substantial the draft, which resulted in a larger volume of water being decelerated when the debris impacted the structure. In the study presented herein, the density (426 kg/m^3) and the draft (0.025 m) were small enough to therefore neglect the influence of the added mass. Future studies will have to further investigate the influence of the density and associated added mass.

The impact forces predicted by the current single DOF equations are based on a simplified impact model derived and validated based on experimental results with different boundary conditions and types of debris. Due to the assumption of full rigidity, these equations predict poorly the debris impact forces in these experiments. To reduce this influence, a dimensionless factor, b_s, was introduced based on the quotient of the stiffness of the structure in this study and is similar to the one used in the Haehnel and Daly (2004).

$$b_s = \frac{k_s}{k_{HD}} \tag{5-3}$$

where k_{HD} is the stiffness of the structure from Haehnel and Daly (2004) (2.46×10^7 N/m). Additionally, Eq. (2-6) has been applied in in-air full scale experiments successfully (Aghl et al. 2014, 2015). To investigate potential scale effects related to the relatively small scale experiments (1:40 length scale (N_L)) presented herein, a scale factor (N_s) was also considered. The scale factor was calculated by scaling the stiffness using the Cauchy criterion (Hughes 1993), resulting in a scale factor of $N_s = N_L^2$.

$$F_i = u\sqrt{b_s k m_d} \tag{5-4}$$

$$F_i = u\sqrt{N_s k m_d} \tag{5-5}$$

Fig. 5-20 shows a comparison of the modified equations (Eq. (5-4) – dotted line, Eq. (5-5) – dashed line) with the Haehnel and Daly (2004) equation and experimental data. Examining solely the influence of scaling from the perspective of the structural stiffness (dashed line), Eq. (5-5) does not accurately represent the measured experimental data. Currently, no comprehensive program examined scale effects

in debris impact modelling. It is therefore difficult to address exactly how scale effects would influence the model. Future research is required to address different scale experiments while achieving the Froude and Cauchy similitude and to address scale effects related to the hydrodynamic and elastic properties of the structure.

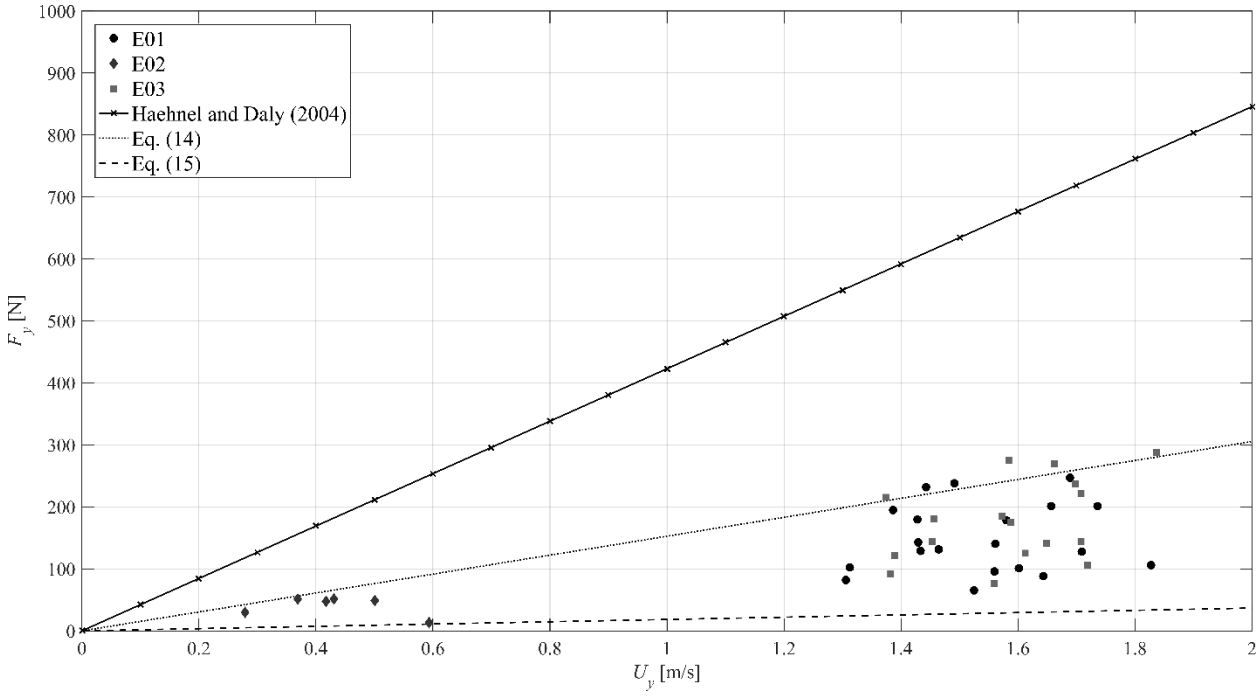

Fig. 5-20. Influence of the non-rigid impact and scale effects on the measured impact loads as a function of impact velocity.

By correcting for the different structural stiffness's in Eq. (5-4), the experimental data is better represented by the single DOF model (dotted line). As discussed earlier, the flexion of the structure results in the structure absorbing a portion of the kinetic energy from the debris impact. The correction applied in Eq. (5-4) includes this absorption. However, in its current form, it only addresses the issue from an empirical perspective. Future research is needed to assess the displacement of the structure, potentially through a full two-DOF model, simultaneously modelling the debris and structural displacement for a more accurate representation of the system.

Equations factoring in the debris impact geometry

The debris impact equation discussed in the previous section addresses a direct, central impact where the center-of-gravity of the debris acts through the impact axis. As outlined in Section 2.2.1, corrections have been developed for Eq. (2-6) to address impacts where oblique and eccentric impact occur. Fig. 5-21 shows forces from the various impact models as compared to the Haehnel and Daly (2004) maximum estimated impact force, as a function of the impact velocity. The direct, central impact would generate the maximum expected force: therefore, all the corrected values would expectedly be at or below the black line in Fig. 5-21. The measured forces are shown as gray solid markers; the marker shape indicates the experimental category. The corrections, outlined in Eq. (2-14) - (2-17) (Section 2.2.1), are shown based on the shade of the marker. The grey filled markers show the data measured from the LC, the black filled markers show the correction from Eq. (2-16), the black hollow markers show the corrections from Eq. (2-14) and (2-15), and the grey hollow markers show the corrections from Eq. (2-17). Comparing the

correction factors show relatively similar values between the different corrections, except in cases with small angles between the velocity vector and the impact axis, the Haehnel and Daly (2004) (Eq. (2-14)) force correction tends to be significantly larger than the others.

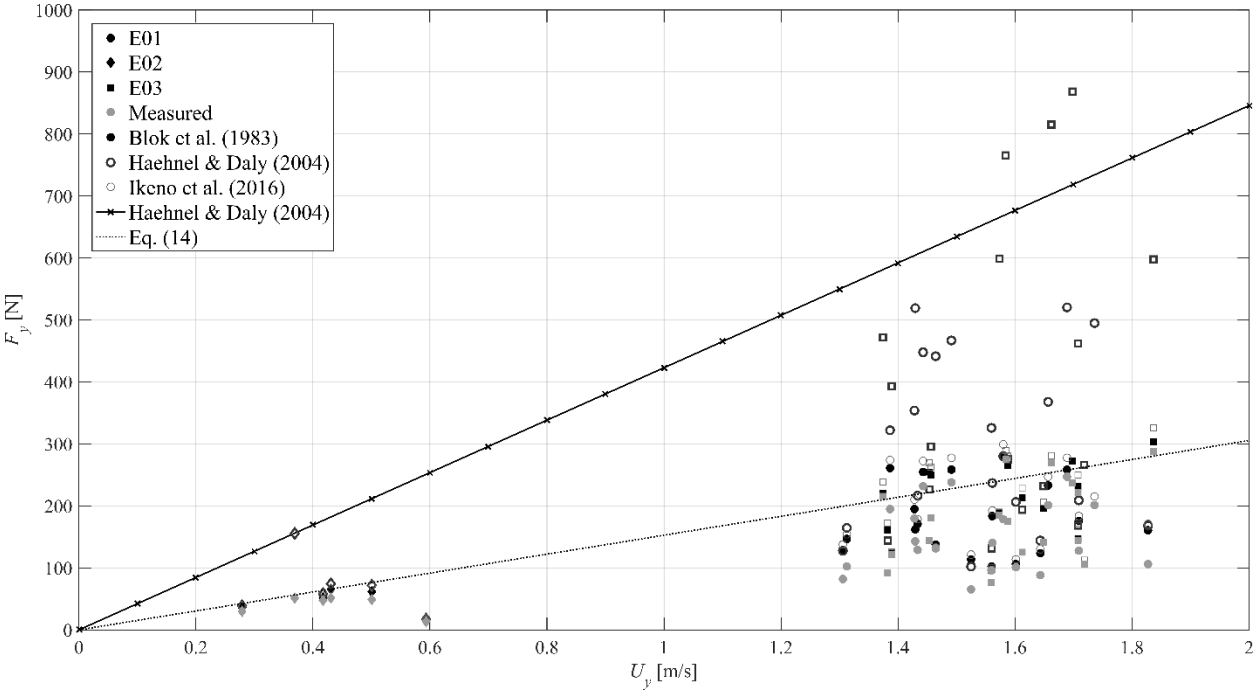

Fig. 5-21. Measured impact forces and corrected ones from Eq. (8) – (11). The experimental category is indicated by the shape of the marker. The black line is the maximum impact force estimated from Haehnel and Daly (2004).

Ikeno et al. (2016) noted that the Haehnel and Daly (2004) correction tended to over-predict the maximum measured forces, particularly when the impact angle was less than 20°. Ikeno et al. (2016) derived a similar correction, however, based on the transfer of kinetic energy to rotational energy when oblique impacts occur. Their correction factor, which varies from 0.50 to 1 as opposed to 0 to 1, results in less substantial increases in the corrected force for the lower impact angles.

As a point of comparison between the three impact geometry models, the corrected forces are compared to the maximum impact force corrected for the stiffness (Eq. (5-4), dotted line). Comparing the coefficient of determination (R^2), the values based on Ikeno et al. (2016) fit the expected impact force (R^2 = 0.282) better than those derived with the equation proposed by Blok et al. (1983) (R^2 = 0.167) and the Haehnel and Daly (2004) correction (R^2 = 0.009). Substantial variations, as can be seen by the low R^2 values, still exist within the corrected impact forces. This is likely a result of the impact model exclusively treating the impact as a 1-D phenomenon. As discussed earlier, complex 3-D debris motion occurs around the structure. However, limitations of the current analysis techniques preclude 3-D corrections of the impact forces.

5.2.4 Discussion

As can be seen from the above comparisons, substantial difficulties exist in adequately estimating the measured debris impact forces. The equations proposed for the single DOF model tends to over-predict the impact forces. The empirical equations (Eq. (2-9) – Eq. (2-13)), based on Hertzian contact mechanics, reproduce more accurately the experimental data. The Hertzian model includes terms to address

penetration into the structure, which will reduce the maximum impact force, by considering the modulus of elasticity. However, the Hertzian model assumes that the penetration is sufficiently small to limit the influence of the size of the structure (Kruggel-Emden et al. 2008). As measured by the LVDT, the displacement of the structure violates the assumptions of the Hertzian contact model and could potentially further reduce the estimated debris impact forces.

The current modifications of the impact force equations focus on impact with a rigid structure. Haehnel and Daly (2004) postulate that a structure is assumed rigid when its stiffness of the structure is less than 10 times the stiffness of the debris. Haehnel and Daly (2004) noted that the debris impact forces are reduced due to the displacement of the structure. To fully model the behavior of the system, the displacement of the structure and debris would need to be considered simultaneously. Extending the current single DOF model to a multi-DOF model may provide a more accurate representation of the measured debris impact forces. Additionally, while including the movement of the structure, the damping as a result of the surrounding water column may also need to be considered (Oumeraci et al. 1993).

Section 5.2.3 outlines the correction methods available to handle oblique and eccentric impacts of debris. While the Ikeno et al. (2016) correction model, where the force is corrected for the rotational energy lost due to the debris rotation around the impact point, improved the estimation of the impact force, it still generates substantial scatter. The primary cause of this scatter is likely a result of the complex 3-D nature of the impact. Current literature has only addressed eccentric and oblique impacts in a 2-D plane (Blok et al. 1983, Ikeno et al. 2016, Shafiei et al. 2016b) which neglects the debris impact angles within the other axes. The assessment of the 3-D orientation of the debris impact is difficult and further developments in experimental methods and sensors will likely address this problem. This type of sensor development could potentially enhance the work started by Goseberg et al. (2016a), in which miniaturized sensors were placed inside the debris to accurately record their position and orientation within a local reference system.

Furthermore, debris motion and impact have inherent stochastic properties (Matsutomi 2009, Stolle et al. 2018c) that cannot be captured using a purely deterministic model. This variability is reflected also by the relatively low R^2 coefficients calculated using the various impact models. Probabilistic models have been proposed to assess aspects of the impact problem. Matsutomi (2009) and Stolle et al. (2018c) independently developed a normal distribution function addressing the likelihood of the debris impact occurring. Ikeno et al. (2016) addressed the variability in impact force through a normal distribution regarding the 1-D impact angle. Lin and Vanmarcke (2010) developed a stochastic framework for assessing debris impact loading in extreme wind conditions, assessing the impact velocity and likelihood of occurrence. However, comprehensive experiments are needed to address, in particular, the 3-D nature of the impact to further develop such probabilistic models.

One concern that cannot be addressed within this study is related to the potential scale effects specific to small-scale testing (Heller 2011). Investigations into the scaling of the hydrodynamic and material properties related to debris impact have yet to be conducted. The added mass was neglected within this study, as the draft of the debris was not large enough to decelerate a significant volume of water. However, while the added mass has been shown to be insignificant in certain small-scale experiments (Riggs et al. 2014), it is unclear whether this would hold for test at prototype scale. While the mass and geometry of the debris model were scaled using Froude similitude, the elastic material properties were not scaled using the Cauchy criterion. While full-scale experiments (Aghl et al. 2014) of impact tests (in-air) have shown that Eq. (2-6) accurately estimated the measured impact forces, it is unclear how the distorted scale of the material properties would influence the measured forces. Moreover, in some cases, the full scale experiments and observations from field investigations (Robertson et al. 2007), showed significant plastic deformation of the debris. No significant plastic deformation was observed throughout the

experiments conducted by the authors, potentially indicating that further work is needed in addressing scale effects related to the material properties.

5.2.5 Conclusions

This study presents results of physical experiments for debris impact on a non-rigid structure in extreme hydrodynamic conditions. Tsunami-like flow conditions in the form of a dam-break waves were generated using the sudden release of a determined volume of water by means of a rapidly-opening swing gate; scaled-down shipping containers were used as debris entrained by the flow. This paper is the companion of a two-paper series: the first one provides a more detailed experimental description, evaluation of the hydrodynamics of the experiments as well as the influences of the wave-structure interaction, flow velocity and the impact geometry on debris impact. Based on the analysis of the experimentally-derived data with a non-rigid structure which were compared with results from existing equations which assume fully-rigid body impact, the following conclusions can be drawn:

- The impact force upon collision generated significant components in all three axes. The force in the flow direction dominates, however, the forces in the lateral and vertical directions exceed those predicted by Coulomb's friction law.
- The impact of debris on a non-rigid structure resulted in reduced impact forces due to the displacement of the structure.
- The Hertzian contact mechanics equations estimated more accurately the measured impact forces in a non-rigid body impact. The inclusions of the material properties of the structure in the proposed equations improved the estimation of the penetration depth of the debris
- The existing single DOF models do not consider the displacement of the structure and, therefore, tend to over-predict the measured impact loads
- An equation by Haehnel and Daly (2004), frequently used in design standards, was modified using a factor, b_s, which linearly correlates the stiffness of the structure used by Haehnel and Daly (2004) and the stiffness of the structure used in the current experiments by the authors. The modified equation significantly improved the agreement with the non-rigid experimental collision forces.

It should be noted that all the results are based on the experimental conditions described in this study and may require further research aimed at variations of hydraulic boundary conditions as well as varying debris such as cars, hydro-poles, dislodged and deteriorated building material. As shown in this study, material properties are of great importance for the debris impact. Therefore, more studies comparing debris interactions with rigid and non-rigid should be conducted. It would be useful to evaluate further experiments with structures of varying stiffness, and compare their results with those employing impacts on a fully-rigid structure to better understand the influence of material properties of both the debris and the structure.

5.2.6 Link to Section 5.3

The results of the study presented in this section showed that the rigidity of the structure had a clear influence on the measured impact forces. Due to this structural behaviour, typical debris impact models that rely on the rigid body assumption are inadequate. The following section will examine how the displacement of the structure will influence the measured impact forces and propose an analytical equation to address debris impacts on flexible structures.

5.3 Debris Impact Forces on Flexible Structures in Extreme Hydrodynamic Conditions

Preprint of an article printed in Journal of Fluids and Structures© 2019 Elsevier.
https://www.sciencedirect.com/science/article/pii/S0889974618304638

5.3.1 Objectives

Previous studies examining debris impact loading as a result of solid objects entrained within an inundating flow have focused on impacts with a rigid structure. The 2DOF model, presented in Section 5.3.2, considers the influence of the structural stiffness on the impact loading. This represents an important extension of the commonly applied SDOF model, as it (i) allows to interpret experimental results where the stiffness ratio of debris and structure differ considerably, and (ii) provides means to design structures against impacts where the rigidity assumption no longer holds. Hence, the objectives of the current study are:

1) To propose and investigate a novel 2DOF model governing debris impact loading that includes displacement of the impacting bodies and, additionally, includes the effect of flexibility of the impacted structure.
2) To evaluate, based on novel experimental data, the accuracy of the 2DOF model in estimating the debris impact loading on the structure.
3) To compare and assess the 2DOF model to the effective stiffness model, presented by Haehnel and Daly (2004), and to the rigid body model.
4) To investigate the influence of the mass and stiffness ratios on the maximum debris impact loading.

The current study investigates the influence of non-rigid structures on debris impact loading. For this purpose, a set of physical experiments was performed at the University of Ottawa, Canada, examining the impact of a single type of debris on a vertical structure. To supplement the experiments presented here, available data from Haehnel and Daly (2004) was used to further investigate the influence of the mass and stiffness ratio.

5.3.2 Two Degree-of-Freedom Impact Model

The debris models outlined above focus on the debris impacting a rigid structure, that is, an applied force will not result in flexing or bending of the structure under consideration. This assumption represents a conservative estimation of the impact force as the structure is not considered to move in response to the impact (Haehnel and Daly 2002). To address the issue of debris impact on a flexible structure, a two degree-of-freedom (2DOF) model with a two body spring-damper system (Fig. 5-22) is required.

Based on Fig. 5-22 and using d'Alembert's principle (Malhotra and Subramanian 1994), the following system of equations can be derived to mathematically describe the problem:

$$\begin{bmatrix} m_s & 0 \\ 0 & m_d \end{bmatrix} \begin{bmatrix} \ddot{x}_s \\ \ddot{x}_d \end{bmatrix} = \begin{bmatrix} k_s + k_d & -k_d \\ -k_d & k_d \end{bmatrix} \begin{bmatrix} x_s \\ x_d \end{bmatrix} + \begin{bmatrix} c_s + c_d & -c_d \\ -c_d & c_d \end{bmatrix} \begin{bmatrix} \dot{x}_s \\ \dot{x}_d \end{bmatrix} \tag{5-6}$$

where m_s is the mass of the structure, x_s is the displacement of the structure, x_d is the displacement of the debris, c_s is the damping coefficient of the structure, and c_d is the damping coefficient of the debris. As the impact occurs over a short duration, damping can be neglected (Haehnel and Daly 2004). The second-order differential equation can then be solved as a system of ordinary differential equations with the initial conditions of $x_s(0) = 0$, $x_d(0) = 0$, $\dot{x}_s(0) = 0$, and $\dot{x}_d(0) = u$.

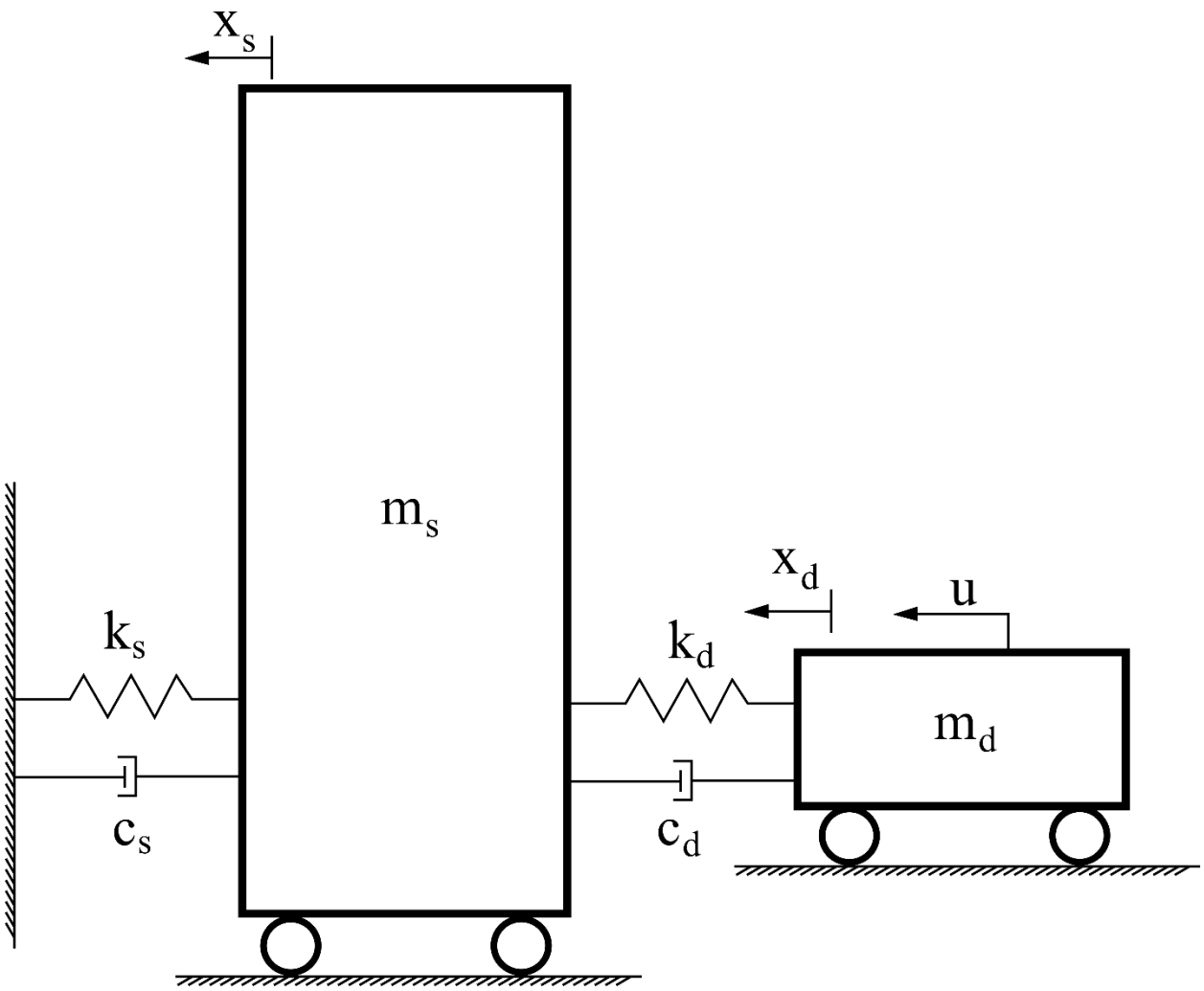

Fig. 5-22. Conceptual two degree-of-freedom (2DOF) model for debris impacts on flexible structures.

A more detailed derivation of the solution can be found in Appendix C of this thesis. The final solution takes the form:

$$F_i = \left|\max\left(k\left((b+1)x_s - x_d\right)\right)\right|_0^{t_i} \tag{5-7}$$

$$\begin{bmatrix} x_s \\ x_d \end{bmatrix} = u\left(C\begin{bmatrix} 1-A \\ 1 \end{bmatrix}\sin(\omega_1 t) + D\begin{bmatrix} 1-B \\ 1 \end{bmatrix}\sin(\omega_2 t)\right) \tag{5-8}$$

where k is the effective stiffness (determined from Eq. (2-7)), ω represents the natural modes of the system, t_i is the impact duraction (defined by the separation of the structure and the debris) and t is the time since impact. As Eq. (5-8) results in an oscillating system, the impact force can be determined by using the maximum value of the first oscillation of the displacements between the debris and the structure multiplied by the effective stiffness of the impact. Constants A through D are determined by the structural and debris properties, defined by the ratios of masses ($a = m_s/m_d$) and stiffness's ($b = k_s/k_d$) involved:

$$A = \frac{(a+b+1) + \sqrt{(a+b+1)^2 - 4ab}}{2a} \tag{5-9}$$

$$B = \frac{(a+b+1) - \sqrt{(a+b+1)^2 - 4ab}}{2a} \tag{5-10}$$

$$C = \frac{1-B}{A-1}\frac{1}{\left(\frac{1-B}{A-1}+1\right)\omega_1} \tag{5-11}$$

$$D = \frac{1}{\left(\frac{1-B}{A-1}+1\right)\omega_2} \tag{5-12}$$

The natural modes of the system are defined by:

$$\omega_1 = \sqrt{A\frac{k}{m}} \tag{5-13}$$

$$\omega_2 = \sqrt{B\frac{k}{m}} \tag{5-14}$$

As it can be observed from Eq. (5-13) and (5-14), the natural frequency of the system is governed by the ratios of the material properties (mass and stiffness). Haehnel and Daly (2004) noted that for cases where the mass and stiffness of the structure was significantly larger than those of the debris, the structure essentially acts as a rigid body. It would then be expected that in case when a shipping vessel impacted a residential structure, the structural response would be sufficiently different than if a shipping container impacted a massive, high-rise structure.

The impact velocity appears outside of these terms, indicating that for a given system the maximum displacement, the impact force will increase linearly with velocity. Fig. 5-23 shows a comparison between the rigid body model (thick solid line), the effective stiffness model (dashed line), and the 2DOF model (solid line). As the rigid body model does not consider the structural stiffness, the single line represents the theoretical maximum impact force. Comparing the effective stiffness and 2DOF model shows that the effective stiffness model estimates a greater impact force for the smaller stiffness ratios. As the latter increases, results for both models converge towards the rigid body model.

Flexibles structures under debris loading have previously been examined. however, these have generally been performed examining debris flows, where debris are considered as non-Newtonian fluids (Shan and Zhao 2014, Dai et al. 2017). Leonardi et al. (2016) extended research into debris flows by considering flexible barriers with a non-Newtonian free surface solver for the debris flow and a Finite Element Method (FEM) for the flexible barrier. Liang et al. (2017), in an examination of the solitary wave impact on movable seawalls using SPH, used a similar technique to that used in the 2DOF model where the seawall was modelled as a spring-mass system. While these techniques provide insight into the transient loading related to debris impact, the coupling between hydraulic and solid models can be computationally expensive and difficult to calibrate. The 2DOF model may aid in providing a method of estimating the maximum loading for the validation of future numerical models.

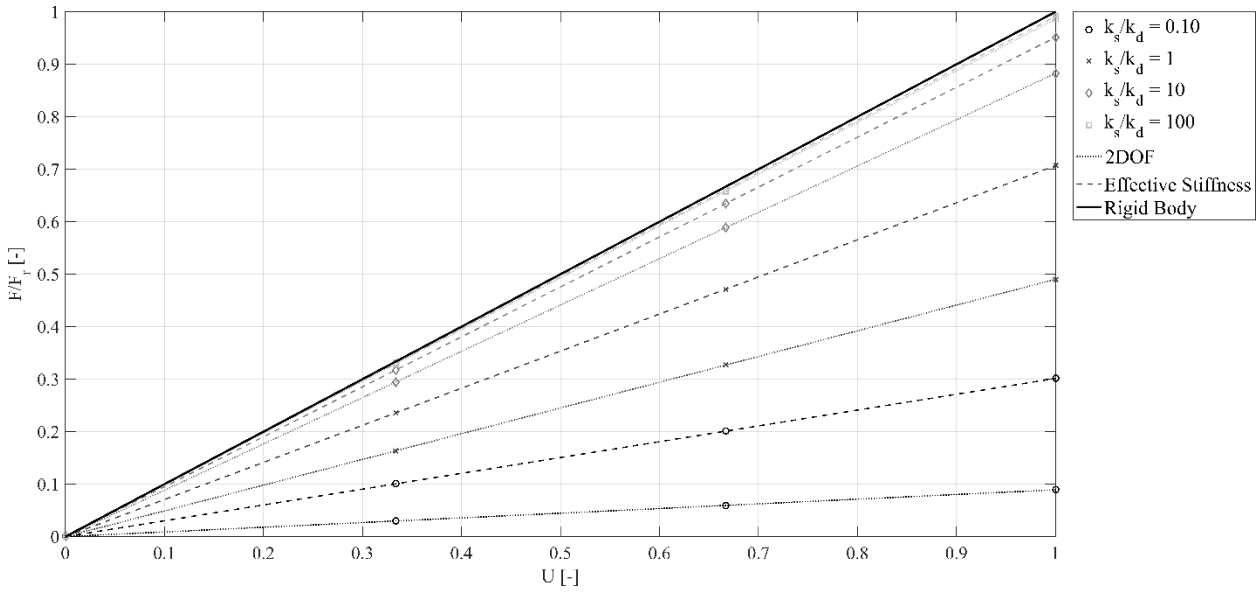

Fig. 5-23. Comparison of the rigid body model (dotted line), the effective stiffness model (dashed line), and the 2DOF model (solid line) as a function of the debris velocity. The figure is normalized by an arbitrary impact velocity (3 m/s) and the maximum force at the impact velocity. The stiffness ratio (between structure and debris) is indicated by the marker type.

5.3.3 Experimental Setup

Experimental Facility

The experiments were performed in the Hydraulics Laboratory of the Department of Civil Engineering, University of Ottawa, Canada. The facility is a 30 m long, 1.5 m wide, and 0.70 m deep (Fig. 5-24) dam-break flume (DBF). The upstream reservoir was 21.55 m long and the water was impounded behind a rapidly swinging gate, installed on top of a 0.15 m false floor. The false floor was covered with a fixed layer of 0.001 m sand grains. The Darcy-Weisbach friction factor (*f*) was determined by fitting the Chanson (2006) diffusive wave model to the instantaneous wave profile in Stolle et al. (2018b), resulting in a value of $f = 0.0293 \pm 0.0023$. The swinging gate was manually opened to generate a dam-break wave; a counter weight was placed on the top of the gate to aid in the rapid opening of the gate.

An in-depth analysis of the hydraulic characteristics of the University of Ottawa dam break flume, Stolle et al. (2018b) has shown that the maximum gate opening time ($T_o = t_o\sqrt{g/h_0}$) of 1.46, is in the range of the suggested values proposed by Lauber and Hager (1998) (T_o = 1.41). The variation in the gate opening time resulted in a mean difference in the wave arrival time of +/- 0.9% at the debris site (y = 3.20 m). Furthermore, Häfen et al. (2018) determined, through numerical modelling, that achieving the Lauber-Hager criterion resulted in minimal errors (~ 1%) in the wave profile when compared to an instantaneously released water column for swinging gates.

The spatial origin of the experiment (0,0,0) was set at the center of the flume, at the upstream edge of gate on top of the false floor. The *y*-axis was chosen positive in the flow direction, using a right-hand coordinate system, the positive *x*-direction was to the right while the positive *z*-direction was up.

The debris was placed on the false floor with the centroid of the debris placed center-flume (x = 0 m) at y = 3.20 m. The model of a vertical structure, 0.20 m long, 0.20 m wide, and 0.80 m high was placed

center-flume with the upstream face at y = 7.03 m. The distance between the centroid of the debris and the upstream face of the structure was 3.43 m.

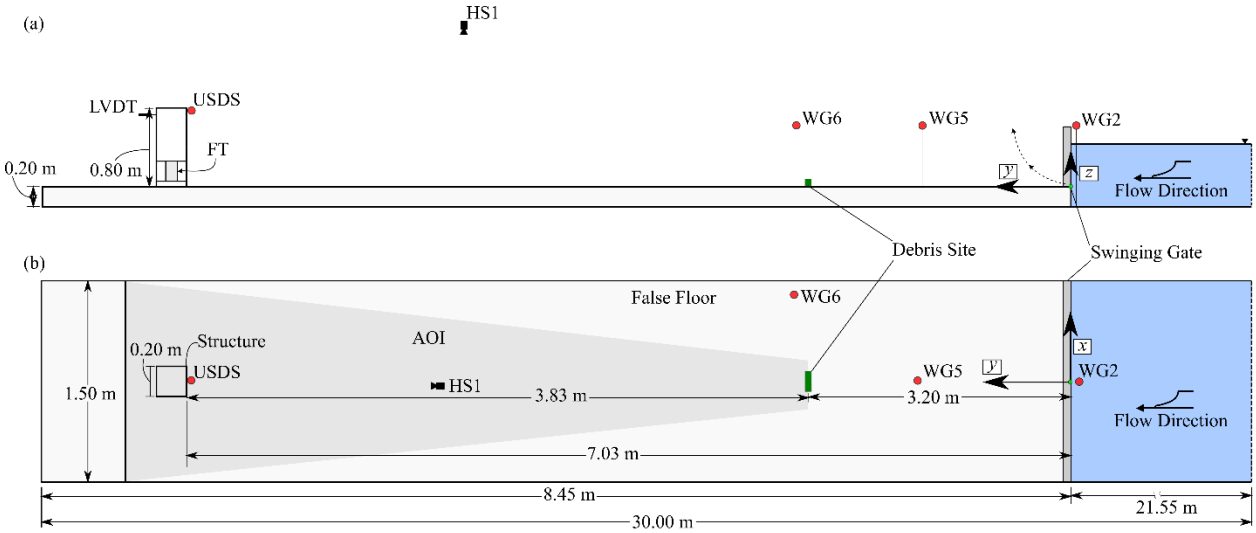

Fig. 5-24. Dam-break Flume (DBF) at the University of Ottawa, Canada: (a) side view and (b) top view. The initial debris site is indicated with a green rectangle. The wave gauge (WG) positions are indicated using red circles.

Instrumentation

The instrumentation used in the experiments are detailed in Fig. 5-24. The time-history of the water depth was measured using capacitance-type wave gauges (WG) (Akamina Technologies WG-50, sampling rate: 1200 Hz, accuracy (percentage of maximum range): +/- 0.15%). Before installation, the WG were calibrated with a calibration coefficient greater than 0.99 for each probe. Wave gauge WG2 was placed within the reservoir at y = -0.10 m (upstream of the gate). The reference time for each experiment was determined as the time that the water depth recorded at WG2 dropped by 0.005 m, signaling thus the opening of the gate. An ultra-sonic wave gauge (USDS) (MassaSonic M-5000, 100 Hz, +/- 0.25%) was placed at the front face of the structure at a height of 0.80 m above the false floor.

The forces of the structure were measure using a 6-axis force-torque transducer (FT) (Interface 6A68E, 19 200 Hz). The base of the FT was attached to the false floor using 4 pieces of threaded rod bolted into the concrete flume floor; these rods then connected through a metal plate, fastened by adjustable nuts. The top of the FT was secured to the structure using two brackets, in the form of angled steel plates. The FT's cable was guided inside the vertical structure such that no biasing forces would occur at any time. A 0.015 m gap was left between the structure and the false floor to allow for the free-motion of the structure. The structure was built from extruded Poly (methyl methacrylate) (acrylic) (modulus of elasticity (E) = 2.50 GPA, 95% Confidence Interval [1.70 3.30]). The structure was hollow with 0.005 m wall thickness. A Linear Variable Differential Transformer (LVDT) (RDPE LSC Transducers DCV025A, 19 200 Hz, +/- 0.1 – 0.5%) was placed on the downstream face of the structure at a height of z = 0.78 m to monitor the head deflection of the structure.

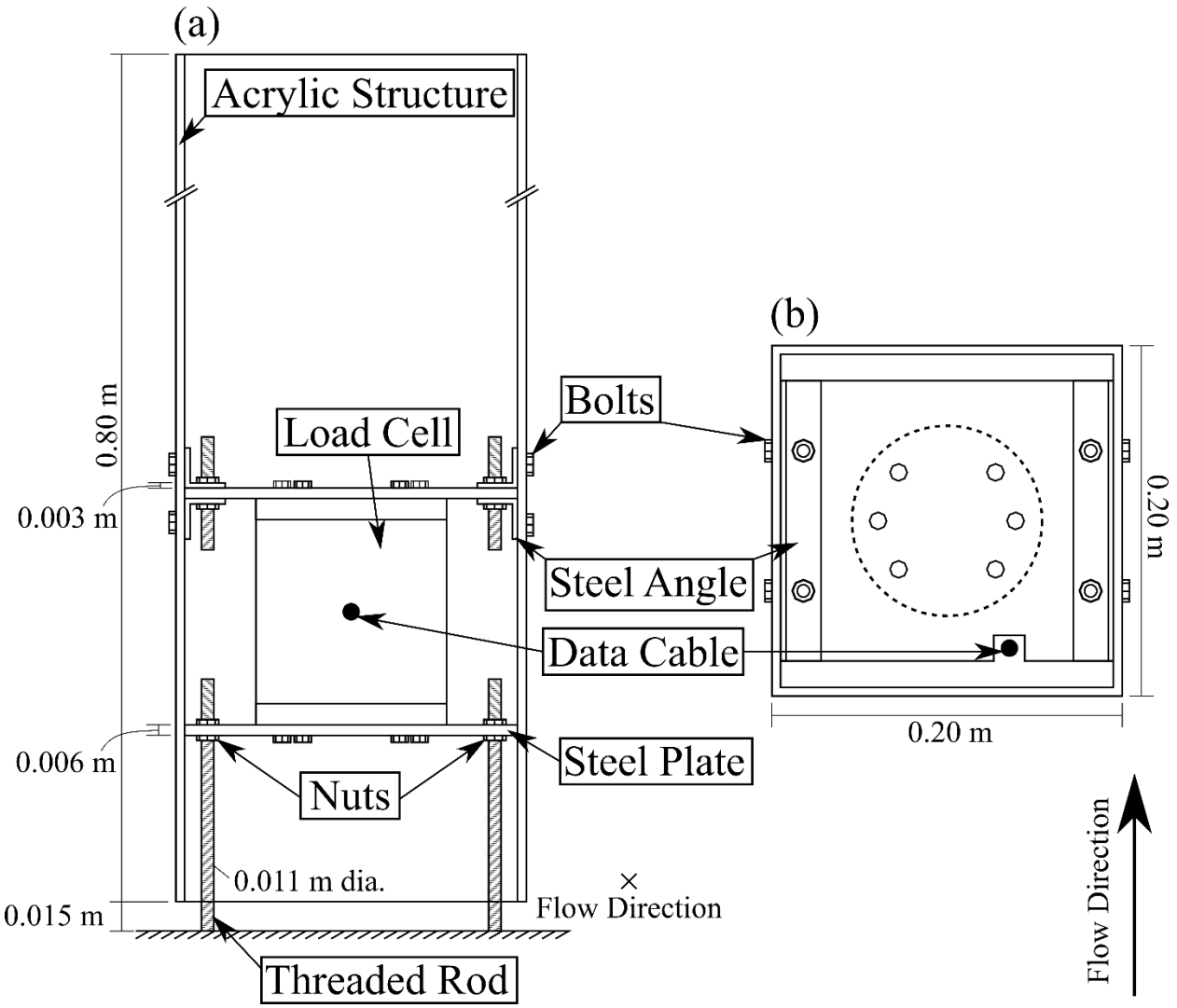

Fig. 5-25. Load cell configuration and connection to the acrylic structure (position shown in Figure 1). (a) Front view; (b) Top view.

Using the latter stage of the flow, where the water depth had essentially reached steady-state conditions and no debris was impacting the structure any longer, a linear relationship was developed for the force measured by the load cell and the deflection from the LVDT. Based on this relationship, the stiffness of the structure was estimated to be approximately $k_s = 4.685 \times 10^5$ ($R^2 = 0.51$, 95% Confidence Interval [4.653×10^5 4.701×10^5]). The relationship between the force and the displacement was assumed to be linear. However, due to friction and slip within the connections between the structure and the load cell, as well as due to the irregularities in the material, some non-linearity's occurs and these result in a lower correlation. As the stiffness of the structure as a whole was significantly less than that of the acrylic, it was assumed there was limited flexure of the structure's face.

The HS camera recorded the experiments with a 70 Hz sampling rate with greyscale resolution. The HS camera was synchronized with the data acquisition system by visually inspecting the images to determine the time that the bore front required to reach the structure and by comparing it to the force signal from the FT. The estimated synchronization accuracy was +/- 0.036 s.

Model Debris

The debris model consisted of downscaled 20-foot shipping containers (ISO668/688) with a geometric scale of 1 in 40. The debris and hydrodynamic properties were scaled considering Froude model scaling. The down-scaled shipping containers were manufactured from positively buoyant polyethylene (PE-HMW, 920 kg/m³). Each down-scaled shipping container had overall dimensions of 0.06 x 0.06 x 0.15 m with an approximate draft of 0.025 m. The thickness of the outer shell of the containers was 0.005 m, with space inside to place additional sensors. The inner space was accessible as the container was made of two pieces, sealed with a custom-made rubber seal, and connected tightly with plastic screws (Goseberg et al. 2016a, 2016b, Nistor et al. 2016). Petroleum jelly was placed on the rubber seals to further prevent water intrusion. The weight of the container, from three weightings, was determined to be 0.234 kg.

The axial stiffness of the debris is critical in evaluating the impact (Aghl et al. 2014). To determine the axial stiffness (k_d) of the model shipping containers, a series of compressive stress-strain test was performed using an Instron ® Model 4482 hydraulic press. The axial stiffness was tested for three different containers to the compressive yield point of the respective container. A different container was used in the hydraulic experiments as all three containers plastically deformed and could no longer be used for the test sequences. From these tests, the axial modulus of elasticity (E) could be determined from the slope of the elastic region (Currey 1988). The average E of the containers was found to be 1.50 GPa compared to the expected E of 1.30 GPa (Gottstein 2013, Aghl et al. 2015) from product data sheets and literature. For the determination of the axial stiffness, the equation presented in Aghl et al. (2014) was used:

$$k_d = \frac{EA}{L} \tag{5-15}$$

where A is the cross-sectional area of the debris and L is the axial length of the impacting debris. The debris had an axial length of 0.15 m and, therefore, a stiffness of 3.04×10^6 N/m.

Experimental Protocol

The experiments performed in the DBF at the University of Ottawa, Canada, examined three different experimental configurations - each configuration was repeated at least 10 times (Table 5-13). The experiments varied the impoundment depth in the reservoir and the orientation of the long-axis of the debris with respect to the horizontal place during initial placement. The impoundment depth was varied between 0.20 m and 0.40 m. The orientation of the long-axis of the debris was placed either perpendicular (0^o) and parallel (90^o) to the flow direction during specific tests. In the following sections, only the cases where the debris impacted the structure are reported. Due to the interaction between the debris and the bed, the lateral (x) spreading of the debris increased with decreasing impoundment depth (Stolle et al. 2018c). This resulted in fewer impacts for the h_0 = 0.20 m cases (6) compared to the cases when the h_0 = 0.40 m impoundment depth was used (36).

For each experiment, the centroid of the debris was placed at y = 3.20 m. To ensure repeatability between the experimental repetitions, the exact placement of the debris was facilitated by position markers drawn on the concrete floor. The accuracy of the initial placement is estimated to be +/- 2 mm in both the x- and z-axis. Subsequently, the reservoir was filled to the prescribed impoundment depth. Long wave components generated during the filling process in the reservoir dissipated over a short period of time prior to the initiation of each test; this ensured a repeatable hydrodynamic boundary condition. The dam-break gate was then opened manually to generate the dam-break wave. Before the beginning of each experiment, the excess water was thoroughly removed from the surface of the false floor.

Table 5-13. Experimental Protocol

Experimental Category	Impoundment Depth [m]	Debris Orientation [°]	Experimental ID [#]	Repetitions [#]
E01	0.40	0	254-263, 274-283	20
E02	0.20	0	294-303	10
E03	0.40	90	264-273, 284-293	20

Data Analysis

Force Measurements

The data signal was filtered to remove instrument noise while maintaining the phase and magnitude of the peaks using the Ensemble Empirical Mode Decompositions (EEMD) method (Huang et al. 1998). EEMD is a method developed for analysing non-linear and non-stationary data sets. This method decomposes the data set into zero-crossing intrinsic mode functions within the characteristic time scale. As an advantage, the EEMD method reliably filters any given time-history retrieved from a sensor while avoiding phase shifts associated with filtering in the frequency domain (Rilling et al. 2003). The development of the filtered signal takes the intrinsic mode functions related to the impact while removing the modes associated with instrument noise and hydrodynamic loads. In this study, as the main variable of concern was the impact force, which needed to be extracted from the time-varying total forces which also includes the hydrodynamic force. To visualize the extraction of the impact force, Fig. 5-26a shows the raw data signal of the forces in the flow direction (y-direction). Fig. 5-26a shows determination of the impact loads from the raw data using the EEMD filter by the removal of the modes associated with the hydrodynamic loading.

The filtered force shown in Fig. 5-26a represents the structural response to the debris impact force. The structural response is the measured signal from the load cell as a result of the displacement of the structure. As the impact force occurs over a short interval (Nouri et al. 2010), compared to the natural oscillation period of the structure, the structural response does not have the opportunity to reach an equilibrium with the load. The Duhamel integral (Clough and Penzien 2003) was used to estimate the debris impact force, similar to the work of Wienke and Oumeraci (2005) who estimated the wave impact loads on columns. The Duhamel integral (Clough and Penzien 2003) calculates the structural response by integrating the differential responses from an estimated loading history:

$$R(t) = \frac{k}{m_s \omega_d} \int_0^t p(\tau) \sin \omega_d (t-\tau) e^{-\xi \omega_d (t-\tau)} d\tau \qquad (5\text{-}16)$$

where ω_d is the damped frequency of the structural oscillation, $p(\tau)$ is impact load applied over a period t, τ is the time elapsed since impact, and ξ is the damping coefficient. The damped frequency of structural oscillation was determined through impact hammer tests. Ten repetitions were performed under various loads resulting in a measured natural frequency of the structure of 70 (± 2.2) Hz. The damping coefficient was estimated by iteratively fitting the structural response to the known impact hammer forces with no water present, resulting in a value of 0.045. The damping coefficient (ξ) is generally difficult to estimate (Moser et al. 2005), therefore a constant value was assumed. Oumeraci et al. (1993) showed in a study on caisson breakwaters that the water depth around the structure can influence the damping of the structural response. As the current experiments were performed in transient flow conditions, an accurate estimation of the varying damping coefficient was not plausible as it changed with the fluctuations observed in the water depth. Using an incremental summation of Eq. (5-16) over t, the structural response to a given impact load can be then estimated (Fig. 5-26b).

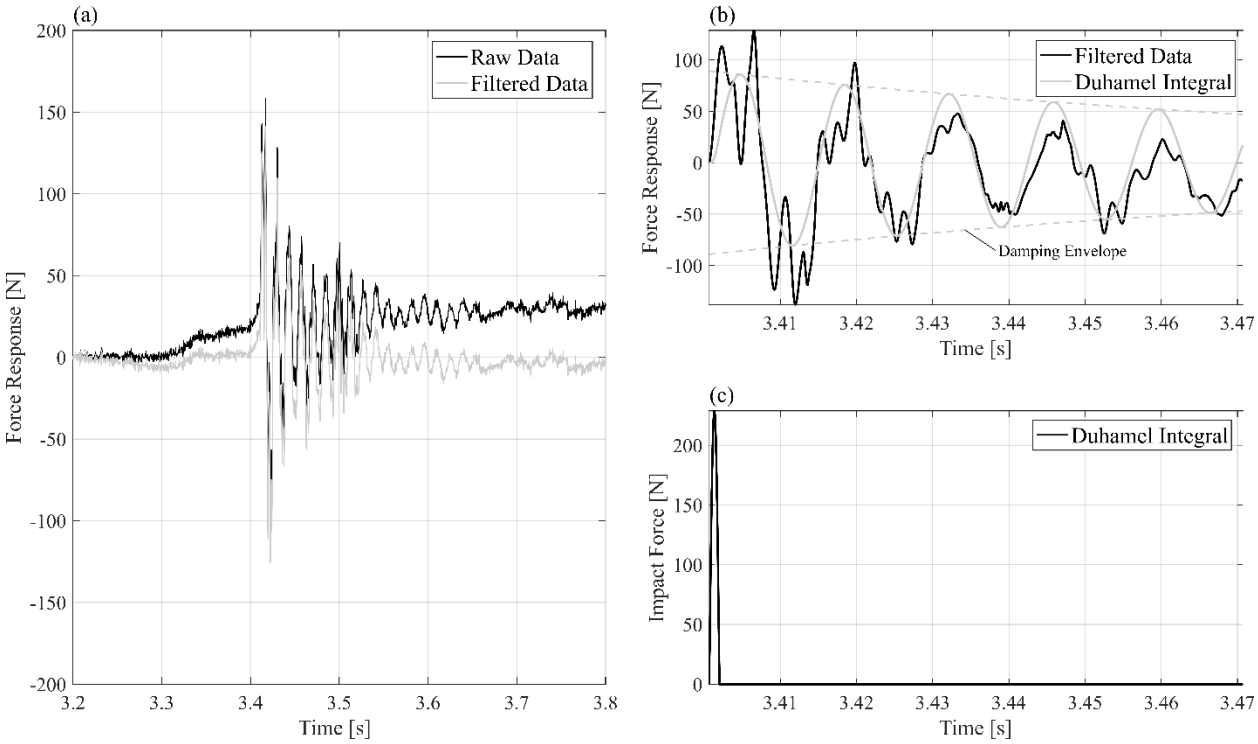

Fig. 5-26. Determination of the impact load. Panel (a) shows the use of the EEMD filter to remove the hydrodynamic loading. Panel (b) shows the estimation of the force response using the Duhamel integral and (c) shows the estimated impact time history based on the Duhamel integral.

By iteratively estimating the impact force and duration (t_d), the structural response can be fit to the experimental data (Navaratnam et al. 2013). The normalized root mean squared error (RMSE) was used as the best fit indicator between the measured force response (f_R)and the estimated response by the Duhamel integral (f_{DI}):

$$RMSE = \frac{\sqrt{\frac{\sum_{i=1}^{n}(f_R - f_{DI})^2 w(i)}{n}}}{F_R} \tag{5-17}$$

where $w(i)$ is a weighting function, and F_R is the maximum value from the measured response. The normalized RMSE was weighted, using a linearly declining function between 1 and 0 for 5 times period of structural oscillation (~0.07 s), to emphasize the error in the initial phase of the impact response. This was due to difficulties in assessing the damping of the structure.

The Duhamel integral method also required an assumption regarding the shape of the impact time history. The ASCE 7 Chapter 6 (2016a) assumed a step function for the impact time history. However, Aghl et al. (2014) performed full-scale in-air impact tests with prototype shipping containers and found that the shape of the impact time history was half-sine. Solving for the half-sine impact time history would result in a larger impact force than would be needed for a step function due to the slower rise time to the peak force. To ensure that forces were not underestimated, the half-sine impact history was assumed for the remainder of this study (Fig. 5-26c).

The experimental force responses were fitted iteratively by varying the impact force and duration using a resolution of 1 N and 0.0001s, respectively. The force and duration with the smallest normalized RMSE was selected. The mean RMSE for the experiments was 0.0748 (standard deviation (σ) = 0.0182). The

ratio of maximum force response to estimated impact force (F_{DI}) ranged from 0.534 – 1.804, with a mean value of 1.070.

Debris Tracking

The debris were manually tracked in order to determine the impact variables, such as obliqueness and eccentricity of the debris at impact. Due to splash-up around the vertical structure, automatic tracking algorithms were not sufficiently accurate to extract consistent results of the impact variable. Therefore, for each experiment, the impact condition was determined using a manual tracking method. The method required the image frame in which the impact occurred. Due to the relatively short duration of the debris impact event (~ 5×10^{-4} s), the last recorded image before the impact occurred was selected. Therefore, the maximum error between the impact event and the selected image was of 0.014 s. It was assumed that there would be minimal change in the debris trajectory and velocity within that period.

For this image frame, as well as the previous four frames, the top four corners of the container were selected. The positions extracted from the five frames where the debris was visible, as well as the impact velocity, velocity vector, debris orientation, and impact point could be determined. The impact velocity was determined based on the trajectory of the centroid of the debris. The distance over which the debris moved was determined based on the displacement of the debris between two image frames. The impact point was defined as the closest point of the debris to the structure in the flow (y) direction. For each experiment, three independent repetitions were performed on the same image frames to diminish inaccuracies from the manual selection of the corners. Based on the variation in the results from the repetitions, the impact velocity was shown to have a mean error of 0.10 m/s and the orientation of the debris axis had an mean error of 2^{o}.

5.3.4 **Results**

Hydrodynamics

The hydrodynamic forcing factor that led to the entrained piece of debris impacting the vertical structure was a dam-break wave. Two impoundment depths were considered for these experiments: 0.20 m and 0.40 m. Fig. 5-27 shows the water elevation profiles from the four WGs installed in each of the experiments (WG2 (a), WG5 (b), WG6 (c), and USDS(d)).

As can be observed in Fig. 5-27, the dam-break wave was repeatable between the various tests. For the different impoundment depths, the time-averaged standard deviation for WG6 was 0.0055 m and 0.0019 m for the 0.40 and 0.20 m impoundment depths, respectively. The Chanson (2006) solution for a dam-break wave with an infinite reservoir is displayed in Fig. 5-27 as a dashed line using the Darcy-Weisbach friction factor from Stolle et al. (2018b) (f = 0.0293). The arrival time of the wave was slightly later than the predicted one by Chanson, potentially due to the thin layer of water left between experimental trials causing excess flow resistance (Chanson 2006, St-Germain et al. 2013).

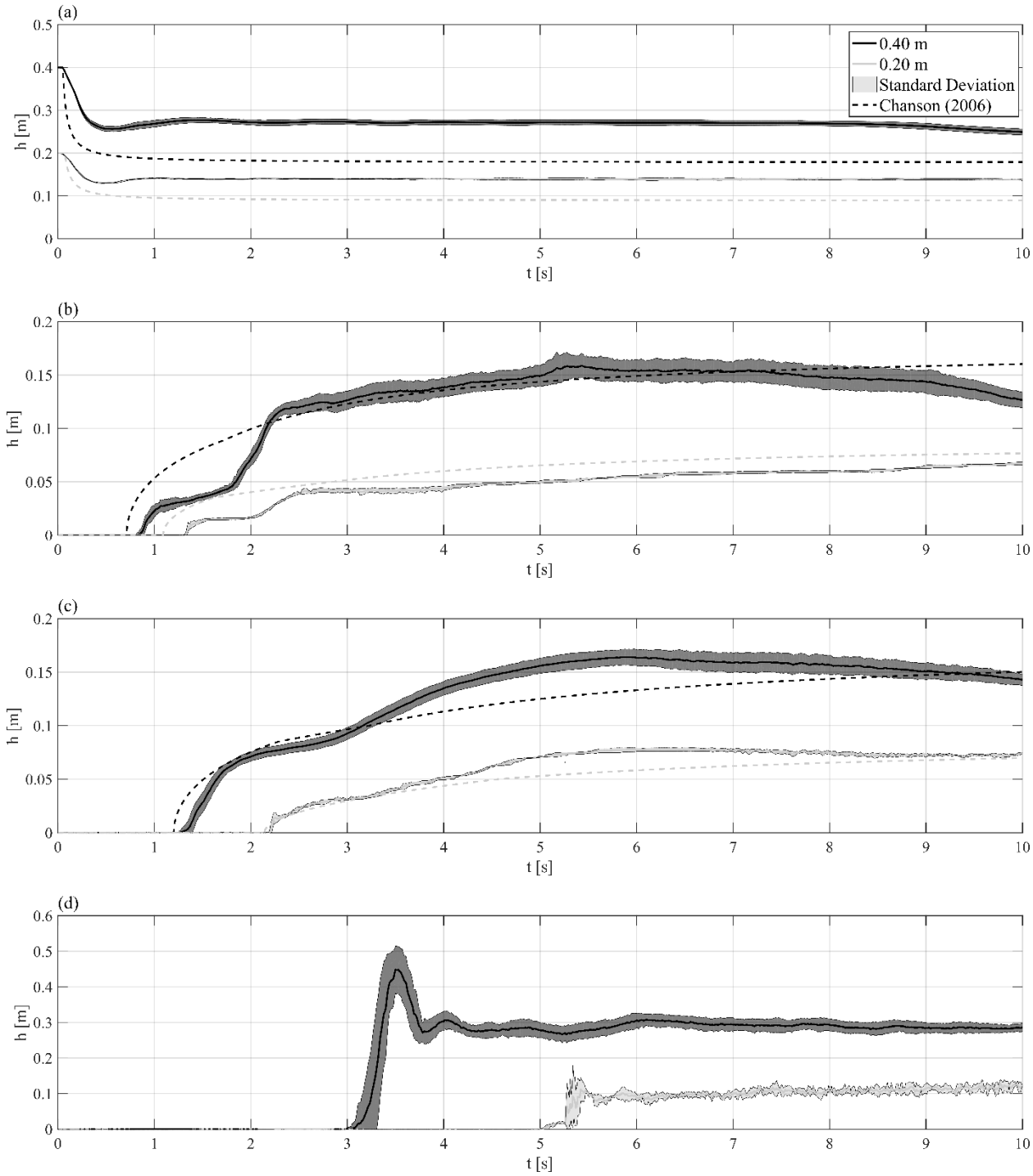

Fig. 5-27. Recorded water surface elevations (h) as a function of time (t) for WG. (a) WG1 (y = -0.10 m); (b) WG5 (y = 2.40 m); (c) WG6 (y = 3.20 m); and (d) USDS (y = 7.03 m). The analytical solution of Chanson (2006) is shown as a dashed line corresponding to the shade of the initial impoundment depth.

The modelling of inundating tsunami waves has always been challenging in a laboratory environment. Solitary waves have commonly been used to evaluate hydrodynamic loads (Arnason et al. 2009, Arikawa 2011, Chinnarasri et al. 2013, Seiffert et al. 2014), as well as debris transport (Yao et al. 2014, Nistor et al. 2016). However, Madsen et al. (2008) indicated the discrepancy in the time scales between solitary

waves and field investigations of tsunami events. Recently, the application of the dam-break wave has become a viable alternative to tsunami engineering experimentation, as Chanson (2006) showed the analogy between the dam-break solution and a tsunami surge on a dry coastal plain. Nouri et al. (2010) and Al-Faesly et al. (2012) applied the dam-break solution to evaluate hydrodynamic tsunami loads on structures. Ikeno et al. (2016) and Shafiei et al. (2016b) used a dam-break to investigate debris impact loads on structures. Imamura et al. (2008) and Matsutomi et al. (2008) examined the transport of debris in a dam-break wave. The dam-break wave here had a maximum water depth of 0.18 m, corresponding to a full-scale inundation height of 7.2 m. The maximum bore front velocity, calculated using the arrival times between WG5 and WG6, was 2.16 m/s, corresponding to 13.66 m/s at prototype scale. Fritz et al. (2012) showed, using PIV analysis of flow during the 2011 Japan Tsunami in Kesennuma Bay, a similar range of flow conditions with water depths ranging from 0.5 – 10 m and flow velocities between 3 and 11 m/s.

It is critical for tsunami modelling that a flow used in experimental research is significantly longer than that associated with solitary wave-induced flows. The dam-break wave can have these longer flow durations and these dependent on the reservoir length (Lauber and Hager 1998). Based on the dam-break experiments of Lauber and Hager (1998), the duration of the flow was defined as the time required for the negative wave of the dam-break to propagate to the end of the reservoir and back to the location of interest (in this case the structure). In these experiments, the duration was 20.34 s and 28.09 s for the 0.40 m and 0.20 m impoundment depths, respectively. As the debris impact for each experiments occurred within 5 s for all the cases, the duration of the flow was well within the flow unaffected by the reservoir length.

Debris Impact

Fig. 5-28 shows the impact forces as a function of the impact velocity. The impact forces, calculated from the Duhamel integral described above, are displayed as filled circular markers. Within each experiment, the impact forces were corrected based on the coefficient presented in Eq. (2-14) - (2-17). The impact forces are compared to the three models presented in Section 2.2.1. The “Rigid Body” model (solid line) refers to Eq. (2-6) where the stiffness is solely the stiffness of the debris. The “Effective Stiffness” model (dotted line) also uses Eq. (2-6), however, the effective stiffness (Eq. (2-7)) is used in place of the debris stiffness. The “2DOF” model (dashed line, Eq. (5-7)) considers the entire system of the structure as a point mass and spring system shown in Fig. 5-22.

Comparing the three models, the rigid body model overestimated the impact forces observed in the experiments, as the model assumed the structure would not be displaced. However, as measured by the LVDT, the structure was displaced between 0.5 – 3.2 mm as a result of the debris impact. The movement of the structure absorbed energy from the impacting the debris, reducing the maximum impact force. Therefore, the rigid body model was demonstratively not an accurate estimation of the debris impact force in these experiments. The effective stiffness model also overpredicted the experimental results. Haehnel and Daly (2004) stated that the effective stiffness model represented the outer envelope of the observed impact experiments in their experiments. As confirmed by these experiments, the effective stiffness model appears to represents the outer extent of the measured impact forces.

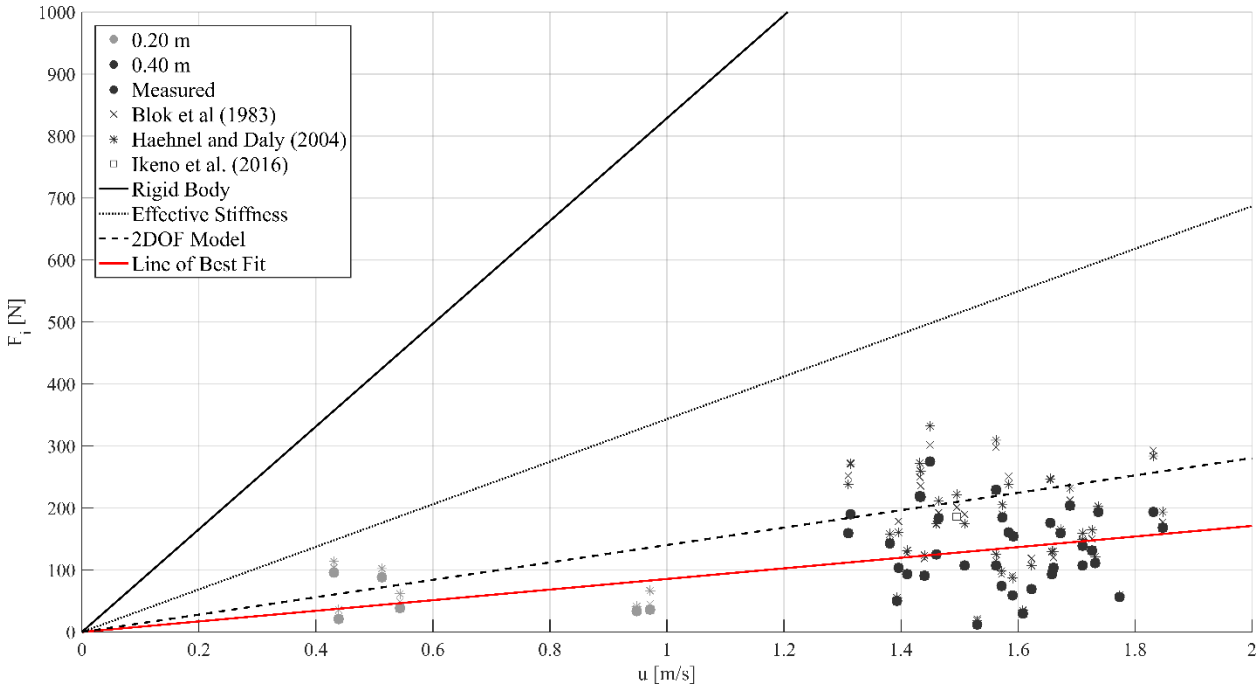

Fig. 5-28. Corrected debris impact force as a function of the impact velocity. The measured forces are represented by the filled circular markers. Forces are corrected by the coefficient from Eq. (2-14) and (2-15)(Haehnel and Daly, 2004), (2-16) (Blok et al., 1983), and (2-17) (Ikeno et al., 2016).

The 2DOF model more accurately estimated the measured impact loads, closely matching the line of best fit (red line) (R^2 = 0.129). However, physically, the model would be expected to overestimate the impact force as the force had not been corrected for oblique or eccentric debris impacts. The assumption of the spring-mass system considers that the entire mass of the debris acts through the impact axis. The likely cause of the discrepancy is due to the estimation of the impact stiffness of the structure and the debris. The impact stiffness of the debris depends on a variety of factors, such as the impact geometry, impact velocity, and material properties (Xu et al. 2016). The examination of the model debris stiffness in this study captured only the materials properties of the debris in a single axis. Due to the dependency of the stiffness on structural geometry, detailed Finite Element Method (FEM) modelling of common debris would likely be necessary to capture the variation in stiffness as a function of the impact geometry (Aghl et al. 2015). Further research will have to evaluate additional effects on the impact stiffness, employing thus more sophisticated experimental and numerical means.

Fig. 5-28 compares the different force correction coefficients, presented in Eq. (2-14) - (2-17). As the correction coefficients are used to capture the influence of the impact geometry, a linearization of the impact loads would be expected. Fig. 5-28 shows little difference in the predicted corrections between the different models. To quantitatively compare the change in variability, the R^2 value was calculated for line of best fit for each of the correction methods. The difference in variability was not significant between the three methods, The correlation coefficient for Blok et al. (1983) equation was R^2 = 0.131, for the Ikeno et al. (2016) model was R^2 = 0.129), and for Haehnel and Daly's (2004) model yielded R^2 = 0.100. Haehnel and Daly (2004) noted a similar variability in their flume tests. The high-variability of the flume tests was likely a result of the free floating debris that generally is subject to random turbulence-induced 3-D motion.

Due to the high variability of the University of Ottawa experiments, the experiments of Haehnel and Daly (2004) were also used to further validate the 2DOF model. Table 5-14 shows the experiments that were used in the validation of the model, each experimental category was performed 3 times. Due to the difference in the experimental objective, some of the physical parameters needed to be estimated. The debris stiffness (wooden logs) was estimated by using the effective stiffness fitted by Haehnel and Daly (2004) (Eq. (2-7)). The mass of their debris varied due to the logs absorbing water throughout the trials. Haehnel and Daly (2004) weighed each of the logs at the beginning and end of each trial period, presenting the minimum and maximum values. As the order of the experiments was not known, the mean debris mass was used.

Table 5-14. Characteristics of the Haehnel and Daly (2004) experiments used in validation of 2DOF model.

Facility	Structural Stiffness [N/m]	Mass of Structure [kg]	Debris Stiffness [N/m]	Mass of Debris [kg]
Flume	1.85×10^6	--	2.694×10^6	--
Basin	0.61×10^6	127	2.694×10^6	255
	0.61×10^6	314		
	22.0×10^6	--		
	32.0×10^6	--		
	120×10^6	--		
Current Study	4.69×10^5	6.3	3.04×10^6	0.226

Fig. 5-29 shows the comparison between the Haehnel and Daly (2004) experiments, the current experiments, and the 2DOF model (solid line) as a function of the ratio of the structural and debris stiffness. With an increasing ratio of the structural to debris stiffness, the maximum impact force tended towards the rigid body model (Eq. (2-6)). Haehnel and Daly (2004) estimated, based on their experiments, that the impact could be considered fully rigid when the structural stiffness was 10 times greater than the debris stiffness (dashed line). Based on the results of the 2DOF model, the structural stiffness should be greater than 100 times the debris stiffness (dotted line in Fig. 5-29) for the rigid body assumption to fully apply.

The flume experiments (represented by crosses in Fig. 5-29) were performed in similar test conditions to the experiments presented here (shown as circles) where the debris were free-floating. In the other experiments performed by Haehnel and Daly (2004), performed in a basin, the debris were constrained to enforce certain impact conditions resulting in the reduced variability in the measured values. The experimental data consistently exceeded the 2DOF model, though they followed the expected trend, with the maximum impact force gradually increasing towards values corresponding to the rigid body impact.

A noticeable discrepancy occurs for the case with the same structural stiffness and different structural mass. Fig. 5-30 examines the influence of the ratio of inertia between the debris and the structure. In the 2DOF model, the structure and debris are both represented as point masses and therefore the inertia was only dependent on the mass of the objects. In Fig. 5-30, the influence of the mass ratio was plotted for specific stiffness ratios. As it can be observed, the influence of the mass ratio varies depending on the stiffness ratio. As the mass ratio increases, the impact force tends towards a constant value. Based on the results of the 2DOF model, the influence of the inertia no longer needs to be considered when the mass of the structure exceeds 50 times that of the debris. Additionally, the influence of the mass ratio is reduced as the stiffness ratio approaches the rigid body solution.

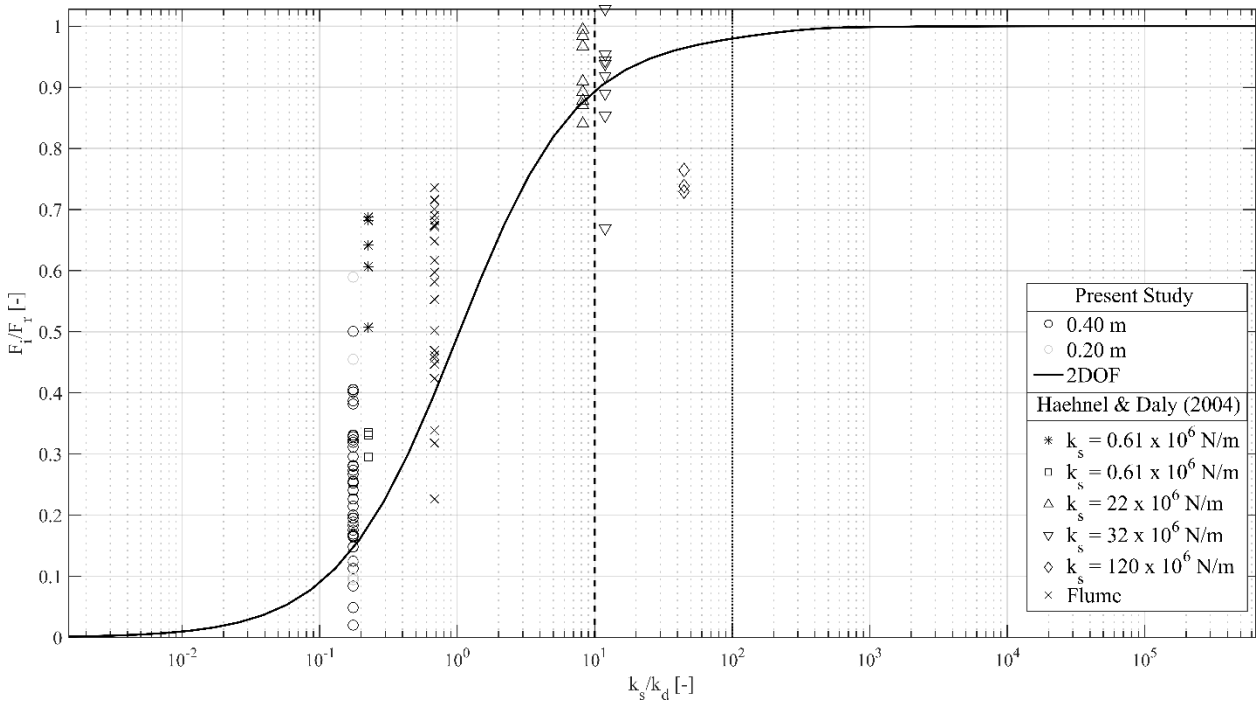

Fig. 5-29. The influence of the stiffness ratio on the maximum impact force. The curve is compared to the experimental data and the Haehnel and Daly (2004) study. The dashed line represents the estimation for a rigid body assumption presented in Haehnel and Daly (2004) study. The dotted line shows the estimation for a rigid body study estimated by the 2DOF model.

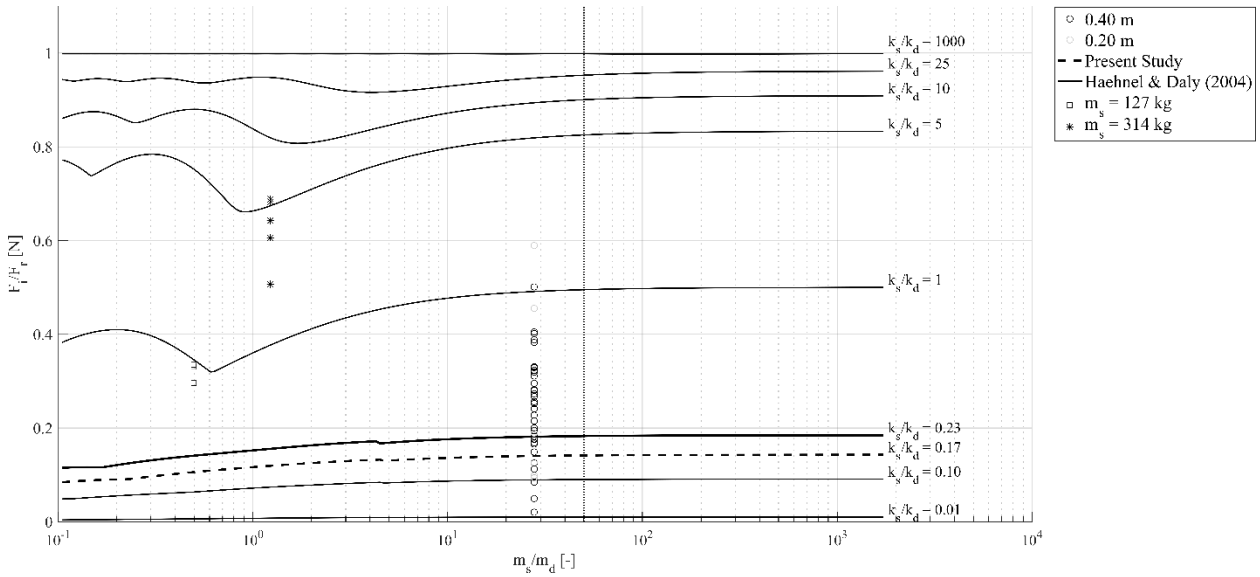

Fig. 5-30. Influence of the mass ratio on the maximum impact force. The dotted line shows the estimation for a rigid body study estimated by the 2DOF model.

In each experimental case, the mass ratio was below the ratio needed to neglect the influence of the inertia on the maximum load. The influence of the inertia may be another reason for the high variability observed

in the both the University of Ottawa and Haehnel and Daly (2004) flume experiments, such as the added mass (discussed in the following section).

The two thick lines shown in Fig. 5-30 represent the stiffness ratios in the current study (dashed line) and Haehnel and Daly (2004) one (solid line). As it can be observed from the Haehnel and Daly (2004), the 2DOF model cannot fully describe the difference in force between the two different inertia cases. Even considering the potential influence of the added mass coefficient, the difference between the two trials exceeds those estimated by the model. Further investigation is needed to address the influence of the mass ratio as difficult to address parameters such as the added mass coefficient should be considered in detail.

5.3.5 Discussion

The following discussion attempts to shed light onto the drawbacks and limitations arising for the nature of the 2DOF model (presented in Section 5.3.2). These limitations necessitate a number of assumptions that influence the application of the model in a design scenario. The masses of both the debris and the structure were assumed to be point mass systems with freedom to move in *x*-direction. Due to the symmetric and cuboid geometry of the debris used within this study, the impact occurred through a relatively small contact area compared to the dimensions of the structure. However, in cases with larger debris or for those with spherical shape, the assumption of a point mass system may no longer be valid and a different impact mechanics system may be necessary, addressing the contact area of the impact. Several studies (Arikawa et al. 2007, Matsutomi 2009, Ikeno et al. 2013) have addressed the impact of large woody debris using empirical equations derived from Hertzian contact mechanics (Hertz 1882), which considers the contact area. Further consideration will also be needed to address the specific type of structure being impacted. Structures with strong foundations would likely act similar to a cantilever beam and may require more complex analysis considering the flexural stiffness using Bernoulli-Euler or Timoshenko beam theory (Abrate 2005).

The debris was permitted free movement, which was not captured by the 2DOF model. The corrections presented in Eq. (2-14) - (2-17) focus on correcting the impact loads in plan view (*x*- and *y*-directions). As the focus of this study is on the application of the 2DOF model, the suggested corrections due to the 3D motion of the debris were outside of the scope – however, the authors stress that they should be investigated in future research. This is of particular importance to this study, due to the transient nature of the hydrodynamic forcing condition, the flow around the structure at the time of impact was still developing, forming significant 3D hydraulic features, such as an upstream surface roller and local flow accelerations (Derschum et al. 2018). Shafiei et al. (2016b), in a study examining debris impact in dam-break waves, noted significant rotation of the debris in *z*-direction, indicating the importance of capturing the 3D motion of the debris under transient forcing conditions. These hydraulic features also incited the lateral motion of debris causing several glancing impacts to be observed. Glancing impacts refers to impacts where the relative velocity of the debris is not parallel to the axis of the target (Frankel and Weihs 1990). The resulting force is then transferred in 2D (*x*- and *y*- directions) through the impact force and friction between the debris and the structure, which are not captured by the impact geometry corrections.

The 2DOF model also does not consider that the impact occurs within a fluid. The presence of the fluid surrounding the debris and structure upon impact will result in fluid reaction forces which are normally interpreted through damping and added mass terms (Chen et al. 1976). The damping of the system is further dependent on the connections within the structure (Shafiei et al. 2016b) and geometry (Oumeraci et al. 1993). Due to the complex nature of estimating the structural damping and the relatively short duration of the impact, damping was neglected from the model.

Shafiei et al. (2016b) noted that the influence of the added mass is dependent on the degree of submergence of the debris. Riggs et al. (2014) found little influence of the added mass coefficient in a study that used debris of similar density (441 kg/m^3) to the debris used in this study (418 kg/m^3). Due to the stochastic nature of the debris impact, the estimation of the added mass coefficient is challenging. The added mass coefficient is dependent on the impact orientation, debris submergence, and surrounding flow field, resulting in a highly variable value dependent on both the impact and the surrounding flow conditions. Additionally, in the 2DOF model, the structure also displaces fluid as a result of its own displacement. The estimation of the added mass of a displaced fixed structure is a more developed field compared to that undertaken for free-floating bodies (Yeung 1981). However, as these experiments were performed in transient flow conditions, the amount of displaced fluid is highly dependent on the flow conditions. These are extremely diverse upon impact, both spatially and temporally. Due to the challenges presented herein, along with potential minimal influence of the coefficient, the added mass was not considered within this study.

Another potential area of uncertainty is related to the assumption of a linear spring response to a load. The elasticity modulus of the debris was estimated using axial compression testing of the debris. The impact stiffness used throughout this study was the debris stiffness along the long axis of the debris. However, as was noted by Haehnel and Daly (2004), the impact stiffness would be dependent on the orientation of impact. Additionally, while there was no visible deterioration of the debris, repetitive impacts could potentially lead to plastic deformations of the debris' edges that would influence the linearity of the debris stiffness. The debris were scaled based on a 1:40 length scale, though the scaling of the material properties of the debris were not addressed within this study. Aghl et al. (2015), in a full-scale study of debris impact loading, noted significant damage to the debris. Proper scaling of debris material properties in laboratory conditions has not yet been addressed in detail and the authors consider that this represents an important future research need (Heller 2011).

The 2DOF model was used in this experiment due to the flexible nature of the structure. The model was shown to more accurately predict the measured impact loading on a structure, matching well with the linear regression fit of the experimental data. The application of the 2DOF model would apply to impact scenarios for "extraordinary" debris impacts (i.e. shipping barges, shipping containers) where the structure's stiffness or mass do not exceed 100 times or 50 time, respectively, that of the debris. The use of the rigid body or effective stiffness model may result in conservative, unfeasible design loads. Otherwise, outside of those ranges, the impact forces tend towards the rigid body model. Scenarios, such as structures built with soft foundations or those pre-damaged by a preceding earthquake (Haehnel and Daly 2002), would also represent instances where the 2DOF model could provide a more accurate estimations of debris impact loading.

While the 2DOF model may capture better the physical phenomena related to an impact with a flexible structure. As shown in Haehnel and Daly (2004), the effective stiffness model represents the outer envelope of the impact loads. As the 2DOF model expanded the impact model to include structural properties, similar uncertainties present in the (Single Degree-of-Freedom) SDOF model which are solely related to the debris, such as added mass and estimation of the stiffness, are also present and related to the structure. For a practicing engineer, the effective stiffness model represents a **conservative estimation of the maximum impact loading**. In extreme cases, where structural properties are unknown, the rigid body model would represent the absolute maximum debris impact force by a single debris acting on a structure.

5.3.6 Conclusions

The study presented herein examines the effects of debris impacting a flexible structure in transient flow conditions. A 2DOF spring-mass system was used to represent the debris-structure interaction. The model

was compared with experimental results from two different studies: one using transient flow conditions and was further validated using those of Haehnel and Daly (2004) study performed in steady-state flow conditions. Based on the results, the following conclusions can be drawn:

- The 2DOF model estimated more accurately the debris impact loads compared to the rigid body and effective stiffness models. It also allowed to distinguish ratios of varying mass and stiffness, previously neglected by studies looking into solid object impact.
- The system can be considered a fully rigid body impact when the stiffness of the structure exceeds 100 times that of the debris.
- The influence of the inertia ratio can be neglected when the mass of the structure exceeds 50 times that of the debris.
- The effective stiffness model was shown to represent the maximum observed impact load, as it was previously determined by Haehnel and Daly (2004).

While the 2DOF model was shown to more accurately estimated the debris impact loading, the measured impact loading tended to be under-predicted by it. This discrepancy was potentially due to the difficulty in evaluating the impact stiffness as well as the inertia of the structure and the debris. To ensure an adequate design of at-risk nearshore structures, the authors recommend the application of the effective stiffness model to ensure a conservative estimation of the debris impact loading in extreme events. Further investigation into the effect of the added mass coefficient and the influence of impact orientation on impact stiffness may further improve the 2DOF model for a wider application in the fields of coastal and hydraulic engineering.

5.3.7 Link to Section 5.4

The study presented here examined the influence on the structural motion of the impact forces exerted by debris. The study showed that, as a conservative estimation, the effective stiffness model should be used in estimating the maximum impact force. This model has so far only been shown the be effective for estimating the impact of a single debris. The following study will extend this study to investigate impacts of multiple debris.

5.4 Multiple Debris Impact in Extreme Hydrodynamic Conditions

5.4.1 Objectives

The present study aims to address the impact of multiple debris on a structure in extreme flow conditions. The specific objective of this study are:

- Determine the influence of the impact conditions (types of agglomeration) on the measured impact forces.
- Examine the effect of the number of debris in a collision on the impact forces.
- Propose and evaluate a method for addressing the number of debris within current debris impact methodologies.

The study examines multiple debris impacts using a single type of uniformly constructed debris (shipping containers) with several initial configurations. Due to limitations of the flume width, the maximum number of debris used within the study was 12. The hydrodynamic forcing condition was a dam-break wave, which was shown to adequately represent a tsunami bore propagating over a coastal plain (Chanson 2006). Two different impoundment depths were used to vary the impact velocities.

5.4.2 Methodology

Experimental Setup

The experiments were performed in the Water Resource Laboratory at the University of Ottawa (Canada). The experimental facility is a 30 m long, 1.5 m wide, and 0.70 m deep dam-break flume (Fig. 5-31). The reservoir (to the right) was 21.55 m long and the water was impounded behind a rapidly-opening swing gate, placed on a 0.15 m false floor. The experimentally-determined Darcy-Weisbach friction factor (f) of 0.0294 (Stolle et al. 2018b). The swing gate was released to generate a dam-break wave; a counter weight was placed on the top of the gate to aid with the fast opening of the gate. A full analysis of the flume hydrodynamics and detailed description can be found in Stolle et al. (2018b).

The spatial origin of the experiment (0,0,0) was selected to be center of the flume at the upstream edge of gate. The y-axis was chosen positive in the flow direction, the positive x-direction was to the flume right and the positive z-direction was in upward direction.

Model Design

The debris consisted of idealized 20-foot shipping containers (ISO668/688) scaled-down based on Froude scaling at a length scale of 1 in 40 (GDV 2003). The down-scaled shipping containers were manufactured from positively buoyant polyethylene (PE-HMW, 920 kg/m^3). Each shipping container had overall dimensions of 0.06 x 0.06 x 0.15 m with an approximate draft of 0.025 m. The thickness of the outer shell of the containers was 0.005 m, with a hollow inside. The inner space was sealed with a custom-made rubber seal, and connected tightly with plastic screws. Additionally, petroleum jelly was placed on the rubber seals to improve water-tightness. The weight of the container, from three repeated weightings, was determined to be 0.234 kg.

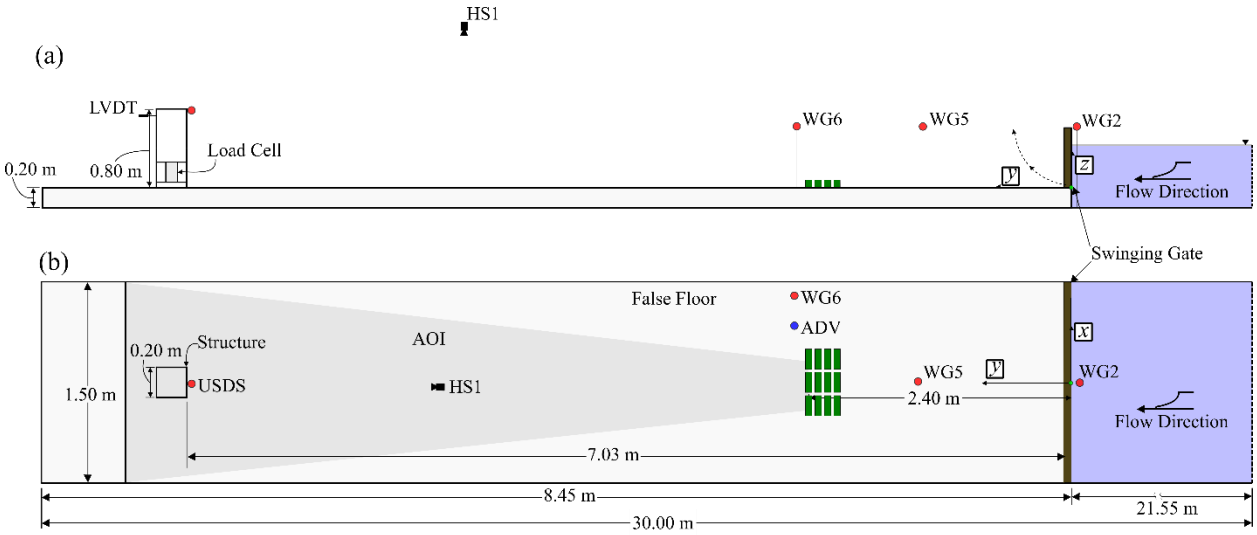

Fig. 5-31. University of Ottawa dam-break flume: (a) side view and (b) top view (not at scale). Dark grey color indicates the area of interest (AOI) of the gate camera (HS1) used. The dam-break wave propagates right to left.

The axial stiffness (k_d) of the model shipping containers was determined through a series of compressive stress-strain test using an Instron® Model 4482 machine. The axial stiffness was tested for three different containers to the compressive yield point of the respective container. A different container was used in the hydraulic experiments as all three containers plastically deformed and could no longer be used for the test sequences. From these tests, the axial modulus of elasticity (E) was determined from the slope of the elastic region (Currey 1988). The mean E of the containers was found to be 1.50 GPa compared to the expected E of 1.30 GPa from product data sheets and literature (Gottstein 2013). For the determination of the axial stiffness, the equation $k_d = EA/L$ was used, where A is the cross-sectional area of the debris and L is the axial length of the impacting debris. The debris stiffness was determined to be 3.04 x 10^6 N/m.

The model of a vertical structure, 0.20 m long, 0.20 m wide, and 0.80 m high, made of acrylic, was placed center-flume at y = 7.03 m. The structure was hollow with 0.005 m thick walls. A linear relationship was fitted to the force measured by the load cell and the deflection from the LVDT yielding a structural stiffness of k_s = 4.685 × 10^5 Pa (R^2 = 0.51, 95% confidence interval [4.653 × 10^5, 4.701 × 10^5]). Impact hammer (PCB Piezotronics, sampling rate 1200 Hz, accuracy as percentage of maximum range: +/- 15%) tests indicated the natural frequency of the model structure was 70 Hz.

Instrumentation

The instrumentation setup is detailed in Fig. 5-31. The water depth was measured using capacitance-type wave gauges (WG) (Akamina Technologies WG-50, sampling rate: 1200 Hz, accuracy as percentage of maximum range: +/- 0.15%). Wave gauge WG2 was placed within the reservoir, behind the dam-break gate at y = -0.10 m. Positions of some of the remaining wave gauges were varying throughout the experimental test program. The reference time for each experiment was determined as the time when the water depth at WG2 dropped 0.005 m (selected threshold value) below the prescribed initial impoundment depth (h_0), identifying the opening of the gate. An ultra-sonic distance sensor (USDS) (MassaSonic M-5000, 100 Hz, accuracy +/- 0.025%) was placed on the upstream face of the structure at z = 0.80 m to measure the time-history of the water surface elevation. An Acoustic Doppler Velocimeter (ADV) (Nortek Vectrino, sampling rate 200 Hz, accuracy: +/- 0.5%) was placed at a fixed position (y = 3.20 m) throughout all experiments with a sampling volume of 7 mm at a height of 0.06 m above the

flume bottom. The data was de-spiked in post-processing using the method developed by Goring and Nikora (2002).

The time history of the forces exerted on the structure were measured using a 6-axis load cell (Interface 6A68E, sampling rate 19 200 Hz, accuracy +/- 0.1%). The base of the load cell was attached to the false floor using 4 pieces of threaded rod bolted into the concrete false floor; the rods were then connected through a metal plate, fastened by adjustable nuts. The load cell was secured to the structure using brackets, in the form of angled steel plates. A 0.015 m gap was set between the acrylic structure and the false floor to allow for the free-motion of the structure. A Linear Variable Differential Transformer (LVDT) (RDPE LSC Transducers DCV025A, sampling rate 19 200 Hz, accuracy +/- 0.1 – 0.5%) was placed on the downstream face of the structure at a height of z = 0.78 m to monitor the deflection of the structure.

A high-speed camera (HS1) (IO Industries Flare 2M360-CL, frame rate: 70 fps, resolution: 2048 × 1088 px) was placed above the flume to analyze the impact conditions. The HS recorded grayscale images with a 60 Hz sampling rate. The HS1 camera was synchronized with the data acquisition system by visually inspecting the images to determine the time when the bore front reach the structure and comparing it to the instant of the first force signal from the FT. The estimated synchronization accuracy was of +/- 0.036 s.

Experimental Protocol

The experimental protocol (Table 5-15) examined the influence of the number of debris (N), initial impoundment depth (h_0), and initial debris orientation (θ). These are the most relevant governing parameters for the process investigated. Additional parameters such as the horizontal distance between the containers and the stacking height will be subject to future studies. As mentioned in Section 0, the debris were configured in the same location with equal horizontal spacing (0.03 m) for each experimental run. The debris were configured in several different initial position to investigate the influence of the configuration on debris transport. The configurations were defined based on the number of debris (N), the rows (r), columns (c), and stacks (s) (Fig. 5-32(a-b)).

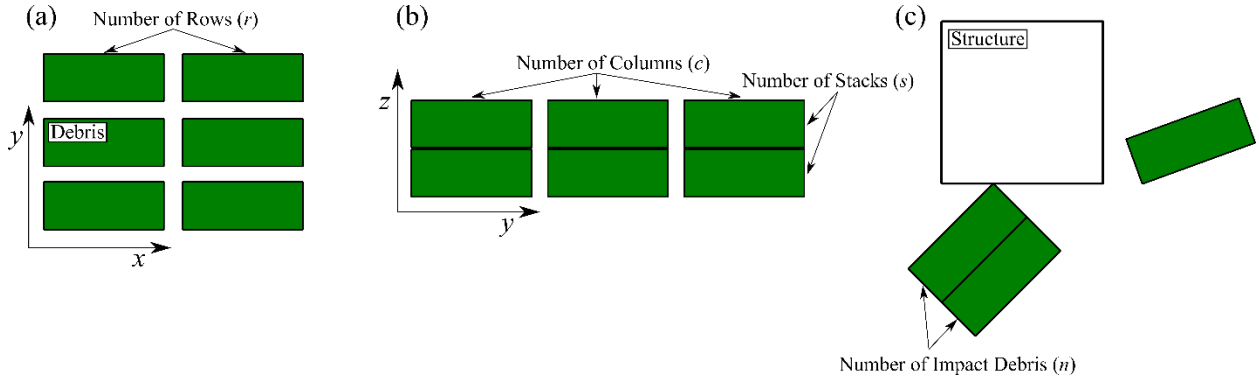

Fig. 5-32. (a) Top view of the initial configuration debris for experimental categories 10 and 11. (b) Side view of experimental categories 8 and 9. (c) Top view of the debris impact (generic).

The hydrodynamic boundary condition (forcing factor), and, therefore, the impact velocity, was varied by changing the initial depth of water impounded in the reservoir between 0.20 m and 0.40 m. The debris orientation, the initial direction of the long axis of the debris, was varied to examine the influence of the initial configuration on the spreading characteristics in a companion study (Stolle et al. 2018c).

Table 5-15. Experimental Protocol.

Experimental Category	Impoundment Depth (h_0) [m]	Number of Debris (N) [-]	Debris Orientation (θ) [°]	Number of Rows (r) [#]	Number of Columns (c) [#]	Number of Stacks (s) [#]	Repetitions [#]
1	0.40	1	0	1	1	1	20
2	0.20	1	0	1	1	1	10
3	0.40	1	90	1	1	1	20
4	0.40	3	0	1	3	1	10
5	0.20	3	0	1	3	1	10
6	0.40	6	0	1	3	2	10
7	0.20	6	0	1	3	2	10
8	0.40	6	0	2	3	1	10
9	0.20	6	0	2	3	1	10
10	0.40	12	0	2	3	2	20
11	0.20	12	0	2	3	2	20
12	0.40	12	90	2	3	2	10
13	0.20	12	90	2	3	2	10

The number of repetitions were selected based on analysis of single debris motion presented in Stolle et al. (2018c). Balancing time restraints and accurate estimation of the debris behaviour, a statistical power (likelihood of correctly rejecting the null hypothesis) of 80% was selected, corresponding to the 10 repetitions used within this study.

Before each experiment, excess water was removed from the bottom of the flume and the debris were configured in their specified position, aided by ground markers and auxiliary spacers. The reservoir was filled to the set impoundment depth and allowed to still for a period of 5 minutes to allow for any internal waves to dampen. The gate was then manually released, allowing the dam-break wave to propagate downstream and subsequently entrain the debris placed in various configurations.

Data Analysis

Impact Geometry

A manual camera-based tracking method was used to determine the impact variables such as impact obliqueness, eccentricity, compactness as well as the number of the impacting debris. The method required the determination of the image frame in which the impact occurred. The later was defined as the last frame (recorded by HS1) to occur before an impact event was recorded by the load cell. From the impact frame, as well as the previous four frames, the top four corners (pixel-based accuracy of the manual selection: +/- 0.01 – 0.02 m) of the container were selected. The centroidal position of the debris was extracted from the five frames, from which the impact velocity, velocity vector, debris orientation, and impact point could be determined. The impact velocity and velocity vector were determined by the mean trajectory of the debris in the five frames to limit errors related to the manual selection. For the cases when the debris impacts occurred as an agglomeration, the velocity vectors for each individual debris were determined. In the following sections, the impact velocity of the debris agglomerations was taken as the mean velocity of all debris in the group.

For each experimental run, three independent repetitions were performed on the same image frames to reduce inaccuracies occurring from the manual selection of the corners. Based on the variation in the

results from the repetitions, the impact velocity had a mean error of 0.10 m/s while the orientation of the debris axis exhibited a mean error of 5°.

Impact Force Analysis

In this study, the main variable of concern was the debris impact force, which had to be extracted from the time-history of the varying hydrodynamic force. An Ensemble Empirical Mode Decomposition (EEMD) (Huang et al. 1998) filter was used to extract the impact response from the hydrodynamic force signal. The EEMD decomposes force-time history from the load cell into zero-crossing intrinsic mode functions. Advantageously, the EEMD method reliably filters any given time-history retrieved from a sensor while avoiding phase shifts associated with filtering in the frequency domain. Through visual analysis, the intrinsic mode functions related to the debris impact were kept while the modes associated with instrument noise and hydrodynamic loads were removed.

The debris impact signal was related to the structural response to the impact force. The structural response is the measured signal from the load cell as a result of the displacement of the structure. As the impact force occurs over a short time interval (Aghl et al. 2014) compared to the period of the structural oscillation, the structural response does not have the opportunity to reach an equilibrium with the load. To estimate the impact force from the structural response, the Duhamel integral (Clough and Penzien 2003) was used to estimate the debris impact force, similar to the work of Wienke and Oumeraci (2005) in estimating wave impact loads. The Duhamel integral (Clough and Penzien 2003) calculates the structural response by integrating the differential responses from an estimated loading history:

$$R(t) = \frac{k_s}{m_s \omega_d} \int_0^t p(\tau) \sin \omega_d (t-\tau) e^{-\xi \omega_d (t-\tau)} d\tau \tag{5-18}$$

where ω_d is the damped frequency of the structural oscillation, $p(\tau)$ is impact load applied over a period t, τ is the time since impact occurred, m_s is the mass of the structure, k_s is the stiffness of the structure, and ξ is the damping coefficient. Using an incremental summation of Eq. (5-16) over t, the structural response to a given impact load can be estimated.

By iteratively estimating the impact force and duration (t_d), the structural response can be fit to the experimental data (Navaratnam et al. 2013). The normalized root mean squared error (RMSE) was used as the fitting indicator between the measure force response (f_R) and the estimated response by the Duhamel integral (f_{DI}):

$$RMSE = \frac{\sqrt{\frac{\sum_{i=1}^{n} (f_R - f_{DI})^2 w(i)}{n}}}{F_R} \tag{5-19}$$

where $w(i)$ is a weighting function, and F_R is the maximum value from the measured response. The normalized RMSE was weighted, using a linearly declining function between 1 and 0 for 5 times the period of structural oscillation (~0.07 s), to estimate the error in the initial phase of the impact response.

The initial error had to be determined due to the challenges in estimating the damping of the structural response. The damping coefficient (ξ) is generally difficult to estimate due to the various losses in a complex structure (Moser et al. 2005). Additionally, Oumeraci et al. (1993) showed that the water depth around the structure can influence the damping of the structural response. As these experiments were performed in transient flow conditions, a time-dependent estimation of the damping coefficient was not plausible, therefore, the RMSE was weighted towards the initial structural response (least influenced by damping).

The Duhamel integral method also requires an assumption regarding the shape of the impact time history. The ASCE7 Chapter 6 (2016a) assumes a step function for the impact time history. However, Aghl et al. (2014), in an examination of full-scale in-air impact tests with shipping containers, determined that the shape of the impact time history was a half-sine. Previous versions of the ASCE7 (2016a) Chapter 5 – Flood Loads used a version of the impact equation that considered the impact force as a half-sine as well. Solving for the half-sine impact time history would result in a larger impact force than when a step function is used due to the slower rise time to the peak force. The half-sine impact history was conservatively assumed for the remainder of this study.

The experimental force responses were fitted iteratively using Eq. (5-16) varying the impact force and duration by a resolution of 1 N and 0.0001s, respectively. The force and duration with the minimum normalized RMSE was selected. The mean RMSE for the experiments was 0.0748 N (with a standard deviation σ = 0.0182 N).

5.4.3 Results

Hydrodynamics

The hydrodynamic forcing condition used throughout these experiments was a dam-break wave. The mean water surface elevation time histories are shown in Fig. 5-33 for the WG indicated in Fig. 5-31. Two initial impoundment depths were used (0.20 m and 0.40 m). The water surface elevation time histories displayed in Fig. 5-33 were ensemble-averaged over the entire experimental data set. The mean standard deviation over all time series was 0.0037 m. The experimental data (solid line) is contrasted with the analytical solution (dotted line) for a dam-break wave propagating over a flat bed (Chanson 2006). The experimental data compares reasonably to the analytical solution and, as the wave propagated further downstream from the gate, the wave approaches the analytical solution (Fig. 5-33c). The initial plateau of the water depth near the wave front was determined to be due to particularities of the gate construction (Stolle et al. 2018b). To ensure a water-tight seal, two side guiding rails were placed on each side of the gate, causing a small constriction of the flume. Khankandi et al. (2012) showed that a constriction of the flume near the reservoir can result in the distinct step profile observed in Figure 3(b). For a full description of the hydrodynamics, Stolle et al. (2018b) examines the specifics of the University of Ottawa dam-break flume.

The wave shown in Fig. 5-33 had a maximum water depth of 0.18 m, corresponding, based on the scale used, to a prototype inundation height of 7.2 m. The maximum measured flow velocities (Fig. 5-33d) were 1.16 (7.33 at prototype) and 1.58 (9.99) m/s for h_0 = 0.20 and 0.40 m, respectively. Due to air entrainment near the wave front and likely the cavitation acting on the stem/legs of the instrument, the ADVs were not able to adequately capture the flow velocities in the initial stages of the flow (~3 s). Therefore, the maximum flow velocities were assumed to be equal to the wave front velocity, calculated using the arrival of the wave between WG5 and WG6. The mean wave front velocities were 1.35 and 2.16 m/s, corresponding to 8.53 and 13.66 m/s at prototype scale. Fritz et al. (2012) showed, using PIV analysis of flow observed during the 2011 Japan Tsunami in Kesennuma Bay, a similar range of flow conditions, with water depths ranging from 0.5 – 10 m and flow velocities with values between 3 and 11 m/s.

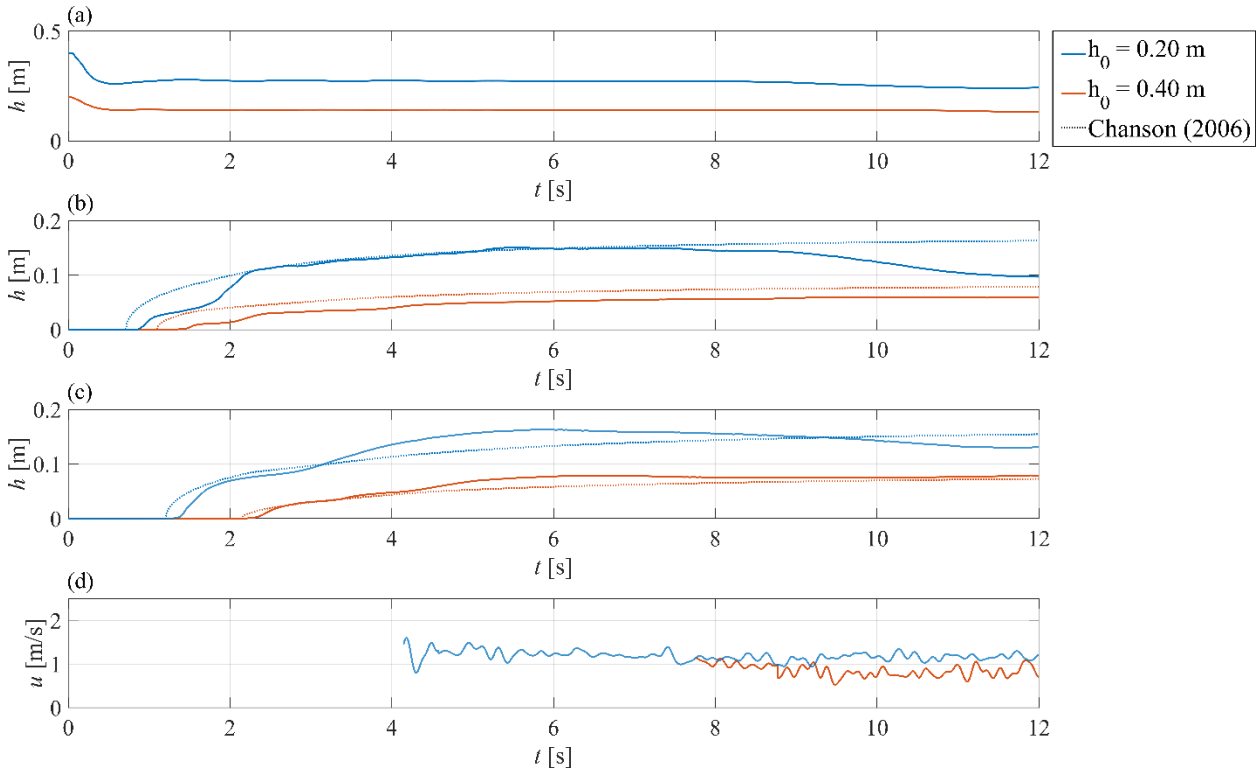

Fig. 5-33. Mean water surface elevation (*h*) time-history for (a) WG2, (b) WG5, and (c) WG6 for each impoundment depth (0.20 and 0.40 m). (d) Mean velocity profile from ADV. The profiles are compared to Chanson's (2006) analytical solution for a dam-break wave including frictional effects on the dam-break front.

Chanson (2006) showed using image analysis of the 2004 Indian Ocean Tsunami coastal inundation that the front of a dam-break wave resembles the wave profile of a tsunami bore inundating over a coastal plain. As a result, dam-break waves have been extensively used to model wave-structure interaction, debris transport, and debris impact (Ikeno et al. 2016, Shafiei et al. 2016b, Derschum et al. 2017) in tsunami-like events.

While the wave front represents adequately that of a tsunami inundating flow, the use of dam-break waves still raise similar concerns with respect to their time scale. This is similar to previous attempts to model tsunami waves, using solitary waves (Madsen et al. 2008). The duration of the dam-break wave is a function of the reservoir length (Lauber and Hager 1998). As the debris, in all experimental cases, was entrained rapidly with the wave front, the debris impact occurred within 5 s after the initiation of the wave. Based on the theoretical velocity of the negative wave propagating upstream in the reservoir ($2\sqrt{gh_0}$), the influence of the reservoir would not be observed at the structure until ~10 s. Therefore, the duration of the wave does not influence the results presented in the following sections examining debris impacts in *initial* wave front of a tsunami-like surge.

Impact Type

Debris impact conditions in the video images were classified into four different impact types observed (shown in Fig. 5-34 along with the impact response time history). A single debris impact (Fig. 5-34a) was the one most commonly observed where a single debris struck the structure. This type of impact can be described by Haehnel and Daly's (2004) model. The second type of impact was the debris striking the

structure as an agglomeration, with several debris propagating as a group (Fig. 5-34b). An agglomeration was identified as a group of debris that have a single impact point from which the inertia would be transferred.

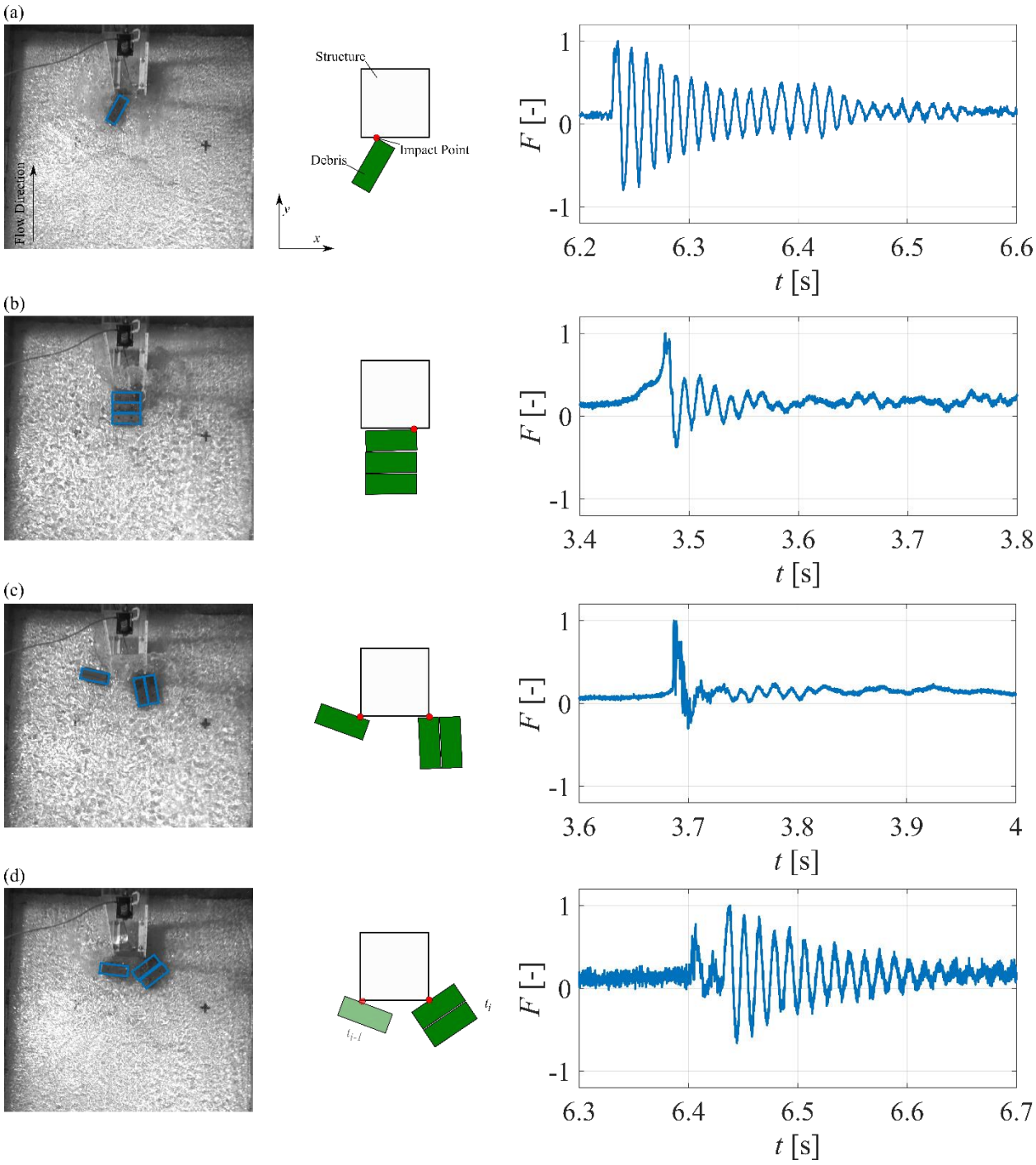

Fig. 5-34. Types of multiple debris impacts. (a) Single; (b) Agglomeration; (c) Simultaneous; and (d) Non-Simultaneous. Image frames taken using the HS camera. The impact response-time history (normalized by the maximum response) from the load cell is shown for each of the impact types shown.

The last two types of impact were the simultaneous (Fig. 5-34c) and non-simultaneous (Fig. 5-34d) ones. Simultaneous impacts occurred when multiple debris hit the structure at different impacts points at the same time (as observed using the video images). The time histories of the structural response measured by the load cell are shown, for each impact type, in Figure 4. As it can be seen, the simultaneous and non-simultaneous impacts show distinct two-peak characteristics compared to the single and agglomeration cases.

In the analysis of simultaneous and near-simultaneous impacts, one of the challenges was related to the occurrence of the impact events. Unlike single impacts, the impact force from a near-simultaneous event cannot be uniquely determined based on impact velocity, independent of time (Quinn and Bairavarasu 2006). Therefore, accurate information regarding the exact occurrence of the impacts is necessary. However, as the theoretical impact duration (~0.002 s) was significantly less than the camera frame rate (~0.02 s), an accurate estimation of the impact occurrence could not be adequately captured for the estimation of the Duhamel integral. Additionally, the overlapping structural response between the impact events makes the application of the Duhamel integral challenging. Further research is required to elucidate the effects of multiple impacts and their contributions towards the total force exerted on a structure.

Non-simultaneous impacts occurred when multiple debris hit the structure at different time instances (t_i) within the natural damping period (~0.07 s) of the structure. Due to the rapid nature of debris impacts, the initial displacement of the structure has an important role in its response, as interference occurs between the structural responses of the individual impacts. Therefore, if the structure is initially in motion due to a recent impact, a second impact would result in a different structural response than that from a static structure. Due to these challenges outlined for the simultaneous and non-simultaneous impacts (jointly named near-simultaneous impacts), these type of impacts were omitted from the analysis due to concerns over the accurate estimation of the impact force. Of the 188 impact events that were observed throughout these experiments, simultaneous and non-simultaneous impacts occurred on 10 occasions. Fig. 5-35 shows the occurrence of the impact types normalized by the number of impact events (P) based on the hydrodynamic forcing condition.

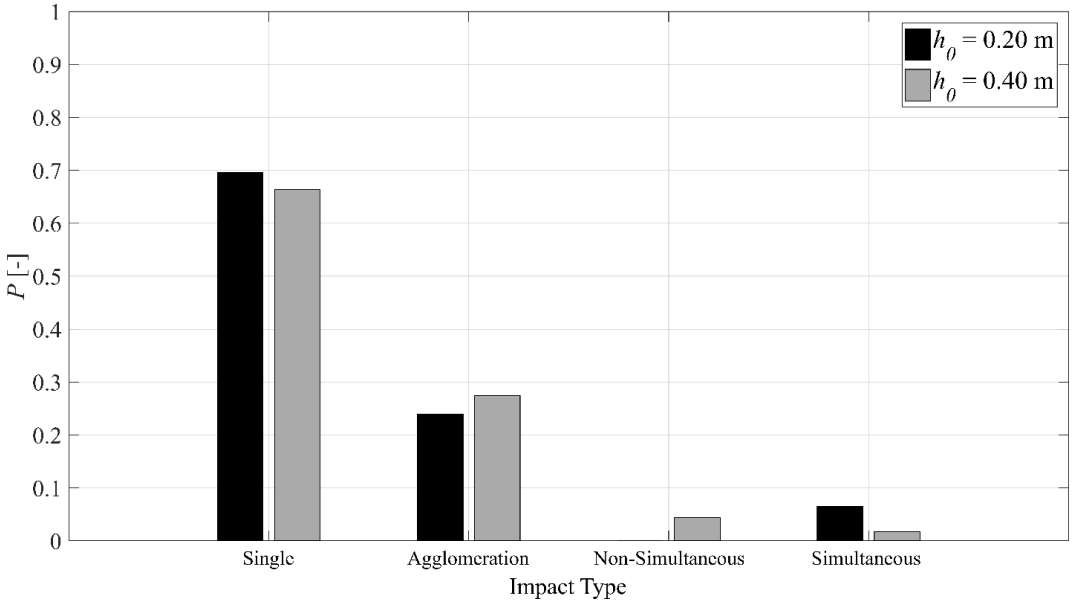

Fig. 5-35. Impact types normalized by the number of impacts (P) observed for each impoundment depth.

The majority of the impacts observed in this study were single debris striking the structure, despite the concentrated initial configuration of the debris (Fig. 5-36). From the initial entrainment of the debris, the debris would further propagate in the form of an agglomeration-type configuration, dictated by the number of columns (*c*) in the initial configuration (Fig. 5-36(b)). A rapid spreading began to occur in the later stages of the flow (Fig. 5-36(c-d)) due to inter-collisions and turbulent eddies (Rueben et al. 2014), exhibiting diffusion-like behaviour. This behaviour was not observed under steady-state conditions (Bocchiola et al. 2008). However, this may have been due to the relatively short debris propagation lengths used within this study.

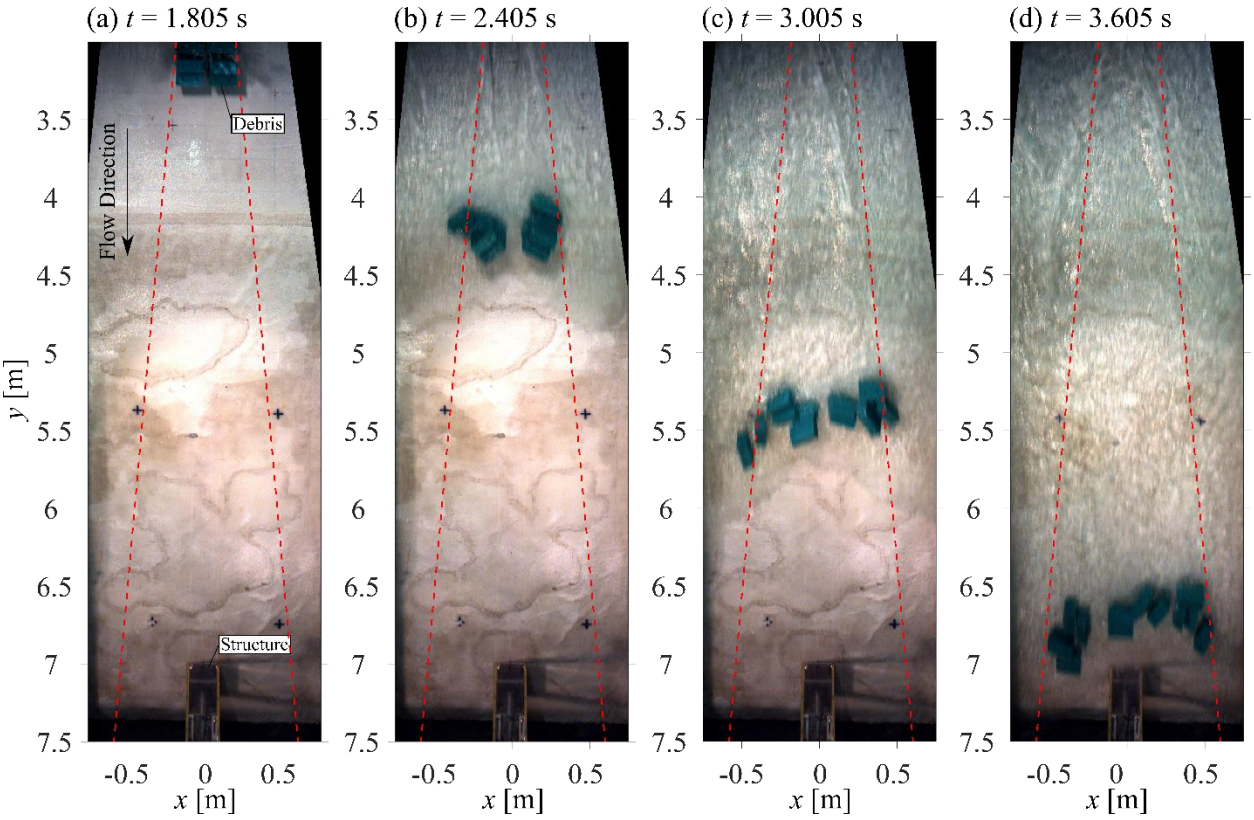

Fig. 5-36. Debris spreading for experimental category 10.

The process of the debris spreading is not well understood; however, it is, clearly, a stochastic process. Rueben et al. (2014) indicated that turbulent eddies may be a cause of the debris spreading, by influencing the breaking up the initial formation of debris agglomerations. Stolle et al. (2019b) demonstrated the influence of bed topography and local flow conditions on the lateral debris displacement. Additionally, interaction between debris, random contact between the bed and debris surface as well as the temporal evolution of the bow wave have also been observed to have an influence on the lateral debris motion while propagating landward (Braudrick and Grant 2001, Goseberg and Schlurmann 2014, Nistor et al. 2016). All these factors likely contribute to the lateral displacement of the debris and to the destruction of debris agglomerations, although it is unclear to what extent each factor plays a role. Stable agglomerations were rarely observed to form in the latter stages of the flow. Highly energetic and turbulent flow of a dam-break wave as well as the initial entrainment of the debris likely caused the rapid diffusion of the debris into commonly observed single impact cases seen in these experiments. The extent of the lateral displacement is likely a function of several variables, including the distance from the initial

debris source, and represents a necessary area of further research to appropriately capture the debris hazard in extreme events.

Furthermore, near-simultaneous impacts occurred predominantly due to the complex flow dynamics around the structure (St-Germain et al. 2013, Derschum et al. 2017). The presence of an obstacle in the flow path results in the formation of a surface roller at the structure's face, a roller which extends towards the walls of the flume. The re-circulating flow patterns occasionally caused the agglomerations to break apart in close proximity to the structure, leading to near-simultaneous impacts. This was particularly prevalent for large debris agglomerations, as they were more unstable. As a result, the maximum observed size of agglomerations impacting the structure was four (4), with those events occurring infrequently (3 times).

Multiple Debris Impact

Impact Forces

The impact forces, estimated through the fitting of the Duhamel integral to the structural response, are depicted as a function of the impact velocity estimated through the video analysis in Fig. 5-37. The impact forces were measured only in the stream-wise direction (*y*-direction). A comparison of the measured impact forces to the impact model presented in Haehnel and Daly (2004) (black dashed line) shows the limitations of the SDOF approach. As the structure is considered to be fully rigid in the analytical equations, the inherent degree flexibility of most of the structures are not fully considered. Most of the regular structure (such as buildings and bridges) would absorb some of the impact energy by deflecting in the stream-wise direction upon impact. Additionally, the debris impact stiffness is highly dependent on the impact geometry (Haehnel and Daly 2002). As the stiffness of the debris in this study was estimated through compression tests parallel to the long and short axis of the debris, the varying impact geometry would influence the estimated effective stiffness. However, from an engineering perspective, the effective stiffness model represents a conservative estimation of the maximum impact force.

To avoid including the limitations of the SDOF model into the analysis of multiple debris impact, the regression slope of the single debris impact was assumed to include the influence of the structural deformation and impact geometry, essentially representing the effective stiffness of the model. It is assumed that within the observed impacts, the structural response would be linear and the distribution of the impact geometry would be normally distributed; therefore, the slope of the line-of-best-fit would include these considerations equally for each impact category.

The line-of-best-fit was determined based on the number of debris impacting the structure, (n) (solid lines in Fig. 5-37). Qualitatively comparing the slopes between the number of impacting debris, as the number of debris increases, the measured impact force increases. An analysis of covariance (ANCOVA) test was performed to examine the difference in the slopes between the number of impacting debris with the null hypothesis that the slopes are all the same. The test found no significant difference between the groups (*p*-value = 0.15, *F*-statistic 1.80, degrees-of-freedom (*dF*) = 3). Intuitively, the more debris present in the agglomeration, the greater the kinetic energy of the debris. This in turn will increase the energy transferred to the impacted structure. However, in the case of free-floating debris, the high variation of impact conditions makes capturing the difference between the kinetic energies challenging without more sophisticated instrumentation.

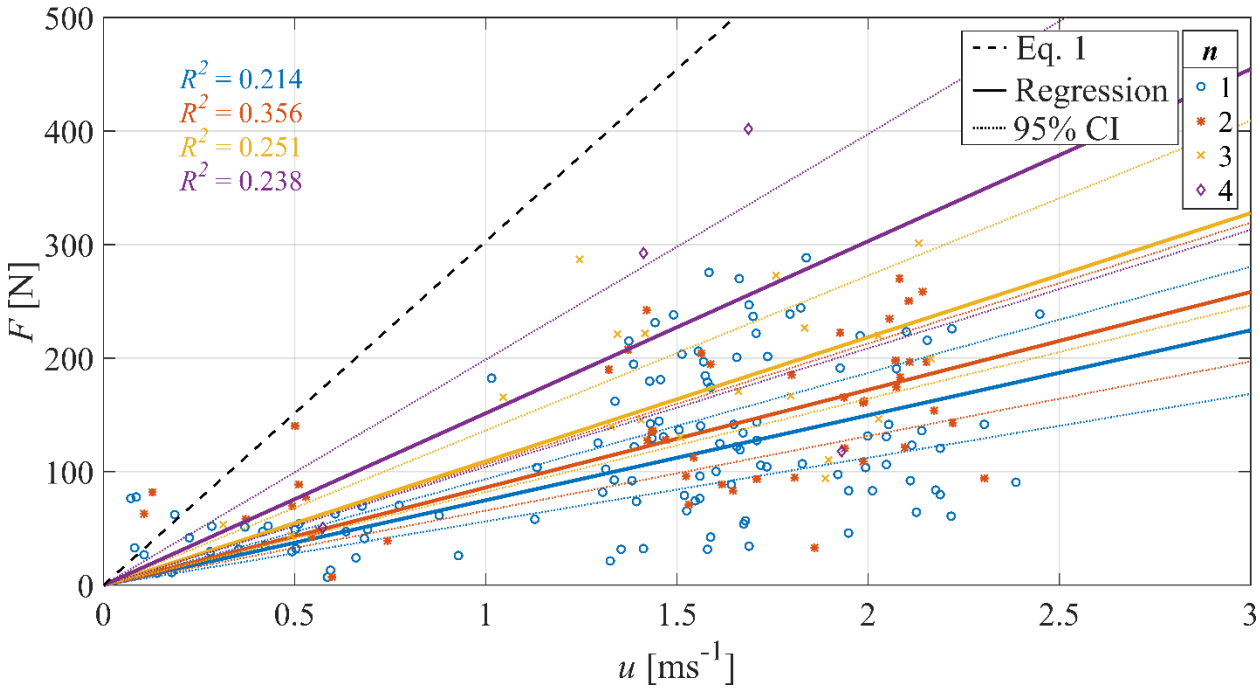

Fig. 5-37. Debris impact force (F) as a function of the impact velocity (u). The marker represents the number of debris impacting the structure. The solid lines represent the line-of-best-fit for the number of debris impacting the structure. The dashed line represents the analytical equation for debris impact (Eq. (2-6)).

As current analytical models do not consider the effect of the number of debris, the maximum impact force imparted onto a structure by an agglomeration of debris could exceed the current design capacity outlined within building design standards. Therefore, to include the influence of multiple debris in assessing maximum design loads, the following section outlines a potential methodology for multiple debris impact analysis.

Adjustment to Current Analytical Equations

Following the methodology of the SDOF model proposed by Haehnel and Daly (2004), the slope of the line-of-best-fit in Fig. 5-37 can be considered as the square root of the product of the impacting mass and debris stiffness (Eq. (2-6)). As the stiffness of the debris is a function of its structural properties (Aghl et al. 2014), the addition of multiple debris to Eq. (2-6) would only influence the impacting mass (m). Stolle et al. (2017a) showed in the analysis of the acceleration of debris agglomerations that the addition of the parameter n, representing the number of debris within the agglomeration, allowed for an accurate theoretical estimation of the velocity profile of entrained debris. Similarly, including parameter n in Eq. (2-4) and considering the number of impact debris results in the equation:

$$F = u\sqrt{nmk} \tag{5-20}$$

As discussed earlier, assuming the impact geometry and impact stiffness were normally distributed, dividing by the single debris impact cases would ideally result in the slopes increasing by a factor of $\sqrt{n}$. However, the measured slopes increased by a lesser value (1.15 for n = 2, 1.46 for n = 3, and 2.00 for n = 4). This is likely due to the assumption that all of the energy within the debris agglomeration was transferred to the structure. Unlike with the single debris case, all of the mass of the projectile does not act

through a single point. Other factors, such as inter-collisions, oblique collisions and rotations within the debris agglomeration, result in energy losses that are not transferred to the structure (D'Alembert 1743).

The losses within the debris agglomerations once again fall within the spectrum of near-simultaneous impacts (Quinn and Bairavarasu 2006) as the stress wave propagates through the individual debris pieces after initial contact with the structure, causing rapid inter-collisions between rear following containers and rotations within the agglomeration. Typical analysis of these types of impacts require pair-wise analysis of the individual impacts (Seghete and Murphey 2010, 2012). However, detailed information regarding the order and duration of the impact are necessary to derive a unique solution. Alternatively, Ivanov (1995) considered multiple near-simultaneous impacts to be a stochastic process, representing the solution as a random variable.

With the objective to maintain the impact analysis within the SDOF model and reduce the required calculation rigor for an engineering estimation, the losses within the agglomeration were assumed to be a function of the impact geometry and compactness of the configuration alone. Both these variables were addressed using a method similar to the ASCE 7 Chapter 6 (2016b) standard for assessing debris loading potential on structures. The coefficient (C_{area}) was calculated as the ratio of the plan area of the debris (blue area in Fig. 5-38(a) and (c)) and the area of the outer plane bounds of the debris agglomeration (the area within red box). Therefore, for increasingly eccentric and oblique impacts, the coefficient will be reduced similar to the orientation coefficient used in the ASCE 7 (2016a), as for cases where the debris agglomeration had a relatively "loose" configuration (Fig. 5-38(a)).

The mean C_{area} value for each number of impacting debris was 0.58 (+/- 0.16), 0.44 (+/- 0.11), 0.44 (+/- 0.13), and 0.37 (+/- 0.07) for n = 1, 2, 3, and 4, respectively. Applying coefficient (C_{area}) to the impacting mass in Eq. (5-20) results in the equation:

$$F = u\sqrt{nC_{area}mk} \tag{5-21}$$

Fig. 5-39 shows the results of using Eq. (5-21), plotting the corrected impact force as a function of the augmented velocity ($u\sqrt{nm}$). Comparing the line-of-best-fit between the number of impacting debris cases shows that the slope collapses (as expected) at an approximately equal value (representing the effective stiffness of the system) for all of the cases.

As the debris were allowed to free-float, the number of impacting debris was not controlled within this experiment, resulting in significantly more single debris impacts. Even within the single debris impacts, significant variation was observed, similar to the findings of Haehnel and Daly (2004). The scatter of the data was likely due to the influence of impact geometry that was not captured by the proposed impact model as impact geometry can influence the impact stiffness, as well as the added mass due to fluid accelerations. The corrections proposed in Eq. (5-21) result in a slight increase in the correlation coefficients compared to Fig. 5-37, however, further investigation into controlled debris agglomeration impact are necessary to further validate the proposed model. Due to the uncertainties related to the estimation of C_{area}, Eq. (5-20) represents a conservative estimation of the impact forces generated from multiple debris impacts.

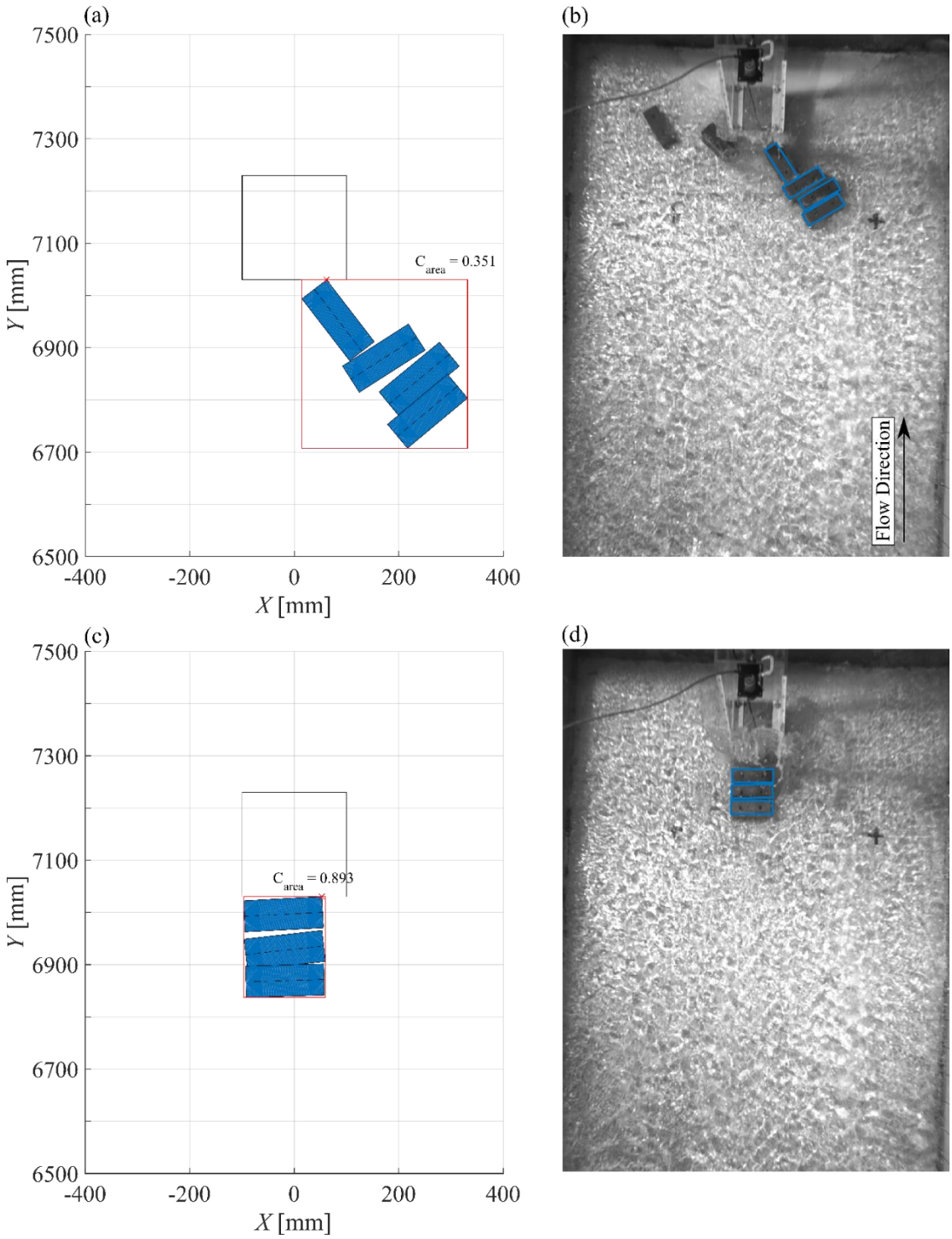

Fig. 5-38. Debris agglomeration impact analysis. (a) and (c) outlines the calculation of the correction coefficient based on the plane area of the agglomeration; (b) and (d) are images taken directly during Experimental Category 4.

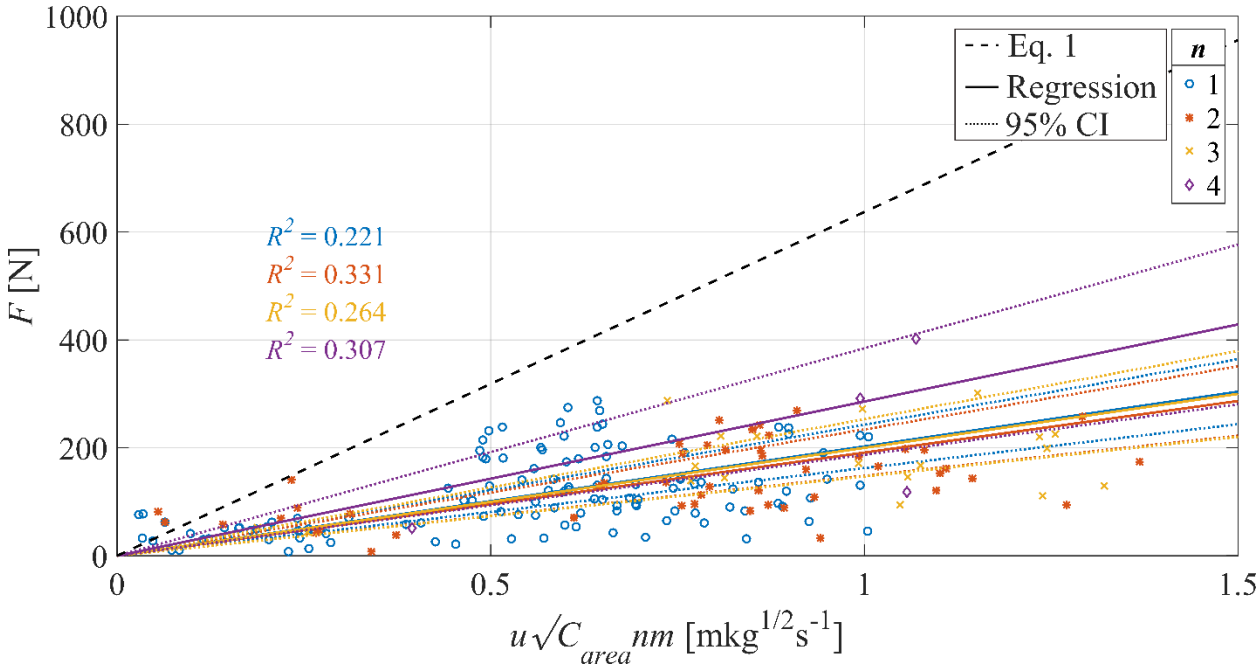

Fig. 5-39. Corrected debris impact forces calculated using Eq. (5-21). The marker represents the number of debris impacting the structure. The solid lines represent the line-of-best fit for the number of debris impacting the structure and the dashed lines represent the 95% confidence interval. The dotted line represents the analytical equation for debris impact (Eq. (2-5)).

Cross-stream Forces

This section examines the cross-stream forces (*x*-direction) from the multi-debris impact cases. For the range of tests analyzed, a correlation between the lateral and the in-stream maximum force was observed (Fig. 5-40). This is in agreement with Hertzian contact mechanics (Hertz 1882) and the impact theory on rigid bodies (Thornton and Yin 1991), as the tangential force is considered to be a direct function of the friction between the impact objects and, therefore, a function of the normal force. Furthermore, based on Coulomb's theory of friction (Coulomb 1771), the tangential forces should be independent of the sliding velocity (*x*-direction) and contact area. Coulomb's theory assumes that the normal force is proportional to the contact area between the objects.

Based on these simplifying assumptions, the cross-stream forces should be linearly dependent on the stream-wise forces, correlated through the coefficient of friction (μ). By performing linear regression (solid lines in Fig. 5-40), the mean coefficient of friction was determined to be 0.34 +/- 0.06. The calculated μ exceeds expected values of ~0.10 for the materials (acrylic, polyethylene) used in these experiments, indicating that Coulomb's law is not capturing the complete mechanics of the tangential forces. Due to the rapid nature of the impact, Coulomb's assumption that the normal force is proportional to the contact area may not be valid (Hertz 1882). Additionally, significant displacements (of up to 0.004 m) were recorded at the top of the structure; therefore, the impact cannot be considered to be fully rigid. Furthermore, due to the 3-D nature of the impact, the impact axis does not pass directly through the *y*-axis, likely transferring momentum in the other axes.

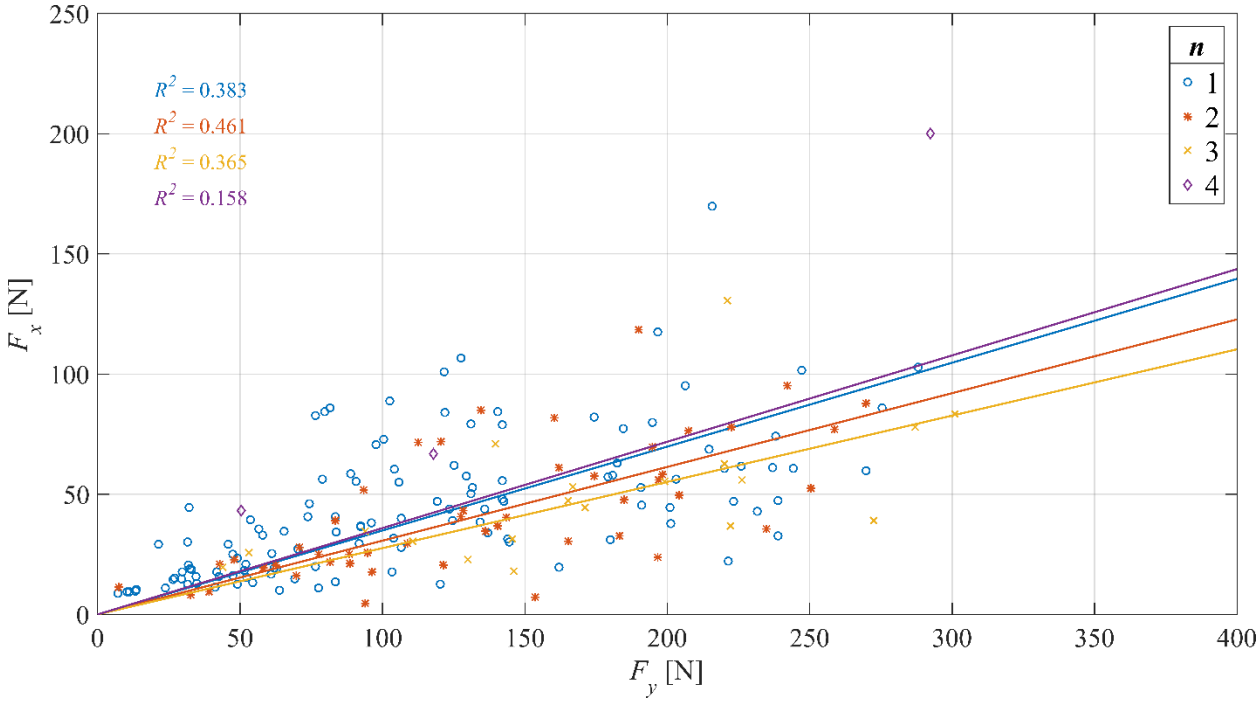

Fig. 5-40. Cross-stream forces as a function of the stream-wise forces for different numbers of impacting debris. The solid lines are the lines-of-best fit.

Impact Moment

Due to the out-of-axis impact of the debris, the impact force exerts an additional moment on the structure, resulting in additional stresses to the building foundations. A comparison of the occurrence of the maximum moment (M_x) measured by the 6-axis force transducer and the stream-wise force (F_y) showed a strong correlation ($R^2 = 0.98$), indicating that the two events occurred at the same time. Using a similar analysis approach as Wüthrich et al. (2018), the cantilever arm (L_z) of the impact can be calculated as:

$$L_z = \frac{M_x}{F_y} \tag{5-22}$$

Fig. 5-41 shows the calculated cantilever arm normalized by the water depth at the front of the structure at the impact time as measured by the USDS as a function of impact velocity. The water depth was averaged over a 0.8 s interval around the impact time to reduce the influence of instrument noise and the presence of the debris. The mean cantilever arm is indicated as the solid line in Fig. 5-41.

The debris used within this study were positively buoyant with a draft of approximately 0.025 m. With a face width of 0.06 m, approximately half of the debris was submerged. Therefore, the expected impact point was around the water surface elevation at the impact time. While scattering was observed, likely a result of interference with the USDS from the splash caused by the impacting wave and debris, as expected, the mean normalized cantilever arm was found to be approximately 1.0, indicating that the debris was impacting the structure at the water line. Further investigation is necessary to evaluate the cantilever arm for negatively buoyant debris such as cars or boulders, as the hydrodynamic conditions, such as wave period and turbulence (Weiss and Diplas 2015), may have a more significant role.

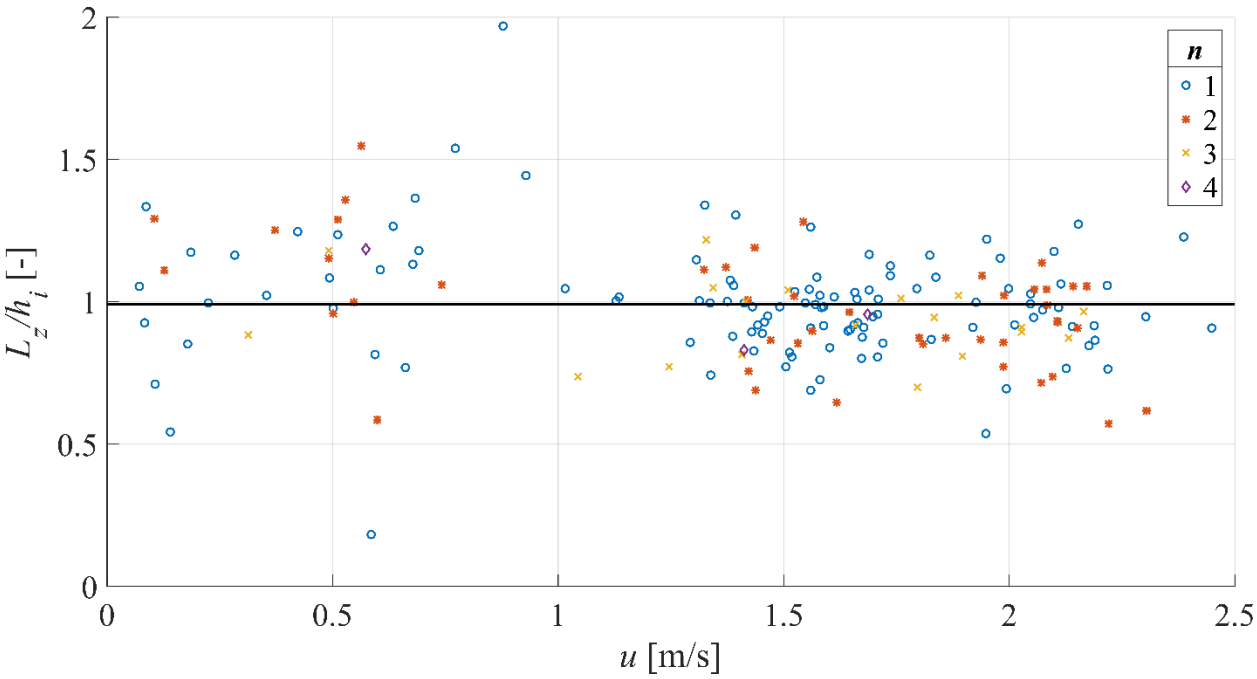

Fig. 5-41. Cantilever arm calculated from Eq. (5-22) normalized by the water depth upon impact as a function of impact velocity. The solid line indicates the mean normalized cantilever arm.

5.4.4 Discussion

Eq. (5-21) presents a methodology of addressing impacts on structures from agglomerations of debris in extreme flooding events, following an accepted engineering approach. However, the suggested methodology has inherent limitations. As it can be seen from Fig. 5-38, the model was developed considering the 1-D motion of the debris, following Haehnel and Daly's (2004) model, and treating the debris agglomeration as a group of debris with a certain compactness. Stolle et al. (2019a) showed the limited effectiveness of these 1-D models in free-floating conditions due to the 3-D motion of the debris. The geometry of the impact in the 2-D horizontal space was attempted to be captured through a correcting compactness coefficient. The cross-stream forces were shown to be correlated with the magnitude of the stream-wise forces. However, the magnitude of the cross-stream forces exceeded those expected from solely a frictional model approach in rigid body impact mechanics. The discrepancy in the forces was likely due to the 3-D motion of the impact debris imparting energy into the other axes. High-resolution data regarding the 3-D motion of the debris upon impact would likely be necessary to accurately assess the partitioning of kinetic energy through the *x*-, *y*-, and *z*-axis.

A second limitation of the model is the use of the rigid body assumption as the foundation of the development. Field evidence of disaster-stricken communities has shown damage from massive pieces of debris, ranging from shipping containers to shipping vessels. As the inertia and stiffness of these type of debris likely exceed the rigid body assumptions, the motion of the structure would likely absorb a portion of the impact energy. In these cases, additional considerations will also need to be given to the plastic deformation of the structure-debris system as the assumption of the behaviour of the structure as a linear spring is no longer be valid.

A third limitation of the present model is related to the correction coefficient (C_{area}) used to evaluate the impact geometry. Haehnel and Daly (2004) had previously shown the effectiveness of correcting the impact forces of constrained debris considering the orientation and eccentricity. However, due to the

complex geometry of the debris agglomerations, the straightforward application of the model was not possible. Potentially developing methods for determining the impact axis of the agglomerations would allow for a more physically relevant correction parameter. Additionally, while the coefficient theoretically aided in the correction of the forces as a result of the varying geometry, the estimation of the value for design purposes is challenging. Potentially, the analysis of the agglomeration behaviour of different debris types under various hydrodynamic conditions would allow for an estimation of a mean value. Lin and Vanmarcke (2010) statistically estimated the number of impacts that would occur using a Poisson distribution, a similar distribution could be developed for estimating the number of impacting debris. As a practical conservative estimation, Eq. (5-20) represents the maximum loading condition for multiple debris impacting a structure under rigid body conditions, assuming no internal energy losses within the moving mass of the debris agglomeration; therefore, a C_{area} equal to one (1.0). From a design perspective, the impact moment for positively buoyant debris could be then estimated using Eq. (5-20), multiplied by the water depth.

One aspect not considered in the current analysis is the influence of the added mass coefficient. As discussed in Shafiei et al. (2016b), the hydrodynamic mass can be challenging to estimate due to its dependence of density and geometry of the debris as well as the orientation of the impact. As the debris properties were kept constant throughout the experiment and assuming that the debris orientation was normally distributed, the influence of the hydrodynamic mass would be included within the slope of the line-of-best fit. Further research is needed into addressing the hydrodynamic mass of a debris agglomeration as water entrained within the agglomeration may have a significant influence on the measured value.

5.4.5 Conclusions

This study examined the influence of multiple debris impacts on the design conditions for debris impact loading in extreme flooding events. The experiments evaluated the impact of shipping containers, entrained within a dam-break wave, on a hollow acrylic structure. Using the Duhamel Integral and video analysis, the impact force and geometry were extracted from the experimental data and classified by the number of debris impacting the structure. A methodology to analyze the impact of multiple debris through the addition of a term is proposed, identifying the number of debris impacting a structure, to the rigid body model, presented by Haehnel and Daly (2004). Based on the present results, the following conclusions can be drawn:

- An increase in the number of debris impacting the structure results in a corresponding increase in the measured impact force, although the observed difference was determined to be not statistically significant due to the high variation in the impact conditions.
- The increase in the measured impact force did not directly scale with the increase in the inertia of the debris. The increase was slightly less due to inter-collisions within the debris agglomerations and the impact geometry.
- An analytical model (Eq. (5-21)) was proposed addressing multiple debris impacts and impact geometry in extreme hydrodynamic flow conditions. The model resulted in a moderate improvement in the estimation of the impact forces. However, due to the challenges in addressing impact geometry in a design setting, Eq. (5-20) represents a conservative estimation of the potential impact forces.
- The cross-stream forces were linearly correlated with the impact force. However, these forces cannot be described completely by rigid body mechanics. The 3-D nature of the free debris impacts imparted a portion of the kinetic energy in the cross-stream direction.
- The impact moments can be described by multiplying the stream-wise force by the water depth for positively buoyant debris.

To maintain continuity with previous debris impact models, the proposed equations builds upon the current methodology for assessing debris impact loads in extreme flooding events. The addition of a term including the number of debris impacting the structure will allow for more robust design in extreme flooding events as field evidence has shown the prevalence of multiple debris within the entraining flow. Additionally, the methodology can be extended to the estimation of the cross-stream forces and moments. As risk assessment methodologies for debris impacts continue to develop, including a consideration for debris agglomerations may aid in the development of more accurate design methods and improved structural resilience.

Chapter 6. Discussion

6.1 Scale Effects

As outlined in Section 1.3, the issue of scale effects influencing debris transport and loading was not explicitly addressed through physical modelling within this thesis. The following section will outline the potential implications of these effects at prototype scale.

One of the most prominent issues is related to the scaling of the viscous forces in tsunami-like conditions. As outlined by Bricker et al. (2015), because coastal engineering models are most often scaled using Froude scaling, the Reynolds number does not match values at prototype scale. The Reynold's number in major flooding events often exceeds 10^6 where as in the studies presented here the Reynolds number was in the range of $10^4 – 10^5$, an order of magnitude smaller. In most coastal models, the viscous forces are assumed to be negligible as long as the flow can be considered fully turbulent (Re > 12 500) (Te Chow 1959, Hughes 1993). However, in the case of debris damming, the Reynolds number plays an important role in the drag force (a portion of the loading captured by C_R) (Sumer and Fredsøe 2006). Limited studies have addressed high Reynolds flow conditions (> 2000) around square cylinders, however, for circular cylinders, transitions from the laminar boundary layer to turbulent (i.e. the drag crisis) occur within the outer range observed within these studies (~ 3.5×10^5). Though transitions of flow regimes for square cylinders tend to occur at lower Reynolds (Saha et al. 2000), it is unclear when the transition to a fully turbulent boundary layer would occur within these experiments and the extent of these effects on the drag forces.

In Chapter 3, the lateral displacement of debris was a critical parameter in estimating the likelihood of debris loading. While several different variables were observed to contribute significantly to the lateral displacement, the extent of those influences at full scale is unclear. While the general observations (i.e. mean lateral displacement equal to 0 and a Gaussian distribution) would be expected to hold, the magnitude of the standard deviation and the influence of the individual variables would likely not. It is unclear the exact mechanisms in which the flow causes the lateral displacement of debris and therefore it is challenging to quantify the influence. Rueben et al. (2014) hypothesized that turbulent eddies contributed to the extent of the lateral displacement. If this is the case, the relative size of the turbulent eddies may not be properly scaled as they would partially depend on the Reynolds number (She and Leveque 1994). Alam et al. (2011) showed in a study of two fixed square cylinders that the gap between the cylinders had an influence on the lift forces (force acting in the lateral direction and similarly influenced by the Reynolds number). At least in the initial stages of debris entrainment, this may have an influence on the displacement of the debris, which again may not be properly scaled due to the Reynold's number.

Furthermore, Bricker et al. (2015) noted the importance of considering surface tension in small-scale tsunami physical models through the Weber number. While throughout these experiments, the Weber number exceeded that suggested by Peakall and Warburton (1996) (We > 120), issues could arise due to aeration within the flow. As the surface tension is the same at prototype and model scale, the size of air bubbles within the dam-break bore are not properly scaled (as the size is a function of the surface tension). Aeration has been shown to influence the forces acting on fixed obstacles (Bullock et al. 2007) and similar effects should logically be expected. However, these forces are most prominent during the

initial impact of the bore, which is not captured in Eq. (2-3). Surface tension may also have an influence when the debris form agglomeration. Due to the small distance between the debris (and therefore small, stagnant film of water), adhesion forces between them may exceed what would typically occur, causing agglomerations and dams of large debris to form more readily than would be the case at prototype scale.

6.2 Model Effects

Due to limitations of the experimental facilities or measurement devices, there is potential errors related to the model setup used within this thesis. This section will address some of the potential errors that existed throughout these experiments.

One of the major challenges in tsunami engineering is the development of an appropriate hydrodynamic forcing condition due to the size and duration of these rare events. In Section 3.1, an elongated solitary wave generated from a falling water column was used as the hydrodynamic boundary condition. The solitary wave has commonly been used in the modelling of tsunami wave impacts on structures (Chinnarasri et al. 2013, Seiffert et al. 2014) and in debris transport studies. However, Madsen et al. (2008) noted that the time scale of a solitary wave is significantly smaller than the time scales necessary to model a tsunami wave. The elongated wave used in Section 3.1 is longer than a solitary wave, however, is still an order of magnitude less than a tsunami wave at prototype scale. Therefore, for the debris transport results discussed within this thesis, only the incipient motion of the debris at prototype scale can be considered to be accurately captured.

For the other experiments, performed in the University of Ottawa flume, the hydrodynamic boundary condition was a dam-break wave. Chanson (2006) showed, using field data from the 2004 Indian Ocean Tsunami, that the dam-break wave well represents a tsunami propagating over a coastal plain. As tsunami are relatively rare events, limited data exists regarding the inundating wave shape. Nouri et al. (2010) used a dam-break wave to examine forces on structures. Similarly, Foster et al. (2017) used a novel wave generation system that enabled the formation of long waves with accurate representation of the temporal and spatial scales at small-scale (1:100). Discrepancies between the force profile upon initial impact of the structure showed that the dam-break wave was significantly steeper. However, the wave steepness is dependent on the flow resistance (Chanson 2005) and the tests may not be accurately capturing flow resistance at prototype scale. Additionally, other aspects that would influence flow resistance, such as the density of fresh-water vs. salt-water and entrained sediment, would also not be accurately captured.

Throughout the studies outlined in Chapters 3 and 5, a single debris type was used (shipping containers). Therefore, there is potential for the shape of the debris to have an influence on the analysis. In Chapter 3, various geometries were incorporated through the application of the characteristic length as this is commonly used to define a wide range of shape in hydraulic problem as the exposed area is often the critical component. However, the shape would also affect the other aspects of debris entrainment and transport, such as the initiation of motion. Throughout the experiments, the debris motion was observed to initially be sliding. In the case of cylindrical debris, such as large woody debris and small petrochemical storage tanks, rolling would initially occur instead of sliding and may not begin to saltate as was observed in Section 3.1. Additionally, flow patterns around different shaped objects may influence the drag and lift forces acting on the debris. Further investigation is needed into different debris shapes to evaluate potential influences on the results.

In the investigation of debris damming, the experiments were performed in a narrow flume (0.40 m) where the dam constricted the width of the flume. The constriction of the flume can have an effect on the

hydrostatic and hydrodynamic forces acting on the structure (Chakraborty et al. 2004). The constriction of the flume results in an associated backwater rise and drop in water depth behind the blockage. The change in water depth results in an unequal distribution of hydrostatic pressure. However, this change in water level is dependent on the hydrodynamic conditions and the percent blockage of the flume width (Fenton 2003). Therefore, at prototype scale, this percent blockage would likely be much less resulting in a reduction in the change in water level.

For the transient flow conditions, the flume width has an influence on the occurrence and magnitude of the maximum force (St-Germain et al. 2013). As the surface roller forms and propagates laterally, the flume width dictates when the surface roller will propagate upstream, resulting in a decrease in the flow velocity, and therefore, force. The reduction in flow velocity likely also has an influence on the formation of the dam, causing it to destabilize in a manner that would not be expected at prototype scale. For the debris impact tests, this phenomenon would not be expected to influence the results as the debris arrived rapidly after the bore arrival.

From the perspective of the hydrodynamic conditions, the constriction results in an increase in the flow velocity around the blockage. Achenbach (1974) studied the drag force acting on a submerged sphere in high Reynolds flow as a function of the blockage ratio (diameter of sphere to diameter of tunnel). Achenbach (1974) determined that the increased blockage resulted in a significant increase in the drag coefficient with blockage ratio. Chakraborty et al. (2004) found a similar conclusion in low Reynolds flow for a cylinder. The change in the drag force appears to be predominantly due to an increase in skin friction associated with the increase in flow velocity. The change in flow regime would likely have a similar effect on the experiments presented in Chapter 4.

In Chapter 5, one of the primary challenges was estimating the debris impact force from the structural response measured by the load cell. The Duhamel integral (Section 5.3.3) was iteratively fit to the filtered structural response. To fit the response, several structural parameters needed to be estimated, most critically, the structural stiffness (k). The structural stiffness was estimated by applying a steady force to the structure and measuring the displacement. However, this assumes that the structural response is linear and there is no flexure of the material at the impact point. While there was no observable plastic deformation of the debris or structure, the response of the structure displayed only a moderate linear response ($R^2 = 0.51$). This could potentially have been due to some rotation of the structure around the connection to the load cell, this was not examined in the analysis.

6.3 Application

The long-term objective of the research presented within this thesis is to provide a framework for assessing debris hazards within extreme flooding events. While the scope of the research focused on tsunami-like events, the findings could also aid in the development of similar frameworks in different instances of extreme flooding events, such as storm surges (Roeber and Bricker 2015), dam-breaks (Pilotti et al. 2011), and flash floods (Alexander and Cooker 2016). For consistency with the research outlined in this thesis, an example will be used to show the application of this framework within tsunami engineering.

To estimate the flow parameters, the Energy Grade Line (EGL) method outlined in Kriebel et al. (2017) and used with the ASCE 7 Chapter 6. The shoreline is assumed to have an mean slope of 1:80 and the maximum run up elevation is 7.50 m at a distance of 600 m from the shoreline. The topography is assumed to always be bare earth (Manning's coefficient = 0.025). The method iteratively back calculates

the water depth and flow velocity from the maximum run-up using the change in the EGL as a function of the slope and friction slope. Fig. 6-1(a) shows the results of the EGL method as a function of distance from the shoreline (x = 0 m). The water depth and velocity at the debris site will be used in the further calculations as this represents the maximum hydrodynamic forcing condition (as water depth and flow velocity decrease over distance).

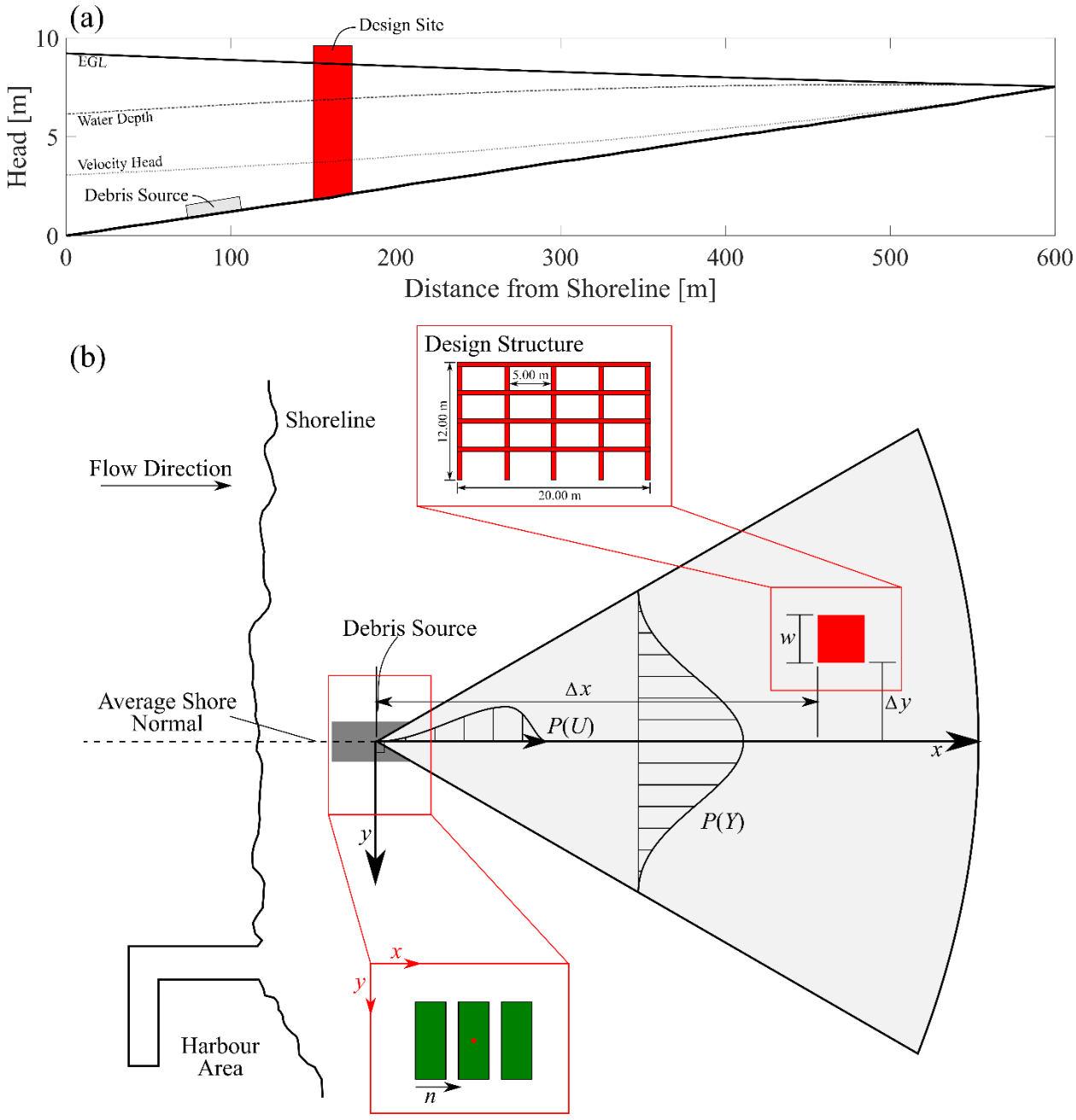

Fig. 6-1. Application of debris hazard assessment in the context of the ASCE 7 Chapter 6 design guidelines. (a) Estimation of flow parameters from the Energy Grade Line (EGL) method. (b) Debris hazard assessment parameters.

The debris source will be considered to be a port where three empty shipping containers (6.10 m × 2.40 m × 2.40 m, mass (m_d) = 2 270 kg, stiffness (k) = 42 900 kN/m) are placed. The shipping containers are placed in the configuration shown in Fig. 6-1(b). The source is located 90 m from the shoreline, where the maximum water depth and flow velocity (from the EGL method) are 6.73 m/s and 5.43 m, respectively. The debris source is 30 m from the design site (Δx), which will be considered to be a vertical evacuation structure, and the centroid of the design site is located 20 m from the average shore normal. The width of the design structure is 20 m. Using the methods proposed in the above thesis, the objective is to calculate the probability of impact occurring and magnitude of the impact force.

In determining the impact velocity, the time for the debris to reach the design site must be determined using Eq. (2-3). To calculate the cross-sectional area exposed to the flow, it will be assumed that the static draft of the debris stays constant (despite the potential for lift force). Using a simple force balance, the draft of the container will be about 0.15 m.

Solving for t and U (using Eq. (2-2)) results in values of 10.34 s and 5.28 m/s, respectively (Fig. 6-2(a)). As shown in Section 3.3 , the debris velocity distribution can be approximately estimated using the Kumaraswamy (1980) distribution. Using the mean velocity, the shape parameters for the probability density function (Eq. (3-13)) (a and b) can be calculated using Eq. (3-15) and (3-16). Using Eq. (3-14), the likelihood of the impact velocity being less than a value could be determined, however, the complement of that probability ($1 - F(U; a, b)$) is the likelihood an impact velocity will exceed a certain value (often referred to as the survival function), which is a more useful value for practicing engineers.

From the impact velocity, the impact force can then be calculated. As shown in Section 5.3, Eq. (2-6) represents a conservative estimation of the impact force from a single debris. In Section 5.4, this was extended to include impacts of debris agglomerations. Therefore, as a conservative estimation, Eq. (5-20) will be used to calculate the design force based on the survival function for impact velocity. Fig. 6-2(c) shows the survival function at the design site.

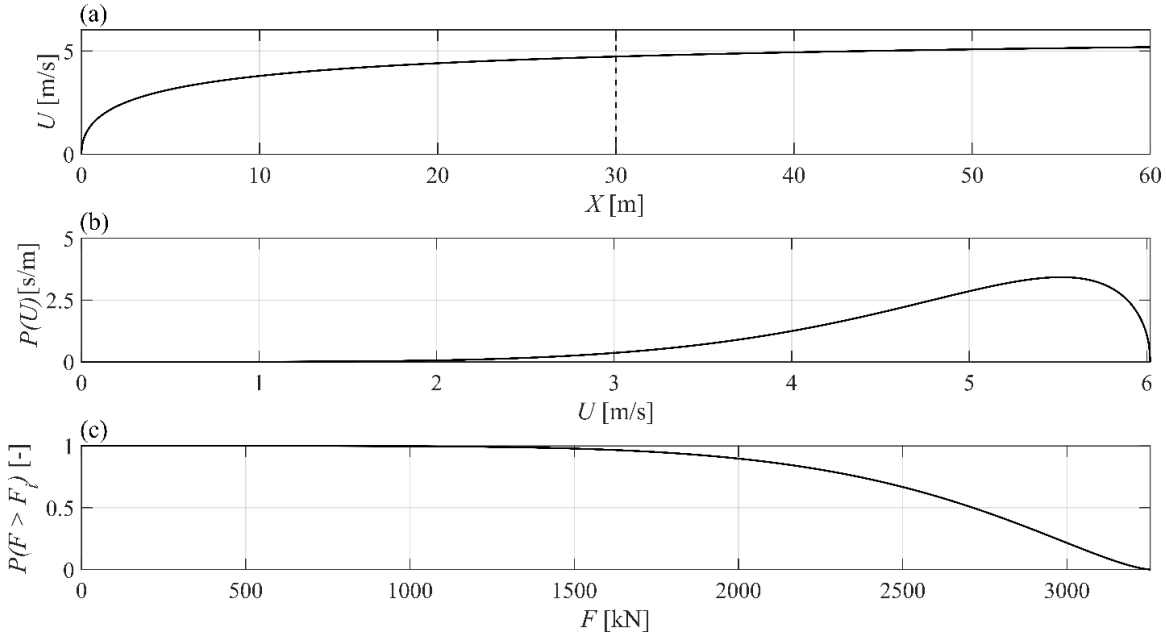

Fig. 6-2. Application of debris hazard assessment framework to calculate (a) the mean impact velocity; (b) probability density function of debris velocity at the design site; (c) survival function for the design site.

As shown in Section 3.2, the mean lateral displacement of the debris is assumed to be 0. The standard deviation in the lateral direction can be calculated using Eq. (3-10), resulting in a value of 17.46 m. The probability density function can then be calculated for a distance of 30 m from the debris source (Fig. 6-3). It is assumed that debris will only make contact with the front face of the structure. Integrating the probability density function across the face of the structure (red faded box in Fig. 6-3), the resulting probability of impact is approximately 23%.

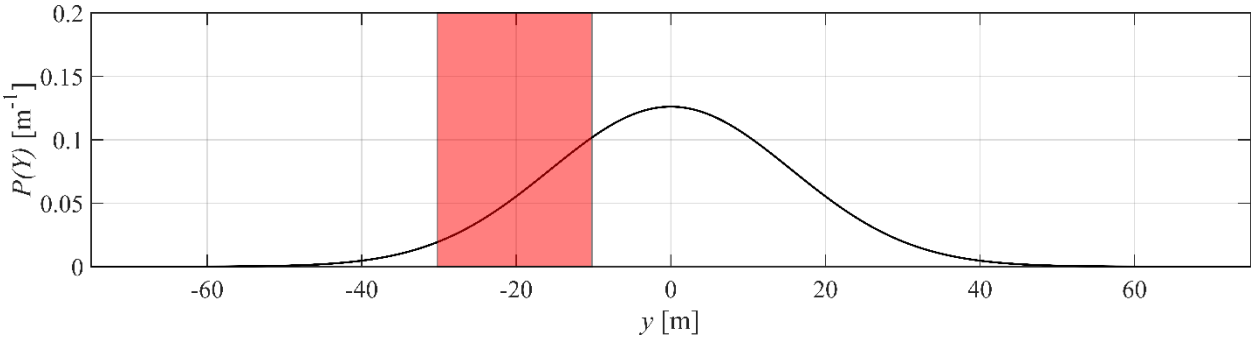

Fig. 6-3. Probability density function of the lateral displacement at the design site.

To extend the model to consider debris damming, the hydrodynamics and geometry of the structure must be considered. Based on the EGL method, the water depth and flow velocity at the structure are 5.32 m and 6.46 m/s, respectively. The geometry of the structure is shown in Fig. 6-1(b), the ratio of the spacing of the structure to the shipping containers was assumed to be similar to the structure outlined in Section 4.2. Using the results from Fig. 4-26(c), the cross-sectional area of the dam is assumed to be 32.3 m^2 and the width (assuming the worst case scenario) is 6.1 m (based on Eq. (4-7)). Calculating the dam Froude and Reynold's number results in values of 0.83 and 3.86×10^7. From Eq. (4-7), the maximum wave runup would be 2.10 m, therefore, the structure should not be overtopped. The estimation of the C_R could not be performed based on Fig. 4-29 due to the limited range of applicability of the correlation (Chaplin and Teigen 2003) to Reynold's numbers an order of magnitude larger than those used in the study.

As outlined in this section, the results of this thesis provide a basic framework in which to estimate the debris hazard in extreme flooding events. However, there are still many considerations that need to be addressed in ensuring the accuracy of the estimation. As outlined in Section 6.1 and 6.2, scale effects, particularly related to the lateral displacement of the debris, and model effects, such as blockage ratio, are of concern. As the exact phenomenon that dictate the magnitude of the displacement are not well understood, research is still necessary to illuminate potential errors with the current estimation. The framework also does not address the influence of debris geometry. As a accurate estimation of the variables impacting the impact geometry could not be determined, the impact geometry was omitted to ensure a conservative estimation of the impact force.

Furthermore, the following study was performed in idealized conditions where complex topographies and the presence of obstacles were not addressed. These parameters would likely significantly influence the displacement of the debris (Goseberg et al. 2016b). Additionally, the motion of the debris was not examined for the retreating wave. In Section 3.1, the retreating debris velocity was 2.5 – 4 times less than inundating debris, however, this could still pose significant risks to the leeside of structures.

6.4 Relevance to the Wider Engineering Community

The hydrodynamic forcing conditions focused predominantly on tsunami-like conditions. However, the results of this thesis can be applied to a wide-range of topics in coastal and hydraulic engineering considering the ubiquity of debris within flooding events. From the hydrodynamic condition perspective, similar conditions have been observed in storm surges in the 2013 Typhoon Haiyan (Philippines) where a rapidly inundating bore formed causing significant damage to local communities (Roeber and Bricker 2015). Similarly, the failure of either natural or artificial dams can cause rapid flooding events which can severely damage local communities (Alexander and Cooker 2016). As disaster management and vulnerable communities continue to develop more complex models of risk assessment, the consideration of debris' influence on design loads and surrounding hydrodynamic conditions should be included.

Outside of debris, the results of this study have parallels to the study of ice loading in riverine environments. Ice jamming (or damming) has resulted in severe damage and flooding due to the constriction during the ice-breakup period (Beltaos et al. 1996). Additionally, it can disrupt power generation (Lu et al. 1999). Free-floating ice can also cause damage through impact structures (Saeki and Ozaki 1980) or ships (Matskevitch 1997). With the changing climate, the occurrence of ice jams due to mid-winter breakups could potentially increase (Beltaos and Prowse 2001) stoking concerns about ice loading. As ice acts as a floating solid body, the results of this thesis could potentially be used to inform future studies into ice hazard assessment.

Chapter 7. Conclusions and Recommendations for Future Work

7.1 Conclusions

The thesis presented herein examined the transport of and loading due to debris in extreme flooding events. The overall research problem was divided in three separate sections: debris transport, debris damming, and debris impact. Based on the results of this study, the following general conclusions can be drawn:

- Debris transport is a complex process influenced by numerous variables. Several main variables were identified in the literature review. Based on the results of this study, the estimation of the magnitude of displacement in the flow direction should consider the bed friction, friction between the debris and bed, the number of debris, and local hydrodynamic conditions.
    - For the estimation of the cross-flow displacement, the initial position of the debris relative to other debris and the local hydrodynamic conditions are the most critical variables.
- The mean displacement in the cross-flow direction for a configuration of debris can be assumed to be zero. The distribution of the cross-flow displacement can be approximately estimated as a Gaussian distribution.
- The evolution of the mean debris velocity in a dam-break wave can be approximately estimated using the bore front velocity. The distribution of the velocity can be approximated using the Kumaraswamy (1980) bounded distribution.
- The steps to debris dam formations seem to exhibit similar properties between steady-state and transient flow conditions. The formation of the surface roller in the transient flow conditions influence the stability of the dam due to the reversing flow velocities.
- The size and shape of the debris have a significant influence on the stability of the debris dam. The larger debris with a high available contact area with the obstacle result in the largest and most stable dams.
- The hydrodynamic conditions dictate the stability and compactness of the debris dam. Higher flow velocities caused the debris to be pushed against the obstacle resulting in more stable and compact dams.
    - Consequently, the higher flow velocities result in greater backwater rise and forces acting on the structure due to the increased constriction of the channel.
- The flow conditions and the momentum of the debris seem to have an influence on the impact geometry. Flow splitting and the surface roller cause changes in the impact axis as the debris rotates, moving from a 1D impact to 3D.
    - As a result, standard methods, such as Coulomb's friction, of estimating forces perpendicular to the primary impact direction do not capture the magnitude of these forces.
- The rigid body, single Degree-of-Freedom (DOF) impact model overestimates the impact forces on a flexible structure as it does not consider the energy absorbed by the structural motion.

    - The proposed two Degree-of-Freedom (2DOF) model considers the structural motion and more accurately estimated the forces, however, due to challenges in estimating the structural stiffness, the model under predicted some cases.
    - As a conservative estimation of the debris impact force, the effective stiffness model proposed by Haehnel and Daly (2004) is the most accurate model.
- The impact of debris agglomerations should be considered in the estimation of design loading conditions. The increased inertia of the impacting debris results in an increase in the impact force.

The thesis provides a simple probabilistic framework for estimating the debris hazard in extreme flooding conditions. The framework provides a basis on which to develop complex models estimating hazard, more accurately representing the physical processes involved in debris transport and impact. The objective of this framework is to provide a methodology for analyzing debris hazard in tsunami, flash floods, and dam-breaks that can be applied by practicing engineers, disaster managements agencies, and insurance companies to estimate the risk and vulnerability of coastal communities.

7.2 Recommendations for Future Work

The studies presented here examines debris hazard assessment methodologies, proposing a basic framework for estimating debris hazards in extreme flooding events. However, further work is necessary to accurately capture the hazard at full-scale, the following additions to the body of knowledge would greatly improve the accuracy of the methodology:

- The development and validation of numerical models capable of addressing debris hazard assessment. Solid body transport has been a challenging endeavour in the numerical modelling of fluid-solid interaction. This is further exacerbated when considering the loading conditions as fluid models often experience instabilities when two solids are in close proximity. Additionally, the temporal resolution for impact conditions must be extremely high.
- High-resolution measurements of the flow conditions around transported debris. This study examined some of the primary variables that may influence the transport of debris though these are predominantly based on variables that would influence the displacement in the flow direction. It is still unclear what the physical processes cause displacement in the cross-flow direction.
- Develop an understanding of the scale effects related to the small-scale testing of debris hazards. To date, no tests have comprehensively examined the scale effects related to debris transport, potentially addressing some of the issues brought up in Section 6.1. Additionally, as shown in Section 5.3, impact forces were sensitive to the stiffness of the debris and structure. Accurately modelling structural elements may be necessary to address this issue in full.
- Examine the full evolution of debris transport in an extreme flooding event. Due to challenges related to accurately modelling the retreating flow in a tsunami, debris motion due to drawdown was not addressed.
- Examine the influence of 3D impact geometry on debris impact forces. This would require a development of sensors or tracking algorithms that can evaluate the 3D position and orientation of debris upon impact.
- Address the issue of added mass on debris impact forces. The added mass results in an increase in the apparent mass of the debris due to the deceleration of fluid around the debris. The contribution of the added mass in the debris impact problem has not been well-established as it is sensitive to the impact geometry and mass of the debris.

- Detailed study of the hydrodynamics around debris dams. Due to the issue of free-floating debris, the hydrodynamics around the dams used in this study could not be evaluated. More detailed measurements may aid in developing an understanding of secondary effects, such as scour, caused by damming.

References

AASHTO. 2012. Bridge design specifications. American Association of State Highway and Transportation Officials, Washington, DC.

Abrate, S. 2005. Impact on composite structures. Cambridge University Press.

Achenbach, E. 1974. The effects of surface roughness and tunnel blockage on the flow past spheres. Journal of Fluid Mechanics 65:113–125.

Aghl, P., C. Naito, and H. Riggs. 2014. Full-scale experimental study of impact demands resulting from high mass, low velocity debris. Journal of Structural Engineering 140:04014006.

Aghl, P. P., C. Naito, and H. Riggs. 2015. Estimation of demands resulting from inelastic axial impact of steel debris. Engineering Structures 82:11–21.

Alam, M. M., Y. Zhou, and X. Wang. 2011. The wake of two side-by-side square cylinders. Journal of Fluid Mechanics 669:432–471.

Alexander, J., and M. J. Cooker. 2016. Moving boulders in flash floods and estimating flow conditions using boulders in ancient deposits. Sedimentology 63:1582–1595.

Anderson, T., T. W. Anderson, T. W. Anderson, T. W. Anderson, and E.-U. Mathématicien. 1958. An introduction to multivariate statistical analysis. Wiley New York.

Anthoine, J., D. Olivari, and D. Portugaels. 2009. Wind-tunnel blockage effect on drag coefficient of circular cylinders. Wind and Structures 12:541–551.

Arikawa, T. 2011. Experimental study on tsunami disaster. 7th Int. Workshop on Coastal Disaster Prevention.

Arikawa, T., D. Ohtsubo, F. Nakano, K. Shimosako, and N. Ishikawa. 2007. Large model tests of drifting container impact force due to surge front tsunami. Proc. of Coastal Engineering 54:846–850.

Árnason, H. 2005. Interactions between an incident bore and a free-standing coastal structure. Washington University.

Arnason, H., C. Petroff, and H. Yeh. 2009. Tsunami bore impingement onto a vertical column. Journal of Disaster Research 4:391–403.

Arrighi, C., F. Castelli, and H. Oumeraci. 2016. Effects of flow orientation on the onset of motion of flooded vehicles. Sustainable Hydraulics in the Era of Global Change:837–841.

ASCE. 2016a. Minimum design loads for buildings and other structures. American Society of Civil Engineers.

ASCE. 2016b. ASCE 7 Chapter 6 Tsunami Loads and Effects. American Society of Civil Engineers.

Baldock, T., D. Peiris, and A. Hogg. 2012. Overtopping of solitary waves and solitary bores on a plane beach. Proceedings of the Royal Society of Science 468:3494–3516.

Bardet, J.-P., C. E. Synolakis, H. L. Davies, F. Imamura, and E. A. Okal. 2003. Landslide tsunamis: recent findings and research directions. Landslide Tsunamis: Recent Findings and Research Directions. Springer.

Barrett, F., and S. Hannoush. 2016. Mitigating the Impacts of Severe Weather. Reports on the Commisoner of the Environment and Sustainable Development Canada.

Bazant, Z. P. 2005. Scaling of structural strength. Butterworth-Heinemann.

Bellos, C., V. Soulis, and J. Sakkas. 1992. Experimental investigation of two-dimensional dam-break induced flows. Journal of Hydraulic Research 30:47–63.

Beltaos, S., B. Burrell, and S. Ismail. 1996. 1991 ice jamming along the Saint John River: a case study. Canadian Journal of Civil Engineering 23:381–394.

Beltaos, S., and T. D. Prowse. 2001. Climate impacts on extreme ice-jam events in Canadian rivers. Hydrological Sciences Journal 46:157–181.

Bernier, C., S. Kameshwar, J. R. Elliott, J. E. Padgett, and P. B. Bedient. 2018. Mitigation Strategies to Protect Petrochemical Infrastructure and Nearby Communities during Storm Surge. Natural Hazards Review 19:04018019.
Blok, J., L. Brozius, J. Dekker, and others. 1983. The impact loads of ships colliding with fixed structures. Offshore Technology Conference. Offshore Technology Conference.
BNPB. 2018. Acceleration of Disaster Casualties Recovery Keeps on Being Intensified in Central Sulawesi, 2113 People Dead. Badan Nasional Penangglulangan Bencana.
Bocchiola, D., M. Rulli, and R. Rosso. 2006. Transport of large woody debris in the presence of obstacles. Geomorphology 76:166–178.
Bocchiola, D., M. Rulli, and R. Rosso. 2008. A flume experiment on the formation of wood jams in rivers. Water Resources Research 44.
BODC. 2018. British Oceanographic Data Center. Natural Environment Research Council. Accessed Jan. 10, 2018.
Boon, J. D. 2012. Evidence of sea level acceleration at US and Canadian tide stations, Atlantic Coast, North America. Journal of Coastal Research 28:1437–1445.
Borrero, J. C., K. Sieh, M. Chlieh, and C. E. Synolakis. 2006. Tsunami inundation modeling for western Sumatra. Proceedings of the National Academy of Sciences 103:19673–19677.
Box, G. E. 1953. Non-normality and tests on variances. Biometrika 40:318–335.
Bradley, K., R. Mallick, D. Alfian, H. Andikagumi, B. Benazir, G. Brocard, G. Feng, E. M. Hill, J. Hubbard, J. Majewski, and others. 2019. Wet rice cultivation was the primary cause of the earthquake-triggered Palu landslides. Earth ArXiV.
Braudrick, C. A., and G. E. Grant. 2000. When do logs move in rivers? Water Resources Research 36:571–583.
Braudrick, C. A., and G. E. Grant. 2001. Transport and deposition of large woody debris in streams: a flume experiment. Geomorphology 41:263–283.
Bremm, G. C., N. Goseberg, T. Schlurmann, and I. Nistor. 2015. Long Wave Flow Interaction with a Single Square Structure on a Sloping Beach. Journal of Marine Science and Engineering 3:821.
Bricker, J. D., S. Gibson, H. Takagi, and F. Imamura. 2015. On the need for larger Manning's roughness coefficients in depth-integrated tsunami inundation models. Coastal Engineering Journal 57:1550005.
Bullock, G., C. Obhrai, D. Peregrine, and H. Bredmose. 2007. Violent breaking wave impacts. Part 1: Results from large-scale regular wave tests on vertical and sloping walls. Coastal Engineering 54:602–617.
Burgett, M., J. Pachuta, E. Padgett, and L. Watson. 2017. Hurricanes and storm events—Lessons learned. Proc. 2017 API Tanks, Valves, and Piping Conference.
Canelas, R. B., A. J. Crespo, J. M. Domınguez, R. M. Ferreira, and M. Gómez-Gesteira. 2016. SPH–DCDEM model for arbitrary geometries in free surface solid–fluid flows. Computer Physics Communications 202:131–140.
Canelas, R. B., J. M. Dominguez, A. J. Crespo, M. Gómez-Gesteira, and R. M. Ferreira. 2015. A Smooth Particle Hydrodynamics discretization for the modelling of free surface flows and rigid body dynamics. International Journal for Numerical Methods in Fluids 78:581–593.
Canelas, R. B., R. M. Ferreira, A. Crespo, and J. Domınguez. 2013. A generalized SPH-DEM discretization for the modelling of complex multiphasic free surface flows. Proceedings of The 8th International SPHERIC workshop.
Carden, L., G. Chock, G. Yu, and I. Robertson. 2015. The new ASCE tsunami design standard applied to mitigate Tohoku tsunami building structural failure mechanisms. Handbook of Coastal Disaster Mitigation for Engineers and Planners. Elsevier.
Chakraborty, J., N. Verma, and R. Chhabra. 2004. Wall effects in flow past a circular cylinder in a plane channel: a numerical study. Chemical Engineering and Processing: Process Intensification 43:1529–1537.

Chanson, H. 2005. Applications of the Saint-Venant equations and method of characteristics to the dam break wave problem. The University of Queensland.
Chanson, H. 2006. Tsunami surges on dry coastal plains: Application of dam break wave equations. Coastal Engineering Journal 48:355–370.
Chanson, H., S. Aoki, and M. Maruyama. 2000. Experimental Investigations of Wave Runup Downstream of Nappe Impact: Applications to Flood Wave Resulting from Dam Overtopping and Tsunami Wave Runup. . Toyohashi University of Technology.
Chanson, H., S. Aoki, and M. Maruyama. 2002. An experimental study of tsunami runup on dry and wet horizontal coastlines. Science of Tsunami Hazards 20:278–293.
Chaplin, J., and P. Teigen. 2003. Steady flow past a vertical surface-piercing circular cylinder. Journal of Fluids and Structures 18:271–285.
Charvet, I., A. Suppasri, and F. Imamura. 2014. Empirical fragility analysis of building damage caused by the 2011 Great East Japan tsunami in Ishinomaki city using ordinal regression, and influence of key geographical features. Stochastic Environmental Research and Risk Assessment 28:1853–1867.
Charvet, I., A. Suppasri, H. Kimura, D. Sugawara, and F. Imamura. 2015. A multivariate generalized linear tsunami fragility model for Kesennuma City based on maximum flow depths, velocities and debris impact, with evaluation of predictive accuracy. Natural Hazards 79:2073–2099.
Chau, K., and J. Bao. 2010. Hydrodynamic analysis of boulder transportation on Phi-Phi Island during the 2004 Indian Ocean Tsunami.
Cheff, I., I. Nistor, and D. Palermo. 2018. Pedestrian evacuation modelling of a Canadian West Coast community from a near-field Tsunami event. Natural Hazards:1–21.
Chen, S., M. Wambsganss, and J. Jendrzejczyk. 1976. Added mass and damping of a vibrating rod in confined viscous fluids. Journal of Applied Mechanics 43:325–329.
Chinnarasri, C., N. Thanasisathit, A. Ruangrassamee, S. Weesakul, and P. Lukkunaprasit. 2013. The impact of tsunami-induced bores on buildings. Proceedings of the Institution of Civil Engineers: Maritime Engineering 166:14–24.
Chock, G., I. Robertson, D. Kriebel, M. Francis, and I. Nistor. 2013. Tohoku, Japan, Earthquake and Tsunami of 2011: Performance of Structures Under Tsunami Loads. ASCE.
Chock, G. Y. 2015. The ASCE 7 Tsunami Loads and Effects Design Standard. Pages 1446–1456 Structures Congress 2015. ASCE.
Chock, G. Y. 2016. Design for tsunami loads and effects in the ASCE 7-16 standard. Journal of Structural Engineering:04016093.
Chouinard, O., S. Plante, and G. Martin. 2008. The community engagement process: A governance approach in adaptation to coastal erosion and flooding in Atlantic Canada. Canadian Journal of Regional Science 31:507–520.
Clague, J. J., A. Munro, and T. Murty. 2003. Tsunami hazard and risk in Canada. Natural Hazards 28:435–463.
Clough, R. W., and J. Penzien. 2003. Dynamics of structures. Computers & Structures, Inc.
Coulomb, C. 1771. Memoires de mathematique et de physique, tirez des registres de l'Academie royale des sciences. . Royal Academy of Science.
Crespo, A., M. Gómez-Gesteira, and R. A. Dalrymple. 2007. Boundary conditions generated by dynamic particles in SPH methods. CMC-TECH Science Press 5:173.
CSA. 2006. Canadian highway bridge design code. CSA.
Currey, J. D. 1988. The effect of porosity and mineral content on the Young's modulus of elasticity of compact bone. Journal of Biomechanics 21:131–139.
D'Alembert, J. L. R. 1743. Traité de Dynamique.
Dai, Z., Y. Huang, H. Cheng, and Q. Xu. 2017. SPH model for fluid–structure interaction and its application to debris flow impact estimation. Landslides 14:917–928.
Derschum, C., I. Nistor, J. Stolle, and N. Goseberg. 2018. Debris impact under extreme hydrodynamic conditions part 1: Hydrodynamics and impact geometry. Coastal Engineering.

Derschum, C., J. Stolle, I. Nistor, and N. Goseberg. 2017. Influence of Wave-Structure Interaction on Tsunami-Driven Debris Impact. International Short Course and Conference on Applied Coastal Research, Santander, Spain.
DFO. 2002. Canada's Oceans Strategy. Department of Fisheries and Oceans Canada.
Donea, J., S. Giuliani, and J.-P. Halleux. 1982. An arbitrary Lagrangian-Eulerian finite element method for transient dynamic fluid-structure interactions. Computer Methods in Applied Mechanics and Engineering 33:689–723.
Douglas, S. 2016. Numerical Modeling of Extreme Hydrodynamic Loading and Pneumatic Long Wave Generation: Application of a Multiphase Fluid Model. University of Ottawa.
El-Alfy, K. 2009. Backwater rise due to flow constriction by bridge piers. Thirteenth International Water Technology Conference:1295–1313.
Elger, D. F., and J. A. Roberson. 2016. Engineering fluid mechanics. Wiley Hoboken (NJ).
Esteban, M., H. Takagi, and T. Shibayama. 2015. Handbook of Coastal Disaster Mitigation for Engineers and Planners.
EU. 2006. Eurocode 1: Actions on structures. EU Science Committee.
Al-Faesly, T., D. Palermo, I. Nistor, and A. Cornett. 2012. Experimental modeling of extreme hydrodynamic forces on structural models. International Journal of Protective Structures 3:477–506.
Farrar, D. E., and R. R. Glauber. 1967. Multicollinearity in regression analysis: the problem revisited. The Review of Economic and Statistics: 92–107.
Fekken, G. 2004. Numerical simulation of free-surface flow with moving rigid bodies. University of Groningén.
FEMA. 2012. P646 Guidelines for Design of Structure for Vertical Evacuation from Tsunamis. Federal Emergency Management Agency.
Fenton, J. 2003. The effects of obstacles on surface levels and boundary resistance in open channels. Proc. of the 30th IAHR Congress.
Fisher, R. A. 1925. Statistical methods for research workers. Genesis Publishing Pvt Ltd.
Foster, A., T. Rossetto, and W. Allsop. 2017. An experimentally validated approach for evaluating tsunami inundation forces on rectangular buildings. Coastal Engineering 128:44–57.
Fourtakas, G., R. Vacondio, and B. D. Rogers. 2015. On the approximate zeroth and first-order consistency in the presence of 2-D irregular boundaries in SPH obtained by the virtual boundary particle methods. International Journal for Numerical Methods in Fluids 78:475–501.
Fraccarollo, L., and E. F. Toro. 1995. Experimental and numerical assessment of the shallow water model for two-dimensional dam-break type problems. Journal of Hydraulic Research 33:843–864.
Frankel, I., and D. Weihs. 1990. Hydrodynamic theory of glancing impact. Journal of Fluid Mechanics 216:213–229.
Friedland, J., H. Cheng, and A. Peleshok. 2014. Water damage risk and Canadian property insurance pricing. Canadian Institute of Actuaries, Ottawa. Prepared by KPMG.
Fritz, H. M., J. C. Borrero, C. E. Synolakis, and J. Yoo. 2006. 2004 Indian Ocean tsunami flow velocity measurements from survivor videos. Geophysical Research Letters 33.
Fritz, H. M., D. A. Phillips, A. Okayasu, T. Shimozono, H. Liu, F. Mohammed, V. Skanavis, C. E. Synolakis, and T. Takahashi. 2012. The 2011 Japan tsunami current velocity measurements from survivor videos at Kesennuma Bay using LiDAR. Geophysical Research Letters 39.
GDV. 2003. Cargo loss prevention information from German marine insurers. Container Handbook.
Gere, J. M., and S. P. Timoshenko. 1984. Mechanics of materials.
Ghobarah, A., M. Saatcioglu, and I. Nistor. 2006. The impact of the 26 December 2004 earthquake and tsunami on structures and infrastructure. Engineering structures 28:312–326.
Glowinski, R., T.-W. Pan, and J. Periaux. 1997. A Lagrange multiplier/fictitious domain method for the numerical simulation of incompressible viscous flow around moving rigid bodies:(I) case where the rigid body motions are known a priori. Comptes Rendus de l'Académie des Sciences-Series I-Mathematics 324:361–369.

Goldfinger, C., C. H. Nelson, A. E. Morey, J. E. Johnson, J. R. Patton, E. Karabanov, J. Gutierrez-Pastor, A. T. Eriksson, E. Gracia, G. Dunhill, and others. 2012. Turbidite event history: Methods and implications for Holocene paleoseismicity of the Cascadia subduction zone. US Geological Survey Professional Paper 1661:170.

Gomez-Gesteira, M., B. D. Rogers, A. J. Crespo, R. Dalrymple, M. Narayanaswamy, and J. M. Dominguez. 2012. SPHysics–development of a free-surface fluid solver–Part 1: Theory and formulations. Computers & Geosciences 48:289–299.

Goring, D. G., and V. I. Nikora. 2002. Despiking acoustic Doppler velocimeter data. Journal of Hydraulic Engineering 128:117–126.

Goseberg, N. 2013a. Reduction of maximum tsunami run-up due to the interaction with beachfront development–application of single sinusoidal waves. Natural Hazards and Earth System Science 13:11.

Goseberg, N. 2013b. Reduction of maximum tsunami run-up due to the interaction with beachfront development - application of single sinusoidal waves. Natural Hazards Earth System Science 1:1119–1171.

Goseberg, N., I. Nistor, T. Mikami, T. Shibayama, and J. Stolle. 2016a. Nonintrusive Spatiotemporal Smart Debris Tracking in Turbulent Flows with Application to Debris-Laden Tsunami Inundation. Journal of Hydraulic Engineering:04016058.

Goseberg, N., and T. Schlurmann. 2014. Non-stationary flow around buildings during run-up of tsunami waves on a plain beach. Coastal Engineering Proceedings 1:21.

Goseberg, N., A. Stahlmann, S. Schimmels, and T. Schlurmann. 2009. Highly-resolved numerical modeling of tsunami run-up and inundation scenario in the city of Padang, West Sumatra. Proc. of the 31st Int. Conference on Coastal Engineering.

Goseberg, N., J. Stolle, C. Derschum, and I. Nistor. 2017. Swing Gate Generated Dam-Break Waves. Proc. of the 37th IAHR World Congress.

Goseberg, N., J. Stolle, I. Nistor, and T. Shibayama. 2016b. Experimental analysis of debris motion due the obstruction from fixed obstacles in tsunami-like flow conditions. Coastal Engineering 118:35–49.

Goseberg, N., A. Wurpts, and T. Schlurmann. 2013. Laboratory-scale generation of tsunami and long waves. Coastal Engineering 79:57–74.

Gottstein, G. 2013. Physical foundations of materials science. Springer Science & Business Media.

Granville, P. S. 1976. Elements of the drag of underwater bodies. DTIC Document.

Greenberg, D. A., T. Murty, and A. Ruffman. 1993. A numerical model for the Halifax Harbor tsunami due to the 1917 explosion. Marine Geodesy 16:153–167.

Gupta, A. K., and S. Nadarajah. 2004. Handbook of beta distribution and its applications. CRC press.

Hadzic, H. 2006. Development and application of finite volume method for the computation of flows around moving bodies on unstructured, overlapping grids. Technische Universität Hamburg.

Haehnel, R. B., and S. F. Daly. 2002. Maximum Impact Force of Woody Debris on Floodplain Structures. USACE.

Haehnel, R. B., and S. F. Daly. 2004. Maximum impact force of woody debris on floodplain structures. Journal of Hydraulic Engineering 130:112–120.

Häfen, H., J. Stolle, N. Goseberg, and I. Nistor. 2018. Lift and Swing Gate Modelling For Dam-break Generation With A Particle-Based Method. Proc. of the 7th IAHR International Symposium on Hydraulic Structures.

Hafsteinsson, H. J., F. M. Evers, and W. H. Hager. 2017. Solitary wave run-up: wave breaking and bore propagation. Journal of Hydraulic Research:1–12.

Hager, W. H. 1989. Supercritical flow in channel junctions. Journal of Hydraulic Engineering 115:595–616.

Hashemi, M., R. Fatehi, and M. Manzari. 2012. A modified SPH method for simulating motion of rigid bodies in Newtonian fluid flows. International Journal of Non-Linear Mechanics 47:626–638.

Hatzikyriakou, A., and N. Lin. 2017. Impact of performance interdependencies on structural vulnerability: A systems perspective of storm surge risk to coastal residential communities. Reliability Engineering & System Safety 158:106–116.
Hay, A. D. 1947. Flow about semi-submerged cylinders of finite length.
Heidarzadeh, M., A. Muhari, and A. B. Wijanarto. 2018. Insights on the Source of the 28 September 2018 Sulawesi Tsunami, Indonesia Based on Spectral Analyses and Numerical Simulations. Pure and Applied Geophysics:1–19.
Heller, V. 2011. Scale effects in physical hydraulic engineering models. Journal of Hydraulic Research 49:293–306.
Heller, V., and W. H. Hager. 2010. Impulse product parameter in landslide generated impulse waves. Journal of Waterway, Port, Coastal, and Ocean Engineering 136:145–155.
Hertz, H. 1882. Über die Berührung fester elastischer Körper. Journal für die reine und angewandte Mathematik 92:156–171.
Higman, B., D. H. Shugar, C. P. Stark, G. Ekström, M. N. Koppes, P. Lynett, A. Dufresne, P. J. Haeussler, M. Geertsema, S. Gulick, and others. 2018. The 2015 landslide and tsunami in Taan Fiord, Alaska. Scientific Reports 8:12993.
Hirt, C. W., and B. D. Nichols. 1981. Volume of fluid (VOF) method for the dynamics of free boundaries. Journal of Computational Physics 39:201–225.
Huang, N. E., Z. Shen, S. R. Long, M. C. Wu, H. H. Shih, Q. Zheng, N.-C. Yen, C. C. Tung, and H. H. Liu. 1998. The empirical mode decomposition and the Hilbert spectrum for nonlinear and non-stationary time series analysis. Proc. of the Royal Society of London A: mathematical, physical and engineering sciences. The Royal Society.
Hughes, S. A. 1993. Physical models and laboratory techniques in coastal engineering. World Scientific.
Hui, G., S. Li, P. Wang, Y. Suo, Q. Wang, and I. D. Somerville. 2018. Linkage between reactivation of the sinistral strike-slip faults and 28 September 2018 Mw7. 5 Palu earthquake, Indonesia. Science Bulletin 63:1635–1640.
Ikeno, M., N. Kihara, and D. Takabatake. 2013. Simple and practical estimation of movement possibility and collision force of debris due to tsunami. J. JSCE, B2 (Coastal Eng.) 69:861–865.
Ikeno, M., D. Takabatake, N. Kihara, H. Kaida, Y. Miyagawa, and A. Shibayama. 2016. Improvement of collision force formula for woody debris by airborne and hydraulic experiments. Coastal Engineering Journal 58:1640022.
Imamura, F., K. Goto, and S. Ohkubo. 2008. A numerical model for the transport of a boulder by tsunami. Journal of Geophysical Research: Oceans (1978–2012) 113.
Ioualalen, M., J. Asavanant, N. Kaewbanjak, S. Grilli, J. Kirby, and P. Watts. 2007. Modeling the 26 December 2004 Indian Ocean tsunami: Case study of impact in Thailand. Journal of Geophysical Research: Oceans 112.
IPCC. 2014. Climate Change 2014–Impacts, Adaptation and Vulnerability: Regional Aspects. . Cambridge University Press.
Iqbal, N., and C. Rauh. 2016. Coupling of discrete element model (DEM) with computational fluid mechanics (CFD): a validation study. Applied Mathematics and Computation 277:154–163.
Ivanov, A. 1995. On multiple impact. Journal of Applied Mathematics and Mechanics 59:887–902.
Jánosi, I. M., D. Jan, K. G. Szabó, and T. Tél. 2004. Turbulent drag reduction in dam-break flows. Experiments in Fluids 37:219–229.
Jones, M. 2009. Kumaraswamy's distribution: A beta-type distribution with some tractability advantages. Statistical Methodology 6:70–81.
Kameshwar, S., and J. E. Padgett. 2018. Storm surge fragility assessment of above ground storage tanks. Structural safety 70:48–58.
Kamphuis, J. W. 2010. Introduction to coastal engineering and management. World Scientific.
Kan, H.-C., H. Udaykumar, W. Shyy, and R. Tran-Son-Tay. 1998. Hydrodynamics of a compound drop with application to leukocyte modeling. Physics of fluids 10:760–774.

Kenney, J. F. 1962a. Mathematics of Statistics. Pages 77–80 *in* E. S. Keeping, editor., 3rd edition. Van Nostrand, Princton, NJ.
Kenney, J. F. 1962b. Mathematics of Statistics. Pages 77–80 *in* E. S. Keeping, editor., 3rd edition. Van Nostrand, Princton, NJ.
Khankandi, A., A. Tahershamsi, and S. Soares-Frazão. 2012. Experimental investigation of reservoir geometry effect on dam-break flow. Journal of Hydraulic Research 50:376–387.
Khowitar, E., H. R. Riggs, and M. H. Kobayashi. 2014. Beam response to longitudinal impact by a pole. Journal of Engineering Mechanics 140:04014045.
Kleefsman, K., G. Fekken, A. Veldman, B. Iwanowski, and B. Buchner. 2005. A volume-of-fluid based simulation method for wave impact problems. Journal of Computational Physics 206:363–393.
Knorr, W., and F. Kutzner. 2008. EcoTransIT: Ecological Transport Information Tool - Environmental Method and Data. IFEU Heidelberg.
Ko, H. T.-S., D. T. Cox, H. R. Riggs, and C. J. Naito. 2015. Hydraulic experiments on impact forces from tsunami-driven debris. Journal of Waterway, Port, Coastal and Ocean Engineering 141:04014043.
Kocaman, S., and H. Ozmen-Cagatay. 2012. The effect of lateral channel contraction on dam break flows: Laboratory experiment. Journal of Hydrology 432:145–153.
Korobkin, A. 1998. Wave impact on the center of an Euler beam. Journal of Applied Mechanics and Technical Physics 39:770–781.
Kriebel, D. L., P. J. Lynett, D. T. Cox, C. M. Petroff, I. N. Robertson, and G. Y. Chock. 2017. Energy method for approximating overland tsunami flows. Journal of Waterway, Port, Coastal, and Ocean Engineering 143:04017014.
Kruggel-Emden, H., S. Wirtz, and V. Scherer. 2008. A study on tangential force laws applicable to the discrete element method (DEM) for materials with viscoelastic or plastic behavior. Chemical Engineering Science 63:1523–1541.
Kulkarni, R., I. Wong, J. Zachariasen, C. Goldfinger, and M. Lawrence. 2013. Statistical Analyses of Great Earthquake Recurrence along the Cascadia Subduction Zone: Statistical Analyses of Great Earthquake Recurrence along the Cascadia Subduction Zone. Bulletin of the Seismological Society of America 103:3205–3221.
Kumaraswamy, P. 1980. A generalized probability density function for double-bounded random processes. Journal of Hydrology 46:79–88.
Lauber, G., and W. H. Hager. 1998. Experiments to dambreak wave: Horizontal channel. Journal of Hydraulic Research 36:291–307.
Leonardi, A., F. K. Wittel, M. Mendoza, R. Vetter, and H. J. Herrmann. 2016. Particle–fluid–structure interaction for debris flow impact on flexible barriers. Computer-Aided Civil and Infrastructure Engineering 31:323–333.
Liang, D., W. Jian, S. Shao, R. Chen, and K. Yang. 2017. Incompressible SPH simulation of solitary wave interaction with movable seawalls. Journal of Fluids and Structures 69:72–88.
Lin, N., and E. Vanmarcke. 2010. Windborne debris risk analysis—Part I. Introduction and methodology. Wind and Structures 13:191.
Lind, S., R. Xu, P. Stansby, and B. D. Rogers. 2012. Incompressible smoothed particle hydrodynamics for free-surface flows: A generalised diffusion-based algorithm for stability and validations for impulsive flows and propagating waves. Journal of Computational Physics 231:1499–1523.
Løvholt, F., G. Pedersen, C. B. Harbitz, S. Glimsdal, and J. Kim. 2015. On the characteristics of landslide tsunamis. Philosophical Transactions of the Royal Society A: Mathematical, Physical and Engineering Sciences 373:20140376.
Løvholt, F., I. Schulten, D. Mosher, C. Harbitz, and S. Krastel. 2018. Modelling the 1929 Grand Banks slump and landslide tsunami. Geological Society, London, Special Publications 477:477–28.
Lu, S., H. T. Shen, and R. D. Crissman. 1999. Numerical study of ice jam dynamics in upper Niagara River. Journal of Cold Regions Engineering 13:78–102.
Lynett, P., J. Borrero, R. Wilson, K. Miller, and S. Son. 2013. Detailed Simulation of Tsunami-Induced Currents in California Ports and Harbors. Ports 2013: Success through Diversification.

Madsen, P. A., D. R. Fuhrman, and H. A. Schaeffer. 2008. On the solitary wave paradigm for tsunamis. Journal of Geophysical Research: Oceans 113.
Malhotra, M., and R. Subramanian. 1994. Textbook in Applied Mechanics. New Age International.
Manson, G. K. 2005. On the coastal populations of Canada and the world. Canadian Coastal Conference 2005.
Marzougui, D., R. R. Samaha, L. Nix, and C.-D. S. Kan. 2013. Extended Validation of the Finite Element Model for the 2010 Toyota Yaris Passenger Sedan (MASH 1100kg Vehicle).
Matskevitch, D. 1997. Eccentric impact of an ice feature: linearized model. Cold regions science and technology 25:159–171.
Matsutomi, H. 2009. Method for estimating collision force of driftwood accompanying tsunami inundation flow. Journal of Disaster Research 4:435–440.
Matsutomi, H., M. Fujii, and T. Yamaguchi. 2008. Experiments and development of a model on the inundated flow with floating bodies. Coastal Engineering:1458–1470.
Matsutomi, H., and K. Okamoto. 2010. Inundation flow velocity of tsunami on land. Island Arc 19:443–457.
McDonald, J. H. 2009. Handbook of biological statistics. Sparky House Publishing Baltimore, MD.
Melville, B. W., and D. Dongol. 1992. Bridge pier scour with debris accumulation. Journal of Hydraulic Engineering 118:1306–1310.
Mitobe, Y., M. B. Adityawan, M. Roh, H. Tanaka, K. Otsushi, and T. Kurosawa. 2016. Experimental Study on Embankment Reinforcement by Steel Sheet Pile Structure Against Tsunami Overflow. Coastal Engineering Journal: 1640018.
Monaghan, J. J. 1992. Smoothed particle hydrodynamics. Annual review of astronomy and astrophysics 30:543–574.
Monaghan, J. J. 1994. Simulating free surface flows with SPH. Journal of computational physics 110:399–406.
Moody, L. F. 1944. Friction factors for pipe flow. Transportation ASME 66:671–684.
Moser, W., H. Antes, and G. Beer. 2005. Soil-structure interaction and wave propagation problems in 2D by a Duhamel integral based approach and the convolution quadrature method. Computational Mechanics 36:431–443.
Naito, C., C. Cercone, H. R. Riggs, and D. Cox. 2014. Procedure for site assessment of the potential for tsunami debris impact. Journal of Waterway, Port, Coastal and Ocean Engineering 140:223–232.
Naito, C., D. Cox, Q.-S. “Kent Yu, and H. Brooker. 2012. Fuel storage container performance during the 2011 Tohoku, Japan, tsunami. Journal of Performance of Constructed Facilities 27:373–380.
Nandasena, N., R. Paris, and N. Tanaka. 2011. Reassessment of hydrodynamic equations: minimum flow velocity to initiate boulder transport by high energy events (storms, tsunamis). Marine Geology 281:70–84.
Navaratnam, C. U., A. Tørum, and Ø. A. Arntsen. 2013. Preliminary analysis of wave slamming force response data from tests on a truss structure in large wave flume, Hannover, Germany. Department of Civil and Transport Engineering, NTNU, Trondheim, Norway.
NG. 2018. The Science of Indonesia’s Surprise Tsunami. National Geographic.
Nistor, I., N. Goseberg, T. Mikami, T. Shibayama, J. Stolle, R. Nakamura, and S. Matsuba. 2016. Hydraulic Experiments on Debris Dynamics over a Horizontal Plane. Journal of Waterway, Port, Coastal and Ocean Engineering: 04016022.
Nistor, I., N. Goseberg, and J. Stolle. 2017. Tsunami-Driven Debris Motion and Loads: A Critical Review. Frontiers in Built Environment 3:2.
Nistor, I., Y. Nouri, D. Palermo, and A. Cornett. 2009. Experimental investigation of the impact of a tsunami-induced bore on structures. Proceedings of the Coastal Engineering Conference.
Nistor, I., and D. Palermo. 2015. Post-Tsunami Engineering Forensics: Tsunami Impact on Infrastructure. Lessons from 2004 Indian Ocean, 2010 Chile, and 2011 Tohoku Japan Tsunami Field Surveys. Handbook of Coastal Disasters. Elsevier.

Nott, J. 2003. Waves, coastal boulder deposits and the importance of the pre-transport setting. Earth and Planetary Science Letters 210:269–276.
Nouri, Y., I. Nistor, D. Palermo, and A. Cornett. 2010. Experimental investigation of tsunami impact on free standing structures. Coastal Engineering Journal 52:43–70.
NRC. 2005. National Building Code of Canada. Canadian Commission on Building and Fire Codes.
Oertel, M., and D. B. Bung. 2012. Initial stage of two-dimensional dam-break waves: Laboratory versus VOF. Journal of Hydraulic Research 50:89–97.
Omidvar, P., P. K. Stansby, and B. D. Rogers. 2013. SPH for 3D floating bodies using variable mass particle distribution. International Journal for Numerical Methods in Fluids 72:427–452.
Oumeraci, H., H. Partenscky, S. Kohlhase, and P. Klammer. 1993. Impact loading and dynamic response of caisson breakwaters - Results of large-scale model tests. Proc. of the International Conference of Coastal Engineering.
Ozmen-Cagatay, H., and S. Kocaman. 2010. Dam-break flows during initial stage using SWE and RANS approaches. Journal of Hydraulic Research 48:603–611.
Ozmen-Cagatay, H., and S. Kocaman. 2011. Dam-break flow in the presence of obstacle: experiment and CFD simulation. Engineering Applications of Computational Fluid Mechanics 5:541–552.
Paczkowski, K., H. R. Riggs, C. J. Naito, and A. Lehmann. 2012. A one-dimensional model for impact forces resulting from high mass, low velocity debris. Structural Engineering and Mechanics 42:831–847.
Pagliara, S., and I. Carnacina. 2010. Temporal scour evolution at bridge piers: Effect of wood debris roughness and porosity. Journal of Hydraulic Research 48:3–13.
Pagliara, S., and I. Carnacina. 2013. Bridge pier flow field in the presence of debris accumulation. Proc. of the Institution of Civil Engineers-Water Management. Thomas Telford Ltd.
Palermo, D., I. Nistor, Y. Nouri, and A. Cornett. 2009. Tsunami loading of near-shoreline structures: a primer. Canadian Journal of Civil Engineering 36:1804–1815.
Palermo, D., I. Nistor, M. Saatcioglu, and A. Ghobarah. 2013. Impact and damage to structures during the 27 February 2010 Chile tsunami. Canadian Journal of Civil Engineering 40:750–758.
Park, H., D. T. Cox, P. J. Lynett, D. M. Wiebe, and S. Shin. 2013. Tsunami inundation modeling in constructed environments: a physical and numerical comparison of free-surface elevation, velocity, and momentum flux. Coastal Engineering 79:9–21.
Parola, A. C. 2000. Debris forces on highway bridges. Transportation Research Board.
Pasha, G. A., and N. Tanaka. 2016. Effectiveness of Finite Length Inland Forest in Trapping Tsunami-Borne Wood Debris. Journal of Earthquake and Tsunami:1650008.
Peakall, J., and J. Warburton. 1996. Surface tension in small hydraulic river models - the significance of the Weber number. Journal of Hydrology New Zealand 35:199–212.
Peskin, C. S. 1977. Numerical analysis of blood flow in the heart. Journal of Computational Physics 25:220–252.
Pfister, M., D. Capobianco, B. Tullis, and A. J. Schleiss. 2013. Debris-blocking sensitivity of piano key weirs under reservoir-type approach flow. Journal of Hydraulic Engineering 139:1134–1141.
Pilotti, M., A. Maranzoni, M. Tomirotti, and G. Valerio. 2011. 1923 Gleno Dam break: Case study and numerical modeling. Journal of Hydraulic Engineering 137:480–492.
Pozzetti, G., and B. Peters. 2018. A multiscale DEM-VOF method for the simulation of three-phase flows. International Journal of Multiphase Flow 99:186–204.
Priest, G. R., C. Goldfinger, K. Wang, R. C. Witter, Y. Zhang, and A. M. Baptista. 2010. Confidence levels for tsunami-inundation limits in northern Oregon inferred from a 10,000-year history of great earthquakes at the Cascadia subduction zone. Natural Hazards 54:27–73.
Qi, Z., I. Eames, and E. Johnson. 2014. Force acting on a square cylinder fixed in a free-surface channel flow. Journal of Fluid Mechanics 756:716–727.
Quinn, D., and K. Bairavarasu. 2006. Near-simultaneous impacts. International Journal of Impact Engineering 32:889–904.
Rachev, S. T. 1991. Probability metrics and the stability of stochastic models. John Wiley & Son Ltd.

Ren, B., M. He, P. Dong, and H. Wen. 2015. Nonlinear simulations of wave-induced motions of a freely floating body using WCSPH method. Applied Ocean Research 50:1–12.
Riggs, H., D. Cox, C. Naito, M. Kobayashi, P. P. Aghl, H.-S. Ko, and E. Khowitar. 2014. Experimental and Analytical Study of Water-Driven Debris Impact Forces on Structures. Journal of Offshore Mechanics and Arctic Engineering 136:041603.
Rilling, G., P. Flandrin, P. Goncalves, and others. 2003. On empirical mode decomposition and its algorithms. IEEE-EURASIP workshop on Non-linear Signal and Image Processing. IEEER.
Ritter, A. 1892. Die fortpflanzung der wasserwellen. Zeitschrift Verein Deutscher Ingenieure 36:947–954.
Robertson, I., L. Carden, R. Riggs, S. Yim, Y. Young, K. Paczkowski, and D. Witt. 2010. Reconnaissance following the September 29th, 2009 Tsunami in Samoa. University of Hawaii UHM/CEE/10-01.
Robertson, I., M. Esteban, J. Stolle, T. Takabatake, H. Mulchandani, T. Kijewski-Correa, D. Prevatt, D. Roueche, and K. Mosalam. 2019. Palu Earthquake and Tsunami, Sulawesi, Indonesia Field Assessment Team Early Access Reconnaissance Report. NHERI DesignSafe-CI.
Robertson, I., H. R. Riggs, S. C. Yim, and Y. L. Young. 2007. Lessons from Hurricane Katrina storm surge on bridges and buildings. Journal of Waterway, Port, Coastal, and Ocean Engineering 133:463–483.
Roeber, V., and J. D. Bricker. 2015. Destructive tsunami-like wave generated by surf beat over a coral reef during Typhoon Haiyan. Nature Communications 6.
Rogers, B. D., R. A. Dalrymple, and P. K. Stansby. 2009. SPH modeling of floating bodies in the surf zone. 01613782:204–215.
Rossetto, T., W. Allsop, I. Charvet, and D. I. Robinson. 2011. Physical modelling of tsunami using a new pneumatic wave generator. Coastal Engineering 58:517–527.
Rueben, M., D. Cox, R. Holman, S. Shin, and J. Stanley. 2014. Optical Measurements of Tsunami Inundation and Debris Movement in a Large-Scale Wave Basin. Journal of Waterway, Port, Coastal, and Ocean Engineering 141.
Rusydi, M., and R. Efendi. 2018. Earthquake Hazard Analysis Use Vs30 Data In Palu. Journal of Physics: Conference Series. IOP Publishing.
Saatcioglu, M., A. Ghobarah, and I. Nistor. 2005. Effects of the December 26, 2004 Sumatra earthquake and tsunami on physical infrastructure. ISET Journal of earthquake technology 42:79–94.
Saeki, H., and A. Ozaki. 1980. Ice forces on piles. Pages 342–350 Physics and Mechanics of Ice. Springer.
Saha, A., K. Muralidhar, and G. Biswas. 2000. Experimental study of flow past a square cylinder at high Reynolds numbers. Experiments in Fluids 29:553–563.
Sassa, S., and T. Takagawa. 2018. Liquefied gravity flow-induced tsunami: first evidence and comparison from the 2018 Indonesia Sulawesi earthquake and tsunami disasters. Landslides:1–6.
Schimmels, S., V. Sriram, and I. Didenkulova. 2016. Tsunami generation in a large scale experimental facility. Coastal Engineering 110:32–41.
Schmocker, L., and W. H. Hager. 2011. Probability of drift blockage at bridge decks. Journal of Hydraulic Engineering 137:470–479.
Schmocker, L., and W. H. Hager. 2013. Scale modeling of wooden debris accumulation at a debris rack. Journal of Hydraulic Engineering 139:827–836.
Seghete, V., and T. Murphey. 2010. Variational solutions to simultaneous collisions between multiple rigid bodies. Pages 2731–2738 Robotics and Automation (ICRA), 2010 IEEE International Conference on. . IEEE.
Seghete, V., and T. Murphey. 2012. Conditions for uniqueness in simultaneous impact with application to mechanical design. Robotics and Automation (ICRA), 2012 IEEE International Conference. IEEE.
Seiffert, B., M. Hayatdavoodi, and R. C. Ertekin. 2014. Experiments and computations of solitary-wave forces on a coastal-bridge deck. Part I: Flat Plate. Coastal Engineering 88:194–209.

Shafiei, S., B. W. Melville, and A. Y. Shamseldin. 2016a. Experimental investigation of tsunami bore impact force and pressure on a square prism. Coastal Engineering 110:1–16.
Shafiei, S., B. W. Melville, A. Y. Shamseldin, S. Beskhyroun, and K. N. Adams. 2016b. Measurements of tsunami-borne debris impact on structures using an embedded accelerometer. Journal of Hydraulic Research 54:1–15.
Shan, T., and J. Zhao. 2014. A coupled CFD-DEM analysis of granular flow impacting on a water reservoir. Acta Mechanica 225:2449–2470.
Shao, S., and H. Gotoh. 2004. Simulating coupled motion of progressive wave and floating curtain wall by SPH-LES model. Coastal Engineering Journal 46:171–202.
Shapiro, S. S., and M. B. Wilk. 1965. An analysis of variance test for normality (complete samples). Biometrika 52:591–611.
She, Z.-S., and E. Leveque. 1994. Universal scaling laws in fully developed turbulence. Physical review letters 72:336.
Smirnov, N. 1948. Table for estimating the goodness of fit of empirical distributions. The Annals of Mathematical Statistics 19:279–281.
Snedecor, G., and W. Cochran. 1989. Statistical Methods. Iowa State. University Press.
Soares-Frazão, S., and Y. Zech. 2007. Experimental study of dam-break flow against an isolated obstacle. Journal of Hydraulic Research 45:27–36.
Stancanelli, L., S. Lanzoni, and E. Foti. 2015. Propagation and deposition of stony debris flows at channel confluences. Water Resources Research 51:5100–5116.
Stansby, P., A. Chegini, and T. Barnes. 1998. The initial stages of dam-break flow. Journal of Fluid Mechanics 370:203–220.
Stevens, B. L., F. L. Lewis, and E. N. Johnson. 2015. Aircraft control and simulation: dynamics, controls design, and autonomous systems. John Wiley & Sons.
St-Germain, P., I. Nistor, R. Townsend, and T. Shibayama. 2013. Smoothed-particle hydrodynamics numerical modeling of structures impacted by tsunami bores. Journal of Waterway, Port, Coastal, and Ocean Engineering 140:66–81.
Stolle, J., C. Derschum, N. Goseberg, I. Nistor, and E. Petriu. 2018a. Debris impact under extreme hydrodynamic conditions part 2: Impact force responses for non-rigid debris collisions. Coastal Engineering 141:107–118.
Stolle, J., B. Ghodoosipour, C. Derschum, I. Nistor, E. Petriu, and N. Goseberg. 2018b. Swing Gate Generated Dam-break Waves. Journal of Hydraulic Research 0:1–13.
Stolle, J., N. Goseberg, I. Nistor, and E. Petriu. 2018c. Probabilistic Investigation and Risk Assessment of Debris Transport in Extreme Hydrodynamic Conditions. Journal of Waterways, Ports, Oceans and Coastal Engineering 144:04017039.
Stolle, J., N. Goseberg, I. Nistor, and E. Petriu. 2019a. Debris Impact Forces on Flexible Structures in Extreme Hydrodynamic Conditions. Journal of Fluids and Structures 84:391–407.
Stolle, J., I. Nistor, and N. Goseberg. 2016. Optical Tracking of Floating Shipping Containers in a High-Velocity Flow. Coastal Engineering Journal 58:1650005.
Stolle, J., I. Nistor, N. Goseberg, T. Mikami, and T. Shibayama. 2017a. Entrainment and Transport Dynamics of Shipping Containers in Extreme Hydrodynamic Conditions. Coastal Engineering Journal 59:1750011.
Stolle, J., I. Nistor, N. Goseberg, T. Mikami, T. Shibayama, R. Nakamura, and S. Matsuba. 2015. Flood-Induced Debris Dynamics over a Horizontal Surface. Coastal Structures and Solutions to Coastal Disasters. ASCE-COPRI.
Stolle, J., T. Takabatake, G. Hamano, H. Ishii, K. Iimura, T. Shibayama, I. Nistor, N. Goseberg, and E. Petriu. 2019b. Debris Transport over a Sloped Surface in Tsunami-Like Flow Conditions. Coastal Engineering Journal 0:1–15.
Stolle, J., T. Takabatake, T. Mikami, T. Shibayama, N. Goseberg, I. Nistor, and E. Petriu. 2017b. Experimental Investigation of Debris-Induced Loading in Tsunami-Like Flood Events. Geosciences 7:74.

Stolle, J., T. Takabatake, I. Nistor, T. Mikami, S. Nishizaki, G. Hamano, H. Ishii, T. Shibayama, N. Goseberg, and E. Petriu. 2018d. Experimental investigation of debris damming loads under transient supercritical flow conditions. Coastal Engineering 139:16–31.
Stronge, W. J. 2004. Impact mechanics. Cambridge University Press.
Sumer, B. M., and J. Fredsøe. 2006. Hydrodynamics around cylindrical structures. World Scientific.
Swidan, A., W. Amin, D. Ranmuthugala, G. Thomas, and I. Penesis. 2013. Numerical prediction of symmetric water impact loads on wedge shaped hull form using CFD. World Journal of Mechanics 3:311.
Takabatake, T., P. St-Germain, I. Nistor, J. Stolle, and T. Shibayama. 2019. Numerical modelling of coastal inundation from Cascadia Subduction Zone tsunamis and implications for coastal communities on western Vancouver Island, Canada. Natural Hazards 0:1-25.
Takahashi, S., Y. Kuriyama, T. Tomita, Y. Kawai, T. Arikawa, and D. Tatsumi. 2011. Urgent survey for 2011 Great East Japan Earthquake and Tsunami disaster in ports and coasts Part I (tsunami). Port and Air Port Research Institute.
Takahashi, S., T. Sugano, T. Tomita, T. Arikawa, D. Tatsumi, H. Kashima, S. Murata, Y. Matsuoka, and T. Nakamura. 2010. Joint survey for 2010 Chilean earthquake and tsunami disaster in ports and coasts. Port and Airport Research Institution.
Te Chow, V. 1959. Open channel hydraulics. McGraw-Hill Book Company, Inc; New York.
Thornton, C., and K. Yin. 1991. Impact of elastic spheres with and without adhesion. Powder technology 65:153–166.
Timoshenko, S. 1914. Zur Frage nach der Wirkung eines Stoßes auf einen Balken. Zeitschrift fur Mathematik und Physik 62:198–209.
Titov, V. V., and C. E. Synolakis. 1997. Extreme inundation flows during the Hokkaido-Nansei-Oki tsunami. Geophysical Research Letters 24:1315–1318.
Tutar, M., and G. Oguz. 2002. Large eddy simulation of wind flow around parallel buildings with varying configurations. Fluid Dynamics Research 31:289–315.
USDA. 2017. Tested Accuracy of GPS Tools. Forestry Services USDA.
USGS. 2018. Earthquake Face and Statistics. U.S. Geological Survey.
Waldner, P., D. Köchli, T. Usbeck, L. Schmocker, F. Sutter, C. Rickli, D. Rickenmann, D. Lange, N. Hilker, A. Wirsch, and others. 2007. Schwemmholz des Hochwassers 2005-Schlussbericht des WSL-Teilprojekts Schwemmholz der Ereignisanalyse BAFU/WSL des Hochwassers 2005. Eidgenössische Forschungsanstalt für Wald Schnee und Landschaft (WSL)(ed.). Birmensdorf.
Weiler, O., and J. Dekker. 2003. Mooring container ships exposed to long waves. Proc. Of the 13th International Harbour Congress. Antwerp, Belgium.
Weiss, R., and P. Diplas. 2015. Untangling boulder dislodgement in storms and tsunamis: Is it possible with simple theories? Geochemistry, Geophysics, Geosystems 16:890–898.
Whitham, G. B. 1955. The Effects Of Hydraulic Resistance In The Dam-break Problem. Proceedings of the Royal Society of London A: Mathematical, Physical and Engineering Sciences 227:399–407.
Wienke, J., and H. Oumeraci. 2005. Breaking wave impact force on a vertical and inclined slender pile—theoretical and large-scale model investigations. Coastal Engineering 52:435–462.
Wu, T.-R., C.-R. Chu, C.-J. Huang, C.-Y. Wang, S.-Y. Chien, and M.-Z. Chen. 2014. A two-way coupled simulation of moving solids in free-surface flows. Computers & Fluids 100:347–355.
Wüthrich, D., M. Pfister, I. Nistor, and A. J. Schleiss. 2018. Experimental study on forces exerted on buildings with openings due to extreme hydrodynamic events. Coastal Engineering 140:72-86.
Xing, Y., I. Hadzic, S. Muzaferija, and M. Peric. 2001. CFD Simulation of Flow- Induced Floating- Body Motions. Proc. of the 16th International Workshop on Water Waves and Floating Bodies, Hiroshima, Japan.
Xu, X., X. Xu, W. Liu, and D. Zhou. 2016. A New Formula of Impact Stiffness in Linear Viscoelastic Model for Pounding Simulation. Shock and Vibration 2016.
Yang, J., and F. Stern. 2015. A non-iterative direct forcing immersed boundary method for strongly-coupled fluid–solid interactions. Journal of Computational Physics 295:779–804.

Yang, L., H. Yang, S. Yan, Q. Ma, and others. 2017. Numerical investigation of water-entry problems using IBM method. International Journal of Offshore and Polar Engineering 27:152–159.
Yao, Y., Z. Huang, E. Y. M. Lo, and H.-T. Shen. 2014. A preliminary laboratory study of motion of floating debris generated by solitary waves running up a beach. Journal of Earthquake and Tsunami 8.
Yeh, H., A. R. Barbosa, H. Ko, and J. G. Cawley. 2014. Tsunami Loadings on Structures: Review and Analysis. Coastal Engineering Proceedings 1:1–4.
Yeh, H., S. Sato, and Y. Tajima. 2013. The 11 March 2011 East Japan earthquake and tsunami: tsunami effects on coastal infrastructure and buildings. Pure and Applied Geophysics 170:1019–1031.
Yeung, R. W. 1981. Added mass and damping of a vertical cylinder in finite-depth waters. Applied Ocean Research 3:119–133.
Yunus, A. C., and J. M. Cimbala. 2006. Fluid mechanics fundamentals and applications. McGraw-Hill Publication 2:136–138.

Appendix A – Hydrodynamics

Swing Gate Generated Dam-break Waves

Preprint of an article printed in Journal of Hydraulic Research© 2018 Taylor & Francis.
https://www.tandfonline.com/doi/full/10.1080/00221686.2018.1489901

Objectives

Without a comprehensive examination of the influence of the swing gate opening times and the subsequently-generated wave hydrodynamics, it is difficult to conclude that the wave generated from such swing-gates display similar characteristics and can be quantitatively compared to the typical dam-break solutions. This may further result in difficulty replicating any study's results, e.g. numerically or in follow-up studies conducted with different swing gate types. Therefore, the following study aims to close this knowledge gap by:

- Investigating the driving influences related to the gate opening time of the swing gate.
- Examining the influence of the swing gate mechanism on the wave arrival time.
- Examining the influence of the swing gate opening time on the downstream wave profile.

This study is the first to investigate the influence of the swing gate on the dam-break wave characteristics. Considering the recent increase in the use of different gate mechanisms for the generation of the dam-break wave, developing an understanding of the gate-water column interaction will help determine the repeatability of these type of experiments across various mechanisms, as the mechanism available or chosen are largely influenced by the available experimental facilities.

Experimental Setup

Flume Facility

This study was performed in the Water Resources Laboratory of the University of Ottawa (Ottawa, Canada). The experimental facility (Fig. A - 1) is a 30 m × 1.5 m × 0.80 m flume, partitioned into a reservoir section (21.55 m long) and the downstream horizontal bed section (8.45 m long). The bed section was a 0.20 m-high false floor. The false floor was covered with a layer of 0.001 m sand grains glued to the surface. A steady-state current test with a Reynolds Number (R) = 1.07×10^5 over the experimental section measuring the surface elevation drop over a defined section yielded a Darcy-Weisbach friction factor (f) of 0.014.

Prior to the first daily test, the dry floor was first wetted and then squeegeed. After each run of the dam-break tests, a squeegee was used to remove excess water from the false floor. The floor was not given time to dry, therefore each experiment was run with a thin layer of water on the bed surface to assure identical experimental conditions throughout the study.

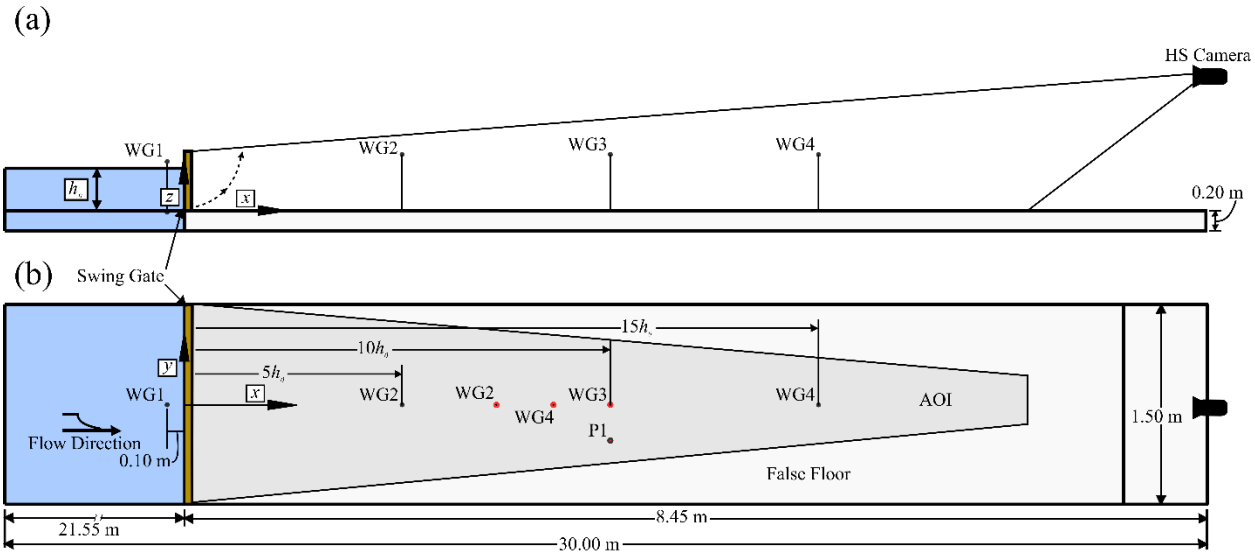

Fig. A - 1. University of Ottawa Flume. Reservoir shown in blue, experimental section shown in grey. The position of the high-speed camera (HS camera) is indicated at the downstream edge of the flume. The red WG apply to the "Hydrodynamics" experimental section, and the black WG apply to the "Examination of Gate" experiments. (a) Side View; (b) Plan View.

The origin of the spatial coordinate system was set at the upstream edge of the gate, center-flume. The positive *x*-, *y*- and *z*-axis selected use the right-hand-rule. The *x*-direction was positive in the direction of the wave propagation, the *y*-direction was positive to the right when facing downstream, and the *z*-direction was positive upwards.

Wave gauge (WG) 1 was maintained in the same position (x = -0.10 m) throughout each of the tests to act as the reference point for time synchronization with the remaining instrumentation and for reporting results. When the water level began to drop at WG1, the gate was considered to be fully opened and time at that point was set to zero.

Dam-break Gate

The gate used to release the impounded water in the reservoir was a hinged swing gate, as shown in Fig. A - 2. The gate was placed on top of the false floor. The gate itself was 1.40 m wide with two lateral supports protruding 0.05 m into the width of flume. The gate face was constructed from marine plywood attached rigidly to a sturdy steel frame. A small 0.03 m protrusion was covered in rubber to maintain a watertight seal around the outer edge of the gate. Due to water level restrictions within the flume, the maximum impoundment depth behind the gate was 0.50 m.

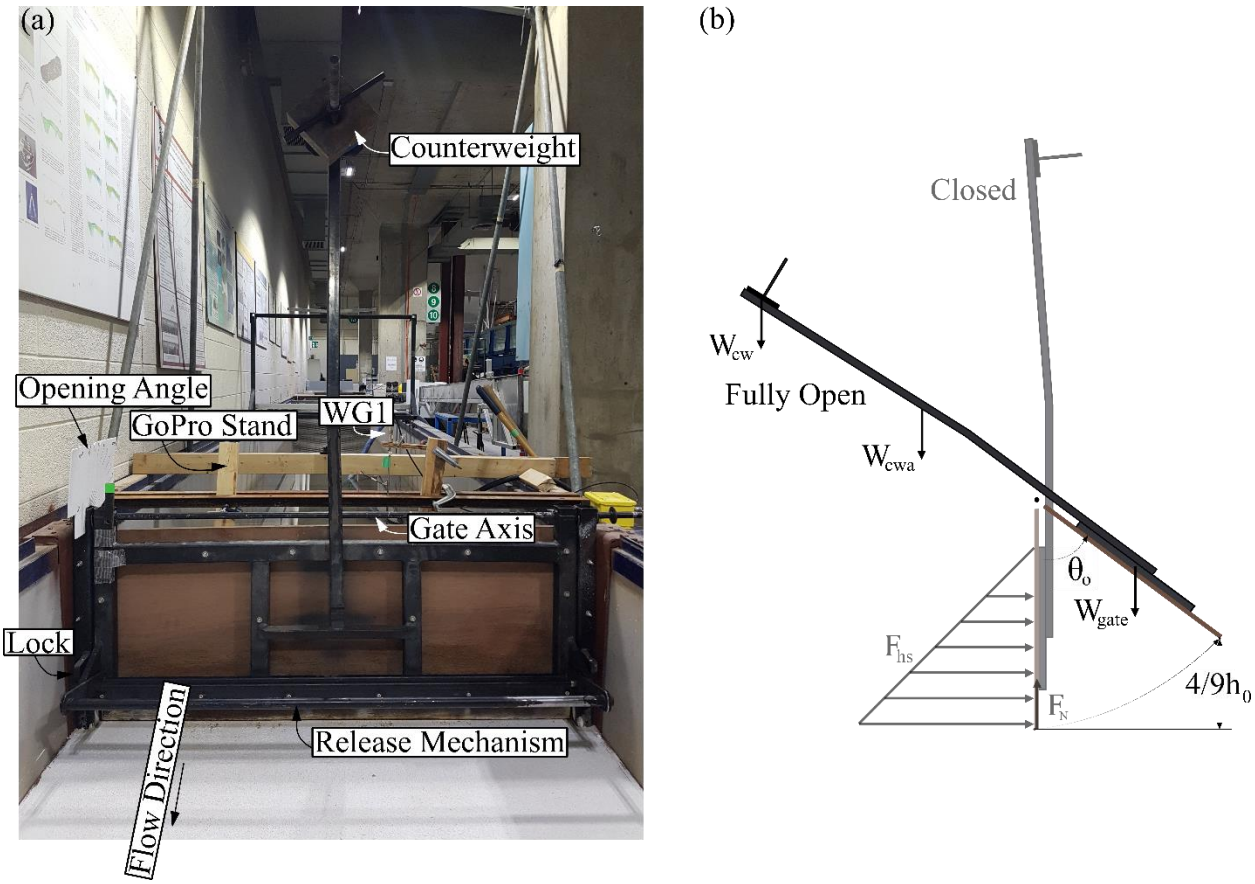

Fig. A - 2. University of Ottawa swing gate. (a) components of the gate system; (b) conceptual side view of the gate with the associated forces. W_{cw} is the weight of the counterweight, W_{cwa} is the weight of the counterweight arm, W_{gate} is the weight of the gate, F_N is the normal force acting on the gate and F_{hs} is the hydrostatic pressure acting on the gate.

A counterweight arm was mounted centrally on the gate, slightly angled so that the center-of-mass of the counterweight was directly over the axis of the gate. The counterweight mass was varied throughout the experiments to influence the length of opening time.

For this given setup, the gate had to be manually released using a release mechanism indicated in Fig. A - 2. The gate was initially placed in the locked position while the reservoir was filled with water. The release mechanism opened to release the gate.

Instrumentation

For each experiment, four WG (RBR WG-50, capacitance-type, ±0.1%, 0.50 m measurement range) were placed along the longitudinal flume axis. The time history of the water surface elevation from each WG was recorded with a sampling rate of 300 Hz. WG1 was always placed inside the reservoir (at x = -0.10 m) to act as the time synchronization reference gauge for the hydrodynamic and camera data. The WG were placed 0.005 m above the bed surface. Before the wave gauges were placed in the flume, they were calibrated ensuring R^2 values greater than 0.99. The mounting frame of the WG consisted of a 0.005 m diameter cylinder that intruded into the water surface; however, the frame was sufficiently far away from the probe to have no observable influence on the measurements or downstream wave profile.

WG2, WG3 and WG4 were placed in the experimental section at the same dimensionless location for each impoundment depth dependent on the experiment type (Fig. A - 2). For the "Hydrodynamics" (HD), the WG (in red) were placed at $X = x/h_0$ = 8, 9, and 10, respectively, to examine the wave profile. A propeller velocity flowmeter (P) (Armfield H33 – high speed, 0 – 3 m/s range, +/-1%) was placed at X = 10, 0.10 m from the center-flume. For the "Examination of the Gate" (EG), the WG (in black) were placed at X = 5, 10, and 15. The WG and P were synchronized through the single data acquisition system (HBM 1601B).

A high-speed (HS) camera (Flare 2M360-CL, 0.14 px/mm) was placed at the downstream edge of the flume to monitor the wave profile. The HS camera recorded the wave profile with 70 fps. A GoPro Hero4 Black (GP) camera (1.7 px/mm) was placed to monitor the opening of the gate (Fig. A - 2) with 120 fps. A full description of the measurement of the gate opening time can be found in the following section.

Gate Opening Time

Due to the differing opening mechanism between the classical vertical release and swing gate, the definition of the full opening of the gate needs to be altered to examine the swing gate mechanism. For a vertical lift gate, the gate was considered fully open when the edge of the gate exceeded the impoundment depth (Lauber and Hager 1998). For this type of gate, this definition had to be modified as the edge of the swing gate moved both horizontally and vertically. The full opening of the gate was considered to be when the bottom edge of the gate exceeded 4/9 of the initial impoundment depth. The 4/9 value was chosen based on Ritter (1892), where at x = 0, the water depth drops to 4/9 the initial impoundment depth immediately upon the release of the water column.

As discussed in the previous section, a GoPro camera was used to monitor the opening of the gate. The camera was directed towards an angular scale constructed by the authors whose center matched the axis of the gate (Fig. A - 2). A rigid needle was attached to the swing gate axis to allow for angle of the gate to be monitored using an automated video tracking algorithm.

Fig. A - 3 outlines the typical snapshot of the tracking algorithm. The GP camera images were rectified in the plane of the angular scale using four control point placed on the outer edges of the scale. The rectified image can be observed in Fig. A - 3a. For each image, a colour threshold was used to select the centroid of the top section of the needle (Stolle et al. 2016, 2017a). The resulting binary image can be observed in Fig. A - 3b, white indicates pixels that fell within the colour threshold. The angle of the needle was determined by finding the orientation of the long axis of the white blob of white pixels (Fig. A - 3b) relative to the x-axis. The opening angle would then be the complementary angle of the orientation displayed in Fig. A - 3. A typical time-history of the opening angle as retrieved from the image processing conducted is shown in Fig. A - 3c where 90° means that the gate is closed; at about a time of t =1.15 s, the opening process is initiated and the rate of change of the opening angle determines the angular opening velocity. The gate opening time was measured between the initiation of motion ($\Delta\theta > 1^o$) to the angle associated with the bottom edge of the gate exceeding 4/9 of the initial impoundment depth. The accuracy of the tracking method determined by manually selecting the angle from each image for one test and found the error to be within +/- 0.54^o.

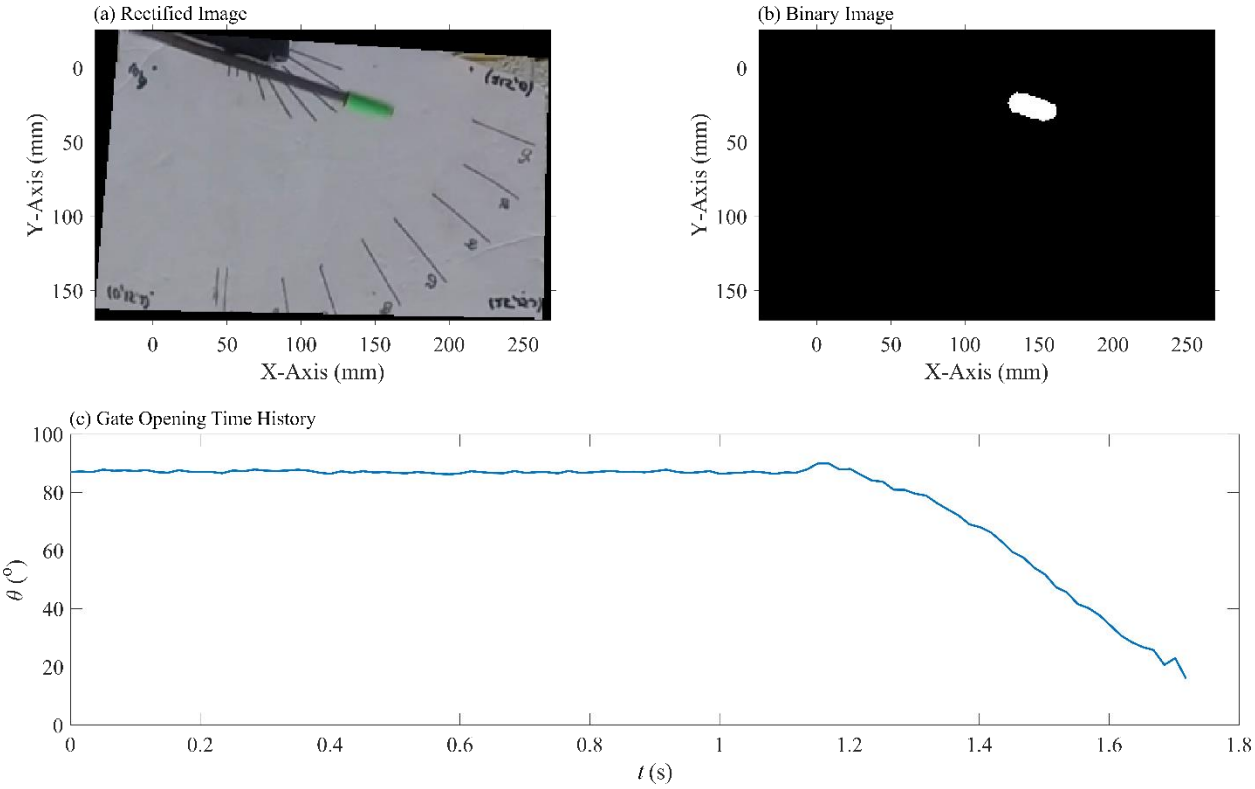

Fig. A - 3. Gate opening tracking algorithm used to determine the gate opening time. (a) GoPro image rectified within the plane of the angular scale, (b) binary image developed using color thresholding; and (c) time history of the gate opening.

Experimental Protocol

Table A - 1 shows the outline of the experimental protocol for this study: a total of 76 tests were conducted. For each experimental type, four impoundment depths (0.20, 0.30, 0.40, and 0.50 m) were examined. The HD experimental type was used to examine the wave profile and flow velocities at $X = 10$.

The EG experimental type examined the influence of the gate opening time on the bore properties. The counterweight was varied between experiments to influence the gate opening times in a repeatable manner. Each experimental condition was repeated 3 times to identify spurious data points. Outliers were identified through visual examination when occurring (>> 3 times the standard deviation of data). The impoundment depth was filled for each experiment to within +/- 0.02% of the expected depth.

The counterweights were standard 4.53 kg (10 lbs) metal plates. To avoid any inconsistencies in the manufacturing, each plate was weighed individually to get a precise measurement of its weight. The same plates were used in experimental series to maintain the same counterweight mass between impoundment depths.

Table A - 1. Experimental protocol. HD – Hydrodynamics; EG – Examination of Gate.

Experiment Type	Impoundment Depth (h_0) (m)	Counterweight (CW) (kg)	Repetitions
HD	0.50	22.30	1
	0.40		
	0.30		
	0.20		
EG	0.50	8.99	3
	0.40	13.42	
	0.30	18.58	
	0.20	22.30	
		26.76	
		31.76	

Results

Gate Opening Time

Fig. A - 4a shows the gate opening profile for a select number of counterweights. The opening angles are normalized by the opening angle (θ_o). The initial intent for the counterweight system was to decrease the gate opening time by increasing the counterweight mass. However, as can be observed in Fig. A - 4a-c, increasing the counterweight mass resulted in an increased gate opening time. Since the gate needed to be flush with the bed surface to maintain the tight seal between the reservoir and experimental sections, the counterweight, initially acting normal to the bed surface, resulted in an increased normal force acting between the gate and the bed surface (Fig. A - 2) which subsequently translated into an increased friction force. During the initiation of the gate motion, the friction reduced the gate acceleration and, therefore, increased the gate opening time. This phenomenon was a function of the particular design of the University of Ottawa swing gate, therefore would likely differ between experimental facilities.

Fig. A - 4d shows the gate opening time (t_o), normalized by the impoundment depth, for each impoundment depth tested. As it can be observed, the mean gate opening time increased with increasing the impoundment depth, as a result of the increased hydrostatic pressure force acting on the gate surface, with an approximately linear relationship:

$$T_o = 1.47 - 1.19h_0 \qquad \text{(A - 1)}$$

where h_0 is the impoundment depth (m) and T_o is the dimensionless gate opening time (-). Eq. (A - 1) is largely specific to the University of Ottawa facility due to the normal and friction forces acting on the gate. However, that the gate opening time was found to decrease with impoundment depth which should apply across facilities. Additionally, the increased impoundment depth resulted in a decrease in the standard deviation between the various experimental tests. As the counterweights between impoundment depths were maintained, the opening process can be seen to be predominantly dominated by the initial hydraulic conditions, that is, the impoundment depth. A different opening mechanism, such as hydraulic lifts, may sufficiently increase the gate velocity to result in a complete detachment of the water column. Therefore, the gate opening velocity would not be influenced by the impoundment depths; however, such opening velocities were not achieved by this facility.

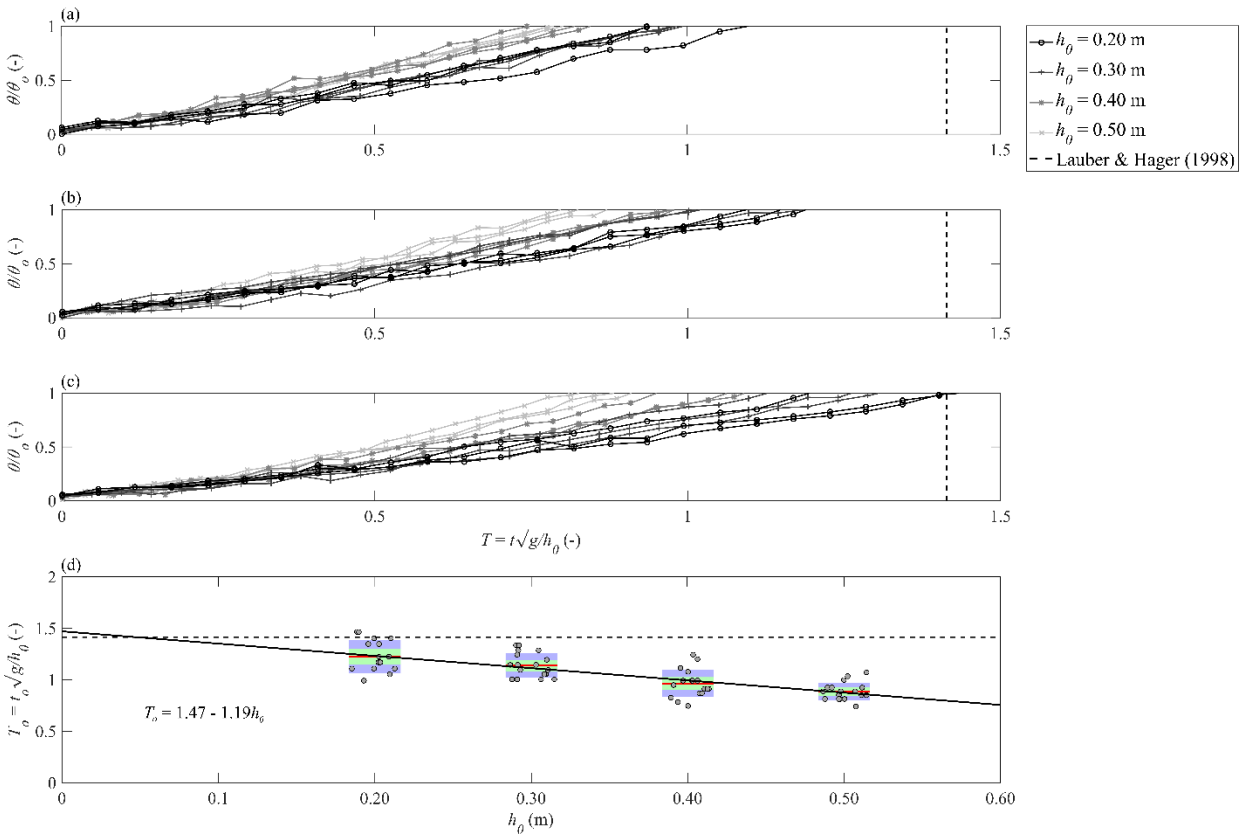

Fig. A - 4. Gate opening time. (a-c) Gate opening time profile normalized by the gate opening definition for different counterweights (CW); (a) CW = 8.99 kg; (b) CW = 18.58 kg; (c) CW = 26.76 kg. (d) Gate opening time as a function of the impoundment depth, compared with Lauber and Hager (1998). The solid line indicates the mean opening time, the patches represent the standard deviation and 95% confidence interval, respectively.

A comparison of the gate-opening time histories shows a similar wave profile regardless of the initial impoundment depth. While the manual opening procedure had influenced the gate opening time, it seemed to have had limited influence on the opening time history. Therefore, the influence of the gate opening time discussed in the following section would theoretically apply regardless of the gate opening technique.

Hydrodynamics

For each of the impoundment depths, an experiment was performed to examine the development of the hydrodynamic conditions at X = 10. This particular location was chosen to maintain the same dimensionless distance to the one used in the following results sections. Lauber and Hager (1998) noted that the Saint-Venant equations were not valid for the initiation of the dam-break ($T = t\sqrt{g/h_0} < 3$) and Chanson (2005) stated that the diffusive wave equation may become invalid when applied to flows over a long time period as the wave tip region becomes sufficiently large. However, to the authors knowledge, that particular limit has not yet been established through experimental tests. To avoid any interference with the boundaries provided in literature, X = 10 was judged to be sufficiently different from these conditions, as the mean dimensionless arrival time ($T_a = t_a\sqrt{g/h_0}$), defined as the time that the wave tip reaches the prescribed dimensionless position (as measured by the WG), was 9.23 s (95% confidence

interval (CI) [9.13 9.31]). The wave arrival time was determined to be when the measured water depth increased by 0.002 m.

Fig. A - 5 shows the dimensionless hydrodynamic conditions at $X = 10$ as a function of time, compared to Ritter (1892) for a frictionless, horizontal bed. $T = 0$ refers to the arrival of the wave tip (T_a), as determined by the rise of the water depth recorded by the WG. As expected, the influence of the bed friction was prominent in the initial flow stages. Chanson (2006) showed that the flow resistance resulted in a decrease in the flow velocity and an increase in the wave steepness and water depth in the wave front (at the wave tip). This reduction in the flow velocity ($V = v/\sqrt{gh_0}$) can be observed in **Error! Reference source not found.**b. In Fig. A - 5a, the flow depth ($H = h/h_0$) rapidly increased, displaying the steeper wave front caused by the bed friction and additional flow resistance due to the thin layer of water (Stansby et al. 1998, Chanson 2006). Following the passage of the wave front, the water depth closely followed the water surface elevation calculated using Ritter (1892).

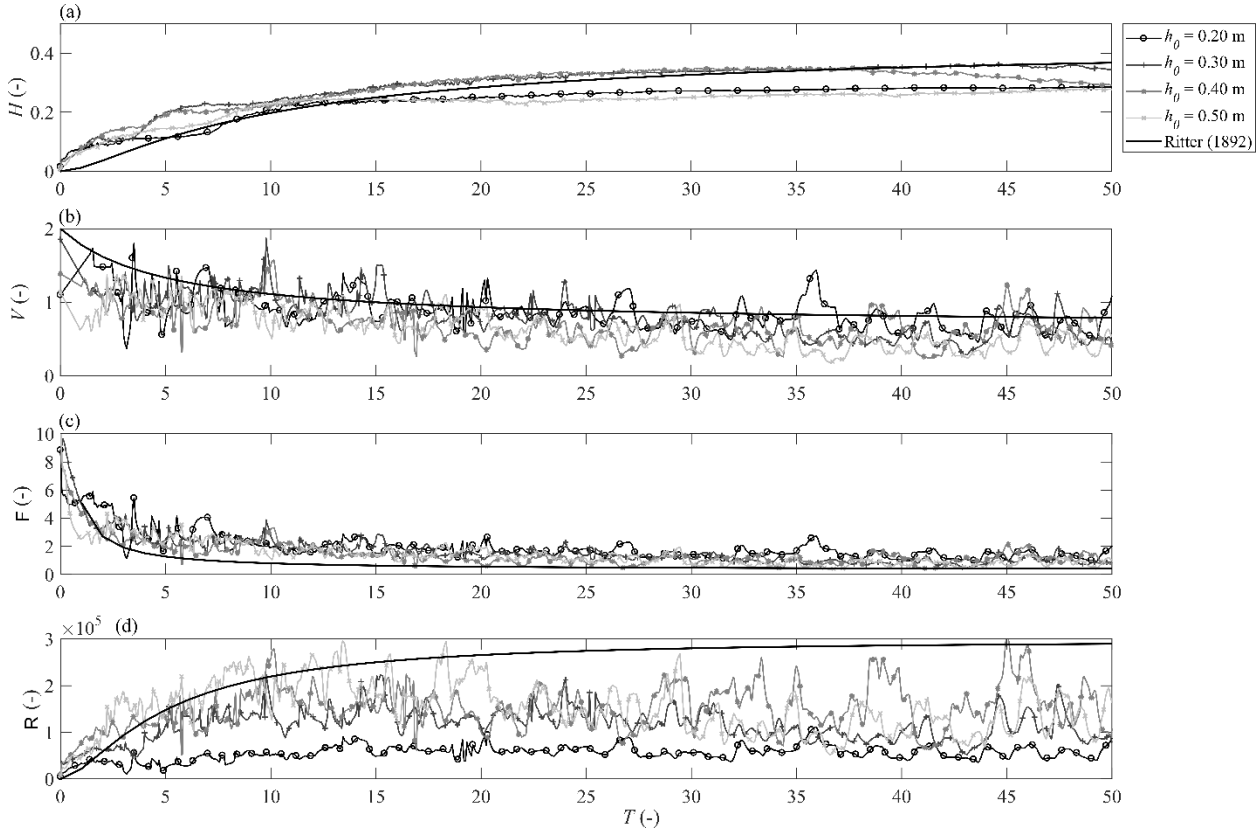

Fig. A - 5. Investigation of the experimental hydrodynamic conditions for X = 10. (a) Water Surface Elevation; (b) Flow Velocity; (c) Froude Number (F); and (d) Reynolds Number (R) (Eq. 6). T = 0 refers to the arrival time of the wave front.

Lauber and Hager (1998) determined that, for impoundment depths ≥ 0.30 m, scale effects are mostly negligible, except in the vicinity of the wave front. Therefore, in cases where the impoundment depth was larger than 0.30 m, the flow was governed by Froude similarity. Fig. A - 5d shows that, for the 0.20 m impoundment depth, the Reynolds number ($R = vh/\nu$) was consistently less than in the cases where the impoundment depth ≥ 0.30 m. As a result, viscous forces were more prominent in the lower impoundment depth; hence, the difficulties with scale effects noted by Lauber and Hager (1998).

The friction factor stated in the experimental setup (f = 0.014) was estimated in steady-state conditions. To compare to the transient conditions in these tests, a Lagrangian estimation of the friction factor was considered using an instantaneous snapshot of the water surface profile (Chanson 2005). Fig. A - 6 shows the instantaneous wave profile for each impoundment depth at the time that wave reached X = 10. WG were placed at an interval of ΔX = 1 to ensure proper recording the wave profile. The diffusive wave model (Chanson 2006) was fitted to the wave profile (black line). The mean friction factor from the fitted data was determined to be 0.0293. The deviation of the WG in the reservoir compared to the analytical solution was due to the constriction of the channel due to the gate construction, this is further described in the following section.

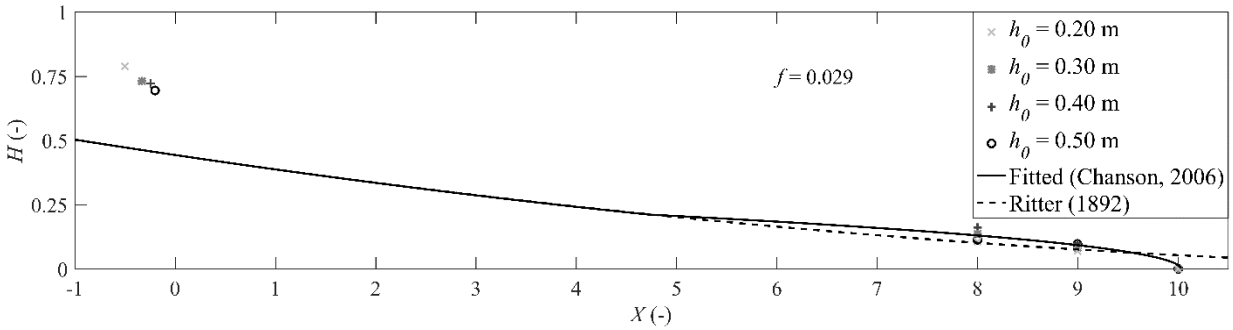

Fig. A - 6. Examination of the friction factor based on the wave profile when the wave first reaches X = 10. Initial impoundment depth shown by the shape of the marker.

The friction factor estimated by the Lagrangian method exceeded that observed in the steady state case. This was likely because the Lagrangian method calculated the friction factor predominantly based on the wave tip region where viscous forces dominate ($1.85 \times 10^4 < R < 7.31 \times 10^4$) (Whitham 1955). As shown in the Moody diagram (Moody 1944), the friction factor increases with decreasing Reynolds numbers for the same roughness. Additionally, the presence of the thin layer of water would result in increased flow resistance that would not be captured by the steady state case.

Influence of Gate Opening

Fig. A - 7 shows the mean dimensionless wave profiles for each of the experiments shown in the EG experimental type. The wave profiles are compared to the analytical solutions from Ritter (1892) and the diffusion wave solution from Chanson (2006), using the friction factor derived from the instantaneous wave profile (f = 0.0293).

Unlike the downstream WG, the position of the reservoir WG (Fig. A - 7a) was kept at a fixed location, as the reservoir WG was required to determine the opening time as well as examine repeatability, regardless of impoundment depth. As a result, the dimensionless position of the reservoir WG was different when using different impoundment depths. This resulted in the discrepancy between the wave profiles. Additionally, to maintain the stability and water-tight seal of the gate, two support columns were placed on the side of the flume walls. The blockage of the flume cross-section resulted in the observed stepped profile. Khankandi et al. (2012) noted a similar profile in an examination of the reservoir geometry on the dam-break wave profile, with an increase in water surface elevation at the reservoir WG of 20-35%, depending on the reservoir, from a straight reservoir. The geometry of the reservoir in this study differed significantly from that used by Khankandi et al. (2012); however a similar increase of 17.5% was observed when compared to the Ritter (1892) solution.

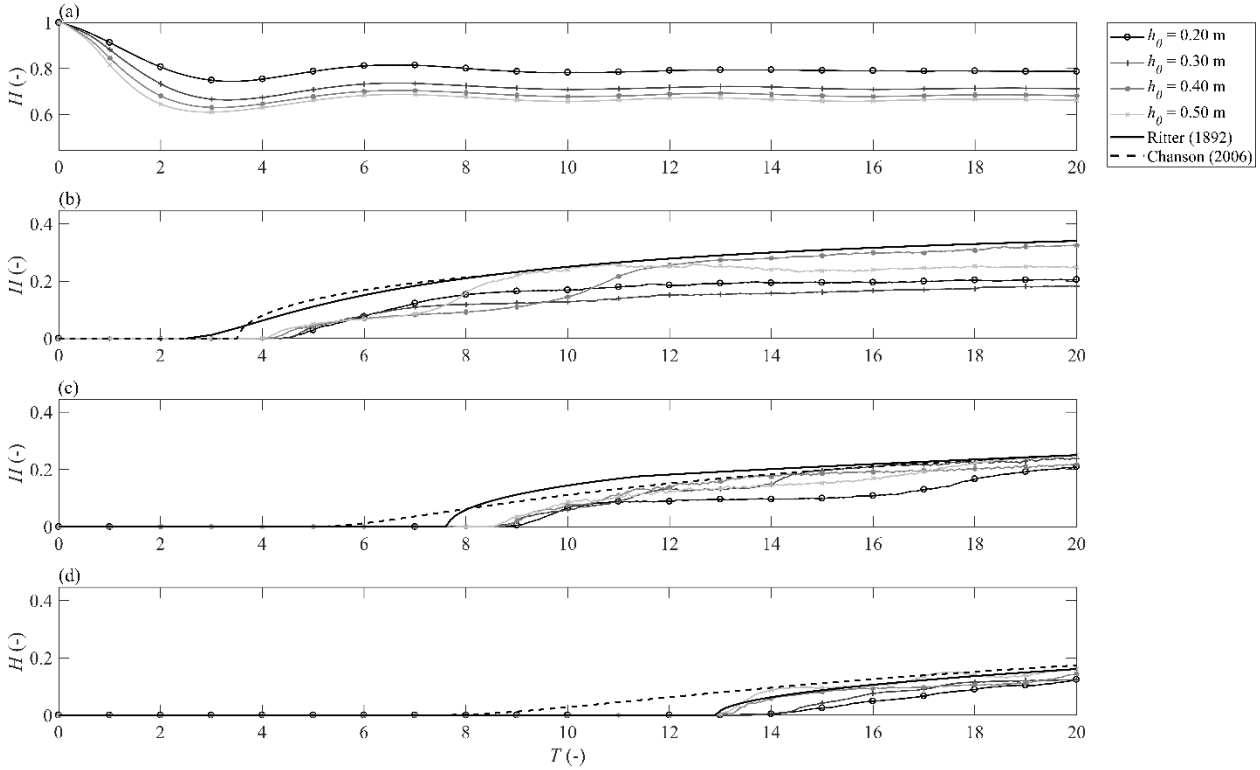

Fig. A - 7. Normalized mean water surface elevation profiles for the four WG: (a) WG1 (x = -0.10 m), (b) WG2 (X = 5), (c) WG5 (X = 10), and (d) WG6 (X = 15). Profiles are compared to analytical solutions of Ritter (1892) and Chanson (2006) (f = 0.0293).

This phenomenon was also observed by Bellos et al. (1992), in an investigation of the two-dimensional flow effects on dam-break wave, which discussed the "bump" feature observed in the downstream wave profiles. The length and velocity of those disturbances are dependent on the gravitational force, and the impoundment depth. This why these disturbances could be starkly observed for the 0.40 m and 0.50 m cases. The "bump" formed in all cases; however, for the 0.20 m and 0.30 m case, the disturbances occurred outside of the displayed time range.

Due to the rapid contraction and expansion of the flume cross-section in the vicinity of the gate frame, significant oscillations of the water surface were observed downstream of the gate in the current experimental tests. As a result, cross-waves formed directly downstream of the gate, propagating off the lateral frame members and eventually meeting about the flume axis. Kocaman and Ozmen-Cagatay (2012) observed a similar phenomenon when investigating dam-break flows through a lateral contraction. The flow at upstream side of the contraction is subcritical and rapidly transitions through the contraction to a supercritical state, resulting in a "mixed flow regime". This transition in the contraction causes diffraction to occur at the downstream end and to be carried downstream as the observed cross-waves. A similar phenomenon has been observed for bottom obstacles (Ozmen-Cagatay and Kocaman 2011) and supercritical steady flow (Hager 1989).

The presence of the cross-waves result in a 3D wave profile (Fraccarollo and Toro 1995). However, this study emphasizes the influence of the gate on the initial wave profile. The increased flow depth as a result of the cross-waves occurred sufficiently after the wave front that the influence of the cross-waves was considered to be negligible.

For the remaining panels in Fig. A - 7b-d, the WG were shifted to the dimensionless position (X = 5, 10, or 15). As it can be observed, wave arrival time lagged behind that of the analytical solutions of Chanson (2006) and Ritter (1892). This discrepancy may be partly due to an inaccurate estimation of the friction factor. However, another reason, and the primary concern of this study, is related to the non-instantaneous opening of the gate used in the experiment. The following section examines the influence of the gate opening on the wave arrival and profile comparing the results to the analytical solutions.

Wave Arrival

To examine the influence of the gate opening on the wave profile, the discrepancy in the wave arrival time was further investigated. Fig. A - 8 shows the comparison of the gate opening time (T_o) with the time of the wave arrival (T_a) for each dimensionless position. For each position, the influence of the gate opening appeared to linearly influence the wave arrival time. However, due to limitations of the experimental facility and its constructional features, the opening times were limited between $0.739 < T_o < 1.46$. Therefore, outside of the experimental range, it is unclear how the wave arrival would be influenced.

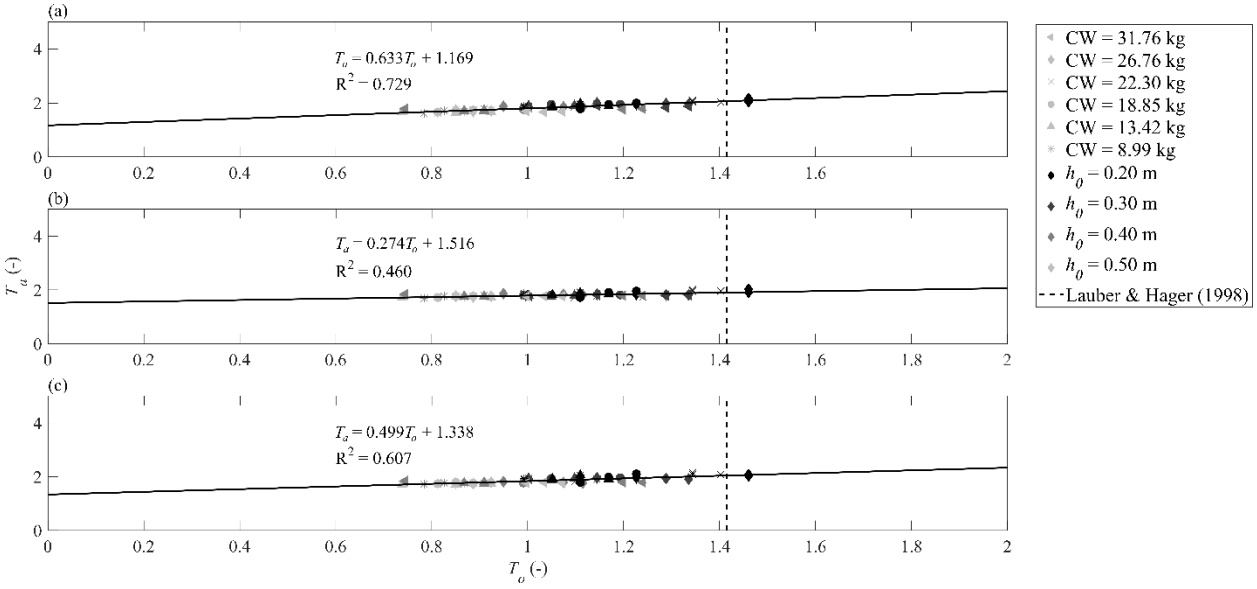

Fig. A - 8. Comparison of the difference in arrival time of the experimental and analytical (Ritter, 1892) surge to the gate opening time for the three WG: (a) X = 5; (b) X = 10; and (c) X = 15.

Lauber and Hager (1998) indicated that a gate opening time of $T_o > 1.41$ would significantly influence the formation of the dynamic wave for a vertical release gate. The value of 1.41 was determined based on the time required for a water particle to drop from the top of the water column to the bottom, thus initiating the horizontal motion of the dam-break wave. In the case of the swing gate, even with gate opening times less than 1.41, the gate opening had an influence on the wave formation. This suggests that the water velocity near the gate likely had a horizontal component which interacted with the gate. Stansby et al. (1998), in an examination of the initial stages of a dam-break wave, observed a horizontal jet that instigated the formation of the dam-break wave and observed differences in the position of that jet based on the gate opening time. The obstruction of this jet by the swing gate could potentially be the cause of the observed delay in the dam-break wave formation.

An additional mechanism for the delay could be due to the difference in the release mechanism of the water column. The vertical lift gate first allows for the release of the water particles at the bottom of the

water column, creating an initial wave before the full impounded water column was released. The water particles were then forced to accelerate in the vertical direction due to the obstruction of the gate and a pressurized flow scenario is briefly realized underneath the gate.

Similarly, the swing gate mechanism would release an initial profile beneath the gate edge. However, as the gate moves both vertically and horizontally, the entire water column was released at the initiation of gate motion. The earlier release of the column potentially resulted in an earlier initialization of the horizontal motion of the wave, which influences the wave profile. Due to the rapid process of this phenomena, numerical or detailed experimental studies of the gate-water column interaction will be required to determine the exact influence of the gate opening mechanisms and the subsequent local hydrodynamics. It will also be of interest whether the detachment of the swing gate surface from the resting water column induces any relevant horizontal acceleration to the water particles.

The empirical relationships displayed in Fig. A - 8 are likely to be specific to the University of Ottawa facility due to its unique construction. However, the general trend would be expected to hold among similar swing gate facilities. The trend shows that there is a significant influence of the gate opening time on the wave for $T_o < 1.41$ suggesting that the criterion established by Lauber and Hager (1998) may not be sufficient to ensure repeatability and replicability of dam-break waves in the case of swing gates.

Water Surface Elevation

To examine the potential influence of the gate opening time on the wave profile, water surface time histories were compared to the analytical profile from Chanson (2006). The water surface elevations were considered to arrive at $T = 0$ and were compared to the analytical solution (thick black line) for $f = 0.0293$ (Fig. A - 9). The first $T = 3$ was examined, as after that point, the stepped wave profile from the two-dimensional effects was observed in the water surface time-histories.

As shown in Fig. A - 9, the analytical solution well represented the water surface elevations. However, in the near-field ($X = 5$ and 10), the water surface elevation was overestimated by the analytical solution of Chanson (2006). The discrepancy in the water surface elevation could be the result of assuming the friction factor to be constant. As previously discussed, the friction factor is a function of the Reynolds number and will therefore vary as the profile and flow velocity change. The estimated friction factor was based on a mean condition and therefore would have likely caused the water profile to converge towards the mean profile in the far-field ($X = 15$).

Fig. A - 10 compares the Root-Mean Squared Error (*RMSE*) of the water surface elevation using:

$$RMSE = \frac{\sqrt{\sum_{i=1}^{n} (h_C - h)^2}}{n} \qquad \text{(A - 2)}$$

where h_C is the water depth calculated from the analytical solution (Chanson 2006), h is the water depth from the WG recording, and n is the number of samples taken between the wave arrival and $T = 3$. The mean *RMSE* ($\overline{RMSE}$) and standard deviation (σ) for each dimensionless positions are shown. Based on results shown in Fig. A - 10, the gate opening time appeared to have no relationship with the bore profile. Oertel and Bung (2012) noted that the wave profile tended to correct from the discrepancies related to the gate opening mechanisms as the wave propagated away from the gate; therefore any discrepancies caused from the gate opening may have been corrected before $X = 5$. A close investigation of the initial phases of the gate opening may therefore derive contradictory results.

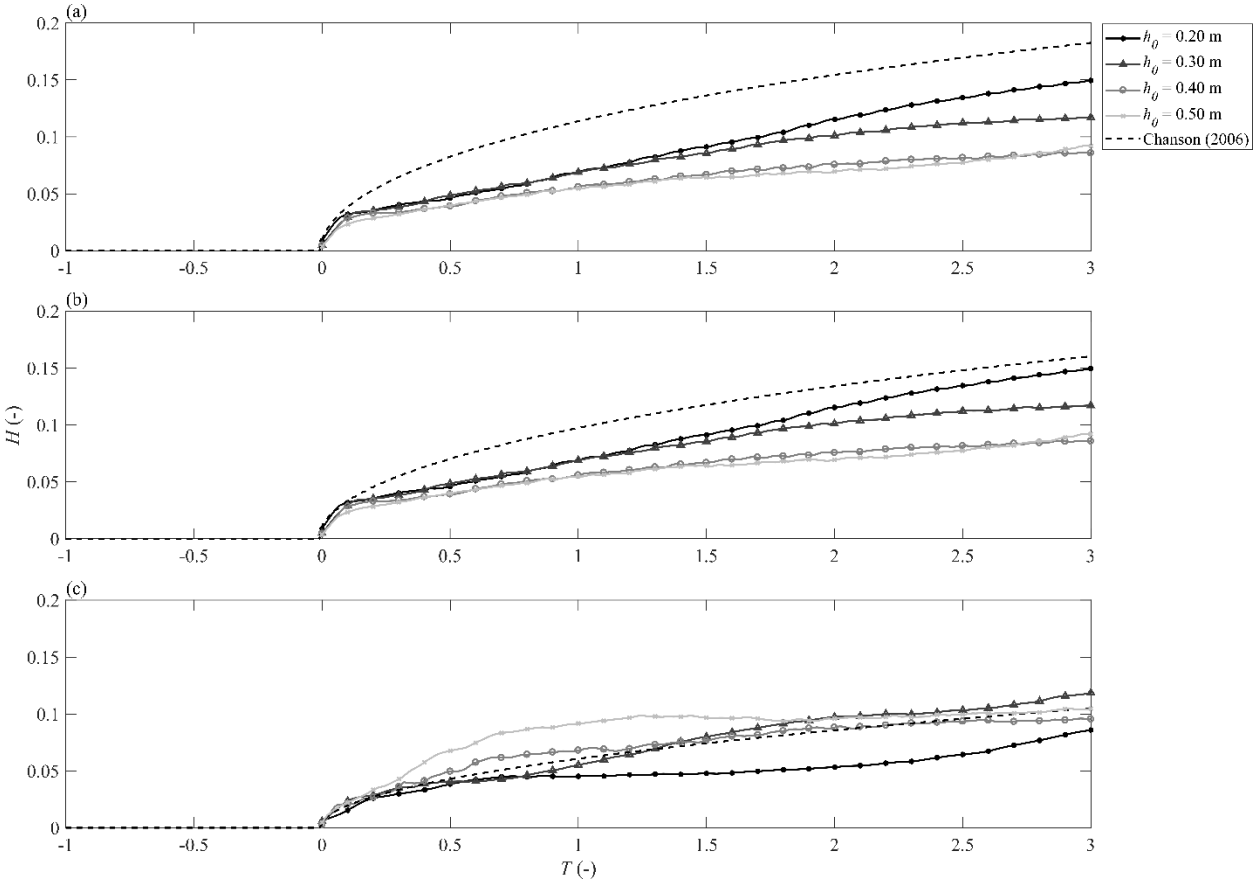

Fig. A - 9. Comparison of the mean experimental bore profiles to the analytical profiles from Chanson (2006) at the WG: (a) X = 5; (b) X = 10; and (c) X = 15.

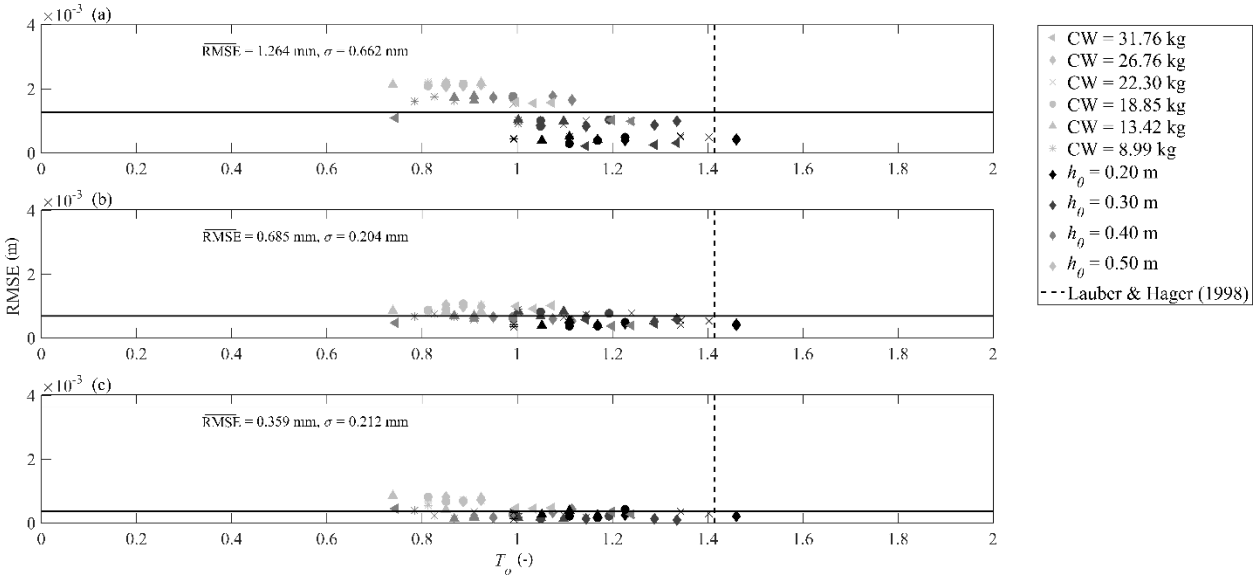

Fig. A - 10. Root mean difference (RMSE) in experimental and analytical (Chanson, 2006) wave profile as a function of gate opening time for WG: (a) X = 5; (b) X = 10; and (c) X = 15. The solid black line shows the mean RMSE for all experiments, and the dashed black line shows the T_o prescribed by Lauber and Hager (1998).

A comparison of the *RMSE* at the various dimensionless positions shows that, in the further field, the water surface elevation approached the analytical solution. In the near-field, Lauber and Hager (1998) showed that the wave initially had two-phases: the initial wave which was the wave formed from the opening of the gate and the dynamic wave which formed from the collapsing of the water column. The initial wave forms earlier in the process, resulting in the initial wave initially being in front of the dynamic wave, until, as determined by Lauber and Hager (1998), $T = 3$, when the dynamic wave overtakes the initial wave. As previously discussed, the different gate opening potentially influenced the formation of the dynamic wave. As the dynamic wave does not reach the initial wave front, the resulting water depth was less than the analytical solution. Further research will be needed to examine the influence of the gate on the dynamic wave formation.

The exact values displayed in Fig. A - 10 are largely dependent on the specific facilities at the University of Ottawa. Moreover, considerations need to be given to the error associated with the initial impoundment depth (+/- 0.02%) and the influence of the aerated flow at the wave tip. The air-water flow properties in the wave tip would potentially influence the measurement values from the capacitance-type wave gauges. However, the general trend would be expected to be translated to similar facilities. The correction of the wave profile towards the analytical solutions have previously been observed in other studies using vertical lift gates (Stansby et al. 1998, Ozmen-Cagatay and Kocaman 2010, Oertel and Bung 2012) and a similar phenomenon was observed in the case of the swing gate presented here.

Conclusions

This study examines the influence of a swing gate on the resulting dam-break wave profile. Understanding the influence of the swing gate mechanisms on the dam-break hydraulics is important in ensuring repeatability between dam-break studies. Four different impoundment depths were examined with a variety of gate-opening times to assess the influence of the gate opening time on the waves characteristics. As a result, the following conclusions can be made:

- As the swing gate was driven by the hydrostatic pressure, an increase in the impoundment depth resulted in a decrease in the gate opening time.
- The wave arrival time was linearly influenced by the gate opening time, even in cases where the opening time was less than the Lauber and Hager criterion. The relationship was likely due to the gate interfering with the horizontal motion of the wave.
- The gate opening time had no significant influence on the wave profile.
- As the wave propagated further away from the swing gate, the water surface elevation approached the analytical solution.

While this study examined the influence of the gate opening mechanism in the relative far-field, an in-depth investigation of the wave profile in the near-field ($X < 3$) may reveal contradictory results due to the influence of the initial wave. Due to the rapid nature of the dam-break problem, near-field studies will need to be performed in future studies using numerical modelling or further experimental studies.

Appendix B – Field Investigation

Engineering Lessons from the 28 September 2018 Indonesian Tsunami: Debris Loading

Preprint of an article in-press at the Canadian Journal of Civil Engineering © 2018 Canadian Science Publishing

Background

On September 28th, 2018, at 18:02:43 local time, a M_w 7.5 strike-slip earthquake occurred along the coast of the Central Sulawesi province of Indonesia (Fig. B - 1) (Hui et al. 2018, USGS 2018). The strike-slip faulting occurred at a depth of 10 km (+/- 1.8 km) within the Molucca Sea Microplate, a part of the larger Sunda tectonic plate system. The earthquake's epicenter was located at a distance of approximately 95 km north from Palu City, the capital of Central Sulawesi. The cascading hazard of earthquake, tsunami, and liquefaction resulted in over 2,100 casualties and 4,500 missing, with the majority occurring within Palu City (BNPB 2018). Due to several rivers draining into Palu Bay through the valley containing Palu City (Rusydi et al. 2018), several alluvial deposits, potentially exacerbated by high water tables from local agricultural irrigation (Bradley et al. 2019), caused widespread liquefaction and severe lateral spreading, affecting over 1,000 homes.

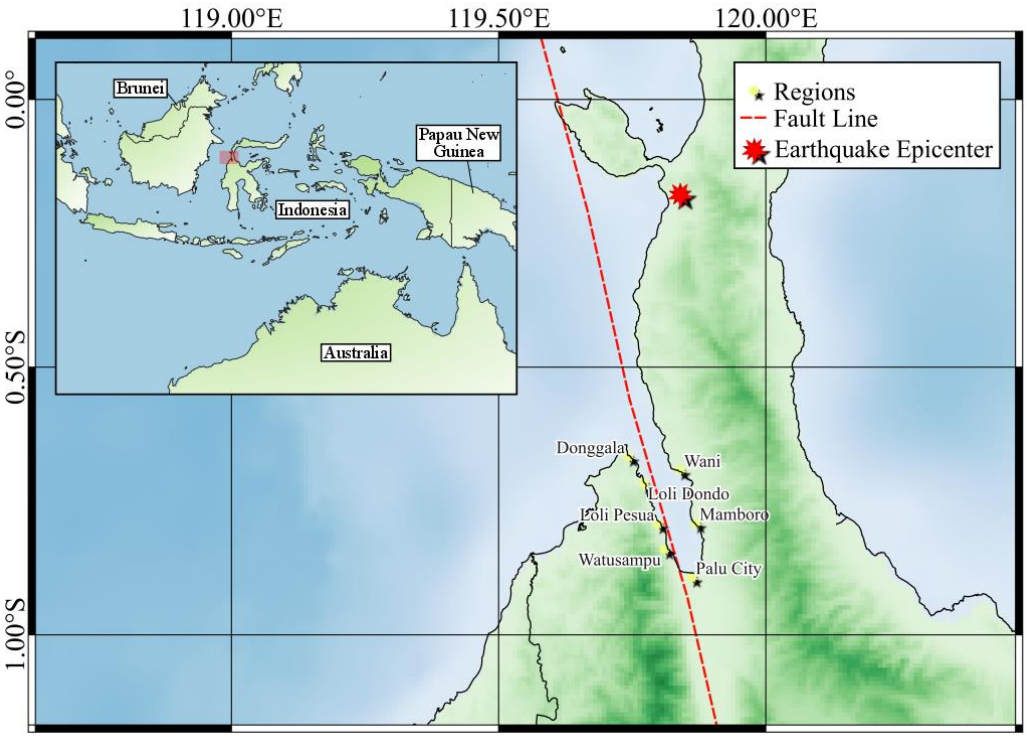

Fig. B - 1. Location of the 2018 Palu Earthquake and surrounding study regions. Positions of the epicenter and fault line being taken from the USGS (2018). Coordinate system is the WGS84 and topographical data is taken from the British Oceanographic Data Center (2018).

The majority of the tsunami damage was localized in Palu Bay, where the field survey took place. While strike-slip faults are generally not regarded as a major tsunami hazard (Heidarzadeh et al. 2018), it is

hypothesized that complex secondary effects, such as landslides, amplified the magnitude of the tsunami. Displacement along the fault line would have potentially caused the displacement of large volumes of water near the earthquake epicenter, then propagating into Palu Bay (NG 2018). Submarine landslides also played an important role, as was observed through video evidence and field observations (Sassa and Takagawa 2018). Several alluvial deposits and reclaimed land in the bay appeared to have disappeared, resulting in the formation of landslide-induced tsunami waves (Bardet et al. 2003, Heller and Hager 2010, Løvholt et al. 2015).

An international survey team, consisting of members from Japan, Germany, the USA, and Canada, conducted a survey along Palu Bay (from October 27th – 31st, 2018), focusing on the following settlements (from west to east): Loli Dondo, Loli Pesua, Watusampu, Palu City, Mamboro, and Wani (a full version of the structural report can be found in Robertson et al. (2019)). The focus of the survey addressed assessments of structures damaged in the event. Debris loading on structures has been identified in previous reconnaissance surveys as a critical load in the failure of structures (Ghobarah et al. 2006, Yeh et al. 2013). This report will focus particularly on the hazards associated with debris entrained within an inundating tsunami wave comparing the observed phenomena to the recently released ASCE 7 Chapter 6 – Tsunami Loads and Effects (ASCE 2016a), which became the first North American standard, written in mandatory language, addressing tsunami hazards and how this applies within the Canadian context. Additionally, the report will aim to identify current gaps in the body of knowledge within the developing field of solid body transport in extreme flooding events (Nistor et al. 2017).

Relevance of Tsunami Preparedness to Canada

Tsunami Hazard

Canadian coasts have experienced many tsunami, though rarely large enough to cause extreme damage (Clague et al. 2003). In November 1929, a M_w 7.2 earthquake triggered a large submarine slump (along the Laurentian slope), potentially from a strike-slip earthquake, which in turn caused a tsunami that struck the Burin Peninsula in Newfoundland, resulting in 28 deaths (Løvholt et al. 2018). In March 1964, a M_w 9.2 earthquake near Alaska caused a tsunami which resulted in over CDN $10 million in damages to Port Alberni, British Columbia (Clague et al. 2003). Tsunami can also be generated from anthropogenic sources, such as the tsunami that killed approximately 200 people in Halifax Harbor during the 1917 Halifax explosion (Greenberg et al. 1993).

Similar to Indonesia, the West Coast of Canada is located along the seismically active Pacific “Ring of Fire”, in particular near the Cascadia Subduction Zone (CSZ), though risks also exist from tsunami generated further afield. Kulkarni et al. (2013) analyzed the historical record of tsunami in the CSZ to calculate time-dependent recurrence intervals and estimated a probability of a M_w 9.0 earthquake occurring at around 17% in the next 100 years. Takabatake et al. (2019) modelled CSZ scenarios at several districts along the Canadian West Coast, estimating inundation heights of 2 – 12 m depending on the magnitude of the earthquake. Cheff et al. (2018) performed pedestrian evacuation modelling of the Tofino, British Columbia, examining the risk to the local population under various run-up scenarios. Glacial retreat has also increased tsunami hazard to the Canadian West Coast, where exposed unstable slopes could potentially fail, causing aerial landslides, as in the Taan Fjord in Alaska which caused massive local wave runup (Higman et al. 2018).

Tsunami Design Practices

The National Building Code of Canada does not explicitly address tsunami loading, with the understanding that urban planning plays a role in protecting inland structures (Palermo et al. 2009).

However, given the predicted run-up levels due to the CSZ, tsunami resilient structures are necessary, particularly along the west coast of Vancouver Island (Takabatake et al. 2019).

The current state-of-the-art design standard for tsunami structures is the ASCE 7 Chapter 6 – Tsunami Loads and Effects (ASCE 2016a). As tsunami hazards in the USA are similar to those in Canada, particularly along the West Coast, this standard should help to inform Canadian practices. Building upon lessons learned from previous field surveys of tsunami-stricken communities over the past decade, the standard became the first to address tsunami hazard from a probabilistic perspective. The standard also provides a comprehensive assessment of the various loads on structures, separated into the following broad categories: hydrostatic, hydrodynamic, debris impact, and erosion. The focus of this study will be on the debris portion of the standard. Debris refers to any solid object entrained within the inundating flows that can potentially impact a structure. ASCE 7 (2016a) separates the types of debris into: wood logs and poles, vehicles, tumbling boulders, shipping containers and barges, and extraordinary impacts.

Debris loading can be separated into two broad categories: impact and damming (Nistor et al. 2017). A debris impact load is defined by a rapid impulse force being exerted by a solid object on a structural element. The general equation for estimating the impact force (F_i) comes from the solution of a spring-mass system representing the debris striking a rigid structure (Haehnel and Daly 2004):

$$F_i = u\sqrt{mk} \tag{B - 1}$$

where u is the impact velocity, m is the mass of the debris, and k is the stiffness of the debris. In ASCE 7, the impact velocity is estimated through numerical modelling of the design site or using an energy grade line method proposed in Kriebel et al. (2017). Debris damming is addressed through calculating the overall drag forces as:

$$F_d = \frac{1}{2}\rho_s I_{tsu} C_d C_{cx} B(hu^2) \tag{B - 2}$$

where C_D is the drag coefficient (dependent on the width to inundation depth ratio), ρ_s is the density of the fluid (considering density changes due to entrained sediment and small debris), I_{tsu} is the importance factor dependent on the type of building, h is the water depth, and u is the flow velocity. C_{cx} is the closure coefficient, calculated as:

$$C_{cx} = \frac{\sum(A_{col} + A_{wall}) + 1.5A_{beam}}{Bh_{sx}} \tag{B - 3}$$

where A_{col} and A_{wall} are the projected area of structural column and wall elements, A_{beam} is the combined projected area of the slab and beam exposed to the flow, B is the width of the building, and h_{sx} is the average story height. Debris damming is incorporated into this equation by restricting the minimum closure coefficient (ratio of debris damming area to the total projected vertical plane area) to 0.70 (Carden et al. 2015).

The field investigation of the 2018 Palu Tsunami will examine the hazards associated with tsunami events, focusing on debris loading, by qualitatively discussing various sites which displayed tsunami-induced structural failures. Through this investigation, potential research needs will be addressed to inform future works.

Field Investigation

Site Locations

The field investigation took place between October 27th and October 31st, 2018 and started work in Donggala (Donggala Regency, Central Sulawesi, Indonesia), located on the northwest side of the Palu

Bay inlet. Within the time of the study, the team covered the total circumference of Palu Bay, covering a distance of approximately 60 km, and finishing in the small town of Wani (Donggala Regency, Central Sulawesi, Indonesia). Fig. B - 2 shows each of the sites that will be discussed within this study and Table B - 1 provides some additional information for each of the sites, which will be expanded upon in the following sections.

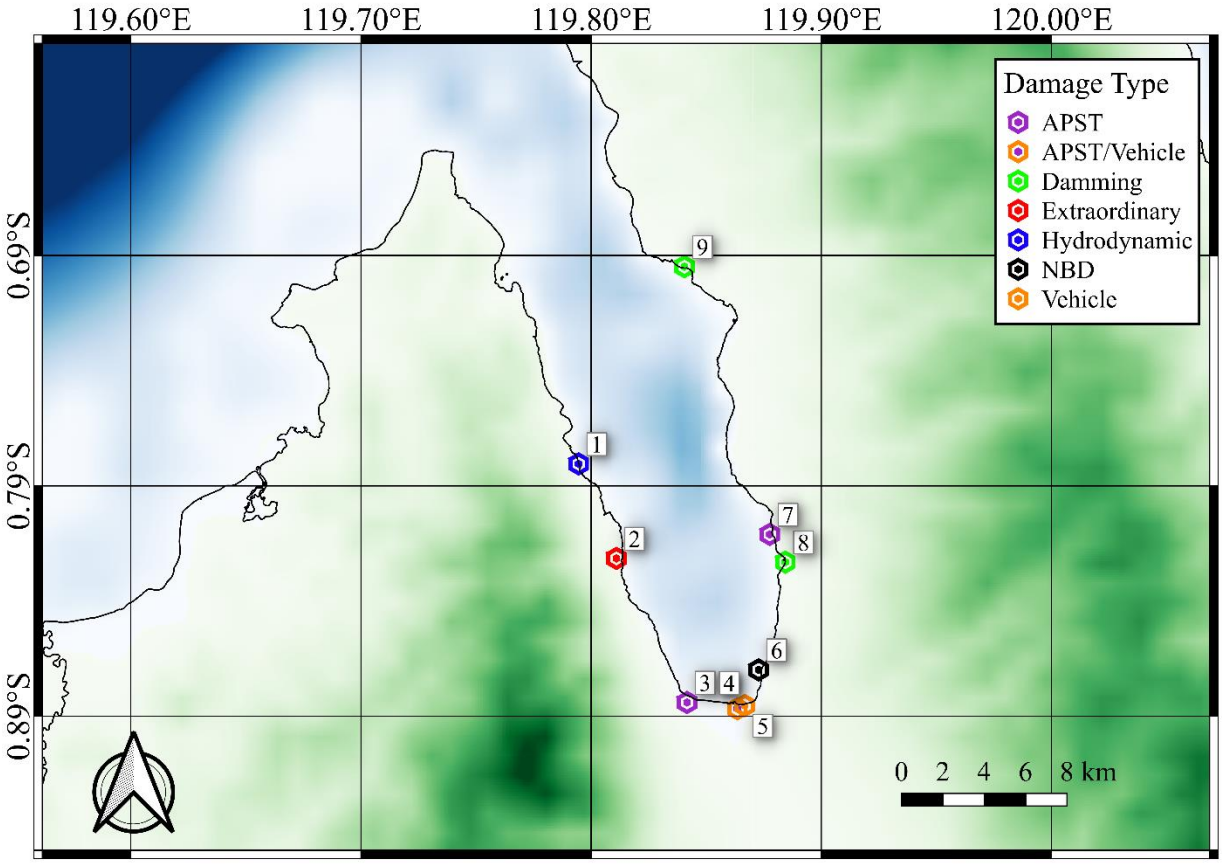

Fig. B - 2. Surveyed locations, labelled by observed damage type. A brief description and the geographical coordinates of the study sites can be found in Table B - 1. The coordinate system is the WGS84 and topographical data is taken from the British Oceanographic Data Center (2018).

Tsunami Characteristics

The 2018 Palu Tsunami was generated and amplified through several different mechanisms. However, the actual tsunami generation and propagation mechanisms are outside the scope of this study, and this section will focus on field evidence and eye-witness testimony regarding the tsunami wave characteristics. These data and information will inform ongoing and future activities pertaining to numerically modelling the hydrodynamic flows inside the Palu Bay, providing valuable information to verify the model results.

Table B - 1. Study locations from field investigation. Coordinates given in the WGS84 coordinate system and time at site given as local time reconnaissance team arrived on site.

Location Number	Location	Longitude	Latitude	Time at Site	Description
1	Loli Pesua	119.795	-0.780	28.10.2018 11:06	Small town with a local house damaged by uplift of structural slab.
2	Watusampu	119.811	-0.821	28.10.2018 12:39	Military naval base with vessels washed onshore by the tsunami.
3	Palu Gas Station	119.842	-0.884	30.10.2018 11:09	Local gas station with propane tanks washed off supports and impacting surround structures.
4	TVRI Palu	119.863	-0.886	29.10.2018 08:36	Local television station where emergency fuel tanks were washed from supports and impacted structures.
5	TotalX Palu	119.866	-0.885	29.10.2018 09:10	Large reinforced concrete building where debris impact loading can be clearly observed.
6	Palu Shopfront 1	119.872	-0.869	29.10.2018 12:17	Reinforced concrete structure close to coast with significant debris and scour damage.
7	Mamboro Warehouses	119.877	-0.811	29.10.2018 18:50	Large, light framed steel structure completely destroyed due to debris from stored goods.
8	Mamboro Fuel Station	119.884	-0.823	29.10.2018 18:28	Fuel station for shipping vessels, damage to anchoring of fuel tanks.
9	Wani	119.840	-0.694	29.10.2018 15:45	Small harbor where large vessels were washed on shore, damaging surrounding structures.

Field evidence around Palu Bay and on the coastline north of the Bay, close to the earthquake's epicenter, showed inundation depths ranging from 0.25 m to 4.82 m. The horizontal coordinate was measured from a handheld GPS instrument (Montana 650, Garmin, approximate accuracy: +/- 7.13 m (USDA 2017)). The inundation depths were measured using a laser ranging instrument (Impulse 200LR, Laser Technology Inc., +/- 0.01 m). Larger flow depths were observed at the end of the bay near Palu City, where the wave amplification was likely most substantial. Significant wave heights were also observed around the Mamboro area (Table B - 1), located directly across the bay from several of the submarine

landslides that occurred. Eye-witness testimonies indicated that the wave arrived between 4 – 6 minutes after the tremor of the earthquake had ceased. Video evidence from a CCTV camera in Wani indicates the wave arrived approximately 3.5 minutes after the end of the earthquake. Locals at Loli Dondo and TVRI Palu also indicated that there were three tsunami waves, with approximately 5 minute intervals between them. The rapid arrival time of the first wave indicates that the primary source of the tsunami was almost certainly within Palu Bay.

Performance of Structures

Generally, low-rise timber and light metal construction suffered the most severe structural damage. In such buildings, the facade was either built as a masonry infill wall, out of timber or with sheet metal. Sheet metal was commonly used as roofing material. Several timber-framed shops were built within a distance of less than 50 m from the coastline. Due to their low lateral force resisting capacity and the proximity to the coastline, these timber structures were dislodged and completely washed away by the tsunami. When the buoyant timber structures disintegrated, building components were entrained inside the onshore tsunami flow and dispersed as waterborne debris. The debris impacted other buildings or accumulated as debris dams, contributing to subsequent failures. Unfortunately, eye-witness reports did not cover the temporal sequence of progressive failure of these light-weight structures. Further research will have to look into temporal progression of failure of light-weight housing.

Near the coastline there were also some smaller reinforced concrete framed houses with unreinforced brick masonry infill walls (Fig. B - 3). The floors were either concrete slab-on-grade, brick infilled slabs, or elevated wood framed structures. As the focus of this study emphasized specific structural loading, the study examines structures that had survived or only partially failed as loading scenarios are more obvious. The structural elements of more substantial reinforced concrete structures generally survived the tsunami loads. Typical reinforcing steel in these areas consisted of 9 - 24 mm diameter smooth and deformed bars with yield strength from 480 to 600 MPa. The quality of concrete varied by location, with in-situ Schmidt impact hammer tests showing a compressive strength between 14 - 28 MPa (Robertson et al. 2019).

Fig. B - 3. Example of a small concrete building observed along the coastline of Palu Bay (photo taken at Loli Pesua). (a) Steel reinforcement of concrete structural columns. (b) Masonry infilled walls and floor slab. The approximate primary flow direction is indicated with a red arrow.

Debris Loading

An important issue to address in the design of tsunami-resilient buildings is debris loading, a type of loading that has not seen sufficient attention in the past. Debris loading refers to any solid object that is entrained within the flow interacting with infrastructure positioned within the trajectory the debris follows. ASCE 7 (2016a) distinguishes several types of debris loads, ranging from wood poles to vehicles, ships or shipping containers. For larger inundation depths and therefore increased buoyancy forces, larger debris must be considered to be entrained within the flow and, therefore, represent a hazard to surrounding structures as it can freely impact structures along its flow path. In the following, the most relevant observations on submerged and floating debris are reported to facilitate future modelling attempts, both numerically and experimentally.

Aboveground Petrochemical Storage Tanks

The transport by the tsunami flows of *Aboveground Petrochemical Storage Tanks* (APST) was observed in several locations around Palu City. At Palu Gas Station, located on the west side of Palu City at a distance of around 200 m from the coastline, five APSTs (5.40 m × 2.60 m diameter) were transported from their initial position to the southeast (Fig. B - 4 (a)). The terrain in this area is relatively flat. The elevation above sea level did not exceed 4 m based GPS measurements conducted in this area. While there was no sign of debris impact on the buildings, the fuel initially held within the APSTs was spread on the ground throughout the site. These hazardous chemicals pose a significant fire and environmental risk, as the contaminants were likely spread by the tsunami wave (Ghobarah et al. 2006, Naito et al. 2012).

Fig. B - 4. APST transport and impact on structures from (a) Palu Gas Station and (b) TVRI Palu. The approximate primary flow direction is indicated with a red arrow.

On the ocean side of Televisi Republik Indonesia (TVRI) building, two APSTs (3.60 m × 1.20 m diameter) were detached from their support structures and transported inland, impacting the structure (Fig. B - 4 (b)). The TVRI station is located on the east side of Palu and lies 100 m inland from the coastline. The APSTs were 3.6 m in length and had a diameter of 1.2 m. A TVRI technician witnessed the incoming tsunami and reported that the inundation depth was lower than 2 m, as it did not reach the second floor. A car, in addition to the APSTs, was noted by the technician to have been transported with the tsunami flow and collided with the TVRI building. The masonry walls and sheet metal roofing were destroyed as a result of the debris and tsunami impact.

Fig. B - 5 (a) shows two APSTs located near Mamboro (northeast of Palu City), used for the refueling of ships. While the APSTs remained in place, cracking could be observed completely around the concrete

anchoring ring. Similar damage was observed in the aftermath of the 2011 Tohoku Tsunami to similar facilities (Naito et al. 2012). Due to the relatively high volume to weight ratio of these structures, particularly if the APSTs were not full, the buoyant force can significantly exceed the corresponding gravity force resulting in flotation of the structure. Fig. B - 5(b) also shows the secondary damage that can occur to these facilities due to flooding, as several connection pipes and the pump house were severely damaged. In this case, the facility appeared to have adequate safety valves to prevent leakage. However, in similar cases, such as 2017 Hurricane Harvey (USA), significant leakage of hazardous chemicals took place (Bernier et al. 2018).

Fig. B - 5. Vertical uplift of fuel storage containers located at the Mamboro Fuel Station (northeast of Palu City). Damage to the foundations was observed due to the buoyant forces due to submergence during tsunami flow. The approximate primary flow direction is indicated with a red arrow.

Damage to APSTs in major flood events has been of increasing concern due to its environmental, economic, and social impacts (Burgett et al. 2017). Due to the relatively low volume to weight ratios of APSTs, the buoyant forces can be significant (as was observed in the damage to the ring structure at Mamboro, Fig. B - 5). These structures can also be damaged due to buckling from laterally induced drag loads (Bernier et al. 2018). Additionally, in cases of high Froude number flow conditions, choked flow conditions could prevail resulting in unbalanced hydrostatic forces acting on the APSTs (Fig. B - 6). Furthermore, in the case of Fig. B - 4, due to the elevated positioning of the APSTs, lift forces could also contribute to failure or improve stability depending on the water level. The combination of buckling, floatation, and overturning could result in the failure of the anchoring system, which in turn could result in the APSTs becoming debris (as in Fig. B - 4).

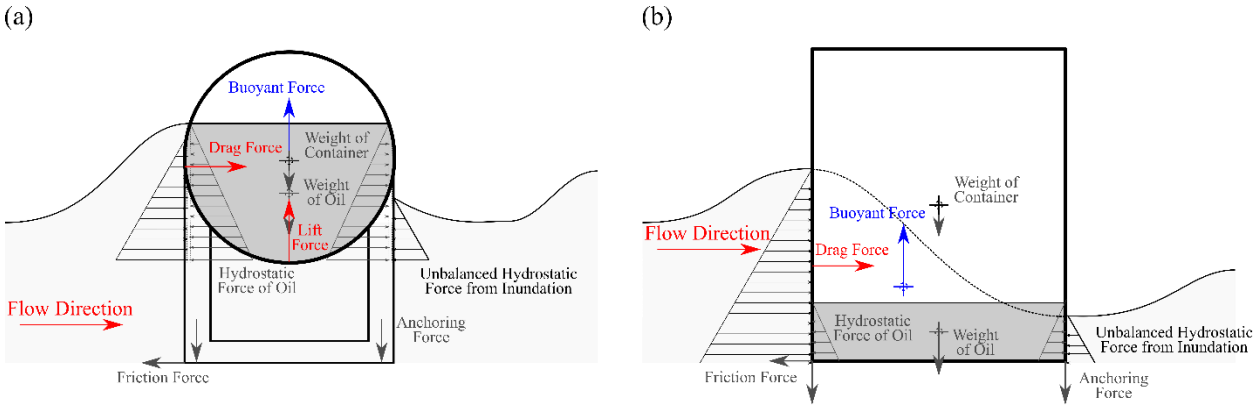

Fig. B - 6. Force balance acting on the APSTs under choked flow conditions for the APST geometry observed in (a) Fig. B - 4 and (b) Fig. B - 5.

While these failure mechanisms have begun to be addressed in the literature (Kameshwar and Padgett 2018), little research has addressed the fate of these objects once they start floating, and the resilience of surrounding infrastructure to their impacts. Coupling APSTs resilience modelling with entrainment characteristics of the different APST geometry may be necessary for the development of comprehensive risk assessments.

Vehicle Impacts

In built environments, such as cities or in residential areas, vehicles are ubiquitous. A vehicle impact was observed near the Mamboro fuel station, where the tsunami entrained a truck which impacted a structural column and the slab of the first floor of an adjacent building (Fig. B - 7 (a)). Minor damage was induced by the vehicle to the slab and its pillar, which were built using reinforced concrete with a facade of masonry. Several cracks could be found on the masonry wall, and a concrete block in front of the building was destroyed as a result of the vehicle impact.

Fig. B - 7. Vehicle impacts at (a) Mamboro Fuel Station, (b) TotalX, and (c) TVRI Palu. (d) Debris damage to internal structural columns observed at TotalX. The approximate primary flow direction is indicated with a red arrow.

A former hotel called TotalX was located on the east side of Palu City, at a distance of 90 m from the coastline. The structure's framing consisted of steel columns and masonry infill walls. The masonry walls facing the coastline were destroyed by the hydrodynamic and debris loads. Two deformed cars were found on the east side of the building (Fig. B - 7 (b)), while one car was found inside the building. The authors presume that the cars outside had already been cleared out of the building at the time of the survey, as several marks of debris impacts were found inside.

Vehicles represent a particular case of debris impact due to the specific way in which they are designed, where they are expected to plastically deform upon impact (to reduce the deceleration and forces acting on the passengers). General debris impact equations used within the ASCE 7 assume that the debris acts as a elastic-plastic model (Haehnel and Daly 2004, Nistor et al. 2017), where the impact force is limited by the plastic response of the debris. However, this is not captured in the case of vehicles. For vehicles, the ASCE 7 assigns a single conservative maximum force of 133 kN based on experimental and numerical analysis of frontal crash impacts of vehicles (Marzougui et al. 2013) (Fig. B - 7 (b-c)). Stolle et al. (2019a) examined the influence of the mass and stiffness ratios between the debris and the structure, which were important in determining the validity of the rigid body model. As vehicles are neutrally buoyant, resulting in a deeper and unequal (due to the engine in the front) draft, the added mass coefficient (caused by the deceleration of the surrounding fluid) could potentially increase the load compared to experiments that do not consider the surrounding fluid (Arrighi et al. 2016, Shafiei et al. 2016b). Further research is needed to address the behaviour of vehicles entrained within the flow.

Judging by the extent of the damage to the vehicles (Fig. B - 7), multiple impacts with the structural components likely took place. Additionally, as shown in Fig. B - 7 (d), debris passed through some of the larger structures, resulting in impacts with interior columns. ASCE 7 specifies that debris impact loading needs to only be considered for exterior structural elements. However, as exterior walls were often destroyed by the initial wave, debris can enter the interior of large building, potentially impacting interior structural elements. Goseberg et al. (2016b) examined the transport of debris through obstacles and observed that they tended to follow the deepest, fastest sections of the flow, which could potentially pass through structures. Therefore, it appears necessary for debris impacts to be included in the design of interior structural elements. However, the impact forces within the structure, due to shielding from exterior elements, would likely be smaller than exterior impacts (Derschum et al. 2018). When passing through buildings, debris' velocity is likely to decrease as a result of vehicle-building interaction. When exiting the building, the question remains how long the debris will require to accelerate to the ambient fluid velocity.

Extraordinary Debris Loading

Extraordinary debris impacts are defined in ASCE 7 (2016a) as impacts from large ships and barges. Ships were observed to be displaced onshore at several locations. Three marine vessels were found onshore at Watusampu Naval Base (Fig. B - 8). Based on the elevation of the vessel in Fig. B - 8(a), the inundation elevation at this point must have exceeded 6.1 m above sea level. In Fig. B - 8(a), the vessel was washed up onshore and appeared to have struck an exterior structural member, causing significant damage. In Fig. B - 8(b) one of the mooring lines remained intact, causing the vessel to repeatedly impact the pier and eventually be lodged under it (likely during the drawdown process). The pier had damage to several piles and the ship appeared to have exerted a vertical force on the deck of the pier, potentially after it had become lodged under the pier. Vertical forces on the piers could have occurred during the sequence of incoming and outgoing tsunami waves. If buoyant debris such as ships or barges become lodged under a pier during drawdown, then the subsequent incoming flow will attempt to raise the

buoyant object, resulting is significant uplift on the pier. Similar damage was observed in Pago-Pago Harbor during the 2009 Samoa Tsunami (Robertson et al. 2010).

Fig. B - 8. Ship impacts with structures at the Watusampu Naval Base. (a) Ship washed onshore, impacting a structure and destroying an exterior column. (b) Ship forced under the pier, causing damage to the pilings and its own hull.

The design of structures for extraordinary impact is generally deemed to be unfeasible, due to the large associated costs. However, ASCE 7 provides an alternative approach by designing for progressive collapse of structures where extraordinary debris hazards exist. In these cases, the residual load carrying capacity of the structure should be assessed in cases where critical structural members fail under debris loading (ASCE 2016a). Designing a structure for progressive collapse prevention can improve the resilience of the system while reducing the initial economic costs, potentially increasing the likelihood of more structures being built with tsunami-resistant designs (Esteban et al. 2015).

Within the ASCE 7, extraordinary debris impact hazard is assessed using an empirical estimation of the spreading of shipping vessels, based on field surveys from the 2011 Tohoku Tsunami (Naito et al. 2014). Research directed towards the transport of shipping vessels when propelled by tsunami currents has increased due to interest in tsunami-induced currents in harbours (Lynett et al. 2013). To date, models generally approximate ships as free-floating objects with no mass following the water currents. However, as is shown in Fig. B - 8(b), the mooring lines may also need to be considered, as they will restrict the initial movement of the ships. As the period of the wave is critical in the design of mooring lines (Weiler and Dekker 2003), models may also need to consider the dynamics of mooring lines when assessing the hazard of extraordinary impacts.

Negatively-Buoyant Debris

The previously discussed debris transport loading is associated with positively- or neutrally-buoyant debris. However, the highly turbulent bore propagation over land can induce uplift forces on negatively-buoyant objects and thereby induce different forces on structures depending on the type of debris. The Palu Shopfront was located approximately one kilometer northeast of Palu City at a distance of 30 m from the coastline and elevated 4 m above sea level. The columns of the shops were built of reinforced concrete with a covering of masonry, while the walls were completely built out of masonry. The asphalt road between the shops and the coastline was severely damaged, and parts of the asphalt were transported by the tsunami. Asphalt patches were found inside the shops, with a particularly high concentration around two exterior columns (Fig. B - 9(a-b)), which resulted in them being more severely damaged than other columns. Just above the base of these columns, the concrete cover around the reinforcing bars was

damaged. One of the columns showed a clear shear failure, possibly due to impact from a rolling section of asphalt pavement.

Fig. B - 9. Debris impact loading from negatively buoyant debris at the Palu Shopfront 1. The approximate primary flow direction is indicated with a red arrow.

Generally, research into debris impacts has primarily focused on positively-buoyant debris, such as wood poles and shipping containers. Some studies have examined the transport of negatively-buoyant debris, though the focus has been on boulder transport as a proxy for studying paleo-tsunami. The ASCE 7 (2016a) assigns a single maximum impact force of 36 kN at a height of 0.61 m above grade for negatively-buoyant debris. This estimation of the impact load is based on a study of the transport of boulders using a simplified static loading approach (Chau and Bao 2010). One of the key concerns of negatively-buoyant debris is the added mass, which is not addressed in the ASCE 7 concerning boulder transport, a result of the deceleration of the liquid around the debris upon impact, which can have a significant influence on the exerted impact loads (Shafiei et al. 2016b). Matsutomi (2009) noted that the estimation of the added mass can be challenging due to its dependency on the degree of submergence, impact orientation, and debris geometry. At the same time, debris impact of negatively buoyant debris will also be a function of the local flow velocity which will determine the impact velocity of the debris strike. As these factors have yet to be examined for negatively-buoyant debris, this should be a key consideration in future research.

Debris Damming

The accumulation of debris on the face of structures is referred to as debris damming (Robertson et al. 2007, Nistor et al. 2017). This obstruction can cause increased drag forces on structural elements (Stolle et al. 2018d), as well as complex secondary effects, such as backwater rise (Schmocker and Hager 2013, Stolle et al. 2017b), scour, and flow channeling (Melville and Dongol 1992).

The warehouse area at Mamboro was located at a distance of 100 m from the shoreline and was generally low-lying. The light steel frame construction forming the building envelope was largely destroyed. Goods inside the warehouses were found accumulated at several points, indicating the building of debris dams in front of structural elements (Fig. B - 10(a)). The tsunami wave propagated through the warehouse area increasing concentrations of debris resulted in large damming forces on interior structural elements (Fig. B - 10(b)), which is not addressed by ASCE 7. It is possible that progressive failure is also related to the formation of debris dams throughout the tsunami; the temporal aspect of this process is not well understood.

Fig. B - 10. (a) and (b) Debris damming on reinforced concrete structures at the Mamboro Warehouses. (c) and (e) Accumulation of shipping vessels in the narrow confines of Wani. (d) Damage of light-framed timber structures in Wani Harbour. The approximate primary flow direction is indicated with a red arrow.

Wani Harbour is a port located near the mouth of Palu Bay, at a distance of 25 km from Palu City. Several ships were washed onshore, indicating inundation heights of at least 2.5 m, which created large debris dams that obstructed the roadways (Fig. B - 10(c-e)). There was severe damage (Fig. B - 10(d)) to structures close to the harbour due to high water depths, with the degree of damage rapidly reducing further inland. Interviews with residents indicated that the debris accumulated across the narrow roadways leading inland perpendicular to the approaching tsunami wave front, reducing the inundation depths on the leeside of the debris dams significantly. Fig. B - 10 (c) shows large amounts of debris from the destroyed light-framed timber houses present around the dam sites indicating the debris potentially

contributed to the dam. This phenomenon possibly explains the high water levels and damage to the harbour area, as the obstructions would result in a rise of water level between the debris dam and the shoreline.

Local residents at both the Mamboro Warehouse and Wani Harbour areas commented on the amount of debris entrained, as well as the relatively slow progression of the wave front. Particularly in the case of Mamboro Warehouse, the high concentration of debris could have potentially increased the resistance to the flow, therefore reducing the wave front velocity. Flow resistance from obstruction, such as buildings, has been well documented through experimental and numerical modelling (Goseberg et al. 2009, Goseberg 2013a, Park et al. 2013). The ASCE 7 (2016a) accounts for high concentrations of suspended sediment and smaller debris in the drag force equation through a fluid density factor, which increases the density of water by a factor of 1.10. However, this is not captured in the flow resistance, which is based on physical modelling of a built environment (which uses clear water) (Bricker et al. 2015). Furthermore, the fluid density factor represents an engineering estimation, assuming an equivalent sediment concentration of 7% and a specific gravity of 2.5, and may not be capturing the sediment and debris concentrations in a real-world event.

Research Needs

Based on the damage sustained by structures during the 2018 Palu Tsunami as well as the current body of literature on the design of tsunami resilient infrastructure, the following topics are proposed as potential research that needs to be addressed to improve current design standards:

Debris Transport in a Built Environment

Current research into debris transport has primarily focused on debris propagating over an idealized flat surface. However, this type of analysis does not consider the influence of obstacles and complex topography which would likely skew the debris trajectory. Complex interactions between debris and structures may influence impact loads through shielding or channeling of flow. Derschum et al. (2018) showed that in the case of multiple impacts by a single debris, the first impact always exerted the maximum force. This reduction in the kinetic energy could provide protection to subsequent structures that are hit. Alternatively, Goseberg et al. (2016b) showed that debris tended to propagate in the deepest, fastest section of the channel, and therefore the presence of obstacles could channelize debris between the obstacles, limiting impact potential. However, the flow velocity in these channels will increase, potentially increasing the impact force when the debris impacts downstream structural elements.

Negatively- and Neutrally-Buoyant Debris

Research into debris hazard assessment has predominantly focused on positively-buoyant debris, where the debris has limited interaction with the bed surface (Shafiei et al. 2016b, Stolle et al. 2017a). Investigation into negatively-buoyant objects, such as boulders and concrete rubble, has also been performed, though not in the context of hazard assessment (Weiss and Diplas 2015). Due to the higher density and deeper draft of the objects, the assumption that the debris reaches the local flow velocity may be overly conservative (Stolle et al. 2017a). The different transport characteristics (i.e. saltation, rolling) would also likely influence the extent of the hazard. The influence of the local flow characteristics (rollers, vertical accelerated flow) is equally relevant when assessing the impact potential of negatively-buoyant debris.

Mass Transport of Debris

As was observed at the Mamboro Warehouses, large concentration of debris (and potentially sediment) can have an influence on the loading conditions. The ASCE 7 outlines how an increased density of the fluid will result in a larger drag load acting on the structure. Alternatively, the increased density of the fluid will also increase shear stress within the fluid (and therefore the flow resistance) resulting in reduced flow velocities and greater water depths (Chanson 2006). As flow resistance in numerical models is normally incorporated as a Manning's roughness value, this may not be capturing the flow behaviour adequately.

Debris Damming

In the current iteration of the ASCE 7, debris damming is addressed through the overall drag forces acting on the structure. However, this potentially ignores secondary effects, such as backwater rise (Fenton 2003) and flow accelerations (Pagliara and Carnacina 2013), which can influence the tsunami resistant capabilities of a structure through overtopping or erosion. Available research mostly uses one or few types of debris when investigating the formation and effects of debris dams, however, as is shown in Fig. B - 10(a) and (b), many debris dams in the context of tsunami damage are comprised of many different types of debris. The variation of individual debris results in stronger likelihood of entangling with each other, such that debris dams potentially form quicker in real tsunami as compared to experimental conditions. The effect of multiple debris types thus requires future attention.

Solid-Fluid Interactions

One of the major challenges in incorporating debris loading into tsunami hazard assessment is including debris dynamics within numerical modelling. Due to the complex nature and scale of debris interactions, physical modelling has potential scale effects which could potentially skew results. Field surveys, such as this one, can provide valuable insights and research direction, though they cannot quantitatively determine loading conditions due to a variety of unknowns. Improving two-way coupled debris transport models would be the most effective method of improving debris hazard assessment in major flooding events. This would allow debris to be incorporated within probabilistic models (Hatzikyriakou and Lin 2017) and fragility curve analysis (Charvet et al. 2015), significantly improving risk analysis in vulnerable communities.

Conclusions

The field survey performed after the 2018 Palu Tsunami provided valuable insight into tsunami loads and effects on structures. The study presented here examined tsunami loads, particularly related to solid objects (debris) entrained within the inundating flows. The paper presents specific examples from various sites around Palu Bay, comparing them to design considerations presented in ASCE 7 Chapter 6. Debris hazard assessment has become a burgeoning field within tsunami engineering, though significant gaps still exist. Field surveys, such as this one, present the opportunity to re-evaluate current progress and identify the research gaps. These studies can provide direction for the development of engineering tools for efficient and accurate assessment of hazards within major flooding events. Additionally, from a Canadian context, the continued development of tsunami engineering can provide a knowledge base on which to build engineering practices to improve community resilience.

Appendix C – Two-Degree of Freedom Model

The following section outlines the solution for the 2DOF model. The system is shown in Fig. 5-22. The equations of motion of the system were derived from d'Alembert's principle, the mass (a) and stiffness (b) ratios were used:

$$\begin{bmatrix} am & 0 \\ 0 & m \end{bmatrix} \begin{bmatrix} \ddot{x}_s \\ \ddot{x}_d \end{bmatrix} = \begin{bmatrix} bk + k & -k \\ -k & k \end{bmatrix} \begin{bmatrix} x_s \\ x_d \end{bmatrix} \quad \text{(C - 1)}$$

$$a = m_s/m_d \quad \text{(C - 2)}$$

$$b = k_s/k_d \quad \text{(C - 3)}$$

where k is the stiffness of the debris, m is the mass of the debris, x_s is the displacement of the structure, and x_d is the displacement of the debris. First, the natural modes of oscillation of the system were determined by assuming harmonic motion passing through the equilibrium position gives structural motion of the following form, for both objects, respectively:

$$x_s = A_s e^{i\omega t} \quad \text{(C - 4)}$$
$$x_d = A_d e^{i\omega t} \quad \text{(C - 5)}$$

where A_s is the amplitude of the structural oscillation, A_d is the amplitude of the debris oscillation, ω is the natural frequency. Inserting the two equations of harmonic motion for the displacement in A.1 yields:

$$\begin{bmatrix} bk + k - am\omega^2 & -k \\ -k & k - m\omega^2 \end{bmatrix} \begin{bmatrix} A_s \\ A_d \end{bmatrix} = 0 \quad \text{(C - 6)}$$

To determine a non-trivial solution, the det(C - 6) = 0 and replacing $\chi = \omega^2$ yields:

$$am^2\chi^2 - (a + b + 1)km\chi + bk^2 \quad \text{(C - 7)}$$

Finding the roots of C – 7 yields:

$$\chi_{1,2} = \frac{(a + b + 1) \mp \sqrt{(a + b + 1)^2 - 4ab}}{2a} \frac{k}{m} \quad \text{(C - 8)}$$

$$A = \frac{(a + b + 1) + \sqrt{(a + b + 1)^2 - 4ab}}{2a} \quad \text{(C - 9)}$$

$$B = \frac{(a + b + 1) - \sqrt{(a + b + 1)^2 - 4ab}}{2a} \quad \text{(C - 10)}$$

The natural frequencies of the system are then equal to $\omega = \sqrt{\chi}$:

$$\omega_1 = \sqrt{A \frac{k}{m}} \quad \text{(C - 11)}$$

$$\omega_2 = \sqrt{B \frac{k}{m}} \quad \text{(C - 12)}$$

Subbing C – 8 into C – 6 yields a ratio of the amplitudes for each natural frequency:

$$\boldsymbol{\varphi_1}(x) = \left(\frac{A_s}{A_d}\right)_{\omega_1} = \begin{bmatrix} 1 - A \\ 1 \end{bmatrix} \quad \text{(C - 13)}$$

$$\boldsymbol{\varphi_2}(x) = \left(\frac{A_s}{A_d}\right)_{\omega_2} = \begin{bmatrix} 1 - B \\ 1 \end{bmatrix} \quad \text{(C - 14)}$$

C – 13 and C – 14 give the ratio of amplitudes of each natural frequency, however, initial conditions are needed to determined the participation of each of the natural modes. The system in free vibration can be given by the equation:

$$\boldsymbol{x} = \begin{bmatrix} x_s \\ x_d \end{bmatrix} = \boldsymbol{\varphi_1} C sin(\omega_1 t + \psi_1) + \boldsymbol{\varphi_2} D sin(\omega_2 + \psi_2) \quad \text{(C - 15)}$$

The initial conditions are given as $x_s(0) = 0$, $x_d(0) = 0$, $\dot{x}_s(0) = 0$, and $\dot{x}_d(0) = u$. Substituting in the initial conditions and natural modes into C – 15 yields the following solution:

$$C = \frac{1 - B}{A - 1} \frac{u}{\left(\frac{1 - B}{A - 1} + 1\right)\omega_1} \quad \text{(C - 16)}$$

$$D = \frac{u}{\left(\frac{1 - B}{A - 1} + 1\right)\omega_2} \quad \text{(C - 17)}$$

Substituting C – 16 and C – 17 into C – 15, the displacements can be determined. The maximum force acting on the structure consists of the maximum difference between the displacement of the structure and the debris multiplied by the effective stiffness (*K*):

$$F_i = \max(K((b + 1)x_s - x_d)) \quad \text{(C - 18)}$$